Atlas

Coordinating Lead Authors:
José Manuel Gutiérrez (Spain), Richard Graham Jones (UK), Gemma Teresa Narisma (Philippines)

Lead Authors:
Muhammad Amjad (Pakistan), Irina V. Gorodetskaya (Portugal, Belgium/Russia), Michael Grose (Australia), Nana Ama Browne Klutse (Ghana), Svitlana Krakovska (Ukraine), Jian Li (China), Daniel Martínez-Castro (Cuba), Sebastian H. Mernild (Denmark/Norway, Denmark), Lincoln Muniz Alves (Brazil), Bart van den Hurk (Netherlands), Jin-Ho Yoon (South Korea)

Contributing Authors:
Gudfinna Adalgeirsdottir (Iceland), Cécile Agosta (France), Mansour Almazroui (Saudi Arabia), Joaquín Bedia (Spain), María Laura Bettolli (Argentina), Ana Casanueva (Spain), Tereza Cavazos (Mexico), Abel Centella-Artola (Cuba), Ruth Cerezo-Mota (Mexico), Haoming Chen (China), Antonio S. Cofiño (Spain), Erika Coppola (Italy), Joseph Daron (UK), Chirag Dhara (India), Arona Diedhiou (Ivory Coast, France), Alessandro Dosio (Italy), Jason Evans (Australia), Sebastian Gerland (Norway, Germany), Natalia Gnatiuk (Russia, Ukraine), Patrick Grenier (Canada), David S. Gutzler (USA), Rafiq Hamdi (Belgium), Cédric Hananel (Belgium, France), Kevin Hennessy (Australia), Sixto Herrera (Spain), Nazrul Islam (Bangladesh, Saudi Arabia), Maialen Iturbide (Spain), Ma. Laurice Preciado Jamero (Philippines), Sanjay Jayanarayanan (India), Eleni Katragkou (Greece), Elena Kharyutkina (Russia), Akio Kitoh (Japan), Erik Kjellström (Sweden), Kenneth Kunkel (USA), Christopher Lennard (South Africa), Marta Pereira Llopart (Brazil), Ian Macadam (Australia), Douglas Maraun (Austria, Germany), Andrew McLean White Orr (UK), Linda Mearns (USA), Wilfran Moufouma-Okia (France), Liew Ju Neng (Malaysia), Thanh Ngo-Duc (Vietnam), Francis Nkrumah (Ghana), Gregory Nikulin (Sweden, Russia/Sweden), Dirk Notz (Germany), Sarah Osima (Tanzania), Tugba Ozturk (Turkey), Mehwish Ramzan (Pakistan), Rosh Ranasinghe (Netherlands, Sri Lanka), Johan Reyns (Netherlands, Belgium), Annette Rinke (Germany), Daniel San Martín (Spain), Chris Shaw (UK), Stefan Sobolowski (Norway, USA), Samuel Somot (France), Anna Amelia Sorensson (Argentina), Mouhamadou Bamba Sylla (Senegal, Rwanda), Fredolin Tangang (Malaysia), Claas Teichmann (Germany), Geert-Jan van Oldenborgh (Netherlands), Jan Melchior van Wessem (Netherlands), Émilie Vanvyve (UK, Belgium), Alejandro Vichot-Llano (Cuba), Yu Xiaoyong (China, Germany)

Review Editors:
Inés Camilloni (Argentina), Jens Hesselbjerg Christensen (Denmark), Fatima Driouech (Morocco)

Chapter Scientists:
Maialen Iturbide (Spain), Ma. Laurice Preciado Jamero (Philippines), Émilie Vanvyve (UK, Belgium)

Date of Draft:
02/03/2020

Note:
TSU compiled version

Table of Content

Executive summary

It is *very likely* that most land areas have warmed by at least 0.1°C per decade over the past 50-100 years with many areas warming faster in recent decades. The latter include most areas of Central and South America, West Antarctica and Western Europe (0.2-0.3°C per decade), the Arabian peninsula, Central Asia and Eastern Europe (0.3-0.5°C per decade) and Arctic land regions warming up to 1°C per decade (or more in a few areas). Consistent with this annual mean warming has been an increase in hot extremes which have shown to be *virtually certain* attributed to anthropogenic climate change in regions such as Europe where a range of extreme event attribution methods have been applied (*high confidence*).

There are no locally significant trends in annual precipitation over most land areas. Regions where significant positive trends have been observed include most of North Asia and parts of Central and Southeast Asia (*medium or high confidence*). Significant negative trends have been observed in the Horn of Africa and south-west Australia (*high confidence*) and southern Africa with the latter attributed to anthropogenic warming of the Indian Ocean. Increases in precipitation intensity have been observed in the Sahel and over Southeast Asia (*medium confidence*).

Warming trends observed in recent decades are projected to continue over the 21st century (*high confidence*) and over most land regions at a rate higher than the global average. Under an RCP8.5 high emissions future it is *likely* that most land areas will experience a further warming of at least 4°C and in some areas significantly more; West, Central and Northern Asia and the Arabian Peninsula (8-10°C) and the Arctic up to 12°C.

There is *high confidence* that the precipitation climatology will change in most regions, either through changes in mean values or the characteristics of rainy seasons or daily precipitation statistics. Regions where mean rainfall is *likely* to increase include East and North Asia, southeast and southern South America, Ethiopian Highlands, northern Europe and North America and the polar regions. Regions were mean rainfall is *likely* to decrease include Indonesia, northern Arabian Peninsula, Central America, southwest South America, northern and southwest southern Africa and the Sahel and southern Europe. Changes in monsoons are *likely* to result in increased precipitation in northern China, increases during the summer monsoon but decreases during the winter monsoon in South Asia (*medium to high confidence*). There is also *high confidence* that precipitation intensity and extremes will increase in many areas including in some where annual mean reductions are *likely* (e.g. Southern Africa).

The subset of CMIP6 results available in the Interactive Atlas at the time of the release of the SOD project more pronounced warming in many regions compared to CMIP5 with these differences clearest in high latitude regions. There is broadscale consistency in the patterns of mean temperature and precipitation change in the CMIP5 and CMIP6 ensembles models over all regions.

Many aspects of the cryosphere either have seen significant changes in the recent past or will see them during the 21st century (*high confidence*). West Antarctica *likely* experienced an increase in surface mass balance mostly seen over the Antarctic Peninsula and the east part of West Antarctica. Also, it is *virtually certain* that snow cover will experience a decline over most regions of North America during the 21st century, in terms of water equivalent, extent and annual duration. Over the Hindukush-Himalaya glacier mass is *likely* to decrease considerably (nearly 50%) under RCP4.5 and RCP8.5 scenarios. However, the surface mass balance in East Antarctica showed strong interannual variability over recent decades, masking any possible existing trends (*medium confidence* due to limited observations). It is also *very likely* that some high-latitude regions will rather experience an increase in winter snow water equivalent, due to the snowfall increase impact prevailing over the warming impact.

It is *virtually certain* that complex climate change information is understood differently by different groups of people. Best-practice guidance is emerging to achieve greater consistency in the understanding and use of climate information.

Use of a narrative structure that converges with the values and experiences of audiences rather than

presenting lists of facts likely improves understanding in the face of this complexity.

Atlas.1 Introduction

Atlas.1.1 Purpose

The Atlas serves several purposes. It expands on and integrates results from other WGI chapters and recent literature to provide summaries of observed and relevant regional/local climate phenomena, historical simulations and projected future climate change across different scales. It includes the description of an online interactive tool (the Interactive Atlas), which allows for a flexible spatial and temporal analysis of these results. One specific focus for the summaries is providing information on climatic impact drivers and hazards relevant to sectoral and regional chapters of the WGII report, being informed by and complementing the work of Chapter 12 in creating a bridge to Working Group II (WGII). Similarly, a specific aim of the integration is synthesising information drawn from across multiple chapters that is relevant to the WGII report and the mitigation and sectoral chapters of the Working Group III (WGIII) report. Finally, the Atlas also assesses approaches to communication of climate information, illustrated with case studies and guidance on how to interpret them.

An overview of the main components of the Atlas Chapter is provided in Figure Atlas.1:.

[START Figure Atlas.1: HERE]

Figure Atlas.1: The main components of the Atlas Chapter with, bottom right, a screenshot from the online Interactive Atlas.

[END Figure Atlas.1: HERE]

Atlas.1.2 Context and framing

Information on global and regional climate change in the form of maps, tables, graphs and infographics has always been a key output of IPCC reports. With the consensus that climate has changed and will continue to do so, policymakers are focusing more on understanding the implications which often requires an increase in regional and temporal details of observed and future climate. In response, the AR5 included in the WGI contribution a globally comprehensive coverage of land regions and some oceanic regions in the Atlas of Global and Regional Climate Projections (Annex I), focusing on projected changes in temperature and precipitation. In the WGII contribution, the Regional Context Chapter (21) included continental scale maps of observed and future temperature and precipitation changes, subcontinental changes in high percentiles of daily temperature and precipitation, and a table of changes in extremes over subcontinental regions (updating an assessment in the SREX report). However, there was only limited coordination between these two contributions despite the largely common data sources and their relevance across the two working groups and to wider communities of climate change-related policy and practice. This resulted in inefficiencies and the potential for confusing or inconsistent messages which the Atlas, with its links with other WGI/II/III chapters, is designed to address.

Given the aims of the Atlas, there are several important factors to consider. There is a clear requirement for climate change information over a wide range of ‘regions’, and classes thereof, and temporal scales. There is also often the need for integrated information relevant for policy, practice and awareness raising. However, most other chapters in WGI are disciplinary, focusing on specific processes in the climate system or on its past or future behaviour, and have limited space to be spatially and temporally comprehensive. The Atlas provides an opportunity to facilitate this integration and exploration of information.

Developing this information often requires a broad range of data sources (various observations, global and

regionally downscaled baselines and projections) to be analysed and combined and, where appropriate, reconciled. This is a topic which is assessed from a methodological perspective in Chapter 10 using a limited set of examples. The Atlas then builds on this work with a more comprehensive treatment of the available results, including (but not exclusively) CMIP5, CMIP6 and CORDEX, to provide wider coverage and to further demonstrate techniques and issues.

Generating information relevant to policy or practice requires understanding the context of the systems that they focus on. In addition to the hazards these systems face, their vulnerability and exposure, and the related socio-economic and other physical drivers, also need to be understood. To ensure this relevance, the Atlas is informed by the assessments in Chapter 12 and the regional and thematic chapters and cross-chapter papers of WG II. It will thus focus on generating messages and information on climatic impact drivers and hazards applicable to assessing risks on human and ecological systems whilst noting the potential relevance of these to related contexts such as the Sustainable Development Goals and the Sendai Framework for Disaster Risk Reduction.

Finally, developing and synthesising all of this information, whilst understanding the context in which it is or could be usefully applied, draws on and further develops methods for communicating climate information. It also provides a series of good practise examples on constructing clear and scientifically credible messages. This is used to provide an assessment of communication methods, with accompanying guidelines on generating relevant climate information and a final section describing the online Interactive Atlas and how to interpret the information it displays.

Atlas.2 Defining temporal, spatial and typological domains and scales

Over the past decades scientists have engaged in a wide array of investigations aimed at quantifying and understanding the state of the components of the land surface-ocean-atmosphere system, the complex nature of their interactions and impacts over different temporal and spatial scales. Through these studies a great deal has been learned about the importance of treating the appropriate temporal and spatial scale when estimating changes due to internal climate variability, trends, characterization of the spatiotemporal variability and quantifying the range of and establishing confidence in climate projections. It is therefore important to be able to explore a whole range of spatial and temporal scales and the Atlas complements the other chapters by facilitating this exploration of their assessments.

This section presents the basic definitions of the temporal and spatial scales and domains of analysis used by the Atlas accounting for potential synergies between WGI and WGII. Noting the approach taken in the recent IPCC Special Report on the impacts of global warming of 1.5°C above pre-industrial levels (SR1.5; IPCC, 2018a), the Atlas will also present key global and regional climate changes at different global warming levels.

In order to increase transparency and FAIR data practises, most of the results reported in this section can be reproduced using the scripts and data provided in the Atlas GitHub repository (Atlas GitHub, 2020).

Atlas.2.1 Baseline and future time-slice periods and temporal scales of analysis

Chapter 1 has extensively explored this topic in Section 1.5.3 and Cross-Chapter Box 1.2. A summary of the main points relevant to the Atlas are provided here.

There is no standard baseline in the literature although the WMO recommends a 30-year baseline approach and the current official climate normal period is 1981–2010. However, it retains the 1961–1990 period as the historical baseline period for the sake of supporting long-term climate change assessments (WMO, 2017). The application of the WMO standards also provides sample sizes relevant to calculating changes in statistics other than the mean. The AR6 WGI has established the 1995–2014 period as modern reference period – for similar reasons to the 1986–2005 period used in AR5 WGI (IPCC, 2013b) – since 2014 (2005)

is the final year of the historical simulations of the models (see more details in Cross-Chapter Box 1.2).

The choice of a baseline and averaging period can significantly influence the analysis results for changes in mean climate (Hawkins and Sutton, 2016) (Cross-Chapter Box 1.2) as well as its variability and extremes. Thus, assessing the sensitivity of results to the reference period is important and can be achieved using figures or tables comparing different climate baseline periods. The Interactive Atlas (see Section Atlas.7) allows users to test the implications of a wide range of different baseline periods, including:

- the AR6 standard 1995–2014 period (20 years),
- the AR5 standard 1986–2005 period (20 years),
- the current WMO climate normal 1981–2010 period (30 years),
- the WMO long-term climate normal 1961–1990 period (30 years).

These baseline periods are relevant to work on impacts and thus would help to promote cross-Working Group consistency. Moreover, using the WMO 1961–1990 period and the AR5 facilitates comparison between CMIP5 (and CORDEX) and CMIP6 simulations since there exist 'current climate' simulations for all these datasets and thus can act as a common baseline for comparing results from AR5 with AR6. However, applying the more modern WMO 1981–2010 period or (particularly) the AR6 standard period would introduce an inconsistency as anthropogenic emissions in the CMIP5 and CORDEX models do not follow the observed trajectory from 2006 onwards. To an extent this can be circumvented by making the pragmatic choice of using scenario data to fill the missing segments (from 2006 to 2010 and from 2006 to 2014, respectively) using the first years of RCP8.5-driven transient projections in which the emissions are close to those observed. This is the approach that is used in the Atlas and Chapter 12. On a more practical level, this also helped to demonstrate how climate scientists can analyse and interpret outputs of simulations following international standards and relevant to applications.

Regarding the future reference periods, for consistency with previous reports, the Interactive Atlas considers the future periods used in AR6: the near-term, mid-term and long-term periods, respectively referring to 2021–2040, 2041–2060 and 2081–2100. Moreover, from the SR1.5 report, global warming is defined as 'The estimated increase in global mean surface temperature (GMST) averaged over a 30-year period, or the 30-year period centred on a particular year or decade, expressed relative to pre-industrial levels unless otherwise specified. For 30-year periods that span past and future years, the current multi-decadal warming trend is assumed to continue.' Therefore, we also consider different global warming levels (GWLs) to support future climate assessment, in particular the +1.5°C, +2°C, +3°C and +4°C GWLs in the Interactive Atlas.

To calculate GWLs for the datasets used in the Atlas (CMIP6 and CMIP5; see Section Atlas.3), we adopted the procedure used in Chapter 11 and quantify the global near-surface air temperature change for the 20-year period centred on the year when each model reaches the defined GWL of +1.5°C, +2°C, +3°C or +4°C for future projections assuming RCP 8.5 emissions, relative to pre-industrial levels as simulated by the historical simulation. Here, the 1851–1900 period is used to define the pre-industrial period and compute the mean pre-industrial temperature as baseline. Then, 20-year running-mean timeseries are computed starting from the 1971–1990 baseline period, and for each GCM (the running mean is centred around each year of the inter-annual time series). As a result, the GWLs are determined by the year when the running mean crosses the GWL threshold. When the projections stabilize before reaching the required threshold and the warming period extends beyond the year 2100, it is discarded (this is indicated by the asterisks in Table Atlas.1:). For CORDEX simulations, the periods of the driving GCM are used, as in Nikulin et al. (2018).

[START Table Atlas.1: HERE]

Table Atlas.1: Time periods for which the +1.5, +2, +3 and +4°C GWLs (compared to pre-industrial times) were reached in the given list of CMIP5 global climate projections for two different scenarios (RCP4.5 and RCP8.5). Values correspond to the central year (n) of the 20-year window (the GWL period is calculated as [n − 9, n +10]). Asterisks indicate that the GWL was not reached before 2100. N/A

means 'not available'. This table (and similar results for CMIP6) can be reproduced from the ATLAS GitHub (warming-levels section) (Atlas GitHub, 2020).

	RCP4.5				RCP8.5			
CMIP5 model name	+1.5º	+2º	+3º	+4º	+1.5º	+2º	+3º	+4º
ACCESS1-0_r1i1p1	2031	2052	*	*	2027	2039	2060	2080
ACCESS1-3_r1i1p1	2036	2055	*	*	2030	2041	2060	2081
bcc-csm1-1_r1i1p1	2022	2045	*	*	2020	2037	2060	2084
bcc-csm1-1-m_r1i1p1	2013	2040	*	*	N/A	N/A	N/A	N/A
BNU-ESM_r1i1p1	2008	2025	2067	*	2009	2023	2046	2065
CanESM2_r1i1p1	2016	2031	2073	*	2013	2026	2049	2067
CCSM4_r1i1p1	2016	2040	*	*	2013	2030	2056	2077
CESM1-BGC_r1i1p1	2019	2043	*	*	2016	2033	2059	2080
CESM1-CAM5_r1i1p1	2029	2046	*	*	2027	2038	2057	2077
CMCC-CM_r1i1p1	2032	2049	*	*	2028	2040	2060	2078
CMCC-CMS_r1i1p1	2034	2052	*	*	2029	2040	2060	2077
CNRM-CM5_r1i1p1	2035	2056	*	*	2029	2043	2066	*
CSIRO-Mk3-6-0_r1i1p1	2034	2047	*	*	2032	2044	2064	2082
EC-EARTH_r12i1p1	2023	2044	*	*	2020	2036	2059	2081
FGOALS-g2_r1i1p1	2038	*	*	*	2030	2046	2074	*
FIO-ESM_r1i1p1	2033	*	*	*	2026	2042	2067	*
GFDL-CM3_r1i1p1	2024	2038	2083	*	2024	2036	2055	2071
GFDL-ESM2G_r1i1p1	2053	*	*	*	2037	2054	2080	*
GFDL-ESM2M_r1i1p1	2044	*	*	*	2034	2051	2080	*
GISS-E2-H-CC_r1i1p1	2018	2044	*	*	N/A	N/A	N/A	N/A
GISS-E2-H_r1i1p1	2022	2049	*	*	2020	2036	2066	*
GISS-E2-H_r1i1p2	2028	2055	*	*	2025	2041	2069	*
GISS-E2-H_r1i1p3	2022	2043	*	*	2019	2034	2059	*
GISS-E2-R-CC_r1i1p1	2037	*	*	*	N/A	N/A	N/A	N/A
GISS-E2-R_r1i1p1	2043	*	*	*	2033	2051	*	*
GISS-E2-R_r1i1p2	2050	*	*	*	2037	2053	*	*
GISS-E2-R_r1i1p3	2033	2056	*	*	2027	2043	2069	*
HadGEM2-AO_r1i1p1	2027	2045	*	*	2034	2045	2062	2079
HadGEM2-CC_r1i1p1	2037	2055	*	*	2028	2040	2057	2074
HadGEM2-ES_r2i1p1	2029	2043	*	*	2025	2037	2055	2071
inmcm4_r1i1p1	2061	*	*	*	2043	2058	2084	*
IPSL-CM5A-LR_r1i1p1	2014	2031	2074	*	2011	2027	2048	2066
IPSL-CM5A-MR_r1i1p1	2016	2035	2080	*	2016	2030	2050	2067
IPSL-CM5B-LR_r1i1p1	2026	2049	*	*	2022	2037	2062	*
MIROC5_r1i1p1	2040	2072	*	*	2033	2048	2071	*
MIROC-ESM-CHEM_r1i1p1	2021	2035	2070	*	2018	2030	2050	2066
MIROC-ESM_r1i1p1	2020	2034	2071	*	2020	2030	2052	2069
MPI-ESM-LR_r1i1p1	2020	2043	*	*	2018	2035	2060	2080
MPI-ESM-MR_r1i1p1	2025	2047	*	*	2021	2038	2061	2082
MRI-CGCM3_r1i1p1	2055	*	*	*	2040	2052	2075	*
NorESM1-ME_r1i1p1	2039	2065	*	*	2032	2046	2069	*
NorESM1-M_r1i1p1	2041	2076	*	*	2033	2048	2073	*

[END Table Atlas.1: HERE]

Climate information at many temporal scales and over a wide range of temporal averaging periods is required for the assessment of climate change and its implications. These range from annual to multi-decadal averages required to characterise low-frequency variability and trends in climate to hourly or instantaneous maximum or minimum values of impactful climate variables. In between, information on seasonal averages of rainfall for example is important to define averaging periods whose relevance are geographically-dependent. As a result, the Atlas presents results over a wide range of timescales and averaging periods with the Interactive Atlas allowing a choice of user-defined seasons and a range of predefined daily to multi-day climate indices.

Atlas.2.2 Spatial domains and scales of analysis

Many factors influence the spatial domains and scales over which climate information can be reliably generated and is required. Despite all efforts in researching, analysing and understanding climate change, a key factor in the spatial scales at which analysis can be undertaken is directly related to the availability and reliability of data, both observational and from model simulations. In addition, information is required over a wide range of spatial domains defined either from a climatological or geographical perspective (e.g., a region affected by monsoon rainfall or a river basin) or from a socio-economic or political perspective (e.g., least-developed countries or nation states). Chapter 1 provides an overview of these topics (see Section 1.5.2). This subsection discusses some relevant issues, summarizes recent advances in defining domains and spatial scales used by AR6 analyses and how these can be explored with the Interactive Atlas.

Recent IPCC reports – AR5 Chapter 14 (IPCC, 2013b) and SR1.5 Chapter 3 (IPCC, 2018a) – have summarized information on projected future climate changes over subcontinental regions defined in the IPCC SREX report and later extended in the AR5 from the 26 regions in SREX to include the polar, Caribbean, two Indian Ocean, and three Pacific Ocean regions (hereafter known as the AR5 WGI reference regions) (Figure Atlas.2:a). In recent literature, new subregions have been used, for example for North and South America, Africa and Central America, together with the new definition of reference oceanic regions (Iturbide et al., submitted). As a result, an updated version of the reference regions has been considered for AR6 (hereafter known as AR6 WGI reference regions) and is shown in Figure Atlas.2:b. The goal of these subsequent revisions was to improve the climatic consistency of the regions so they represented sub-continental areas of greater climatic coherency.

[START Figure Atlas.2: HERE]

Figure Atlas.2: Reference AR5 (a) and AR6 (b) WGI regions (Iturbide et al., submitted). The latter includes both land and ocean regions and it is used as the standard for the regional analysis of atmospheric variables in the Atlas Chapter and Interactive Atlas. The definition of the regions and companion notebooks and scripts are available at the ATLAS GitHub (reference-regions section) (Atlas GitHub, 2020).

[END Figure Atlas.2: HERE]

The rationale followed in Iturbide et al. (submitted) for the definition of the reference regions was guided by two basic principles: 1) climatic consistency and better representation of regional climate features and 2) representativeness of model results (i.e., sufficient number of model grid boxes). The finer resolution of CMIP6 models (as compared to CMIP5) yields better model representation of the reference regions allowing them to be revised for better climatic consistency (e.g., dividing heterogeneous regions) while preserving the model representation. Figure Atlas.3: illustrates this issue displaying the number of (land) grid boxes in each of the AR6 and AR5 reference regions for two reference grid horizontal resolutions of 1° and 2°, representative of the typical resolution of CMIP6 and CMIP5 models, respectively. This figure shows that the new reference regions are better suited for the assessment of model results due to the improvement in model resolution, with a minimum model coverage for the New Zealand (NZ), the Caribbean (CAR) and Southern South America (SSA) regions with only 20-40 land grid boxes.

[START Figure Atlas.3: HERE]

Figure Atlas.3: Number of land grid boxes (blue number) for the (a) AR6 and (b) AR5 reference regions for the representative grid-boxes of the CMIP6 (1° horizontal resolution) and CMIP5 (2° horizontal resolution) model outputs. Colour shading indicate regions with fewer than 250 grid-boxes (darkest shading if fewer than 20 grid-boxes). The polygons in the figures show the climate reference regions shown in Figure Atlas.2:; adapted from Iturbide et al. (submitted). This figure can be reproduced from the ATLAS GitHub (reference regions and grids sections) (Atlas GitHub, 2020).

[END Figure Atlas.3: HERE]

AR6 WGI (land and open ocean) reference regions are used in the Interactive Atlas as the default regionalization for atmospheric variables. However, these regions are not optimum for the analysis of oceanic variables since, for instance, the five upwelling regions (Canary, California, Peru, Benguela and Somali) are mostly included in 'land' boxes. Therefore, the alternative set of oceanic regions defined by their biological activity (Figure Atlas.4:) is used in the Interactive Atlas for the regional analysis of oceanic variables.

[START Figure Atlas.4: HERE]

Figure Atlas.4: Ten oceanic regions defined by their biological activity used for the regional analysis of oceanic variables in the Interactive Atlas.

[END Figure Atlas.4: HERE]

However, due to the many potential definitions of the regions relevant for WGI and WGII, it is important to keep some flexibility in the definition of regions in the Interactive Atlas, so new regions (e.g., typological domains) could be added. However, the Atlas should be a useful instrument for AR6, and not necessarily cover all particular regions relevant to specific chapters.

Atlas.2.3 Typological domains

In addition to contiguous spatial domains discussed in the previous subsection, some domains are defined by specific climatological, geographical, ecological or socio-economic regions where climate is an important determinant or influencer. The domain will be subject to particular physical processes that are important for its climatology or that involve systems affected by the climate in a way that observations and climate model simulations can be used to understand. Many of these are the basis of the cross-chapter working papers of the AR6 WGII report, namely biodiversity hotspots, tropical forests, cities, coastal settlements, deserts and semi-arid areas, the Mediterranean, mountains and polar regions. It is therefore important to generate climate information relevant to these typological domains and some examples of this are provided in Section Atlas.5.10 and expanded upon in the Interactive Atlas. Figure Atlas.5: shows an example of typological domains (monsoon regions) that can be used in the Interactive Atlas.

[START Figure Atlas.5: HERE]

Figure Atlas.5: Land monsoon regions of North America (NAM), South America (SAM), Africa (WAM), Asia (SASM and EAM) and Australasia (AUSMC). These regions can be used alternatively to the reference regions for the regional analysis of atmospheric variables in the Interactive Atlas.

[END Figure Atlas.5: HERE]

Atlas.2.4 Higher resolution reference regions

Besides the definition of generic reference/typological regions, further regionalisations have been used by the regional modelling communities. They can provide further insight compared to using the subcontinental reference regions, for example being relevant for model evaluation purposes and to developing climate information relevant to the AR6 WGII and III reports.

As an illustrative example, CORDEX simulation results are validated for the Southeast Asia region (treated as a single AR6 WGI reference region) and for the subregions shown in Figure Atlas.6: (Cruz and Sasaki, 2017; Juneng et al., 2016; Ngo-Duc et al., 2017). These subregions are based on the historical behaviour of rainfall identified by previous studies of the Southeast Asia region. For example, there are two subregions over the Philippines, based on two dominant climate types strongly influenced by the synoptic-scale southwest and northeast monsoon systems (Manzanas et al., 2015). Over Vietnam, there is a north-south division of subregions as rainfall is highest in the north during summer but peaks in the south in winter. More information about the climatic subregions in Southeast Asia can be found in Juneng et al. (2016).

[START Figure Atlas.6: HERE]

Figure Atlas.6: CORDEX-SEA subregions based on historical rainfall climatology and variability (Juneng et al., 2016).

[END Figure Atlas.6: HERE]

Atlas.3 Combining multiple sources of information for regions

This section introduces the observational data sources and reanalyses that are used in the assessment of regional climate change and for evaluating and bias adjusting the results of models (more information on observational reference datasets in Annex I). Also, it introduces the different global and regional climate model output that are used for regional climate assessment considering both historical and future climate projections (see Annex III). Many of these models are run as part of coordinated Model Intercomparison Projects (MIPs), including the global Coupled Model Intercomparison Projects (CMIP5 and CMIP6) and the COordinated Regional Downscaling EXperiment (CORDEX), which are also described below. Combining information from these multiple data sources is a significant challenge (see Chapter 10 for an in-depth treatment of the problem) though if clear messages on regional climate change can be generated then they can be used to guide policy and support decisions responding to these changes. An important and necessary part of this process is to check for consistency amongst the data sources which is discussed in the final section.

Atlas.3.1 Observations

There are various sources of observational information available with disparity, inadequacy and contradictions in these as well as applications of observations being assessed in Chapter 10. Observational uncertainty is a key factor when assessing and attributing historical trends, so assessment should build on integrated analysis from different datasets. The Atlas can supplement and complement Chapter 10 by providing the opportunity to visualise and expand on its assessment. This includes displaying maps of density of stations observations (including those that are used in the different datasets) and assessing observational uncertainty by using multiple datasets and applying the concept of model (observational references in this case) agreement.

Two of the most commonly used variables in climate studies are gridded monthly surface air temperature and precipitation. There are many datasets available, commonly used ones including the Climatic Research Unit CRU TS4.0 (version 4.03 used here; Harris et al., 2014), the Berkeley surface temperature dataset

(BEST, Rohde et al., 2013, here referred to as BERKELEY), and EWEMBI (Lange, 2019) for temperature and CRU TS4.0, the Global Precipitation Climatology Centre (GPCC, v2018 used here; Schneider et al., 2011), and Global Precipitation Climatology Project (GPCP; monthly version 2.3 used here; Huffman et al., 2009). Although the ultimate source of these datasets is surface station reported values (GPCP and EWEMBI also include satellite and reanalysis information, respectively), each has access to different numbers of stations and lengths of records and employs different ways of creating the gridded product and ensuring quality control.

The most widely used SST datasets are HadSST3 (Kennedy et al., 2011b, 2011a), ERSST (Huang et al., 2017a), and KaplanSST (Kaplan et al., 1998). The largest difference among the three datasets lie in how inconsistency in number of observations during early and recent years is treated.

For example, Figure Atlas.7: shows the spatial coverage of the total number of observation stations for, respectively, 1901–1910, 1971–1980, and 2001–2010 and illustrates spatially the declining trend of observation station data used in the precipitation dataset for certain regions (South America, Africa) after the 1990s in the CRU TS4.0 dataset (left) and the SST data in the HadSST3 (right). This demonstrates the regional inhomogeneity and temporal change in station density. During early years a limited number of observations are available.

[START Figure Atlas.7: HERE]

Figure Atlas.7: Left: Number of stations per 0.5 x 0.5 grid cell reported over the period of 1901–1910, 1971–1980, and 2001–2010 (top 1-3) and global total number of stations reported over the entire globe for precipitation for CRU TS4.0 dataset (bottom). Right: same as left except the HadSST3 dataset.

[END Figure Atlas.7: HERE]

In addition to surface observation, satellites have been widely used to produce rainfall estimates. The advantage of satellite-based rainfall products is their globally uniform coverage including remote areas. However, there have been reported inconsistencies among different satellite-based rainfall products over complex terrain (Rahmawati and Lubczynski, 2018; Satgé et al., 2019). Another recent development has been on gridded dataset for climate extremes based on surface stations.

Atlas.3.1.1 Consistency and differences in observational data

There are some recent studies assessing observational datasets globally (Beck et al., 2017; Sun et al., 2018b) that report large differences among them. Regional studies have also been undertaken on comparing and assessing observational datasets with similar results (Manzanas et al., 2014; Salio et al., 2015; Prakash, 2019), thus stressing the importance of considering observational uncertainty in regional climate assessment studies. For example, Indasi (2019) assessed rainfall characteristics of ten gridded precipitation datasets over Southern Africa (Table Atlas.2:). They demonstrated that those sharing similar source data displayed similar rainfall characteristics while station-based datasets showed the least similarities. No single dataset was found to capture the rainfall characteristics across the entire Southern Africa region, and each performed better or worse depending on location. They also noted the decline in the number of stations available, mainly due to insufficient resources but also a tendency by country meteorological services to restrict free access, increasing relevance of satellite data and significant relationships between some of the datasets (Figure Atlas.8:). Another important aspect is that many stations do not report to the WMO networks, with their data being kept domestically or regionally, which has made regional datasets become more important in the recent years.

[START Table Atlas.2: HERE]

Table Atlas.2: Gridded precipitation datasets assessed in Indasi (2019) over South Africa, indicating the different data sources used in each case.

Dataset	GHCN stations	WMO GTS stations	FAO station data	Other station data	CFS	NCEP/ NCAR Reanalysis	ERA-Interim	TRMM	Thermal IR satellite
CRU	X	X		X					
GPCC	X	X	X	X					
UDEL	X			X					
ARC		X							X
CHIRP					X			X	X
CHIRPS		X		X	X			X	X
CMAP	X	X	X	X		X			X
GPCP	X	X	X	X					X
WFDEI_CRU	X	X		X			X		
WFDEI_GPCC	X	X	X	X			X		

[END Table Atlas.2: HERE]

[START Figure Atlas.8: HERE]

Figure Atlas.8: Relationship between gridded precipitation dataset and three classes of input data; station, satellite and reanalysis. Input datasets are shown in green, blue shows gridded datasets that are used as input to others shown in orange. (Indasi, 2019)

[END Figure Atlas.8: HERE]

Uncertainty in observations is a key limitation for the evaluation of climate models over most regions. This is highlighted in various other chapters and the Atlas expands on the treatment of this, complementing the discussions on discrepancies/conflicts in observations presented in Chapter 10 and expanding on and replicating their results for other regions. For example, Sylla et al. (2013) assessed uncertainties in climate observation products by intercomparing three gridded observed daily rainfall datasets over Africa – FEWS (Famine Early Warning System), GPCP and TRMM (Tropical Rainfall Measuring Mission). Different observation products were shown to exhibit differences in mean rainfall, higher order daily precipitation statistics, such as frequency of wet days, precipitation intensity and extremes as well as maximum length of wet and dry spells. FEWS showed mostly higher frequency and lower intensity events than TRMM and GPCP. Figure Atlas.9: shows a sample figure from Juneng et al., (2016) on the differences in precipitation values in the observation data in Southeast Asia. Figure Atlas.10: replicates this for Africa.

[START Figure Atlas.9: HERE]

Figure Atlas.9: Differences in precipitation values in the different observation datasets in Southeast Asia (from Juneng et al., 2016).

[END Figure Atlas.9: HERE]

[START Figure Atlas.10: HERE]

Figure Atlas.10: Similar to Figure Atlas.9: but for Africa.

[END Figure Atlas.10: HERE]

Atlas.3.2 Reanalysis

There are currently many atmospheric reanalysis datasets with different spatial resolution and assimilation algorithms (see Annex I, Observations). There are also substantial differences among those datasets and the Atlas will show and intercompare those that are used in the report. These differences are due to the types of observations assimilated into these reanalyses, the assimilation techniques that are used, and the resolution of the outputs amongst other reasons. For example, 20CR only assimilates surface pressure and sea surface temperature to achieve the longest record but at relatively low resolution, while ERA20C only surface pressure and surface marine winds. At the other extreme, very sophisticated assimilation systems using multiple surface, upper air and earth observation data sources are employed, e.g. for ERA5, ERA-Interim and JRA-55, which also have much higher resolutions. Most of reanalysis dataset covers the entire globe. However, there are also high-resolution regional reanalysis datasets (see, e.g. Section Atlas.5.6.2 for the case of Europe).

Atlas.3.3 Global model data (CMIP5 and CMIP6)

The Atlas (and the Interactive Atlas) uses global model simulations from both CMIP5 (full AR5 dataset curated by the IPCC Data Distribution Centre) and CMIP6 (the latter only partially since this dataset is not entirely available yet). This facilitates comparison of the assessments from two IPCC cycles and thus the detection of new features and findings coming from recent science and the latest CMIP6 ensemble. The selection of the models is based on availability of scenario data for the variables of interest (see Table Atlas.3:); in particular, in order to avoid unbalanced results and to harmonize the results obtained from the different scenarios as much as possible, we chose only models providing data for the historical scenario and at least two emission scenarios: RCP2.6 (SSP1-2.6), RCP4.5 (SSP2-4.5) and/or RCP8.5 (SSP5-8.5).

Building on this information, the Interactive Atlas displays a number of (mean and extreme) indices and climate impact drivers considering both atmospheric and oceanic variables (see Section Atlas.7). Some of these indices have been selected in coordination with Chapters 11 and 12, in order to support and extend the assessment performed in these Chapters (see Annex VII Hazards and Extreme Indices for details on the indices).

[START Table Atlas.3: HERE]

Table Atlas.3: CMIP5 (left) and CMIP6 (right) models used in the Atlas (and also in the Interactive Atlas) for the historical scenario and the RCP2.6 (SSP1-2.6), RCP4.5 (SSP2-4.5) and RCP8.5 (SSP5-8.5) emissions-driven future projections; the full inventory of models for different scenarios and variables is given in the Atlas GitHub repository (AtlasHub-inventory section) (Atlas GitHub, 2020). The variables analysed are both atmospheric – mean (tas, in ºC), maximum (tx, in ºC) and minimum (tn, in ºC) temperatures, precipitation (pr, in mm day^{-1}) – and oceanic – sea surface temperature (tos, ºC), pH (PH) and oxygen (O2, in mol m^3) – variables. Salient features of these models are described in IPCC AR5 Appendix 9.A (model names are taken from Table 9.A.1) and in Annex III. Columns lon and lat indicate the horizontal longitude and latitude effective resolutions of each model (in º).

#	CMIP5 Model	lon	lat	CMIP6 Model	lon	lat
1	ACCESS1-0	1.88	1.25	CNRM-CERFACS_CNRM-ESM2-1	1.41	1.39
2	ACCESS1-3	1.88	1.25	EC-Earth-Consortium_EC-Earth3-Veg	0.70	0.70
3	bcc-csm1-1	2.81	2.77	BCC_BCC-CSM2-MR	1.13	1.11
4	bcc-csm1-1-m	1.13	1.11	AWI_AWI-CM-1-1-MR	0.94	0.93

5	BNU-ESM	2.81	2.77	NASA-GISS_GISS-E2-1-G	2.50	2.00
6	CanESM2	2.81	2.77	BCC_BCC-ESM1	2.81	2.77
7	CCSM4	1.25	0.94	CCCma_CanESM5	2.81	2.77
8	CESM1-BGC	1.25	0.94	NCAR_CESM2-WACCM	1.25	0.94
9	CMCC-CESM	3.75	3.68	NCAR_CESM2	1.25	0.94
10	CMCC-CM	0.75	0.74	CNRM-CERFACS_CNRM-CM6-1	1.41	1.39
12	CNRM-CM5	1.41	1.39	NOAA-GFDL_GFDL-CM4	1.25	1.00
13	CSIRO-Mk3-6-0	1.88	1.85	NCC_NorESM2-LM	2.50	1.89
14	EC-EARTH	1.13	1.11	MOHC_HadGEM3-GC31-LL	1.88	1.25
15	FGOALS-g2	2.81	6.13	IPSL_IPSL-CM6A-LR	2.50	1.27
16	GFDL-CM3	2.50	2.00	MRI_MRI-ESM2-0	1.13	1.11
17	GFDL-ESM2G	2.50	1.52	NUIST_NESM3	1.88	1.85
18	GFDL-ESM2M	2.50	1.52	MOHC_UKESM1-0-LL	1.88	1.25
19	HadGEM2-CC	1.88	1.25	SNU_SAM0-UNICON	1.25	0.94
20	HadGEM2-ES	1.88	1.25			
21	inmcm4	2.00	1.50			
22	IPSL-CM5A-LR	3.75	1.89			
23	IPSL-CM5A-MR	2.50	1.27			
24	IPSL-CM5B-LR	3.75	1.89			
25	MIROC-ESM	2.81	2.77			
26	MIROC-ESM-CHEM	2.81	2.77			
27	MIROC5	1.41	1.39			
28	MPI-ESM-LR	1.88	1.85			
29	MPI-ESM-MR	1.88	1.85			
30	MRI-CGCM3	1.13	1.11			
31	NorESM1-M	2.50	1.89			

[END Table Atlas.3: HERE]

The Atlas also aims to cover as much information on regional climate changes as possible, so information from the existing CMIP5 as well as the CMIP6 datasets is supplemented with downscaled regional climate simulations from CORDEX. This facilitates an assessment of the effects from higher resolution including whether this modifies the projected climate change signals compared to global models and adds any value, especially in terms of high-resolution features and extremes.

Atlas.3.4 Regional model data (CORDEX)

Global model data, as generated by the CMIP ensembles, are available everywhere, but their spatial resolution is limited for reproducing certain processes and phenomena relevant for regional analysis (around 2º and 1º for CMIP5 and CMIP6, respectively). The Coordinated Regional Climate Downscaling Experiment – CORDEX (Gutowski et al., 2016) – coordinates regional downscaling experiments worldwide over a number of domains as represented in Figure Atlas.11: (more details are provided in Annex III; Table AIII.1) with a typical resolution of 0.44º (but also at 0.22º and 0.11º over particular regions, such as Europe). However, in some domains only a few simulations are available and in others it is not easy to access data (see the list of contributing models in Table AIII.2 and the data inventory in Table AIII.3). This limits the level of analysis and assessment that can be done using CORDEX data in some regions. Moreover, there are regions where several domains overlap, e.g. the Mediterranean or Central Asia, thus providing alternative lines of evidence which may lead to conflicting messages. There is still limited guidance on the synthesis and use of this information for scientifically rigorous analysis and generation of reliable climate information for

stakeholder use, but some studies have recently proposed the use of multi-domain grand ensembles to work globally with CORDEX data (Spinoni et al., 2019; Legasa et al., submitted). Ongoing efforts, such as the multi-domain CORDEX CORE simulations (Gutowski et al., 2016), are promoting more homogeneous coverage thus allowing more systematic treatment of CORDEX domains (see BOX ATLAS.1:).

[START Figure Atlas.11: HERE]

Figure Atlas.11: CORDEX domains and the topography corresponding to 0.44º resolution.

[END Figure Atlas.11: HERE]

A lot of progress has been made in the different CORDEX domains since AR5 to produce and make available downscaled climate information for evaluation (driven by ERA-Interim) and historical and future climate scenarios (under a range of future emissions, i.e. RCP2.6, RCP4.5 and RCP8.5). As a result, datasets obtained with ensembles of RCMs are now available on the Earth System Grid Federation (ESGF), for most of the domains (see Annex III; Tables AIII.2 and AIII.3) and for CORDEX CORE, and more information is expected to be available in the coming months.

Data available at ESGF (as of 30 September 2019) from both the individual CORDEX domains and from CORDEX CORE have been used to define the CORDEX regional datasets used in the Atlas (and included in the Interactive Atlas) starting with a number of domains where data was readily available: North and South America, Europe, Africa, South Asia and Antarctica (all domains with sufficient data available by the cut-off date will be included in the final version). In particular, in order to harmonize the information across domains and to maximize the size of the resulting ensembles, all the available simulations for each individual CORDEX domain (including the available 0.22º CORDEX CORE simulations) were interpolated to a common regular 0.5º resolution grid to provide a grand ensemble covering the historical and future emission RCP2.6, RCP4.5 and RCP8.5 scenarios, and also the reanalysis-driven simulations for evaluation purposes. As an example, Table Atlas.4: shows the simulations available for the South Asia domain, including the reanalysis-driven simulations (used for validation purposes) and the GCM-driven simulations under different scenarios, with a total of 12 different GCMs and 6 RCMs; the full inventory of models for different scenarios and variables for the different domains is given in the Atlas GitHub repository (AtlasHub-inventory section) (Atlas GitHub, 2020).

[START Table Atlas.4: HERE]

Table Atlas.4: GCM/RCM simulations (12/6 different models) available for the South Asia domain (from the WAS-44 and WAS-22 CORDEX domains) for the historical and RCP2.6, RCP4.5 and RCP8.5 scenarios (as from ESGF at September 2019). The six first rows show the reanalysis driven simulations, used for validation purposes. For details on the GCMs see Table Atlas.3: for details on the RCMs see Annex III models; Table AIII.2). The table is sorted by GCMs (greying repetitions to ease identification).

Domain	GCM_run	RCM_version
WAS44	ECMWF-ERAINT (evaluation)	RegCM4-4_v5
WAS44	ECMWF-ERAINT (evaluation)	HadRM3P_v1
WAS44	ECMWF-ERAINT (evaluation)	RCA4_v2
WAS22	ECMWF-ERAINT (evaluation)	COSMO-crCLIM-v1-1_v1
WAS22	ECMWF-ERAINT (evaluation)	REMO2015_v1
WAS22	ECMWF-ERAINT (evaluation)	RegCM4-7_v0
WAS44	CCCma-CanESM2_r1i1p1	RegCM4-4_v5
WAS44	CCCma-CanESM2_r1i1p1	RCA4_v2
WAS44	CNRM-CERFACS-CNRM-CM5_r1i1p1	RegCM4-4_v5
WAS44	CNRM-CERFACS-CNRM-CM5_r1i1p1	RCA4_v2
WAS44	CSIRO-QCCCE-CSIRO-Mk3-6-0_r1i1p1	RegCM4-4_v5

WAS44	CSIRO-QCCCE-CSIRO-Mk3-6-0_r1i1p1	RCA4_v2
WAS44	ICHEC-EC-EARTH_r12i1p1	RCA4_v2
WAS44	IPSL-IPSL-CM5A-LR_r1i1p1	RegCM4-4_v5
WAS44	IPSL-IPSL-CM5A-MR_r1i1p1	RCA4_v2
WAS44	MIROC-MIROC5_r1i1p1	RCA4_v2
WAS22	MIROC-MIROC5_r1i1p1	RegCM4-7_v0
WAS44	MOHC-HadGEM2-ES_r1i1p1	RCA4_v2
WAS22	MOHC-HadGEM2-ES_r1i1p1	REMO2015_v1
WAS44	MPI-M-MPI-ESM-LR_r1i1p1	REMO2009_v1
WAS44	MPI-M-MPI-ESM-LR_r1i1p1	RCA4_v2
WAS22	MPI-M-MPI-ESM-LR_r1i1p1	REMO2015_v1
WAS44	MPI-M-MPI-ESM-MR_r1i1p1	RegCM4-4_v5
WAS22	MPI-M-MPI-ESM-MR_r1i1p1	RegCM4-7_v0
WAS44	NCC-NorESM1-M_r1i1p1	RCA4_v2
WAS22	NCC-NorESM1-M_r1i1p1	REMO2015_v1
WAS22	NCC-NorESM1-M_r1i1p1	RegCM4-7_v0
WAS44	NOAA-GFDL-GFDL-ESM2M_r1i1p1	RegCM4-4_v5
WAS44	NOAA-GFDL-GFDL-ESM2M_r1i1p1	RCA4_v2

[END Table Atlas.4: HERE]

Section Atlas.5 assesses research on CORDEX simulations over different regions analysing past and present climate, as well as future climate projections. It also focuses on regional model validation in order to extend and complement the validation of global models done in Chapter 3, taking into account the specificity of regional climate models. Besides the literature assessment, comprehensive validation information for the available simulations across the different CORDEX domains is computed using the VALUE validation framework for downscaling methods assessed in Chapter 10 (Section 10.3.3) (Maraun et al., 2015). The goal is to provide some basic validation results for the CORDEX models, in particular on the biases for different validation indices, characterizing different aspects (temporal structure, extremes, etc.). The diagnostic indices and measures used are those proposed in the synthesis paper (Maraun et al., 2018), which are shown in Table Atlas.5:.

[START Table Atlas.5: HERE]

Table Atlas.5: Diagnostic indices considered for the evaluation of CORDEX data (see Maraun et al., 2018). Relative biases (%) are used as performance measure for all indices.

Code	Index/Diagnostic	Description
Mean	Mean	Mean precipitation
R01	Wet day frequency	Number of wet days (≥1mm)
SDII	Wet day intensity	Mean on wet days only
WWProb	Wet–wet transition probability	Probability of a wet day, given that the previous was wet
DWProb	Dry–wet transition probability	Probability of a wet day, given that the previous was dry
WetMaxSp	Longest wet spell	Median of the annual max. wet (≥1 mm) spell duration
DryMaxSp	Longest dry spell	Median of the annual max. dry (<1 mm) spell duration
AnnualCRA	Relative amplitude of the annual cycle	Difference between maximum and minimum value (30-day moving window over calendar days), relative to the mean of these two values.
P98Wet	98th percentile of rainfall for wet days	98th percentile of wet (≥ 1 mm) amounts
P98WetAm	Total precipitation over P98	Accumulated rainfall from days above P98Wet

[END Table Atlas.5: HERE]

Figure Atlas.12: shows the validation results for the European domain (only for precipitation) using EWEMBI (see Atlas.3.1) as the observational reference dataset. The validation indices are computed annually and seasonally (DJF and JJA), both for the RCMs and the driving GCMs, thus allowing to analyse the global and regional seasonal biases. Firstly, results are computed for the reanalysis-driven RCMs, in order to assess the intrinsic model errors (driven by "perfect" boundary conditions), and the results are displayed for each reference region indicating both the spatial mean and standard deviation. The latter is included to characterize the spatial homogeneity of the results and to inform of potential misleading spatial mean biases due to bias compensation. As shown in Figure Atlas.12: this is particularly relevant in the Mediterranean region. This same analysis is performed for the GCM-driven RCM simulations over the historical period (sorted by driving GCM). Overall, results are region dependent and RCMs tend to improve GCM biases particularly over NEU and CEU.

These results will be reproduced for all the domains with the final CORDEX data sets defined after the cut-off date.

[START Figure Atlas.12: HERE]

Figure Atlas.12: Evaluation (relative bias) of precipitation-based diagnostics shown separately for the three European subdomains NEU, CEU and MED for reanalysis- and historical GCM-driven RCM simulations showing annual and seasonal results (as shown in the legend). The colour matrices show the mean spatial biases of the different diagnostics (in rows) and columns are organized in blocks corresponding to each of the GCMs (blue labels, including ERA-Interim in first place slightly separated) together with their coupled RCMs (black labels). This allows to compare the bias of the RCM with that of the driving GCM. All diagnostic biases are relative with respect to the observational reference (EWEMBI).

[END Figure Atlas.12: HERE]

[START BOX ATLAS.1: HERE]

BOX ATLAS.1: CORDEX-CORE

The main objective of the CORDEX-CORE initiative is to provide a world-wide homogeneous foundation of high-resolution regional climate model projections to improve the understanding of local phenomena and to allow impact and adaptation research world-wide (Gutowski et al., 2016). The experimental framework was designed to produce homogeneous regional projections for most of the land regions and, therefore, it is requested that the contributing RCMs run projections over most CORDEX domains at 0.22° resolution driven by the same core set of GCMs for the two scenarios RCP2.6 and RCP8.5 (see Box Atlas.1, Figure 1:). Due to the computational requirements, three GCMs were selected to drive the simulations, covering the spread of high, medium, and low (HADGEM2ES, MPI-ESM, and NorESM, respectively) equilibrium climate sensitivity from the CMIP5 ensemble at a global scale (using MIROC5, EC-Earth, GFDL-ES2M as secondary GCMs). Two RCMs have contributed so far to this initiative (REMO and RegCM4) constituting an initial homogeneous downscaled ensemble to analyze mean climate change signals and hazards (Coppola et al., submittedb; Teichmann et al., submitted; see also Chapter 12), and there are ongoing efforts to extend the CORDEX-CORE ensemble with additional regional simulations (e.g. the COSMO-CLM community) to further increase the ensemble size and the representation of possible future climate change pathways.

CORDEX-CORE spans the spread of the CMIP5 ensemble climate change signals for temperature and precipitation for most of the covered reference regions (Teichmann et al., submitted; see Box Atlas.1, Figure 2). However, it is still a small ensemble and for other variables the coverage of the ensemble spread might be

different and would need to be assessed before further use of the CORDEX-CORE ensemble.

[START BOX ATLAS.1, FIGURE 1 HERE]

Box Atlas.1, Figure 1: Nine domains used for global coverage in CORDEX CORE; see Figure Atlas.11: for the full list of CORDEX domains (Teichmann et al., submitted).

[END BOX ATLAS.1, FIGURE 1 HERE]

[START BOX ATLAS.1, FIGURE 2 HERE]

Box Atlas.1, Figure 2: Temperatures (left) and precipitation (right) climate change signals at the end of the century (2070-2099) for the entire CMIP5 ensemble (box-whisker plots) and the CORDEX-CORE driving GCMs of the respective CORDEX-CORE results in the SAS (South Asia) reference regions. The driving GCMs with low, medium and high equilibrium climate sensitivity are plotted as gray triangles pointing upwards, circle and triangle pointing downwards, respectively and the corresponding RCM results are drawn using the same symbols as before, but in orange for REMO and in blue for RegCM (Teichmann et al., submitted).

[END BOX ATLAS.1, FIGURE 2 HERE]

[END BOX ATLAS.1: HERE]

Atlas.4 Global synthesis

Most other chapters in WGI focus on past or future behaviour of the global climate system or specific components within it. Noting the overall WGI contribution aims to have wide-ranging application that frequently requires integration of information sources, this section combines findings from these other chapters (2–9) with a focus on messages that are relevant to WGII and WGIII contexts. It also provides a global overview assessment of findings from the CMIP5 and CMIP6 ensembles focusing on climate indices underpinning the regional assessments in Section Atlas.5 and the results displayed in the Interactive Atlas. Thus, its aim is not to provide information relevant to deriving messages about regional climate changes but to provide the global context for such messages derived later in the Atlas. The first subsection (Atlas.4.1) considers global atmospheric and land-surface results, with findings on the global oceans in the second (Atlas.4.2) and the third (Atlas.4.3) focusing on extreme events.

Atlas.4.1 Global atmosphere and land surface

The principal atmospheric quantities of interest for understanding how climate change may impact human and ecological systems, as well as being key global indicators of change, are surface air temperature and precipitation. They are therefore a significant focus of the regional climate assessments in Section Atlas.5 and of the Interactive Atlas. Observed changes in these variables over land during the recent past (1980–2014) are shown in Figure Atlas.13: using results from three global datasets for each variable to illustrate where the clearest messages can be found (Figure Atlas.14:) and to illustrate observational uncertainty. For temperature, a clear signal of warming is seen over most land areas with an amplification at high latitudes, though all continents apart from Europe also have regions where trends are not significant. Significant changes in annual mean precipitation are seen over much more limited areas though with consistent drying trends over parts of South and North America and the Middle East and wetting trends over some northern high latitude regions. The information conveyed in Figure Atlas.14: on both consensus in the signal of change and on observational uncertainty is used in this chapter as a line of evidence to assess historical observed trends.

[START Figure Atlas.13: HERE]

Figure Atlas.13: Observed trends of annual mean surface air temperature (left-hand column) and precipitation (right-hand column) – see Section Atlas.3 for details of the datasets. Observed linear trends are calculated for the common 1980–2014 period from three different datasets and are expressed as ºC per decade and relative change (with respect to the climatological value) per decade, respectively. Hatching indicates regions where trends are not significant (at a 0.1 significance level) and the black lines mark out the reference regions defined in Section Atlas.2.

[END Figure Atlas.13: HERE]

[START Figure Atlas.14: HERE]

Figure Atlas.14: Consensus on the observed trends from the three observational datasets shown in Figure Atlas.13: (CRU TS, BERKELEY and EWEMBI for temperature; CRU TS, GPCC and GPCP for precipitation). Hatching indicates regions where no or only one dataset provides a significant trend. Linear trends are calculated for the common 1980–2014 period and expressed in °C per decade (temperature) and % relative change per decade (precipitation) with respect to the climatological mean over this period.

[END Figure Atlas.14: HERE]

Projected changes in annual mean surface air temperature from the CMIP5/6 ensembles (Figure Atlas.15:) show similar patterns to the observed warming and a high level of consistency between the two ensembles in terms of the patterns and magnitude of change. However, for the long-term future, warming in the CMIP6 ensemble is generally higher, reflecting the increase in the top end of the range of climate sensitivities amongst the CMIP6 GCMs.

[START Figure Atlas.15: HERE]

Figure Atlas.15: Future projected changes of annual mean surface air temperature in the CMIP5 (left-hand column) and CMIP6 (right-hand column) ensembles. Projected changes are calculated as the climatology differences for near-term (2021–2040), medium-term (2041–2060) and long-term (2081–2100) periods for the emissions scenario RCP8.5 (SSP5-8.5 for CMIP6) with respect to the historical (1986–2005) period; values are expressed as ºC. Hatching indicates lack of model agreement (less than 80% of agreement; as defined in Nikulin et al., 2018) and the black lines mark out the reference regions defined in Section Atlas.2. Similar analysis for other indices and scenarios (including warming levels) are available at the Interactive Atlas (http://ipcc-atlas.ifca.es).

[END Figure Atlas.15: HERE]

As described earlier, information on projected future changes is required both at different time periods in the future under a range of emissions scenarios but also for different global warming levels. Figure Atlas.16: shows the global surface air temperature change projection calculated from the ensemble mean of nine CMIP5 models for the middle of the century under the RCP4.5 and RCP8.5 emissions scenarios compared to the end of the century warming under RCP8.5 and for a global mean warming levels of 2°C.

[START Figure Atlas.16: HERE]

Figure Atlas.16: Global temperature changes projected for mid-century (left-hand column) under RCP4.5 (top) and RCP8.5 (bottom) compared to, in the right column, a global mean warming level of 2°C (top) and at the end of the century under RCP8.5 emissions (bottom) from an ensemble of nine CMIP5 GCMs. Note that the future period warmings are calculated against a baseline period of 1986–2005 whereas

the global mean warming level is defined with respect to a 'pre-industrial' baseline of 1861–1890. Thus, the other three RCP-based maps would show greater warmings with respect to this earlier baseline.

[END Figure Atlas.16: HERE]

Figure Atlas.16: presents a mean projection from averaging the changes from nine CMIP5 models but it is also important to explore the full range of outcomes from the ensemble, for example when undertaking a comprehensive risk assessment in which temperature is an important hazard. This is displayed in Figure Atlas.17: for the global average surface air temperature increases projected by the models throughout the century under the RCP8.5 emissions scenario. Of course, information of this nature is also important regionally and this can be explored within the Interactive Atlas over the AR6 WG I reference regions defined by the polygons on the maps in Figure Atlas.16: (and described in Section Atlas.2). These regional results demonstrate how temperature is projected to increase for all regions, and at a greater rate than the global average over many land regions and the North Pole.

[START Figure Atlas.17: HERE]

Figure Atlas.17: Global average surface air temperature increases projected by nine CMIP5 models under the RCP8.5 emissions scenario from 2005 to 2100 relative to a 1986–2005 baseline.

[END Figure Atlas.17: HERE]

Changes in annual mean precipitation present a more complex picture with regions of decrease as well as increase and areas where there is model disagreement on the sign of the change, even when the signal is strong in the long-term future period as shown in Figure Atlas.18:. However, as with the temperature changes, there is a high level of consistency in the patterns and magnitude of the precipitation changes, with changes in some areas being larger in the long-term future.

[START Figure Atlas.18: HERE]

Figure Atlas.18: Future projected changes of annual mean precipitation in the CMIP5 (left-hand column) and CMIP6 (right-hand column) ensembles. Projected changes are calculated as the climatology differences for near-term (2021-2040), medium-term (2041-20160| and long-term (2081-2100) periods for the emissions scenario RCP8.5 (SSP5-8.5 for CMIP6) with respect to the historical period (1986-2005); values are expressed relative differences (%). Hatching indicates lack of model agreement (less than 80% of agreement; as defined in Nikulin et al., 2018) and the black lines mark out the reference regions defined in Section Atlas.2. Similar analysis for other indices and scenarios (including warming levels) are available at the Interactive Atlas (http://ipcc-atlas.ifca.es).

[END Figure Atlas.18: HERE]

Considering changes over land, Figure Atlas.18: also shows that at lower warming levels there are many regions, especially in the southern hemisphere, where there is no robust signal of change from the models. In particular this is shown in Figure Atlas.19: comparing projected changes at 2°C global mean warming relative to pre-industrial levels with those in the long-term period under RCP8.5 emissions compared to the recent past (displaying the ensemble mean changes corresponding to the right-hand panels of Figure Atlas.16:).

[START Figure Atlas.19: HERE]

Figure Atlas.19: Global precipitation changes projected at 2°C global mean warming compared to pre-industrial levels (left) and for 2081–2100 under RCP8.5 emissions compared to the 1986–2005 period (right) from an ensemble of nine CMIP5 GCMs. Regions are stippled where less than six out of the nine models agree on the sign of the change (noting that this assessment does not take into account whether the individual models' projected changes are significant).

[END Figure Atlas.19: HERE]

In addition to displaying results from global model ensembles as maps of projected changes and their robustness or as timeseries of the projected temporal evolution of the median and range of a climate statistic, it is often useful to generate area-averaged summaries of these statistics under different future emissions scenarios or at specific global warming levels. This is demonstrated in Figure Atlas.20: showing a range of projected changes compared to the recent historical baseline period of 1995-2014. The first four panels show: (a) the additional warming to reach global warming levels (with respect to the pre-industrial baseline period of 1851-1900) of 1.5°C and 2°C; and (b) the warming at three future time periods this century; both sets summarise projections from the CMIP5 and CMIP6 ensembles with the latter showing results under the RCP2.6/SSP1-2.6 and RCP8.5/SSP5-8.5 forcing scenarios. The last two panels summarise the previous box-plots for the CMIP6 projections by plotting precipitation against temperature change at the different time periods, but also including an additional post-2050 period (2061-2080) and results from an additional forcing scenario, SSP2/RCP4.5.

[START Figure Atlas.20: HERE]

Figure Atlas.20: Changes in annual mean surface air temperature and precipitation averaged over global land (left) and the global oceans (right). The top two rows show the median (dots) and 10th–90th percentile range across each model ensemble for temperature and precipitation changes respectively, for two datasets (CMIP5 and CMIP6) and two scenarios (SSP1-2.6/RCP2.6 and SSP5-8.5/RCP8.5). The first four bars represent the additional warming projected relative to the historical baseline period of 1995-2014 to reach the two global warming levels (GWL; +1.5°C and +2°C) and the remaining six the projected changes over three time periods (near-term 2021–2040, mid-term 2041–2060 and long-term 2081–2100) compared to this same historical baseline period.
The bottom row shows scatter diagrams of temperature against precipitation changes, displaying the median (dots) and 10th–90th percentile ranges for four future periods (2021–2040, 2041–2060, 2061–2080, 2081–2100) compared to the historical baseline period, as obtained from CMIP6 projections for three scenarios (SSP1-2.6, SSP2-4.5 and SSP5-8.5). Changes are absolute for temperature and relative for precipitation.
(The script used to generate this figure is available online (Atlas GitHub, 2020) and similar results can be generated in the Interactive Atlas for flexibly defined seasonal periods.)

[END Figure Atlas.20: HERE]

Global warming leads to systematic changes in regional climate variability via various mechanisms such as thermodynamic responses via altered lapse rates (Kröner et al., 2017; Brogli et al., 2019) and land-atmosphere feedbacks (Boé and Terray, 2014). These can modify temporal and spatial variability of temperature and precipitation, including an altered seasonal and diurnal cycle and return frequency of extremes. Regional influences from and feedbacks with sea surface, clouds, radiation and other processes also modulate the regional response to enhanced warming, both locally and, via teleconnections, remotely. Given their potential to influence extremes in both temperature, precipitation and other climatic impact drivers and hazards, and thus risks to human and ecological systems, it is important to understand these links for developing adaptations in response to clear anthropogenic influences on individual hazards. This will also support the related fields of disaster risk reduction and global sustainable development efforts as noted by Steptoe et al. (2018). They demonstrated that 15 regional hazards shared connections via the El Niño–

Southern Oscillation, with the Indian Ocean Dipole, North Atlantic Oscillation and the Southern Annular Mode being secondary sources of significant regional interconnectivity (Figure Atlas.21:). Understanding these connections and quantifying the concurrence of resulting hazards can support adaptation planning as well as multi-hazard resilience and disaster risk reduction goals.

[START Figure Atlas.21: HERE]

Figure Atlas.21: Influence of major modes of variability on regional extreme events relevant to assessing multi-hazard resilience (Steptoe et al., 2018). Ribbon colours define the driver from which they originate and their width is proportional to the correlation. Hatching represent where there is conflicting evidence for a correlation or where the driver is not directly related to the hazard and dots represent drivers that have both a positive and negative correlation with the hazard.

[END Figure Atlas.21: HERE]

Atlas.4.2 Global oceans

As with the atmosphere, there are several key ocean-related quantities which are relevant for understanding how climate change may impact human and ecological systems and/or key global indicators of change. These include ocean surface temperature and heat content, sea ice cover and thickness, and certain chemical properties such as ocean acidity and oxygen concentration. For example, there is growing awareness of the threat presented by ocean acidification to ecosystem services and its socio-economic consequences are becoming increasingly apparent and quantifiable (Hurd et al., 2018) and the IPCC Special Report on Global Warming of 1.5ºC (IPCC, 2018c) noted a significant impact of low levels of global warming on the state of the global oceanic ecosystems and food security. For instance, 70-90% of coral reefs are projected to decline at a warming level of 1.5º, with larger losses (>90%) at 2ºC (SR1.5).

Thus, because of their importance to ocean ecosystems, the Interactive Atlas focuses on ocean temperature, pH and dissolved oxygen and projected changes in the subset of nine CMIP5 models used to establish a reference for the CMIP6 results. Figure Atlas.22: shows projected changes in these variables at the end of the century under RCP4.5 and RCP8.5 emissions, demonstrating the much larger changes seen with the higher emissions scenario.

[START Figure Atlas.22: HERE]

Figure Atlas.22: Projected changes in sea surface temperature (top), ocean pH (middle) and dissolved oxygen (bottom) for 2081–2100 under the RCP4.5 (left-hand column) and 8.5 (right-hand column) emissions compared to a 1986–2005 baseline period from an ensemble of nine CMIP5 GCMs. Regions are stippled where less than six out of the nine models do not agree on the sign of the change (noting that this assessment does not take into account whether the individual models' projected changes are significant)

[END Figure Atlas.22: HERE]

Atlas.4.3 Extremes

Many of the most severe impacts of climate are felt through extreme events and climate change has been demonstrated to increase either the frequency or intensity of many types of such hazardous events. Thus, the third important area of focus for this global synthesis section is on the implications of global warming for high-impact extreme climate events. This topic is a focus for Chapter 12 in its treatment of hazards relevant to risk assessment and Chapter 11 is devoted entirely to extreme events, so the results presented here are intended to complement these more in-depth treatments whilst providing context for the regional assessments presented in the following section (and expanded on in the Interactive Atlas) and synthesis

material relevant to the WGII assessment.

As an example, Figure Atlas.23: shows the projected increase in the number of days in which maximum temperature exceeds a high absolute threshold of 35°C, a hazard relevant to risks to human well-being, as derived from the ensemble mean of nine CMIP5 GCMs. The two rows show results for 2046–2065 compared to 1986–2005 under the RCP4.5 and 8.5 emissions scenarios respectively, with those in the left column derived from raw output from the models and those in the right when a bias adjustment has been applied to these model outputs. This figure demonstrates that significant increases are *likely* to occur in many areas of all inhabited continents.

[START Figure Atlas.23: HERE]

Figure Atlas.23: Projected changes in the number of days per year in which the maximum temperature exceeds 35°C from an ensemble of nine CMIP5 GCMs (the ensemble mean is considered in all cases). The top/bottom rows correspond to a future mid-term period 2046–2065 (compared to 1986–2005) under the RCP4.5/8.5 emissions scenarios respectively considering the raw model data (left-hand column) and bias adjusted (EQM method) data (right-hand column). Regions are stippled where less than six out of the nine models agree on the sign of the change (noting that this assessment does not take into account whether the individual models' projected changes are significant). The Interactive Atlas shows the results for two alternative bias adjustment methods; see Annex VII for more details.

[END Figure Atlas.23: HERE]

The Interactive Atlas shows the results for two alternative bias adjustment methods (see Annex VII for more details). The reason for using bias adjustment for some of the results displayed in Figure Atlas.23: is that the historical simulations of the climate models used to generate these projected changes often validate poorly when compared with observations. If the mean of the distribution of daily maximum temperatures is shifted by a few °C then even if the shape of the distribution is well captured the frequency of exceedance of a high threshold event will be significantly biased. In order to correct results from the models for these biases and to provide a basis for a reasonable comparison between them, this issue is generally addressed by applying bias correction to the model data based on comparing distributions from the historical simulations with observations. As there are several approaches to bias adjustment and no clearly preferred method (see Chapter 10) the results in Figure Atlas.23: should be taken as indicative of the direction of change and of the relative impact of different future scenarios with *low confidence* in the absolute values. In order to provide an idea of the implications of using different bias adjustment approaches, the Interactive Atlas displays the results obtained for this index from raw and bias corrected model data, using two different bias adjustment techniques (see Annex VII).

Atlas.5 Regional syntheses and case studies

This section aims to synthesise information enabling an understanding of the climate change context across all land regions, documenting findings that are relevant to applications of regional information in WGII and III contexts. Its structure aligns most closely with that of the regional chapters and cross-chapter papers in the WG II report, with sections on Small Island States, the main continental and polar regions (subdivided where relevant) and case studies relevant to typological domains. It focuses on assessing observed, attributed and projected changes in mean surface air temperature and precipitation and the regional evaluation of global and regional models, drawing out and illustrating key findings which can be explored further in the Interactive Atlas. In particular, changes in mean and extreme temperatures and precipitation are displayed in the Interactive Atlas in terms of a number of illustrative indices (including some of the indices assessed in Chapter 12, thus supporting and extending the assessment performed in this chapter) and allowing for a regional analysis of the results. This also builds and expands on and complements the assessment of extremes in Chapter 11. The Interactive Atlas then presents the different regional information that has been assessed in these chapters and in the CORDEX and other region-specific literature assessed in the Atlas,

including different climate variables and indices as well as relevant climate processes.

Atlas.5.1 Information sources for regional synthesis

In the following regional sub-sections, the Atlas presents information on observations (station data, gridded data sets, reanalysis, and satellite-based) and observed trends, extremes and variability and also how they are applied in the literature in validating CORDEX output (drawing on the assessment of methodologies in Chapter 10, section 10.6). It also provides summary information on projections of mean climate change from the CMIP5, CMIP6 and CORDEX ensembles, synthesises regional information based on the assessments in Chapters 11 and 12 and provides some examples of attribution of regional climate changes. Datasets and issues related to availability and integrity of observational data are described in Section Atlas.3.

For illustrative purposes and to provide a general climate change context for each region, in the following region by region synthesis sections, we include summary figures of observed trends and future projections of annually averaged surface air temperature and precipitation. Three observed datasets are used for each variable to illustrate where the clearest messages on changes in the recent past can be found and to illustrate observational uncertainty. Future projection information is taken from the CMIP5 and CMIP6 ensembles, illustrating ensemble mean changes and model agreement for mid- and end-of-century timescales compared to a recent past baseline. In many regional sections, results and figures from region-specific analyses are included for additional context.

Atlas.5.2 Africa

Regional executive summary

The rate of temperature increase has generally been more rapid in Africa than the global average *(high confidence)*. Minimum temperatures have increased more rapidly relative to maximum temperatures over inland southern Africa (*medium confidence*). Since 1980, mean temperature over East Africa has shown an increasing trend but showed a decreasing trend in the past (*medium confidence*). Mean temperature over northern Africa and West Africa have increased over the last 50 years (*high confidence*). {Atlas.5.2.2}

The Horn of Africa has experienced significantly decreased rainfall during the long rains season March to May *(high confidence)* and drying trends in this and other parts of Africa are attributable to oceanic influences *(high confidence)* both internal variability in some cases and human-induced in other cases. Drying over the Sahel is attributed to an increase in the South Atlantic SST and over southern African as a response to anthropogenic-forced Indian Ocean warming. Drying over East Africa is associated with decadal natural variability in SSTs over the Pacific Ocean. The enhanced rainfall intensity over the Sahel in the last two decades is associated with increased greenhouse gases indicating an anthropogenic influence *(medium confidence).* {Atlas.5.2.2}

Relative to the late 20th century, annual mean temperature over Africa is projected to rise faster than the global average *(very high confidence)* with the increase likely to exceed 4°C by the end of the century under RCP 8.5 emissions. All parts of Africa will have increased maximum and minimum temperatures with a commensurate increase in the number of warm days in all seasons (*high confidence*) with North Africa, central interior of southern Africa and West Guinea likely to warm at a faster rate (*high confidence*). {Atlas.5.2.4}

There are contrasting signals in the projections of rainfall over some parts of Africa until the end of 21st century *(high confidence)* though changes in any given region are projected *with medium confidence.* In regions of high or complex topography such as the Ethiopian Highlands, downscaled projections indicate *likely* increases in rainfall by the end of the 21st century. However, the Northern Africa and the south-western parts of South Africa are *likely* to have a reduction in precipitation. Over West Africa, rainfall will *likely* decrease in the Western Sahel subregion (*medium confidence*) and increase in the central

Sahel subregion (*low confidence*) and along the Guinea Coast subregion (*medium confidence*). Rainfall amounts over western part of the East Africa is *likely* to reduce but increase in the eastern part of the region (*medium confidence*). Southern Africa is projected to have a reduction in annual mean rainfall but *likely* to have an increased intensity by 2100 (*medium confidence*). {Atlas.5.2.4}

Atlas.5.2.1 Key features of the regional climate and findings from previous assessments

Key features of the regional climate

Africa has many varied climates and can be categorized as dry regime in the Saharan region, tropical humid regime in West and East Africa except for parts of the Greater Horn of Africa (alpine) and the Sahel (semi-arid), and a dry/wet season regime in the southern African region and each climate region has its local variations resulting in very high spatial and temporal variations (Peel et al., 2007).

Previous findings from IPCC assessments

The most recent IPCC reports, AR5 and SR1.5 (IPCC, 2013b, 2018c), state that over most parts of Africa, minimum temperatures have warmed more rapidly than maximum temperatures during the last 50 to 100 years (*medium confidence*). In the same period minimum and maximum temperatures have increased by more than 0.5°C (*high confidence*). While the quality of ground observational temperature measurements tends to be high compared to that of measurements for other climate variables, Africa remains an under represented region (IPCC, 2018c). Based on the Coupled Model Intercomparison Project Phase 5 (CMIP5) ensemble, surface air temperatures in Africa are projected to rise faster than the global average increase and *likely* to increase by more than 2°C by the end of the century (IPCC, 2013; 2018) relative to the late 20th century. Higher temperature increases are projected during boreal summer. Southern Africa is *likely* to exceed the global mean land surface temperature increase in all seasons by the end of the century. Temperature projections for East Africa indicate considerable warming under RCP 8.5 where average warming across all models is approximately 4°C by the end of the century. According to SROCC, eastern Africa like other regions with smaller glaciers is projected to lose more than 80% of its glaciers by 2100 under RCP8.5 (*medium confidence*) (IPCC, 2019b).

West Africa has also experienced an overall reduction of rainfall over the 20th century, with a recovery towards the last 20 years of the century (IPCC, 2013). Over the last 3 decades rainfall has decreased over eastern Africa especially between March and May/June. Projected rainfall changes over Africa in the mid- and late 21st century are uncertain. In regions of high or complex topography such as the Ethiopian Highlands, downscaled projections indicate *likely* increases in rainfall and extreme rainfall by the end of the 21st century. However, the Northern Africa and the south-western parts of South Africa are *likely* to have a reduction in precipitation.

The consequence of increased temperature and evapotranspiration, and decreased precipitation amount, in interaction with climate variability and human activities, have contributed to desertification in dryland areas in Sub-Saharan Africa (*medium confidence*) as reported in SRCCL 2019 (IPCC, 2019a).

Atlas.5.2.2 Assessment and synthesis of observations, trends and attribution

Figure Atlas.24:a shows observed annual mean temperature trends (ºC per decade) and indicates that temperatures have been rising rapidly over Africa over 1980-2014 and that, at most locations, the increases are statistically significant. However, over a longer period (1961-2018) and subjected to a different statistical analysis (Engelbrecht et al. (2015), there is a larger area of non-statistically significant temperature increases compared to Figure Atlas.24:. More specifically over the Horn of East Africa, the long-term mean annual temperature change between 1930 and 2014 showed two distinct but contrary trends: temperature trends were significantly negative between 1930 and 1969 but significantly positive from 1970 to 2014 (Ghebrezgabher et al., 2016). North Africa has an overall warming in observed seasonal temperature

(Barkhordarian et al., 2012; Lelieveld et al., 2016) with positive trends in annual minimum and maximum temperatures (Vizy and Cook, 2012). Temperatures over West Africa have increased over the last 50 years (Mouhamed et al., 2013; Niang et al., 2014) with a spatially variable gradual warming reaching 0.5°C per decade from 1983 through 2010 (Sylla et al., 2016). West Africa has also experienced a decrease in the number of cool nights as well as more frequent warm days and warm spells (Mouhamed et al., 2013; Ringard et al., 2016). Similarly, East Africa has experienced a significant increase in temperature since the beginning of the early 1980s (Anyah and Qiu, 2012) with an increase in seasonal mean temperature. Over South Africa, positive trends were found in the annual mean, maximum and minimum temperatures for 1960–2003 in all seasons, except for the central interior (Kruger and Shongwe, 2004; Zhou et al., 2010; Collins, 2011; Kruger and Sekele, 2013; MacKellar et al., 2014), where minimum temperatures have decreased significantly (MacKellar et al., 2014). Inland southern Africa, minimum temperatures have increased more rapidly relative to maximum temperatures (New et al., 2006). In the recent years Africa experienced hotter, longer and more extensive heat waves than in the last two decades of the 20th century (Russo et al., 2016).

There is a general decrease in annual total rainfall over Africa (Mouhamed et al., 2013). Most areas of the African continent lack enough observational data to draw conclusions about trends in annual precipitation over the past century. In addition, many regions of Africa have discrepancies between different observed precipitation data sets according to (Sylla et al., 2013; Panitz et al., 2014). A statistically significant (95% confidence level) decrease in rainfall and the number of rainy days is reported in autumn over central and north-eastern parts of South Africa in spring and summer during the period of 1960–2010 (MacKellar et al., 2014). Central Africa has experienced a significant decrease in total precipitation, which is likely associated with a significant decrease of the length of the maximum number of consecutive wet days (Aguilar et al., 2009). Furthermore, rainfall decreased significantly in the Horn of Africa (Tierney et al., 2015) and more pronounced during the long raining season March to May (Lyon and Dewitt, 2012; Viste et al., 2013; Rowell et al., 2015). Over mountainous areas significant increases are found in the number of rain days around the southern Drakensberg in spring and summer during the period of 1960–2010 (MacKellar et al., 2014). Similarly, southern West Africa is observed to have had more intense rainfall from 1950 to 2014 during the second rainy season of September–November (Nkrumah et al., 2019) and throughout the raining season over the Sahel region within the period (Panthou et al., 2014, 2018b, 2018a; Sanogo et al., 2015; Gaetani et al., 2017; Taylor et al., 2017; Biasutti, 2019) in the last two decades (1980-2010).

Temperature increases over Africa in the 20th century can be attributed due to the strong evidence of a continent-wide anthropogenic signal in the warming (Hoerling et al., 2006; Min and Hense, 2007; Stott et al., 2010, 2011; IPCC, 2013). More specifically over West Africa, higher temperature increases are due to the relatively small natural climate variability in the region that generates narrow climate bounds which can be easily surpassed by relatively small climate changes (IPCC, 2013b). Warming over North Africa is due to natural (internal) variability (Barkhordarian et al., 2012), which is in turn attributed largely to the North Atlantic Oscillation (NAO) (Knippertz et al., 2003). Over southern Africa there is a strong link between ENSO and droughts (Meque and Abiodun, 2015). The drying trends in parts of Africa during each monsoon season is attributable to oceanic influences where air-sea interactions have been most relevant (Hoerling et al., 2006). In particular, they demonstrated that the drying over the Sahel can be attributed to warming of the South Atlantic SST and southern African drying as a response to Indian Ocean warming (Hoerling et al., 2006; Dai, 2011).

The enhanced rainfall intensity in the last two decades over the Sahel is associated with increased greenhouse gases suggesting an anthropogenic influence (Biasutti, 2019). In the last decade, the changes in the timing of onset and cessation over Africa have been linked to changes in the progression of the tropical rain-band and the Saharan Heat Low (Dunning et al., 2018; Wainwright et al., 2019). Over East Africa, the drying trend is associated with an anthropogenic-forced relatively rapid warming of Indian Ocean SSTs (Williams and Funk, 2011; Hoell et al., 2017); a shift to warmer SSTs over the western tropical Pacific and cooler SSTs over the central and eastern tropical Pacific (Lyon and Dewitt, 2012); multidecadal variability of SSTs in the tropical Pacific, with cooling in the east and warming in the west (Lyon, 2014); and the strengthening of the 200-mb easterlies (Liebmann et al., 2017). However, decadal natural variability from SST variations over the Pacific Ocean has also been associated with the drying trend of the East Africa (Wang et al., 2014; Hoell et al., 2017). Moreover, later onset and earlier cessation of Eastern Africa rainfall

is associated with a delayed and then faster movement of the tropical rain-band northwards during the boreal spring and the Saharan Heat Low (Wainwright et al., 2019).

Atlas.5.2.3 Assessment of model performance

Model development has advanced in the world, but Africa still lags in its contribution (James et al., 2018). Furthermore, none of the current generation of general circulation models (GCMs) was developed in Africa (Watterson et al., 2014), and the relevant processes in the continent have not always been the priority for model development (James et al., 2018). However, there are growing efforts to boost African climate science by running and evaluating climate models over Africa (Endris et al., 2013; Kalognomou et al., 2013; Gbobaniyi et al., 2014; Engelbrecht et al., 2015; Klutse et al., 2016; Gibba et al., 2019).

CORDEX models simulate the occurrence of the West African Monsoon jump and the timing and amplitude of mean annual cycle of precipitation and temperature over the homogeneous subregions of West Africa (Gbobaniyi et al., 2014). CORDEX RCMs simulate eastern Africa rainfall adequately (Endris et al., 2013). Over Southern Africa, CORDEX models capture the observed climatological spatial patterns of extreme precipitation (Pinto et al., 2016). They simulate also the phasing and amplitude of monthly rainfall evolution and the spatial progression of the wet season onset well over Southern Africa (Shongwe et al., 2015). The southern African rainfall trend is found to have a significant downtrend of -0.013 mm/day per year and -0.003 mm/day per year for longer periods over the 20th century from 1900 to 2010 (Jury, 2013). However, discrepancies and biases in present-day rainfall are reported over Uganda from the RCM-simulated rainfall compared to three gridded observational datasets (Kisembe et al., 2018). Specifically, they reported that the CORDEX models underestimate annual rainfall of Uganda and struggle to reproduce the variability of the long and short rains seasons.

The CMIP project has not resulted in improved performance for Africa (Flato et al., 2013b; Rowell, 2013; Whittleston et al., 2017) and culling ensembles based on existing metrics for Africa fails to reduce the range of uncertainty in precipitation projections (Roehrig et al., 2013; Yang et al., 2015; Rowell et al., 2016) but CMIP6 presents less bias compared to CMIP5 over Africa (Adamu et al., submitted). Nonetheless, CMIP5 has been evaluated over Africa to advance the understanding of climate science (Biasutti, 2013; Rowell, 2013; Dike et al., 2015; McSweeney and Jones, 2016; Onyutha et al., 2016; Wainwright et al., 2019) and recently, CMIP6 (Adamu et al., submitted; Almazroui et al., submitted, b).

Atlas.5.2.4 Assessment and synthesis of projections

Research over Africa (Druyan and Fulakeza, 2013; Hernández-Díaz et al., 2013; Panitz et al., 2014; Sarr et al., 2015; Careto et al., 2018; Sylla et al., 2018) has improved since AR5 and even though the SR1.5 has synthesised new information for the continent, there is still not enough information on specific areas for assessment. A large ensemble of CORDEX Africa simulations have been used to present the impact of 1.5°C and 2°C global warming levels (GWLs) (Klutse et al., 2018; Lennard et al., 2018; Maure et al., 2018; Mba et al., 2018; Nikulin et al., 2018b; Osima et al., 2018). While a few studies addressed the whole African continent (Lennard et al., 2018; Nikulin et al., 2018a), some focused on specific regions of Africa (Diedhiou et al., 2018; Klutse et al., 2018; Kumi and Abiodun, 2018; Maure et al., 2018; Mba et al., 2018). CORDEX simulations give a robust warming over Africa to exceed the mean global warming (Lennard et al., 2018; Nikulin et al., 2018a). The rate of increase in minimum temperatures will exceed that of maximum temperatures (Vizy and Cook, 2012). Over North Africa, summer mean temperatures from CORDEX, CMIP5 (RCP8.5) and CMIP6 (SSP5-8.5) are projected to increase beyond 6.0°C by the end of the century with respect to the period 1970–2000 (Schilling et al., 2012; Ozturk et al., 2018; Almazroui et al., submitted, b). Over West Africa, a continuous stronger warming is projected to occur 1 to 2 decades earlier than the global average (IPCC, 2013; Mora et al., 2013; Sylla et al., 2016; Klutse et al., 2018) by 2100. The Sahel and tropical West Africa are hotspots of climate change for both RCP4.5 and RCP8.5 pathways from CMIP5 (Diffenbaugh and Giorgi, 2012). Temperature increases projected under RCP8.5 over Sudan and northern Ethiopia implying that the Greater Horn of Africa would warm faster than the global mean relative to

1971−2000 (Osima et al., 2018). Projections from CMIP5 show that East Africa is *likely* to warm by 1.7–2.8 °C and 2.2–5.4 °C under the RCP4.5 and RCP8.5 scenarios respectively in the period 2071-2100, relative to 1961-1990 (Ongoma et al., 2018). Over southern Africa, areas in the south-western region of the subcontinent, covering South Africa and parts of Namibia and Botswana are projected to experience the largest increase in temperature, which are expected to be greater than the global mean warming (Maure et al., 2018). CMIP5 and CMIP6 projections (Figure Atlas.24:) are for a continuous warming exceeding 4°C and up to 6°C or more till the end of the century under RCP8.5 emissions. Some areas (e.g., central interior of South Africa, North Africa, and West Guinea) of the continent are *likely* to warm faster than other areas (like the Democratic Republic of Congo).

Projected rainfall changes over sub-Saharan Africa in the mid and late 21st century are uncertain in many regions, highly variable spatially and with differing levels of model agreements (Figure Atlas.24:). Some uncertainties are reported over parts of Africa from CORDEX projections (Dosio and Panitz, 2016; Endris et al., 2016; Klutse et al., 2018). For example, large uncertainties are found to be associated with projections at 1.5°C and 2°C over Central Africa (Mba et al., 2018) and over the Sahel (Sylla et al., 2016). Biases in RCMs from CORDEX vary in both magnitude and spatial extent from model to model (Gbobaniyi et al., 2014). Over southern Africa, enhanced warming is projected to result in a reduction in mean rainfall across the region (Maure et al., 2018) and in particular, up to 0.4 mm/day over the Limpopo Basin and smaller areas of the Zambezi Basin in Zambia, and also parts of Western Cape, South Africa, under a global warming of 2°C. However, projected rainfall intensity over southern Africa is likely to increase and be magnified under RCP8.5 compared with RCP4.5 for the period 2069–2098 relative to the reference period (1976–2005) (Pinto et al., 2018). For West Africa, rainfall is projected to decline consistently through the periods 2021-2040 to 2081-2100 and West African river basins would decline in the basin-scale irrigation potential under 2°C global warming (Sylla et al., 2018). The western and eastern Sahel are projected as hotspots for a delayed rainfall onset dates and reduced length of rainy season in the 1.5°C to 2°C warmer climates under RCP4.5 and RCP8.5 scenarios (Kumi and Abiodun, 2018). They are also projected a delay in rainfall cessation dates and a longer length of rainy season over the western part of the Guinea coast. North Africa is also projected to have a reduction in precipitation (Sellami et al., 2016), (Figure Atlas.24:). There is a tendency towards an increase in annual mean precipitation over central/eastern Sahel and eastern Africa (Figure Atlas.24:) (Nikulin et al., 2018a) especially over the Ethiopian highlands with up to 0.5 mm day^{-1} increase in rainfall (Osima et al., 2018).

[START Figure Atlas.24: HERE]

Figure Atlas.24: (a–b) Mean observed trends of annual mean surface air temperature and precipitation for three datasets (CRU TS, BERKELEY and EWEMBI for temperature; CRU TS, GPCC and GPCP for precipitation). Hatching indicates regions where no or only one dataset provides a significant trend. Linear trends are calculated for the common 1980–2014 period and expressed in °C per decade (temperature) and % relative change per decade (precipitation) with respect to the climatological mean over this period.
(c–f) Climate change projections of annual mean surface air temperature and precipitation from CMIP5 (30 models) and CMIP6 (17 models) calculated as the differences in the climatological average for RCP8.5 and SSP5-8.5 respectively, for the period 2041–2060 with respect to the historical 1995–2014 period and expressed as °C (temperature) and % relative change (precipitation). Hatching indicates weak model agreement on the sign of the change (less than 80% as defined in Nikulin et al., 2018).
(g–n) Regional mean changes in annual mean surface air temperature and precipitation for the eight African regions (MED, SHA, WAF, CAF, NEAF, CEAF, SWAF and SEAF). The top row shows the median (dots) and 10th–90th percentile range across each model ensemble for annual mean temperature changes, for two datasets (CMIP5 and CMIP6) and two scenarios (SSP1-2.6/RCP2.6 and SSP5-8.5/RCP8.5). The first four bars represent the additional warming projected relative to the historical baseline 1995–2014 period to reach the two global warming levels (GWL; +1.5°C and +2°C) and the remaining six projected changes over three time periods (near-term 2021–2040, mid-term 2041–2060 and long-term 2081–2100) compared to this same historical baseline period. The bottom row shows scatter diagrams of temperature against precipitation changes, displaying the median (dots) and 10th–90th percentile ranges for four future periods (2021–2040, 2041–2060, 2061–

2080, 2081–2100) compared to the historical baseline period, as obtained from CMIP6 projections for three scenarios (SSP1-2.6, SSP2-4.5 and SSP5-8.5). Changes are absolute for temperature and relative for precipitation.
(The script used to generate this figure is available online (Atlas GitHub, 2020) and similar results can be generated in the Interactive Atlas for flexibly defined seasonal periods.)

[END Figure Atlas.24: HERE]

Atlas.5.3 Asia

Atlas.5.3.1 East Asia

Regional executive summary

In most East Asia areas annual mean temperature has been increasing since the 1950s. This is documented based on historical meteorological observations. It is *very likely* that the linear trend of annual mean surface air temperature exceeded 0.1°C per decade over most of East Asia from 1980-2014. Annual precipitation over most of East Asia does not show significant change for the period of 1980-2014 (*high confidence*). {Atlas.5.3.1.2}

GCMs still show poor performance in simulating the mean rainfall and its variability over East Asia, especially over regions characterized by complex topography (*high confidence*). The RCMs produce relatively more detailed regional features, but do not always produce superior simulations compared with the driving GCMs (*medium confidence*). {Atlas.5.3.1.3}

It is *very likely* that the surface temperature over the East Asian continent will increase under global warming. Larger warming magnitudes will occur in the northern part of East Asia (*high confidence*). {Atlas.5.3.1.4}

Precipitation is projected to increase over land in most of East Asia at the end of the 21st century under the high emissions scenario (RCP8.5, SSP5-8.5). Stronger precipitation increase occurs in northern China, corresponding to the strengthened monsoon circulation in the lower troposphere. (*high confidence*) {Atlas.5.3.1.4}

Atlas.5.3.1.1 Key features of the regional climate and findings from previous assessments

Key features of the regional climate

East Asia is significantly influenced by monsoon systems. The seasonal advance or retreat of the monsoon rainbelt is crucial to local climate. The East Asian monsoon exhibits considerable variability on a wide range of time scales, including significant inter-decadal variation in the 20th century. The thermal conditions of both the Tibetan Plateau and related oceans play key roles in modulating the intensity of the monsoon circulation. GCMs still show poor performance in simulating the monsoon rainfall and its variability over East Asia. There will be an increasing trend of both surface temperature and the monsoon circulation.

Previous findings from IPCC assessments

The findings of the most recent IPCC reports (AR5, SR1.5, SRCCL and SROCC) stated that both the East Asian summer and winter monsoon circulations have experienced an inter-decadal scale weakening since the 1970s due to natural variability of the coupled climate system, leading to enhanced mean precipitation along the Yangtze River Valley (30°N) but deficient mean precipitation in North China in summer, and a warmer climate in winter. The summer rainfall amount over East Asia shows no clear trend during the 20th century. Regional trends in frequency and intensity of drought during 1950–2012 are evident in East Asia. The winter monsoon circulation weakened significantly after the 1980s. Since the middle of the 20th century, it is *likely* that there has been an increasing trend in winter temperatures across much of Asia. The numbers of cold days and nights have decreased and the numbers of warm days and nights have increased over Asia.

The findings of the AR5 stated that model skill in representing regional monsoons is lower compared to the global monsoon and varies across different monsoon systems. For East Asia, there is only *low confidence* in more specific details of the projected changes due to the still limited skill of CMIP5 models in simulating monsoon features such as the East Asian monsoon rainband.

The most recent IPCC reports (AR5, SR1.5, SRCCL and SROCC) also stated that there is a significant increase in mean, daily maximum and minimum temperatures in south-eastern China, associated with a decrease in the number of frost days under the SRES A2 scenario. The CMIP5 model projections indicate an increase of temperature in both boreal winter and summer over East Asia for RCP4.5. Based on CMIP5 model projections, there is *medium confidence* that with an intensified EASM, summer precipitation over East Asia will increase. More than 85% of CMIP5 models show an increase in mean precipitation of the EASM, while more than 95% of models project an increase in heavy precipitation events. Future projections of annual precipitation indicate increases of the order of 5 to 20% over the 21st century in many mountain regions, including the Himalaya and East Asia (SROCC).

Atlas.5.3.1.2 Assessment and synthesis of observations, trends and attribution

Based on historical meteorological observations, the best estimations of linear trends of annual mean surface air temperature for China with 95% uncertainty ranges are 0.121° ± 0.009°, 0.379° ± 0.045°, and 0.079° ± 0.13°C (not significant) decade^{-1} for 1900–2015, 1979–2015, and 1998–2015, respectively (Li et al., 2017). The annual temperature increased in large cities at a rate of 0.29 ± 0.08 °C decade^{-1} compared with 0.11 ± 0.08 °C decade^{-1} in other stations in South Korea, which is associated with the general increase in greenhouse gases in East Asia (Kim et al., 2016a). Summer (June–August) mean temperature in Eastern China has increased by 0.82°C since reliable observations were established in the 1950s (Sun et al., 2014). East Asia has experienced more cold winters and a number of unusually harsh cold winters have occurred in many parts of East Asia in the past few years, which is related to the recovered and re-amplified East Asian winter monsoon (EAWM) in the mid-2000s (Wang and Chen, 2014; Kug et al., 2015). The winter cooling has contributed to the 1998–2012 hiatus in China, when the warming trend in China was replaced by a decrease in mean maximum temperature (Li et al., 2015b). In contrast to the warming hiatus post-1990s, an accelerated warming trend has appeared over the Tibetan Plateau during 1998–2013 (0.25 °C decade^{-1}), compared with that during 1980–1997 (0.21 °C decade^{-1}) (Duan and Xiao, 2015). Figure Atlas.25:a shows the trend of annual temperature for the period of 1980-2014. Most areas of East Asia have significant warming trends exceeding 0.1°C per decade, and the strongest warming (0.42-0.52°C per decade) occurs in the northern China.

The change in East Asian summer monsoon (EASM) presents a clear interdecadal variation rather than a linear trend since the 1900s (Zhang, 2015; Zhou et al., 2017b). Evidence indicates that the "southern flood and northern drought" (SFND) anomalous pattern in eastern China after the 1970s has been changed with the recovering EASM since the early 1990s. Summer flooding events have increased in the Huaihe River valley and the monsoon rain belt has tended to move northward in eastern China (Liu et al., 2012; Zhao et al., 2015). The summer rainfall daily frequency and intensity over East Asia show significantly decreasing and increasing trends from 1961 to 2014, respectively (Zhou and Wang, 2017b). Accompanied by the recovery of the summer monsoon, the summer rainfall characteristics exhibit enhanced trends from 1979 to 2014, based on highly-resolved in-situ observations and eight current reanalysis products (Zhou and Wang, 2017a). Mean and extreme rainfall and the number of rainy days during the Meiyu/Baiu/Changma period from June to September have increased, and the dry spell has become shorter (Lee et al., 2017). Precipitation amounts exhibited a substantial decrease at both the annual and seasonal scales in Japan for the period 1901–2012 (Duan et al., 2015). The decadal precipitation trend has caused a large increase in summer precipitation at a rate of 40.6 ± 4.3 mm decade^{-1}, resulting in an increase of annual precipitation of 27.7 ± 5.5 mm decade^{-1} in South Korea from 1960 to 2010 (Kim et al., 2016a). Figure Atlas.25:b shows the trend of annual precipitation for the period of 1980-2014. Precipitation trends over most of East Asia is not significant but for a small region on the north-eastern edge of the Tibetan Plateau.

GHG and anthropogenic aerosols played an important role in driving the weakened low-level monsoon circulation during 1958–2001. The enhanced cooling over continental East Asia caused by aerosols affects

the monsoon circulation through reducing the land-sea thermal contrast (Chapter 8). An event attribution study using the large-ensemble simulations with and without human-induced climate change showed that the July 2018 high temperature event in Japan would never have happened without anthropogenic global warming (Imada et al., 2019).

Atlas.5.3.1.3 Assessment of model performance

Current climate models perform poorly in simulating the mean precipitation in East Asia, including the seasonal phase of the northward progression of rain band (Zhang et al., 2018b). Although there has been an improvement in the simulation of mean states, interannual variability, and past climate changes in the progression from CMIP3 to CMIP5, some previously documented biases (such as the ridge position of the western North Pacific subtropical high and the associated rainfall bias) are still evident in CMIP5 models (Zhou et al., 2017a). Some CMIP6 models show improvements in simulating the mean precipitation and interannual variation, but the deficiencies are still evident (Sellar et al.; Tatebe et al., 2019; Wu et al., 2019). The performance of models is sensitive to cumulus convection schemes and horizontal resolution (Haarsma et al., 2016; Wu et al., 2017; Kusunoki, 2018b). The high-resolution AGCM is successful in reproducing the intensity and the spatial pattern of the EASM rainfall (Li et al., 2015a; Yao et al., 2017) and improves the simulation of the diurnal cycle of precipitation rates and the probability density distributions of daily precipitation over Korea, Japan and northern China (Lin et al., 2019).

Recent studies using CORDEX-EA models showed that the RCMs produce relatively more detailed regional features of the temperature distribution compared with the driving GCMs (Tang et al., 2016). But RCMs also show large biases in simulating East Asian climatology and variability (Park et al., 2016; Zhou et al., 2016; Zou and Zhou, 2016), and do not always show added value compared to the driving GCMs (Li et al., 2018a). For example, by comparing inter-GCM and inter-RCM differences around the Japan archipelago, it was found that RCMs bring about a relatively large difference in precipitation (Suzuki-Parker et al., 2018). The multi-model ensemble (MME) overall produces superior simulation compared with a single RCM (Huang et al., 2015; Jin et al., 2016; Guo et al., 2018a).

Topography has a strong effect on the precipitation patterns over East Asia, and the simulation of precipitation over regions with complicated topography is a major challenge. Over the Tibetan Plateau, RCMs consistently show similar spatial patterns, but there is a mean cold (wet) bias in the temperature (precipitation) climatology compared to station observations (Guo et al., 2018a). Over steep mountains such as the southern edge of the Tibetan Plateau, the overestimation of heavy rainfall is found to be caused by the "overshoot" of water vapor to the high-altitude region of the windward slopes (Yu et al., 2015).

Evaluation of the ability of CORDEX-EA models in simulating tropical cyclone (TC) activity over the western North Pacific indicates that models reasonably capture the observed climatological spatial distribution and interannual variability of TC activity. But due to the low horizontal resolutions (~50 km), RCMs tend to underestimate TC intensity (Jin et al., 2016).

Atlas.5.3.1.4 Assessment and synthesis of projections

Coupled model simulations indicate that East Asia will experience ~0.2°C higher warming than the global mean conditions in the 1.5°C and 2°C warming conditions at the end of the 21st century. Larger warming magnitudes are projected to occur in the southern, north-western, and north-eastern regions of China, parts of Mongolia, the Korean Peninsula, and Japan than in other regions (Li et al., 2018b). The increases in the monthly minimum values of daily minimum temperature (TNn) and maximum values of daily maximum temperature (TXx) over mainland China tend to show a similar spatial pattern during the period 2070–2099 (relative to the baseline 1961–1990) under the RCP4.5 and RCP8.5 scenarios. The largest increases in TNn (more than 5 °C in RCP4.5 and 8 °C in RCP8.5) are projected to occur mainly in northeast China and most parts of western China (Xu et al., 2019a).

Figure Atlas.25:c,e show the projected temperature changes under CMIP5 RCP85 and CMIP6 SSP5-85. Both CMIP5 and CMIP6 models show uniform warming in East Asia. The warming is stronger in the

northern part of East Asia and decreases south-eastward.

The EASM circulation and precipitation are projected to increase (Kitoh, 2017; Moon and Ha, 2017). Simulations from CMIP5 models show that compared with the current summer climate, both surface air temperature and precipitation increase significantly over the East Asian continent during the 1.5 °C warming period (Wang et al., 2018; Chen et al., 2019a). The monsoon circulation in the lower troposphere is strengthened due to the enhanced land–sea thermal contrast, which causes the increased summer precipitation over the East Asian continent. Precipitation over eastern China increases for almost all months under global warming in projections from GCMs with different horizontal resolutions (Kusunoki, 2018a). However, the geographical distribution of precipitation change tends to depend relatively on the cumulus convection scheme and horizontal resolution of models rather than on SST distributions. Under the RCP4.5 and the RCP8.5 scenarios, the interannual variability in EASM rainfall is projected by the multi-model ensemble mean (MME) to increase in the 21st century (Ren et al., 2017b). Further studies showed a projected increase in heavy rainfall together with increases in rainfall intensity (Endo et al., 2017). Multi-model intercomparison indicates significant uncertainties in the future projection of East Asian climate change, although precipitation increases consistently across models (Zhou et al., 2017a).

Figure Atlas.25:d,f shows the projected precipitation changes under CMIP5 RCP8.5 and CMIP6 SSP5-8.5 respectively. CMIP5 and CMIP6 models present similar patterns: most land areas have positive precipitation changes and the strongest precipitation increase occurs in the northern China. Compared with CMIP5, the CMIP6 models have better agreement in precipitation changes over East Asia. Figure Atlas.26: shows the simulated historical changes and projected future changes of the EASM index. Under SSP5-8.5, CMIP6 models present an increase in summer monsoon circulation in East Asia in the 21st century.

The increasing temperature trends of RCP scenarios were consistently reproduced in projections using CORDEX-EA models (Kim et al., 2016b) as reported in AR5 using GCMs. However, changes in annual and seasonal mean precipitation exhibit significant inter-RCM differences and possess larger magnitude and variability than GCMs (HAM et al., 2016; Ozturk et al., 2017; Sun et al., 2018a; Zhang et al., 2018a). Dynamical downscaling simulations showed that the Meiyu-Baiu-Changma heavy rainfall will significantly increase in northern Japan and Japan Sea at the end of the 21st century under the RCP8.5 scenario (Osakada and Nakakita, 2018), but precipitation amount and number of precipitating days in summer around and over Japan differ among members, which comes from RCM uncertainty (Suzuki-Parker et al., 2018).

[START Figure Atlas.25: HERE]

Figure Atlas.25: (a–b) Mean observed trends of annual mean surface air temperature and precipitation for three datasets (CRU TS, BERKELEY and EWEMBI for temperature; CRU TS, GPCC and GPCP for precipitation). Hatching indicates regions where no or only one dataset provides a significant trend. Linear trends are calculated for the common 1980–2014 period and expressed in °C per decade (temperature) and % relative change per decade (precipitation) with respect to the climatological mean over this period.
(c–f) Climate change projections of annual mean surface air temperature and precipitation from CMIP5 (30 models) and CMIP6 (17 models) calculated as the differences in the climatological average for RCP8.5 and SSP5-8.5 respectively, for the period 2041–2060 with respect to the historical 1995–2014 period and expressed as °C (temperature) and % relative change (precipitation). Hatching indicates weak model agreement on the sign of the change (less than 80% as defined in Nikulin et al., 2018).
(g) Regional mean changes in annual mean surface air temperature and precipitation for the East Asian region. The left plot shows the median (dots) and 10th–90th percentile range across each model ensemble for annual mean temperature changes, for two datasets (CMIP5 and CMIP6) and two scenarios (SSP1-2.6/RCP2.6 and SSP5-8.5/RCP8.5). The first four bars represent the additional warming projected relative to the historical baseline 1995–2014 period to reach the two global warming levels (GWL; +1.5°C and +2°C) and the remaining six projected changes over three time periods (near-term 2021–2040, mid-term 2041–2060 and long-term 2081–2100) compared to this same historical baseline period. The right plot shows a scatter diagram of temperature against precipitation changes, displaying the median (dots) and 10th–90th percentile ranges for four future

periods (2021–2040, 2041–2060, 2061–2080, 2081–2100) compared to the historical baseline period, as obtained from CMIP6 projections for three scenarios (SSP1-2.6, SSP2-4.5 and SSP5-8.5). Changes are absolute for temperature and relative for precipitation.
(The script used to generate this figure is available online (Atlas GitHub, 2020) and similar results can be generated in the Interactive Atlas for flexibly defined seasonal periods.)

[END Figure Atlas.25: HERE]

[START FIGURE ATLAS.26: HERE]

Figure Atlas.26: Time series of East Asian Summer Monsoon index (21-year running mean) over 1900-2100. Historical (grey), SSP5-8.5 (red) simulations by 12 CMIP6 model ensembles are shown in 10th and 90th (shading), and 50th (thick line) percentile. The index is defined as normalized June-July-August sea level pressure difference between 110°E and 160°E from 10°N to 50°N (Wang et al., 2008).

[END FIGURE ATLAS.26: HERE]

Atlas.5.3.2 Middle East Asia

Regional executive summary

Observations over the Arabian Peninsula for the period 1978–2018 exhibit an increase in annual surface air temperature estimated at 0.52°C per decade and *very likely* in the range of 0.21–0.73°C per decade *(high confidence)* and a decrease in annual precipitation estimated at 6.3 mm per decade and *likely* in the range –30 mm–9.0 mm per decade *(medium confidence).* The highest warming and precipitation decrease is observed in the northern Peninsula and the lowest warming and highest precipitation increase in the south. As the annual precipitation total in the region comes mostly in a wet season from a few scattered extreme events, decrease in their frequency has resulted in a negative precipitation trend (*medium confidence*), nevertheless intensity of extreme precipitation has increased (*low confidence*). {Atlas.5.3.2.2}

A strong increase of annual surface air temperature and precipitation amount continued over West and Central Asia in the last half century based on observational and gridded datasets including satellite products. The observed trend in the period 1960–2013 *very likely* was in the range 0.27°C–0.47°C per decade for temperature and 1.3–4.8 mm per decade for precipitation. In mountainous areas the scarcity of observation stations and the decline of observation sites after the collapse of the former Soviet Union in 1991 *very likely* increase the uncertainty of the long-term temperature and precipitation estimates. {Atlas.5.3.2.2}

Extensive land-use and land-cover changes had different impacts on the local temperature and precipitation in Central Asia *(medium confidence).* Agriculture intensification through oasis expansion in the Xinjian region has increased summer precipitation (*medium evidence*, *high agreement*). The shrinking of the Aral Sea has induced an increase of local surface air temperature in the range of 2°C to 6°C (*very high confidence*), but its impact on precipitation can be attributed only with *very low confidence*. {Atlas.5.3.2.2}

There is *medium evidence* about performance of RCMs in the Middle East region as publications on regional model evaluation have only recently emerged. Published studies have *medium to high agreement* for mean temperature and precipitation biases in RCMs. Regional models simulate colder temperatures than observed over mountainous and high plateau regions including the Himalayas and Plateau of Tibet (*limited evidence*, *high agreement*). Mean temperature bias of RCMs is within ± 3°C over West Asia (*high confidence*), but RCMs have a tendency to overestimate precipitation amounts in almost all parts of the region (*low confidence*). {Atlas.5.3.2.3}

Over the Arabian Peninsula the highest rate of warming (0.98°C per decade) is projected for its northern part under the higher emission scenario during the 21st century *(high confidence).* Strong decreases in precipitation (–30% to –50%) are projected in the north-western part of the Arabian

Peninsula with the area of largest increase (8.6% per decade) found over the southern part *(medium confidence).* Projected warming is between 1°C and 2°C for SSP1-2.6 and 4°C and 6°C for SSP5-8.5, while precipitation is projected to change by –3% to 41% for SSP1-2.6 and 12% to 126% for SSP5-8.5 (*medium confidence*). {Atlas.5.3.4.4}

Widespread warming over West and Central Asia is projected at the end of the 21st century compared to 1971–2000, varying from 2.5°C to 8°C depending on the season and scenario *(high confidence)* with the maximum warming rate in the northern part of the region in summer *(medium confidence)*. {Atlas.5.3.4.4}

Strong spatiotemporal differences with overall decreasing precipitation are projected over West Asia *(low confidence)* and in the central and northern parts of Central Asia in summer, while relatively stronger increasing rates are projected over north of Central Asia in winter *(medium confidence)*. {Atlas.5.3.4.4}

Atlas.5.3.2.1 Key features of the regional climate and previous findings from IPCC assessments

Key features of the regional climate

The climatic regions defined for Middle East Asia include the Arabian Peninsula [ARP] and the West and Central Asia region [WCA] (see Figure Atlas.2:).

The Arabian Peninsula region is composed of seven countries located in southwest Asia and experiences semi-arid or arid desert climate. It has very low annual mean precipitation and very high temperature. The climate of the Arabian Peninsula is influenced by ENSO. The wet season is mainly from November to April (NDJFMA) and the dry season is from June to August (JJA). Rainfall is confined mostly to the south-western part of the Peninsula

The West and Central Asia region is separated from Eastern Europe by the Caucasus Mountains and borders the West Siberia subregion to the north. It is adjacent to the [ARP] and South Asia [SAS] regions to the south and extends west to east from the Mediterranean region [MED] to the Tibetan Plateau [TIB]. The local climate of West and Central Asia is typically semi-arid or arid with a strong gradient in both precipitation and temperature from the mountains to the plains and from north to south.

Previous findings from IPCC assessments

Recent AR6 IPCC Special Reports have stated for the Middle East subregions particularly the following.

Even for 1.5°C and 2°C of warming, the strongest increase in hot extremes is projected in both subregions ARP and WCA, with more urban populations exposed to severe droughts in West Asia, while an increase of heavy precipitation events is projected in mountainous regions of Central Asia (IPCC, 2018d).

These changes in temperature and precipitation regimes will *likely* result in a higher risk of desertification in Central Asia, second after the South Asia subregion in the number of dryland population exposed and vulnerable to water stress, with increasing drought intensity and habitat degradation. Higher temperatures with less precipitation will result in higher risks of wildfire and dust storms exacerbated by land-use and land-cover changes in the region with consequent effects on human health due to transport of particulate matter, pollutants, pathogens and potential allergens over large distances. Further drying up of the Aral Sea in Central Asia will *likely* have negative impacts on the regional microclimate adding to the growing wind erosion in adjacent deltaic areas and deserts. Another effect of the Aral Sea desiccation is the salinization of the major rivers Amudarya and Syrdarya used for irrigation, that is already resulting in a reduction of the vegetation productivity including croplands. At the same time, projected increase of precipitation intensity in Central Asia and the Arabian Peninsula are also *likely* to lead to higher soil erosion by water particularly in winter and spring due to floods caused by increasing number of heavy precipitation events (SRCCL; IPCC, 2019a).

Middle East Asia includes high mountains where temperature increases have outpaced the global rate,

indicating enhanced warming above 500m above sea level. The warming peaks above 5,000m above sea level. according to evidence based on combining in situ observations (often scarce at high elevations) with remote sensing and modelling approaches on the Tibetan Plateau. A very strong interannual and decadal variability as well as scarce in situ records of mountain snow cover prevent from quantifying recent trends in High Mountain Asia. However, the most pronounced effect of a further warming is projected on snow cover and glaciers in high latitudes and mountains where projections indicate a continued increase in winter runoff in many snow and/or glacier-fed rivers over the 21st century (*high confidence*) regardless of the climate scenario due to increased winter snowmelt and more precipitation falling as rain in addition to increases in precipitation in some basins in the region. There is *high confidence* that summer runoff will decline over the 21st century in many basins for all emission scenarios due to less snowfall and decreases in glacier melt after peak water which will generally be reached before or around the middle of the century (*robust evidence*, *high agreement*) . A global-scale projection suggests that decline in glacier runoff by 2100 (RCP8.5) may reduce basin runoff by 10% or more in at least one month of the melt season in several large river basins originated in High Mountain Asia during dry seasons (SROCC; IPCC, 2019b).

There is a growing amount of climate research involving climate models in the Middle East Asia region compared with AR5 stimulated by the CORDEX results in particular (Top et al., submitted).

CMIP5 models generally have difficulties in reproducing the present mean temperature and precipitation climatology for the subregions represented in this area, which is partly related to the poor spatial resolution of the models preventing the resolution of the complex mountainous terrain dominating Middle East Asia. However, the scarceness of observational data and issues related to comparison of observations with coarse-resolution models add to the uncertainty regarding model quality (Christensen et al., 2013). The IPCC AR5 stated that temperature is generally better simulated than precipitation in terms of the amplitude and phase of the seasonal cycle in accordance with a comparison of CMIP3 and CMIP5 seasonal cycles for different regions. Even though the multi-model mean is close to observations, the inter-model spread remains large, particularly in high-latitude regions in winter and in regions with steep orography such as Central Asia. The largest systematic biases occur in annual total precipitation over land regions occur in regions which are characterized by high orography and/or a large fraction of solid precipitation such as Tibetan Plateau, both of which are expected to introduce a negative bias in gauge-based precipitation (Flato et al., 2013b). The IPCC AR5 stated that CMIP5 models tend to be able to simulate West Asia's basic climate state as well as the main phenomena affecting it with some fidelity, but the region is at the fringes of the influence of different drivers of European, Asian and African climates and remains poorly analysed in the peer-reviewed literature with respect to climate model performances (Christensen et al., 2013).

According to the IPCC AR5, it is *very likely* that temperatures will continue to increase over West Asia due to models' *high agreement*. On the other hand, projections of an overall reduction in precipitation had *medium confidence* due to models' *medium agreement* on projected precipitation changes. The CMIP5 model projections for this century are for further warming in all seasons, while precipitation shows some distinct subregional and seasonally dependent changes, characterized by model scatter (Christensen et al., 2013). Over Central Asia, the IPCC AR5 stated that CMIP5 projected a temperature increase for both summer and winter seasons. Less annual variation is found in temperature rise over Central Asia and the Tibetan Plateau. Model agreement is lower on changes for both winter and summer precipitation for the whole region. According to the AR5, the level of agreement in projections of precipitation was positive and significantly above the 20-year natural variability, and therefore suggested that there is *medium confidence* in the sign of the projected change in future precipitation (Christensen et al., 2013). One of the conclusions of AR5 was that in order to have a better understanding of climate of the region, results of fine resolution regional climate models also need to be assessed.

Atlas.5.3.2.2 Assessment and synthesis of observations, trends and attribution

Since the AR5, there has been an increasing number of studies on climate in the region, particularly over the Arabian Peninsula, which were based on surface observations, and regional and global climate model simulations. These studies indicated a warming as well as an increasing trend for climate extremes (see also Figure Atlas.27:). Estimated observed trends in precipitation indicate declines over most of the region where

the trends are significant, though some areas of increase are also found (Figure Atlas.27:).

[START Figure Atlas.27: HERE]

Figure Atlas.27: (a–b) Mean observed trends of annual mean surface air temperature and precipitation for three datasets (CRU TS, BERKELEY and EWEMBI for temperature; CRU TS, GPCC and GPCP for precipitation). Hatching indicates regions where no or only one dataset provides a significant trend. Linear trends are calculated for the common 1980–2014 period and expressed in °C per decade (temperature) and % relative change per decade (precipitation) with respect to the climatological mean over this period.
(c–f) Climate change projections of annual mean surface air temperature and precipitation from CMIP5 (30 models) and CMIP6 (17 models) calculated as the differences in the climatological average for RCP8.5 and SSP5-8.5 respectively, for the period 2041–2060 with respect to the historical 1995–2014 period and expressed as °C (temperature) and % relative change (precipitation). Hatching indicates weak model agreement on the sign of the change (less than 80% as defined in Nikulin et al., 2018).
(g–h) Regional mean changes in annual mean surface air temperature and precipitation for the two Middle East Asia regions (WCA and ARP). The top row shows the median (dots) and 10th–90th percentile range across each model ensemble for annual mean temperature changes, for two datasets (CMIP5 and CMIP6) and two scenarios (SSP1-2.6/RCP2.6 and SSP5-8.5/RCP8.5). The first four bars represent the additional warming projected relative to the historical baseline 1995–2014 period to reach the two global warming levels (GWL; +1.5°C and +2°C) and the remaining six projected changes over three time periods (near-term 2021–2040, mid-term 2041–2060 and long-term 2081–2100) compared to this same historical baseline period. The bottom row shows scatter diagrams of temperature against precipitation changes, displaying the median (dots) and 10th–90th percentile ranges for four future periods (2021–2040, 2041–2060, 2061–2080, 2081–2100) compared to the historical baseline period, as obtained from CMIP6 projections for three scenarios (SSP1-2.6, SSP2-4.5 and SSP5-8.5). Changes are absolute for temperature and relative for precipitation.
(The script used to generate this figure is available online (Atlas GitHub, 2020) and similar results can be generated in the Interactive Atlas for flexibly defined seasonal periods.)

[END Figure Atlas.27: HERE]

Observed warming over the northern part of the Arabian Peninsula is higher than over the southern part. The rate of increase in mean temperature is 0.10°C per decade for the period 1901–2010 (Attada et al., 2019). The rate of increase was 0.52°C (*likely* in the range 0.21 to 0.73°C) per decade over the Arabian Peninsula for the period 1978–2018 (Almazroui et al., submitted, a). The highest (lowest) rate of temperature increase is observed in the northern (southern) Peninsula. Over the region, the number of warm days and nights increased, while the number of cold days and nights decreased (Almazroui et al., 2014; Islam et al., 2015). In the region, the temperature is likely to be influenced by SST variations over the tropical oceans and closely associated with ENSO, NAO and AO (Attada et al., 2019). Enhanced rainfall may occur in the wet season during the El Niño phase of ENSO (Kang et al., 2015; Niranjan Kumar et al., 2015; Abid et al., 2018; Kamil et al., 2019), while precipitation may reduce during the La Niña phase of ENSO (Atif et al., 2020). Observational records for the Arabian Peninsula show a decreasing trend of precipitation with mean value of 6.3 mm (*likely* in the range –30 mm to 9.0 mm) per decade for the period 1978–2018 with large interannual variability over Saudi Arabia, which covers 80% of the Arabian Peninsula (AlSarmi and Washington, 2011; Almazroui et al., 2012; Donat et al., 2014). Almazroui and Saeed (2020) showed that extreme events contributed enormously (20–70%) to total precipitation over the Arabian Peninsula.

The region of Central Asia accounts for one third of all arid and semi-arid regions globally. Huang et al. (2017) pointed out that the dryland showed an enhanced warming over the past century, when surface warming over global drylands (1.2°C to 1.3°C) has been 20–40% higher than that over humid lands (0.8°C to 1.0°C). The meteorological stations located in Central Asia are sparsely scattered and most of them are distributed in the plains with elevation less than 2 km. Meanwhile some weather stations have stopped operating since 1991 when the Soviet Union collapsed (Huang et al., 2014a). There is *very high confidence*

based on *robust evidence* and *high agreement* that the scarcity of observation stations in mountainous areas with the decline of observation sites in Central Asia increase the uncertainty of the long-term warming estimates.

Giese et al. (2007) used observed data from 1950 to 2000 in lowland basins and foothills in valley and basin locations in Central Asia. They showed a warming with a rate of 3.1°C to 3.7°C per 100 years. Chen et al. (2009) found that the average annual mean temperature increase rate of four subregions in Central Asia is 0.18℃ per decade, with a greater increase rate in winter (0.21℃ per decade). Feng et al. (2018) analysed the extreme temperature by using 108 stations in Central Asia from 1981 to 2015. All extreme temperature values exhibited a positive trend on an annual scale, but maximum temperature increased faster than minimum temperature, and most warm extreme events mainly occurred in spring and summer. Based on data from 22 observed meteorological stations operating between 1960 and 2011 in northern Xinjiang, Xu et al. (2015) reported that both temperature and precipitation have increased significantly (0.35℃ per decade, 11.2 mm per decade). Aizen et al. (1997) analysed 110 sites located in Tien Shan mountain, the average warming rate was 0.01℃ yr^{-1} and the precipitation increased by 1.2 mm yr^{-1} over the past half century while a decrease in snow resources have been observed.

A strong increase in surface air temperature with range 0.27°C – 0.47°C per decade and an overall wetting tendency with precipitation trend between 1.3 mm – 4.8 mm per decade have been found over central Asia between 1960 and 2013 (*very high confidence*) (Han and Yang, 2013; Li et al., 2013; Hu et al., 2014, 2017; Huang et al., 2014a; Deng and Chen, 2017; Zhang et al., 2019a, 2017; Guo et al., 2018b; Haag et al., 2019; Yu et al., 2019).

Recently gridded data have been used to detect the variations in temperature and precipitation in Central Asia. Based on reanalysis data, CRU and observed data, Hu et al. (2014) showed a strong increase in near-surface air temperature of 0.39℃ (ranging from 0.36℃ to 0.42℃) per decade averaged over Central Asia from 1979 to 2011. Warming is most prominent in the spring with rates ranging between 0.64℃ and 0.82℃ per decade. Hu et al. (2017) examined the temporal variation of annual precipitation over Central Asia based on GPCC V7 data. An overall increasing trend (0.66 mm per decade) is found for the entire region from 1901 to 2013. Song and Bai (2016) used GPCC precipitation data to detect the spatial and temporal trend of precipitation in Central Asia from 1960 to 2013. No significant trends were observed for annual precipitation in Central Asia, while precipitation in winter displayed a significant increase (0.11 mm y^{-1}). However, the performance of the satellite-based precipitation products vary greatly (Guo et al., 2017c). These gridded products have difficulties in accurately estimating the mountainous precipitation (Chen et al., 2019b). Guo et al. (2017) found that CMORPH and TRMM products fail to capture the precipitation events in the ice/snow covered region in winter and show great false-alarm percentage in summer. They found that satellite-only products have large systematic and random errors and that the gauge-corrected GSMAP performs better than other products with skill in reducing various type of errors. Over Central Asia, the satellite precipitation products have difficulties in accurately estimating the mountainous precipitation. Satellite-only products have large systematic and random errors (*very high confidence*) (Song and Bai, 2016; Guo et al., 2017c; Hu et al., 2017; Chen et al., 2019b).

There is *medium evidence* but *high agreement* that agriculture intensification through oasis expansion in Xinjian region has increased summer precipitation in the Tianshan mountain (Zhang et al., 2009, 2019b; Deng et al., 2015; Guo and Li, 2015; Yao et al., 2016; Xu et al., 2018; Cai et al., 2019). However, there is *very low confidence* of the impact of oasis expansion on the temperature warming trend (Han and Yang, 2013; Li et al., 2013; Yuan et al., 2017).

There is *very high confidence* (*robust evidence*, *high agreement*) that the shrinking of the Aral sea has induced an increase of surface air temperature around the Aral sea region in the range of 2℃ to 6℃ (Baidya Roy et al., 2014; McDermid and Winter, 2017; Sharma et al., 2018). There is however *very low confidence* on its impact on precipitation (Chen et al., 2011; Jin et al., 2017).

An overview of observational datasets for North, West and Central Asia is given in Table Atlas.A.1 with the corresponding domain covered, climate variable available, data type, spatial and temporal resolution and

period covered for each data set.

Atlas.5.3.2.3 Assessment of model performance

There is *limited evidence* about performance of regional climate models in representing the mean present climate of West and Central Asia subregions due to the limited number of studies on evaluating models over this region, but scientific publications on the topic are just emerging (Russo et al., 2019; Top et al., submitted) particularly from the CORDEX initiative (Giorgi et al., 2009). The evaluation of regional climate models REMO and ALARO-0 driven by ERA-Interim at 25 km resolution over the domain CORDEX-CA showed that the choice of the observational dataset has an impact on the scores but in general both models reproduce reasonably well the spatio-temporal patterns for temperature and precipitation (Top et al., submitted). The evaluation of minimum and maximum temperature demonstrates that both models underestimate the daily temperature range. The evaluation of regional climate model RegCM3 for the winter climate of Central Southwest Asia, focusing on the mean model climatology of temperature and precipitation, showed that the model driven by ERA40 reanalysis dataset can reproduce well the climatology of temperature, precipitation and storms over the region. (Syed et al., 2010) also found that RegCM3 captures the observed influence of NAO and ENSO on climate, particularly in the region of northern Pakistan, Afghanistan and Kazakhstan.

According to results based on implementation of the high-resolution regional climate model REMO driven by the ECHAM dataset over the region centred over Central Asia, the simulated large-scale precipitation and temperature patterns are in good agreement with observations. Results show that in the high altitudes of the mountainous regions of the study area, REMO simulates colder temperatures than observed but the pattern of simulated precipitation is quite close to observations thanks to the higher resolution of the regional model. Nevertheless, it is difficult to evaluate the performance of regional climate models, because the model simulations have a higher resolution than the observational data and station coverage is low. Those stations which exist are usually situated in valleys and not at the high elevations (Mannig et al., 2013). RegCM4.3.5 simulations driven by two different global climate models adequately reproduced the observed climatology in the region with very few exceptions which are *very likely* due to the high topographical characteristics of the domain (Figure Atlas.28:). Results show that a cold bias occurred in air temperatures over mountainous and high plateau regions of the domain including the Himalayas and Tibetan Plateau respectively, regardless of seasons and the boundary conditions used. According to the study, this result can be explained by inadequate observational data due to a lack of climatological and meteorological stations in that region of the domain. According to the results, global models and regional climate models show better performance than the ERA-Interim reanalysis dataset with respect to observational datasets (Ozturk et al., 2017).

[START Figure Atlas.28: HERE]

Figure Atlas.28: Seasonal air temperature (°C, blue to red) and precipitation (mm day^{-1}, pale green to blue) for the domain centred over Central Asia for the period 1981–2000, for ERA-Interim dataset (ERA; a–d), RegCM4.3.5 driven by the ERA-Interim (MOD; e–h) and CRU observational dataset (OBS; i–l), for spring (a, e, i), summer (b, f, j), autumn (c, g, k) and winter (d, h, l) seasons (Ozturk et al., 2017).

[END Figure Atlas.28: HERE]

According to a study which focuses on the evaluation of 30-year long WRF climate simulations and the comparison between three different radiation parameterization configurations over the MENA-CORDEX domain including West Asia, for most of the extent of the domain (≈ 70%), the temperature biases are lower than ± 2°C (Zittis and Hadjinicolaou, 2017) in the model simulations. Most of the mean temperature biases are related to night-time minimum temperature misinterpretations that are mostly connected to biases of the long-wave radiation fluxes of the surface. Therefore, they suggest its use for climate/weather simulations over similar environments (Zittis and Hadjinicolaou, 2017). Another study based on ERA-Interim driven COSMO-CLM simulations over the CORDEX-MENA domain (Bucchignani et al., 2016) stated that the

model proved to be very sensitive to changes in physical parameters. The optimized configuration characteristics consist in the new parameterization of albedo, based on Moderate Resolution Imaging Spectroradiometer data, and the new parameterization of aerosols, based on NASA-GISS aerosol optical depth (AOD) distributions. Mean absolute error values obtained for the considered variables are about 1.2°C for temperature, about 15 mm per month for precipitation, about 9% for total cloud cover, and about 0.6 hPa for mean sea-level pressure. COSMO-CLM is relatively able to improve the simulated main climate features of this very complex area (Bucchignani et al., 2016). The ability of the RegCM4.4 regional climate model to reproduce the observed climatology over the same domain is found sufficient especially for dry regions with an overall temperature bias of the model within ± 3.0°C. Precipitation amounts were overestimated by the RCM in almost all parts of the domain for all seasons except the Sahara Desert, the Western Sahara, and the Sahel regions with hyper-arid/arid and semiarid climates (Ozturk et al., 2018).

For 22 CMIP3 models, most of them simulate warm (cold) bias over the southern (central and northern) parts of the Arabian peninsula. Similar to the temperature, the precipitation bias also varies among the CMIP3 models (Almazroui et al., 2017c). A large portion of the Arabian Peninsula is dominated by the dry bias in most of the model simulations. However, some CMIP3 models also display a wet bias, especially over the south-eastern parts of the peninsula. For 30 CMIP5 models, the simulated temperature bias with respect to the surface observation indicates that overall 18 models fall within one standard deviation and 12 fall outside this range (Almazroui et al., 2017b). Over the Arabian Peninsula, a cold bias for most of the months and warm bias for summer months are reported by Lelieveld et al. (2016) in 26 CMIP5 models. The model precipitation bias with respect to the surface observation indicates that most of the models underestimate wet season precipitation and overestimate dry season precipitation with 26 models falling within one standard deviation. For the Arabian Peninsula, the evaluation of five GCMs (HadGEM2, GFDL, CNRM, CanESM2, and ECHAM6) downscaled with an RCM over the CORDEX-MENA domain identified that most models had a cold bias (of about 0.70°C) and underestimated precipitation over the Arabian Peninsula by 13% compared to observations (Almazroui, 2016). A warm (cold) bias over the south-eastern (western) parts of the peninsula is reported by Syed et al. (2019).

Atlas.5.3.2.4 Assessment and synthesis of projections

Individual studies based on the future climate projections using global climate model outputs over West and Central Asia countries including Armenia (Vermishev and Moir, 2015; Gevorgyan et al., 2016a), Azerbaijan (Osborn et al., 2016), Georgia (GMENR, 2015), Iran (IDOE, 2017), Iraq (Salman, Shahid, Ismail, Chung, & Al-Abadi, 2017), Tajikistan (Aalto et al., 2017) and Turkmenistan (Allaberdiyev, 2010) (for more detail see Table Atlas.A.2) stated that an increase in temperatures are expected by the end of the century. The intensity of future warming depends on season, timescale and scenario and will be approximately up to 7°C. On the other hand, there is a large uncertainty about future projections of precipitation. Results show a general decrease in precipitation and an opposite change is predicted over high-mountain regions, where precipitation is projected to increase (Aalto et al., 2017; Salman et al., 2018).

Projections from the CMIP5 and CMIP6 ensembles shown in Figure Atlas.27: are for temperatures to continue to increase into the future with further annual mean warming of over 2°C by mid-century and up to 6°C by the end of century under the RCP8.5 scenario (with greater warming projected by the CMIP6 ensemble). Conversely there is no clear signal in precipitation. Overall, the projections by the end of the century (2081–2100) indicate little overall change, although with a tendency for reduced precipitation, particularly for the higher emission scenarios. However, regardless of the sign of precipitation change in the high-mountain regions of Central Asia, the influence of warming on the snow pack will *very likely* cause important changes in the timing and amount of the spring melt (Diffenbaugh et al., 2013).

According to the results based on dynamical downscaling of global climate models, widespread warming will occur in the Central Asia region in the 21st century. Results of the regional climate model REMO driven by ECHAM global dataset based on the SRES-A1B emission scenario show a warming which is above the global average in the largest part of the model domain for the 2071–2100 period compared to 1971–2000. The warming peaks are projected over high elevations and the northern part of the domain during winter. On the other hand, results show a decrease in summer precipitation in the monsoonal region and an increase in

winter precipitation over the northern part of the model domain (Mannig et al., 2013). For the highest emission scenario outputs (RCP8.5) of the regional climate model RegCM4.3.5 driven by two boundary conditions of the HadGEM2-ES and the MPI-ESM-MR global models for the 2071–2100 period, the increase in temperature will be stronger, varying from 5°C up to 8°C. In the future, a decrease in precipitation is also expected over some countries such as Turkey, Iran, Afghanistan and Pakistan (Ozturk et al., 2017).

According to the results based on statistical downscaling of 18 CMIP5 general circulation models (GCMs) under RCP4.5, precipitation increases at an average rate of 4.63 mm per decade in Central Asia during the 2021–2060 period relative to 1965–2004, while the temperature increases at a rate 0.37°C per decade. Results show that changes in precipitation are projected to have strong spatiotemporal differences with decreasing trends occurring in the central and southern parts of Central Asia during summer. The maximum expected warming rate appeared in the northern part of Central Asia while warming was most conspicuous in summer among all seasons (Luo et al., 2019).

Based on the outputs of the five out of 28 CMIP5 models that performed best in simulating the current climate of the region, relatively strong increasing rates in annual precipitation (over 3 mm per decade in RCP2.6 and over 6 mm per decade in RCP4.5 and RCP8.5) are located over northern Central Asia and the north-eastern Tibetan Plateau (Huang et al., 2014a).

According to the projections of changes in temperature and precipitation from these five GCMs for the 2071–2099 period compared to the 1951–1980 baseline for the Central Asia region, warming over the land is expected to be greater than the global mean. The multi-model mean of boreal summer warming in 2071–2099 is projected to be about 2.5°C and 6.5°C above 1951–1980 at 2°C and 4°C global warming levels respectively. Projections are for drier conditions over the southwest part and wetter over the northeast. At a 4°C warming level, Turkmenistan and parts of Tajikistan and Uzbekistan *likely* receive less rain, with the multi-model mean annual precipitation dropping by about 20% and somewhat stronger relative decreases in summer (Reyer et al., 2017).

Lioubimtseva and Cole (2006) examined the key uncertainties of climate change in Central Asia. Global climate models project temperatures in arid Central Asia will increase by 1°C–2°C in 2031–2050, with the greatest increases in wintertime, but some models project greater aridity in the future although others project less aridity. Yang et al. (2017) using 21 GCMs to detect future climate change in Central Asia, showed that at the end of the 21st century (2070–2099) under RCP8.5, compared to the control period (1976–2005), annual mean temperature and mean annual precipitation will rise by 4.8°C and 5.2% respectively, while mean annual snowfall will decrease by 26.5%. Luo et al. (2018) used 37 GCMs outputs statistically downscaled for precipitation and temperature in Xinjiang, China in order to define spatiotemporal characteristics of climate trends. For the 2021–2060 period, a pronounced increase of 0.27°C to 0.51°C per decade is projected for temperature while precipitation change is estimated to be between –1.7% to 6.8% per decade varying seasonally and spatially; a decrease of precipitation emerged in the western region of Xinjiang during summer. More extreme rainfall events are predicted to occur during summer and autumn.

Results of studies for the CORDEX-MENA domain comprising West Asia have found an overall strong warming for both the RCP4.5 and RCP8.5 scenarios (Bucchignani et al., 2018; Ozturk et al., 2018). This warming is characterized by a marked seasonality, ranging from a minimum of 2.5°C in winter to a maximum of 8°C in summer. In winter and spring seasons, the largest increases were projected over high-altitude areas of Turkey, northern Iran and Afghanistan, in particular over the Hindu Kush (see Atlas.5.10.1) – an 800-km long mountain range that separates climate zones B and D based on Köppen-Geiger evaluation. Large increases were also projected at the boundary between Iran and Iraq. Results of precipitation projections over subregion B and D which includes West Asia were not significant (Bucchignani et al., 2018).

In order to reduce knowledge gaps at the time of the AR5 on changes in climate over the Arabian Peninsula, simulations of CMIP3 and CMIP5 models were analysed (e.g. Barfus and Bernhofer, 2014; Almazroui et al., 2016, 2017b, 2017c; Almazroui, 2019; Syed et al., 2019). The 30 CMIP5 models ensemble under RCP8.5

scenario displayed an increase in temperature over the Arabian Peninsula that varies spatially from 1°C to 2°C in the near future (2021–2050), and 3.4°C to 5.0°C in the far future (2070–2099) (Almazroui et al., 2017b). The ensemble of 30 CMIP5 model datasets over the Arabian Peninsula indicates an increase in temperature, higher in the northern Peninsula than the southern part (Almazroui et al., 2017a). In the northern (southern) Peninsula, the projected warming is *likely* to be 0.60°C (0.53°C) per decade under a high-emission (RCP8.5) scenario. Three CMIP5 models (HadGEM2, CanESM and ECHAM6) downscaled by an RCM over the CORDEX-MENA domain indicate that the number of hot days (daily maximum temperature ≥ 50°C) in the future is *likely* to increase and the number of cold nights (daily minimum temperature ≤ 5°C) is *likely* to decrease faster over the Arabian Peninsula (Almazroui, 2019). Three CMIP5 models (ECHAM6, GFDL and HadGEM2) downscaled by an RCM indicate that the summer maximum average temperature over the Gulf Cooperation Council (GCC) states is not projected to exceed 52°C, while daily maximum temperature is projected to exceed 55°C in some cities in the GCC region by the end of the 21st century under RCP8.5 (Almazroui, submitted). The 19 CMIP6 models indicate the continuation of increase in temperature in the future climate, increase of projected temperature is 1.6°C (1.2°C to 2.0°C) and 5.3°C (4.1°C to 5.8°C) under SSP1-2.6 and SSP5-8.5 respectively at the end of 21st century with respect to the base period of 1981–2010 (Almazroui et al., submitted, a). The same higher temperature increasing in the northern peninsula (5.7°C) is projected as compared to the southern Peninsula (4.8°C) under SSP5-8.5. Under the high-emission scenario, a higher rate of warming (0.98°C per decade) is projected for the northern peninsula as compared to the southern peninsula (0.75°C per decade).

Precipitation is projected to *likely* decrease over the northern area of the Arabian Peninsula and increase over the southern parts. However, at the central area of the peninsula, high variability of precipitation is projected. At the annual scale, it is very likely that precipitation will decrease (increase) at the rate of −0.14% (3.0%) per decade for RCP8.5 in the northern (southern) Arabian Peninsula (Almazroui et al., 2017a). For SSP1-2.6 and SSP5-8.5, precipitation is projected to increase by 1.1 % (–2.6 to 40.8%) and 28.4 % (12.0 to 125.8%) respectively over the Arabian Peninsula at the end of 21st century while the north-western region is projected to get less precipitation and the southern region is projected to get more precipitation (Almazroui et al., submitted, a). The largest increase is projected over the southern peninsula (8.6% per decade), while for the north-western part a decrease is projected with maximum change (-30% to 50%). The results of CMIP6 are in line with the results of CMIP3 and CMIP5, however for precipitation the variability in the central area is less in case of CMIP6 models as compared to CMIP5. The uncertainty associated with precipitation over the Arabian Peninsula is large because of very low annual amounts and high variability. In a recent study, Almazroui and Saeed (2020) found that, irrespective of the frequency, projected extreme precipitation events are *likely* to intensify over the peninsula.

Table Atlas.A.2 gives on overview of national and other climate change assessments for the countries in North, West and Central Asia. Country specific assessments have different reference periods and time horizons for projected climate change. These also vary in terms of the emissions scenarios used.

Atlas.5.3.3 North Asia

Regional executive summary

Annual surface air temperature *very likely* has increased over most territories of North Asia based on observational datasets. The most pronounced warming has been found in spring in East Siberia and over the Russian Far East, strengthening from the South to North territories of the sub-regions with linear trend 0.8°C-1.2°C per decade for the 1976–2014 period (*high confidence*). Temperature decrease was identified just in winter in the southern part of Western and Eastern Siberia *likely* due to midlatitude circulation variability, but the decrease has moderated from –0.6°C per decade for 1976–2012 to –0.3°C per decade for the longer 1976–2018 period due to warmer winters in the last years (*high confidence*). {Atlas.5.3.3.2}

Annual precipitation sums *very likely* have increased over the most territory of North Asia based on observational datasets. The highest precipitation increase predominantly was observed over some regions of Siberia and the Russian Far East with estimated trends of 5–15 mm per decade for the 1976–2014 period

(*medium confidence*). The decrease in annual precipitation sums was observed to be up to –20 mm per decade for the 1976–2014 period over the southern and north-eastern parts of the Russian Far East, namely over the Kamchatka and the Chukchi Peninsulas (*medium confidence*). {Atlas.5.3.3.2}

Most of the CMIP5 GCMs overestimate the annual mean air temperature and precipitation over the North Asia region (*medium confidence*). The biases in the simulated annual surface air temperature primarily comes from winter (DJF) season, while the model biases in other seasons are relatively smaller (*medium confidence*). Most of the GCMs are able to represent the observed decadal temperature trend (*medium confidence*), but CMIP5 GCMs fail to capture the decreasing temperature trend over the southern East Siberia in winter (*high confidence*). {Atlas.5.3.3.3}

Surface air temperature and precipitation in the North Asia region are projected to further increase based on CMIP5/CMIP6 projections (*medium confidence*). Temperature change is projected in the range from 3°C in summer to 4.9°C in winter based on RCP4.5 scenario, and from 5.6°C in summer to 9.7°C in winter based on RCP8.5 scenario, whereas the projected precipitation increase is 9–22% (summer-winter in RCP4.5) and 9–56% (summer-winter in RCP8.5) for the 2080–2099 period comparatively to the 1981–2000 period (*medium confidence*). {Atlas.5.3.3.4}

Atlas.5.3.3.1 Key features of the regional climate and previous findings from IPCC assessments

Key features of the regional climate

The North Asia region, extending from the Tibetan plateau to the Arctic and mostly covering the interior of a large continent, is mainly influenced by weather systems coming from the west or south, giving some dependency on the atmospheric angular momentum (AAM) and the North Atlantic Oscillation/Northern Annular Mode (NAO/NAM), with associated atmospheric blocking as an additional phenomenon of influence related to the latter. In particular, the variability and long-term change of the climate system in the region are closely related to variations of the NAO and NAM. In addition, weather and climate of the region are strongly influenced by the Siberian High that exhibited a pronounced decadal-to-multidecadal variability with a recent (1998 to 2012) strengthening and northwest-ward expansion. As part of the polar amplification, large warming trends (particularly strong in the cold season November to March) were observed in North Asia in recent decades associated with increasing trends of heavy precipitation events (Christensen et al., 2013).

The climatic region defined as North Asia lies from the Ural Mountains in the west to the Pacific Ocean in the east and from the Russian Arctic [RAR] in the north to West and Central Asia [WCA], Tibetan Plateau [TIB] and East Asia [EAS] in the south. In AR6 it includes three subregions in the reference regions (see Figure Atlas.2:):

- [WSB] West Siberia has a continental type of climate with warm summers and cold winters.
- [ESB] East Siberia is characterized by the severely continental climate with harsh, long winters and short, hot summers. This region is influenced by high atmospheric pressure areas and there is a high amplitude in daily and seasonal temperature variations.
- [RFE] Russian Far East is a monsoon-influenced region with cold winters and wet summers in the south and cold winters almost without precipitation in the north.

The most recognizable features of the region are boreal forests and permafrost. Substantial permafrost carbon exists below 3 m depth. Deep carbon (> 3 m) has been best quantified for the Yedoma region of Siberia, characterized by wind- and water-moved permafrost sediments tens of meters thick. The Yedoma region covers a 1.4 x 10^6 km^2 area that remained ice-free during the last Ice Age and accounts for 327–466 Pg C in deep sediment accumulations below 3 m (SROCC; IPCC, 2019b). Permafrost thaw and loss of ground ice due to warming causes the land surface to subside and collapse into the volume previously occupied by ice, resulting in disturbance to overlying ecosystems and human infrastructure. Ice rich permafrost areas where impacts of thaw could be the greatest include not only the Yedoma deposits but Gydan peninsulas of West Siberia, and smaller portions of Eastern Siberia contain buried glacial ice bodies of significant thickness and extent (SROCC).

WGII AR5 and SR1.5 (IPCC, 2018a) identified Siberian ecosystems in Asia as one of the threatened systems (*Reason for Concern 1 – RFC1*), where impacts accrue with greater warming and impacts at 2°C are expected to be greater than those at 1.5°C with *medium confidence*.

The aridisation of the climate has been identified in the south of Eastern Siberia between 1976 and 2016 that caused an extension of the steppes polewards with corresponding migration of mammal species. In the forest areas of the subregion, both positive and negative effects of climate change have been observed recently. There has been an increase in forest productivity in most of boreal Siberia due to the extension of the vegetation period. At the same time, there has been a decrease in forest productivity due to increased risk of wildfire, natural disturbances and tree mortality caused by migrating insects and other tree diseases (SRCCL; IPCC, 2019a).

Previous findings from IPCC assessments

In the previous IPCC assessment cycles three subregions defined in the current AR6 as North Asia merged with East Europe and partly Arctic subregions and were considered as either Northern Eurasia, or Russia in AR4/AR5. Analysis of North Asia together with Arctic is appropriate particularly for river discharge since the main rivers of Arctic drainage flow over West and East Siberia.

In WGI AR5 (IPCC, 2013b) for the Arctic drainage areas, it was found that upward trends in streamflow were not accompanied by increasing precipitation, especially over Siberia, based on available observations. Observation data are known to be sparse and exhibit large cold-season biases in the Arctic drainage areas and hence there are large uncertainties in using these datasets to investigate the influence of precipitation on streamflow. Surface water area reduction has been observed in discontinuous permafrost of central and southern Siberia. Increased evaporation from warmer/longer summers, decreased recharge due to reductions in snow melt volume, and dynamic processes such as ice-jam flooding are important considerations for understanding observed surface water area change across the Arctic (SROCC). In AR5 WGII, although the most evident flood trends appear to be in northern high latitudes, where observed warming trends have been largest, in some regions no evidence of a trend in extreme flooding has been found, e.g. over Russia, based on daily river discharge. Other studies for Asia show varying trends in the magnitude and frequency of floods and there is currently no clear and widespread evidence for observed changes in flooding except for earlier spring flows in snow-dominated regions.

SROCC has concluded that boreal forest vegetation shows trends of both greening and browning over multiple years in different regions in satellite records (*high confidence*). Here, patterns of changing vegetation are a result of direct responses to changes in climate (temperature, precipitation and seasonality) and other driving factors for vegetation (nutrients, disturbance) similar to what has been reported in tundra. While boreal forest may expand at the northern edge, climate projections suggest that it could diminish at the southern edge and be replaced by lower biomass woodland/shrublands (*medium confidence*). Furthermore, changes in fire disturbance are leading to shifts in landscape distribution of early and late successional ecosystem types. Fires that burn deeply into the organic soil layer can alter permafrost stability, hydrology and vegetation. Loss of the soil organic layer exposes mineral soil seedbeds, leading to recruitment of deciduous tree and shrub species that do not establish on organic soil. This recruitment has been shown to shift post-fire vegetation to alternate successional trajectories of increasing deciduous forest at the expense of evergreen forest in Russian boreal forests (*medium confidence*).

In WGI AR5, North Asia is considered together with Central Asia in the regional chapter (Christensen et al., 2013). The CMIP5 models generally have difficulties in representing climatological means of both temperature and precipitation for the sub-regions represented in this area, which is partly related to the coarse resolution that is not able to resolve the complex mountainous terrain on the south border of the region. But the scarceness of observational data in northern parts of the region and issues related to estimation of biases with coarse resolution models add to the uncertainty in the model results (Christensen et al., 2013).

SREX (IPCC, 2012) indicate increases in all precipitation extreme indices for northern Asia. These projections are supported by CMIP5 model results under different RCP scenarios. CMIP5 projections over North Asia show that temperatures will rise more in boreal winter (DJF) than in boreal summer (JJA).

In North Asia, all CMIP5 models project an increase in precipitation in both the winter half year and summer half year. The ability of these CMIP5 models to simulate precipitation over this region varies. There is a reasonable level of agreement in model projections of precipitation to be positive and significantly above the 20-year natural variability, and therefore this suggests that there is *medium confidence* in the sign of the projected change in future precipitation. In summary, all the areas are projected to warm and there is a stronger than global mean warming trend projected for northern Asia during winter. Precipitation in northern Asia will *very likely* increase, and extreme precipitation events will *likely* increase (Christensen et al., 2013).

Atlas.5.3.3.2 Assessment and synthesis of observations, trends and attribution

Based on observational datasets from the All-Russian Institute for Hydrometeorological Information (RIHMI-WDC), Institute of Global Climate and Ecology (IGCE), HadCRUT and Hadley/CRU, temperature increase has been observed since the mid 70s of the 20th century over the whole territory of North Asia (the Asian territory of Russia: Western Siberia, Eastern Siberia and the Russian Far East) (Frolov et al., 2014), and especially over the north-eastern part of Russia (Gruza et al., 2015) (see also Figure Atlas.29:). More intense climate warming was observed in spring in East Siberia and over the Russian Far East, strengthening from south to north territories with linear trend of 0.8°C–1.2°C per decade for the 1976–2014 period (Frolov et al., 2014; Ippolitov et al., 2014; Kokorev and Sherstiukov, 2015). Trends of annual averaged temperature in the northern part of the region during the last decades were twice as strong as that averaged over the globe (Frolov et al., 2014; Mokhov, 2015; Sherstyukov, 2016). This tendency has been accompanied by winter cooling in mid-latitude regions and well-pronounced in Western and Eastern Siberia, especially in its southern part (Cohen et al., 2014; Ippolitov et al., 2014; Gruza et al., 2015; Kharyutkina et al., 2016; Overland et al., 2016; Perevedentsev et al., 2017; Wegmann et al., 2018). This phenomenon has been called 'warm Arctic – cold Eurasia (Siberia)' or WACE (WACS) – the appearance of a cold anomaly over Siberia was observed in conjunction with warming over the Arctic region (see Section Atlas.5.9.2), in particular over the Barents-Kara sea region, where the last 15 years warming trend is larger than 2.5°C per decade (Outten and Esau, 2012; Semenov et al., 2012; Overland et al., 2016; Semenov, 2016; Wegmann et al., 2018; Meleshko et al., 2019; Susskind et al., 2019). While the temperature decrease is strongly correlated with the Barents-Kara sea ice loss, recent studies by (Blackport et al., 2019; Clark and Lee, 2019) have shown that both phenomena are caused by a midlatitude circulation variability. Negative temperature trends in winter in Siberia were also observed in the whole troposphere for the 1981–2010 period based on radiosonde observations (Komarov et al., 2010). However, the trend of winter temperature decrease has moderated in recent years, from –0.6°C per decade for the 1976–2012 period to –0.3°C per decade for the 1976–2018 period (Frolov et al., 2014; ROSHYDROMET, 2019). Extremality of cold days has also strengthened in the south of Siberia, but in general, the total number of days with frost became less and in spring the situation was reversed. The tendency to warming extends over the whole Asian territory of Russia and reached values of 1.2°C per decade, compensating the cooling in winter (Frolov et al., 2014). Temperature trends and means derived from reanalysis datasets (JRA-25, MERRA) correctly represented temperature variability shown in observational data over the Asian territory of Russia for the 1976–2010 period (Loginov et al., 2014).

Precipitation increased over the whole territory with a mean trend of 0.8 mm/month per decade for Russia in the 1976–2012 period (Frolov et al., 2014). The highest precipitation increase predominantly was observed over some regions of Siberia and the Russian Far East with estimated trends of 5–15 mm per decade for the 1976–2014 period (Kokorev and Sherstiukov, 2015) or 5% per decade for the 1976–2018 period (ROSHYDROMET, 2019), which is also seen in Figure Atlas.29:. Decreasing tendency was observed in the centre of Western Siberia, in the north of Eastern Siberia, the Baikal and Transbaikal regions, the Amur River region and Primorye territories. The highest decrease in annual precipitation sums was observed over the southern and north-eastern part of the Russian Far East namely over the Kamchatka and the Chukchi Peninsulas up to –20 mm per decade for the 1976–2014 period (Kokorev and Sherstiukov, 2015) or 15–20% per decade for the 1976–2018 period (ROSHYDROMET, 2019).

Over North Eurasia, the number of days with light precipitation has decreased but moderate, heavy, and very heavy precipitation have increased, enhancing the amount and intensity of precipitation over the 1951–2010 period (Wen et al., 2014). The growth of precipitation intensity maxima was most evident in Yakutia for the warm season (Khlebnikova et al., 2019b). The largest increase in precipitation was over the southern part of Russian Far East mostly due to positive changes in convective precipitation intensity in the region that has increased by over 1 mm per day per decade, implying a 13.8% increase per 1°C warming over the 1966–2016 period (Chernokulsky et al., 2019). Other studies have shown this major role of convective precipitation in the increase in precipitation intensity and extremes over Northern Eurasia (Ye et al., 2017a). In the central part of Western Siberia, frozen precipitation and the frequency of freezing rain increased while freezing drizzle frequency decreased over entire Russia (Groisman et al., 2016). Showery precipitation dominates in Northern Eurasia over the 1966–2016 period (Chernokulsky et al., 2019) and the amount of solid precipitation predominantly decreased. Total number of days without precipitation rose almost over the whole territory in winter, and in summer in the Kamchatka Peninsula and Chukchi Peninsula (Frolov et al., 2014). Based on All-Russian Institute for Hydrometeorological Information data, over the 1966–2010 interval, the longest dry day periods (up to 14.6 days) were observed along the southern border of Siberia in winter. Significant positive changes in consecutive dry days over the 1991–2015 period (relative to 1966–1990) were identified in the southern parts of Eastern Siberia and in most of the Russian Far East. At the same time, the zone of significant negative changes was clearly pronounced in Eastern Siberia (Ye, 2018).

Figure Atlas.29: shows observations based on three datasets for annual mean temperature (a) and precipitation (b) trends. Significant warming is evident in the northern regions of North Asia. Precipitation changes are mostly not significant except for increasing trends in the eastern regions.

Atlas.5.3.3.3 Assessment of model performance

In order to assess model performance, gridded datasets as reference values should be evaluated against observations first. For seasonal values, ERA-Interim reanalysis data underestimate mean temperature over North-East Asia in spring (MAM), autumn (SON), and winter (DJF) and overestimate it in summer (JJA). The data set also underestimates summer (JJA) precipitation and shows large wet biases over North-East Asia during spring compared with CRU dataset (Ozturk et al., 2017; Top et al., submitted).

In terms of the main synoptic processes affecting North Asia, GCMs are able to capture the temporal evolution of the Siberian High (SH) over the historical 1872–2005 period for both magnitude and position. On decadal and multi-decadal time scales, the CMIP5 multi-model ensemble also captures the pronounced reduction (between the 1981–2000 and 1881–1900 periods) and the recovery (during the 1991–2005 period) of the SH intensity (Fei and Yong-Qi, 2015). Both CMIP3 and CMIP5 indicate a weakening of intensity of the winter SH and a strengthening of the interannual variability compared to the historical period (Lupo and Kininmonth, 2013; Fei and Yong-Qi, 2015). The main blocking characteristics of the current climate obtained from reanalysis data, including number of blocking events and their duration, intensity and frequency in the region was reasonably well reproduced by GCMs (Mokhov et al., 2014). However, GCMs do not sufficiently simulate the Northern Hemisphere Eurasian warming pattern (Lupo and Kininmonth, 2013) and most of the GCMs overestimate the annual mean temperature over Northern Eurasia (*high confidence)*. Generally, the bias in the simulated annual surface air temperature simulation primarily comes from winter (DJF) season, while the model biases in other seasons are relatively smaller (Miao et al., 2014; Peng et al., 2019). Most of the GCMs can approximate the decadal SAT trend, but the accuracy of annual SAT simulation is relatively low (Miao et al., 2014). Moreover CMIP5 GCMs fail to capture the decreasing temperature trend over East Siberia (Fei and Yong-Qi, 2015). For CMIP5, models with higher resolution do not always perform better than those with lower resolutions (Miao et al., 2014).

The performance of 16 CMIP5 models in simulating SAT variability over Eurasia in the 20th century was evaluated with respect to CRU observations for permafrost subregions (Peng et al., 2019). Results show warm bias in the northwest of Eurasia when both CMIP5 ensemble averages and CRU observations demonstrate climate warming over the 20th century, with acceleration during the late 20th century. Further, CMIP5 GCMs generally underestimate daily temperature range (DTR) compared with observations over

north-eastern Russia (Sillmann et al., 2013a). In winter, the Northern Hemisphere is dominated by a large decrease (reaching as low as –2.7°C) in DTR north of approximately 45°N (Lindvall and Svensson, 2015).

Analysis of CMIP5 models against observations (HadEX2) shows warmer temperature extremes than the models and reanalysis and underestimates dry day index compared to observations (Sillmann et al., 2013a).

Currently, there are only a few studies that analyse CMIP6 models performance in comparison with CMIP5 in the region. A GCM from CMIP6 (BCC-CSM2-MR) show cold biases amplified at high latitudes in the Northern Hemisphere, in particular in Siberia, compared with CMIP5 (Voldoire et al., 2019). In another GCM (CNRM-CM6-1) from CMIP6, warm bias over Siberia is amplified in winter but in summer biases are much smaller than in CMIP5 (Wu et al., 2019).

There is limited work on the use of regional climate models for the North Asia region. CORDEX-CAS has almost full cover of North Asia except parts of Russian Far East, and the ARCTIC-CORDEX domain covers the northern regions. For CORDEX-CAS three RCMs (REMO, ALARO-0 and CLMcom) with different boundary conditions were applied. Results show that RCMs have warmer biases for maximum temperatures and colder biases for minimum temperatures (Top et al., submitted). The models also have a wet bias for precipitation in the north during the winter months compared with the CRU data. Rain gauges, however, are known to have problems in terms of measuring properly solid precipitation, e.g. drifting snow, and this can greatly affect the accuracy of the CRU dataset over Northern Asia (Harris et al., 2014).

Atlas.5.3.3.4 Assessment and synthesis of projections

Projections from the CMIP5 and CMIP6 ensembles shown in Figure Atlas.29: are for temperatures to continue increasing into the future with further warming of over 2°C–3°C by mid-century. Temperature change will be up to 8°C in northern regions by the end of the 21st century under the higher emissions future (with greater warming projected by the CMIP6 ensemble). Similarly, annual precipitation is projected to continue increasing, by up to 30% more, by the end of the century with higher emissions.

Looking across a range of emissions futures, CMIP5 projections of temperature increases over Northern Eurasia in the 21st century are 1.03°C per 100 years, 3.11°C per 100 years and 7.14°C per 100 years under the RCP2.6, RCP4.5 and RCP8.5 scenarios, respectively (Miao et al., 2014). Another study for permafrost sub-regions in Eurasia by (Peng et al., 2019) indicate that the RCP2.6, RCP4.5 and RCP8.5 scenarios exhibit statistically significant increases in annual temperature during the 21st century at a rate of 0.08°C, 0.23°C and 0.72°C per decade during the 2006–2100 period, respectively, resulting in an increase of ensemble area-averaged mean SAT for the 2081–2100 period relative to the 1986–2005 period of 1.68°C (RCP2.6), 3.18°C (RCP4.5), or 6.41°C (RCP8.5). This confirms that the warming rate of SAT in permafrost regions is faster than global and in non-permafrost regions.

Projected future changes in the number of dry days can both amplify and damp precipitation intensity growth expected in the process of climate warming (Sillmann et al., 2013c). Since precipitation is projected to increase and the internal and inter-model uncertainties are relatively small at both annual and seasonal scales, North Asia is projected to experience a decrease in dry extremes, such as decreases in days without precipitation and the CDD index (Sillmann et al., 2013c). Further, increased extreme precipitation events and increased flood risk are projected over the region (*high confidence)* (Shkolnik et al., 2018; Khlebnikova et al., 2019c).

Studies on the projection of blocking in the 21st century using two scenarios RCP2.6 and RCP8.5 showed a general increase in the blocking frequency and intensity for the Euro-Atlantic region in all seasons. There is also an increasing likelihood of extreme winter and summer conditions due to the total blocking duration longer than seven weeks. Changes of the opposite sign are characteristic for the Northern Hemisphere as a whole with no change in the interannual or interdecadal variability (Lupo and Kininmonth, 2013; Mokhov et al., 2014).

As for regional climate models, North Asia is partly included with the Arctic (northern parts) and Central-

Asia (almost all territory except part of the Russian Far East) in CORDEX domains. Regional climate modeling projections developed at MGO (Voeikov Main Geophysical Observatory) for the Arctic-CORDEX domain for RCP8.5 scenario show changes in the temperature-precipitation indices for the 2006–2100 period relative to the 1951–2005 period. In wintertime, there is a) a decrease of wintertime duration and in the number of degree-days with negative air temperature; b) a decrease in the number of very cold days with air temperature below –30°C; and c) an increase in total annual precipitation. Further, there is an increase in summertime extremes and in the number of days with hot weather. There is also an increase in the storm activity and precipitation intensity (Khlebnikova et al., 2018). For the Central Asia CORDEX domain, which includes North Asia, RegCM4.3.5 simulations driven by two different CMIP5 global climate models (HadGEM2-ES and MPI-ESM-MR) for two scenarios (RCP4.5 and RCP8.5) and three time slices (2011–2040, 2041–2070, and 2071–2100) with respect to the 1971–2000 reference period were analysed (Ozturk et al., 2017). The warming trend is projected to intensify and will increase by about 3-4°C during the summer season in all parts of the region for the 2071–2100 period for RCP4.5 and by more than 7°C for almost all parts of the domain and for all seasons for RCP8.5. Warming will be most evident at the large continental Siberian Plateau with boreal and sub-boreal climates and biomes (i.e., taiga forests and tundra) during the winter season. In almost all seasons and for all future periods, precipitation in Siberia will not change with respect to the reference 1971–2000 period, except in the RCP8.5 scenario for the winter and autumn seasons (Ozturk et al., 2017).

Over the whole territory of Russia, MGO RCM simulations using five CMIP5 GCMs as boundary conditions for RCP8.5 scenario show relatively faster increase in the upper limit of predicted variations in the annual minimum temperature as compared with maximum temperature for the 2050–2059 and 2090–2099 periods relative to the 1990–1999 period. For precipitation, results show a significant increase in the upper limit of the variation range of intense precipitation over most of the region in winter and a decrease in summer over East Siberia (Kattsov et al., 2017b). Assessment of future forestry conditions with the same RCM MGO for RCP8.5 and RCP4.5 scenarios shows the smallest change in the sum of active temperatures (i.e., over 5°C, 10°C and 15°C when different types of vegetation start to grow) expected in the area of northern taiga in Western and Eastern Siberia in the 2090–2099 period relative to the 1990–1999 period (Torzhkov et al., 2019).

Further, a maximum increase in rare annual temperature maxima by the end of the 21st century is projected in the south of European Russia as well as in the southern regions of the Urals and West Siberia. During the cold season, the variability of extremes is reduced (to 30% of base values for the 1990–1999 period) in most of Siberia and the Russian Far East. The growth of annual minima variability is projected in Chukotka (to 20%) and a slight increase (5–10%) is projected in the southern regions of Western Siberia and in the south west of European Russia (Khlebnikova et al., 2019a).

[START Figure Atlas.29: HERE]

Figure Atlas.29: (a–b) Mean observed trends of annual mean surface air temperature and precipitation for three datasets (CRU TS, BERKELEY and EWEMBI for temperature; CRU TS, GPCC and GPCP for precipitation). Hatching indicates regions where no or only one dataset provides a significant trend. Linear trends are calculated for the common 1980–2014 period and expressed in °C per decade (temperature) and % relative change per decade (precipitation) with respect to the climatological mean over this period.
(c–f) Climate change projections of annual mean surface air temperature and precipitation from CMIP5 (30 models) and CMIP6 (17 models) calculated as the differences in the climatological average for RCP8.5 and SSP5-8.5 respectively, for the period 2041–2060 with respect to the historical 1995–2014 period and expressed as °C (temperature) and % relative change (precipitation). Hatching indicates weak model agreement on the sign of the change (less than 80% as defined in Nikulin et al., 2018).
(g–j) Regional mean changes in annual mean surface air temperature and precipitation for the four North Asia regions (RAR, WSB, ESB and RFE). The top row shows the median (dots) and 10th–90th percentile range across each model ensemble for annual mean temperature changes, for two datasets (CMIP5 and CMIP6) and two scenarios (SSP1-2.6/RCP2.6 and SSP5-8.5/RCP8.5). The first four bars represent the additional warming projected relative to the historical baseline 1995–2014 period to

reach the two global warming levels (GWL; +1.5°C and +2°C) and the remaining six projected changes over three time periods (near-term 2021–2040, mid-term 2041–2060 and long-term 2081–2100) compared to this same historical baseline period. The bottom row shows scatter diagrams of temperature against precipitation changes, displaying the median (dots) and 10th–90th percentile ranges for four future periods (2021–2040, 2041–2060, 2061–2080, 2081–2100) compared to the historical baseline period, as obtained from CMIP6 projections for three scenarios (SSP1-2.6, SSP2-4.5 and SSP5-8.5). Changes are absolute for temperature and relative for precipitation.
(The script used to generate this figure is available online (Atlas GitHub, 2020) and similar results can be generated in the Interactive Atlas for flexibly defined seasonal periods.)

[END Figure Atlas.29: HERE]

Atlas.5.3.4 Southeast Asia

Regional executive summary

El Niño events have strongly influenced observed warming over Southeast Asia (*medium confidence).* However, there is *low confidence* in the exact effect of El Niño on mean, extreme, and night time temperatures. {Atlas.5.3.4.2}

There has been an increase in maximum daily precipitation during La Niña events over Southeast Asia (*medium confidence*). Changes in daily mean precipitation are less spatially coherent (*low confidence*) and the effect of ENSO variability on extreme precipitation trends vary between subregions (one day extreme rainfall decreasing over the Maritime Continent and increasing over Indochina and Thailand) (*low confidence).* {Atlas.5.3.4.2}

Temperature is projected to increase over Southeast Asia by at least 3°C by the end of the 21st century under the RCP8.5 scenario (*very likely).* This regional warming is consistent across CORDEX, CMIP5 and CMIP6 ensembles. {Atlas.5.3.4.4}

Projected changes in rainfall over Southeast Asia will be season dependent with significantly drier conditions over most regions during boreal summer (June, July, August) (*medium confidence*) at the end of the 21st century under the RCP 8.5 scenario. Over Indonesia, a 20-30% decrease in mean rainfall is *very likely*. During boreal winter (December, January, February) there will be an increase in mean rainfall over Indochina and the Philippines while there is a drying tendency over the Maritime Continent (*medium confidence*). {Atlas.5.3.4.4}

Atlas.5.3.4.1 Key features of the regional climate and findings from previous assessments

Key features of the regional climate

The Southeast Asia (SEA) region is composed of countries that are part of Indochina (or Mainland Southeast Asia) and countries that are very archipelagic in nature and have strong land-ocean-atmosphere interactions, including those that are part of the maritime continent. Rainfall seasonal variability in the region is affected by tropical cyclones from the Northwest Pacific and the synoptic scale monsoon systems (northeast and southwest) while intraseasonal variability can be influenced by the Madden-Julian Oscillation (MJO). Temperature and especially rainfall are also affected by the El Niño-Southern Oscillation (ENSO).

Previous findings from IPCC assessments

A key finding of the AR5 is the lack of sufficient observational records to allow for full understanding of precipitation trends over the past century in most of the Asian region, including SEA and that precipitation trends that are available differ vastly across the region and between seasons. Still, WGI AR5 showed that the mean annual temperature of SEA has been increasing at a rate of 0.14°C to 0.20°C per decade since the 1960s, along with an increasing number of warm days and nights, and a decreasing number of cold days and nights.

On projected changes in climate, the AR5 showed future increases in precipitation extremes related to the monsoon that are *very likely* in SEA. Further, the annual total wet-day rainfall and rainfall from extreme rainy days have increased by 22 mm and 10 mm per decade, respectively and the ratio of rainfall in wet to dry season in SEA have also increased between 1955 and 2005. Findings of the AR5 also show that the frequency of extreme rainfall events has been increasing in the northern parts of SEA, although it is decreasing in Myanmar. In SR1.5, there is a projected increase in flooding and runoff over Southeast Asia for a 1.5 to 2°C global warming, and these will increase even more for a greater than 2°C level of warming.

Findings from WGII AR5 also showed warming is *very likely* in the mid- and late-21st century over all land areas of Asia based on CMIP5 simulations under all four RCP scenarios. For SEA in particular, WGII AR5 assessed that, under the RCP8.5 scenario, the ensemble-mean changes in mean annual temperature over the region will *likely* exceed 3°C above the late 20th-century baseline in the late 21st century.

Atlas.5.3.4.2 Assessment and synthesis of observations, trends and attribution

Within the last decade, there has been an increasing number of studies on climatic trends over Southeast Asia. These studies were either carried out on regional basis (Thirumalai et al., 2017; Cheong et al., 2018) or focused on specific countries (Cinco et al., 2014; Villafuerte et al., 2014; Mayowa et al., 2015; Villafuerte and Matsumoto, 2015; Guo et al., 2017b; Sa'adi et al., 2017; Supari et al., 2017).

Temperatures are strongly influenced by ENSO in the region, including extreme temperatures. Thirumalai et al. (2017) reported that almost all April extreme temperatures occur in El Niño years and that global warming contributed to about half of the warming observed in 2016. In most of Southeast Asia (except for the north-eastern areas), Cheong et al. (2018) detected an increase in the number of warm nights with El Niño episodes within the period of 1972–2010. Over the Philippines, the largest positive anomaly in mean temperatures since the 1960s occurred in 1998 at the end of a strong El Niño event (Cinco et al., 2014).

Changes in mean precipitation are less spatially coherent over Southeast Asia. Over Thailand, Limsakul and Singhruck (2016) analysed station data and concluded that on the average, rain day events have decreased by a rate of –0.99 days/decade while simple daily intensity has increased by 0.17mm/day per decade. The increase in rainfall extremes and annual total wet-day rainfall are consistent with AR5 findings.

As with temperature, precipitation is also affected by ENSO events. There has been a significant increase in the amount of maximum daily precipitation with La Niña episodes in 1972–2010, especially during the winter monsoon period between December and February (Cheong et al., 2018). Over the Maritime Continent and Thailand, the likelihood of extreme rainfall events and greater amounts of precipitation are higher during La Niña and lower during El Niño years (Villafuerte and Matsumoto, 2015; Limsakul and Singhruck, 2016).

Figure Atlas.30: shows changes in mean temperature and precipitation relative to a baseline period 1980-2014 for three datasets (CRU TS, BERKELEY and EWEMBI for temperature; CRU TS, GPCC and GPCP for precipitation). Observation data show that there has been a significant overall warming over SEA with higher rates of warming in Malaysia, Indonesia, and the southern areas of mainland Southeast Asia. Precipitation trends, however, over the region are mostly not significant except for southern Philippines, Malaysia, and East Kalimantan Indonesia.

It is important to note that the availability, quality, and temporal and spatial density of observation data can introduce uncertainties to the detected changes in historical climate. This may lead to varying results because of the uncertainty in the temporal and spatial characteristics of observations in the region. Juneng et al. (2016) showed root mean square differences (RMSD) in precipitation values of up to 8 mm/day when comparing four different observation datasets available for Southeast Asia.

[START Figure Atlas.30: HERE]

Figure Atlas.30: (a–b) Mean observed trends of annual mean surface air temperature and precipitation for three datasets (CRU TS, BERKELEY and EWEMBI for temperature; CRU TS, GPCC and GPCP for precipitation). Hatching indicates regions where no or only one dataset provides a significant trend. Linear trends are calculated for the common 1980–2014 period and expressed in °C per decade (temperature) and % relative change per decade (precipitation) with respect to the climatological mean over this period.
(c–f) Climate change projections of annual mean surface air temperature and precipitation from CMIP5 (30 models) and CMIP6 (17 models) calculated as the differences in the climatological average for RCP8.5 and SSP5-8.5 respectively, for the period 2041–2060 with respect to the historical 1995–2014 period and expressed as °C (temperature) and % relative change (precipitation). Hatching indicates weak model agreement on the sign of the change (less than 80% as defined in Nikulin et al., 2018).
(g) Regional mean changes in annual mean surface air temperature and precipitation for the Southeast Asia region. The left plot shows the median (dots) and 10th–90th percentile range across each model ensemble for annual mean temperature changes, for two datasets (CMIP5 and CMIP6) and two scenarios (SSP1-2.6/RCP2.6 and SSP5-8.5/RCP8.5). The first four bars represent the additional warming projected relative to the historical baseline 1995–2014 period to reach the two global warming levels (GWL; +1.5°C and +2°C) and the remaining six projected changes over three time periods (near-term 2021–2040, mid-term 2041–2060 and long-term 2081–2100) compared to this same historical baseline period. The right plot shows a scatter diagram of temperature against precipitation changes, displaying the median (dots) and 10th–90th percentile ranges for four future periods (2021–2040, 2041–2060, 2061–2080, 2081–2100) compared to the historical baseline period, as obtained from CMIP6 projections for three scenarios (SSP1-2.6, SSP2-4.5 and SSP5-8.5). Changes are absolute for temperature and relative for precipitation.
(The script used to generate this figure is available online (Atlas GitHub, 2020) and similar results can be generated in the Interactive Atlas for flexibly defined seasonal periods.)

[END Figure Atlas.30: HERE]

Atlas.5.3.4.3 Assessment of model performance

Compared to AR5, the number of publications on climate modelling and projections have greatly increased for Southeast Asia. However, there are difficulties in validating high-resolution simulations due to the inadequacies of coarse-scale observed gridded datasets (Van Khiem et al., 2014) or, as previously mentioned, the uncertainties in the observations themselves (Juneng et al., 2016). Some efforts have been done to produce better observationally-based gridded datasets for the region (e.g. APHRODITE2; Nguyen-Xuan et al., 2016; SA-OBS; van den Besselaar et al., 2017).

Regional climate models (RCMs) have been intensively used over this region in recent years. There is *high confidence* that RCMs can reproduce reasonably well seasonal climate patterns of temperature, precipitation and large-scale circulation over the different subregions of SEA (Van Khiem et al., 2014; Kwan et al., 2014; Ngo-Duc et al., 2014, 2017; Juneng et al., 2016; Katzfey et al., 2016; Loh et al., 2016; Raghavan et al., 2016; Cruz et al., 2017; Ratna et al., 2017; Trinh-Tuan et al., 2018). The performance of GCMs was assessed before being used as boundary conditions for the RCM experiments (Siew et al., 2013; Katzfey et al., 2016). Performance in simulating rainfall varies among GCMs over the region (*high confidence*). Some GCMs are capable of simulating the precipitation seasonal cycle reasonably well but with weaker interannual variations (Siew et al., 2013). The CMIP5 models could simulate the spatial pattern of the winter monsoon rainfall but with a large spread of wet bias magnitude (Siew et al., 2013). Raghavan et al. (2018b) analysed randomly 10 CMIP5 models and revealed that no particular model performed well in simulating historical rainfall over SEA. Li et al. (2019) analysed the outputs of 31 CMIP5 GCMs over the mainland Southeast Asia and found that the performance of the models in simulating precipitation during wet season was superior to that for annual and dry season precipitation.

Some RCMs generally showed a systematic cold bias for near surface temperature (Manomaiphiboon et al., 2013; Kwan et al., 2014; Ngo-Duc et al., 2014; Loh et al., 2016; Cruz and Sasaki, 2017; Cruz et al., 2017).

Cold biases are mainly due to model physics (Manomaiphiboon et al., 2013; Kwan et al., 2014) and/or the biases in the SST forcing (Ngo-Duc et al., 2014). Thus, Katzfey et al. (2016) bias corrected the GCM SST before using it for downscaling. Van Khiem et al. (2014) however showed a slight warm bias of simulated temperature over some subregions of Vietnam. Temperature was shown to be strongly influenced by the choice of cumulus scheme (Cruz et al., 2017). The biases for precipitation were found to be greater and less systematic with wet or dry biases depending on the subregions (Manomaiphiboon et al., 2013; Kwan et al., 2014; Van Khiem et al., 2014; Juneng et al., 2016). Systematic wet biases were found in model simulations in both DJF and JJA (Kwan et al., 2014; Van Khiem et al., 2014; Kirono et al., 2015; Juneng et al., 2016). The wet biases over mainland Indochina could be linked to the lack of summer air-sea interactions in the RCM experiments (Juneng et al., 2016). Regional climate models differ in simulating rainfall interannual variability. Juneng et al. (2016) found stronger interannual variability of rainfall compared to observations while Kirono et al. (2015) showed model underestimation of interannual variability. Simulated rainfall amount is sensitive to the choice of convective scheme (Juneng et al., 2016; Ngo-Duc et al., 2017) and the choice of land-surface scheme (Chung et al., 2018). Rainfall biases can be greatly reduced if a bias correction method such as the quantile mapping is applied (Trinh-Tuan et al., 2018).

Extreme indices have been generally estimated using the core indices recommended by the joint WMO Commission for Climatology (CCI)/World Climate Research Programme (WCRP) Climate Variability and Predictability (CLIVAR) project's Expert Team on Climate Change Detection, Monitoring and Indices (ETCCDMI) (Manomaiphiboon et al., 2013; Ngo-Duc et al., 2014, 2017). There is better coherence for temperature extreme indices than for precipitation extreme indices. Over Thailand, the occurrence frequency of dry days is under-predicted (Manomaiphiboon et al., 2013). Climatic heavy rainfall centres can be well captured (Kieu-Thi et al., 2016). The pattern of tropical cyclone numbers can be reasonable represented by RCM outputs (Van Khiem et al., 2014; Kieu-Thi et al., 2016).

Multi-model experiments have been conducted (Cruz et al., 2017; Juneng et al., 2016; Katzfey et al., 2016; Ngo-Duc et al., 2014, 2017; Raghavan et al., 2018a; Van Khiem et al., 2014). Ngo-Duc et al. (2014) showed that the ensemble mean product tends to outperform the individual model in representing the climatological mean state. By examining the similarity index omega (Koster et al., 2000, 2002) to assess how model simulations agree or disagree in simulating historical climate for temperature and precipitation extreme indices, Ngo-Duc et al. (2017) found that there are relatively high similarities among the simulations over mainland Asia compared to those over the Maritime Continent for both seasonal and inter-annual variability. (The similarity index quantifies the degree of similarity among ensemble members in terms of phase and shape.) The extreme rainfall indices had a lower similarity index compared to that of temperature. Figure Atlas.31: shows the similarity index omega for the CORDEX-SEA historical simulations for extreme indices of temperature and rainfall.

[START Figure Atlas.31: HERE]

Figure Atlas.31: Similarity index omega between the different CORDEX-SEA historical simulations for different temperature-based (a-e) and precipitation extreme indices (f-h) (from Ngo-Duc et al., 2017).

[END Figure Atlas.31: HERE]

Atlas.5.3.4.4 Assessment and synthesis of projections

There has been limited published literature on future climate projections for Southeast Asia that are based on multi-model regional climate simulations. Many of the previous works were country specific and were based on either limited GCMs or RCMs or both. Ngo-Duc et al. (2014) used three RCMs for projecting future climate in Vietnam and some extreme indices until the 2050s for the SRES A1B scenario. The temperature trend was found to be positive and significant over the study area and may increase up to 1.8ºC in the boreal summer (JJA). Loh et al. (2016) concluded that the projected temperature increments over Malaysia were uniform, ranging from 2.7 to 4.2°C and 1.7 to 3.1°C for A2 and B2 scenarios, respectively.

More recent works that use the RCP scenarios over the region are consistent with previous results that used the SRES scenarios. The completion of multi-model and high-resolution (25 km) simulations under CORDEX Southeast Asia provided more opportunity for robust assessment of future climate changes over SEA. Based on ten ensemble members, (Tangang et al., 2018) showed that the projected temperature increase over SEA ranges from 3.6 to 5.6°C by the end of 21st century under RCP8.5. These findings on regional warming in Southeast Asia are consistent with WGII AR5 findings that showed warming is *very likely* in the mid- and late-21st century over all land areas of Asia based on CMIP5 simulations under all four RCP scenarios. For SEA in particular, WGII AR5 assessed that, under the RCP8.5 scenario, the ensemble-mean changes in mean annual temperature over the region will *likely* exceed 3°C above the late 20th-century baseline in the late 21st century.

Projections of future rainfall changes are highly variable. Over the 2020–2050 period, an increase in precipitation is projected over most of Southeast Asia, with the change being more pronounced in the Maritime Continent under RCP4.5. However, towards the end of the century, a high increase in precipitation over the northern areas of Southeast Asia is projected under RCP8.5 (Raghavan et al., 2018a). Over Vietnam, future changes in precipitation vary from –25% to +15% depending on regions and seasons, with the most significant increasing trend over the coastal area during the rainy season, suggesting more severe water-related disasters in this region in the future (Ngo-Duc et al., 2014). Based on 14 ensemble members of CORDEX Southeast Asia simulations, which are comprised of 11 GCMs and 7 RCMs, Tangang et al. (submitted) showed significant and robust increases of mean rainfall over Indochina and the Philippines while there is a drying tendency over the Maritime Continent during DJF for early, mid and end of the 21st century periods at both RCP4.5 and 8.5 (Figure Atlas.32:). At the end of the 21st century during DJF under RCP8.5, an increase of 20% in mean rainfall is projected over Myanmar, northern-central Thailand and northern Laos, and a 5-10% increase over the eastern Philippines and northern Vietnam. During JJA, significant and robust drier conditions are projected over almost the entire Southeast Asia except over Myanmar and northern Borneo. The projected increase of mean rainfall over Thailand is consistent with those of (Tangang et al., 2019). Over the Indonesian region, especially Java, Sumatra and Kalimantan, as much as a 20% - 30% decrease in mean rainfall is projected during JJA by the end of the 21st century. Nevertheless, inter-model variations can be large depending on sub-region and season. However, the projected drier condition over Indonesia is consistent with that of Giorgi et al. (2019), Kang et al. (2019) and Kusunoki (2017). This is also consistent with projected annual and seasonal (JJA and SON) increase of CDD over the Indonesian region described by Tangang et al. (2018) and Supari et al. (submitted), particularly by the middle and end of the 21st century. Therefore, it is *very likely* (*high confidence*) that the Indonesian region will be experiencing enhanced dryness, especially from the mid- 21st century onwards for both RCPs. This drying tendency over Indonesia is associated with enhanced subsidence over the region (Kang et al., 2019; Tangang et al., submitted).

Figure Atlas.30: show projected changes in temperature (c,e) and precipitation (d,f) calculated as the climatology differences for the medium-term (2040-2060) period for the scenario RCP85 (SSP5-85 for CMIP6) with regards to the historical (1986-2005) values. Significant warming is projected to continue over the entire region with temperatures increasing to about 1.5°C over land regions by mid-century. Changes in precipitation, however, are more uncertain. In general, there is an overall increase in mean precipitation but CMIP5 and CMIP6 differ in terms of the magnitude and location of these changes. In particular, the CMIP5 ensemble shows significant (stronger model agreement) increase in precipitation over the Philippines and the northern regions of mainland SEA (Burma), while the CMIP6 ensemble projects significant changes over the southern regions of Borneo island (Indonesia).

[START Figure Atlas.32: HERE]

Figure Atlas.32: The projected changes in mean precipitation expressed as a percentage (%) relative to the mean in the historical period. Hatching indicates the changes are significant at the 95% level above random noise while dots are showing robustness at 95% (Tangang et al., submitted).

[END Figure Atlas.32: HERE]

Atlas.5.3.5 South Asia

Regional executive summary

The South Asian monsoon has shown contrasting behaviour over India and Pakistan (in the monsoon dominated region only), with a strengthening trend over the core monsoon zone in Pakistan (*low confidence*) and weakening trend over central north India (*high confidence*). Vertically Integrated (0–500 hPa) Meridional Moisture Transport (VIMMT) and extra-tropic connections are mainly forming this dipole like mechanisms since the 1950s. {Atlas.5.3.5.2}

Minimum and maximum daily temperatures in South Asia are increasing and winters are getting warmer faster than summers (*high confidence*). There is *high confidence* that there is an increasing trend in heat wave occurrence in many regions over South Asia. {Atlas.5.3.5.2}

It is *likely* that temperatures over South Asia will increase by 5.0±0.9°C during 2081-2100 when comparing with the 1995-2014 baseline period under both CMIP5 RCP8.5 and CMIP6 SSP5-8.5 scenarios. {Atlas.5.3.5.4}

Summer monsoon precipitation in South Asia is *likely* to increase by the end of the 21st century while winter monsoons are projected to be drier. Based on CMIP6 models (available in the Interactive Atlas), an increase (> 22%) in mean annual precipitation is projected over South Asia under RCP 8.5 at the end of the century (*medium confidence*). {Atlas.5.3.5.4}

Atlas.5.3.5.1 Key features of the regional climate and findings from previous assessments

Key features of the regional climate

The climate of the South Asia region is mainly governed by the combination of large scale forcing phenomena, intense air-sea interaction, and topographic effects. Precipitation falls over the region mainly in summer as the monsoon system and the associated troughs approach relatively warm land. The countries in this region are mostly semi-arid to arid and therefore depend heavily on the summer monsoon precipitation (June–September, JJAS) to replenish fresh water supplies. In winter, westerly winds bring moisture from the Atlantic Ocean, which cause precipitation over northern and western parts of South Asia.

Previous findings from IPCC assessments

IPCC AR5 assessed that there is *high confidence* that high resolution regional downscaling, which is complementary to results obtained directly from global climate models, adds value to the simulation of spatial variations in climate in regions with highly variable topography (e.g., distinct orography, coastlines), and for mesoscale phenomena and extremes (Flato et al., 2013a). Recent IPCC reports AR5, SR1.5, SRCCL and SROCC assessed that it is *very likely* that the mean annual temperature over South Asia has increased during the past century (see Figure 2.21 in Hartmann et al., 2013 and Figure 24-2 in Hijioka et al. 2014), and the frequency of cold (warm) days and nights have decreased (increased) across most of Asia since about 1950 (based on Figure 2.32 in Hartmann et al., 2013). IPCC AR5 assessed that there is *high confidence* that the large-scale patterns of surface temperature are well simulated by the CMIP5 models in agreement with observations except in certain regions, particularly at higher elevations over the Himalayas (Flato et al., 2013a). It is with *high confidence* and *robust evidence* that CMIP5 models projected a clear increase in temperature over South Asia, and there is *medium confidence* in summer monsoon precipitation increase in the future projections for South Asia based on IPCC AR5 (Collins et al., 2013).

Inconsistent evidence was found on the declining trends in mean precipitation and increasing droughts from 1950 onwards considering 1960 -1990 as the base period. Similarly, the IPCC AR5 reported *low confidence* (due to lack of literature) in trends in climate indices related to extreme precipitation events. The Indian summer monsoon circulation was found to have weakened, but this was compensated by increased atmospheric moisture content leading to more rainfall (*medium confidence)*. It is *likely* that snowfall occurrence events are decreasing in southern Asia along with other regions along with increase in winter temperatures. Based on satellite- and surface-based remote sensing it is *very likely* that aerosol optical depth

(AOD) has increased over southern Asia since 2000.

It was assessed with *high confidence* in SRCCL that risks from desertification are projected to increase under shared socioeconomic pathway SSP2 ("Middle of the Road") at 1.5°C, 2°C and 3°C of global warming, and around 3,398 million people will be exposed to various impacts related to the water, energy and land sectors and around half of them will be living in South Asia.

It is projected with *medium confidence* that the projected weakening of the Atlantic Meridional Overturning Circulation (AMOC) will result in decline in summer rainfall over South Asia. With *low confidence*, it is projected that the frequency of Indian Ocean Dipole events will increase in future.

Atlas.5.3.5.2 Assessment and synthesis of observations, trends and attribution

Recent studies show that the Indian annual mean land temperatures warmed at a rate of around 0.6°C per century during 1901−2018, which was primarily contributed by a significant increase in annual maximum temperature by 1.0°C per century, while the annual minimum temperature showed a lesser increasing trend of 0.18°C per century during this period, with significant rise only in the recent few decades (1981-2010) at a rate of 0.17°C per decade (Srivastava et al., 2017b, 2019). The observed frequency, total duration and maximum duration of heat waves are increasing over central and north-western parts of India during the summer months (April to June) (Rohini et al., 2016).

There has been a noticeable declining trend in rainfall with monsoon deficits occurring with higher frequency in different regions in South Asia. Concurrently, the frequency of heavy precipitation events have increased over India, while the frequency of moderate rain events have decreased since 1950 (high confidence) (Goswami et al., 2006; Dash et al., 2009; Christensen et al., 2013; Krishnan et al., 2016; Kulkarni et al., 2017; Roxy et al., 2017). There is a considerable spread in the seasonal and annual mean precipitation climatology and interannual variability among the different observed precipitation data sets over India (Collins et al., 2013; Prakash et al., 2014; Kim et al., 2018; Ramarao et al., 2018). Yet, the regions of agreement among datasets lends *high confidence* that there has been a decrease in mean rainfall over most parts of the eastern and central north regions of India (Krishnan et al., 2016; Jin and Wang, 2017; Juneng et al., 2016; Latif et al., 2017; Pulak Guhathakurta and Jayashree V Revadekar, 2017; Roxy et al., 2015; Sabin and Mujumdar, 2016; Singh et al., 2014).

A dipole-like structure in the summer monsoon rainfall trends is observed over the northern Indo-Pakistan region on seasonal and inter-annual timescales, with significant increasing trends observed over Pakistan and decreasing trends over central north India (*low confidence*) (Latif et al., 2017); the likely reason is the strengthening (weakening) trend of vertically integrated meridional moisture transport (VIMMT) over the Arabian Sea (Bay of Bengal). This is confirmed by measurements from 35 meteorological stations located in the monsoon-dominated strip in Pakistan found that the mean monsoon onset has observed a shift to an earlier time in Pakistan over 40 years (1971-2010) (Ali et al., 2019).

It was assessed using a state-of-the-art global climate model with high-resolution zooming over South Asia (Sabin et al., 2013) that a juxtaposition of regional land-use changes, anthropogenic-aerosol forcing and the rapid warming signal of the equatorial Indian Ocean was crucial to produce the observed Indian summer monsoon weakening in recent decades, which significantly enhanced the occurrence of localized intense precipitation events, as compared to the global-warming response (Krishnan et al., 2016).

Figure Atlas.33: shows changes and trends (calculated from a common 1980-2014 period) in temperature (a) and precipitation (b) from three different data sets over South Asia. There is significant warming trend over the region with faster rates of increase in temperature over the Hindu Kush Himalayan region. There are no significant observed precipitation changes over most of South Asia but for some regions in southern India.

Atlas.5.3.5.3 Assessment of model performance

There was evident improvement in the CMIP3 to CMIP5 multi-model ensemble mean in the simulation of

the amplitude and phase of the seasonal cycles of temperature and precipitation in South Asia. However, there was no appreciable improvement in regions with steep orography, and there has remained substantial inter-model spread in seasonal and annual mean temperatures over South Asia.

The Indian summer monsoon rainfall (ISMR) simulations have improved in the CMIP3 to CMIP5 multi-model ensembles, specifically in terms of northward propagation, time for peak monsoon and withdrawal (Sperber et al., 2013). However they fail to simulate the trends in monsoon rainfall and the post-1950 weakening of monsoon circulation (Saha et al., 2014). This is partially attributed to the failure of coarse resolution (about 3°) CMIP5 models in simulating fine resolution process such as orography, land surface feedback and problems in cloud parameterization resulting in overestimation of convective precipitation fraction (Singh et al., 2017).

Regional climate models (RCMs) were used to perform dynamical downscaling of the coarse resolution CMIP5 models to higher resolution (50 km) over South Asia (called CORDEX South Asia) with improved surface fields such as topography and coastlines, with the aim of better resolving the complexities of the monsoon and other hydrological processes (Giorgi et al., 2009).

The added value obtained from CORDEX RCM simulations, relative to the driving GCMs, presents a complex picture. Certain aspects of climate are better represented in CORDEX RCM simulations, such as the spatial patterns of temperature (Sanjay et al., 2017d), and the spatial features of precipitation distribution associated with the Indian summer monsoon (Choudhary et al., 2018). Clear improvements are also found in simulating the active and break composite precipitation (Karmacharya et al., 2016). On the other hand, an assessment of the CORDEX South Asia RCM ensemble showed that RCMs follow the driving CMIP5 GCMs in underestimating seasonal mean surface air temperature but overestimating spatial variability in precipitation. The cold bias in the driving CMIP5 model is found to have amplified after downscaling over almost the entire region, with larger magnitudes during winter season over the Hindu Khush Himalayan region, Afghanistan and southwest Pakistan (Iqbal et al., 2017). Neither RCMs nor their driving CMIP5 GCMs reproduce well the observed climatology of precipitation (Mishra, 2015b) and temperature over the Himalayan watersheds of the Indus Basin with substantial cold biases of 6–10 °C (Hasson et al., 2019; Nengker et al., 2018). In addition, important characteristics of ISMR such as northward and eastward propagation, onset, seasonal rainfall patterns, intra-seasonal oscillations and patterns of extremes did not show consistent improvement (Singh et al., 2017). Also, these RCM simulations have not indicated added value in capturing the observed changes in ISMR characteristics over recent decades.

Atlas.5.3.5.4 Assessment and synthesis of projections

Summer precipitation changes in South Asia are consistent between CMIP3 and CMIP5 projections, but model spread is large in winter precipitation change. Changes in the summer monsoon will dominate the annual rainfall change over South Asia (Woo et al., 2019).

CMIP5 GCMs generally project increasing moisture convergence and summer monsoon precipitation over South Asia with global warming (Mei et al., 2015). Under the RCP8.5 scenario, 23 CMIP5 GCMs showed an increase in South Asian Monsoon precipitation due to anthropogenic climate change (Srivastava and Delsole, 2014). Out of 20 CMIP5 GCMs, four showed increase in magnitude and lengthening of all-India summer monsoon under the RCP8.5 scenario. Both strong and weak monsoon intensity are expected to increase during the period 2051−2099.

CMIP5 GCMs under the RCP4.5 and RCP8.5 scenarios for the time period of 2006-2050 show a possible decline in JJAS rainfall over India due to the anti-cyclonic circulation over the Arabian Sea at 850 hPa and cyclonic circulation at 200 hPa (40^{o}N and 70^{o}E−90^{o}E respectively) (Sarthi et al., 2015). CORDEX−South Asia projections over northeast India under the RCP4.5 scenario for the time period of 2011-2060 show a decreasing seasonal precipitation trend (Soraisam et al., 2018) but most of the literature do not agree with this finding. There is consistency among all 36 CMIP5 GCMs, with regard to the projected increase in the moisture transport over the Arabian Sea and Bay of Bengal towards the end of 21st century. The increase in the magnitude of rainfall and VIMMT trends is higher for RCP8.5 compared to the RCP4.5 scenario over the

Indo-Pakistan region (Latif, 2017). For the time period 2011–2030, 2046–2065, and 2080–2099 using IPCC AR4-based AOGCMS, there will be a gradual increase in annual precipitation in the Jammu and Kashmir, Khyber Pakhtunkhwa and Punjab regions of Pakistan, but an increase and then decrease in rainfall in Balochistan and Sindh. In humid and semi-arid climate areas, there is an increase in annual precipitation in all three projected periods (Saeed and Athar, 2018).

ECHAM5 downscaled by RegCM4 at 30 km resolution for South Asia shows steadily progressing warming, which would be widespread across the region with increases of 4°C to 5°C by the 2080s under the A2 scenario (Ahmed and Suphachalasai, 2014). Warming of 2.5ºC to 5°C are projected over northern Pakistan and India sub-regions (Syed et al., 2014). CORDEX-South Asia projections over northeast India under RCP4.5 scenario, for time period of 2011-2060, shows increasing trends for both seasonal maximum and minimum temperature over northeast India. The finding of the Figure Atlas.33: are also produced in (Rehman et al., 2018) on the performance of CMIP5 models over Pakistan and South Asia .

Figure Atlas.33: show projected changes in temperature (c,e) and precipitation (d,f) over South Asia calculated as the climatology differences for medium-term (2041-2060) periods for the scenario RCP85 (SSP5-85 for CMIP6) with regards to the historical (1986-2005). The increase in temperature in terms of magnitude and pattern for mid future is consistent for both scenarios (CMIP5 RCP85 and CMIP6 SSP5-85) with strong model agreement in the ensembles. Both CMIP5 and CMIP6 show significant increase in annual rainfall over western regions in India and there is model agreement in the projected increase in rainfall over the Himalayas in CMIP6.

[START Figure Atlas.33: HERE]

Figure Atlas.33: (a–b) Mean observed trends of annual mean surface air temperature and precipitation for three datasets (CRU TS, BERKELEY and EWEMBI for temperature; CRU TS, GPCC and GPCP for precipitation). Hatching indicates regions where no or only one dataset provides a significant trend. Linear trends are calculated for the common 1980–2014 period and expressed in °C per decade (temperature) and % relative change per decade (precipitation) with respect to the climatological mean over this period.
(c–f) Climate change projections of annual mean surface air temperature and precipitation from CMIP5 (30 models) and CMIP6 (17 models) calculated as the differences in the climatological average for RCP8.5 and SSP5-8.5 respectively, for the period 2041–2060 with respect to the historical 1995–2014 period and expressed as °C (temperature) and % relative change (precipitation). Hatching indicates weak model agreement on the sign of the change (less than 80% as defined in Nikulin et al., 2018).
(g–h) Regional mean changes in annual mean surface air temperature and precipitation for the Tibetan Plateau and South Asia. The top row shows the median (dots) and 10th–90th percentile range across each model ensemble for annual mean temperature changes, for two datasets (CMIP5 and CMIP6) and two scenarios (SSP1-2.6/RCP2.6 and SSP5-8.5/RCP8.5). The first four bars represent the additional warming projected relative to the historical baseline 1995–2014 period to reach the two global warming levels (GWL; +1.5°C and +2°C) and the remaining six projected changes over three time periods (near-term 2021–2040, mid-term 2041–2060 and long-term 2081–2100) compared to this same historical baseline period. The bottom row shows scatter diagrams of temperature against precipitation changes, displaying the median (dots) and 10th–90th percentile ranges for four future periods (2021–2040, 2041–2060, 2061–2080, 2081–2100) compared to the historical baseline period, as obtained from CMIP6 projections for three scenarios (SSP1-2.6, SSP2-4.5 and SSP5-8.5). Changes are absolute for temperature and relative for precipitation.
(The script used to generate this figure is available online (Atlas GitHub, 2020) and similar results can be generated in the Interactive Atlas for flexibly defined seasonal periods.)

[END Figure Atlas.33: HERE]

Atlas.5.4 Australasia

Regional executive summary

There is *very high confidence* that the climate of Australia warmed by just over 1°C and New Zealand by around 1°C since reliable records began in 1910 and 1909 respectively, and this warming is projected to continue with a magnitude roughly equal to or slightly more than the global average temperature (for example, Australasian land area warming in CMIP6 from 1995-2014 to 2°C global warming since pre-industrial is 1.0°C to 1.5°C compared to the global average of 0.8°C to 1.4°C). {Atlas.5.4.2}

There is *high confidence* that human influence has been the dominant driver of the warming trend and contributed to greater intensity and duration of atmospheric and marine heat events. Drying of southwest Western Australia in April to October has been attributed with *medium to high confidence*, some other trends and events have been attributed with some confidence, including snow cover declines, increase in fire risk in southern Australia and intensity of New Zealand extreme rainfall. {Atlas.5.4.2}

There is *medium confidence* that model representation of aspects of the Australasian region has somewhat improved between CMIP5 and the CMIP6 ensemble available at the time of writing, including temperature and rainfall climatology, ENSO and IOD and their teleconnection with Australian rainfall, and ocean currents, however CMIP6 is far from complete. {Atlas.5.4.3}

There is *high confidence* for a significant ongoing rainfall decline in southwest Australia in the cool season (April-October) and a rainfall increase in parts of New Zealand in winter, with similar results in CMIP5 and CMIP6, other rainfall changes are less significant or less certain. {Atlas.5.4.4}

There is *high confidence* that dynamical downscaling and statistical downscaling performed for regional studies have produced 'added value' in the climate change projected signals in regional temperature, rainfall and extremes related to topography and coasts in Australia and New Zealand, however care must be taken in placing projections using different model inputs and downscaling methods in context, and regional downscaling does not fully sample uncertainties encompassed by the latest CMIP and CORDEX simulations. {Atlas.5.4.4}

Atlas.5.4.1 Key features of the regional climate and findings from previous assessments

Key features of the regional climate

Australasia is divided into four regions for the Atlas, as follows: New Zealand (NZ), with a varied climate with diverse landscapes, mainly maritime temperate with four distinct seasons; Northern Australia (NAU) which is mainly tropical with monsoonal summer-dominated rainfall, but with a hot, semi-arid climate in the south of the region; Central and Eastern Australia (CAU) with a hot, dry desert climate in the west and centre, ranging to a temperate climate in the east; and Southern Australia (SAU) which ranges from Mediterranean and semi-arid in the west to mainly cool temperate maritime climate in the southeast. Various remote drivers have notable teleconnections to regions within Australasia, including an effect of the El Niño Southern Oscillation and the Indian Ocean Dipole. Much of southern NZ and SAU are affected by systems within the westerly mid-latitude circulation, in turn affected by the Southern Annular Mode. The monsoon and the Madden-Julian Oscillation affect rainfall variability in northern Australia.

Previous findings from IPCC assessments

AR5 WGI and WGII report *very high confidence* that air and sea temperatures in the region have warmed (values of change see Table Atlas.6:), cool extremes have become rarer in Australia and New Zealand since 1950, while hot extremes have become more frequent and intense (e.g., *very likely* that warm days and nights have increased). AR5 reported it is *virtually certain* that mean air and sea temperatures will continue to

increase, with *very high confidence* that the greatest increase will be experienced by inland Australia and the least increase by coastal areas and New Zealand. AR5 reported a range of different precipitation trends within the region. For example, while annual rainfall has been significantly increasing in north-western Australia since the 1950s (*very high confidence*), it decreased in the northeast of the South Island of New Zealand over 1950–2004 (*very high confidence*) and over the southwest of Western Australia. In line with these trends, WGI reported it is *likely* that drought has decreased in northwest Australia. Future projections for precipitation extremes indicate an increase in most of Australia and New Zealand, in terms of rare daily rainfall extremes (i.e., current 20-year return period events) and of short duration (sub-daily) extremes (*medium confidence*). Likewise, however, there is a projected increase the frequency of drought in southern Australia (*medium confidence*) and in many parts of New Zealand (*medium confidence*). Owing to hotter and drier conditions, there is *high confidence* that fire weather will increase in most of southern Australia, and *medium confidence* that the fire danger index will increase in many parts of New Zealand.

AR5 also reported that mean sea levels have also increased in Australia and New Zealand at average rates of relative sea-level rise of 1.4 ± 0.6 mm/yr from 1900 to 2011, and 1.7 ± 0.1 mm/yr from 1900 to 2009, respectively (*very high confidence*), that the volume of ice in New Zealand declined by 36–61% from the mid-late 1800s to the late 1900s (*high confidence*), while late season significant snow depth also declined in three out of four Snowy Mountain sites in Australia between 1957 and 2002 (*high confidence*). As mean sea-level rise is projected to continue for at least several more centuries, there is *very high confidence* that this will lead to large increases in the frequency of extreme sea-level events in Australia and New Zealand. On the other hand, the volume of winter snow and the number of days with low-elevation snow cover in New Zealand are projected to decrease in the future (*very high confidence*), while both snow depth and area are projected to decline in Australia (*very high confidence*).

The Special Report on the Ocean and Cryosphere in a Changing Climate (SROCC) reports on the observed and projected decline in snow cover in Australasia, as well as the retreat of New Zealand glaciers following an advance in 1983-2008 due to enhanced local snow precipitation. The report also discusses the vulnerability of some Australian communities and ecosystems to sea level rise, the increase in the intensity and duration of marine heatwaves driven by human influence (*high confidence*), the decrease in frequency of tropical cyclone landfall on eastern Australia since the late 1800s (*low confidence* in an anthropogenic signal), and presented a case study on the multiple hazards, compound risk and cascading impacts from climate extremes in Tasmania in 2015/16 (including an attributable human influence on some events). The Special Report on Climate Change and Land assessed the land vegetation ‘greening’ in parts of Australia, desertification and trends in drought.

Atlas.5.4.2 Assessment and synthesis of observations, trends and attribution

Australia and New Zealand have continued to warm, and many rainfall trends have continued since the AR5. Figure Atlas.34:(a,b) shows changes and trends in temperature and precipitation for a common 1980-2014 period from three different global data sets. All the datasets show significant (at 0.1 significance level) warming trends over the southern half of Australia. Most of the observed changes in precipitation over the region are not significant over this period, although two of the observed datasets (GPCC and GPCP) agree on a significant drying trend in the Southern regions of New Zealand.

For a longer-term perspective based on high-quality regional datasets, Figure Atlas.35: shows that Australian mean temperature has increased by just over 1°C during the period 1910-2019 and 2019 was Australia’s hottest year on record using the updated observed temperature dataset ACORN-SATv2 (Trewin, 2018). Most of the warming has occurred since 1950, with eight of the top ten warmest years on record occurring since 2005, with a clear attribution of anthropogenic influence (Bureau of Meteorology and CSIRO, 2018). Regionally, the highest temperature trends have occurred in central and eastern Australia, with a regional warming minimum in the northwest of Australia since the 1970s (CSIRO and Bureau of Meteorology, 2015). On a seasonal basis, spring has seen the highest trend with fairly similar trends in other seasons (Bureau of Meteorology and CSIRO, 2018). In New Zealand, an increase of 1°C has been measured from 1909-2016 using the NIWA NZ temperature record (New Zealand Ministry for the Environment & Statistics, 2017).

These mean changes have been accompanied by positive trends in daytime and night-time maximum and minimum temperatures and a greater number of hot days and nights and fewer cold days and nights (Alexander and Arblaster, 2017; New Zealand Ministry for the Environment & Statistics, 2017).

Detectable anthropogenic increases in precipitation in Australia have been reported particularly for north central Australia and for a few regions along the south-central coast for the period 1901-2010 (Knutson and Zeng, 2018). Seasonally, there is a decline in cool season (April to October) precipitation in southwest Western Australia, see Figure Atlas.35:, with an attributable human influence (Delworth and Zeng, 2014, and others).

In New Zealand between 1960 and 2016, winter rainfall increased in Whangarei, Wellington, and New Plymouth, while summer rainfall increased in Dunedin and Kerikeri (New Zealand Ministry for the Environment & Statistics, 2017). Note however, for the most part, the above reported trends have been classified as statistically not significant. Trends in gridded climate data in summer and winter for 1979 to 2006 taken from (Ummenhofer et al., 2009) are shown in Figure Atlas.35:.

Atlas.5.4.3 Assessment of climate model performance

Most studies reviewed by WGII AR5 were based on Coupled Model Inter-comparison Project Phase 3 (CMIP3) models and Special Report on Emission Scenarios (SRES) scenarios, as well as CMIP5 model results whenever available. WGI AR5 reported that model biases in annual temperature and rainfall are similar to or lower than other continental regions outside the tropics, with temperature biases generally <1°C in the multi-model mean and <2°C in most models over Australia compared to reanalysis, and a wet bias over the Australian inland region but a dry bias near coasts and mountain regions of both Australia and New Zealand.

Early results from CMIP6 suggest incremental improvements compared to CMIP5 in the simulation of the mean annual climatology of temperature and precipitation of the Indo-Pacific region surrounding Australasia, the teleconnection between ENSO and IOD and Australian rainfall and other relevant climate features (Grose et al., submitted). These assessments suggest that confidence in projections is similar to AR5 or incrementally improved. CORDEX Australasia simulations are found to have cold biases in daily maximum temperature and an overestimation of precipitation but overall showed some added value on the simulation of the current climate.

Atlas.5.4.4 Assessment and synthesis of projections

This section is limited to mean temperature and precipitation, projected changes to other variables for Australasia are summarised in Chapter 12 of WGI and Chapter 11 of WGII. Figure Atlas.34: and Table Atlas.6: show projected changes in temperature and precipitation over the Australasia region calculated as the climatology differences for medium-term (2040-2060; c-f) periods for the scenario RCP8.5 (SSP5-8.5 for CMIP6) with respect to the historical (1986-2005) values and are expressed as ºC and relative differences (%), for temperature and precipitation, respectively.

CMIP5 and CMIP6 both indicate mean temperature in Australasia is projected to continue to rise through the 21st century (*very high confidence*) as illustrated in Figure Atlas.34:. CMIP5 projections as reported in the Australian national climate projections using the AR5 baseline are shown in Table Atlas.6:, indicating increases of around 0.5 to 1.5°C over the century under RCP2.6 and around 2.7 to 5.0°C under RCP8.5 in all four tailored regions within the country. For New Zealand, the Ministry for the Environment (2018) projects an increase of mean temperature of 0.7°C (RCP2.6) and 1.0°C (RCP8.5) to 2040, and 0.7°C (RCP2.6) and 3.0°C (RCP8.5) by 2090 relative to 1986-2005, with higher increase in summer than in winter and more pronounced in mountainous areas. Temperature projections in the CMIP6 ensemble as it stands in the Atlas are not significantly different than CMIP5, except for a warmer high end of the range (see Figure Atlas.34:), for example the 10–90th percentile range of modelled temperature change averaged over the land regions of

Australasia for 1995–2014 to 2081–2100 under high emissions is 3.0°C to 4.4°C in CMIP5 (RCP8.5) and 3.0°C to 4.9°C in CMIP6 (SSP5-8.5). This higher projection is produced by a group of models with high climate sensitivity (Forster et al., 2019), resulting in higher temperature projections after 2050 for the region(Grose et al., submitted). Changes in mean annual temperature for 1.5°C and 2°C global warming since preindustrial are similar to this change in the global average in most regions but higher than the global average in central Australia.

There is more than 80% model agreement for projected mean annual rainfall decrease in southwest Western Australia for both mid (2041-2060) and far future (2081-2100) and a significant increase in rainfall in the far future (2081-2100) for the southern regions of New Zealand, with less model agreement elsewhere (Figure Atlas.34:). However, there are some important seasonal and regional projections worth further explanation, also see a review of Australian rainfall changes found in (Dey et al., 2019). Almost all models project Southern Australia to continue getting drier in winter (JJA) and spring (SON), but a few models show little change in rainfall, e.g., the CMIP5 projections for JJA under RCP8.5 between 1986-2005 and 2081-2100 is -32 to -2% (CSIRO and Bureau of Meteorology, 2015). Studies of winter rainfall change in southern Australia and circulation suggest the wetter end of the range may possibly be rejected (Grose et al., 2017, 2019a). The CMIP5 projections of northern Australian wet season rainfall change are uncertain, from a large and significant decrease to a large and significant increase, with CMIP5 projections for DJF under RCP8.5 between 1986-2005 and 2081-2100 of -24 to 18% (CSIRO and Bureau of Meteorology, 2015). Evidence from warming patterns suggests a constraint on the dry end of projections (Brown et al., 2016), and currently the CMIP6 ensemble has no models with a large projected rainfall decline. Ferguson et al. (2018) project that between 1976-2005 and 2070-2099, summers will become wetter (mainly in northern Australia) under RCP 8.5. There is also evidence for a projected increase in rainfall variability in northern Australia in scales from days to decades (Brown et al., 2017). Projections for eastern Australia vary by season, with moderate agreement on a decrease in rainfall in winter and spring with less model agreement in summer and autumn. Liu et al. (2018) find that under 1.5°C warming, central and northeast Australia is projected to become wetter.

Projected patterns in annual precipitation exhibit increases in the west and south of New Zealand and decreases in the north and east (Ministry for the Environment, 2018). However, projected changes in mean precipitation in New Zealand are expected to vary around the country and with season, where the west and south are projected to experience increases in annual mean precipitation in future, while the north and east are projected to experience decreases (*medium confidence*). Liu et al. (2018) project that the north island will be drier, while the South Island will be wetter under both 1.5°C and 2°C warming.

CORDEX Australasia simulations at ~50 km spatial resolution reveal some more detail in projected temperature and rainfall change associated with important features such as orography. For temperature, enhanced warming at high elevation has been reported. For rainfall, areas where there is coincident ‘added value’ in the simulation of the current climate and ‘potential added value’ as new information in the projected climate change signal (collectively termed ‘realised added value’) in Australia include the Australian Alps, Tasmania and parts of northern Australia (Di Virgilio et al., submitted). There have been several studies of regional climate change for New Zealand and states of Australia at fine resolution (5-12 km), domains shown in Figure Atlas.36:, that have produced insights into regional climate change. One important insight is enhanced drying in cool seasons on the windward slopes of the southern Australian Alps (decreases of 20-30% compared to 10-15% in host models), and conversely a chance of enhanced rainfall increase on the peaks of mountains in summer (Grose et al., 2019b), with the summer finding in line with the European Alps (Giorgi et al., 2016).

[START Figure Atlas.34: HERE]

Figure Atlas.34: (a–b) Mean observed trends of annual mean surface air temperature and precipitation for three datasets (CRU TS, BERKELEY and EWEMBI for temperature; CRU TS, GPCC and GPCP for precipitation). Hatching indicates regions where no or only one dataset provides a significant trend. Linear trends are calculated for the common 1980–2014 period and expressed in °C per decade

(temperature) and % relative change per decade (precipitation) with respect to the climatological mean over this period.
(c–f) Climate change projections of annual mean surface air temperature and precipitation from CMIP5 (30 models) and CMIP6 (17 models) calculated as the differences in the climatological average for RCP8.5 and SSP5-8.5 respectively, for the period 2041–2060 with respect to the historical 1995–2014 period and expressed as °C (temperature) and % relative change (precipitation). Hatching indicates weak model agreement on the sign of the change (less than 80% as defined in Nikulin et al., 2018).
(g-j) Regional mean changes in annual mean surface air temperature and precipitation for the four Australasian regions (NAU, CAU, SAU and NZ). The top row shows the median (dots) and 10th–90th percentile range across each model ensemble for annual mean temperature changes, for two datasets (CMIP5 and CMIP6) and two scenarios (SSP1-2.6/RCP2.6 and SSP5-8.5/RCP8.5). The first four bars represent the additional warming projected relative to the historical baseline 1995–2014 period to reach the two global warming levels (GWL; +1.5°C and +2°C) and the remaining six projected changes over three time periods (near-term 2021–2040, mid-term 2041–2060 and long-term 2081–2100) compared to this same historical baseline period. The bottom row shows scatter diagrams of temperature against precipitation changes, displaying the median (dots) and 10th–90th percentile ranges for four future periods (2021–2040, 2041–2060, 2061–2080, 2081–2100) compared to the historical baseline period, as obtained from CMIP6 projections for three scenarios (SSP1-2.6, SSP2-4.5 and SSP5-8.5). Changes are absolute for temperature and relative for precipitation.
(The script used to generate this figure is available online (Atlas GitHub, 2020) and similar results can be generated in the Interactive Atlas for flexibly defined seasonal periods.)

[END Figure Atlas.34: HERE]

[START Figure Atlas.35: HERE]

Figure Atlas.35: Observed trends in temperature and rainfall for Australia and New Zealand from high-quality regional datasets; Left: time series of anomalies from the 1961-1990 average, Australian northern wet season is Oct-Apr and southern wet season is Apr-Oct (adapted from BoM and CSIRO 2018); Centre: maps show annual linear trends for 1970-2019 for temperature to illustrate warming minimum in northwest Australia in this period, 1950-2019 in mean annual rainfall; right: New Zealand mean annual temperature from NIWA, maps show trends in summer and winter rainfall in 1979 to 2006 in the NIWA climate database taken from (Ummenhofer et al., 2009).

[END Figure Atlas.35: HERE]

[START Figure Atlas.36: HERE]

Figure Atlas.36: Domains of notable regional dynamical downscaling studies in Australasia offering the potential for regional added value in climate change projections. NIWA projections for New Zealand (red), NARCliM work for eastern Australia (purple) and southwest Western Australia regional projections (black) use limited area models and the entire model domain is shown, Victorian Climate Projections 2019 (green), Queensland (brown), Climate Futures for the Alps (light brown) and Climate Futures for Tasmania (blue) use stretched-grid global models and the high-resolution domain is shown. Surface height is indicated by the colour scale, showing studies are generally focused on areas of notable topographic features, where cases of ‘added value’ in temperature and rainfall projections were found.

[END Figure Atlas.36: HERE]

[START Table Atlas.6: HERE]

Table Atlas.6: Temperature changes and warming rates in mean annual temperature reported in previous assessments and literature and the Atlas, projected changes are for the AR5 periods 1986-2005 to 2081-2100 to allow comparison, ranges are the 10-90 percentile values.

Region	Historical change	Projected RCP2.6/ SSP1-2.6 (°C)	Projected RCP8.5/ SSP5-8.5 (°C)	Source
New Zealand (air)	Around 1°C or 0.09 ± 0.03°C per decade since 1909	Atlas CMIP5: 0.2 to 0.9 CMIP6: 0.7 to 1.2	Atlas: CMIP5: 2.2 to 3.7 CMIP6: 2.7 to 4.0	Observed:(IPCC, 2013a) and (New Zealand Ministry for the Environment & Statistics, 2017)
New Zealand seas	Around 0.07°C per decade in 1909-2009			(IPCC, 2013a)
Australia (air)	Just over 1°C or 0.09 ± 0.03°C per decade since 1910	Atlas: CMIP5: 0.9 to 1.7 CMIP6: 0.7 to 1.7	Atlas: CMIP5: 3.3 to 5.2 CMIP6: 3.3 to 5.5	Observed: (IPCC, 2013a) and (Bureau of Meteorology and CSIRO, 2018)
North-western and north-eastern Australian seas	0.12°C per decade since 1950			(IPCC, 2013a)
South-eastern Australian seas	0.2°C per decade since 1950			(IPCC, 2013a)
Southern Australia		0.5 to 1.4	2.7 to 4.2	(CSIRO and Bureau of Meteorology, 2015)
Northern Australia		0.5 to 1.6	2.7 to 4.9	(CSIRO and Bureau of Meteorology, 2015)
Eastern Australia		0.6 to 1.6	2.8 to 5.0	(CSIRO and Bureau of Meteorology, 2015)
Australian Rangelands (central)		0.6 to 1.8	2.9 to 5.3	(CSIRO and Bureau of Meteorology, 2015)

[END Table Atlas.6: HERE]

Atlas.5.5 Central and South America

Atlas.5.5.1 Central America

Regional executive summary

Warming trends have been observed in most of Central America *(high confidence*). Significant warming trends within 0.2°C and 0.3°C per decade have been observed in all the subregions of Central America in the last 30 years, with the largest increases in the North America monsoon region (*high confidence*), with some local cooling trends reported for certain small regions. Trends in precipitation are non-significant and highly variable all over the region. {Atlas.5.5.1.2}

Warming trends observed in recent decades are projected to continue to increase over the 21st century *(high confidence).* Under the middle emissions scenario (SSP2-4.5) surface warming is *likely* to exceed 1.5°C for continental Central America before the mid-century, becoming *very likely* by the end of the century; in the Caribbean islands, the warming trends are lower. Under the high emissions scenario (SSP5-8.5) surface warming is *very likely* to exceed 1.5°C before the mid-century and 3°C before the end of the century, but it is *likely* to exceed 4.5°C by the end of the century. The Caribbean Islands warming will *likely* exceed 1.5°C in the mid-century and 3°C by the end of the century and will *very likely* exceed 2.3°C by the

end of the century. {Atlas.5.5.1.4}

Projected change in mean annual precipitation shows a large spatial variation across Central America. Mean annual precipitation is *likely* to decrease as an average in the whole of Central America *(low confidence).* Under the middle emissions scenario there are overall negative but non-significant (*low confidence*) precipitation trends during the 21st century. Under the high emissions scenario, average precipitation is *likely* to decrease in most of the region, particularly in the north-western and central Caribbean and part of continental Central America. {Atlas.5.5.1.4}

Atlas.5.5.1.1 Key features of the regional climate and previous findings from IPCC assessments

Key features of the regional climate

For the purpose of this assessment, the Central America and Caribbean region is split into three subregions: Central America isthmus (including the Yucatan peninsula), Mexico (centre and north) and the Caribbean (see Figure Atlas.2:).

The dominant annual cycle of the Central American region, except for the central part of its Atlantic coast, is monsoonal, with highest temperatures in April and lowest temperatures in January. Precipitation in most of Central America is characterized by two maxima in June and September, an extended dry season from November to May, and a shorter dry season in July and August, known as the midsummer drought (MSD) (Magaña et al., 1999). To some extent, precipitation seasonality is explained by the migration of the Intertropical convergence zone (ITCZ) (Taylor and Alfaro, 2005).

The climate of Mexico is temperate to the north of the Tropic of Cancer, with marked difference between winter and summer, modulated by the North American monsoon (NAM), while generally arid and tropical to the south. The precipitation cycle in the southeast presents a midsummer drought (MSD), as most of Central America.

The Caribbean islands have two main seasons, characterized by differences in temperature and precipitation. The wet or rainy season, with higher values of temperature and accumulated precipitation, occurs during the boreal summer and part of spring and autumn. The MSD is also present in most of the Caribbean, particularly in the Greater Antilles (Taylor and Alfaro, 2005). A persistent climatological feature of the low level circulation is the Caribbean low level jet (CLLJ), with a characteristic semi-annual cycle with maxima in the summer (main) and winter (secondary) (Amador, 1998; Magaña et al., 1999; Whyte et al., 2008).

One of the most prominent features of the regional climate is the incidence of tropical cyclones (TCs), which represent an important hazard for almost all the countries of the region between June and November. In the cyclogenetic regions of the Atlantic and Pacific Oceans and the Gulf of Mexico, TCs frequently enter land, with strong winds and high precipitation (Hobgood, 2005). The El Niño Southern Oscillation (ENSO) influences the frequency of TCs developing and passing over the Caribbean, with evidence of multidecadal variation in storm activity (Taylor and Alfaro, 2005), positively correlated with the Atlantic multidecadal oscillation (AMO) (Goldenberg et al., 2001). Mexico is also affected by TCs from the Eastern Pacific, which are modulated by the interannual (ENSO) and decadal and multidecadal (PDO and AMO) fluctuations (Martinez Sanchez and Cavazos, 2014).

Previous findings from IPCC assessments

According to the AR5 (IPCC, 2013b), significant positive trends of temperature have been observed in Central America (*high confidence*), while significant precipitation trends are regionally dependent, especially during the summer. In addition, changes in climate variability and in extreme events have severely affected the region (*medium confidence*). A decrease in mean precipitation and an increase in extreme precipitation are projected in continental Central America, associated with tropical cyclones making landfall along the eastern and western coasts. El Niño and La Niña (teleconnections) are *very likely* to move eastwards in the future (*medium confidence*), while changes in their climate impacts on other regions including Central America and the Caribbean is uncertain (*medium confidence*). There is *medium confidence* in projections showing an increase in seasonal mean precipitation on the equatorial flank of the ITCZ affecting parts of

Central America and the Caribbean.

In relation to the 1986–2005 baseline period, temperatures are *very likely* to increase by the end of the century by approximately 0.6°C to 2°C for the RCP2.6 scenario, and by 3.6°C to 5.2°C for the RCP8.5 scenario. Precipitation is projected to vary between +10 and –25% (*medium confidence*).

Following the SR1.5 (IPCC, 2018c), there is a *high agreement* and *robust evidence* that mean surface temperature will increase in Small Island Development States (SIDS) at the 1.5°C global warming level. The Caribbean region will experience a 0.5°C to 1.5°C warming compared to the 1971–2000 baseline period, with greatest warming over larger land masses. The frequency of warm spell conditions is projected to increase up to 50% in the Caribbean at the 1.5°C global warming level with a further increase by up to 70 days at 2°C.

Atlas.5.5.1.2 Assessment and synthesis of observations, trends and attribution

There is *high confidence* in enhanced trends of temperature (Cavazos et al., 2019) and its extremes (heatwaves, hot days, tropical nights, etc.) during the second half of the 20th century over parts of Mexico (Cueto et al., 2013; Martínez-Austria et al., 2016; Martinez-Austria and Bandala, 2017; Navarro-Estupiñan et al., 2018) and the Caribbean (Peterson et al., 2002; Cueto et al., 2013; Stephenson et al., 2014; Melissa McLean et al., 2015). Significant warming trends have been found for most of Central America and the Caribbean (Planos Gutiérrez et al., 2012; Jones et al., 2016a; Hidalgo et al., 2017; Cavazos et al., 2019), with significant warming between 0.3°C and 0.4°C per decade for most of the region, but cooling trends have been detected by Hidalgo et al. (2017) in part of Honduras and northern Panama.

Changes in mean precipitation rates are less consistent and long-term trends are generally weak. Small positive trends were observed in the total annual precipitation, daily intensity, maximum number of consecutive dry days, and episodes of heavy rains (Stephenson et al., 2014). In the Central America Isthmus region, trends in annual precipitation are generally non-significant, with the exception of small significant positive trends reported by Hidalgo et al. (2017) for Guatemala, El Salvador and Panama. Planos Gutiérrez et al. (2012) used a local gridded dataset based on 900 rain gauges for Cuba and found small non-significant wet trends. Jones et al. (2016a) reported an increase of positive annual precipitation anomalies for the Caribbean for the 1979–2012 period as a consequence of the rainfall increase during the rainy period. Local high-resolution surface air temperature and precipitation datasets were used by Hidalgo et al. (2017) to study climate variability in the Central American isthmus. It was found that the 1970–1999 trends in precipitation are generally non-significant.

Figure Atlas.37: shows regional trends in temperature and precipitation for the recent past (1980–2014), showing a consistent warming in the whole region reaching 0.5°C per decade in Mexico and southern Baja California. Significant but smaller warming (0.2°C) is also detected in the Yucatan Peninsula, the Guatemala Pacific coastal region and the Caribbean and the Bahamas, in agreement with Planos Gutiérrez et al. (2012) who investigated trends in the Cuban climate using a network of 11 local surface meteorological stations for the 1951–2008 period and of Jones et al. (2016b) who analysed CRU TS-3.1 data for the Caribbean for the 1979–2012 period. In the case of precipitation, there is a large regional variability and no consensus on significant trends from the three global gridded datasets, in agreement with the finding reported above with local data.

A significant positive correlation between precipitation rates in the Caribbean and the AMO index was found by Enfield et al. (2001). A similar result was found in southern Mexico in the MSD region (Méndez and Magaña, 2010; Cavazos et al., 2019). On the other hand, ENSO favours wet conditions in Mexico during summers of low Pacific Decadal Oscillation (PDO) and during winters of high PDO. Cooler conditions are favoured during La Niña summers and El Niño winters, regardless of the PDO phase, while summers with high PDO and El Niño condition favour warmer temperature. In the Pacific coast of the Central America Isthmus, the MSD intensity and magnitude are correlated with the Niño 3.4 and CLLJ indices in stations, so that warm anomalies in the Niño 3.4 region correspond to an enhanced CLLJ and a drier MSD (Maldonado et al., 2016). Positive trends in the duration of the MSD have been found in this region over the past four

decades (*low confidence*) (Anderson et al., 2019).

Increasing trends have been observed in the intensities and precipitation yield of Atlantic TCs in the past few decades *(high agreement),* particularly from the 1970s to 1980s (Kossin et al., 2013; Holland and Bruyère, 2014; Walsh et al., 2016; Kossin, 2018). However, this trend cannot be considered as a long-term one because of the high multidecadal variability (William Landsea, 2015). For the northeast Pacific cyclogenetic region, no significant trends in intense TCs have been found (Walsh et al., 2016), but interdecadal variability in TC occurrence over the Pacific coast of Mexico is very important and is likely to be related to the PDO (Raga et al., 2012; Pazos and Mendoza, 2013). The variation of TC intensity in the region is affected by the detected poleward migration trend of the location of the moment of maximum intensity of TCs (Kossin et al., 2014).

Atlas.5.5.1.3 Assessment of model performance

The ability of climate models to simulate the climate in this region has improved in many key aspects (Karmalkar et al., 2013; Fuentes-Franco et al., 2014, 2015, 2017; Vichot-Llano et al., 2014; Vichot-Llano and Martínez-Castro, 2017; Martínez-Castro et al., 2018). Particularly relevant for this region are increased model resolution and a better representation of the land-surface processes.

Regional climate models (RCMs) forced with a reanalysis product and atmosphere-only global climate model (AGCM) provide time-slice simulations with a reasonably good performance over the core Mexican monsoon and southwest United States regions (Bukovsky et al., 2013). They found that the RCMs do add value to the GCM simulations. There is *high confidence* in the ability of RCMs to reproduce the seasonal spatial patterns of temperature and the bimodal characteristics of the Caribbean rainfall. The PRECIS model is also skilful at reproducing the observed temperature trends in the whole region, but it has problems reproducing trends of precipitation in the tropical parts of the domain, underestimating precipitation (Karmalkar et al., 2013; Centella-Artola et al., 2015). The simulated rainfall climatology of the central Caribbean basin captures the bimodal characteristics of rainfall in the Caribbean, southern Mexico and part of the Central America isthmus (Cavazos et al., 2019) though overestimating the late season peak rainfall and displacing the rainfall maximum to November. The placement of the November-December-January rainfall maximum south of Jamaica is interesting and suggests that the model may be over- or underestimating the strength of the CLLJ. It is *likely* that the PRECIS simulations do not improve with the size of the domain, as important features of the regional circulation and key rainfall climate features, such as the CLLJ and MSD, are well represented for a variety of domains of different sizes (Centella-Artola et al., 2015). Recent results show that the RCA4 model (Samuelsson et al., 2011) also reproduces well climate patterns and features in the region (Cavazos et al., 2019). Using CORDEX output, Cerezo-Mota et al. (2015) evaluated the capability of four RCMs – RCA 3.5 (Samuelsson et al., 2011), HadGem3-RA (Hewitt et al., 2011), REMO (Jacob, 2001) and RegCM4 –, using ERA-Interim as driving data, to reproduce the climate of the North American Monsoon region, including the northern part of Mexico. They especially analysed two years of extremely low and high precipitation within the period of simulations, with good results in the reproduction of the key climatic features of the region. Cabos et al. (2018) applied the ROM oceanic model (Sein et al., 2015) coupled with the REMO model to the Central America isthmus and Mexico to simulate the climate in the region, showing improvements in the reproduction of the onshore and offshore precipitation and of regional climate features such as the MSD and CLLJ. The PRECIS model also showed skill in reproducing the observed negative trends in consecutive wet days (CWD) and negative trends in extreme rainfall events (R95p) over the Caribbean, as other extreme precipitation and temperature indexes, including their correct regional distribution (McLean et al., 2015).

About RegCM4, there is *high confidence* that the model provides consistent reproductions of the main climate features of the region, for horizontal resolutions of 50 and 25 km and different combinations of physical parameterizations (*robust evidence)*, including climatic features such as the MSD and CLLJ (Martínez-Castro et al., 2006, 2016, 2018; Diro et al., 2012; Vichot-Llano et al., 2014).

Representation of tropical cyclones in numerical models

The representation of TCs in numerical models (Serreze et al., 2000; Nguyen, 2001; Walsh et al., 2004; Diro et al., 2014; Fuentes-Franco et al., 2014, 2017) is one of the most important challenges in tropical regions and particularly in Central America and the Caribbean. As these cannot be obtained directly from the wind fields, it is necessary to develop algorithms for their detection, which identify in the fields the grid-point structure that meets the characteristics defining a TC. Fuentes-Franco et al. (2014) used a simple detection algorithm to detect days with cyclonic vortices, namely at least once a day the wind speed is greater than or equal to 21 m s^{-1}, the pressure at sea level is less than or equal to 1005 hPa and the highest precipitation intensity greater or equal to 15 mm day^{-1}. In the same way, Diro et al. (2014) examined the characteristics of TCs in the CORDEX Central America (CAM) domain for present and future periods, with the aim of reducing the scale to 50 km and increasing the capacity of vortex detection. It is *very likely* that the regional climate model RegCM4 adequately reproduces the cyclogenetic zones of the region (Diro et al., 2014; Fuentes-Franco et al., 2014) using reanalysis fields as boundary conditions. The results showed good agreement with the observed climatology, with some overestimation in the tropical North Atlantic and the Caribbean, and underestimation in the tropical eastern Pacific. Fuentes-Franco et al. (2017) used the same methodology – but removing the precipitation threshold –, to evaluate the occurrence of cyclonic vortices at different grid intervals of 50 and 25 km. The model showed a response dependent on the specific cyclogenetic zone, with greater sensitivity to physics schemes than to resolution. The parameterization of ocean flows strongly influenced the frequency of estimated vortices and their intensity. However, the methodology applied to assess the sensitivity to resolution could be questioned, since the same detection thresholds are used for different resolutions, not taking into account the experience of previous investigations (Walsh et al., 2007).

Atlas.5.5.1.4 Assessment and synthesis of projections

Results have been reported for this region based on the GCM outputs from CMIP3 and CMIP5, and on regional projections downscaling these GCMs, using the CORDEX CAM domain or similar smaller domains (Taylor et al., 2013; Vichot-Llano et al., 2019). Statistical downscaling methods of CMIP5 projections have been also applied to obtain bias-adjusted regional projections (Colorado-Ruiz et al., 2018; Taylor et al., 2018; Vichot-Llano et al., 2019). Figure Atlas.37: summarizes the results for this region for CMIP5 and CMIP6.

Global and regional models highly coincide in projecting warming in the whole region for the end of the century, under scenarios A2 and B2 for CMIP3 projections and under RCP4.5 and RCP8.5 for CMIP5 projections. Herein, the projected warming was greater for continental than insular territories, generally reaching values between 2°C and 4°C (*high confidence*) (Campbell et al., 2011; Karmalkar et al., 2011; Cavazos and Arriaga-Ramírez, 2012; Cantet et al., 2014; Colorado-Ruiz et al., 2018). The greatest warming of 5.8°C for the end of the century was projected for northern Mexico by Colorado-Ruiz et al. (2018) under RCP8.5, using an ensemble of CMIP5 GCMs (see also Figure Atlas.37:). On the other hand, high-resolution regional projections for the 2021–2050 period relative to the 1961–1990 baseline period were made by Imbach et al. (2018) using the Eta regional climate model at an 8-km resolution and driven by HadGEM2-ES with the RCP4.5 scenario. They projected a warming in the Central America isthmus for 2021–2050 of about 1.6°C to 2.4°C.

Much more uncertainty is found in the precipitation projections. Using the PRECIS model under the A2 and B2 scenarios and for the end of the century, Karmalkar et al. (2011) projected a precipitation increase in the dry season for the northern Caribbean region and a precipitation decrease for the southern Caribbean (25–50%). They also projected a drying of up to 35% under the A2 scenario during the wet season for the whole Caribbean.

Twenty first century projections were developed by Cavazos and Arriaga-Ramírez (2012) by applying bias-correction and statistical downscaling methods to the projections output of six CMIP3 GCMs for the NAM region and north-western Mexico. The projections showed larger interannual variations and larger uncertainties for precipitation than for temperature. The A2 scenarios show the largest reductions of precipitation in the last 20 years of the 21st century and a decrease of 30% is projected for Baja California mainly in winter and spring, while precipitation in the NAM region is projected to decrease by 20% during

winter, spring and summer.

Maloney et al. (2014) examined 21st-century climate projections of north American climate in CMIP5 models under RCP8.5, including Central America and the Caribbean. Summertime drying was projected in the Caribbean and southern Mexico for most of the models, with good agreement. The strongest drying is projected to occur during July and August which are the months when the MSD occurs in many subregions. The maximum MSD signal increases from 2.5 mm day^{-1} to 3–4 mm day^{-1} in the RCP4.5 forcing experiment, with slight intensification in amplitude and expansion in the affected area for RCP8.5.

Similar results were obtained by Colorado-Ruiz et al. (2018) who developed climate change experiments with ensembles of 14 GCMs from CMIP5 for a 1971–2000 baseline period and with future scenarios RCP4.5 and RCP8.5, finding that precipitation may decrease between 5 and 10% by the end of the century for the RCP4.5 and RCP8.5 scenarios respectively. The largest impacts are expected during summer with a possible decrease of 13%, especially in southern Mexico, Central America and the Caribbean. Dynamically downscaled simulations by Bukovsky et al. (2015) also projected a decrease of precipitation for the middle of the century (2041–2069) relative to 1971–1999 for the north of Mexico (*low confidence*), even though there was good agreement among the members of the applied model ensemble.

Decreased precipitation was projected for the Central America isthmus by Imbach et al. (2018) with the 8-km resolution Eta RCM during the rainy season, including an intensification of the MSD, although no significant change was projected for the CLLJ.

Figure Atlas.37: shows the climate fields for temperature and precipitation for CMIP5 RCP8.5 and CMIP6 SSP5-8.5 and the 2041–2060 time slice with very similar results for temperature, with projected consistent and significant warming for all the subregions, with higher values for the north of Mexico and central southern USA (above 2.5°C). Most of the rest of the continental land of the region would warm up to 2°C, while the Caribbean would reach 1.5°C of warming, while for the south-eastern Caribbean and the Lesser Antilles the warming would be limited to 1°C. For precipitation, there is large uncertainty in the region for this period (mid-term). However, there is *high agreement* in the projected decrease of precipitation by the end of the century for most of the region particularly for annual and summer precipitation, but there is *low confidence* on the magnitude of this decrease which varies between 5 and 50% for different projections and different subregions (see extended information in the Interactive Atlas).

The status of climate extreme trends and projections for the region has been reviewed in Chapter 11 and the main findings are synthesized below.

There is a *high confidence* that estimated trends of temperature and its extremes (heatwaves, hot days, tropical nights, etc.) over parts of Mexico (Cueto et al., 2010, 2013; Martínez-Austria et al., 2016; Martinez-Austria and Bandala, 2017; Navarro-Estupiñan et al., 2018) and the Caribbean (McLean et al., 2015) have increased in the last 30 to 40 years. The severity of droughts increased in the Caribbean Islands from 1950 to 2016 (Herrera and Ault, 2017; Stennett-Brown et al., 2017) and severe drought events have been partially attributed to anthropogenic warming (Herrera et al., 2018) (*medium confidence*). Several studies have found drought trends in different parts of the region (*low confidence*).

There is also *high confidence* in the projections of an increase in surface air temperature over Central America (Chou et al., 2014a; Coppola et al., 2014a; Hidalgo et al., 2017; Imbach et al., 2018), including massive heatwaves events at the end of the century in the Central America isthmus region (Angeles-Malaspina et al., 2018) and an increase in warm days and warm nights over this region and the Caribbean (Stennett-Brown et al., 2017). For the Caribbean islands, using CMIP3 models, Karmalkar et al. (2013) found evidence for an increase in drought severity at the end of the century, mainly due to precipitation decrease during the early wet season. In the Central America isthmus, projections suggest an increase in the MSD (Imbach et al., 2018) and consecutive dry days (CDD) (Chou et al., 2014a; Giorgi et al., 2014). This is consistent with the projections of Stennett-Brown et al. (2017).

[START Figure Atlas.37: HERE]

Figure Atlas.37: (a–b) Mean observed trends of annual mean surface air temperature and precipitation for three datasets (CRU TS, BERKELEY and EWEMBI for temperature; CRU TS, GPCC and GPCP for precipitation). Hatching indicates regions where no or only one dataset provides a significant trend. Linear trends are calculated for the common 1980–2014 period and expressed in °C per decade (temperature) and % relative change per decade (precipitation) with respect to the climatological mean over this period.
(c–f) Climate change projections of annual mean surface air temperature and precipitation from CMIP5 (30 models) and CMIP6 (17 models) calculated as the differences in the climatological average for RCP8.5 and SSP5-8.5 respectively, for the period 2041–2060 with respect to the historical 1995–2014 period and expressed as °C (temperature) and % relative change (precipitation). Hatching indicates weak model agreement on the sign of the change (less than 80% as defined in Nikulin et al., 2018).
(g–i) Regional mean changes in annual mean surface air temperature and precipitation for the three Central American regions (NCA, SCA and CAR). The top row shows the median (dots) and 10th–90th percentile range across each model ensemble for annual mean temperature changes, for two datasets (CMIP5 and CMIP6) and two scenarios (SSP1-2.6/RCP2.6 and SSP5-8.5/RCP8.5). The first four bars represent the additional warming projected relative to the historical baseline 1995–2014 period to reach the two global warming levels (GWL; +1.5°C and +2°C) and the remaining six projected changes over three time periods (near-term 2021–2040, mid-term 2041–2060 and long-term 2081–2100) compared to this same historical baseline period. The bottom row shows scatter diagrams of temperature against precipitation changes, displaying the median (dots) and 10th–90th percentile ranges for four future periods (2021–2040, 2041–2060, 2061–2080, 2081–2100) compared to the historical baseline period, as obtained from CMIP6 projections for three scenarios (SSP1-2.6, SSP2-4.5 and SSP5-8.5). Changes are absolute for temperature and relative for precipitation.
(The script used to generate this figure is available online (Atlas GitHub, 2020) and similar results can be generated in the Interactive Atlas for flexibly defined seasonal periods.)

[END Figure Atlas.37: HERE]

Atlas.5.5.2 South America

Regional executive summary

Warming trends have been observed across most of South America *(high confidence).* It is *very likely* that the average temperatures across the South America regions have warmed almost 0.2°C per decade from 1980 to 2014, particularly in central and northern South America (*high confidence*), while the southern regions are warming at a slower rate (*low confidence*). {Atlas.5.5.2.2 Figure Atlas.39:}

Warming trends observed in recent decades are projected to continue over the 21st century *(high confidence).* There is *high confidence* that the surface temperature is projected to *very likely* exceed 1.5°C before mid century over the South America regions under all emission scenarios (RCPs and SSPs). Warming is *likely* to exceed 4°C for the end of the 21st century (2081–2100) under the high-emission scenario (RCP8.5/SSP5-8.5). {Atlas.5.5.2.4 Figure Atlas.39:}

Projected change in mean annual precipitation shows a large spatial variation across South America. However, it is *likely* projected to increase in southeast South America (SES) and decrease in southwest South America (SWS) with increased levels of warming *(medium confidence).* For the period 2081–2100, compared to present day, the northern and southwest South America are *projected* to experience a decrease in annual mean precipitation in the range of about –22 to –0.3 % (5–95% range of available CMIP6 projections). An increase (> 50%) in mean annual precipitation is projected over southern South America (*medium confidence*). The projected change in rainfall exhibits a large spatial variation across other South America regions with larger uncertainty (*low confidence*). {Atlas.5.5.2.4 Figure Atlas.39:}

Atlas.5.5.2.1 Key features of the regional climate and previous findings from IPCC assessments

Key features of the regional climate

The South America region is characterized by numerous regional and local climates which are influenced by multiple forcings. The main large-scale drivers include the interdecadal modes of natural variability – the Atlantic Multi-decadal Oscillation (AMO), the North Atlantic Oscillation (NAO), the Pacific Decadal Oscillation (PDO) –, the interannual to annual modes of natural variability – the El Niño-Southern Oscillation (ENSO), the Indian Ocean Dipole (IOD), the Quasi-Biennial Oscillation (QBO) –, the seasonal variability driven by the meridional migration of the Intertropical Convergence Zone (ITCZ) and the timing and intensity of the South American Monsoon System, the Madden-Julian Oscillation (MJO) subseasonal mode of natural variability, and the behaviour at finer scales of the tropical easterly waves.

At the subregional scale, several phenomena drive climate variability. In the Amazon (SAM), key drivers include the South-Atlantic Convergence Zone (Marengo et al., 2012), the Bolivian high, the 40- to 60-day intraseasonal oscillation, and the forcing of the high Andes Mountains to the west (Almeida et al., 2017). In the south-western South America (SWS) strip, climate is driven by seasonal changes in the position of subtropical high-pressure air masses in the South Atlantic and South Pacific oceans, the Antarctic Oscillation, the dynamics of the cold Humboldt ocean current, and the icy cold fronts and mid-latitude westerlies (Valdés-Pineda et al., 2016). In the densely populated, highly productive subregion of south-eastern South America (SES), climatic conditions are strongly tied to ENSO, whose influence is moderated by local air-sea thermodynamics in the South Atlantic (Barreiro, 2010). Lastly, the climate of the southern tip of South America (SSA) is influenced by the Southern Annular Mode, and the interaction between the wetter Pacific winds and the Andean Cordillera (Aceituno, 1988; Silvestri and Vera, 2009).

Given that climates and biomes transcend national political boundaries, new regions have been used for the assessment (see Figure Atlas.2:) that have a consistent climate change response signal and are climatically consistent (Solman et al., 2008; Neukom et al., 2010; Barros et al., 2015; Nobre et al., 2016). Several studies have also used these regions for analysis and impact studies (Fu et al., 2013; Cabré et al., 2016).

Previous findings from IPCC assessments

Some of the main findings of the most recent IPCC assessment reports – the Fifth Assessment Report (AR5) for the Working Group I (IPCC, 2013b) and Special Report on 1.5°C Global Warming (IPCC, 2018b) are outlined below.

AR5 WGI (Flato et al., 2013b) noted that climate simulations from CMIP3 and CMIP5 models were able to well represent the main climatological features, such as seasonal mean and annual cycle (*high confidence*), although some biases remained over the Andes, Amazon basin and for the South America Monsoon. On the other hand, climate models from CMIP5 showed better results when compared to CMIP3.

CMIP5 models have projected increased surface temperatures for South America. A temperature change exceeding 2°C at the end of the century under all assessed emission scenarios throughout South America is expected (*high confidence*).

Projections for precipitation are more uncertain, but the highlights are *robust* increases in mean precipitation in SES and rainfall decrease in northern South America (NSA) and northeast South America (NES) (*high confidence*).

The projected frequency and magnitude of extreme events, such as floods and droughts in some areas are smaller under 1.5°C than under 2°C of warming (*medium confidence*). The differences in the risks among areas are strongly influenced by local socio-economic conditions (*medium confidence*).

Atlas.5.5.2.2 Assessment and synthesis of observations, trends and attribution

Studies on climate trends in South America indicate that mean temperature and extremely warm maximum

and minimum temperatures have shown an increasing trend (*high confidence*), particularly for a large region in northern South America and south-western Andes (NSA, SAM, NES, SWS and the north of SES regions) (Figure Atlas.38:a; Figure Atlas.39:a) (Skansi et al., 2013; de Barros Soares et al., 2017a). The observed temperature anomalies showed an increase in intensity and in frequency of heatwave events in an area covering most of South America between 1980 and 2014 (Ceccherini et al., 2016) (see Chapter11). Conversely, there has been no significant change for cold waves. Also, the trend of the difference between the annual mean of the daily maximum temperature and the annual mean of the daily minimum temperature was positive – up to 1°C per decade – over the extratropics with the maximum temperature generally increasing faster than the minimum temperature, while a negative trend – up to –0.5°C per decade – was observed over the tropics.

Regionally, analyses of temperatures point to an increased warming trend (*high confidence*) over Amazonia over the last 40 years, which reached approximately 0.6°C–0.7°C (Figure Atlas.39:a) and with stronger warming during the dry season and over the southeast. The analyses also showed that 2016 was the warmest year since at least 1950 (Marengo et al., 2018). In many areas in Brazil the frequency and length of heatwaves has increased over the last five decades (Bitencourt et al., 2016) (see Chapter 11). Trends for temperature extremes are also positive over most of Argentina during the recent decades (Barros et al., 2015) (Figure Atlas.38:). In central Argentina, the trends of temperature extremes show warming in several months with clear increases in heatwaves. However, in other parts of the country, combinations of different trends and decadal variability resulted in some cases in a decrease of extreme heatwaves (Rusticucci et al., 2016). In addition, analysis of the Hadley Centre extremes dataset, HadEX2 (Donat et al., 2013), showed a decrease in the annual maximum of daily maximum temperature values over south-eastern South America (SES) in the second half of the 20th century mostly caused by stratospheric ozone depletion over the South Pole (Wu and Polvani, 2017). Andean temperatures showed significant warming trends, especially at inland and higher elevation sites, while trends are non-significant or negative at coastal sites (Vuille et al., 2015; Burger et al., 2018; Vicente-Serrano et al., 2018). The analysis over central Chile also showed that the positive trends are largely restricted to austral spring, summer and autumn seasons for mean, maximum and minimum temperatures (Burger et al., 2018; Vicente-Serrano et al., 2018). Over Peru maximum air temperature trends mainly amplified during the austral summer, but cold season minimum air temperature trends showed an opposite pattern, with the strongest warming being recorded in the austral winter (Vicente-Serrano et al., 2018).

In general, the spatial patterns of observed trends in temperature are more consistent than for precipitation across the whole South America as can be seen in Figure Atlas.38: where the trends in annual precipitation totals are shown. However, significant changes in the spatial and temporal rainfall variability were observed over South America in recent decades, although subject to observational uncertainty (de Barros Soares et al., 2017a) (*medium confidence*). In southeast Brazil there is a region of highly significant decrease of rainfall in both wet and dry seasons recorded in the period 1979–2011 (Rao et al., 2016). In contrast, southern South America has experienced significant increase of the annual precipitation since the beginning of the 20th century, mostly explained by positive trends in austral summer (Saurral et al., 2017). In eastern Argentina, southern Brazil and western Uruguay, a positive significant increase of total annual precipitation and intensity of rainfall events has been observed (Figure Atlas.38:) (Scian and Pierini, 2013; Barros et al., 2015; Cavalcanti et al., 2015; Hannart et al., 2015a; Vera and Díaz, 2015; Wu and Polvani, 2017) from the late 1960s which increase the probability of extreme flows over the main rivers of the Plata Basin. An increase in precipitation in eastern Patagonia and a marked decrease in rainfall in Chile was also found in agreement with the trends in annual precipitation totals (Vera and Díaz, 2015) displayed in Figure Atlas.38:.

The Amazon biome is perhaps the most-studied in South America due to the important role it plays in the global energy balance, hydrological cycle and carbon balance. The Amazon Basin has experienced more frequent floods and droughts over the past two decades (Espinoza et al., 2013; Gloor et al., 2015; Marengo and Espinoza, 2016). Observational studies also show that the dry-season length over southern Amazonia has increased significantly since 1979, and accompanied by a prolonged fire season (Fu et al., 2013; Alves, 2016). On the other hand, recent analyses of Amazon hydrological and precipitation data suggest an intensification of the hydrological cycle over the past few decades (Gloor et al., 2015). In general, these changes are attributed mainly to decadal climate fluctuations (*high confidence*), El Niño-Southern

Oscillation (ENSO), the Atlantic SST north-south gradient, feedbacks between fire and land-use change mainly across south south-eastern Amazon and changes in the frequency of organized deep convection (Fernandes et al., 2015; Sánchez et al., 2015; Tan et al., 2015).

[START Figure Atlas.38: HERE]

Figure Atlas.38: Local robust trends estimated annually for the 1969–2009 period for (a) cold nights (upper left), cold days (upper right), warm nights (bottom left) and warm days (bottom right) and (b) for annual total rainfall (upper left), very wet days (upper central), extremely wet days (upper right), annual maximum consecutive 5-day precipitation (bottom left), annual maximum 1-day precipitation (bottom central) and consecutive dry days (bottom right). (Skansi et al., 2013)

[END Figure Atlas.38: HERE]

Anthropogenic forcing in CMIP5 models explains with the overall warming (*high confidence*) over the entire South American continent, including the increase in the frequency of extreme temperature events (Hannart et al., 2015) such as the Argentinian heatwave of December 2013. It has a detectable influence in explaining the precipitation positive and negative trends observed in regions such as SES and the Southern Andes (Vera and Díaz, 2015; de Barros Soares et al., 2017b; Boisier et al., 2018; de Abreu et al., 2019). Despite that, there is *limited evidence* that human-induced greenhouse gas emissions had an influence on the 2014/15 water shortage in Southeast Brazil (Otto et al., 2015).

In general, analyses of historical temperature time series strongly point to an increased warming trend (*high confidence*) across many South American regions, except for a cooling off the Chilean coast. Annual rainfall has increased over south-eastern South America and decreased in most tropical land regions (*high confidence*). The number and strength of extreme events, such as extreme temperatures, droughts and floods, have already increased (*medium confidence*) (see Chapter 11).

It is still noted that the major barrier to the study of climate change in many regions of South America is the absence or insufficiency of long time series of observational data. Most national datasets were created in the 1970s and 1980s, preventing a more comprehensive long-term trend analysis. To fulfil the users demand for climatological and meteorological data products covering the whole region, several interpolation techniques have been used – reanalysis and gridded gauge-analysis products – that add the necessary spatial detail to the climate analyses over land and for climate variability and trend studies, however subject to uncertainties (Skansi et al., 2013).

Atlas.5.5.2.3 Assessment of model performance

As reported in Chapter 9 of the WGI AR5 (Flato et al., 2013b), the global models are able to reproduce quite well the general features of the regional-scale mean surface temperature (*high confidence, robust agreement*). However, the models continued to perform less well for precipitation (although regional-scale patterns have improved) than for surface temperature, and the assessment remains difficult owing to observational uncertainties. In addition, the multi-model mean is closer to observations than most of the individual models (*high confidence*). Since AR5 the number of publications on climate model performance and their projections in South America has increased, particularly for regional climate modelling studies (Ambrizzi et al., 2019).

Most global and regional climate models can simulate reasonably well the current climatological features of South America, such as seasonal mean and annual cycles, while underestimating rainfall over tropical South America including the Amazon, northeast Brazil and the Andes (Joetzjer et al., 2013; Torres and Marengo, 2013a; Yin et al., 2013; Fernandes et al., 2015; Yoon, 2016). During the dry season, both convective and large-scale precipitation are underestimated in most models over Amazonia (Yin et al., 2013). Over regions with complex orography, such as the subtropical central Andes, the CMIP5 models were found to reproduce

adequately well the regional and seasonal surface temperature and precipitation, as well as sea-level pressure and circulation (Zazulie et al., 2017). These improvements in climate modelling have advanced understanding of climate variability in South America; however, significant biases persist mainly at regional scales (Blázquez and Nuñez, 2013; Gulizia et al., 2013; Joetzjer et al., 2013; Jones and Carvalho, 2013; Torres and Marengo, 2013a; Gulizia and Camilloni, 2015; Zazulie et al., 2017; Abadi et al., 2018; Barros and Doyle, 2018). The biases in seasonal precipitation, annual precipitation and climate extremes over several regions of South America were reduced, including the Amazon, central South America, Bolivia, eastern Argentina and Uruguay, in the CMIP5 models when compared to those of CMIP3 (*medium confidence*) (Díaz and Vera, 2017). In general, the multi-model ensemble results have demonstrated better performance compared to individual models in most seasons and regions (Sillmann et al., 2013b; Torres and Marengo, 2013a; Gulizia and Camilloni, 2015). The representation of the South America Monsoon System (SAMS) life cycle exhibited a significant improvement in some CMIP5 models when compared to their versions in the CMIP3 whereas others continue to have problems in representing accurately the main SAMS features, such as amplitude and length (Jones and Carvalho, 2013; Reboita et al., 2014; de Carvalho and Cavalcanti, 2016).

RCM simulations showed a systematic temperature underestimation over the Amazon, temperature overestimation and precipitation underestimation over La Plata Basin, with the warm bias amplified for austral summer and the dry bias amplified for the rainy season (Solman et al., 2013; Reboita et al., 2014; Solman, 2016a). The dry bias shown by most RCMs in the La Plata Basin is partially due to errors in representing cold-front passages over southern Brazil (de Jesus et al., 2016). In summer the precipitation bias is explained by too few passages of cold fronts, while in winter it is explained by the fact that low pressure systems are not deep enough and that there is a lack of moisture availability in low levels.

The evaluation of statistical downscaling models (ESD) in representing the different regional climate features in South America has increased since the AR5 assessment, however there are still few ESD studies over the different subregions. Precipitation simulations based on ESD models properly reproduce mean precipitation over tropical and subtropical South American regions, especially with maximum precipitation areas in western Colombia, south-eastern Peru, central Bolivia and the La Plata basin (Souvignet et al., 2010; Mendes et al., 2014; Palomino-Lemus et al., 2015, 2017, 2018; Soares dos Santos et al., 2016; Troin et al., 2016; Bettolli and Penalba, 2018; Bettolli et al., submitted). Major discrepancies are linked with dry areas or with unreliable coverage of data. Temperature simulations are fewer but satisfactory over the La Plata Basin plains as well as the complex orography of north central Chile (Souvignet et al., 2010; Bettolli and Penalba, 2018).

Overall, climate modelling has made some progress in the past decades, but the results reveal that there is no model that performs well in simulating all aspects of the present climate over South America. The performance of the models varies according to the region, time scale, and variables analysed (Abadi et al., 2018). There is also a fairly narrow spread in the representation of temperature and precipitation over South America by the CMIP5 GCMs and also the RCMs, with biases that can be associated with the parametrizations and schemes of surface, boundary layer, microphysics and radiation used by the models. Finally, observational reference datasets, such as reanalysis products, used in the calibration and validation of climate models also can be quite uncertain and may explain part of the important biases present in climate models.

Atlas.5.5.2.4 Assessment and synthesis of projections

Previous assessments, as was shown in AR5 WGI Chapter 12, AR5 WGII Chapter 27 and SR1.5 Chapter 3, based on the CMIP5 multi-model projections, have suggested that substantial warming (2°C to 6°C) would occur in a large portion of South America at the end of 21st century for all emission scenarios (RCPs) (*high confidence*). Rainfall changes for South America vary geographically, most notably showing a reduction in northeast Brazil, and an increase in southern South America (*high confidence*).

Anthropogenic GHG emissions are indeed expected to alter substantially the climate over South America in the coming decades (Solman et al., 2013; Reboita et al., 2014, 2016, 2018; Coppola et al., 2014a; da Rocha

et al., 2014; Llopart et al., 2014a, 2019; Sánchez et al., 2015a; Cabré et al., 2016; Ruscica et al., 2016a; Menéndez et al., 2016a; Fernandez et al., 2017; Palomino-Lemus et al., 2017, 2018; Ambrizzi et al., 2019; Zaninelli et al., 2019a). Increases in extreme events, such as flood, drought, and heatwaves (Batista et al., 2016; Giorgi et al., 2014; López-Franca et al., 2016; Marengo et al., 2017; Sillmann et al., 2013) associated with climate change may pose severe stresses on natural ecosystems and various sectors of society in the continent (see Chapter 12).

According to GCM, RCM and ESD projections, it is *very likely* that temperature will increase over South America by a wide range – from 1.0°C up to 6.0°C – by the end of the 21st century under all emission scenarios (Souvignet et al., 2010; Coppola et al., 2014b; Sánchez et al., 2015b; Solman, 2016b; Ambrizzi et al., 2019; Llopart et al., 2019), with the highest warming projected over the central South America as shown in Figure Atlas.39: (Chou et al., 2014b; Coppola et al., 2014b; Cabré et al., 2016; Menéndez et al., 2016a; Ruscica et al., 2016a; Llopart et al., 2019) (*high confidence*). The temperature change is larger than the interannual variability range for the entire South America (*high confidence*) (Torres and Marengo, 2013b).

The precipitation changes expected for the late 21st century are complex due to the large spread exhibited by the future projections, but the ensemble average changes indicate a general drying of northern and wetting of southern South America east of the Andes (*medium confidence*) (Solman, 2013; Chou et al., 2014b; Llopart et al., 2014b; Reboita et al., 2014; Sánchez et al., 2015a; Menéndez et al., 2016b; Ruscica et al., 2016b; Zaninelli et al., 2019a; Reboita et al., submitted), though with a large inter-model spread (Solman, 2013; Coppola et al., 2014b; Llopart et al., 2014b, 2019; Sánchez et al., 2015a). A decline in precipitation in the Chilean Andes and an increase in the west of Colombia is also *likely* expected (Souvignet et al., 2010; Palomino-Lemus et al., 2017, 2018). Alves et al.(submitted) suggest that all the Brazilian regions will experience more rainfall variability in the future, i.e., drier dry periods and wetter wet periods on daily, weekly, monthly and seasonal timescales, despite the future changes in mean rainfall being currently uncertain. These changes will clearly impact natural and agricultural ecosystems (Camilo et al., 2018). On the other hand, according to Torres and Marengo (2013) the projected changes of precipitation have the same magnitude as the natural variability, however these results do not apply to the climate projections of climate extremes (see Chapter 11).

To assess the future climate changes in precipitation and mean temperature due to the global warming, the mean changes over seven key regions in South America (NSA, SAM, NWS, NES, SWS, SES, and SSA; see Figure Atlas.39:) are shown in tables Atlas.A.3 to Atlas.A.9 (see Appendix Atlas.A) that summarize the projected changes expected for the end of this century, relative to the present day. The baseline depends on the reference article – for example, Coppola et al. (2014) used 1975–2005 as reference period while Mourão et al. (2016) used 1961–1990.

As shown in Figure Atlas.39: mean temperature is expected to increase according to simulations of both CMIP5 and CMIP6 models over all South America. The projected increases in temperature are greater in the latter dataset with the highest values reaching 6°C over the SAM region by the end of the 21st century (*high confidence*). For precipitation, there is a *high agreement* over the whole continent with significant decreases in the south of Chile and Argentina of up to 40% (south of SWS and SSA) and increases in the coastal areas of Peru and Ecuador of up to 50% (NWS).

[START Figure Atlas.39: HERE]

Figure Atlas.39: (a–b) Mean observed trends of annual mean surface air temperature and precipitation for three datasets (CRU TS, BERKELEY and EWEMBI for temperature; CRU TS, GPCC and GPCP for precipitation). Hatching indicates regions where no or only one dataset provides a significant trend. Linear trends are calculated for the common 1980–2014 period and expressed in °C per decade (temperature) and % relative change per decade (precipitation) with respect to the climatological mean over this period.
(c–f) Climate change projections of annual mean surface air temperature and precipitation from CMIP5 (30 models) and CMIP6 (17 models) calculated as the differences in the climatological average for RCP8.5 and SSP5-8.5 respectively, for the period 2041–2060 with respect to the historical

1995–2014 period and expressed as °C (temperature) and % relative change (precipitation). Hatching indicates weak model agreement on the sign of the change (less than 80% as defined in Nikulin et al., 2018).
(g–m) Regional mean changes in annual mean surface air temperature and precipitation for the seven South American regions (NWS, NSA, SAM, NES, SWS, SES and SSA). The top row shows the median (dots) and 10th–90th percentile range across each model ensemble for annual mean temperature changes, for two datasets (CMIP5 and CMIP6) and two scenarios (SSP1-2.6/RCP2.6 and SSP5-8.5/RCP8.5). The first four bars represent the additional warming projected relative to the historical baseline 1995–2014 period to reach the two global warming levels (GWL; +1.5°C and +2°C) and the remaining six projected changes over three time periods (near-term 2021–2040, mid-term 2041–2060 and long-term 2081–2100) compared to this same historical baseline period. The bottom row shows scatter diagrams of temperature against precipitation changes, displaying the median (dots) and 10th–90th percentile ranges for four future periods (2021–2040, 2041–2060, 2061–2080, 2081–2100) compared to the historical baseline period, as obtained from CMIP6 projections for three scenarios (SSP1-2.6, SSP2-4.5 and SSP5-8.5). Changes are absolute for temperature and relative for precipitation.
(The script used to generate this figure is available online (Atlas GitHub, 2020) and similar results can be generated in the Interactive Atlas for flexibly defined seasonal periods.)

[END Figure Atlas.39: HERE]

Atlas.5.6 Europe

Regional executive summary

In most European areas it is *very likely* that positive trends in extreme precipitation and warm temperatures are persistent. This is documented using new datasets with homogenized observations at higher spatial and temporal resolution. {Atlas.5.6.2}

It is *very likely* that a substantial number of weather events involving extreme temperatures in Europe can be attributed to human contributions to climate change. This is following the application of a range of methods (*high confidence*). Increasing trends in surface shortwave radiation are *likely* attributed to decreasing trends in aerosol concentrations. {Atlas.5.6.2}

Model representation of the climatology of European mean and extreme temperature and precipitation has improved compared to AR5 (*likely*). This is aided by continuous model development, the existence of new coordinated modelling initiatives dedicated to Europe such as Euro-CORDEX and Med-CORDEX, and the release of new (high-resolution) observational data sets and reanalysis data. {Atlas.5.6.3}

There is *medium confidence* that high-resolution, convection permitting RCMs have a better representation of characteristics of extreme precipitation (e.g., diurnal cycles, mesoscale convective events, extremes) and exhibit stronger responses in the tails of the precipitation distribution than coarser resolution models. {Atlas.5.6.3}

The subset of CMIP6 results available in the Interactive Atlas at the time of the release of the SOD shows higher future warming in the European regions in DJF and JJA than CMIP5, corresponding to a larger climate sensitivity of the CMIP6 models (*likely*). JJA precipitation in NEU and EEU is *likely* lower in CMIP6 than in CMIP5. {Figure Atlas.40:, Figure Atlas.41:}

It is *very likely* that strong winter warming in Northern Europe and strong summer warming in Southern Europe will continue. It is *likely* that the associated northern European increase in seasonal mean precipitation and reduced summer mean precipitation in southern Europe will continue. Different regional warming levels will be reached depending on the level of global warming. {Atlas.5.6.4}

Projections of summer surface radiation, surface temperature and precipitation of RCMs and GCMs

are frequently inconsistent. There is *limited evidence* that some of these inconsistencies can be attributed to the treatment of aerosols and that internal variability of large-scale atmospheric circulation also plays a role. {Atlas.5.6.4}

Atlas.5.6.1 Key features of the regional climate and findings from previous assessments

Key features of the regional climate

The main climatic features that characterize daily to inter-annual variability in the European region are westerly winds and the accompanying Atlantic storm track with cyclones and anticyclones travelling mainly from the Atlantic towards inland Europe. The Siberian High in winter determines cold weather in East Europe and can affect Central and even West and South Europe with cold outbreaks. Intra-seasonal and inter-annual variations are driven by modes of climate variability such as the North Atlantic Oscillation (Hurrel et al., 2003), and atmospheric flow patterns characterized as "weather regimes" in winter or summer seasons (Michelangeli et al., 1995; Cassou et al., 2005). Feedbacks may amplify climate variability, in particular soil moisture temperature feedbacks in Central Europe in summer (Boé and Terray, 2014) and feedbacks related to snow cover in winter (Henderson and Leathers, 2009).

Global warming can lead to systematic changes in regional climate variability via various mechanisms. Thermodynamic responses such as altered lapse rates (Kröner et al., 2017; Brogli et al., 2019) and land-atmosphere feedbacks (Boé and Terray, 2014) modify temporal and spatial variability of temperature and precipitation, including altered seasonal and diurnal cycles and return frequencies of extremes. Regional feedbacks involving the sea surface, land surface, clouds, aerosols, radiation and other processes modulate the regional response to enhanced warming.

The climatic regions defined for Europe include (see Figure Atlas.2:):

- [MED] The Mediterranean region in the south characterized by mild winters and hot and dry summers (Mediterranean climate). The climate is determined by sinking motion on the eastern flank of the climatological high pressure in the Atlantic region in boreal summer, and by the Atlantic storm track in boreal winter.
- [CEU] The continental region in central Europe characterized by warm summers and cold winters with increasing continentality of climate eastwards.
- [NEU] The northern regions, close to the Atlantic Ocean, characterized by high humidity and relatively mild winters, and strong exposure to the Atlantic storm track.
- [EEU] The western part of Russia and neighbouring territories, with continental characteristics.

Previous findings from IPCC assessments

Previous findings from IPCC assessments on observed trends

The AR5 WGI and SREX assessments reported that it is *likely* that heatwave frequency has increased since 1950 in large parts of Europe and that there is *high confidence* that the frequency and intensity of precipitation have increased. Central and southern Europe, including the Mediterranean region, are highlighted as the regions with the highest levels of warming for extreme hot days.

According to the SRCCL report frequency and intensity of droughts have increased due to climate change in southern Europe and the Mediterranean (*medium confidence*). A vegetation greening and has been observed in the last 30 years over all European land due to extended growing season, increased CO_2 emissions, nitrogen deposition and land management (*high confidence*) but also due to an increase of forest area. There is *high agreement* that this forestation cools summertime surface temperature and warms winter temperature due to decreased snow cover and increased snow shading in forested areas. Warmer and drier climate has been also the cause of yield decline in part of Southern Europe.

SROCC reports with *high confidence* that a reduction in snow cover at low elevation, glacier extent and

permafrost area is observed, with consequent changes in annual and seasonal runoff patterns. Permafrost temperature shows an increase in the European Alps. In the Russian European north, a considerable reduction in permafrost thickness and areal extent has been observed over the 1975–2005 period *(medium confidence)*.

Since the 1970s, it is *virtually certain* that the frequency and intensity of storms in the North Atlantic have increased, although the reasons for this increase are debated. With *high confidence*, floods recorded in the 20th century have been larger than those occurring during the past five centuries in northern and central Europe, and the western Mediterranean region.

It is *very likely* that aerosol column amounts have declined over Europe since the mid-1990s.

Previous findings from IPCC assessments on model performance

AR5 reports that the ability of models to simulate the climate in Europe has improved in many important aspects. Particularly relevant for this region are increased model resolution and a better representation of the land-surface processes in many of the models that participated in CMIP5. The spread in climate model projections is still substantial, partly due to large amounts of natural variability in this region (particularly NAO and AMO). Storm track biases in the North Atlantic have improved slightly, but models still produce a storm track that is too zonal and underestimate cyclone intensity.

Studies assessed in SR1.5 have clearly identified a possible amplification of temperature extremes by changes in soil moisture, acting as a mechanism that further magnifies the intensity and frequency of heatwaves related to summer drying conditions. Other studies indicate that European winter variability may be related to sea-ice reductions in the Barents-Kara Sea.

Previous findings from IPCC assessments on future projections

AR5 reports it is *likely* that in the next decades the frequency of warm days and warm nights will increase in most land regions, while the frequency of cold days and cold nights will decrease. Models also project increases in the duration, intensity and spatial extent of heatwaves and warm spells for the near term. Several studies project that European high-percentile summer temperatures are projected to warm faster than mean temperatures.

SRCCL reports that warming in high latitude is also projected to increase disturbance in boreal forest, like drought wildfires and pest outbreaks (*high confidence*). Also the Mediterranean area may be increasingly affected by wildfire. Global warming and urbanization can increase the heat island effect in cities, particularly during heat wave events. This will mainly affect night time temperatures (*high confidence*).

SROCC reports with *very high confidence* that snow cover and glaciers are projected to decrease all along the 21st century. For RCP8.5 in Central Europe and Caucasus the small glaciers are projected to lose more than 80% of their mass by the end of century.

AR5 reports that in the winter half year, NEU and CEU are projected to have increased mean precipitation associated with increased atmospheric moisture, increased moisture convergence and intensification in extratropical cyclone activity and no change or a moderate reduction in the MED. In the summer half year, NEU and CEU mean precipitation are projected to have only small changes whereas there is a notable reduction in MED. These precipitation changes are more pronounced at 2°C than with a 1.5°C global warming.

For a 2°C global warming, an increase in runoff is projected for north-eastern Europe while decreases are projected in the Mediterranean region, where runoff differences between 1.5°C and 2°C global warmings will be most prominent. At high latitudes high river flows are expected to be more frequent. Probabilities associated with increases in drought frequency and magnitude are substantially larger at 2°C than at 1.5°C in the Mediterranean region *(medium confidence)*.

The AR5 WGII European chapter (Chapter 23) reports that there is *medium confidence* in extreme wind increase in central and northern Europe, and *low confidence* of a small decreasing trend in Southern Europe by the end of the 21st century.

SROCC reports that a *likely* decline in AMOC will lead to an increase in winter storms in Europe.

The AR5 assessed with *high confidence* a projected increase in extreme sea level events. The frequency of 100-year return period river-discharge events is expected to increase in continental Europe and decrease in some northern and southern European regions. Snowmelt flood may decrease by the end of the 21st century and peak floods in northern Europe may increase in autumn and winter due to increased rainfall in these seasons. A decline in low flow is projected by 2100 for United Kingdom, Turkey, France and rivers fed by Alpine glaciers.

Atlas.5.6.2 Assessment and synthesis of observations, trends and attribution

An assessment of more recent literature largely confirms the findings of previous IPCC reports but with additional detail and (for some measures) higher confidence due to improvements in observations and refinement in methods.

In Northern Europe continued warming has been observed, particularly during spring. Between 1970-2008 Rutgersson et al. (2015) report an annual mean temperature increase of 0.4°C per decade. In Poland Degirmendžić et al. (2004) report positive temperature trends in spring over 1951-2000 (3°C in March and 1.5°C in May). In Ukraine annual mean surface air temperature has increased by 0.57°C (0.3 – 0.7°C) per decade in the period 1961 – 2010, with a particularly strong warming of 1.1 °C per decade for JJA maximum air temperature in the south-east steppe (Boychenko et al., 2016; Balabukh and Malitskaya, 2017). Loginov et al. (2018) argued that the summer diurnal temperature range has decreased particularly in cities, but no significant trend in winter mean air temperatures is shown between 1881 and 2016 in Belarus. In this area the number of extreme weather events has decreased since 2001 attributed to a decrease in the meridional south circulation. In Western Europe land-only observations analysed by Dong et al. (2017) indicate a rapid increase in summer (JJA) mean surface air temperature since the mid-1990s. The change in temperature during 1996–2011 relative to 1964–1993 ranges from 0.93 to 1.10 °C. Ringard et al. (2019) report a significant annual mean temperature increase since 1979 of 0.4 °C per decade over Paris, with 0.52 and 0.46 °C per decade in spring and summer, respectively. Also over Spain spring and summer temperatures are reported to increase faster than in the other seasons (Vicente-Serrano et al., 2017). Gonzalez-Hidalgo et al. (2016) found the temperature increase to be maximum between 1970 and 1990.

Trends in mean precipitation are generally small and non-significant. Tímea and Anda (2017) report a decrease of annual mean precipitation in Hungary of 11% between 1901 and 2004 (mostly in spring). Trend analysis from 1966 to 2000 based on 3-hourly synoptic observations at 547 stations over Northern Eurasia by Ye et al. (2017b, 2017a) indicated an increase of the number of convective precipitation days in winter of 4.3 day/decade, while an increase of 0.7 day/decade was seen in summer. While the precipitation fraction falling as snow decreased, in Ukraine the intensity of heavy snowfall events has increased significantly and shifted from the north-north-western parts in the past to south-south-eastern regions recently (Balabukh et al., 2018). These trends were significantly correlated with surface warming and moistening. However, negative trends in number of non-convective precipitation days were larger, leading to a small net decrease in the number of wet days in spring, summer and fall. Murphy et al. (2019) re-evaluated the trends identified with the England Wales Precipitation (EWP) series, and blame the widely reported trend to wetter winters (DJF) and drier summers (JJA) over north-western Europe by gauge undercatch of snowfall for pre-1870 winters. For summer, pre-1820 precipitation totals were too high, likely due to decreasing network density and less certain data at key stations.

A substantial fraction of temperature extremes in Europe can be attributed to anthropogenic activity (Coumou and Rahmstorf, 2012; Fischer and Knutti, 2015). However, for precipitation at local to regional

scales, this attribution is less straightforward (Stott, 2016). During the northwest European dry and warm spell in the spring and summer of 2018, the temperature extremes could be attributed to global warming (Leach et al., 2019; Yiou et al., 2019). Land-atmosphere interactions involving soil moisture-atmosphere feedbacks are shown to be able to amplify temperature and precipitation anomalies in Central Europe, suggesting that global warming can increase the probability of large scale precipitation deficits (Vogel et al., 2018). Gudmundsson and Seneviratne (2015) show a gradient in trends of (particularly multi-annual) droughts across Europe, with a decreasing trend in Northern Europe and increasing trends in the South. However, a formal attribution of European droughts to global warming has not been documented.

The increasing trend in surface shortwave radiation, documented in AR5 to have occurred since the 1980s and referred to as a brightening effect, is substantiated over Europe and the Mediterranean region (Nabat et al., 2014; Sanchez-Lorenzo et al., 2015). This increasing trend has been attributed to the decrease in anthropogenic sulphate aerosols over the 1980–2012 period (Nabat et al., 2014). In model sensitivity experiments, the aerosol trend has been quantified to explain 81 ± 16% of the European surface shortwave trend and 23 ± 5% of the European surface temperature warming.

To support climatological analyses and model evaluation, national meteorological and hydrological services are increasingly making available high spatial and temporal resolution gridded and in situ homogenized and quality-checked datasets. The inclusion of additional station data lead to a better representation of extreme precipitation statistics than the global-scale CRU or continental-scale E-OBS datasets. For example, in Norway a 1km gridded daily precipitation and temperature dataset is available from 1957 to the present (Lussana et al., 2018). Switzerland, Sweden, France, Germany, Poland, Spain and the Carpathians also boast gridded observation-based datasets at resolution of 2 to 25 km (Déqué and Somot, 2008; Vidal et al., 2010; Rauthe et al., 2013; Noël et al., 2015; Spinoni et al., 2015; Herrera et al., 2016; Ruti et al., 2016; Fantini et al., 2018). Recent gridded products merging radar and station data allow to reach higher spatial and temporal resolutions (Tabary et al., 2011; Berg et al., 2016; Fumière et al., 2019). Spatial pooling of climate change signals enhances the statistical robustness of the observed and projected trends (Fischer et al., 2013).

While the emergence of very high-resolution observation-based gridded datasets does provide additional information for climate assessments and model evaluation, a number of caveats exists. The gridded European datasets are unreliable over data-sparse regions. Also, many datasets employ different approaches to interpolation and gridding, which adds to their uncertainty and complicates comparative evaluations (Kotlarski et al., 2017; Berthou et al., 2018; Fantini et al., 2018). For example, differences between different precipitation datasets have been shown to be of the same magnitude as errors in regional climate models (Prein et al., 2016; Prein and Gobiet, 2017; Fantini et al., 2018).

Atlas.5.6.3 Assessment of model performance

Regional climate models driven by reanalysis have been extensively evaluated regarding a range of climate features over Europe and the Mediterranean (Casanueva et al., 2016; Vaittinada Ayar et al., 2016; Ivanov et al., 2017; Krakovska et al., 2017; Terzago et al., 2017; Cavicchia et al., 2018; Drobinski et al., 2018; Fantini et al., 2018; Harzallah et al., 2018; Panthou et al., 2018b). Standard assessments of RCMs, typically run at 12– 25 km spatial resolution, confirm that the Euro-CORDEX and Med-CORDEX ensembles are capable of reproducing the salient features of European climate, corresponding to the ENSEMBLES simulations (Kotlarski et al., 2014; Krakovska, 2018). They have been shown to be able to represent realistically circulation features such as coastal low-level jet (over Portugal, (Cardoso et al., 2016), medicanes (Gaertner et al., 2018), Mediterranean cyclones (Flaounas et al., 2018; Sanchez-Gomez and Somot, 2018), cyclonic activity in high latitudes including Northern Europe (Shkolnik and Efimov, 2013), characteristics of heating periods (Krakovska et al., 2019) and intensity, direction and inland penetration of the sea breeze (south of France, (Drobinski et al., 2018).

RCMs run at 12 km generally show similar area-averaged, seasonal mean features compared to coarser-scale simulations (with GCMs and lower-resolution RCMs). However, higher-resolution simulations do show improved performance in reproducing the spatial patterns and seasonal cycle of mean precipitation over all

European regions (Mayer et al., 2015; Soares and Cardoso, 2018), extreme precipitation (Torma et al., 2015; Prein et al., 2016; Ruti et al., 2016; Fantini et al., 2018), snow-melt driven runoff in the Alps (Coppola et al., 2018), and mountainous zones (Torma, in press). This is mainly due to the better representation of orography at high resolution (e.g. Dyrrdal et al., 2018). Precipitation improvements in summer are attributed to better representation of larger spatial convection structures. Limited added value was noted for heatwaves (Vautard et al., 2013; Jury et al., 2018) and surface solar radiation (Vautard et al., submitted).

However, systematic errors persist in RCM simulations, such as cold and wet biases over much of the continent and warm dry biases in the south in summer (Vautard et al., submitted). Seasonal and regionally averaged temperature biases generally do not exceed 1.5°C, while precipitation biases can be up to ±40% (Kotlarski et al., 2014). The warm and dry summer bias over southern and south-eastern Europe is reduced compared to the previous ENSEMBLES simulations (Katragkou et al., 2015; Giot et al., 2016; Prein and Gobiet, 2017; Dell'Aquila et al., 2018), but over the Mediterranean, RCMs generally underestimate the observed long-term temperature trend, mostly in summer, even with respect to the driving reanalysis. They show rather limited ability to reproduce decadal variability in temperature and precipitation over the Euro-Mediterranean region (Dell'Aquila et al., 2018), which is strongly related to the considerable natural variability at this time scale (Aalbers et al., 2018). In some cases these biases are mitigated by compensating errors further complicating the picture within the Euro-CORDEX ensemble (García-Díez et al., 2015; Katragkou et al., 2015).

Coupled RCMs for the Baltic, North Sea and Mediterranean Sea have been further explored since AR5. New, or updated, higher-resolution, coupled atmosphere-ocean-ice model systems have been found to simulate realistically the observed climate over the Baltic area with some improvement with respect to stand-alone atmosphere model versions in features, like the correlation between precipitation and SST, between surface heat-flux components and SST, and for weather events like convective snow bands over the Baltic Sea (e.g. Gröger et al., 2015; Pham et al., 2017; Tian et al., 2013; Van Pham et al., 2014; Wang et al., 2015). Coupled atmosphere-land-river-ocean Regional Climate System Models (RCSMs) from Med-CORDEX have similar skill as the ENSEMBLES ensemble and the Euro-CORDEX ensemble to represent decadal variability of Mediterranean climate and its extremes (Cavicchia et al., 2018; Dell'Aquila et al., 2018; Gaertner et al., 2018). A number of single model studies over the North Sea and Baltic Sea region (Tian et al., 2013; Gröger et al., 2015; Wang et al., 2015) have shown that ocean-atmosphere coupling improves the representation of atmosphere and ocean compared to standalone model versions. Panthou et al. (2018) also showed that over land differences between atmosphere-only and coupled RCMs are confined to coastal areas that are directly influenced by SST anomalies. In contrast, Van Pham et al. (2014) showed significant differences in seasonal mean temperature across a widespread continental domain. Sea wind (Akhtar et al., 2018), the turbulent air-sea fluxes (Sevault et al., 2014; Akhtar et al., 2018), and the seasonal cycle of the medicane frequency (Gaertner et al., 2018) are shown to be improved in coupled RCSMs.

Convection-Permitting RCMs (CPRCM, running at a resolution of typically 1 to 3 km) are better able to capture observed extreme precipitation behaviour than 12-km RCMs (Kendon et al., 2014; Prein et al., 2015; Lind et al., 2016; Berthou et al., 2018; Fumière et al., 2019; Ban et al., submitted). Precipitation on daily and shorter time scales shows more coherent results than coarser resolution RCMs (Kendon et al., 2016). Ban et al. (2014) found Clausius-Clapeyron (CC) scaling between temperature and moderate (90th percentile value) hourly precipitation events, while super-CC scaling was noted for the extreme (99th percentile and up) tails of hourly precipitation.

The role of aerosol forcing is increasingly analysed as new and more realistic aerosol datasets become available (Nabat et al., 2013; Pavlidis et al., submitted), and as RCMs begin to include interactive aerosols (Nabat et al., 2012, 2015a; Drugé et al., 2019; Nabat et al., submitted). Explicitly accounting for aerosol effects in RCMs leads to improved representation of the surface shortwave radiation at various scales: long-term means (Gutiérrez et al., 2018), day-to-day variability (Nabat et al., 2015a), and long-term trends (Nabat et al., 2014). It is *likely* that including a realistic representation of aerosol past trends in climate models over Europe increases positive land- and sea-surface temperature trends, with associated reductions in evaporation and precipitation, and increases the deep-water formation rate in the Mediterranean Sea (Nabat et al., 2014). For favourable circulation types, the representation of aerosols affects the simulated heatwave intensity over

Europe (Nabat et al., 2015b).

Atlas.5.6.4 Assessment and synthesis of projections

[START Figure Atlas.40: HERE]

Figure Atlas.40: (a–b) Mean observed trends of annual mean surface air temperature and precipitation for three datasets (CRU TS, BERKELEY and EWEMBI for temperature; CRU TS, GPCC and GPCP for precipitation). Hatching indicates regions where no or only one dataset provides a significant trend. Linear trends are calculated for the common 1980–2014 period and expressed in °C per decade (temperature) and % relative change per decade (precipitation) with respect to the climatological mean over this period.
(c–f) Climate change projections of annual mean surface air temperature and precipitation from CMIP5 (30 models) and CMIP6 (17 models) calculated as the differences in the climatological average for RCP8.5 and SSP5-8.5 respectively, for the period 2041–2060 with respect to the historical 1995–2014 period and expressed as °C (temperature) and % relative change (precipitation). Hatching indicates weak model agreement on the sign of the change (less than 80% as defined in Nikulin et al., 2018).
(g–j) Regional mean changes in annual mean surface air temperature and precipitation for the four European regions (NEU, CEU, MED and EEU). The top row shows the median (dots) and 10th–90th percentile range across each model ensemble for annual mean temperature changes, for two datasets (CMIP5 and CMIP6) and two scenarios (SSP1-2.6/RCP2.6 and SSP5-8.5/RCP8.5). The first four bars represent the additional warming projected relative to the historical baseline 1995–2014 period to reach the two global warming levels (GWL; +1.5°C and +2°C) and the remaining six projected changes over three time periods (near-term 2021–2040, mid-term 2041–2060 and long-term 2081–2100) compared to this same historical baseline period. The bottom row shows scatter diagrams of temperature against precipitation changes, displaying the median (dots) and 10th–90th percentile ranges for four future periods (2021–2040, 2041–2060, 2061–2080, 2081–2100) compared to the historical baseline period, as obtained from CMIP6 projections for three scenarios (SSP1-2.6, SSP2-4.5 and SSP5-8.5). Changes are absolute for temperature and relative for precipitation.
(The script used to generate this figure is available online (Atlas GitHub, 2020) and similar results can be generated in the Interactive Atlas for flexibly defined seasonal periods.)

[END Figure Atlas.40: HERE]

Regional climate change simulations from Euro-CORDEX have been assessed for levels of global warming of 1.5 and 2.0 °C (Schaller et al., 2016; Dosio and Fischer, 2017; Kjellström et al., 2018; Teichmann et al., 2018). The projections indicate enhanced local warming even at relatively low global warming levels, particularly towards the north in winter. Changes in precipitation include increases in the north and decreases in the south with a borderline that migrates from a northerly position in summer to a southerly one in winter (Jacob et al., 2018; Coppola et al., submitteda). Extreme temperature and precipitation exhibit a different response to global warming than mean values. Precipitation extremes, particularly on daily and shorter time scales, are projected to increase even for some regions where the mean precipitation is projected to decrease (Ban et al., 2015; Rajczak and Schär, 2017; Tramblay and Somot, 2018; Coppola et al., submitteda). Large impacts on water availability, agriculture and forestry are reported in Eastern Europe (Shvidenko et al., 2017). In a surrogate warming experiment representing a 2°C warming, Lenderink et al. (2019) found super-CC scaling in humid areas over and close to the Mediterranean Sea and over western Europe while over the drier inlands of the Iberian Peninsula scaling was reduced to CC. Also in Eastern Europe regional climate projections have been analysed (Partasenok et al., 2015; Kattsov et al., 2017b), but their quantitative estimations of climate change features have *low confidence* due to the use of relatively small ensembles of GCMs and/or RCMs, and limited evaluation of model performance in the region.

High resolution climate projections reveal an enhanced likelihood of tropical cyclones reaching the European domain (Haarsma et al., 2013; Baatsen et al., 2015; Dekker et al., 2018). The findings have been confirmed by (Liu et al., 2017b), and is addressed in depth in the HighResMIP experiment (Haarsma et al., 2016b).

RCMs and CPRCMs modify some signatures of climate change projected by GCMs. (Kjellström et al., 2018) show that projections of temperature, precipitation and wind in RCMs may deviate from GCM signals dependent on the dominant atmospheric circulation. In many areas RCMs produce lower warming levels and higher precipitation (less drying) in both summer and winter (Coppola et al., submitteda). Over specific geographic features such as high mountains, RCMs modify the climate change signal of extreme precipitation simulated by the low-resolution GCMs (Giorgi et al., 2016; Torma and Giorgi, submitted). This is especially true for summer precipitation over the Alps where opposite signs of changes in mean and extreme precipitation are generated by the CMIP5 GCM ensemble and the 12-km Med-CORDEX and Euro-CORDEX RCM ensemble (Giorgi et al., 2016). Chan et al. (submitted) evaluate the UK CPRCM over a large European domain, and conclude that the application of their high resolution model changes the seasonal signature of the change of extreme precipitation, with lower responses in summer and higher responses in autumn and winter than in earlier RCM experiments. Pichelli et al. (submitted) found with an ensemble of convection-permitting models at 3km resolution that projections of daily precipitation intensity and heavy precipitation can have a different sign in some regions, a stronger amplitude of the diurnal cycle change for mean, intensity, frequency and extreme precipitation, and a larger positive change of high and extreme precipitation distribution for both daily and hourly resolution.

Also for mean surface shortwave radiation, surface temperature and precipitation systematic differences between GCM and RCM outputs are found (Boe et al.; Bartók et al., 2017; Fernández et al., 2018; Sørland et al., 2018a; Gutierrez et al., submitted). This is especially true for the summer season in which RCM ensembles warm and dry significantly less than their corresponding driving GCM ensemble. Some authors claim that RCMs are more realistic because they have smaller bias for the present climate (Sørland et al., 2018a), or better cloud representation (Bartók et al., 2017). Other authors claim that GCMs are more reliable due to representation of aerosol forcing (Boe et al.; Gutierrez et al., submitted), air-sea coupling (Boe et al., submitted) or vegetation response to elevated atmospheric CO_2 (Schwingshackl et al., 2019) that are all missing in many RCMs (Boe et al., submitted) (see case study in section Atlas.6.2).

Figure Atlas.40: shows observed and modelled trends of annual mean temperature and precipitation for a range of observational data sets, CMIP5 and the CMIP6 subset ensemble in the Interactive Atlas for each of the four European subregions. To zoom in on a DJF and JJA seasons specifically, Figure Atlas.41: shows projected changes in seasonal mean temperature and precipitation, derived from the CMIP5 and the CMIP6 subset ensemble. Shown are land-area averaged results from RCP2.6/SSP1, RCP4.5/SSP2 and RCP8.5/SSP5 scenarios for early, mid and late 21st century relative to the 1995-2014 baseline period (see Section Atlas.3 for details on model data selection and processing). Also seasonal mean temperature and precipitation change normalized by the annual mean global mean surface temperature change (over land and sea) obtained from the respective CMIP ensemble are shown.

[START Figure Atlas.41: HERE]

Figure Atlas.41: Regional mean changes in seasonal mean temperature and precipitation for DJF and JJA for the European regions NEU, CEU, EEU and MED for CMIP5 and a subset of CMIP6. Left 2 columns show absolute temperature and relative precipitation change for 3 emission scenarios and 4 20-year time slices between 2020 and 2100 relative to 1995-2014; right 2 columns show the change normalized by the global mean annual mean temperature change. Horizontal and vertical error bars represent the 10% and 90% percentile value from the mean values calculated across the ensemble of included models. See text for details. Results are generated with the Interactive Atlas (http://ipcc-atlas.ifca.es, system version 24 January 2020).

[END Figure Atlas.41: HERE]

The results in Figure Atlas.41: show a consistent meridional gradient of changes in precipitation, with a clear DJF precipitation increase in NEU, CEU and EEU, and reduced precipitation over MED. JJA precipitation is strongly reduced in MED and CEU, and smaller signals are shown in NEU and EEU. The temperature is

increasing in all European domains, but warming is strongest in the continental area EEU away from the Atlantic, in Northern Europe during winter and in MED during summer. In Europe, the increased climate sensitivity of CMIP6 (Forster et al., 2019) is expressed particularly by the regional temperature response in JJA for the strong emission scenarios end of century, where CMIP6 warming is exceeding CMIP5 warming in all areas. DJF temperature response is similar in CMIP5 and CMIP6. JJA precipitation in EEU is clearly reduced in CMIP6, while little change is shown in CMIP5.

Local amplification of global warming (regional temperature change normalized by global mean temperature change) and precipitation change per degree global warming show similar results for CMIP6 and CMIP5 for both winter and summer. Winter precipitation increases by 5 to 7% per °C global warming in the NEU, CEU and EEU regions, and is smaller in CMIP6 than CMIP5 in these regions. Also JJA precipitation in the CEU and EEU regions is reduced in CMIP6 compared to CMIP5. The regional difference between CMIP5 and CMIP6 found here is subject to the selection of models included in the Interactive Atlas, but is broadly consisting with findings from for example (Coppola et al., submitteda).

Darmaraki et al. (2019) used an ensemble of five fully coupled RCSMs and a total of 11 projections to assess the future evolution of the Mediterranean SST and related marine heatwaves at high resolution. By the end of the 21st century and under RCP8.5, Mediterranean extreme SSTs (99th daily percentile) are expected to rise by 3.6°C, significantly more than the annual mean SST increase (3.1°C). Despite different methodologies and time periods, Med-CORDEX RCSM and CMIP5 GCM results agree well on the Mediterranean SST warming rate (Mariotti et al., 2015; Darmaraki et al., 2019). Similarly, an ensemble with one coupled atmosphere-ocean-ice RCSM for the Baltic Sea and the North Sea downscaling five different GCMs show that both seas undergo warming, strong freshening and, for some simulations, changes in the circulation as regional warming continues (Gröger et al., 2015). For the same model ensemble, Dietrich et al. (submitted) found spatially non-uniform changes in air-sea interaction over the North Sea indicating the importance of simulating the coupled system.

Atlas.5.7 North America

Regional executive summary

In most North American areas it is *very likely* that positive trends of warm temperatures are persistent. The observed trends in annual temperature indicate that across near-Arctic latitudes of North America surface air temperature increases are exceptionally pronounced (> 0.5°C per decade) and relatively well-defined as seen in the consistency across multiple data analyses *(high confidence*). {Atlas.5.7.2}

In most North American areas it is *likely* that no clear trends in precipitation are present in the period of 1980 to 2014. Since 1980, it is *likely* that precipitation has decreased in the south-western U.S. and north-western Mexico. Nearly everywhere else, there is no trend in precipitation. {Atlas.5.7.2}

Model representation of the climatology of mean and extreme temperature and precipitation has *likely* improved compared to AR5 over North America. This is aided by continuous model development, the existence of new coordinated modelling initiatives such as NA-CORDEX. {Atlas.5.7.3}

The subset of CMIP6 results available in the Interactive Atlas at the time of the release of the SOD project more pronounced warming in most North American regions compared to CMIP5 with this difference clearest in northern regions. {Atlas.5.7.3 Figure Atlas.42:}

Spanning the range of available climate sensitivities in CMIP ensembles is very likely critical for producing a representative range of dynamically downscaled projections. {Atlas.5.7.3 Figure Atlas.44:}. This is the case for both temperature and precipitation.

It is *very likely*, based on global and regional model future projections, that on an annual time scale precipitation will increase over North America north of about 40°N, and it is *likely* that the direction

of change of precipitation is uncertain below 40°N. {Atlas.5.7.4}

There is *high confidence*, based on results from a large number of regional climate model experiments of varying spatial resolutions, that extreme precipitation will increase in the future though the complexity of interpreting results from models with different resolutions prevents quantification of these increases for specific extreme events. {Atlas.5.7.3, Atlas.5.7.4}

It is virtually certain that the snow cover will experience a decline over most regions of North America during the 21st century, in terms of water equivalent, extent and annual duration. It is however *very likely* that some high-latitude regions will rather experience an increase in winter snow water equivalent, due to the snowfall increase impact prevailing over the warming impact. {Atlas.5.7.4}

Atlas.5.7.1 Key features of the regional climate and previous findings from IPCC assessments

Key features of the regional climate

The recent-past climate of North America is characterized by high spatial heterogeneity and by variability at diverse temporal scales. Considering the traditional Köppen-Geiger classification, North America covers all main climate types, i.e., cold (northern USA and most of Canada), arid (western USA and northern Mexico), temperate (western coast of Canada and USA, south-eastern USA and central Mexico), polar (northern coast of Alaska and northern Canada) and tropical (extreme south-east of Florida, southern Mexico) (Peel et al., 2007). Important geographical features influence local climates over various distances, like the Rocky Mountains through cyclogenesis (Grise et al., 2013) and the Great Lakes through lake-effect snowfall (Wright et al., 2013). The cryosphere is an important component of the climate system in North America, with fundamental roles for the sea ice cover, the snow cover, the permafrost and the Greenland ice sheet. Oceans surrounding the continent also influence its climate, with water temperatures strongly influencing hurricane activity which impacts Caribbean Islands and the coasts of eastern Mexico and south-eastern USA (Elsner, J.B., Jagger, 2010). Temporal variability is influenced by several large-scale atmospheric modes with the North Atlantic Oscillation (NAO) affecting north-eastern USA and eastern Canada precipitation (Whan and Zwiers, 2017), and El Niño–Southern Oscillation (ENSO) impacting California temperature and precipitation, although in a complex and not yet fully understood manner (Yoon et al., 2015; Yeh et al., 2018).

Previous findings from IPCC assessments

The IPCC AR5 (IPCC, 2013b) found that the climate of North America has changed due to anthropogenic causes (*high confidence*) and many climate stressors that carry risk – severe heat, heavy precipitation, and declining snowpack – will increase in frequency and/or severity in the next decades (*high confidence*). SR1.5 (IPCC, 2018c) found that limiting global warming to 1.5°C would limit increases in hazardous heavy precipitation events (*medium confidence*).

Atlas.5.7.2 Assessment and synthesis of observations, trends, and attribution

The observed trends in annual mean surface air temperature (Figure Atlas.42:) across near-Arctic latitudes are exceptionally pronounced (> 0.5°C per decade) and relatively well-defined as seen in the consistency across multiple data analyses. Trends are smaller in magnitude but still quite significant across subtropical western North America. Temperatures have not increased over southern Alaska, western and south-central Canada, and the north-central USA over the period 1980-2014 (Figure Atlas.42:). Compared to temperature, trends in annual precipitation over the past 35 years are generally non-significant, as illustrated by the widespread hatching across most of North America in Figure Atlas.42:. It is *likely* that precipitation has decreased in the south-western U.S. and north-western Mexico (Figure Atlas.42:).

Several factors account for the differences in temperature and precipitation trend significance. Observed

trends in precipitation are relatively modest compared to the very large natural interannual variability of precipitation. Furthermore, the precipitation observing network is spatially inadequate and temporally inconsistent over some regions of North America, so that detection of multidecadal trends is difficult, especially for regions with summertime convective precipitation maxima that may be spatially patchy (Easterling et al., 2017) (Chapter 12).

These differences in observed climate change between temperature and precipitation affect the nature of hazards associated with these variables. Although Figure Atlas.42: emphasizes continental temperature change, the upward trend in temperature is also observed over near-coastal oceans resulting in transient heat waves (*very high confidence*; Chapter 9, WG II Chapter 14). Increasing temperature is also associated with sea-level rise and associated flooding hazards which have seen significant increases during the past several decades (Chapters 9 and 12).

Temperature-related hazards are particularly extreme in high latitudes: sea ice and permafrost are melting rapidly, presenting coastal hazards associated with increasing storminess and diminished coastal protection by ice. In forested regions of North America, probability of wildfire is increasing due to warmer temperature and increased dryness of vegetation (Abatzoglou and Williams, 2016). Increased temperature is associated with increasing severity of episodic, naturally occurring drought, increasing risks to water supplies and ecosystem health, and exacerbating wildfire risk (Chapter 11).

Snowfall and snow cover concern a large portion of North America (Estilow et al., 2015) and have high societal and environmental impacts (Fyfe et al., 2017). Snow interacts in a complex way with temperature and total precipitation, and with other variables like cloud cover and humidity as well (Mioduszewski et al., 2014a). Snow-related reference datasets are ultimately based on in situ and/or satellite measurements (Larue et al., 2017; Brown et al., 2018), which include large uncertainties due to a certain number of technical challenges (Mudryk et al., 2015; Wang et al., 2017), and these may in turn impact long-term trends found in snow datasets (Kunkel et al., 2007).

Observations suggest a rather complex evolution of the snow cover over the continent during recent decades. For example, large spatial heterogeneity was found in the trend sign and amplitude of snow water equivalent (SWE) in situ local records over Canada during the 1967–2016 period (Brown et al., 2019). Only a few of these investigated records show statistically significant trends, but in these cases the trend tends to be negative. Findings in Brown et al. (2019) are similar for snow depth but opposite for snow density (the low number of statistically significant trends tend to be positive). Trends in average snow depth, snow cover extent, and snow onset and retreat dates also show heterogeneous spatial patterns over the U.S. (Knowles, 2015).

Some characteristics of the snow cover show same-sign trends over large parts of the continent. For example, Kunkel et al. (2016) found a general decrease in the annual maximum of SWE between 1961 and 2015, but again with trends generally not statistically significant (see Figure Atlas.43:). Vincent et al. (2015) also report a general decrease in annual maximum SWE for snow monitoring stations across Canada between 1950 and 2012, as well as earlier dates for the occurrence of the snow-depth peak, and shorter snow season duration. For the period of 1981 to 2015, Bush and Lemmen (2019) reported regional declines in snow cover fraction over Canada in all seasons but most widespread from October to December. Analogously, Knowles (2015) found decreases in snow season duration at the contiguous U.S. stations between 1950 and 2010 (using two complementary duration metrics). Mote et al. (2018) report marked declines in April 1st SWE at most monitoring sites of the western US mountains between 1955 and 2016.

Attribution of causes to snow-related changes is often a complex task, as there are regional particularities in climate change (Mioduszewski et al., 2014b). For example, at high latitudes, warming-induced melting may be offset by precipitation increases (Rupp et al., 2013). Some event-based attribution studies indicate these complex relationships. For example, an attribution study for the record low SWE values of winter 2014–15 in the western U.S. concluded that circumstantial Pacific sea surface temperature patterns were about twice as important as anthropogenic warming in Oregon and Washington, with relatively smaller roles for both causes in California (Mote et al., 2016). Teufel et al. (2019) used a 5-member CRCM5 ensemble to

investigate the role of climatic drivers in the April-May 2017 floods along the Ottawa River basin, and found that event-related precipitation accumulation is 2–3 times more likely to occur in the present compared to pre-industrial climate conditions due to increased atmospheric moisture in warmer air, whereas event-related snowpack mass is half as likely to occur due to warmer temperature, resulting in no substantial change in the risk of spring flood. Other drivers (e.g., land use changes) were not explicitly considered in this study.

Elements of the cryosphere other than the snow cover also experienced recent changes, especially in the Arctic part of the continent (AMAP, 2017) which is covered in Section Atlas.5.9.2.

[START Figure Atlas.42: HERE]

Figure Atlas.42: (a–b) Mean observed trends of annual mean surface air temperature and precipitation for three datasets (CRU TS, BERKELEY and EWEMBI for temperature; CRU TS, GPCC and GPCP for precipitation). Hatching indicates regions where no or only one dataset provides a significant trend. Linear trends are calculated for the common 1980–2014 period and expressed in °C per decade (temperature) and % relative change per decade (precipitation) with respect to the climatological mean over this period.
(c–f) Climate change projections of annual mean surface air temperature and precipitation from CMIP5 (30 models) and CMIP6 (17 models) calculated as the differences in the climatological average for RCP8.5 and SSP5-8.5 respectively, for the period 2041–2060 with respect to the historical 1995–2014 period and expressed as °C (temperature) and % relative change (precipitation). Hatching indicates weak model agreement on the sign of the change (less than 80% as defined in Nikulin et al., 2018).
(g–k) Regional mean changes in annual mean surface air temperature and precipitation for the five North American regions (NWN, NEC, WNA, CNA and ENA). The top row shows the median (dots) and 10th–90th percentile range across each model ensemble for annual mean temperature changes, for two datasets (CMIP5 and CMIP6) and two scenarios (SSP1-2.6/RCP2.6 and SSP5-8.5/RCP8.5). The first four bars represent the additional warming projected relative to the historical baseline 1995–2014 period to reach the two global warming levels (GWL; +1.5°C and +2°C) and the remaining six projected changes over three time periods (near-term 2021–2040, mid-term 2041–2060 and long-term 2081–2100) compared to this same historical baseline period. The bottom row shows scatter diagrams of temperature against precipitation changes, displaying the median (dots) and 10th–90th percentile ranges for four future periods (2021–2040, 2041–2060, 2061–2080, 2081–2100) compared to the historical baseline period, as obtained from CMIP6 projections for three scenarios (SSP1-2.6, SSP2-4.5 and SSP5-8.5). Changes are absolute for temperature and relative for precipitation.
(The script used to generate this figure is available online (Atlas GitHub, 2020) and similar results can be generated in the Interactive Atlas for flexibly defined seasonal periods.)

[END Figure Atlas.42: HERE]

[START Figure Atlas.43: HERE]

Figure Atlas.43: Grid box trends (mm yr^{-1}) in annual maximum snow depth for cold season periods of 1960/1961 to 2014/2015. (top) Numbers indicate number of stations available in that grid box. (bottom) Boxes with 'x' indicate statistically significant trends at the $p < 0.05$ level of significance (Vose et al., 2017).

[END Figure Atlas.43: HERE]

Atlas.5.7.3 Assessment of model performance

The North American region has been extensively used as a testbed for regional climate model experiments, such as the North American Regional Climate Change Assessment Program (NARCCAP) (Mearns et al., 2009) and the MultiRCM Ensemble Downscaling (MRED) (Yoon et al., 2012). Therefore, a wide range of performance evaluation was conducted with a focus on specific climate features in North America. For example, multi-model performance evaluation was done for North American monsoon region (Cerezo-Mota

et al., 2015; Tripathi and Dominguez, 2013; Bukovsky et al., 2013) or a single member performance (Lucas-Picher et al., 2013; Martynov et al., 2013; Šeparović et al., 2013). These studies have demonstrated the added value of regional climate models, particularly newly available runs in CORDEX through improved summertime precipitation associated with the North American Monsoon (Tripathi and Dominguez, 2013; Cerezo-Mota et al., 2015) as well as relative agreement between observations and the simulated climatological wintertime storm tracks across the western United States. In comparison to previous sets of RCMs in the NARCCAP, those in NA-CORDEX have better performance in simulating annual and semi-annual modes of precipitation variability in the North American Monsoon region and within the intermountain west (Meyer et al., submitted).

Prein et al. (2019) investigated the ability of RCMs to capture large-scale weather types by examining NA-CORDEX and the WRF large perturbed-physics ensemble (WRF36). Twelve different hydrologically relevant weather types were investigated. NA-CORDEX simulations were found to be more successful at reproducing the weather types compared to the WRF36 ensemble, though it should be noted that there were a number of differences in the suite of experiments that could account for this (e.g., size of domain).

However, a few deficiencies were reported. For example, excessive storm occurrence was found (Poan et al., 2018), and amplitude in the simulated annual cycle was generally excessive in both the lower and higher resolution NA-CORDEX simulations. Summertime precipitation continued to show dry bias except for over the Colorado Rockies) by low-resolution RCMs. An over-active monsoon was simulated by high-resolution RCMs, presumably due to explicitly simulated mesoscale processes and thermodynamics driving the convective precipitation. Additionally, a common trait of NA-CORDEX RCMs that outperformed the ensemble average was the use of spectral nudging. Regional climate models also have been used to evaluate extreme rainfall and temperature. In general, the annual cycle and spatial patterns of extreme temperature are generally better than those of extreme precipitation (Whan and Zwiers, 2016; Meyer et al., submitted submitted).

Recently, convective-permitting RCMs were used to simulate North American climate features and generated better simulations. For example, summer precipitation over the south-western United States was improved due to better representation of organized mesoscale convective systems at subdaily scale (Castro et al., 2012; Liu et al., 2017a; Prein et al., 2017b; Pal et al., 2019) and the diurnal cycle convection (Nesbitt et al., 2008). It has been suggested that the convective-permitting regional downscaling could perform better in terms of mean and extremes for the north-eastern United States (Komurcu Bayraktar et al., 2018).

The lack of long-term high-quality high-resolution gridded datasets limits the assessment of model performance for snow-related variables, especially at regional and local scales (Mccrary et al., 2017; Xu et al., 2019b). Nevertheless, a few studies have focused on model bias estimation over specific regions, and studies on future projections often include recent-past bias estimates. Model biases potentially have various sources, like temperature biases, poor temperature-precipitation co-variability, and model structural/parameter limitations in aspects relevant for snow dynamics (Rhoades et al., 2018).

For the NARCCAP regional simulations ensemble, McCrary and Mearns (2019) found that biases in snow-related variables are more sensitive to the RCM choice than to the driving GCM choice. Biases in winter SWE are mostly positive, except for two models (WRFG and MM5I). Biases are markedly strong over the western mountain chains, and the snow cover generally extends farther in the south than it does in observational datasets. Continental-average snow cover extent and SWE values exceed observational uncertainty in several simulations, for all cold months. NARCCAP snow cover duration biases show different signs from one model to another, but a recurrent feature is a large positive bias over the western US. Biases in snow cover duration occur at both ends of the cold season.

Biases in four NA-CORDEX models (RegCM4, CRCM5, CanRCM4 and WRF) over the California Sierra Nevada were investigated by Xu et al. (2019), who found that all models overestimate snow ablation, and that each of these RCMs has distinct biases regarding snow accumulation processes, compared to the Landsat-Era Sierra Nevada Snow Reanalysis (SNSR) dataset. This study also suggests that increasing spatial resolution (from 0.44° to 0.11° with CRCM5) leads to a substantial improvement in SWE, due to

improvement in mean precipitation and topography-related temperature. However, other snow-related aspects are not improved with higher resolution. Rhoades et al. (2018) emphasize that relatively good model skill for winter SWE averages in simulations may hide compensating errors in more subtle SWE metrics. For example, melt rate biases are prevalent throughout most simulations of NA-CORDEX RCMs (HIRHAM5, RCA4, RegCM4, CRCM5, CanRCM4 and WRF) over the Sierra Nevada, and all GCM-driven RCM simulations have a shorter total snow season length (on average, 44 fewer days) when compared with SNSR.

Rain-on-snow characteristics from the CRCM5 and CanRCM4 models have been assessed by Jeong and Sushama (2018). When driven by ERA-Interim, the two RCM simulations capture reasonably well the spatial distributions of the observed rain-on-snow days; however, they tend to overestimate the observed frequency, particularly over the central parts of North America. This study also shows the ability of both models in reproducing rain-on-snow-related hydro-meteorological features leading to spring flood events, for the St. John River basin in April 2008 and for the Red River basin in March 2009 (Canadian basins).

An evaluation of the NA-CORDEX models has been carried out using the data included in the Interactive Atlas portal (Section Atlas.7). A detailed description of the reference data, metrics and models being evaluated is given in Section Atlas.3.

Atlas.5.7.4 Assessment and synthesis of projections

CMIP5 and CMIP6

Projected temperature and precipitation changes during the 21st century are summarised in Figure Atlas.42: for two different RCPs and SSPs: RCP2.6 and SSP1-2.6 for the lower scenario and RCP8.5 and SSP5-8.5 for the higher scenarios using 30 CMIP5 models for the RCPs and 15 and 17 CMIP6 models for SSP1-2.6 and SSP5-8.5 respectively. The number of model results used to generate these figures differs, and this sample size difference may affect the results but the patterns of change are generally consistent and there is a tendency for higher projected temperature change in the CMIP6 ensemble in the northern regions. Table Atlas.7: summarizes annual temperature and precipitation projections for the end of the century for these scenarios over the far north and south of North America (taken from figures generated by the Interactive Atlas).

[START Table Atlas.7: HERE]

Table Atlas.7: Temperature and precipitation changes at the end of the 21st Century for the far northern and southern parts of North America for the two RCPs indicated under CMIP5 and CMIP6. UC represents lack of model agreement.

		CMIP5		CMIP6	
		RCP2.6	RCP8.5	SSP1-2.6	SSP5-8.5
Temperature	North	2.5°C	>8.0°C	3.5°C	>8.0°C
	South	1.0°C	4.0°C	1.5°C	3.5°C
Precipitation	North	10-15%	45-50%	15-20%	45-50%
	South	UC	UC	UC	UC

[END Table Atlas.7: HERE]

For CMIP5, RCP2.6, annual temperature changes by the end of century progress from 2.5°C in far northern Canada and Alaska down to 1°C in the southern US and northern Mexico. For RCP8.5 temperature changes exceed 8°C in the far northern part of Canada and diminish to about 4°C in the southern US and northern Mexico.

CMIP5 results have been analysed extensively and used in major climate change assessments. The most recent US National Climate Assessment (USGCRP, 2017) used CMIP5 results to project anticipated climate changes over the US (USGCRP, 2017) and adjacent areas, focusing on RCP4.5 and RCP8.5 for two future time periods. Canada's Changing Climate Report (Bush and Lemmen, 2019) present changes in temperature and precipitation, as well as other variables such as snow for future periods in Canada using results from CMIP5.

Regarding precipitation, in the far northern part of the domain increases of 10–15% are projected under RCP2.6 concentrations, but to the south, in the western southern prairies and in most of Mexico, smaller increases (*low confidence*) and some decreases (also *low confidence*) are projected. For RCP8.5, only in the far northern parts of Canada and Alaska are substantial increases (40–50%) projected, and to the south there is considerable uncertainty regarding the direction and amount of change, but there is a tendency for decreases though with little model agreement.

In the case of SSP1-2.6, results for CMIP6 contrast somewhat with those from CMIP5 (Table Atlas.7:). For temperature change at the end of the century larger values are obtained. Temperatures increases by about a degree more than in the CMIP5 ensemble. Projected temperature change ranges from 3.5°C in the far north to 1.5°C in the southern US and northern Mexico. Based on 17 results from the CMIP6 models for RCP8.5 by mid-century, on an annual time scale (Figure Atlas.42:), projected changes greater than 6°C (8°C by end of century) are seen in the northern part of the North American domain, through mid-Alaska and northern Canada, bending down in an arc over Hudson Bay and then arcing back further north. This sinusoidal pattern of temperature change continues throughout the continent down to 3-4°C further south (5°C by end of century), but with somewhat larger warming over the US Rocky Mountains. Lowest values are seen in the Florida panhandle (about 2.5°C or 4.5°C end of century) and on the west coast in the US and the Yucatan in Mexico.

Regarding precipitation for RCP2.6, CMIP6, increases of up to 20% are projected in the far north, decreasing to 15% increase in Alaska and central Canada. For RCP8.5 in northern Canada increases of over 40% are projected, with this amount reducing toward the south to about 10% increase along the US west coast. Increases of 5–10% are seen in the northern part of the US, but below about 40°N decreases are seen although these are uncertain. For the most part, projected changes in Mexico are highly uncertain for most of the country, except for the mid-west coast area where decreases of 10–15% are projected. The overarching patterns of change in the two ensembles are very similar as are the ranges of temperature and precipitation change on an annual basis, except for annual temperature change for RCP2.6, which is somewhat larger in the case of CMIP6.

NA-CORDEX and other regional model projections

The full NA-CORDEX matrix includes considerable spread across multiple GCMs that sample the full range of climate sensitivity, with multiple RCMs, at two different spatial resolutions (25 and 50 km) and considering different RCPs (in most cases RCP4.5 and RCP8.5). The GCM-driven simulations available in the NA-CORDEX archive (Mearns et al., 2017) are discussed, focusing on simulations that used RCP8.5 for future projections (Bukovsky and Mearns, submitted).

The current period (1970–1999) is compared to the future at the end of the 21st century (2070–2099). Bukovsky and Mearns (submitted) focus on the differences in the climate changes in relation to the TCR (Transient Climate Response) of the driving models. Karmalkar (2018) noted that the NA-CORDEX model set does a better job of covering subregional ranges of temperature change from the CMIP5 GCMs than NARCCAP did for the CMIP3 models. Two RCMs driven by the same three GCMs with TCRs that span the range of the CMIP5 models are highlighted here (Figure Atlas.44:). Domain-wide changes in temperature follow the TCR of the global models (low – GFDL, medium – MPI-LR, high – HadGEM2), and this association continues down to the grid-point level. Moreover, there is a tendency for WRF to produce higher domain-wide changes than RegCM, suggesting that at least in some cases there is evidence for different RCMs having something akin to a TCR (Figure Atlas.44:) (Bukovsky and Mearns, submitted). The pattern of warming is as seen in CMIP5 and CMIP6. Greater detail in the RCM responses compared to their driving

GCMs is seen (Figure Atlas.44:) such as over the Rocky Mountains in the US West.

Regarding precipitation, there is also a tendency for the RCMs, domain wide, to follow the TCRs of the driving models, but this tendency is limited to the domain-wide scale on the annual time scale and in winter. The typical increases of precipitation are seen in the far north, and down into lower Canada, and most of the northern US. But there are mixed decreases and increases in the western part of the US, and the west coast when the RCMs are driven by MPI-LR and HadGEM2. Both WRF and RegCM4 follow the pattern of the MPI-LR GCM in most of the domain. Large parts of Mexico (Figure Atlas.44:) exhibit decreases when RegCM is driven by all the GCMs and for WRF when driven by MPI-LR. However, there are also simulations (Mearns et al., 2017; Rendfrey et al., 2018) where there are large increases in the west, particularly in those RCMs driven by CanESM2. These analyses demonstrate that spanning the range of available climate sensitivities in the CMIP5 group is critical for producing a representative range of dynamically downscaled projections.

[START Figure Atlas.44: HERE]

Figure Atlas.44: Changes in the annual mean surface air temperature (top) and precipitation (bottom) by three GCMs (GFDL ESM2M, MPI ESM-LR, HadGEM2-ES) and two RCMs (WRF and RegCM4) nested in the GCMs.

[END Figure Atlas.44: HERE]

Prein et al. (2019) investigated two sets of RCMs regarding weather types and found that under future conditions the NA-CORDEX simulations showed substantial changes in certain weather types, e.g., related to increased monsoonal flow frequency and drying of the northern Great Plains in summer.

In addition to NA-CORDEX, other researchers (Wang and Kotamarthi, 2015; Ashfaq et al., 2016) have produced higher-resolution simulations over large parts of North America. Wang and Kotamarthi (2015) used the WRF RCM at 12 km resolution nested in the CCSM4 over a domain covering much of North America for both RCP4.5 and RCP8.5 for mid and late 21st century in addition to a current period. Annual changes in precipitation include decreasing intensity over the southwest, increasing intensity over the eastern US and much of Canada and an increase in days with heavy precipitation in most areas. This pattern is similar to the changes seen in CCSM4 (their Figure 9), as well as the changes seen in the NA-CORDEX model simulations, which are driven by different GCMs. Ashfaq et al. (2016) analysed results of RegCM4 at 18 km nested in 11 different global models for current and a near-term future period (2010–2050). Both winter (snow) and summer (liquid) extremes are projected to increase across the US. The ensemble mean pattern of precipitation change resembles what is found in NA-CORDEX and the Wang and Kotamarthi simulations, but the changes are less intense at least partially because of the earlier time period examined. They also note, however, that many areas show decreases or increases depending on the driving GCM.

A collection of research articles has considered changes in precipitation extremes in NA-CORDEX, particularly through analysis of changes in Intensity-Duration-Frequency (IDF) curves, calculations frequently used in hydrologic engineering. Higher-resolution modelling is used to analyse changes in IDFs since better reproduction of extremes tends to occur at higher spatial resolutions. DeGaetano and Castellano (2017) used a small set of NA-CORDEX simulations to determine future changes in extreme precipitation in New York State, along with several other downscaling techniques. The dynamically downscaled simulations yielded much larger changes (35%) in 100-year extremes compared to those calculated through an analogue statistical approach (15%). These results have important implications for choice of downscaling method when extreme precipitation is an important consideration (see Chapter 10). Cook et al. (submitted) investigated in 34 cities how choice of spatial resolution of the RCM ensemble affects future IDF curves. The resolution effect was complex in that it depended partially on what duration event was considered. The higher-resolution model results produced larger changes for the 24-hour duration event, but not necessarily for the 1-hour duration event. This indicates greater complexity in potential changes in IDFs based on the

nature of the event under investigation than earlier thought. Other papers (e.g., Ganguli and Coulibaly, 2019; Requena et al., 2019; Schardong and Simonovic, 2019) focused particularly on Canada. For example, Requena et al. (2019) used NA-CORDEX for the entire Canadian domain for 24-hour duration events (and multiple return periods), and in general found substantial increases in the frequency and intensity of events. These results taken together reaffirm earlier analyses that precipitation extremes are *very likely* to increase in the future, but they also enrich the discussion indicating that there may be important differences in these extremes based on which extreme event is analysed and the spatial resolution of the modelling.

As discussed in Atlas.5.7.3 an important advance in regional modelling over the past decade or so is the use of convection-permitting regional models (CPMs) (Prein et al., 2015, 2017b). There have been a number of experiments using CPMs over North America (e.g., Rasmussen et al., 2014; Prein et al., 2015, 2019; Liu et al., 2017a; Komurcu Bayraktar et al., 2018). Prein et al. (2017a) used a CPM over North America to investigate changes in Mesoscale Convective Systems by the end of the century and found that their frequency more than triples by the end of the century, assuming an RCP8.5 scenario, with up to an 80% increase in associated total precipitation volume. Komurcu Bayraktar et al. (2018) used multiple nesting of WRF over the north-eastern US to downscale the CESM to 3 km and investigated the downscaling effect on a future scenario (RCP8.5) and found a different pattern of precipitation change in the CESM (increases every month) and in WRF (mixed increases and decreases). It is clear from these investigations that very high-resolution simulations add important dimensions to our understanding of regional climate change, although they do not necessarily lead to reduced uncertainty.

The development of ensembles of initial conditions of global models affords the opportunity to investigate the effects of such ensembles in a regional modelling context particularly regarding extremes and natural variability (Fan et al., 2014; Leduc et al., 2019). Leduc et al. (2019) produced a 50-member ensemble with the Canadian Regional Model (CRCM5) at 12 km resolution driven by the CanESM2 50-member initial conditions ensemble over Europe and north-eastern North America for the 1950–2099 period, following the RCP8.5 scenario. More robust results were obtained using the multiple ensemble members for investigating changes in variability and extremes. Moreover, CRCM5 allowed for a much more realistic representation of regional features regarding extreme precipitation

On snow-related variables

The snow cover over North America is projected to decline during the 21st century based on CMIP5 (e.g., Brutel-Vuilmet et al., 2013; Maloney et al., 2014a) as well as NARCCAP (e.g., McCrary and Mearns, 2019) simulations. However, at sub-continental scales, projections for specific snow-related indices are often highly uncertain in both amount and sign, because drivers of change like temperature and precipitation may have opposing effects and will evolve with spatial and temporal heterogeneity. In terms of mean winter SWE, a decline could occur over most regions except at higher latitudes consistent with projected changes in snowfall (Krasting et al., 2013).

A recent study using the NARCCAP ensemble (McCrary and Mearns, 2019) reports that continental-averaged SWE and snow cover extent are both projected to decrease from the recent past (1971–1999) to mid-century (2041–2069), for all months of the year, in all of the models. Regional exceptions occur, with for example winter (January to March) SWE projected to increase at high latitudes. This increase is also found in CMIP3 and CMIP5 ensembles, although over slightly different areas in these ensembles. Snow cover duration is expected to decrease practically everywhere, with later first snow date (in autumn) and earlier last snow date (in spring). In terms of snow cover fraction, Mudryk et al. (2018) found a mixed picture of decreasing and weak trends during the 2020–2050 period across seasons and regions over Canada, using a CMIP5 ensemble. Fyfe et al. (2017) demonstrated using the CanESM large ensemble and the CanRCM4 that changes in SWE in the near term (to 2038) could reach 60% decrease in the western US and that natural variability greatly mediates potential future changes in SWE.

The fraction of precipitation falling as snow could decrease practically everywhere over North America, including in the Great Lakes basin where lake-effect precipitation is important (Suriano and Leathers, 2016). In this basin, the frequency of heavy lake-effect snowstorms is expected to decrease during the 21st century,

except for a possible temporary increase around Lake Superior by the mid-century, if local air temperatures remain low enough (Notaro et al., 2015). CMIP5 simulations of the periods 1981–2000 and 2081–2100 over Central and Eastern US suggest a northward shift in the transition zone between rain-dominated and snow-dominated areas, by about 2° latitude under the RCP4.5) scenario and 4° latitude under the RCP8.5 scenario (Ning and Bradley, 2015).

Rain-on-snow events should also evolve during the 21st century. Analysing projected changes from the recent past (1976–2005) to mid-century (2041–2070) in simulations from regional models CRCM5 and CanRCM4, Jeong and Sushama (2018) found increases in rain-on-snow frequency, amount and runoff north of the future freezing line (including the US Rocky Mountains and most parts of Canada during the coldest months), due to enhanced winter rainfall. South of the future freezing line, decreases are found in these rain-on-snow indices, due to reduced autumn and spring snow cover.

Atlas.5.8 Small islands

Regional executive summary

It is *very likely* that the tropical Western Pacific has warmed by 0.15-0.18°C decade^{-1} over the period 1953 to 2011 whilst daily maximum and minimum temperatures have increased by 0.19°C and 0.28°C decade^{-1} respectively during 1961 to 2010. There are few significant trends in precipitation in these regions though some locations in the Caribbean have detectable decreasing trends, in part attributable to anthropogenic forcings (*medium confidence*). {Atlas.5.8.2}

Small islands regions Western and equatorial Pacific, and Southern Ocean small island regions are projected to be wetter in the future but drier over parts of the Caribbean, central and eastern Pacific, Atlantic Ocean, and Indian Ocean (*medium confidence*). {Atlas.5.8.3}

Atlas.5.8.1 Key features of the regional climate and previous findings from IPCC assessments

Key features of the regional climate

Many small islands lie in tropical regions and their climate varies depending on a range of factors with location, extent and topography having major influences. In general their climate is determined by that of the broader region in which they lie as they have little influence on the regional climate though steep topography can induce locally higher rainfall totals. Temperature variability tends to be low due to the influence of the surrounding oceans, most marked in the tropics where oceanic temperature ranges are small. However, seasonal rainfall variability can often be significant, both through the annual cycle and also interannually. Many small islands are exposed to tropical cyclones and the associated hazards of high winds, storm surges and extreme rainfall and many low lying islands are exposed to regular flooding from natural high tide and wave activity. In the Pacific phases of the El Niño Southern Oscillation result in periods of warmer or cooler than average temperatures following the upper ocean warming of El Niño events or cooling of La Niña events and respectively weaker and stronger trade winds. El Niño conditions also lead to drought in Melanesian islands and increased typhoons and storm surges in French Polynesia with La Niña conditions causing drought in Kiribati. Other islands experience increased rainfall during these periods.

Previous findings from IPCC assessments

The following summary is derived from the SROCC special report (IPCC, 2019b). Ocean warming rates have *likely* increased in recent decades with marine heatwaves increasing which are *very likely* to have become longer-lasting, more intense and extensive as a result of anthropogenic warming. Open ocean oxygen levels have *very likely* decreased and oxygen minimum zones have *likely* increased in extent. There is *very high confidence* that global mean sea level rise has accelerated in recent decades which combined

with increases in tropical cyclone winds and rainfall, and increases in extreme waves has exacerbated extreme sea level events and coastal hazards (*high confidence*). It is *virtually certain* that during the 21st century, the ocean will transition to unprecedented conditions with further warming *virtually certain*, increased upper ocean stratification *very likely*, further acidification *virtually certain* and continued oxygen decline (*medium confidence*). There is very *high confidence* that marine heatwaves and *medium confidence* that extreme El Niño and La Niña events will become more frequent. It is *very likely* that these changes will be reduced under scenarios with low greenhouse gas emissions. Similarly, global mean sea level will continue to rise and there is *high confidence* that the consequent increases in extreme levels will result in local sea levels in most locations that historically occurred once per century occurring at least annually by the end of the century under all RCP scenarios (high confidence). In particular, many small islands (including SIDS) are projected to experience historical centennial events at least annually by 2050 under RCP2.6, RCP4.5 and RCP8.5 emissions. The proportion of Category 4 and 5 tropical cyclones and associated precipitation rates along with average tropical cyclone intensity are projected to increase with a 2°C global temperature rise.
This will exacerbate coastal hazards from increased intensity and magnitude of storm surge and precipitation rates of tropical cyclones.

Atlas.5.8.2 Assessment and synthesis of observations, trends and attribution

Significant positive trends in temperature ranging from 0.15°C decade^{-1} (over the period 1953–2010) to 0.18°C decade^{-1} (over the period 1961–2011) are noted in the tropical Western Pacific, where the significant increasing trends in the warm and cool extremes are also spatially homogeneous (Jones et al., 2013; Whan et al., 2014; Wang et al., 2016). Similarly, much of the Caribbean region showed statistically significant warming (at the 95% level) over the 1901–2010 period (Jones et al., 2016b). Observation records in the Caribbean region indicate a significant warming trend of 0.19°C decade^{-1} and 0.28°C decade^{-1} in daily maximum and minimum temperatures, respectively, with statistically significant increases (at the 5% level) in warm days and warm nights during 1961–2010 (Taylor et al., 2012; Stephenson et al., 2014; Beharry et al., 2015).

Observation datasets have revealed no significant long-term trends in Caribbean rainfall over 1901–2012, when analysed seasonally and for data grouped into large subregions of the Caribbean, with inter-decadal variability shown in wetter and drier conditions (Jones et al., 2016b). In contrast, a gridpoint based annual precipitation trend analysis for gridpoints with available data over 1901–2010 in the Caribbean region does indicate some gridboxes with detectable decreasing trends (Knutson and Zeng, 2018), which were attributable in part to anthropogenic forcing. The regions included south of Cuba, the northern Bahamas, and the Windward Islands. These findings did not hold over the shorter time intervals they analysed (1951–2010 and 1981–2010). In general, the positive regional trend in precipitation at 2% and trends in extremes from 1961 to 2010 are not statistically significant (at the 5% level) in the Caribbean (Stephenson et al., 2014; Beharry et al., 2015). Over the western Pacific, interannual and decadal variabilities also drive long-term trends in rainfall. Recent analysis of station data showed spatial variations in the mostly decreasing but non-significant trends in the annual total and extreme rainfall over the Western Pacific from 1961–2011 (*low confidence*) (McGree et al., 2014).

Atlas.5.8.3 Assessment and synthesis of projections

Projections indicate increases in median values ranging from 1°C (RCP 4.5) to 1.5°C (RCP 8.5) in the period 2046–2065, and from 1.3°C (RCP 4.5) to 2.8°C (RCP 8.5) by 2081–2100, relative to 1986–2005 (*very likely*) (Harter et al., 2015). Spatial variations in the warming trend are projected to increase by the end of the 21st century, with relatively higher increases in the arctic and sub-arctic islands, and in the equatorial regions compared with islands in the Southern Ocean (Harter et al., 2015). [*Placeholder: future projections to be updated with AR6 values*]. In the western Pacific, temperatures are projected to increase by 2.0°C to 4.5°C by the end of the 21st century relative to 1961–1990 (Wang et al., 2016). The warming over land in the Lesser Antilles is estimated to be about 1.6 (3.0)°C by 2071–2100 for the RCP 4.5 (RCP8.5) scenario,

relative to 1971–2000 (Cantet et al., 2014).

While some small islands in parts of the western and equatorial Pacific, and Southern Ocean are projected to have wetter conditions in the future, drier conditions are projected over parts of the Caribbean, central and eastern Pacific, Atlantic Ocean, and Indian Ocean (*low/medium confidence*). A recent study using CMIP5 multi-model projections noted a slight median increase in precipitation for the majority of the small islands globally from around 1–2% in the period 2046–2065, to 2–3% in the period 2081–2100 for RCP2.6 to RCP8.5, relative to 1986–2005 (*low/medium confidence, model agreement*) (Harter et al., 2015) [*Placeholder: to be updated with AR6 numbers*]. However, there is notable variability among islands, wherein precipitation is projected to decrease up to -16% over the Caribbean, Atlantic Ocean, and parts of Indian Ocean and central and eastern Pacific Ocean, and increase up to 10% over parts of the western Pacific and Southern Ocean, and up to 55% in the equatorial Pacific islands in the period 2081–2100 under RCP 6.0, relative to 1986–2005 (Harter et al., 2015) (*low/medium confidence, model agreement*). A projected decrease in annual precipitation is also noted over the Lesser Antilles under the RCP4.5 and RCP8.5 scenarios (Cantet et al., 2014). Seasonal rainfall is projected to decrease in most areas in Hawaii, except for the climatically wet windward side of the mountains, which would increase the wet and dry gradient over the area (*low confidence*) (Timm et al., 2015). The average precipitation changes in Hawaii are estimated to be about -11% to -28% under RCP 4.5 (-31% under RCP 8.5) during the wet season, and about -4% to -28% under RCP 4.5 (-53% under RCP 8.5) during the dry season in the period 2041-2071 relative to 1975–2005 (*low confidence*) (Timm et al., 2015). There are still uncertainties in the projected changes, which have been attributed to factors including insufficient model skill in representing topography in the small islands, and high variability in climate drivers (Harter et al., 2015).

Atlas.5.9 Polar regions

This section assesses climate change over the polar regions, Antarctica and the Arctic. Climatic regions (see Figure Atlas.2:) defined for Antarctica include West Antarctica (WAN – including the Antarctic Peninsula), East Antarctica (EAN) and the Southern Oceans (SOO) and for the Arctic include: Arctic Ocean (ARCO), Greenland/Iceland (GIC), northeast Canada (NEC), north-western North America (NWA), and Russian Arctic (RAR).

Atlas.5.9.1 Antarctica

Regional executive summary

Atlas - Antarctica section focuses on changes in surface air temperatures and precipitation (represented also by surface mass balance).

The annual mean surface air temperature in West Antarctica *likely* increased by 0.2°C to 0.3°C per decade from 1958 to 2012, whereas that in East Antarctica *likely* showed no significant trends in temperature over the same period. The largest warming within West Antarctica has been observed in austral winter (0.28 ± 0.27°C) and spring (0.39 ± 0.21°C) (*medium confidence* due to limited observations). The Antarctic Peninsula *very likely* experienced the fastest warming with a rate of 0.3°C to 0.5°C per decade since around 1950. {Atlas.5.9.1.2}

West Antarctica *likely* experienced an increase in surface mass balance mostly seen over the Antarctic Peninsula and the east part of West Antarctica, while the surface mass balance in East Antarctica showed strong interannual variability over recent decades, masking any possible existing trends (*medium confidence* due to limited observations). Changes in surface mass balance are *likely* driven by changes in precipitation. The surface mass balance in West Antarctica showed a significant increase in the east side and significant decrease in the west side (respectively 5 to 15 mm water equivalent and -5 to -15 mm water equivalent per decade from 1957 to 2000). The Antarctic Peninsula has *very likely* experienced an increase in surface mass balance over the last century (beginning in about 1930 and accelerating during the

1990s). It is *likely* that the increased surface mass balance has slightly compensated for the total Antarctic ice-sheet mass loss. {Atlas.5.9.1.2}

Whether the 21st century evolves under low-, intermediate- or high-emission scenarios, both West and East Antarctica will *likely* experience higher annual mean surface air temperatures and more precipitation, which will have a dominant influence on determining future changes in the surface mass balance. The projected Antarctic mean increase in temperature and in precipitation (median for CMIP6 models compared to the 1986–2005 baseline period) will *likely* be up to 1°C and 7% by 2050 and 1.4°C and 7% by 2100 under the sustainable (low emission) scenario SSP1-2.6, while up to 2°C and 12% by 2050 and 5°C and 30% by 2100 under the high-emission scenario SSP5-8.5. Although the projected increases in temperature and precipitation are largest over the interior of Antarctica, it is *likely* that the warming around the coastal margins by the end of the century under the high-emission scenario will lead to enhanced surface melting that has been historically leading to the ice-shelf collapse. {Atlas.5.9.1.4}

Atlas.5.9.1.1 Key features of the regional climate and previous findings from IPCC assessments

Key features of the regional climate

The current climate in Antarctica and the Southern Ocean is influenced by interactions between the ice sheet, the ocean, sea ice, and the atmosphere, and their responses to climate drivers – see Chapters 9, 10, 11; SROCC (IPCC, 2019b).

Snowfall is the largest positive component of the surface mass balance, exhibiting significant spatial and temporal variability over the ice sheet while surface air temperatures affect snowmelt amounts mainly at the ice sheet margins (Chapter 9). Even though Antarctica is the coldest continent on Earth, meltwater production over its ice shelves can be significant, leading to meltwater ponding. While it is more common in summer, the intense winter surface melt can be driven by episodes of foehn winds on the leeside of the mountains and by warm air intrusions from the ocean. Local snow accumulation is also influenced by sublimation and snow transport. These variables have a direct impact on the total ice-sheet mass balance and consequently on the ocean state (Chapter 9) and are tightly linked with the global climate (Chapter 10).

The total ice-sheet mass change is also strongly influenced by oceanic processes – changes in the total ice sheet mass balance, sea ice and other key parameters and processes relevant to the Antarctic ice sheet are discussed in Chapter 9 and the SROCC report (IPCC, 2019b). The Antarctic contribution to sea-level results from the small imbalance between mass loss by ice discharge into the ocean and mass gain by net snow accumulation, i.e. the surface mass balance. Overall the Antarctic ice sheet has been losing mass and its recent contribution to global mean sea-level rise has been estimated at 7.6 ± 3.9 mm between 1992 and 2017 corresponding to the loss of 2,720 ± 1,390 billion tonnes of ice (Chapter 9).

Previous findings from IPCC assessments

The following summary from previous IPCC reports is derived from the SROCC report (IPCC, 2019b) unless otherwise stated.

Unlike the Arctic, the Antarctic ice sheet showed more variability in the surface air temperature changes over the past 30 to 50 years. Parts of the West Antarctica experienced warming, while no significant overall change was observed over East Antarctica. These trend estimates have *low confidence* due to the sparse in situ measurements and large interannual to interdecadal variability.

Record surface warmth was experienced in West Antarctica during the 1990s relative to the past 200 years. The Antarctic Peninsula surface melting has intensified since the mid 20th century with the last three decades of the 20th century showing a melt unprecedented over the past 1,000 years. More positive Southern Annular Mode caused increased foehn winds and consequently increased surface melting on the Larsen ice shelves. Strong warming between the mid-1950s and the late 1990s lead to the collapse of the Larsen B ice shelf in 2002, which had been intact for the 11,000 years.

Snowfall has increased over the ice sheet by 4 ± 1 Gt then 14 ± 1 Gt per decade over the 19th and 20th centuries (*high confidence*): the largest increase was found over East Antarctica, followed by the Antarctic Peninsula and West Antarctica, offsetting the 20th century sea-level rise respectively by 7.7 ± 4.0 mm, 6.2 ± 1.7 mm and 2.8 ± 1.7 mm per century (*medium confidence*). Longer records suggest either an Antarctic ice sheet snowfall decrease over the last 1000 years or a statistically negligible change over the last 800 years (*low confidence*).

There is *medium agreement* but *limited evidence* of anthropogenic forcing impact on Antarctic ice-sheet mass balance through both surface mass balance and glacier dynamics (*low confidence*). Partitioning between natural and human drivers of atmospheric and ocean circulation changes remains very uncertain – see SROCC (IPCC, 2019b) for a detailed description.

Atlas.5.9.1.2 Assessment and synthesis of observations, trends and attribution

Surface air temperature trend estimates are available during the instrumental period – which starts at the end of 1950s in Antarctica –, based on station observations and automatic weather stations (see Figure Atlas.45:). Longer-term estimates (century and longer) are available from reconstructions, based on regional composites of a stable water isotope ($\delta^{18}O$) in ice cores.

The Antarctic Peninsula has warmed much faster than the global average since 1950 with recent estimates of 0.5°C per decade from 1951 to 2006 (Turner et al., 2014) and 0.33 ± 0.17°C per decade from 1958 to 2012 (Nicolas and Bromwich, 2014) (*high confidence*). Reconstructions during the last century showed a significant warming trend from 1915 to 2010 ranging from 0.20 ± 0.08°C per decade to 0.29 ± 0.11°C per decade, depending of the reconstruction method (Stenni et al., 2017). This century-scale warming trend is unusual in the context of natural variability over the last 2000 years (Stenni et al., 2017). As detailed in the SROCC special report (IPCC, 2019b), the recent warming in the Antarctic Peninsula and consequent ice-shelf collapses are linked to anthropogenic ozone and greenhouse-gas forcing via the Southern Annular Mode and to anthropogenically-driven Atlantic sea-surface warming via the Atlantic Multidecadal Oscillation. This warming trend in the Antarctic Peninsula is strong and significant, despite its short recent slowdown (since the 2000s), attributed to a greater frequency of cyclonic conditions in the Weddell sea which result in cold, south-easterly winds (Turner et al., 2016).

West Antarctica experienced warming between 1950 and 2010: an increase of 0.42 ± 0.24°C per decade from 1958 to 2010 was measured at Byrd station (Bromwich et al., 2012, 2014) as was an increase of 0.22 ± 0.12°C per decade from 1958 to 2012 averaged over the West Antarctica but excluding the Antarctic Peninsula (Nicolas and Bromwich, 2014). The strongest warming signal in West Antarctica has *likely* been observed in austral winter and spring (0.28 ± 0.27°C and 0.39 ± 0.21°C respectively). Reconstructions show a century-scale temperature increase ranging from 0.10 ± 0.08°C per decade to 0.11 ± 0.09°C per decade from 1915 to 2015 (Stenni et al., 2017). This warming trend falls in the high end of century-scale trends over the last 2000 years (Stenni et al., 2017). Figure Atlas.45: shows changes in surface air temperature, sea surface temperature, sea-ice extent and near-surface winds during the enhanced instrumental period (1979-2014) demonstrating significant warming over the Antarctic Peninsula and West Antarctica, cooling over parts of East Antarctica, strengthening of the westerlies, and high variability in sea-ice extent with an increasing trend in southern hemispheric mean values (Jones et al., 2016a).

In contrast to West Antarctica, no significant warming was measured over East Antarctica from 1958 to 2012 (Nicolas and Bromwich, 2014). A particularly strong difference between the east and west sides of the Trans-Antarctic mountains – marking the divide between the East and West Antarctic ice sheets – is found during winter (cooling or weak warming) and spring (strong warming) (Nicolas and Bromwich, 2014). The only station with a significant warming in East Antarctica is Kohnen Station in Queen Maud Land, showing warming at a rate of 1.15 ± 0.71°C per decade from 1998 to 2016 (Medley et al., 2018). Reconstructions over the last century show no significant trend for East Antarctica (Stenni et al., 2017). A significant warming signal is found in Queen Maud Land Coast of 0.01 ± 0.07°C to 0.13 ± 0.09°C per decade from 1915 to 2010, which falls into the centennial internal variability (Stenni et al., 2017).

[START Figure Atlas.45: HERE]

Figure Atlas.45: a) Surface air temperature (SAT) and sea surface temperature (SST) change over the 1979–2014 period based on observational records (Jones et al., 2016a). b) Air temperature change during the 1995–2014 period based on EWEMBI data (from Interactive Atlas available at http://ipcc-atlas.ifca.es). Thin black lines denote WAN and EAN, the two main reference regions as used in the Interactive Atlas for Antarctica.

[END Figure Atlas.45: HERE]

Since the late 1990s, **surface melting** of the ice shelves and coastal margins of West Antarctica has increased due to more frequent and stronger intrusions of warm marine air onto the ice sheet caused by Amundsen Sea blocking anticyclones and the negative polarity of the Southern Annular Mode, which are both related to El Niño conditions (Scott et al., 2019). A similar circulation pattern directs atmospheric rivers toward Antarctica, which are associated with around 40% of the total summer meltwater generated across the Ross Ice Shelf to nearly 100% in the higher elevation Marie Byrd Land and 40–80% of the total winter meltwater generated on the Wilkins, Bach, George IV and Larsen B and C ice shelves (Wille et al., 2019). It is *likely* that meltwater ponding have led to the rapid ice-shelf collapses of the Larsen B (De Rydt et al., 2015) and Larsen C (Borstad et al., 2013; Luckman et al., 2014; Kuipers Munneke et al., 2018) ice shelves in the Antarctic Peninsula, which caused an ice-discharge acceleration due to the removal of ice shelves buttressing effect (Scambos et al., 2014; Rignot et al., 2019).

Precipitation in Antarctica occurs mostly in the form of snowfall and diamond dust, with rainfall present mostly only during the short summer period in the coastal regions, the Antarctic Peninsula and sub-Antarctic islands. Recently, warm events in the West Antarctica associated with drizzle were observed (Nicolas et al., 2017; Wille et al., 2019). In the current climate, most rain falling on the Antarctic continent refreezes in the snowpack due to the low temperature and thus also contributes to ice-sheet mass accumulation (Agosta et al., 2019; Lenaerts et al., 2019).

Direct observations of snowfall using traditional gauges are highly uncertain due to strong winds and blowing snow. Only a few stations have started to be equipped with precipitation radars (Gorodetskaya et al., 2015; Grazioli et al., 2017) with records still not long enough to allow for the assessment of trends. Trends in precipitation cannot be assessed with reanalyses because spurious changes are introduced by the increase in assimilated satellite observations (Nicolas and Bromwich, 2011). Assessment of the Antarctic-wide snowfall climatology is available using satellite-borne radar observations (CloudSat): it provides a mean snowfall rate of 171 mm $year^{-1}$ from August 2006 to April 2011 (Palerme et al., 2014) (*medium confidence*). Precipitation trends in CMIP5 models which simulate snowfall rates within ±20 % of the CloudSat estimates give an average Antarctic precipitation increase of 2.1 mm per decade from 1956 to 2000 (Palerme et al., 2017).

In the context of lack of precipitation measurements, observations of surface mass balance (net snow accumulation on the surface) through various techniques (summarized by Lenaerts et al. (2019)) – including annually resolved radar transects (Eisen et al., 2008), stake lines (Favier et al., 2013), sonic snow height meters on automatic weather stations (Gorodetskaya et al., 2013) and ice core records (Thomas et al., 2015, 2017) –, are considered as a good proxy of precipitation if averaged over a sufficiently long period (e.g., yearly).

The Antarctic Peninsula has experienced a significant increase in surface mass balance, beginning in about 1930 and accelerating during the 1990s (Thomas et al., 2017). This is the only region in Antarctica where both the most recent 50-year and 100-year trends are outside of the observed range for the past 300 years. West Antarctica overall has shown a stable surface mass balance from 1980 to 2009 but with high regional variability (Medley et al., 2013). Significant increases in accumulation are observed on the east side of the West Antarctic ice sheet divide of 5 to 15 mm water equivalent per decade from 1957 to 2000 with significant decreases on the west side of -1 to -5 mm water equivalent per decade from 1901 to 1956 and -5 to -15 mm water equivalent per decade from 1957 to 2000 (Medley and Thomas, 2019). Overall, the

increasing accumulation trend over the Antarctic Peninsula and eastern West Antarctica mitigated global mean sea-level rise by 0.28 ± 0.17 mm per decade over the 20th century (Medley and Thomas, 2019).

The surface mass balance of East Antarctica increased during the 20th century, which *likely* mitigated global mean sea-level rise by 0.77 ± 0.40 mm per decade (Medley and Thomas, 2019). A significant increase in snow accumulation of 5.2 ± 3.7% per decade from 1920 to 2011 was recorded by an ice core in western Dronning Maud Land, near the Kohen station (Medley et al., 2018). The surface mass balance was found to decrease significantly in eastern Dronning Maud Land and western Wilkes Land from 1957 to 2000 (Medley and Thomas, 2019). The surface mass balance was found stable during the 1901–2000 period and the last decades in the interior of the East Antarctic plateau (Thomas et al., 2017; Medley and Thomas, 2019), stable over western Dronning Maud Land (Syowa-Dome F annual stake line, 1975–2006 period) (Wang et al., 2015), and stable in Adelie Land (annual stake line, 1971–2008 period) (Agosta et al., 2012). In the second half of the 20th century, ice-shelf cores showed a negative trend of the surface mass balance but an increase on the plateau in western Dronning Maud Land (Altnau et al., 2015). Regional trends of the last 50 years (1961–2010) and 100 years (1911–2010) fall into centennial variability of the past 1,000 years, except for coastal Dronning Maud Land (unusual 100-year increase in accumulation) and for coastal Victoria Land (unusual 100-year decrease in accumulation) (Thomas et al., 2017). This contradicts some previous studies which suggest a negligible change in the Antarctic surface mass balance, both over West and East Antarctica, since 1957 (Monaghan et al., 2006) and that the current surface mass balance is not exceptionally high compared to the past 800 years (Frezzotti et al., 2013; Medley and Thomas, 2019).

Queen Maud Land (East Antarctica) experienced extreme surface mass balance anomalies in 2009 and 2011, unprecedented in the last 60 years (Lenaerts et al., 2013). These have been related to a handful of regionally extreme anomalous snowfall events attributed to the large-scale atmospheric blocking directing intense moisture flux within extra-tropical cyclones towards Antarctica (Gorodetskaya et al., 2014) and frequency of such events in Antarctica has been increasing since 1979 (Turner et al., 2019; Wille et al., 2019).

As noted also in the SROCC Special Report (IPCC, 2019b), disentangling natural and human drivers of atmospheric and ocean circulation changes which may influence the surface mass balance remains very uncertain. The geographic pattern of accumulation changes since 1957 bears a strong imprint of a trend towards more positive phases of the Southern Annular Mode (e.g., Medley and Thomas, 2019). At the same time, large-scale blocking and increased meridional moisture flow causing moist and warm air intrusions in West Antarctica was found to be associated with a negative Southern Annular Mode (Scott et al., 2019). There is some recent limited evidence from modelling, observations and reanalyses that increased Antarctic precipitation might have mitigated dynamical ice-mass losses by about 50 Gt yr^{-1} since about 1990 (Lenaerts et al., 2018; Medley and Thomas, 2019) and at lower rates over the entire 20th century (Medley and Thomas, 2019). The cause of this possible increase, which could be circulation changes linked to ozone depletion (Lenaerts et al., 2018) or large-scale warming (Frieler et al., 2015; Medley and Thomas, 2019), is unclear – see the SROCC Special Report (IPCC, 2019b) for a more detailed discussion of attribution and its uncertainties.

Atlas.5.9.1.3 Assessment of model performance

Because Antarctica is an exceptionally data-sparse region, regional and local surface mass balance and climate information for the present day from relatively coarse general circulation models (GCMs) or high-resolution regional climate models (RCMs) are needed. Fewer than 10 out of 41 CMIP5 GCMs have reasonable biases when compared to ERA-Interim reanalysis with simulated present-day temperature increases highly sensitive to Southern Ocean sea-ice biases in the models (Agosta et al., 2015; Bracegirdle et al., 2015).

Comparison of CMIP5 models with Cloudsat satellite products and ERA-Interim reanalyses showed that almost all the models overestimate current Antarctic precipitation, some by more than 100% (Palerme et al., 2017), hence resulting in large biases in the surface mass balance. GCM simulations of surface snow-melt processes are of variable quality, with the processes represented extremely simply in the models or even non-existent (Agosta et al., 2015; Trusel et al., 2015). This is not overly important for current climate simulations

as most meltwater refreezes in the snowpack and does not run off into the ocean. However, run-off is expected to increase in the future climate under global warming. Snowpack models and related processes are being further improved by several research groups around the world for better future projections. The new generation of Earth system models, such as CESM2 (included in CMIP6), have been updated with improved snow-layer scheme to represent better polar conditions (Lenaerts et al., 2016). Surface melting is still considerably overestimated in CESM2 compared to RCMs and satellite products, because of the reduced potential for refreezing and overestimation of the net energy available for melt (Trusel et al., 2015; Lenaerts et al., 2016). This emphasizes the need for better snow-melt parameterizations and representation of feedback processes such as melt-albedo and cloud radiative forcing.

Assimilation of observations in reanalysis products yield realistic temperature patterns and seasonal variations, with the newest dataset (ERA5 reanalysis) performing the best. The reanalyses' ability to simulate precipitation and the surface mass balance is more variable, and they generally overestimate the surface mass balance, except for ERA5 which shows an underestimation and the lowest bias (Gossart et al., 2019), but are well suited to provide atmospheric and sea-surface boundary conditions to drive RCMs.

Gorte et al. (submitted) selected a subset of the top 10th percentile of models, when compared to ice-core reconstructions from Medley and Thomas (2019), from both the CMIP5 and currently released CMIP6 models. The resulting refined projections for the surface mass balance integrated over the entire Antarctic ice sheet during the 2000–2100 period for RCP 2.6, 4.5, and 8.5 are 2295 ± 1222 Gt, 2382 ± 1316 Gt, and 2648 ± 1530 Gt per year respectively.

To date, published studies of higher-resolution hindcast RCM simulations covering mainly Antarctica are limited to a few model simulations with a grid spacing of 12 to 50 km, and including RACMO2 (van Wessem et al., 2018), MAR (Agosta et al., 2019), COSMO-CLM2 (Souverijns et al., 2019), HIRHAM5 (Lucas-Picher et al., 2012), and MetUM (Walters et al., 2017; Mottram et al., submitted). These models are typically forced by reanalysis products such as ERA-Interim, and their simulations agree reasonably well with available measurements of temperature, surface melt, and surface mass balance, including the coast-to-plateau surface mass balance gradients (see Figure Atlas.46:). These studies also often highlight important processes that are sometimes missing or under-represented in the models, such as drifting-snow transport (Agosta et al., 2019) and cloud-precipitation microphysical processes (van Wessem et al., 2018). Other studies using regional climate models have employed much finer grid spacings of around 5 km to run successful hindcast climate simulations of particular regions of Antarctica, such as the Antarctic Peninsula using MAR and RACMO2 models (Datta et al., 2018; van Wessem et al., 2018) and West Antarctica using the RACMO2 and/or MAR models (Lenaerts et al., 2018; Donat-Magnin et al., 2019) and the Weddell Sea region using the CCLM model (Zentek, R. and Heinemann, 2019). The latest estimates, using model mean ensemble estimates of the surface mass balance from Polar-CORDEX using nine high-resolution RCMs, are 2122 Gt yr^{-1} for the grounded ice sheet (excluding ice shelves) and 2485 Gt yr^{-1} for the whole ice sheet including ice shelves for the period of 1980 to 2010. The standard deviation amongst models is 306 Gt yr^{-1} for the whole ice sheet and 266 Gt yr^{-1} for the grounded ice sheet, and is largely explained by differences in boundary-forcing methodology and cloud microphysics (Mottram et al., submitted).

For the 1979–2015 period, a cross-evaluation of two RCMs specifically applied to Antarctica, MAR and RACMO2 both forced by ERA-Interim reanalysis products, identified missing and underrepresented processes in both models (Agosta et al., 2019). In particular, despite MAR and RACMO2 simulating the coast-to-plateau surface-mass-balance gradient well, comparison of the simulated surface mass balance with observations also highlighted the importance of drifting-snow transport that is not included in MAR and is underestimated in RACMO2, suggesting a need to simulate better and constrain drifting-snow fluxes in climate models.

Using non-hydrostatic regional models, such as Polar-WRF (Grosvenor et al., 2014; Elvidge et al., 2015; Elvidge and Renfrew, 2016; King et al., 2017; Hines et al., 2019; Vignon et al., 2019) or HARMONIE-AROME (Mottram et al., 2017) up to finer resolutions approaching 2 km, could solve remaining discrepancies in RCM simulations, but are still often unable to resolve accurately the relevant feedbacks and foehn processes (Turton et al., 2017; Bozkurt et al., 2018).

[START Figure Atlas.46: HERE]

Figure Atlas.46: Maps of Antarctic mean surface mass balance from Polar CORDEX forced by ERA-Interim reanalysis (taken from Mottram et al. (submitted)). The models are MetUM, COSMO-CLM2, RACMO2.1p, HIRHAM, MAR v3.10 and RACMO2.3p2. The period is 1980 to 2010 with the exception of COSMO-CLM2 where the time series starts in 1987.

[END Figure Atlas.46: HERE]

Atlas.5.9.1.4 Assessment and synthesis of projections

The Antarctic region is *very likely* to experience an increase in annual mean temperature and precipitation by the end of this century under the high-emissions scenario (Collins et al., 2013; Bracegirdle et al., 2015; Frieler et al., 2015; Lenaerts et al., 2016; Previdi and Polvani, 2016; Palerme et al., 2017). Figure Atlas.47: shows that there is a relatively good agreement under the high-emissions scenario between the CMIP5 RCP8.5 and CMIP6 SSP5-8.5 ensemble mean, with them both showing warming of over 2°C for the 2041–2060 period over much of Antarctica, and a median warming of 4°C for CMIP5 RCP8.5 and nearer 5°C for CMIP6 SSP5-8.5 for the 2081–2100 period (relative to 1986–2005). Figure Atlas.47: also shows projected increases in precipitation of up to 20% over Antarctica for the 2041–2060 period and median changes of around 30% for the 2081–2100 period for CMIP6 SSP5-8.5 scenario projections (relative to 1986–2005). Both the warming and increase in precipitation are largest over the interior of Antarctica, with a projected increase in precipitation of around 30% by the end of the century when averaged over the entire Antarctic ice sheet. By contrast, for the medium stabilisation scenario there is warming of up to 2°C by the mid century and 3°C by the end of century based on CMIP5 RCP4.5 (Collins et al., 2013). Based on CMIP5 models, the projected increase in precipitation will also result in an increase in surface mass balance, which would correspond to a negative contribution to sea-level rise (Palerme et al., 2017).

Projections of all RCMs from Polar-CORDEX for total annual precipitation change in the middle of the 21st century for RCP8.5 show precipitation increasing over most of the Antarctic continent (this and other results from these RCMs can be visualised in the Interactive Atlas). According to regional climate model projections (Lenaerts et al., 2013), East Antarctica is increasingly likely to experience snow accumulation anomalies towards the end of the 21st century attributed to anomalously high snowfall of the scale as during the first half of 2009 and 2011 in Queen Maud Land, East Antarctica (Boening et al., 2012; Gorodetskaya et al., 2014). A combination of observations and regional climate model simulations has shown that the relationship between summer air temperatures and surface melting over Antarctic ice shelves is highly non-linear (Trusel et al., 2015). CMIP5 models, bias-corrected based on regional climate model simulations, showed that the projected warming around the periphery of Antarctica is expected to result in increased surface melting over its ice shelves, with melt on several ice shelves under the high-emission scenario (such as Larsen C, Wilkins, George VI) approaching or surpassing intensities that were linked with the collapse of Larsen A and B ice shelves (Trusel et al., 2015).

[START Figure Atlas.47: HERE]

Figure Atlas.47: (a–d) Climate change projections of annual mean surface air temperature and precipitation from CMIP5 (30 models) and CMIP6 (17 models) calculated as the differences in the climatological average for RCP8.5 and SSP5-8.5 respectively, for the period 2041–2060 with respect to the historical 1995–2014 period and expressed as °C (temperature) and % relative change (precipitation). Hatching indicates weak model agreement on the sign of the change (less than 80% as defined in Nikulin et al., 2018).
(e–f) Regional mean changes in annual mean surface air temperature and precipitation for the two Antarctic regions (WAN and EAN). The top row shows the median (dots) and 10th–90th percentile range across each model ensemble for annual mean temperature changes, for two datasets (CMIP5 and CMIP6) and two scenarios (SSP1-2.6/RCP2.6 and SSP5-8.5/RCP8.5). The first four bars represent the additional warming projected relative to the historical baseline 1995–2014 period to reach the two global warming levels (GWL; +1.5°C and +2°C) and the remaining six projected

changes over three time periods (near-term 2021–2040, mid-term 2041–2060 and long-term 2081–2100) compared to this same historical baseline period. The bottom row shows scatter diagrams of temperature against precipitation changes, displaying the median (dots) and 10th–90th percentile ranges for four future periods (2021–2040, 2041–2060, 2061–2080, 2081–2100) compared to the historical baseline period, as obtained from CMIP6 projections for three scenarios (SSP1-2.6, SSP2-4.5 and SSP5-8.5). Changes are absolute for temperature and relative for precipitation.
(The script used to generate this figure is available online (Atlas GitHub, 2020) and similar results can be generated in the Interactive Atlas for flexibly defined seasonal periods.)

[END Figure Atlas.47: HERE]

Atlas.5.9.2 Arctic

Regional executive summary

It is *very likely* that the Arctic has warmed at more than twice the global rate over the past 50 years and *likely* that annual precipitation has increased with the highest increases during the cold season. This is based on thermodynamic changes that includes the increase in surface absorption of solar radiation due to changes in sea ice, ice, and snow cover contributing to the amplified warming (*high confidence*). It is *likely* that the frequency of rainfall increased over the Arctic by 2.7–5.4% over the 2000–2016 period with more frequent rainfall events being reported for northern Europe and Svalbard. {Atlas.5.9.2.2}

It is *likely* that the Arctic annual mean temperature and precipitation will continue to increase reaching 12.5 ± 2.9°C and 54.7 ± 13.7 mm over the 2081–2100 period (with respect to a 1995–2014 baseline) under the SSP5/RCP8.5 scenario or 4.0 ± 1.4°C and 17.3 ± 6.6 mm under the SSP1/RCP2.6 scenario. These are preliminary results from the current set of CMIP6 results available in the Interactive Atlas at the time of the release of the Second-Order Draft. These CMIP6 results show *likely* higher Arctic annual mean temperatures and precipitation compared to CMIP5 for both SSP5/RCP8.5 and for SSP1/RCP2.6. {Atlas.5.9.2.4}

It is *likely* that the Arctic annual precipitation will increase twice as fast as the global annual precipitation over the 2081–2100 period (with respect to a 1995–2014 baseline). This is the case for the CMIP6 GCMs for both SSP5/RCP8.5 and SSP1/RCP2.6 scenarios. {Atlas.5.9.2.4}

Atlas.5.9.2.1 Key features of the regional climate and previous findings from IPCC assessments

Key features of the regional climate

The Arctic has a polar climate, which is governed by mid-latitude atmospheric circulation, baroclinicity at the polar front, the planetary wave meanders of the jet stream and blocking highs. The potential for Arctic climate to change due to increased greenhouse gases was established in modelling in the 1980s (Manabe and Stouffer, 1980) and clearly demonstrated in more recent observational studies (Serreze et al., 2000). A number of physical processes contribute to amplified Arctic temperature variations as compared to the global temperature in particular thermodynamic changes that include the increase in surface absorption of solar radiation due to surface albedo feedbacks related with sea-ice, ice, and snow-cover retreat as well as poleward energy transports, water-vapour-radiation and cloud-radiation feedbacks (Screen and Simmonds, 2010; Serreze and Barry, 2011; Pithan and Mauritsen, 2014; Bintanja and Krikken, 2016; Graversen and Burtu, 2016; Franzke et al., 2017; Stuecker et al., 2018).

Previous findings from IPCC assessments

The following summary from previous IPCC reports is derived from the SROCC Special Report (IPCC, 2019b) unless otherwise stated. Arctic surface air temperatures have increased from the mid-1950s, with feedbacks from loss of sea ice and snow cover contributing to the amplified warming (*high confidence*) (IPCC, 2018b), and have *likely* increased by more than double the global average over the last two decades (*high confidence*). During the winters (January–March) of 2016 and 2018, surface temperatures in the central Arctic were 6°C above the 1981–2010 average. The frequency of marine heatwaves is *very likely* to increase

for the Arctic Ocean by 2081–2100 under RCP2.6 and RCP8.5, relative to the frequency of occurrence during the 1850–1900 period (*medium confidence*) (IPCC, 2019b). Further, changes in precipitation will not be uniform. The high latitudes are *likely* to experience an increase in annual mean precipitation under the RCP8.5 scenario (IPCC, 2013b).

Arctic snow cover in June has declined by 13.4 ± 5.4% per decade from 1967 to 2018 (*high confidence*). Autumn and spring snow cover duration are projected to decrease by a further 5–10% from current conditions in the near term (2031–2050). No further losses are projected under the RCP2.6 emissions scenario whereas a further 15–25% reduction in snow cover duration is projected by end of century under RCP8.5 (*high confidence*). Arctic glaciers are losing mass (*very high confidence*) and this along with changes in high-mountain snow melt have caused changes in river runoff and Arctic hydrology that are projected to continue in the near term (*high confidence*). The rate of ice loss from the Greenland ice sheet has increased (*extremely likely*, *very high confidence*) with the mass loss being dominated by surface melting (*high confidence*). For the 2006–2015 period, the rate of ice-mass loss was 278 ± 11 Gt yr^{-1} with the rate for the 2012–2016 period higher than for the 2002–2011 period, and several times higher than for the 1992–2001 period (*extremely likely*, *high confidence*).

The Arctic sea-ice extent is declining in all months of the year (*high confidence*) with the September sea-ice minimum *very likely* having reduced by 12.8 ± 2.3% per decade during the satellite era (1979 to 2018) to levels unprecedented for at least 1,000 years (*high confidence*). It is *virtually certain* that Arctic sea ice has thinned, concurrent with a shift to younger ice, since 1979 with the areal proportion of thick ice at least five years old declining by approximately 90%. Approximately half of the observed sea-ice loss is attributed to anthropogenic global warming (*medium confidence*). The direct relationship between summer Arctic sea-ice extent, global temperatures and cumulative CO_2 emissions provides a basis for estimating the probability of a sea-ice-free Arctic ocean in September to be around once per century for stabilised global warming of 1.5°C to at least one per decade with 2°C global warming (*high confidence*) (IPCC, 2018b, 2019b).

Atlas.5.9.2.2 Assessment and synthesis of observations, trends and attribution

Recent literature largely confirms the findings of the previous reports but with additional detail and higher confidence (for some measures) due to improvements in observations and refinement in methods. During the Medieval Climate Anomaly (MCA; around 950–1400 AD), portions of the Arctic and sub-Arctic experienced periods warmer than any subsequent period, except for the most recent 50 years (Kaufman et al., 2009; Kobashi et al., 2010, 2011; Vinther et al., 2010; Spielhagen et al., 2011). Tingley and Huybers (2013) provided a statistical analysis of northern high-latitude temperature reconstructions back to 1400 and found that recent extreme hot summers are unprecedented over this time span. It is assessed that despite the uncertainties, there is sufficiently strong evidence that it is *likely* there has been an anthropogenic contribution to the very substantial warming in Arctic land surface temperatures over the past 50 years. That recent increases are due to different primary climate processes. For example, when the 2007 sea-ice minimum occurred, Arctic temperatures had been rising and sea-ice extent had been decreasing over the previous two decades (Stroeve et al., 2007; Screen and Simmonds, 2010).

The Arctic has *very likely* warmed at more than twice the global rate over the past 50 years with the greatest increase during the cold season (Davy et al., 2018; Box et al., 2019). The annual average Arctic surface air temperature (north of the Arctic Circle) increased by 2.7°C from 1971 to 2017, with a 3.1°C increase in the cold season (October–May) and a 1.8°C increase in the warm season (June–September) (AMAP, 2019) (Figure Atlas.48:). Satellite-based data, which provide continuous coverage of the Arctic Ocean, estimate the rate of warming for 1981–2012 above 64°N as about 0.60 ± 0.07°C per decade in the Arctic. The trend in temperature over sea-ice covered regions was estimated to be 0.47°C per decade (*very likely* between 0.37°C and 0.57°C per decade at a 90% confidence level), whereas the trend was significantly higher at 0.77°C per decade (*very likely* between 0.60°C and 0.94°C per decade) over Greenland (Comiso and Hall, 2014). February and March are the months with the largest temperature increase of almost 5°C for the 2003–2012 period, averaged over the ocean and sea-ice area north of 70°N (Kohnemann et al., 2017). It is likely that the largest Arctic warming in the last 15 years occurred over the Barents and Kara Seas with trends larger than 2.5°C per decade (Susskind et al., 2019). Arctic temperatures for the recent five years (2014 to 2018) have

very likely exceeded all previous records since 1900 (Blunden and Arndt, 2019). There is a positive trend in the overall duration of winter warming events (temperature above –10°C) for both the North Pole region (4.25 days per decade) and Pacific Central Arctic (1.16 days per decade), due to an increased number of events of longer duration (Graham et al., 2017). In the permafrost region of the northern hemisphere, annual air temperatures showed trends of 0.13°C per decade for the 1901–2014 period, 0.39°C per decade for the 1979–2014 period, and 0.32°C per decade for the 1998–2014 period (*high confidence*) (Guo et al., 2017a). Winter air temperatures *very likely* showed the greatest increase during the 1901–2014 period, while autumn air temperatures increased the most during the 1979–2014 period. Generally, the Arctic warming pattern has been attributed to a decline in sea-ice, changing atmospheric circulation, and advection of heat and moisture (Dahlke and Maturilli, 2017; Champagne et al., 2019; Clark and Lee, 2019; Hao et al., 2019; Kim and Kim, 2019).

Over the ARCO region, long-term temperature trends and variability are available from Spitsbergen (Svalbard). For the entire period of 1898 to 2012 available at Svalbard Airport, the annual mean warming is 2.6°C per century, with the largest trend in spring (3.9°C per century) (Nordli et al., 2014). The winter warming is also large (2.9°C per century) with six of the 10 warmest winters occurring after 2000 (Nordli et al., 2014). Over the recent period of 1994 to 2013, the largest trend (3.1 ± 2.4°C per decade) *very likely* occurs in winter and the annual mean trend is *very likely* 1.3 ± 0.7°C per decade (Maturilli et al., 2015). Isaksen et al. (2016) report on the substantial warming in western Spitsbergen, particularly in winter (3.4–4.6°C), while the summer warming is moderate (0.7–1.4°C). A multi-dataset analysis for the Canadian Arctic (NEC) shows a consistent warming (Rapaić et al., 2015), with the largest annual temperature trend (> 0.3°C per decade, from 1981 to 2010) *likely* over eastern NEC and also significant warming over northern Quebec and most of the Canadian Arctic north of the treeline. For the longer 1950–2010 period, a consistent warming is found over central and western NEC, but no trend or no consensus is found over the Labrador coast. The latter is related with cooling of the North Atlantic region during the 1970s. In Northern Europe (NEU), based on the 1914–2013 period, statistically significant warming trends were found from March to May at all nine stations analysed by (Kivinen et al., 2017) and from September to October at most of them. In particular, this is seen in a significant decrease of extremely cold climate events (10th percentile of mean seasonal temperature) in all seasons and increase of extremely warm climate events particularly in spring and autumn in the recent 1994–2013 period, compared to earlier 20-year periods. (Saros et al., 2019) showed a step change in summer temperature (2.2°C in June, 1.1°C in July) over west Greenland after the mid-1990s.

The Arctic Monitoring and Assessment Programme (AMAP) reported Arctic precipitation increases of 1.5–2.0% per decade, with the strongest increase in the cold season (October–May) (AMAP, 2019). However, annual precipitation trends derived from different reanalyses do not agree, differ in sign and have low significance (Lindsay et al., 2014; Boisvert et al., 2018) (Figure Atlas.48:). Direct precipitation measurements are difficult and include uncertainties, therefore precipitation estimates in the Arctic rely on climate models and reanalyses.

Based on the ‘best’ five CMIP5 model means, the mean annual precipitation in the Arctic (70-90°N; 2006 to 2015) is dominated by snowfall, with 65 ± 5% of precipitation currently falling in solid form (this model estimate compares to the 68 ± 2% from the observationally driven JRA-55 reanalysis) (Bintanja and Andry, 2017). However, the estimates of different reanalyses vary largely. According to an estimate of five reanalyses over the 2000–2010 period, on average, around 40% of the precipitation falls over the entire Arctic Ocean (north of 60°N) as snow (200 mm yr^{-1}), with a prominent across-reanalyses standard deviation of 60–70 mm (Boisvert et al., 2018). The frequency of rainfall increased over the Arctic by 2.7–5.4% (*high confidence*) over the 2000–2016 period (Boisvert et al., 2018). More frequent rainfall events have been reported for example for NEU and ARCO (Svalbard) (Maturilli et al., 2015; AMAP, 2019). Further for NEU, the contribution of heavy daily precipitation amounts to the total precipitation has increased since 1950 (Hartmann et al., 2013).

Observational records (1966 to 2010) for the Russian-Arctic (RAR) region from 517 historical Russian surface weather stations over northern Eurasia show changing precipitation characteristics (Ye et al., 2016), providing values and geographical distribution of mean seasonal precipitation total, frequency, and intensity. Higher precipitation intensity but lower frequency and little change in annual precipitation total occurred. It

is *likely* that precipitation intensity has increased in all seasons, strongest in winter and spring, weakest in summer, and at a rate of about 1–3% per 1°C of air temperature increase (*high confidence*). Chernokulsky et al. (2019) connect the moderate increase in the total precipitation over the last five decades (1966 to 2016) with the increase of convective precipitation and the concurrent reduction of stratiform precipitation. For NEC, the CANGRD dataset indicates locally significant increases of 20–30% for the 1981–2010 period, but there is little consensus for increasing precipitation as multiple datasets analysed both for the 1981–2010 and longer 1950–2010 periods showed no consensus on trends (Rapaić et al., 2015).

A type of event with major impact in the Arctic is rain on snow. For example, Hansen et al. (2014) examined the recent occurrence of such events in Svalbard and concluded that the frequency of rain-on-snow events is *likely* to increase in the Arctic (AMAP, 2017). Based on reanalyses, the trend in such events across the Arctic is mixed, i.e. region and season (autumn–winter) dependent (Cohen et al., 2015). In autumn, it is *likely* that an increasing trend of rain-on-snow events has been seen over North East Canada (NEC) and a decreasing trend over NEU (particularly Norwegian Arctic, Groisman et al., 2016). In winter, rain-on-snow trends show less coherence. Considering GIC, rain-on-snow events have increased over the south-western coast of Greenland where increased rainfall directly contributed to more rain-on-snow events (Cohen et al., 2015). Further, Groisman et al. (2016) provided a long-term climatology of freezing rain and freezing drizzle events for the past four decades and assessed changes in the frequency and intensity of these events (e.g., by comparing the 2005–2014 period to the previous 30-year baseline period). In NEC, the frequency was *likely* found to increase by about 1 day yr^{-1}.

Atlas.5.9.2.3 Assessment of model performance

Evaluating simulated temperature and precipitation is problematic and uncertain in the Arctic due to sparse observations, with relatively few weather stations that are only over land. This leads to inconsistencies between observational datasets. Precipitation estimates over the Arctic Ocean are particularly uncertain as they mainly rely on reanalyses or observationally-constrained products such as the merged gridded datasets combining gauge measurements and satellite estimates – such as GPCC (Global Precipitation Climatology Centre, Schneider et al., 2014), CMAP (CPC Merged Analysis of Precipitation, Xie and Arkin, 1996), GPCP (Global Precipitation Climatology Project, Adler et al., 2003) – which are not well constrained over the poorly observed Arctic Ocean. Reanalyses also suffer from sparse observations over the central Arctic and thus their precipitation estimates depends largely on the atmospheric model used, its resolution and parametrizations, and estimates for the Arctic can differ by more than 50% (Boisvert et al., 2018). A newer satellite products, CloudSat, has recently become available, but it could also be biased as it is very sensitive to light rain and snowfall (Behrangi et al., 2016). The lack of reliable precipitation observation datasets for the Arctic thus makes it *likely* impossible to evaluate objectively the skill of models to reproduce precipitation patterns (Takhsha et al., 2018).

CMIP5 models reasonably reproduce the observed Arctic warming during the long 1900–2005 (Hao et al., 2018) and 1900–2014 (Chylek et al., 2016) periods. The simulated mean (40 CMIP5 models) Arctic (north of 64°N) warming over the 1900–2014 period is 2.7°C compared to the observed values of 2.2°C (NASA GISS data smoothed using a 1200-km radius) or 1.7°C (using a 250-km smoothing radius) (Chylek et al., 2016). However, a large inter-model difference in the simulated warming magnitudes is obvious and ranges from 1.2°C to 5.0°C. Although the CMIP5 models reasonably reproduce the observed warming over the past 50 to 100 years, the spatial pattern is quite different from that of observations and reanalysis (Xie et al., 2016; Franzke et al., 2017; Hao et al., 2018). The zonal mean temperature trends indicate that the CMIP5 models overestimate the warming in the cold season over high latitudes in the northern hemisphere (Xie et al., 2016). Possible reasons are modelled sea surface temperature biases and an overestimated temperature response to the Arctic sea-ice decline. Furthermore, some models, which have a warm or weak bias in their Arctic temperature simulations, closely relate the Arctic warming to changes in the large-scale atmospheric circulation. In other models, which show large cold biases, the albedo feedback effect plays a more important role for the temperature trend magnitude. This stark difference in model biases might indicate that the dominant Arctic warming mechanism and trend may be dependent on the bias of the model mean state (Franzke et al., 2017).

Arctic CORDEX RCMs show adequate skills in capturing the warming patterns. Generally, the surface air temperature bias of the RCMs is a cold bias and largest in winter (Koenigk et al., 2015; Matthes et al., 2015; Hamman et al., 2016; Cassano et al., 2017; Brunke et al., 2018; Takhsha et al., 2018). However, the bias largely depends on the reference dataset that is used; the bias with respect to the CRU dataset is twice that with respect to the UDEL dataset (Takhsha et al., 2018). Arctic Ocean biases are smaller in simulation using RCM downscaling approaches than in CMIP5 models in all seasons (Koenigk et al., 2015). Cassano et al. (2017) showed a large sensitivity of the simulated surface climate to changes in atmospheric model physics. In particular, large changes in radiative flux biases, driven by changes in simulated clouds, lead to large differences in temperature and precipitation biases. CORDEX models simulate Arctic annual temperature trends of 0.40°C per decade over the 1979–2014 period which are less than that from ERA-Interim (0.55°C per decade) and station observations (0.60°C per decade) (Zhou et al., 2019). The maximum temperature trend of 2°C per year during the 2003–2012 period over the Kara and Barents Seas in March is well captured (Kohnemann et al., 2017).

CMIP5 models perform well in simulating 20th-century snowfall for the northern hemisphere, although there is a positive bias in the multi-model ensemble relative to the observed data in many regions (Krasting et al., 2013). Lack of sufficient spatial resolution in the model topography has a serious impact on the simulation of snowfall. The patterns of relative maxima and minima of snowfall, however, are captured reasonably well by the models. The magnitude of annual snowfall is in better agreement over the eastern half of North America (coincides with the relatively flat terrain and a higher density of stations that allow the capture the regional variations of snowfall), while the largest absolute errors are found in the western part of the continent (consistent with the coarse representation of the Rocky Mountains in the models as well as with biases that may be present in the observational data) (Krasting et al., 2013). Over Eurasia, the snowfall maximum in the central plateau of Siberia is significantly over-estimated by the models by as much as 250–300 cm.

Arctic CORDEX RCMs reproduce the dominant features of regional precipitation pattern, including the precipitation magnitude and seasonal cycle, as for example shown in the Regional Arctic System Model (RASM1; Hamman et al., 2016). Due to the higher spatial resolution, the RCM simulates larger amounts of orographic precipitation compared to reanalyses. Overall, the simulated precipitation is within the reanalysis and global model (CESM1) ensemble spread, but the Arctic river basin precipitation compares better to observations (Brunke et al., 2018). However, Takhsha et al. (2018) show that the RCMs precipitation bias highly depends on the observational reference dataset used. Glisan and Gutowski (2014) showed the capability of RCMs to reproduce extreme daily precipitation over the western Arctic in summer. Although the models underestimate extreme precipitation amounts and simulate fewer high-intensity precipitation events compared to the station observations, the spatial patterns and interannual variability are roughly equivalent to the observations. Years with the highest and lowest occurrences of observed extreme events are simulated well.

Annual mean precipitation of ensemble global atmospheric simulations with a high horizontal resolution (60 km) agrees well with the observed precipitation maximum over the Greenland Sea and the Norwegian Sea (Kusunoki et al., 2015). The regional average annual precipitation according to the model is 1.1 mm, which is larger than the observed value of 0.88 mm. This positive bias of 22% is partly due to model overestimates of precipitation in the North Pole region, where observations show a local minimum. The spatial correlation coefficient between observations and simulations is as high as 0.84. Excessive precipitation over Alaska and the western Arctic is consistent with the results of Kattsov et al. (2017), but in this later study the bias over the eastern Arctic and the Norwegian/Barents Sea region is opposite to the results of Kattsov et al. (2007). These differences in the bias distribution can be attributed to differences in models used and in the time periods of the analyses.

An ensemble of global atmospheric simulations with high horizontal resolution have been used to evaluate extreme precipitation. The simulations reproduce Simple Daily Precipitation Intensity Index (SDII; defined as the total annual precipitation divided by the number of rainy days) over the Greenland Sea, but underestimate precipitation over other regions (Kusunoki et al., 2015). Arctic average SDII from the model is 8% smaller than the observed value, a difference which originates from the overestimated number of rainy days and indicates that the model tends to predict too many weak rainfall events. The spatial correlation

coefficient between observations and the simulations is 0.68. Furthermore, the model reproduces the observed maximum 5-day precipitation total (R5d) distribution reasonably well but overestimates it around Svalbard. The Arctic-averaged R5d from the model shows a positive bias of 17% and the spatial correlation coefficient between observations and the simulation is 0.69.

Atlas.5.9.2.4 Assessment and synthesis of projections

[START Figure Atlas.48: HERE]

Figure Atlas.48: (a–b) Mean observed trends of annual mean surface air temperature and precipitation for three datasets (CRU TS, BERKELEY and EWEMBI for temperature; CRU TS, GPCC and GPCP for precipitation). Hatching indicates regions where no or only one dataset provides a significant trend. Linear trends are calculated for the common 1980–2014 period and expressed in °C per decade (temperature) and % relative change per decade (precipitation) with respect to the climatological mean over this period.
(c–f) Climate change projections of annual mean surface air temperature and precipitation from CMIP5 (30 models) and CMIP6 (17 models) calculated as the differences in the climatological average for RCP8.5 and SSP5-8.5 respectively, for the period 2041–2060 with respect to the historical 1995–2014 period and expressed as °C (temperature) and % relative change (precipitation). Hatching indicates weak model agreement on the sign of the change (less than 80% as defined in Nikulin et al., 2018).
(g–k) Regional mean changes in annual mean surface air temperature and precipitation for the five Arctic regions (ARO, RAR, GIC, NEC and NWN). The top row shows the median (dots) and 10th–90th percentile range across each model ensemble for annual mean temperature changes, for two datasets (CMIP5 and CMIP6) and two scenarios (SSP1-2.6/RCP2.6 and SSP5-8.5/RCP8.5). The first four bars represent the additional warming projected relative to the historical baseline 1995–2014 period to reach the two global warming levels (GWL; +1.5°C and +2°C) and the remaining six projected changes over three time periods (near-term 2021–2040, mid-term 2041–2060 and long-term 2081–2100) compared to this same historical baseline period. The bottom row shows scatter diagrams of temperature against precipitation changes, displaying the median (dots) and 10th–90th percentile ranges for four future periods (2021–2040, 2041–2060, 2061–2080, 2081–2100) compared to the historical baseline period, as obtained from CMIP6 projections for three scenarios (SSP1-2.6, SSP2-4.5 and SSP5-8.5). Changes are absolute for temperature and relative for precipitation.
(The script used to generate this figure is available online (Atlas GitHub, 2020) and similar results can be generated in the Interactive Atlas for flexibly defined seasonal periods.)

[END Figure Atlas.48: HERE]

Projections from 40 CMIP5 models of the 2014–2100 Arctic (north of 64°N) annual warming under RCP4.5 emissions vary from 0.9°C to 6.7°C, with a multi-model mean of 3.68°C (Chylek et al., 2016). The largest warming is simulated over the Barents Sea. Climate models with fully interactive aerosol-cloud interactions lead to projections of a warmer Arctic. Arctic warming trends projected by models that include a full direct and indirect aerosol effect ('fully interactive') are significantly higher (the mean projected Arctic warming is about 1.5°C higher) than those projected by models without a full indirect aerosol effect (Chylek et al., 2016).

Projected Arctic warming exhibits a very pronounced seasonal cycle, with exceptionally strong warming in the winter. In projections from 30 CMIP5 models, winter warming over the Arctic Ocean varies regionally with 3°C–5°C by the mid-century and 5°C–9°C by the late century under RCP4.5 (AMAP, 2017). Averaged over the Arctic (60–90°N) and based on 36 CMIP5 models, winter warming is 5.8 ± 1.5°C by the mid-century and 7.1 ± 2.3°C by 2100 under RCP4.5 (Overland et al., 2019) and exceptionally strong warming of up to 14.1 ± 2.9°C is projected in December under RCP8.5 with more moderate warming during the summer (Bintanja and Krikken, 2016). Bintanja and Van Der Linden (2013) also estimated the Arctic winter warming over the 21st century to exceed the summer warming by at least a factor of four, irrespective of the magnitude of the climate forcing. Averaged over the Arctic (70–90°N) projected warming increases linearly

with about 0.78°C per 1% reduction in sea-ice concentration until temperature changes of about 10°C (Koenigk et al., 2015). For further ice concentration reductions, the temperature response gets slightly smaller (0.48°C per 1% ice concentration reduction).

Overland et al. (2014) highlighted the difference between the near-term 'adaptation timescale' and the long-term 'mitigation timescale' for the Arctic (60–90°N). Only in the latter half of the century do the projections under RCP4.5 and RCP8.5 emissions noticeably separate. End-of-the-century warming is approximately twice as large under RCP8.5 demonstrating the impact of the lower emissions under RCP4.5 (AMAP, 2017). More specifically under the strong forcing scenario, annual mean surface air temperatures in the Arctic (70–90°N) is projected to increase by 8.5 ± 2.1°C (model-mean value and inter-model standard deviation) over the course of the 21st century (Bintanja and Andry, 2017). Koenigk et al. (2015) show that the end-of-the-century warming (2080–2099 period relative to 1890–1999 period) can exceed 15°C in autumn and winter over the Arctic Ocean.

Projections averaged over the four best-performing CMIP5 models over the Arctic are for annual mean surface air temperature to warm 4.1°C, 5.7°C, and 10.6°C by 2100 compared to the 1951–1980 period under RCP2.6, RCP4.5 and RCP8.5 respectively (Hao et al., 2018). The largest annual warming is simulated over the Arctic Ocean with CMIP5 ensemble median projections for Svalbard of about 10°C for RCP8.5 and 7°C (van der Bilt et al., 2019). Projected temperatures show strongest increase over northern Fennoscandia and the high Arctic, exceeding 7°C by end of the 21st century for a typical 'warm winter' under RCP4.5, and much stronger warming under RCP8.5 with increases exceeding 18°C in some places (Benestad et al., 2016).

The ensemble of CMIP6 (15-17 models depending on the scenario) shows generally greater warming compared to CMIP5 (Figure Atlas.48:). There is weak agreement among the models in projected temperature change over the Arctic North Atlantic under SSPs until the mid-century (Figure Atlas.48:), but a robust warming signal clearly emerges even there by 2100. Generally, the largest annual warming is simulated over the Arctic Ocean, particularly over the Barents Sea (Figure Atlas.48:).

Future warming in CORDEX RCMs and the CMIP5 models are similar. Koenigk et al. (2015) show that the RCM warming over the Arctic Ocean is smaller, while the warming over land is larger in winter and spring but smaller in summer, compared with CMIP5.

The CMIP5 multi-model mean projected precipitation increase in the Arctic is in the order of 50% under RCP8.5 by the end of 21st century, which is among the highest globally (Bintanja and Selten, 2014). Over 70–90°N, the precipitation increase is 61.9 ± 20.5% and 56.4 ± 13.2% for RCP4.5 and RCP8.5 respectively. In the near future (2030 to 2049), this corresponds to an increase of 2–10 mm per month and substantially more for the Barents Sea (up to 50 mm per month) under RCP8.5, and the increase is expected to continue until the end of the century (Koenigk et al., 2015). For ARCO (Svalbard), van der Bilt et al. (2019) estimate the increase in annual precipitation by 2100 to be about 65% for RCP8.5 and 45% for RCP4.5 (CMIP5 ensemble median). However importantly, the simulated Arctic (70–90°N) precipitation increase varies by a factor of three to four between models (Bintanja and Selten, 2014). The projected increase is strongest in late autumn and winter.

The CMIP6 projections confirm precipitation will *likely* increase almost everywhere in the Arctic (Figure Atlas.48:). The largest increase is simulated over the Barents Sea and Chukchi Sea regions, and over northeast Greenland. A pronounced uncertainty in the projection exists over the Arctic North Atlantic and south Greenland. There, the precipitation signal is not significant even by the end of the 21st century and under strong scenarios (RCP8.5, SSP5-8.5). According to the generally higher warming in CMIP6, compared to CMIP5, the projected precipitation increase is higher in CMIP6.

The increase in Arctic mean annual-average precipitation sensitivity has been estimated at 4.5% per 1°C temperature rise, compared to a global average of 1.6–1.9% per 1°C temperature rise (Bintanja and Selten, 2014) based on a set of 37 CMIP5 GCMs. Koenigk et al. (2015) stress the different precipitation sensitivity in winter (0.8 mm per month per 1°C temperature rise) and summer (2 mm per month per 1°C temperature rise), based on RCM downscaling of four CMIP5 models. Dobler et al. (2016) support the high precipitation

sensitivity for the projected temperature changes. Relative and absolute sensitivities following the RCP8.5 scenario show the biggest increases along the Norwegian west coast in summer and autumn. Relative sensitivity is about 4% per 1°C temperature rise in the Barents area. The pattern and amplitude of precipitation changes agree in CORDEX simulations with their driving CMIP5 models (Koenigk et al., 2015). However, more small-scale variations over land and coastlines and significantly larger precipitation changes in summer are obvious in the downscaling.

Rain is projected to become the dominant form of precipitation in the Arctic region by the end of the 21st century. CMIP5 models show a decrease in annual Arctic (70–90°N) snowfall under both RCP4.5 and RCP8.5 (Krasting et al., 2013; Bintanja and Andry, 2017). In the central Arctic (north of 80°N), the snowfall fraction barely remains larger than 50%, with only Greenland still having snowfall fractions larger than 80% (Bintanja and Andry, 2017). The most dramatic reductions in snowfall fraction are projected to occur over the North Atlantic and especially the Barents Sea, associated with the large warming there. The reduction in Arctic snowfall is expected to be most pronounced during summer and autumn when temperatures would be close to the melting point, but winter rainfall is also projected to intensify considerably. CORDEX simulations project a general increases of rain-on-snow events over the NEC region (north of the future freezing line) during the November–May period for both RCP4.5 and RCP8.5 (Jeong and Sushama, 2018).

Atlas.5.10 Case studies relevant to typological domains

The previous material in this section has focused on climate change over large mainly continental land regions, with the exception of the Polar Arctic (a significantly oceanic domain) and Small islands. This is in alignment with the regional chapters in the AR6 WGII report but does not comprehensively cover all possible types of domains which is acknowledged in the WGII report which also contains Cross Chapter Papers entitled *Biodiversity hotspots (land, coasts and oceans); Cities and settlements by the sea; Deserts, semi-arid areas and desertification; Mediterranean region; Mountains; Polar regions; Tropical forests.* This section then describes examples of generating climate change assessments relevant to these typological domains in three cases studies relevant to the *Mountains* and *Polar regions* cross-chapter papers. The first looks at observed and projected climate change in the Hindu Kush Himalaya (HKH) and the Tibetan plateau and the others at two important features of Arctic climate.

Atlas.5.10.1 Mountains: The Hindu Kush Himalaya (HKH)

Regional executive summary

The glacier mass is *likely* to decrease considerably (nearly 50%) under RCP 4.5 and 8.5 scenarios while the snowmelt is higher in central and eastern Himalaya than western Himalaya. Karakoram glaciers are in approximately balanced state, however elevation dependent warming is evident over the HKH region (*high confidence*). {Atlas.5.10.1.4}

Minimum temperatures are increasing more than maximum temperatures with high values for winter temperatures (*high confidence*). The sparseness of observational data is a major source of uncertainty in the estimates of long-term trends of mean and extreme climatic indices in the HKH. {Atlas.5.10.1.2}

Heavy precipitation events will intensify in future, which may cause more Glacial Lake Outburst Flood (GLOF events) (*medium confidence*). It is *likely* that annual mean precipitation will increase in the future with most of the increase coming from winter precipitation (*medium confidence*). {Atlas.5.10.1.4}

Atlas.5.10.1.1 Key features of the regional climate and findings from previous assessments

Key features of the regional climate

The climate is mostly alpine over the Himalaya but varies within HKH significantly with snow-capped

higher elevations to tropical/subtropical climates at lower slopes (Krishnan et al., 2019a). The HKH climate modulates the global weather patterns by serving as a heat source in summer and heat sink in winter. The HKH and the elevated Tibetan Plateau exert significant influence on the Asian summer monsoon system. The HKH is sensitive to climate change and variability (Krishnan et al., 2019). The atmospheric features of the region are influenced by three distinct weather systems, known as westerly storms, summer monsoon and anticyclonic clear weather conditions (Bashir et al., 2017).

Previous findings from IPCC assessments

In 2007, the Intergovernmental Panel on Climate Change (IPCC's) Fourth Assessment Report (Pachauri and Reisinger, 2007) pointed to the lack of consistent long-term monitoring in the HKH. Little progress was made in the HKH by the time of the IPCC's Fifth Assessment Report (Pachauri and Meyer, 2014). The precipitation is not simulated well at regional scales by global climate models used in CMIP5 experiments for the IPCC Assessment Report 5 (AR5), and the assessment is hampered by observational uncertainties (Flato et al., 2013). The AR5 highlights that the projected changes in the water cycle at regional scale will be strongly influenced by natural internal variability and may be affected by anthropogenic aerosol emissions. The monsoon winds are likely to weaken, however the monsoon precipitation is likely to intensify due to the availability of more moisture in the atmosphere (Krishnan et al., 2013; KITOH, 2017). The HKH region is projected to warm over the 21st century based on the analyses performed on future projections of annual mean surface temperature change relative to 1976–2005, based on a CMIP5 multi-model ensemble mean (a subset of 25 models), which are higher than the likely ranges reported for global and South Asian regions by the recent IPCC assessment. They indicate continuous warming over the entire HKH in the 21st century. SR1.5 says that the risks from heavy precipitation events are projected to be higher at 2°C compared to 1.5°C of global warming in several northern hemisphere high-latitude and/or high-elevation regions (*medium confidence*).

Atlas.5.10.1.2 Assessment and synthesis of observations, trends and attribution

The topographic variations, the annual cycle of seasons, and variability of weather patterns have strong controls on the spatial pattern of temperatures across different geographic regions of the HKH (Hasson et al., 2014; Kapnick et al., 2014; Krishnan et al., 2019a). The HKH has seen significant warming in the past decades nearly equal to the global average (Krishnan et al., 2019a). The annual mean surface air temperature has increased significantly in the HKH at a rate of about 0.1 °C per decade during 1901–2014, with larger change of more than 0.2°C per decade in the Tibetan Plateau (TP) and southern Pakistan (Ren et al., 2017a). The annual mean temperature in the Tibetan Plateau (TP) is warming at a rate of 0.316°C per decade during 1961–2012 (Yan and Liu, 2014), which is almost twice the previous estimate for 1955–1996 period by Liu and Chen (2000). The observed annual and winter mean temperatures at high elevation sites (>2,000 m) of the eastern TP have increased at a rate of about 0.42°C per decade and 0.61°C per decade respectively during 1961–2006, while the low-elevation sites (<500 m) have warmed at a rate of about 0.2°C per decade during the same period (Liu et al., 2009).

The variability of seasonal weather patterns together with the confluence of different mountain ranges makes the topography of the HKH region so complex that the relationship between rainfall and topography is poorly defined (Palazzi et al., 2013). These complexities had posed difficulties in discerning precipitation trends within the HKH in recent decades though using satellite rainfall estimates, reanalyses, and gridded in situ rain gauge data they assessed that the observed summer monsoon precipitation in Himalaya is decreasing significantly (Palazzi et al., 2013).

The datasets used for the study of seasonal mean temperature and precipitation over the Himalayan region are gridded datasets CRU and APHRODITE, which have been used by regional climate modelling, model evaluation and inter comparison studies, e.g., CORDEX South Asia (Latif et al., 2017; Sanjay et al., 2017b; Choudhary and Dimri, 2018b; Ghimire et al., 2018; Nengker, T.; Choudhary, A.; Dimri, 2018). Monthly and daily pre-1950 data are lacking for most parts of the HKH, and the gap is particularly large for areas outside of India. The daily data post-1950 are also insufficient in some areas, including Afghanistan, Pakistan, Myanmar, Bhutan, and Nepal, and the north-western part of the Tibetan Plateau (TP). The sparseness of

observational data is the major source of uncertainties in the estimates of long-term trends of mean and extreme climatic indices in the HKH. In addition, major uncertainty with the estimates of extreme temperature trends comes from the systematic bias of the historical temperature data series caused by urbanization (Wester et al., 2019).

Observation data ranging from 1980–2016 obtained from 46 weather stations in Nepal showed an increase in maximum temperature (~0.04°C yr^{-1}) that is higher than the minimum temperature (~0.02°C yr^{-1}). This trend is more prevalent over the mountainous region than in valleys and lowlands and during the pre-monsoon season than for the rest of the year. A consistent higher increasing trend for warm days (13 days per decade) than for warm nights (4 days per decade) is observed, whereas the rates of decrease for cold days and cold nights are the same (6 days per decade). Less snowfall and cloud coverage are attributed for this trend, which cause positive geopotential height anomalies and strengthens the anticyclonic circulations in the mid-to-upper troposphere. The winter cooling is attributed to the stable lower atmosphere causing prolonged and frequent periods of fog over lowlands regions (Karki et al., 2019).

Figure Atlas.49: shows changes and trends relative to 1980–2014 period in temperature (a) and precipitation (b) from three different data sets over south and central Asia that covers the HKH region. There is a widespread significant warming trend over the HKH, especially in the Tibetan Plateau, of about 0.3–0.4°C per decade. Changes in precipitation, however, are less spatially coherent with a mix of decreasing and increasing trends in rainfall over the region that are not statistically significant.

Atlas.5.10.1.3 Assessment of model performance

The CMIP5 models used in IPCC AR5 were able to simulate the 20th century mean annual cycles of temperature and precipitation in the eastern and western Himalayan sub-regions within the HKH (Panday et al., 2015). However these coarse resolution global models showed large spread in capturing the weather station based observational precipitation regimes as they were not able to resolve fine-scale processes and represent the complex topography in the western Himalayas. Hence these climate models could not realistically simulate the reductions in mean annual temperature observed across stations in the western Himalayas (Panday et al., 2015). As the horizontal resolution of GCMs increased to ~50km, the spatial pattern of rainfall along the southern edge of the Himalayas became more realistic and the overestimation of light rainfall over the Tibetan Plateau also reduced (Li et al., 2016).

Higher resolution (50 km) dynamical downscaling in CORDEX over South Asia using regional climate models (RCMs) with improved topographic representation of the HKH region are expected to better resolve the complexities of the monsoon and other hydrological processes at regional scales. The CORDEX South Asia multi-RCM ensemble does exceptionally well in capturing the spatial patterns of temperature climatology over Himalayas for the present (Dimri et al., 2018b). These downscaled high resolution RCM simulations were also able to show added value relative to their driving CMIP5 GCM simulations in a few aspects for the HKH such as the spatial pattern of temperature during summer monsoon and winter season and its changes over the Himalayan water towers in the Indus, Ganges, and Brahmaputra river basins (Mishra, 2015c), and the climatology of temperature and precipitation seasonality over Himalayan watersheds of the Indus basin (Hasson et al., 2019b). Further, the CORDEX RCMs reliably capture the overall increasing trend of surface temperature variations over the South Asian region (Sanjay et al., 2017a) with varying magnitude across regions, seasons, averaging periods and scenarios.

CORDEX South Asia RCM simulations, however, still show cold bias when compared to the driving CMIP5 GCMs over the Himalayas water towers and tend to overestimate the total precipitation in the HKH sub-regions during the summer monsoon and winter seasons (Choudhary and Dimri, 2018; Ghimire et al., 2018; Mishra, 2015; Nengker, T.; Choudhary, A.; Dimri, 2018; Sanjay et al., 2017). Over the Indus Basin (Jhelum, Kabul and upper Indus basin), results showed that the downscaled RCMs and their driving CMIP5 experiments consistently feature low fidelity in terms of the chosen skill metrics, suggesting substantial cold (6–10°C) and wet (up to 80%) biases and underestimation of observed precipitation seasonality (Hasson et al., 2019c) and showed uncertainty for far future climate projection under the RCP8.5 scenario. The biases of both RCMs and of their driving CMIP5 GCMs were higher in magnitude than the projected changes under

the RCP8.5 scenario by the end of 21st century, indicating uncertain future climates for the Indus Basin watersheds.

Atlas.5.10.1.4 Assessment and synthesis of projections

The assessment of future temperature changes over HKH indicated that CORDEX multi-RCMs provided relatively better confidence than their driving CMIP5 GCMs in projecting the magnitude of seasonal warming for the hilly sub-region within the Karakoram and north-western Himalaya. The projected temperature change (5.4°C) is higher during winter (December to February) than during summer monsoon (June-September) season (4.9°C) by the end of 21st century under the RCP8.5 high emissions scenario (Sanjay et al., 2017c, 2017d). However, less agreement was found among these RCMs on the magnitude of future warming over other hilly sub-regions within the HKH for both seasons. In particular, there is higher RCM uncertainty in the climate projections over the hilly parts of central Himalaya. Over the Indian Himalayan region, an assessment of future temperature changes in four CORDEX RCMs indicated statistically significant strong rates of warming (increasing with intensification of greenhouse gas emission RCP scenarios) of about 0.03–0.09°C per year (Dimri et al., 2018a), but with large spatial variations and inter-model spread (*medium confidence*). Further, there is a higher warming rate (0.23–0.52°C per decade) for both minimum and maximum air temperature (Tmin and Tmax) along with the diurnal temperature range (DTR) predominated by rise of the Tmax as compared to Tmin (Dimri et al., 2018b) over the region under both RCP4.5 and RCP8.5 scenarios. Overall temperature across the mountainous HKH will increase by about 1–2°C (and in some places by up to 4–5°C) by 2050 (Shrestha et al., 2015) and will increase up to 5.5 ± 1.5 °C by the end of the 21st century. For RCP4.5 this change will be 2.5 ± 1.5 ° C (van Vuuren et al., 2011).

Results from the CMIP5 models suggest that the projected changes in the surface mean temperature over the HKH are larger compared to the global mean change by the end of the 21st century. The projected warming differs by more than 1°C between the eastern and western HKH, with relatively higher values in winter (Sanjay et al., 2017b). The projected temperature changes with RCP4.5 and RCP8.5 scenarios for time slices of 2036–65 and 2066–95 relative to 1976–2005 in three HKH subregions suggest that during summer (winter) relatively higher (lower) warming will occur over the hilly regions of the north-western Himalaya and Karakoram (HKH1) than in the central Himalaya (HKH2) and south-eastern Himalaya and TP (HKH3) (Wester et al., 2019). In general, future projections of surface temperature from the CMIP5 models and CORDEX RCM seem to agree on the overall warming trends over the HKH region with differences in magnitude (Wester et al., 2019).

The summer monsoon precipitation will intensify by about 22% in the hilly sub-region within the south-eastern Himalaya and Tibetan Plateau for the far-future period under the RCP8.5 scenario (Krishnan et al., 2019b). CMIP5 GCM projections for RCP4.5 and RCP8.5 scenarios show summer monsoon rainfall increase over the Himalayas (Palazzi et al., 2015). Three different hydrological models tested over snow and glacier-covered river basins of Hunza-, Gilgit- and Astore using CORDEX RCM-simulations for future scenarios showed an increase in precipitation but decline in intensity of rise over high-altitude zones, for the period 2071–2099 (2090s) under the RCP8.5 scenario with significant increase in snow- glacier-melt runoff and precipitation runoff in the Hunza-, Gilgit- and Astore-River basins, respectively (Azmat et al., 2019). Another result from a regional climate model (PRECIS) over a river basin scale (Indus Basin) did not show any trends in precipitation changes in the future in the western HKH (Rajbhandari et al., 2015). However, in the eastern Himalaya (Koshi Basin), for both RCP4.5 and RCP8.5 scenarios, a 10–20% increase in rainfall during the summer monsoon and about a 5% increase in the winter season over the trans-Himalayan part of the basin was observed (Rajbhandari et al., 2016). Unlike temperature, the precipitation response to climate change over the HKH region is subject to larger uncertainties both in the CMIP5 and CORDEX models (Dimri et al., 2018; Hasson et al., 2013, 2015; Mishra, 2015a; Sanjay et al., 2017b). The CORDEX RCM, in particular, still have inherent limitations in reproducing the observed characteristics of the summer monsoon rainfall variability (Singh et al., 2017), and future projections of precipitation extremes are unresolved, both across studies and across regions (Palazzi et al., 2013).

Figure Atlas.49: show projected changes in temperature (c,e) and precipitation (d,f) over the HKH region

calculated as the climatology differences for medium-term (2041–2060) periods for the scenario RCP8.5 (SSP5-8.5 for CMIP6) with regards to the historical (1986–2005). Warming over the region will continue to increase significantly and temperatures will increase by as much as 2.5–3°C, especially in the TP, by mid-century in both CMIP5 and CMIP6. Precipitation is projected to increase over the TP by as much 20–25% with strong model agreement within members of the ensemble for both scenarios.

[START Figure Atlas.49: HERE]

Figure Atlas.49: (a–b) Mean observed trends of annual mean surface air temperature and precipitation for three datasets (CRU TS, BERKELEY and EWEMBI for temperature; CRU TS, GPCC and GPCP for precipitation). Hatching indicates regions where no or only one dataset provides a significant trend. Linear trends are calculated for the common 1980–2014 period and expressed in °C per decade (temperature) and % relative change per decade (precipitation) with respect to the climatological mean over this period.
(c–f) Climate change projections of annual mean surface air temperature and precipitation from CMIP5 (30 models) and CMIP6 (17 models) calculated as the differences in the climatological average for RCP8.5 and SSP5-8.5 respectively, for the period 2041–2060 with respect to the historical 1995–2014 period and expressed as °C (temperature) and % relative change (precipitation). Hatching indicates weak model agreement on the sign of the change (less than 80% as defined in Nikulin et al., 2018).
(g–h) Regional mean changes in annual mean surface air temperature and precipitation for the Tibetan Plateau and South Asia. The top row shows the median (dots) and 10th–90th percentile range across each model ensemble for annual mean temperature changes, for two datasets (CMIP5 and CMIP6) and two scenarios (SSP1-2.6/RCP2.6 and SSP5-8.5/RCP8.5). The first four bars represent the additional warming projected relative to the historical baseline 1995–2014 period to reach the two global warming levels (GWL; +1.5°C and +2°C) and the remaining six projected changes over three time periods (near-term 2021–2040, mid-term 2041–2060 and long-term 2081–2100) compared to this same historical baseline period. The bottom row shows scatter diagrams of temperature against precipitation changes, displaying the median (dots) and 10th–90th percentile ranges for four future periods (2021–2040, 2041–2060, 2061–2080, 2081–2100) compared to the historical baseline period, as obtained from CMIP6 projections for three scenarios (SSP1-2.6, SSP2-4.5 and SSP5-8.5). Changes are absolute for temperature and relative for precipitation.
(The script used to generate this figure is available online (Atlas GitHub, 2020) and similar results can be generated in the Interactive Atlas for flexibly defined seasonal periods.)

[END Figure Atlas.49: HERE]

Atlas.5.10.2 Polar regions: glaciers in the Arctic

Atlas.5.10.2.1 Background and overall conditions

Glaciers in the Arctic, including Greenland, are located in remote and hard-to-get-to places where continuous measurements are both physically difficult and expensive to maintain. With the increased use of satellite and newly available remote sensing data, the observational dataset for glaciers is becoming more detailed and new inventories that gather the monitoring efforts are enabling leaps in the state of knowledge of glaciers. The coming few years will see huge improvements in monitoring of glaciers in the Arctic and in the world. The data presented in AR6 are made available in open access from Global Terrestrial Network for Glaciers (GTN-G), which provides an umbrella for existing and operational monitoring services and is jointly run by three operational bodies – the World Glacier Monitoring Service (WGMS), the US National Snow and Ice Data Center (NSIDC), and the Global Land Ice Measurements from Space (GLIMS) initiative.

The WGMS and its predecessor organizations have internationally coordinated glacier monitoring since 1894, resulting in an unprecedented database on glacier changes in length, area, volume and mass with the longest time series reaching back to the 16th century (Zemp et al., 2015; WGMS, 2017). Since IPCC AR5, the glacier mass-balance dataset from geodetic surveys has been boosted from a few hundred to almost 20,000 glaciers with available observations (Zemp et al., 2015, 2019). An inventory of digital global glacier

outlines called the Randolph Glacier Inventory (RGI) was developed to inform the AR5 and facilitate assessment of past and future mass evolution of glaciers in the world (Pfeffer et al., 2014; RGI Consortium, 2017). GLIMS and RGI have been fundamental in gathering global inventories of glacier outlines. In AR6, version 6.0 of the RGI inventory is used, yielding *high confidence* that the current area of the glaciers is 706 ± 30 x 10^3 km^2 (Chapter 9, Section 9.5.1.1, Table 9.4).

Several new data sources and access to archives of old satellite and remote sensing data have become available for assessing both changes in area and elevation of glaciers and ice caps. For elevation changes and geodetic mass-balance estimates, a number of new or recently made available data sources are used. This includes archived aerial photographs; declassified satellite photoreconnaissance missions from the 1960–1984 period; Hexagon KH-9 Mapping Camera images (e.g. Bindschadler and Vornberger, 1998; Surazakov and Aizen, 2010); optical stereo-imagery that includes ASTER (Raup et al., 2007; Brun et al., 2017), SPOT (Zheng et al., 2018), CryoSat2 (Foresta et al., 2018), High-Resolution SAR Interferometry, like TanDEM-X (Krieger et al., 2007; Braun et al., 2019); and high-resolution digital elevation models with submeter uncertainty from Lidar, Pleiades (Berthier et al., 2014), Worldview (Shean et al., 2016) and Arctic DEM (Porter et al., 2018). This is a breakthrough in both spatial and temporal resolution that will revolutionize monitoring of glaciers in the coming years. Increase in computational power and the use of large-scale batch processing, like the Ames Stereo Pipeline (Shean et al., 2016), are allowing for the assessment of glacier elevation changes at continental or large mountain range scales (Brun et al., 2017; Braun et al., 2019).

Atlas.5.10.2.2 Glacier volume thus sea level change

To estimate the total volume and thus the sea-level equivalent mass of the glaciers in the Arctic and globally, the thickness of all the glaciers needs to be known. A standardised database of glacier thickness (GlaThiDa, containing observations from roughly 1,100 glaciers, (Gärtner-Roer et al., 2014; GlaThiDa Consortium, 2019) is used to validate the global estimation approaches which come with large uncertainties (median relative absolute deviation of around 30%) and a tendency to overestimate the glacier thickness. Since AR5, a coordinated effort to assess the quality of glacier thickness estimates has been made in the framework of the Ice Thickness Models Intercomparison Experiment (ITMIX; Farinotti et al., 2017). Only a few models are currently capable of operating on an Arctic and global scale, and the differences in the results of the 17 models assessed in ITMIX highlight the importance for an internationally consistent database against which models can be calibrated and validated (Farinotti et al., 2017). A consensus estimate of world's glaciers thicknesses made from five models of variable spatial extent (Huss and Farinotti, 2012; Frey et al., 2014; Fürst et al., 2017; Ramsankaran et al., 2018; Maussion et al., 2019) indicates that there still remains a large uncertainty in the estimated thickness and subsequent sea-level contribution, due to both model uncertainty and input data (Farinotti et al., 2019). This new estimate of the thickness of all glaciers in the Arctic and the world and thereby their volume is presented in Chapter 9.

The continued synthesis of ever-longer time series from multi-platform observations and combined datasets is rapidly improving understanding of the present and past cryosphere. Focusing on the Earth's ice masses, including glaciers in the Arctic, several studies (e.g., Bamber et al., 2018; Box et al., 2018; Shepherd et al., 2018, 2019; Zemp et al., 2019) integrate and assess estimates from gravity, altimetry and mass change measurements. These new syntheses are able to reduce uncertainties and provide clearer insights into interannual and decadal trends.

Atlas.5.10.2.3 Assessment and synthesis of observations, trends and attribution

While temperatures in the Arctic have warmed considerably, datasets show that Greenland, as well as the ocean south of it, have cooled over the last 15 years (Susskind et al., 2019). This cooling over Greenland is a relatively recent phenomenon. However, McGrath et al. (2013) showed that previous in situ measurements at Greenland Summit suggested that the annual mean near-surface air temperature had increased by 0.9 ± 0.1 °C per decade from 1982 to 2011. The long-term weather data over west Greenland show that since 1994 mean June air temperatures are 2.2°C higher and mean winter precipitation has doubled from 21 to 40 mm; and since 2006, mean July air temperatures are 1.1°C higher (Saros et al., 2019).

The summer air temperature 'viability threshold' that triggers irreversible wastage of the Greenland ice sheet was previously estimated to be for an annual global temperature increase of 2°C–5°C (Gregory and Huybrechts, 2006; Huybrechts et al., 2011). An updated estimate based on a higher-resolution simulation that explicitly incorporates albedo and elevation feedbacks suggests a lower loss threshold: 0.8°C–3.2°C (95% confidence range) with 1.6°C above pre-industrial conditions as a best estimate implying it is likely that the Greenland ice sheet enters a phase of irreversible loss under the RCP4.5 scenario (Overland et al., 2019).

Atlas.5.10.3 Polar Regions: Snow on sea ice in Arctic

Atlas.5.10.3.1 Background and overall conditions

Snow covering sea ice in the polar regions alters and affects the surface energy fluxes, the sea-ice mass balance, habitat conditions, and mechanical properties of the combined snow—sea-ice system (SROCC 3.2.1.1.6; AR6 WGI 2.3.2.1.9). The connection between precipitation, temperature, and deposited snow is different for sea ice compared to snow over land. This is because sea ice usually provides a heat source to the bottom of the snow cover, the sea-ice cover is not necessarily around for a long period, and sea-ice drift actively transports snow over large distances.

Snow thickness observations on sea ice are sparse and no continuous dataset with a sufficient spatial coverage exists. Existing sporadic data indicate regional differences with a negative trend in snow thickness over the sea ice for the western Arctic, and a rather thick snow cover in the Atlantic sector (Section 2.3.2.1) (Webster et al., 2014, 2018; Rösel et al., 2018). Available observations from drifting buoys do not show significant trends in snowfall rate (Webster et al., 2014). Changes in snow thickness on sea ice are therefore primarily driven by changes in the prevailing sea-ice type and sea-ice age: multi-year ice (MYI), which is sea ice that has survived a summer, will capture all snowfall throughout the entire annual cycle. On the other hand, first-year ice (FYI, that only forms throughout autumn and winter) will not carry any of the snow that fell before the ice formed. Hence, there is a clear connection between snow depth and ice type, with up to double the snow depths on MYI compared with FYI (Kurtz and Farrell, 2011; Blanchard-Wrigglesworth et al., 2015). To reflect this, snow climatologies used for the satellite inference of sea-ice thickness based on altimeter measurements are usually corrected using a thinner snow thickness for FYI compared with MYI (Laxon et al., 2013; Ricker et al., 2017).

Atlas.5.10.3.2 Key processes and impacts

Two processes are known to lead to sea-ice growth at the ice surface: snow-ice formation, which implies freezing of a slush layer at the snow-sea ice interface after flooding by sea water, and superimposed ice formation, freezing of a similar layer, but with the contribution of freshwater from rain or snow melt instead of sea water (Onstott, 1992; Eicken, 1998). The snow cover in the Arctic Ocean has, in the past, generally been too thin to load the ice to the point where negative freeboard occurs, and surface flooding can result in snow-ice formation (Haapala et al., 2013; Granskog et al., 2017). However, thinning of the sea ice, as observed in the Arctic (Section 2.3.2.1; SROCC 3.2.1.1.2), decreases the freeboard, unless the snow cover in parallel also becomes substantially less. Hence, snow-ice formation is expected to increase in the Arctic in the future (Merkouriadi et al., 2019). Depending on future changes in atmospheric temperature and precipitation phases, occurrence of superimposed ice might also become a scenario seen more often than today.

Radiative fluxes and the snow cover on sea ice are closely connected. Snow has a higher surface albedo than a bare sea ice surface (Figure Atlas.50:). The timing of snow precipitation and snow melt relative to solar elevation is therefore important for the surface energy balance in a sea-ice covered region (e.g., Perovich et al., 2017; Perovich and Polashenski, 2012). Snow along with atmospheric forcing and sea-ice topography determines how and when melt ponds on sea ice form in summer months. Melt ponds however lower the albedo.

The snow cover on sea ice has a major influence on the light budget available for ice-associated biota in and

below the sea ice (Nicolaus et al., 2012; Lange et al., 2019). Conditions at the snow-ice interface can provide living conditions for certain algae species (Fernández-Méndez et al., 2018). The snow cover can also play a role for upper trophic levels such as ring seals, which use snow caves for raising their pups (Kovacs et al., 2012; Iacozza and Ferguson, 2014; Hamilton et al., 2018).

Mechanical properties of the sea-ice and snow system are relevant for ice dynamics, such as ridging and rafting of sea ice, but also for human activity (shipping). With the latter, snow on sea ice has a direct societal relevance. A snow cover on sea ice increases the mechanical friction for a ship navigating through the ice.

[START Figure Atlas.50: HERE]

Figure Atlas.50: Conceptual flow diagram of relevant snow-on-sea-ice processes.

[END Figure Atlas.50: HERE]

Atlas.6 Climate change communication

Atlas.6.1 Approaches to communicating climate change information

The primary purpose of IPCC assessment reports is to provide policymakers and practitioners at all levels with the scientific information they need to develop climate policies. The information needs to be provided in a manner which is accessible, relevant and usable for the intended audience. This requires that the science be communicated in a way that allows non-scientific audiences to recognise easily and without ambiguity the implications of that science for their decision-making. The term 'policymaker' in itself covers a wide range of users with varying societal and cultural perspectives, expertise and specialist scientific knowledge. Aside from feeding into international, national and local climate policy, region-specific information on climate impacts and projected changes under different scenarios contained within the IPCC reports serves a practical purpose and provides input into designing better forecasting systems, spatial planning and early warning systems. The detailed technical findings in IPCC reports also serve as an important benchmark resource for the research community. Finally, growing societal engagement with climate change means IPCC reports are increasingly used directly by businesses, the financial sector, health practitioners, civil society, the media and educators at all levels. While the primary audience remains decision makers, the IPCC reports could effectively be considered a tiered set of products with information relevant to a range of audiences.

Information on observed or projected climate change can be aggregated to different levels across a range of spatial and temporal scales, from global mean long-term climate characteristics to regionalized and tailored records of observed or projected impacts on a specific group of people. The aggregation scale not only affects the (un)certainty level or confidence in the presented findings, but also the perception of the information by recipients. Assessing impacts of climate change does require integration of climate and non-climatic information, which makes communication between inter- and transdisciplinary teams necessary. Although 'neutral' communication about climate change is difficult to achieve or define, communication actions aimed at informing the general public about the assessed scientific findings regarding climate change have a different purpose and format from actions that are intended to inform a specific target audience in order to support adaptation or mitigation policies (Whetton et al., 2016).

Scientists tend to focus on what they do not know before emphasizing points of agreement (National Academies of Sciences and Medicine, 2017). This focus on uncertainty obscures the level of scientific consensus on main climate change features (Lewandowsky et al., 2015). In addition, it can lead to 'action paralysis', when a weighting or comparison of available adaptation or mitigation actions is complicated by the large number of unresolved drivers for determining an optimal mix of measures.

Rather than stressing the inherent uncertainty in the understanding of past phenomena or future pathways, an emphasis on a 'likely' or 'plausible' range of conditions is being advocated to be an effective approach in

climate change communication. A number of approaches and an evaluation of their effectiveness are under development.

Empirical research on the effectiveness of climate information communication shows trade-offs in conveying complicated information whilst ensuring ease of interpretation and use. Communication approaches favoured by users are not always the approaches that achieve greatest accuracy in interpretation. Best-practice guidance is emerging to achieve greater consistency in the understanding and use of climate information.

Here, a brief overview of concepts of climate change communication is given, also listed in Chapter 10.5.1, including the effectiveness of the various communication strategies some of which are followed by the IPCC.

Atlas.6.1.1 Interpretation and extrapolation of historical trends

Observed trends at the global, local and regional scale provide empirical evidence of a non-stationary climatology. Issues with quality, representativity, and consistency with other lines of evidence are often illustrated in this assessment report (see for example the comparison of various observational datasets in the regional climate change assessments in Section Atlas.5). These issues lead to systematic constraints on their use for attribution of causes of trends (see Section Atlas.5). The practice of attributing trends and extreme events to human causes gives confidence that these trends may be expected to continue in the (near) future, provided the human drivers of climate change remain unchanged. However, large internal variability at decadal time scales can be mistaken for a systematic human impact on the likelihood of extreme events, and in that case extrapolation of trends cannot be expected to be a reliable estimator for the future (Schiermeier, 2018).

Extrapolation of trends can be a viable approach when the time scale of the quantity of interest is long compared with the time window for which the information on future conditions is required. This applies for instance to sea level rise, where observed trends at the local scale are generally extrapolated to near-future time ranges to assist planning of beach nourishment programs and near-term adaptation interventions (Daron, 2015; Baart et al., 2018).

Atlas.6.1.2 Direct use of the output from GCMs, including high resolution GCMs

Outputs from Global Climate Models (GCMs) are a basic repository of many climate change information programs (see Chapter 4 for a review). Issues of systematic biases, drifts, internal variability, assumptions on forcings, spatial and temporal scale, data availability, experimental design and aggregation of ensembles of projections have been assessed in multiple sections of this report. Scenario storylines are needed to interpret the outcome of future projections using a specific time-varying forcing. Even after careful filtering and correcting for all these issues, GCM outputs generally give a relatively coarse picture of climate change, which is deemed useful to feed global mitigation planning but are rarely applicable to local climate change adaptation (van den Hurk et al., 2018). Interactions between the physical and socio-economical elements of the climate system is included in the methodology in choosing scenario assumptions and following driver-effect cascades from the climate response to anthropogenic forcings to regional impacts and risk changes (Berkhout et al., 2013). In this ‘top-down’ mapping approach, uncertainty generally increases with longer time scales and smaller spatial and sectoral domains.

Atlas.6.1.3 Application of downscaling of GCMs

Downscaling global projections with regional climate models (RCMs) or statistical downscaling adds spatial detail, but also adds a source of uncertainty, related to the selection of the chosen downscaling method (see Section 10.3).

An increasing number of national and international climate change assessment programs have been performed, aiming at mapping climate change information relevant for adaptation and mitigation decision support. For instance, Bessembinder et al. (2018) provide an overview of European national climate change scenario programs. In most programs use is made of CMIP5 (or earlier) global climate change ensembles driven by an agreed set of greenhouse-gas emission scenarios, followed by downscaling using RCMs and/or statistical methods, in order to arrive at regionally representative hydrometeorological indicators of climate change. In some cases output of a selection of downscaled global and regional models is provided to users (Whetton et al., 2012; Daron et al., 2018). Uptake by users is strongly dependent on guidance provided on the motivation of the selection, the clarity of the downscaling procedure, and further steps needed to tailor the information to the local scale (Lemos et al., 2012). More comprehensive programs provide probabilistic climate information by careful interpretation, correction and aggregation of ensembles of model outputs (Lowe et al., 2018). The information provided is generally tailored to professional practitioners with expertise to interpret and process this probabilistic information. It is argued that this top-down probabilistic information chain is not able to highlight the essential climate change information for users, and alternative bottom-up approaches are encouraged (Frigg et al., 2013).

Atlas.6.1.4 Inferring regional climate change from an assessment of changes in driving processes

Regional climate is governed by a mixture of physical drivers, such as circulation patterns, seasonal monsoons, annual cycles of snow, regional land-atmosphere feedbacks, etc. Global warming may affect regional climate characteristics by altering the dynamics of their drivers. Regional climate change information can be generated by mapping the consequences of changing the frequency, intensity or impact of drivers. As an example, the KNMI climate change scenarios are constructed by aggregating climate change information from a large ensemble of regional climate projections, and stratifying these according to levels of global warming and the projected change of patterns of atmospheric circulation, an important driver of the regional atmospheric moisture balance and precipitation characteristics (Lenderink et al., 2014). Each of the climate change scenario thus created is based on a physical climate storyline referring to these major drivers.

Atlas.6.1.5 Storylines and narratives

Communicating the full extent of available information on future climate for a region, including a quantification of uncertainties, can act as a barrier to the uptake and use of such information (Lemos et al., 2012; Daron et al., 2018). To address the need to simplify and increase the relevance of information for specific contexts, recent studies have adopted narrative and storyline approaches (Hazeleger et al., 2015; Shepherd et al., 2018b) (see Chapter 1 for definitions, and Chapter 10 for further discussion on these concepts). Narratives and storylines (see Section 1.4.4 and Section 10.5.3) can also be used to help describe relationships between physical climate processes across spatial and temporal scales, and how these influence the climate of a region (e.g., Zappa et al., 2017; Dessai et al., 2018) but here their role in communicating future climate information to address societal challenges is emphasized.

Some uses of climate narratives also focus on the process of their construction and demonstrate the added value of co-produced narratives to enhance knowledge integration in decision-making contexts (e.g., de Bruijn et al., 2016). The success of co-production depends on the degree to which clarity of underlying values and purposes of the different co-production partners is ensured (Bremer and Meisch, 2017). An IPCC expert meeting on assessing and combining multi-model climate projections (IPCC, 2010) recommended that in cases when quantitative information is limited or missing, regional climate assessments could use narratives in addition or as an alternative. It may now be argued that information needs not be missing or limited for narratives to have value, both as a tool to communicate climate information and as a process for knowledge integration.

Atlas.6.1.6 Utilizing expert knowledge and theory

Regional climate characteristics that are extremely rare or result from a complex interplay of compound drivers are frequently assessed by involving expert knowledge and basic theory (Thompson et al., 2016). The information can be aggregated from solicited expert judgments on the likelihood or potential impacts of such a rare event, triggered by its past occurrence or by evidence derived from analyses of model projections. For instance, Dessai et al. (2018) use expert elicitation to characterise narratives of changes in the Indian monsoon. Bamber et al. (2019) concluded that since AR5 uncertainty about sea level rise projections has increased, based on expert opinions on the likelihood of an increased contribution from an unstable Antarctic ice mass.

The scientific credibility (and uptake) of this climate information is sensitive to the reputation and track record of the experts involved (National Academies of Sciences and Medicine, 2017). In addition the protocol used to collect and aggregate the expert information is sensitive to biases, when interaction between experts allows mutual influence between the experts' opinions.

Atlas.6.2 Communicating uncertainty: the role of language and visuals

The communication of uncertainty has a profound influence on the perception of information that is exchanged during the communication process. In climate science, uncertainty refers to the inherent inability to quantify the past, current or expected state of (components of) the climate system (Ho and Budescu, 2019). It is usually expressed by displaying information with an associated likelihood range, generated by the use of ensembles of datasets or model projections (Slingo and Palmer, 2011). Major sources of uncertainty in (IPCC) climate change assessments include imperfection of observational records, model formulation, natural variability and socio-economic pathways.

Uncertainty in climate science communication can lead different audiences to interpret the information in different ways (Corner et al., 2012). Audiences who do not understand that science is a debate and an ongoing process of reducing uncertainty are more likely to dismiss scientific messages that highlight uncertainty in the findings (Rabinovich and Morton, 2012). Leading with what is known, rather than what is uncertain, leads to improved engagement with climate science messages (Trenberth, 2012). Some research has recommended reframing uncertainty information using the closely related concept of 'risk', with which as the language of the insurance, health and national security sectors, most people are more familiar (Howe et al., 2019). It is also argued that scientists must realize that their engagement in advocacy does not necessarily hurt their credibility (Kotcher et al., 2017).

A narrative structure can simplify otherwise complex issues and help audiences make decisions in the face of this complexity (Mohan and Topp, 2018). Understanding and engagement with narratives can be made more effective if the scientific information is presented in a narrative format congruent with the audiences' values, rather than presented as a list of facts (Jones and Song, 2014; Nisbet and Markowitz, 2016; Harris, 2017). On the other hand, many studies suggest that the framing of information is crucial to the way in which it is disseminated or discussed (Lakoff, 2010; Berkhout et al., 2013; Kause et al., 2019).

The visual communication of climate science can take many forms, including graphs, infographics, animations and photographs. The emergence of social media has emphasised the role of visuals, illustrated by the rapid dissemination and uptake of for example the 'warming stripes' (Royal Meteorological Society, 2019) and also used in the Interactive Atlas (Figure Atlas.51:). Studies have used interviews and online surveys to assess interpretations of visualizations used to communicate climate uncertainties to decision makers (Daron et al., 2015; Lorenz et al., 2015; McMahon et al., 2015; Retchless and Brewer, 2016). They commonly find wide-ranging interpretations of the same information and distorted understanding that can be caused by seemingly arbitrary visualization choices. Taylor et al. (2015) found that preferences for a particular visualization approach does not always align with the approaches that achieve greatest accuracy in interpretation.

With new insights from a range of scientific disciplines, including the cognitive and psychological sciences (Harold et al., 2016), best-practice guidance for communicating and visualizing climate data is emerging. Budescu et al. (2012) showed that using a dual verbal-numerical scale allows for greater consistency in understanding confidence and uncertainty; an approach advocated by Harris et al. (2013) who find differences in interpretations of probability expressions between the Chinese and British public. Kaye et al. (2012) and Retchless and Brewer (2016) provided guidance on the use of colour, masking and other graphical approaches to represent uncertainty. Beyond communication of climate information through papers, reports and web-based platforms, new World Meteorological Organization guidance discusses the value of different user-engagement approaches (WMO, 2018) to improve climate information communication, particularly in developing climate services. The guidance provides examples from passive to interactive and focused engagements, showing that deeper and more valuable engagement is best achieved through face-to-face interaction.

In addition, new evidence is emerging about the potential of photographic imagery to build trust in scientific communication. Photographs which connect people and climate in ways deemed credible and authentic support positive engagement with climate change messaging (Chapman et al., 2016). Effective visual communication needs to connect with the values and identity of its audience (Ballantyne et al., 2018).

Besides the standard visual products typically used for communicating global and regional climate information to practitioners (e.g., maps, time series or scatter diagrams), the Interactive Atlas incorporates new visuals (e.g., stripes) facilitating the communication of key messages (e.g., warming and consistency across models) to a less technical audience (Figure Atlas.51:). The various tabular and graphical representation alternatives included as options in the Interactive Atlas facilitate exploring the information interactively from different perspectives and for different levels of detail thus favouring the communication with the larger and diverse audience of IPCC products.

[START Figure Atlas.51: HERE]

Figure Atlas.51: The Interactive Atlas incorporates different visualisations to present climate information such as standard spatial maps (top) and time series (middle), but also more modern visual representations like the (piled) stripes plots (bottom). These examples correspond to CMIP6 annual mean temperature for the SSP5-8.5 scenario. The spatial map shows the climate change signal for the long-term period (2081–2100) with respect to the 1995–2014 baseline period. Regional information – for the aggregated European regions selected in the map – for both the historical and future periods are displayed using time series (middle panel, historical 1950–2014 period in grey and 2015–2100 projections in red) and, alternatively, as a stripe plot formed by the piled stripes of the different models (this figure illustrates a strong warming pattern emerging from the interannual and model variability).

[END Figure Atlas.51: HERE]

Atlas.6.3 Selected case studies

[PLACEHOLDER TO BE ENHANCED DURING THE PERIOD THAT THE INTERACTIVE ATLAS IS BEING FINALISED BUT BEFORE THE SOD GOES OUT FOR REVIEW: MORE CASE STUDIES WILL BE ADDED, INCLUDING ILLUSTRATIONS OF THE USE OF THE INTERACTIVE ATLAS]

Atlas.6.3.1 Communicating regional climate change in a case of inconsistency between various lines of evidence

Sometimes GCM- and RCM-based ensembles can disagree concerning the future projections for some key variables even over large areas. These examples of inconsistency can create issues in communicating future climate change assessment towards stakeholders or the public. Following Boé et al. (submitted), Figure

Atlas.52: illustrates the GCM-RCM inconsistency for European surface temperature projections at the end of the 21st century in summer under the RCP8.5 scenario between the CMIP5 GCM and CORDEX RCM ensembles. This inconsistency remains to be definitively attributed but various hypotheses have been proposed (Sørland et al., 2018b; Schwingshackl et al., 2019; Boé et al., submitted). When assessing future climate change, documenting understanding and taking into account GCM-RCM inconsistencies are required to create a comprehensive and effective narrative on regional climate change.

[START Figure Atlas.52: HERE]

Figure Atlas.52: Mean European June-July-August surface temperature change between the 1970–1999 and 2070–2099 periods for RCP8.5 using an ensemble of CMIP5 GCMs (black), a subset of these used to drive an ensemble of RCMs (green) and the RCMs (red). (Source: Boé et al., submitted).

[END Figure Atlas.52: HERE]

Atlas.7 Description of the online 'Interactive Atlas'

The Interactive Atlas is developed in collaboration with WGI and WGII chapters, focusing on relevant variables, indices and climate impact drivers and allowing for a spatial and temporal analysis with a predefined granularity (e.g. flexible seasons and a number of predefined alternatives for subregions and baseline and future periods, including warming levels; see Section Atlas.2). The Second order Draft (SOD) version presented here includes some basic atmospheric (temperatures and precipitation) and oceanic (sea surface temperature, pH and Oxygen) variables and some illustrative extreme indices (used in Chapter 11) and climate impact drivers (used in Chapter 12). In particular, the Interactive Atlas provides global information in the form of interactive maps for observations (climatologies and trends) and model outputs (climatologies and climate change signals for both time slices and warming levels) of these variables and indices considering a number of alternative reference baselines. It also provides regional information (aggregated spatial values) for a number of predefined (reference and typological) regions in the form of time series, annual cycle plots, scatter plots (e.g. temperature versus precipitation), tabular summaries and stripe plots. This allows for an in-depth comprehensive analysis (and intercomparison) of the different datasets at a global and regional scale. Figure Atlas.53: illustrates the key functionalities of the Interactive Atlas.

[START Figure Atlas.53: HERE]

Figure Atlas.53: Screenshots from the Interactive Atlas showing the main interface and WGI Reference regions (top map) and various formats for displaying summary information over the reference regions (bottom five graphics panels). Other details of model ensembles, resolutions etc are displayed in the text of the figure.

[END Figure Atlas.53: HERE]

In order to ensure transparency and promote FAIR principles (Wilkinson et al., 2016), the reproducibility of results has been a major concern when developing the Interactive Atlas. As a result, full metadata is provided in the Interactive Atlas for each of the products (only for spatial maps in the SOD) and the scripts used to generate the intermediated products (e.g. indices) and plots are available online (Atlas GitHub, 2020), together with simpler notebooks more suitable for reusability. These scripts are based on the climate4R open source framework (Iturbide et al., 2019).

The Interactive Atlas SOD is available for review at ipcc-atlas.ifca.es (login details and indications are provided upon registration as reviewer).

Atlas.7.1 Why an interactive online Atlas in AR6?

The idea of an interactive online Atlas was first discussed in the IPCC Expert Meeting on Assessing Climate Information for the Regions, ICTP, Trieste, 16–18 May 2018. One of the main limitations of previous static global and regional information (including the AR5 Atlas) was the limited options available in order to be informative for different regions and applications. For instance, the use of standard seasons limits the assessment in many cases, such as regions affected by monsoons or seasonal rainband migrations or other phenomena driven seasons. The limited number of variables which can be treated on a printed Atlas also prevents the inclusion of relevant indices and climate impact drivers. One of the main general concerns raised by this online alternative was the potential danger of having an unmanageable number of final products impossible to assess following the IPCC assessment process. All the recommendations and concerns have been taken into account in the design of the Interactive Atlas, implementing a tool for flexible regional and temporal analysis, but with limited predefined functionality and granularity. Moreover, links have been established with other chapters (e.g. using common tools) in order to support their assessment and adopt their methodological recommendations.

In order to facilitate the assessment of the Interactive Atlas, it has been implemented tracking relevant navigation information in the URL, so any product visualized by the Interactive Atlas (as characterized by the particular dataset, region, variable, season, scenario, future and baseline periods, and analysis tool) can be reproduced using the review code provided by the Interactive Atlas for the particular page viewed. This serves as a sort of ID which facilitates the review process of the granular products shown by the Interactive Atlas.

Atlas.7.2 Description of the Interactive Atlas: functionalities and datasets

The Interactive Atlas builds on the work done in the framework Spanish National Adaptation Plan (PNACC – AdapteCCa; http://escenarios.adaptecca.es) to develop a regional scenarios portal to assist the Spanish climate change impact and adaptation community. The basic functionalities initially included in the AR6 WGI Interactive Atlas were based on those already implemented in AdapteCCa and have been adapted and extended to cope with the particular requirements of the datasets and functionalities planed for the Interactive Atlas. In particular, the functionalities available in the SOD have been designed to showcase the possibilities that offers interactivity building on six basic products (see Figure Atlas.53:):

- global maps, uncertainty is represented as in Nikulin et al. (2018), using both model agreement and signal to noise ratio,
- temporal series,
- stripe plots,
- annual cycle plots,
- two-variable scatter plots (e.g. temperature vs. precipitation), and
- tables with summary information.

The first of these products provides spatial information of the ensemble mean and the latter five convey (spatially) aggregated information of the multi-model ensemble for particular region(s) selected by the user from a number of predefined alternatives (currently ‘AR6 WGI reference regions’ and ‘monsoon regions’ for atmospheric variables, and ‘ocean biomes’ for oceanic ones; see Section Atlas.2.2 for more details on regional definitions).

Figure Atlas.54: shows a screenshot of the Interactive Atlas land page displaying a global map with the climate change for the default configuration of dataset, variable, scenario and season (as shown in the tabs at the top of the window). In order to provide a measure of uncertainty, hatching is used to represent low or no model agreement (less than 80%, main hatching at 45º) and low signal to noise ratio (less than 1, secondary hatching at -45º) following Nikulin et al. (2018).

[START Figure Atlas.54: HERE]

Figure Atlas.54: A screenshot illustrating the main window of the AR6 WGI Interactive Atlas, which displays a global map of the climate change signal for annual mean temperature from the CMIP6 dataset for the long-term future period (2081-2100) using the AR6 baseline (1995-2014). The main controls at the top of the window allow selecting the *dataset* (CMIP6, CMIP5 or different CORDEX domains, at 2º, 1º and 0.5º horizontal resolution, respectively), *variable* (atmospheric and oceanic variables and indices), *scenario* (currently SSP1-2.6, 2-4.5 and 5-8.5 –or RCP2.6, 4.5 and 8.5– for different time slices and 1.5º, 2º and 3º warming levels) and *season* (annual, standard seasons and user-defined ones). Regional information for a particular region can be obtained interactively by clicking on the map over one or several sub-regions; see Figure Atlas.55:). Note that the full URL (as copied from the browser) tracks all the information of the current choice (a short 'review code' can be obtained as shown in the figure).

[END Figure Atlas.54:HERE]

The Interactive Atlas includes both atmospheric (daily mean, minimum and maximum temperatures and precipitation) and oceanic (sea surface temperature, pH and oxygen) variables, as well as some illustrative (ETCCDI) extreme indices used in Chapter 11 and a selection of climate impact drivers used in Chapter 12 (see Annex VII, Tables AVII.1 and AVII.2 for more details):

- Maximum of maximum temperatures (TXx)
- Minimum of minimum temperatures (TNn)
- Maximum 1-day precipitation (RX1day)
- Frost days (FD)
- Heating Degree Days (HDD)
- Cooling Degree Days (CDD)
- Days with maximum temperature above 40ºC (TX35), both raw and bias adjusted.
- Days with maximum temperature above 35ºC (TX40), both raw and bias adjusted.
- Days with mean temperature above 21.5ºC (T21.5)
- 99th percentile of daily precipitation (R99)

Some of the above indices (in particular TX35 and TX40) are highly sensitive to model biases and the application of bias adjustment techniques is recommended to alleviate this problem (see Cross-Chapter Box 10.2 on bias adjustment). Bias adjustment is performed using an observational reference (preferable with a resolution similar to the model to avoid 'downscaling' artifacts) and adjusting the historical model output distribution towards the observed one; here we use the EWEMBI (Lange, 2019) observational reference (used in the ISI-MIP initiative), upscaled to the model resolution. As there are several approaches to bias adjustment and no clearly preferred method (see Cross-Chapter Box 10.2) here we use a popular bias adjustment method (empirical quantile mapping, EQM; see Casanueva et al. submitted), but will extended the analysis in the final draft to include an additional trend-preserving method to allow assessing the uncertainty due to bias adjustment techniques. We follow the recommendations given in Chapter 10 and provide the results for both the adjusted and the raw model output.

The basic variables are available in the Interactive Atlas for the global and regional datasets (CMIP5 on a common 2º grid, CMIP6 on a 1º grid, and CORDEX on a 0.5º; see Sections Atlas.3.3 and Atlas.3.4), whereas the indices and climate impact drivers are available only for the global datasets (the final version will include also the indices for CORDEX, for the final dataset available at the cut-off date). Data from the historical, SSP1-2.6, SSP2-4.5 and SSP5-8.5 scenarios (or RCP2.6, RCP4.5 and RCP8.5 for CMIP5 and CORDEX) is available in all cases, and the user can select a baseline from three alternatives (AR6: 1995–2014, AR5: 1986-2005 and WMO: 1981–2010) and the future period of analysis as either a time slice (considering the AR6 future periods 2021–2040, 2041-2060 and 2081-2100 for near-, mid- and long-terms, respectively), or as a warming level (1.5ºC, 2ºC or 3ºC; see Section Atlas.2.1 for full details).

Regionally aggregated information can be obtained interactively by selecting (clicking on) the region(s) of

interest and indicating the type of product from a number of options: temporal series (ensemble plumes), stripes, annual cycle plots, two-variables scatter plots, summary tables (see Figure Atlas.53:). In this case, uncertainty is explicitly represented in the products (e.g. by the ensemble spread for the time series), since the Interactive Atlas shows the individual results for each of the models (see Figure Atlas.55:). Note that the dataset, variable, scenario and season can be changed at any time and the regional information (for the currently selected region) will be change accordingly, thus providing high interactivity in the exploration of products. Note that the information displayed in these products will correspond to the aggregated results of the region(s) selected and displays higher granularity since the results of individual models are represented and not only the ensemble mean (or ensemble statistics).

[START Figure Atlas.55: HERE]

Figure Atlas.55: Regional information for a selected region (the Mediterranean) in the form of a time series for a mid-term time slice (top) and a 2ºC warming level (bottom). Note that the corresponding periods are indicated with grey shading (with intensity proportional to the number of models including each particular year for the case of the warming levels). Fine granularity is provided by hovering over a particular point, obtaining information of particular models. These figures have been exported directly from the Interactive Atlas (as bitmap or PDF files).

[END Figure Atlas.55: HERE]

Atlas.7.3 Accessibility and reproducibility

The accessibility and reproducibility of scientific results is nowadays a major concern in all scientific disciplines (Baker, 2016). During the design and development of the Interactive Atlas, special attention has been paid to these problems in order to ensure the transparency of the products feeding the Interactive Atlas (which are all publicly available). Accessibility will be established in collaboration with the IPCC Data Distribution Centre, since all final products provided by the Atlas will be based on curated IPCC-DDC datasets and will include full provenance information as part of the provided metadata (see Atlas.7.4). The Atlas products are generated using open source frameworks –e.g. the climate4R framework (Iturbide et al., 2019)– based on free software community tools (e.g. R) for data post-processing (re-gridding, aggregation, adjustment, etc.) and evaluation and quality control (when applicable). Full metadata is generated for all final products using the METACLIP RDF-based framework (Bedia et al., 2019), describing the datasets and the post-processing workflow (see Atlas.7.4 for some examples).

In summary, a number of actions have been conducted in order to facilitate the open access and reproducibility of results, including:

- Open access to raw data and derived Atlas products;
- Provision of full provenance metadata describing the product generation workflow;
- Free availability of the software and code used. As an example, code for reproducing some of the figures of the Atlas Chapter is available online at a GitHub repository (Atlas GitHub, 2020),
- Use of standards and open-source tools.

All Atlas products and flexibility options for extended analysis build on recommendations and assessments made in WGI Chapters. For instance, products based on bias adjustment follow the recommendations done in Chapter 10, and the variables and indices included have been assessed in Chapters 11, 12 or the Atlas. The incorporation of new products in the Atlas expanding the analysis provided in other chapters need to be a collaborative process. A number of requirements are listed:

- The scripts/code used to generate the dataset supporting a new product would be based on and incorporated into the package used to generate the other interactive Atlas datasets and made publicly available; the Atlas team can collaborate in this process integrating and harmonizing tools;
- The dataset generated would need to be assessed in the relevant chapter;
- The Interactive Atlas would provide functionality to select reference periods, emissions, regions,

plotting options as agreed with the chapter as being appropriate for the relevant dataset.

Atlas.7.4 Provenance for the full workflow from the data source to the final product

Provenance is defined as a 'record that describes the people, institutions, entities, and activities involved in producing, influencing, or delivering a piece of data or a thing'. This information can be used to form assessments about their quality, reliability or trustworthiness. In the context of the outcomes of the Interactive Atlas, having an effective way of dealing with data provenance is a necessary condition to ensure not only the reproducibility of results, but also to build trust on the information provided. However, the relative complexity of the data and the post-processing workflows involved may prevent from a proper communication of data provenance with full details for reproducibility. Therefore, a special effort has been made in order to build a comprehensive provenance metadata model for the Interactive Atlas products.

Provenance frameworks are typically based on RDF (Resource Description Framework), a family of World Wide Web Consortium (W3C) specifications originally designed as a metadata model – RDF Working Group 2014: www.w3.org/RDF (Candan et al., 2001). It is an abstract model that has become a general method for conceptual description of information for the Web, using a variety of syntax notations and serialization formats. Designed to provide a framework that ensures interoperability between metadata frameworks, RDF allows for structured and semi-structured data to be mixed, exposed, and shared across different applications. As a result, RDF has been widely adopted in many different fields. To this aim, specific vocabularies have been written in RDF, containing a conceptual model of a particular – more or less broad – domain of knowledge. Vocabularies list the types of objects, the relationships that connect them and constraints on the ways that objects and relationships can be combined, being used for description, classification and reasoning. METACLIP (Bedia et al., 2019) exploits RDF through specific vocabularies, written in the OWL ontology language, describing different aspects involved in climate product generation, from the data source to the post-processing workflow, extending international standard vocabularies such as PROV-O (Moreau et al., 2015). The METACLIP vocabularies are publicly available in the METACLIP GitHub repository (github.com/metaclip/vocabularies).

METACLIP makes an emphasis in the delivery of 'final products' (understood as any piece of information that is stored in a file, such as a plot or a map) with a full semantic description of its origin and meaning attached to it. METACLIP ensures 'machine readability' through the reuse of well-defined, standard metadata vocabularies, providing semantic interoperability and the possibility of developing database engines supporting advanced provenance analytics. Therefore, this framework has been adopted in order to generate provenance information and attach it as metadata to the products generated by the interactive Atlas. A specific vocabulary (IPCC_TERMS) is created alongside the inclusion of new products in the Interactive Atlas and use the controlled vocabularies existing from CMIP and CORDEX experiments. As an example, Figure Atlas.56: shows the semantic vocabularies needed to encode the information of the typical workflow for computing (from bias-adjusted data) any of the climate indices (extreme or climate impact drivers) included in the Interactive Atlas.

[START Figure Atlas.56: HERE]

Figure Atlas.56: Schematic representation of the generation workflow, from database description, subsetting and data transformation to final graphical product generation (maps and plots). Product-dependent workflow steps are depicted with dashed borders. METACLIP specifically considers the different intermediate steps consisting of various data transformations, bias adjustment, climate index calculation and graphical product generation, providing a semantic description of each stage and the different elements involved. The different controlled vocabularies describing each stage are indicated by the colors. The gradient indicates that both ipcc_terms and datasource vocabularies are involved, usually meaning that specific individual instances have been defined in ipcc_terms extending generic classes of datasource. Both datasource and ipcc_terms vocabularies, dealing with the primary data sources, have specific annotation properties linking their own features with the CMIP5, CMIP6 and CORDEX Data Reference Syntax, taking as reference their respective controlled vocabularies. All products

generated by the Interactive Atlas provide a METACLIP provenance description, including a persistent link to a reproducible source code under version control.

[END Figure Atlas.56: HERE]

Atlas.7.5 Exporting products (including metadata) in different formats

All the products visualized in the Interactive Atlas can be exported in a variety of formats, including PNG files (and also PDF in cases with vector information, e.g. for temporal seriers). Moreover, products with spatial information (only the global maps in the current version) can be downloaded in GIS format (GeoTIFF). These options can be selected in the right-hand side buttons of the main screen (see Figure Atlas.54:) under the zooming options.

For some test products of the Interactive Atlas (only global maps in this version), a comprehensive provenance metadata description has been generated, including all details needed for reproducibility, from the data sources to the different post-processes applied to obtain the final product (detailed information on the specific metadata provenance model used, METACLIP, is given in next section). In these cases, there is also the possibility to download a PNG file augmented with attached metadata information (in JSON format). This metadata information (including the source code generating the product) can be accessed and interpreted automatically using specific JSON software/libraries. However, for the sake of simplicity, a human readable version of the metadata is accessible directly from the Interactive Atlas (see metadata option in Figure Atlas.54:) describing the key information along the workflow.

In order to facilitate full metadata consultation, the METACLIP framework has an interactive interpreter designed as an interactive provenance visualization tool to navigate through complex data workflows and obtain, for each step, a semantic description of the operations undertaken, thereby allowing for an easy interpretation of the provenance information by users with different levels of expertise. This is a drag-and-drop facility where users can drop the files downloaded from the Interactive Atlas to visually explore the metadata. For example, Figure Atlas.57: shows the metadata for the augmented PNG file corresponding to the default selection of the Interactive Atlas, and obtained by clicking on the METACLIP button. The visualization interface provides provenance description at different levels of granularity, in such a way that the most technical details (e.g. command calls which are only relevant for expert users) remain hidden unless explicitly queried.

[START Figure Atlas.57:HERE]

Figure Atlas.57: Screenshot of the METACLIP Interpreter for provenance visualization (metaclip.org), displaying the provenance of a temperature anomaly map downloaded from the Interactive Atlas as a PNG file with attached METACLIP metadata (METACLIP export option). The blow-up shows a specific dataset (CMIP5 RcP8.5) used to produce the map. It shows details about the dataset provenance such as its DOI identifying the source of data, the experiment (RCP 8.5), the modelling centre, GCM information, data provider and associated Project (CMIP5). The interface allows the user to expand the detail of information if needed by clicking in each of the nodes and reading the metadata in the left panel. It is also possible zooming in/out, scrolling and saving a user-defined position of the graph.

[END Figure Atlas.57: HERE]

Atlas.8 Limits to the assessment

Knowledge gaps

Frequently Asked Questions

[FAQs will be further developed in the final draft]

FAQ ATLAS.1: Why is there an AR6 WG I Interactive Atlas?

One of the main limitations of static (printed or electronic) climate products (e.g. maps or summary tables) is the limited options available to extract relevant information for regional analysis. For instance, the use of standard seasons limits the assessment in many cases (such as regions affected by monsoons or seasonal rainband migrations) and the limited number of variables prevents the inclusion of relevant indices and climate impact drivers. These factors limited the scope of the AR5 Atlas, which provided global and regional information only for temperature and precipitation for the standard seasons due to space limitation. The Interactive Atlas has been conceived as a tool for flexible regional and temporal analysis, but with limited predefined functionality and granularity to prevent misuse. Moreover, links have been established with other chapters in order to adopt their methodological recommendations and to support their assessment.

FAQ ATLAS.2: How can I use the Interactive Atlas for mitigation and adaptation studies?

FAQ ATLAS.3: How can I use the Interactive Atlas for climate risk assessment?

FAQ ATLAS.4: Where can I find the information that was used to produce the figures in the Interactive Atlas?

In order to ensure transparency and promote FAIR principles (findable, accessible, interoperable and reproducible results), the reproducibility of results has been a major concern when developing the Interactive Atlas. As a result, metadata is provided in the Interactive Atlas for the full workflow, from the data sources to the final products (only for spatial maps in the SOD) and the scripts used to generate the intermediated products (e.g. indices) as well as the figures are available online in a GitHub repository (Atlas GitHub, 2020). Moreover, in order to increase reusability, simple notebooks have been produced illustrating the different steps of the process (data collocation, transformation, etc.) using smaller subsets. These scripts are based on the climate4R open source framework (Iturbide et al., 2019). FAQ Atlas.4, Figure 1shows a screenshot of the repository for a particular topic (calculation of warming levels).

[START FAQ ATLAS.4, FIGURE 1 HERE]

FAQ Atlas 4, Figure 1: Screenshot of the GitHub repository containing the scripts and results of the warming level calculations for CMIP5 and CMIP6 models, together with some sensitivity studies to the effect of the length of the moving window.

[END FAQ ATLAS.4, FIGURE 1 HERE]

References

Aalbers, E. E., Lenderink, G., van Meijgaard, E., and van den Hurk, B. J. J. M. (2018). Local-scale changes in mean and heavy precipitation in Western Europe, climate change or internal variability? *Clim. Dyn.* 50. doi:10.1007/s00382-017-3901-9.

Aalto, J., Kämäräinen, M., Shodmonov, M., Rajabov, N., and Venäläinen, A. (2017). Features of Tajikistan's past and future climate. *Int. J. Climatol.* 37, 4949–4961. doi:10.1002/joc.5135.

Abadi, A. M., Oglesby, R., Rowe, C., and Mawalagedara, R. (2018). Evaluation of GCMs historical simulations of monthly and seasonal climatology over Bolivia. *Clim. Dyn.* 51, 733–754. doi:10.1007/s00382-017-3952-y.

Abatzoglou, J. T., and Williams, A. P. (2016). Impact of anthropogenic climate change on wildfire across western US forests. *Proc. Natl. Acad. Sci. U. S. A.* 113, 11770–11775. doi:10.1073/pnas.1607171113.

Abid, M. A., Almazroui, M., Kucharski, F., O'Brien, E., and Yousef, A. E. (2018). ENSO relationship to summer rainfall variability and its potential predictability over Arabian Peninsula region. *npj Clim. Atmos. Sci.* doi:10.1038/s41612-017-0003-7.

Aceituno, P. (1988). On the functioning of the Southern Oscillation in the South American sector. Part I: surface climate. *Mon. Weather Rev.* 116, 505–524. doi:10.1175/1520-0493(1988)116<0505:OTFOTS>2.0.CO;2.

Adamu, M., Ongoma, V., Mcgregor, S., Gallant, A., and Galvin, S. (submitted). Evaluation of CMIP6 and CMIP5 Global Climate Models over Africa: Precipitation. *Theor. Appl. Climatol.* (submitted.

Adler, R. F., Huffman, G. J., Chang, A., Ferraro, R., Xie, P.-P., Janowiak, J., et al. (2003). The Version-2 Global Precipitation Climatology Project (GPCP) Monthly Precipitation Analysis (1979–Present). *J. Hydrometeorol.* 4, 1147–1167. doi:10.1175/1525-7541(2003)004<1147:TVGPCP>2.0.CO;2.

Agosta, C., Amory, C., Kittel, C., Orsi, A., Favier, V., Gallée, H., et al. (2019). Estimation of the Antarctic surface mass balance using the regional climate model MAR (1979–2015) and identification of dominant processes. *Cryosph.* 13, 281–296. doi:10.5194/tc-13-281-2019.

Agosta, C., Favier, V., Genthon, C., Gallée, H., Krinner, G., Lenaerts, J. T. M., et al. (2012). A 40-year accumulation dataset for Adelie Land, Antarctica and its application for model validation. *Clim. Dyn.* 38, 75–86. doi:10.1007/s00382-011-1103-4.

Agosta, C., Fettweis, X., and Datta, R. (2015). Evaluation of the CMIP5 models in the aim of regional modelling of the Antarctic surface mass balance. *Cryosph.* 9, 2311–2321. doi:10.5194/tc-9-2311-2015.

Aguilar, E., Barry, A. A., Brunet, M., Ekang, L., Fernandes, A., Massoukina, M., et al. (2009). Changes in temperature and precipitation extremes in western central Africa, Guinea Conakry, and Zimbabwe, 1955-2006. *J. Geophys. Res. Atmos.* doi:10.1029/2008JD011010.

Ahmed, M., and Suphachalasai, S. (2014). *Assessing the Costs of Climate Change and Adaptation in South Asia*. Available at: http://www.adb.org/sites/default/files/pub/2014/assessing-costs-climate-change-and-adaptation-south-asia.pdf.

Aizen, V. B., Aizen, E. M., Melack, J. M., and Dozier, J. (1997). Climatic and Hydrologic Changes in the Tien Shan, Central Asia. *J. Clim.* 10, 1393–1404. doi:10.1175/1520-0442(1997)010<1393:CAHCIT>2.0.CO;2.

Akhtar, N., Brauch, J., and Ahrens, B. (2018). Climate modeling over the Mediterranean Sea: impact of resolution and ocean coupling. *Clim. Dyn.* 51, 933–948. doi:10.1007/s00382-017-3570-8.

Alexander, L. V., and Arblaster, J. M. (2017). Historical and projected trends in temperature and precipitation extremes in Australia in observations and CMIP5. *Weather Clim. Extrem.* 15, 34–56. doi:https://doi.org/10.1016/j.wace.2017.02.001.

Ali, S., Khalid, B., Kiani, R. S., Babar, R., Nasir, S., and Rehman, N. (2019). Spatio-Temporal Variability of Summer Monsoon Onset over Pakistan.

Allaberdiyev, G. (2010). Climate change and Turkmenistan. Ashgabat Available at: https://www.undpcc.org/docs/National issues papers/Climate Change/29_Turkmenistan NIP_Climate Change.pdf [Accessed April 3, 2019].

Almazroui, M. (2016). RegCM4 in climate simulation over CORDEX-MENA/Arab domain: selection of suitable domain, convection and land-surface schemes. *Int. J. Climatol.* 36, 236–251. doi:10.1002/joc.4340.

Almazroui, M. (2019). Temperature Changes over the CORDEX-MENA Domain in the 21st Century Using CMIP5 Data Downscaled with RegCM4: A Focus on the Arabian Peninsula. *Adv. Meteorol.* doi:10.1155/2019/5395676.

Almazroui, M. (submitted). Summer maximum temperature over the Gulf Cooperation Council states in the 21st century: multimodel simulations overview. (submitted.

Almazroui, M., Islam, M. N., Athar, H., Jones, P. D., and Rahman, M. A. (2012). Recent climate change in the Arabian Peninsula: Annual rainfall and temperature analysis of Saudi Arabia for 1978-2009. *Int. J. Climatol.* 32. doi:10.1002/joc.3446.

Almazroui, M., Islam, M. N., Dambul, R., and Jones, P. D. (2014). Trends of temperature extremes in Saudi Arabia. *Int. J. Climatol.* doi:10.1002/joc.3722.

Almazroui, M., Islam, M. N., Saeed, F., Alkhalaf, A. K., and Dambul, R. (2017a). Assessing the robustness and uncertainties of projected changes in temperature and precipitation in AR5 Global Climate Models over the

Arabian Peninsula. *Atmos. Res.* 194, 202–213. doi:10.1016/j.atmosres.2017.05.005.
Almazroui, M., Islam, M. N., Saeed, S., Alkhalaf, A. K., and Dambul, R. (2017b). Assessment of uncertainties in projected temperature and precipitation over the Arabian Peninsula using three categories of CMIP5 multimodel ensembles. *Earth Syst. Environ.* doi:10.1007/s41748-017-0027-5.
Almazroui, M., Islam, M. N., Saeed, S., and Ismail, M. (submitteda). Future changes in climate over the Arabian Peninsula based on CMIP6 multimodel simulations. (submitted.
Almazroui, M., Saeed, F., Islam, M. N., and Alkhalaf, A. K. (2016). Assessing the robustness and uncertainties of projected changes in temperature and precipitation in AR4 Global Climate Models over the Arabian Peninsula. *Atmos. Res.* 182. doi:10.1016/j.atmosres.2016.07.025.
Almazroui, M., and Saeed, S. (2020). Contribution of extreme daily precipitation to total rainfall over the Arabian Peninsula. *Atmos. Res.* 231, 104672. doi:10.1016/j.atmosres.2019.104672.
Almazroui, M., Saeed, S., Islam, M., and Al., E. (submittedb). CMIP6 simulated changes of projected temperature and precipitation over Africa CMIP6. *Earth Syst. Environ.* (submitted.
Almazroui, M., Saeed, S., Islam, M. N., Khalid, M. S., Alkhalaf, A. K., and Dambul, R. (2017c). Assessment of uncertainties in projected temperature and precipitation over the Arabian Peninsula: a comparison between different categories of CMIP3 models. *Earth Syst. Environ.* 1, 12. doi:10.1007/s41748-017-0012-z.
Almeida, C. T., Oliveira-Júnior, J. F., Delgado, R. C., Cubo, P., and Ramos, M. C. (2017). Spatiotemporal rainfall and temperature trends throughout the Brazilian Legal Amazon, 1973–2013. *Int. J. Climatol.* doi:10.1002/joc.4831.
AlSarmi, S., and Washington, R. (2011). Recent observed climate change over the Arabian Peninsula. *J. Geophys. Res. Atmos.* doi:10.1029/2010JD015459.
Altnau, S., Schlosser, E., Isaksson, E., and Divine, D. (2015). Climatic signals from 76 shallow firn cores in Dronning Maud Land, East Antarctica. *Cryosph.* 9, 925–944. doi:10.5194/tc-9-925-2015.
Alves, L. (2016). Análise estatística da sazonalidade e tendências das estações chuvosas e seca na Amazônia: Clima presente e projeções futuras. Available at: http://urlib.net/8JMKD3MGP3W34P/3L9KTPH.
Alves, L. M., Chadwick, R., Moise, A., Brown, J., and Marengo, J. A. (submitted). Assessment of Rainfall Variability and Change in Brazil across Multiple Timescales. *Int. J. Climatol.* (submitted.
Amador, J. (1998). A climatic feature of the tropical Americas: The trade wind easterly jet. *Top. Meteor. Ocean.* 5, 91–102.
AMAP (2017). *Snow, Water, Ice and Permafrost in the Arctic (SWIPA) 2017*.
AMAP (2019). Arctic Climate Change Update 2019.
Ambrizzi, T., Reboita, M. S., da Rocha, R. P., and Llopart, M. (2019). The state of the art and fundamental aspects of regional climate modeling in South America. *Ann. N. Y. Acad. Sci.* 1436, 98–120. doi:10.1111/nyas.13932.
Anderson, T. G., Anchukaitis, K. J., Pons, D., and Taylor, M. (2019). Multiscale trends and precipitation extremes in the Central American Midsummer Drought. *Environ. Res. Lett.* 14, 124016. doi:10.1088/1748-9326/ab5023.
Angeles-Malaspina, M., González-Cruz, J. E., and Ramírez-Beltran, N. (2018). Projections of Heat Waves Events in the Intra-Americas Region Using Multimodel Ensemble. *Adv. Meteorol.* 2018, 1–16. doi:10.1155/2018/7827984.
Anyah, R. O., and Qiu, W. (2012). Characteristic 20th and 21st century precipitation and temperature patterns and changes over the Greater Horn of Africa. *Int. J. Climatol.* doi:10.1002/joc.2270.
Ashfaq, M., Rastogi, D., Mei, R., Kao, S.-C., Gangrade, S., Naz, B. S., et al. (2016). High-resolution ensemble projections of near-term regional climate over the continental United States. *J. Geophys. Res. Atmos.* 121, 9943–9963. doi:10.1002/2016JD025285.
Atif, R. M., Almazroui, M., Saeed, S., Abid, M. A., Islam, M. N., and Ismail, M. (2020). Extreme precipitation events over Saudi Arabia during the wet season and their associated teleconnections. *Atmos. Res.* 231, 104655. doi:10.1016/j.atmosres.2019.104655.
Atlas GitHub (2020). doi:10.5281/zenodo.3691646.
Attada, R., Dasari, H. P., Chowdary, J. S., Yadav, R. K., Knio, O., and Hoteit, I. (2019). Surface air temperature variability over the Arabian Peninsula and its links to circulation patterns. *Int. J. Climatol.* 39, 445–464. doi:10.1002/joc.5821.
Azmat, M., Wahab, A., Huggel, C., Uzair Qamar, M., Hussain, E., Ahmed, S., et al. (2019). Climatic and Hydrological Projections to Changing Climate under CORDEX-South Asia Experiments over the Karakoram-Hindukush-Himalayan Water Towers. *Sci. Total Environ.*, 135010. doi:10.1016/j.scitotenv.2019.135010.
Baart, F., Rongen, G., Hijma, M., Kooi, H., Winter, R. de, and Nicolai, R. (2018). Zeespiegelmonitor 2018 (in Dutch). Delft, The Netherlands Available at: https://www.deltares.nl/app/uploads/2019/03/Zeespiegelmonitor-2018-final.pdf.
Baatsen, M., Haarsma, R. J., Van Delden, A. J., and de Vries, H. (2015). Severe Autumn storms in future Western Europe with a warmer Atlantic Ocean. *Clim. Dyn.* 45, 949–964. doi:10.1007/s00382-014-2329-8.
Baidya Roy, S., Smith, M., Morris, L., Orlovsky, N., and Khalilov, A. (2014). Impact of the desiccation of the Aral Sea on summertime surface air temperatures. *J. Arid Environ.* 110, 79–85. doi:https://doi.org/10.1016/j.jaridenv.2014.06.008.
Baker, M. (2016). 1,500 scientists lift the lid on reproducibility. *Nature*. doi:10.1038/533452a.
Balabukh, V., Lavrynenko, O., Bilaniuk, V., Mykhnovych, A., and Pylypovych, O. (2018). “Extreme Weather Events

in Ukraine: Occurrence and Changes," in *Extreme Weather* (InTech). doi:10.5772/intechopen.77306.
Balabukh, V., and Malitskaya, L. (2017). Assessment of current changes in the thermal regime of Ukraine. *Geoinformatika* 64, 5–20.
Ballantyne, A. G., Glaas, E., Neset, T.-S., and Wibeck, V. (2018). Localizing Climate Change: Nordic Homeowners' Interpretations of Visual Representations for Climate Adaptation. *Environ. Commun.* 12, 638–652. doi:10.1080/17524032.2017.1412997.
Bamber, J. L., Oppenheimer, M., Kopp, R. E., Aspinall, W. P., and Cooke, R. M. (2019). Ice sheet contributions to future sea-level rise from structured expert judgment. *Proc. Natl. Acad. Sci. U. S. A.* 166, 11195–11200. doi:10.1073/pnas.1817205116.
Bamber, J. L., Westaway, R. M., Marzeion, B., and Wouters, B. (2018). The land ice contribution to sea level during the satellite era. *Environ. Res. Lett.* 13, 63008. doi:10.1088/1748-9326/aac2f0.
Ban, N., Brisson, E., Caillaud, C., Coppola, E., Pichelli, E., Sobolowski, S., et al. (submitted). The first multi-model ensemble of regional climate simulations at kilometer-scale resolution , Part I : Evaluation of precipitation. *Clim. Dyn.* (submitted.
Ban, N., Schmidli, J., and Schär, C. (2015). Heavy precipitation in a changing climate: Does short-term summer precipitation increase faster? *Geophys. Res. Lett.* 42, 2014GL062588. doi:10.1002/2014GL062588.
Barfus, K., and Bernhofer, C. (2014). Assessment of GCM performances for the Arabian Peninsula, Brazil, and Ukraine and indications of regional climate change. *Environ. Earth Sci.* doi:10.1007/s12665-014-3147-3.
Barkhordarian, A., Bhend, J., and von Storch, H. (2012). Consistency of observed near surface temperature trends with climate change projections over the Mediterranean region. *Clim. Dyn.* doi:10.1007/s00382-011-1060-y.
Barreiro, M. (2010). Influence of ENSO and the South Atlantic Ocean on climate predictability over Southeastern South America. *Clim. Dyn.* 35, 1493–1508. doi:10.1007/s00382-009-0666-9.
Barros, V. R., Boninsegna, J. A., Camilloni, I. A., Chidiak, M., Magrín, G. O., and Rusticucci, M. (2015). Climate change in Argentina: trends, projections, impacts and adaptation. *Wiley Interdiscip. Rev. Clim. Chang.* 6, 151–169. doi:10.1002/wcc.316.
Barros, V. R., and Doyle, M. E. (2018). Low-level circulation and precipitation simulated by CMIP5 GCMS over southeastern South America. *Int. J. Climatol.* 38, 5476–5490. doi:10.1002/joc.5740.
Bartók, B., Wild, M., Folini, D., Lüthi, D., Kotlarski, S., Schär, C., et al. (2017). Projected changes in surface solar radiation in CMIP5 global climate models and in EURO-CORDEX regional climate models for Europe. *Clim. Dyn.* 49, 2665–2683. doi:10.1007/s00382-016-3471-2.
Bashir, F., Zeng, X., Gupta, H., and Hazenberg, P. (2017). A Hydrometeorological Perspective on the Karakoram Anomaly Using Unique Valley-Based Synoptic Weather Observations. *Geophys. Res. Lett.* 44, 10,470-10,478. doi:10.1002/2017GL075284.
Batista, R. J. R., Gonçalves, F. L. T., and da Rocha, R. P. (2016). Present climate and future projections of the thermal comfort index for the metropolitan region of São Paulo, Brazil. *Clim. Change* 137, 439–454. doi:10.1007/s10584-016-1690-5.
Beck, H. E., Vergopolan, N., Pan, M., Levizzani, V., Van Dijk, A. I. J. M., Weedon, G. P., et al. (2017). Global-scale evaluation of 22 precipitation datasets using gauge observations and hydrological modeling. *Hydrol. Earth Syst. Sci.* doi:10.5194/hess-21-6201-2017.
Bedia, J., San-Martín, D., Iturbide, M., Herrera, S., Manzanas, R., and Gutiérrez, J. M. (2019). METACLIP : A semantic provenance framework for climate products. *Environ. Model. Softw.*
Beharry, S. L., Clarke, R. M., and Kumarsingh, K. (2015). Variations in extreme temperature and precipitation for a Caribbean island: Trinidad. *Theor. Appl. Climatol.* 122, 783–797. doi:10.1007/s00704-014-1330-9.
Behrangi, A., Christensen, M., Richardson, M., Lebsock, M., Stephens, G., Huffman, G. J., et al. (2016). Status of high-latitude precipitation estimates from observations and reanalyses. *J. Geophys. Res. Atmos.* 121, 4468–4486. doi:10.1002/2015JD024546.
Benestad, R. E., Parding, K. M., Isaksen, K., and Mezghani, A. (2016). Climate change and projections for the Barents region: What is expected to change and what will stay the same? *Environ. Res. Lett.* 11. doi:10.1088/1748-9326/11/5/054017.
Berg, P., Norin, L., and Olsson, J. (2016). Creation of a high resolution precipitation data set by merging gridded gauge data and radar observations for Sweden. *J. Hydrol.* 541, 6–13. doi:10.1016/J.JHYDROL.2015.11.031.
Berkhout, F., van den Hurk, B., Bessembinder, J., de Boer, J., Bregman, B., and van Drunen, M. (2013). Framing climate uncertainty: socio-economic and climate scenarios in vulnerability and adaptation assessments. *Reg. Environ. Chang.* 14, 879–893. doi:10.1007/s10113-013-0519-2.
Berthier, E., Vincent, C., Magnússon, E., Gunnlaugsson, P., Pitte, P., Le Meur, E., et al. (2014). Glacier topography and elevation changes derived from Pléiades sub-meter stereo images. *Cryosphere* 8, 2275–2291. doi:10.5194/tc-8-2275-2014.
Berthou, S., Kendon, E. J., Chan, S. C., Ban, N., Leutwyler, D., Schär, C., et al. (2018). Pan-European climate at convection-permitting scale: a model intercomparison study. *Clim. Dyn.* doi:10.1007/s00382-018-4114-6.
Bessembinder, J. J. E., Bouwer, L. M., and Scheele, R. (2018). Climate and climate change: protocol for use and generation of statistics on rainfall extremes. Available at:

https://www.cedr.eu/download/other_public_files/research_programme/call_2015/climate_change/watch/WATCH-Climate-and-climate-change_Protocol-for-use-and-generation-of-statistics-on-rainfall-extremes.pdf.
Bettolli, M. ., Solman, S., da Rocha, R. P., Llopart, M., Gutierrez, J. M., Fernández, J., et al. (submitted). The CORDEX Flagship Pilot Study in Southeastern South America: a comparative study of statistical and dynamical downscaling models in simulating daily extreme precipitation events. *Clim. Dyn.* (submitted.
Bettolli, M. L., and Penalba, O. C. (2018). Statistical downscaling of daily precipitation and temperatures in southern La Plata Basin. *Int. J. Climatol.* 38, 3705–3722. doi:10.1002/joc.5531.
Biasutti, M. (2013). Forced Sahel rainfall trends in the CMIP5 archive. *J. Geophys. Res. Atmos.* doi:10.1002/jgrd.50206.
Biasutti, M. (2019). Rainfall trends in the African Sahel: Characteristics, processes, and causes. *Wiley Interdiscip. Rev. Clim. Chang.* doi:10.1002/wcc.591.
Bindschadler, R., and Vornberger, P. (1998). Changes in the West Antarctic Ice Sheet since 1963 from declassified satellite photography. *Science (80-.).* 279, 689–692. doi:10.1126/science.279.5351.689.
Bintanja, R., and Andry, O. (2017). Towards a rain-dominated Arctic. *Nat. Clim. Chang.* 7, 263–267. doi:10.1038/nclimate3240.
Bintanja, R., and Krikken, F. (2016). Magnitude and pattern of Arctic warming governed by the seasonality of radiative forcing. *Sci. Rep.* 6, 1–7. doi:10.1038/srep38287.
Bintanja, R., and Selten, F. M. (2014). Future increases in Arctic precipitation linked to local evaporation and sea-ice retreat. *Nature* 509, 479–482. doi:10.1038/nature13259.
Bintanja, R., and Van Der Linden, E. C. (2013). The changing seasonal climate in the Arctic. *Sci. Rep.* 3, 1–8. doi:10.1038/srep01556.
Bitencourt, D. P., Fuentes, M. V., Maia, P. A., and Amorim, F. T. (2016). Frequência, Duração, Abrangência Espacial e Intensidadedas Ondas de Calor no Brasil. *Rev. Bras. Meteorol.* 31, 506–517. doi:10.1590/0102-778631231420150077.
Blackport, R., Screen, J. A., van der Wiel, K., and Bintanja, R. (2019). Minimal influence of reduced Arctic sea ice on coincident cold winters in mid-latitudes. *Nat. Clim. Chang.* 9, 697–704. doi:10.1038/s41558-019-0551-4.
Blanchard-Wrigglesworth, E., Farrell, S. L., Newman, T., and Bitz, C. M. (2015). Snow cover on Arctic sea ice in observations and an Earth System Model. *Geophys. Res. Lett.* 42, 10,342-10,348. doi:10.1002/2015GL066049.
Blázquez, J., and Nuñez, M. N. (2013). Performance of a high resolution global model over southern South America. *Int. J. Climatol.* 33, 904–919. doi:10.1002/joc.3478.
Blunden, J., and Arndt, D. S. (2019). State of the Climate in 2018. *Bull. Am. Meteorol. Soc.* 100, Si-S306. doi:10.1175/2019BAMSStateoftheClimate.1.
Boé, J., Somot, S., and Corre, L. (submitted). Large differences in summer climate change over Europe as projected by global and regional climate models: causes and consequences. (submitted.
Boe, J., Somot, S., Corre, L., and Nabat, P. (submitted). Large discrepancies in summer climate change over Europe as projected by global and regional climate models: causes and consequences. (submitted.
Boé, J., and Terray, L. (2014). Land–sea contrast, soil-atmosphere and cloud-temperature interactions: interplays and roles in future summer European climate change. *Clim. Dyn.* 42, 683–699. doi:10.1007/s00382-013-1868-8.
Boening, C., Lebsock, M., Landerer, F., and Stephens, G. (2012). Snowfall-driven mass change on the East Antarctic ice sheet. *Geophys. Res. Lett.* doi:10.1029/2012GL053316.
Boisier, J. P., Alvarez-Garretón, C., Cordero, R. R., Damiani, A., Gallardo, L., Garreaud, R. D., et al. (2018). Anthropogenic drying in central-southern Chile evidenced by long-term observations and climate model simulations. *Elem Sci Anth* 6, 74. doi:10.1525/elementa.328.
Boisvert, L. N., Webster, M. A., Petty, A. A., Markus, T., Bromwich, D. H., and Cullather, R. I. (2018). Intercomparison of precipitation estimates over the Arctic ocean and its peripheral seas from reanalyses. *J. Clim.* 31, 8441–8462. doi:10.1175/JCLI-D-18-0125.1.
Borstad, C. P., Rignot, E., Mouginot, J., and Schodlok, M. P. (2013). Creep deformation and buttressing capacity of damaged ice shelves: Theory and application to Larsen C ice shelf. *Cryosphere* 7, 1931–1947. doi:10.5194/tc-7-1931-2013.
Box, J. E., Colgan, W. T., Christensen, T. R., Schmidt, N. M., Lund, M., Parmentier, F. J. W., et al. (2019). Key indicators of Arctic climate change: 1971-2017. *Environ. Res. Lett.* 14. doi:10.1088/1748-9326/aafc1b.
Box, J. E., Colgan, W. T., Wouters, B., Burgess, D. O., O'Neel, S., Thomson, L. I., et al. (2018). Global sea-level contribution from Arctic land ice: 1971–2017. *Environ. Res. Lett.* 13, 125012. doi:10.1088/1748-9326/aaf2ed.
Boychenko, S., Voloshchuk, V., Movchan, Y., Serdjuchenko, N., Tkachenko, V., Tyshchenko, O., et al. (2016). FEATURES OF CLIMATE CHANGE ON UKRAINE: SCENARIOS, CONSEQUENCES FOR NATURE AND AGROECOSYSTEMS. *Proc. Natl. Aviat. Univ.* 69. doi:10.18372/2306-1472.69.11061.
Bozkurt, D., Rondanelli, R., Marín, J. C., and Garreaud, R. (2018). Foehn Event Triggered by an Atmospheric River Underlies Record-Setting Temperature Along Continental Antarctica. *J. Geophys. Res. Atmos.* 123, 3871–3892. doi:10.1002/2017JD027796.
Bracegirdle, T. J., Stephenson, D. B., Turner, J., and Phillips, T. (2015). The importance of sea ice area biases in 21st century multimodel projections of Antarctic temperature and precipitation. *Geophys. Res. Lett.* 42, 10832–10839.

doi:10.1002/2015GL067055.
Braun, M. H., Malz, P., Sommer, C., Farías-Barahona, D., Sauter, T., Casassa, G., et al. (2019). Constraining glacier elevation and mass changes in South America. *Nat. Clim. Chang.* 9, 130–136. doi:10.1038/s41558-018-0375-7.
Bremer, S., and Meisch, S. (2017). Co-production in climate change research: reviewing different perspectives. *Wiley Interdiscip. Rev. Clim. Chang.* 8. doi:10.1002/wcc.482.
Brogli, R., Kröner, N., Sørland, S. L., Lüthi, D., Schär, C., Brogli, R., et al. (2019). The Role of Hadley Circulation and Lapse-Rate Changes for the Future European Summer Climate. *J. Clim.* 32, 385–404. doi:10.1175/JCLI-D-18-0431.1.
Bromwich, D. H., Nicolas, J. P., Monaghan, A. J., Lazzara, M. A., Keller, L. M., Weidner, G. A., et al. (2012). Central West Antarctica among the most rapidly warming regions on Earth. *Nat. Geosci.* 6, 139. Available at: https://doi.org/10.1038/ngeo1671.
Bromwich, D. H., Nicolas, J. P., Monaghan, A. J., Lazzara, M. A., Keller, L. M., Weidner, G. A., et al. (2014). Erratum: Central west antarctica among the most rapidly warming regions on Earth (Nature Geoscience (2013) 6 (139-145)). *Nat. Geosci.* 7, 76. doi:10.1038/ngeo2016.
Brown, J. R., Moise, A. F., and Colman, R. A. (2017). Projected increases in daily to decadal variability of Asian-Australian monsoon rainfall. *Geophys. Res. Lett.* 44, 5683–5690. doi:10.1002/2017GL073217.
Brown, J. R., Moise, A. F., Colman, R., and Zhang, H. (2016). Will a Warmer World Mean a Wetter or Drier Australian Monsoon? *J. Clim.* 29, 4577–4596. doi:10.1175/JCLI-D-15-0695.1.
Brown, R. D., Fang, B., and Mudryk, L. (2019). Update of Canadian Historical Snow Survey Data and Analysis of Snow Water Equivalent Trends, 1967–2016. *Atmos. - Ocean* 57, 149–156. doi:10.1080/07055900.2019.1598843.
Brown, R., Tapsoba, D., and Derksen, C. (2018). Evaluation of snow water equivalent datasets over the Saint-Maurice river basin region of southern Québec. *Hydrol. Process.* 32, 2748–2764. doi:10.1002/hyp.13221.
Brun, F., Berthier, E., Wagnon, P., Kääb, A., and Treichler, D. (2017). A spatially resolved estimate of High Mountain Asia glacier mass balances from 2000 to 2016. *Nat. Geosci.* 10, 668–673. doi:10.1038/ngeo2999.
Brunke, M. A., Cassano, J. J., Dawson, N., Duvivier, A. K., Jr, W. J. G., Hamman, J., et al. (2018). Evaluation of the atmosphere – land – ocean – sea ice interface processes in the Regional Arctic System Model version 1 (RASM1) using local and globally gridded observations. 4817–4841. doi:10.5194/gmd-11-4817-2018.
Brutel-Vuilmet, C., Ménégoz, M., and Krinner, G. (2013). An analysis of present and future seasonal Northern Hemisphere land snow cover simulated by CMIP5 coupled climate models. *Cryosphere* 7, 67–80. doi:10.5194/tc-7-67-2013.
Bucchignani, E., Cattaneo, L., Panitz, H. J., and Mercogliano, P. (2016). Sensitivity analysis with the regional climate model COSMO-CLM over the CORDEX-MENA domain. *Meteorol. Atmos. Phys.* 128, 73–95. doi:10.1007/s00703-015-0403-3.
Bucchignani, E., Mercogliano, P., Panitz, H. J., and Montesarchio, M. (2018). Climate change projections for the Middle East–North Africa domain with COSMO-CLM at different spatial resolutions. *Adv. Clim. Chang. Res.* 9, 66–80. doi:10.1016/j.accre.2018.01.004.
Budescu, D. V., Por, H.-H., and Broomell, S. B. (2012). Effective communication of uncertainty in the IPCC reports. *Clim. Change* 113, 181–200. doi:10.1007/s10584-011-0330-3.
Bukovsky, M., and Mearns, L. O. (submitted). Regional Climate Change Projections from NA-CORDEX and their Relation to Climate Sensitivity. *Clim. Change* (submitted.
Bukovsky, M. S., Carrillo, C. M., Gochis, D. J., Hammerling, D. M., McCrary, R. R., and Mearns, L. O. (2015). Toward assessing NARCCAP regional climate model credibility for the North American monsoon: Future climate simulations. *J. Clim.* 28, 6707–6728. doi:10.1175/JCLI-D-14-00695.1.
Bukovsky, M. S., Gochis, D. J., and Mearns, L. O. (2013). Towards Assessing NARCCAP Regional Climate Model Credibility for the North American Monsoon: Current Climate Simulations*. *J. Clim.* 26, 8802–8826. doi:10.1175/JCLI-D-12-00538.1.
Bulygina, O. N., Korshunova, N. N., and Razuvaev, V. N. (2014). Specialized datasets for climate research. *Tr. VNIIGMI-WDC* 177. Available at: http://meteo.ru/publications/125-trudy-vniigmi/trudy-vniigmi-mtsd-vypusk-177-2014-g/518-spetsializirovannye-massivy-dannykh-dlya-klimaticheskikh-issledovanij.
Bureau of Meteorology, and CSIRO (2018). State of the Climate. Melbourne, Australia Available at: isbn: 978-1-925315-97-4.
Burger, F., Brock, B., and Montecinos, A. (2018). Seasonal and elevational contrasts in temperature trends in Central Chile between 1979 and 2015. *Glob. Planet. Change* 162, 136–147. doi:10.1016/j.gloplacha.2018.01.005.
Bush, E., and Lemmen, D. S. (2019). *Canada's Changing Climate Report*. Ottawa, Ontario, Canada: Government of Canada.
Cabos, W., Sein, D. V, Durán-Quesada, A., Liguori, G., Koldunov, N. V, Martínez-López, B., et al. (2018). Dynamical downscaling of historical climate over CORDEX Central America domain with a regionally coupled atmosphere--ocean model. *Clim. Dyn.* doi:10.1007/s00382-018-4381-2.
Cabré, M. F., Solman, S., and Núñez, M. (2016). Regional climate change scenarios over southern South America for future climate (2080-2099) using the MM5 Model. Mean, interannual variability and uncertainties. *Atmósfera* 29, 35–60. doi:10.20937/ATM.2016.29.01.04.

Caesar, J., Alexander, L., and Vose, R. (2006). Large-scale changes in observed daily maximum and minimum temperatures: Creation and analysis of a new gridded data set. *J. Geophys. Res.* 111, D05101. doi:10.1029/2005JD006280.

Cai, P., Hamdi, R., Luo, G., He, H., Zhang, M., Termonia, P., et al. (2019). Agriculture intensification increases summer precipitation in Tianshan Mountains, China. *Atmos. Res.* 227, 140–146. doi:10.1016/j.atmosres.2019.05.005.

Camilo, J. A., Andrade, C. L. T., Amaral, T. A., Tigges, C. H. P., Melo, M. L. A., Chou, S. C., et al. (2018). Impact of climate change on maize grown in the Brazilian cerrado. in *2018 Detroit, Michigan July 29 - August 1, 2018* (St. Joseph, MI: American Society of Agricultural and Biological Engineers). doi:10.13031/aim.201800967.

Campbell, J. D., Taylor, M. A., Stephenson, T. S., Watson, R. A., and Whyte, F. S. (2011). Future climate of the Caribbean from a regional climate model. *Int. J. Climatol.* 31, 1866–1878. doi:10.1002/joc.2200.

Candan, K. S., Liu, H., and Suvarna, R. (2001). Resource Description Framework : Metadata and Its Applications. *SIGKDD Explor.* doi:10.1145/507533.507536.

Cantet, P., Déqué, M., Palany, P., and Maridet, J.-L. (2014). The importance of using a high-resolution model to study the climate change on small islands: the Lesser Antilles case. *Tellus A Dyn. Meteorol. Oceanogr.* 66, 24065. doi:10.3402/tellusa.v66.24065.

Cardoso, R. M., Soares, P. M. M., Lima, D. C. A., and Semedo, A. (2016). The impact of climate change on the Iberian low-level wind jet: EURO-CORDEX regional climate simulation. *Tellus A Dyn. Meteorol. Oceanogr.* 68, 29005. doi:10.3402/tellusa.v68.29005.

Careto, J. A. M., Cardoso, R. M., Soares, P. M. M., and Trigo, R. M. (2018). Land-Atmosphere Coupling in CORDEX-Africa: Hindcast Regional Climate Simulations. *J. Geophys. Res. Atmos.* doi:10.1029/2018JD028378.

Casanueva, A., Kotlarski, S., Herrera, S., Fernández, J., Gutiérrez, J. M., Boberg, F., et al. (2016). Daily precipitation statistics in a EURO-CORDEX RCM ensemble: added value of raw and bias-corrected high-resolution simulations. *Clim. Dyn.* 47, 719–737. doi:10.1007/s00382-015-2865-x.

Cassano, J. J., DuVivier, A., Roberts, A., Hughes, M., Seefeldt, M., Brunke, M., et al. (2017). Development of the Regional Arctic System Model (RASM): Near-surface atmospheric climate sensitivity. *J. Clim.* 30, 5729–5753. doi:10.1175/JCLI-D-15-0775.1.

Cassou, C., Terray, L., and Phillips, A. S. (2005). Tropical Atlantic influence on European heat waves. *J. Clim.* doi:10.1175/JCLI3506.1.

Castro, C. L., Chang, H.-I., Dominguez, F., Carrillo, C., Schemm, J.-K., and Henry Juang, H.-M. (2012). Can a Regional Climate Model Improve the Ability to Forecast the North American Monsoon? *J. Clim.* 25, 8212–8237. doi:10.1175/JCLI-D-11-00441.1.

Cavalcanti, I. F. A., Carril, A. F., Penalba, O. C., Grimm, A. M., Menéndez, C. G., Sanchez, E., et al. (2015). Precipitation extremes over La Plata Basin – Review and new results from observations and climate simulations. *J. Hydrol.* 523, 211–230. doi:10.1016/j.jhydrol.2015.01.028.

Cavazos, T., and Arriaga-Ramírez, S. (2012). Downscaled Climate Change Scenarios for Baja California and the North American Monsoon during the Twenty-First Century. *J. Clim.* 25, 5904–5915. doi:10.1175/JCLI-D-11-00425.1.

Cavazos, T., Luna-Niño, R., Cerezo-Mota, R., Fuentes-Franco, R., Méndez, M., Pineda Martínez, L. F., et al. (2019). Climatic trends and regional climate models intercomparison over the CORDEX-CAM (Central America, Caribbean, and Mexico) domain. *Int. J. Climatol.*, joc.6276. doi:10.1002/joc.6276.

Cavicchia, L., Scoccimarro, E., Gualdi, S., Marson, P., Ahrens, B., Berthou, S., et al. (2018). Mediterranean extreme precipitation: a multi-model assessment. *Clim. Dyn.* 51, 901–913. doi:10.1007/s00382-016-3245-x.

Ceccherini, G., Russo, S., Ameztoy, I., Romero, C. P., and Carmona-Moreno, C. (2016). Magnitude and frequency of heat and cold waves in recent decades: the case of South America. *Nat. Hazards Earth Syst. Sci.* 16, 821–831. doi:10.5194/nhess-16-821-2016.

Centella-Artola, A., Taylor, M. A., Bezanilla-Morlot, A., Martinez-Castro, D., Campbell, J. D., Stephenson, T. S., et al. (2015). Assessing the effect of domain size over the Caribbean region using the PRECIS regional climate model. *Clim. Dyn.* 44, 1901–1918. doi:10.1007/s00382-014-2272-8.

Cerezo-Mota, R., Cavazos, T., Arritt, R., Torres-Alavez, A., Sieck, K., Nikulin, G., et al. (2015). CORDEX-NA: Factors inducing dry/wet years on the North American Monsoon region. *Int. J. Climatol.* 36. doi:10.1002/joc.4385.

Champagne, O., Pohl, B., McKenzie, S., Buoncristiani, J. F., Bernard, E., Joly, D., et al. (2019). Atmospheric circulation modulates the spatial variability of temperature in the Atlantic–Arctic region. *Int. J. Climatol.* 39, 3619–3638. doi:10.1002/joc.6044.

Chan, S. C., Kendon, E. J., Giorgia, B., Elizabeth, F., and Fowler, H. J. (submitted). Europe-wide precipitation projections at convection permitting scale with the Unified Model. (submitted.

Chapman, D. A., Corner, A., Webster, R., and Markowitz, E. M. (2016). Climate visuals: A mixed methods investigation of public perceptions of climate images in three countries. *Glob. Environ. Chang.* 41, 172–182. doi:10.1016/j.gloenvcha.2016.10.003.

Chen, F., Huang, W., Jin, L., Chen, J., and Wang, J. (2011). Spatiotemporal precipitation variations in the arid Central Asia in the context of global warming. *Sci. China Earth Sci.* 54, 1812–1821. doi:10.1007/s11430-011-4333-8.

Chen, F., Wang, J., Jin, L., Zhang, Q., Li, J., and Chen, J. (2009). Rapid warming in mid-latitude central Asia for the past 100 years. *Front. Earth Sci. China* 3, 42. doi:10.1007/s11707-009-0013-9.

Chen, H., Zhou, T., Neale, R. B., Wu, X., and Zhang, G. J. (2010). Performance of the New NCAR CAM3.5 in East Asian Summer Monsoon Simulations: Sensitivity to Modifications of the Convection Scheme. *J. Clim.* 23, 3657–3675. doi:10.1175/2010jcli3022.1.

Chen, L., Qu, X., Huang, G., and Gong, Y. (2019a). Projections of East Asian summer monsoon under 1.5 {\textdegree}C and 2 {\textdegree}C warming goals. *Theor. Appl. Climatol.* 137, 2187–2201. doi:10.1007/s00704-018-2720-1.

Chen, S., Hamdi, R., Ochege, F. U., Du, H., Chen, X., Yang, W., et al. (2019b). Added value of a dynamical downscaling approach for simulating precipitation and temperature over Tianshan mountains area, Central Asia. *J. Geophys. Res. Atmos.* 0. doi:10.1029/2019JD031016.

Cheong, W. K., Timbal, B., Golding, N., Sirabaha, S., Kwan, K. F., Cinco, T. A., et al. (2018). Observed and modelled temperature and precipitation extremes over Southeast Asia from 1972 to 2010. *Int. J. Climatol.* 38, 3013–3027. doi:10.1002/joc.5479.

Chernokulsky, A., Kozlov, F., Zolina, O., Bulygina, O., Mokhov, I. I., and Semenov, V. A. (2019). Observed changes in convective and stratiform precipitation in Northern Eurasia over the last five decades. *Environ. Res. Lett.* 14. doi:10.1088/1748-9326/aafb82.

Chou, S. C., Lyra, A., Mourão, C., Dereczynski, C., Pilotto, I., Gomes, J., et al. (2014a). Assessment of Climate Change over South America under RCP 4.5 and 8.5 Downscaling Scenarios. *Am. J. Clim. Chang.* 03, 512–527. doi:10.4236/ajcc.2014.35043.

Chou, S. C., Lyra, A., Mourão, C., Dereczynski, C., Pilotto, I., Gomes, J., et al. (2014b). Assessment of Climate Change over South America under RCP 4.5 and 8.5 Downscaling Scenarios. *Am. J. Clim. Chang.* 03, 512–527. doi:10.4236/ajcc.2014.35043.

Choudhary, A., and Dimri, A. P. (2018a). Assessment of CORDEX-South Asia experiments for monsoonal precipitation over Himalayan region for future climate. *Clim. Dyn.* 50, 3009–3030. doi:10.1007/s00382-017-3789-4.

Choudhary, A., and Dimri, A. P. (2018b). Assessment of CORDEX-South Asia experiments for monsoonal precipitation over Himalayan region for future climate. *Clim. Dyn.* 50, 3009–3030. doi:10.1007/s00382-017-3789-4.

Christensen, J. H., Kumar, K. K., Aldria, E., An, S.-I., Cavalcanti, I. F. A., Castro, M. de, et al. (2013). "Climate Phenomena and their Relevance for Future Regional Climate Change Supplementary Material," in *Climate Change 2013: The Physical Science Basis. Contribution of Working Group I to the Fifth Assessment Report of the Intergovernmental Panel on Climate Change*, 62. doi:10.1017/CBO9781107415324.028.

Chung, J. X., Juneng, L., Tangang, F., and Jamaluddin, A. F. (2018). Performances of BATS and CLM land-surface schemes in RegCM4 in simulating precipitation over CORDEX Southeast Asia domain. *Int. J. Climatol.* 38, 794–810. doi:10.1002/joc.5211.

Chylek, P., Vogelsang, T. J., Klett, J. D., Hengartner, N., Higdon, D., Lesins, G., et al. (2016). Indirect aerosol effect increases CMIP5 models' projected arctic warming. *J. Clim.* 29, 1417–1428. doi:10.1175/JCLI-D-15-0362.1.

Cinco, T. A., de Guzman, R. G., Hilario, F. D., and Wilson, D. M. (2014). Long-term trends and extremes in observed daily precipitation and near surface air temperature in the Philippines for the period 1951–2010. *Atmos. Res.* 145–146, 12–26. doi:10.1016/J.ATMOSRES.2014.03.025.

Clark, J. P., and Lee, S. (2019). The Role of the Tropically Excited Arctic Warming Mechanism on the Warm Arctic Cold Continent Surface Air Temperature Trend Pattern. *Geophys. Res. Lett.* doi:10.1029/2019gl082714.

Cohen, J., Screen, J. A., Furtado, J. C., Barlow, M., Whittleston, D., Coumou, D., et al. (2014). Recent Arctic amplification and extreme mid-latitude weather. *Nat. Geosci.* 7, 627–637. doi:10.1038/ngeo2234.

Cohen, J., Ye, H., and Jones, J. (2015). Trends and variability in rain-on-snow events. *Geophys. Res. Lett.* 42, 7115–7122. doi:10.1002/2015GL065320.

Collins, J. M. (2011). Temperature variability over Africa. *J. Clim.* 24, 3649–3666. doi:10.1175/2011JCLI3753.1.

Collins, M., Knutti, R., Arblaster, J., Dufresne, J.-L., Fichefet, T., Friedlingstein, P., et al. (2013). Long-term Climate Change: Projections, Commitments and Irreversibility. *Clim. Chang. 2013 Phys. Sci. Basis. Contrib. Work. Gr. I to Fifth Assess. Rep. Intergov. Panel Clim. Chang.*, 1029–1136.

Colorado-Ruiz, G., Cavazos, T., Salinas, J. A., De Grau, P., and Ayala, R. (2018). Climate change projections from Coupled Model Intercomparison Project phase 5 multi-model weighted ensembles for Mexico, the North American monsoon, and the mid-summer drought region. *Int. J. Climatol.* 38, 5699–5716. doi:10.1002/joc.5773.

Comiso, J. C., and Hall, D. K. (2014). Climate trends in the Arctic as observed from space. *Wiley Interdiscip. Rev. Clim. Chang.* 5, 389–409. doi:10.1002/wcc.277.

Consortium, R. (2017). Randolph glacier inventory–a dataset of global glacier outlines: version 6.0: technical report, global land ice measurements from space, Colorado, USA. *Digit. Media*. doi:https://doi.org/10.7265/N5-RGI-60.

Cook, L., McGinnis, S., and Samaras, C. (submitted). The effect of modeling choices on updating intensity duration frequency curves and stormwater infrastructure designs for climate change. *Clim. Change* (submitted.

Coppola, E., Giorgi, F., Raffaele, F., Fuentes-Franco, R., Giuliani, G., LLopart-Pereira, M., et al. (2014a). Present and

future climatologies in the phase I CREMA experiment. *Clim. Change* 125, 23–38. doi:10.1007/s10584-014-1137-9.

Coppola, E., Giorgi, F., Raffaele, F., Fuentes-Franco, R., Giuliani, G., LLopart-Pereira, M., et al. (2014b). Present and future climatologies in the phase I CREMA experiment. *Clim. Change* 125, 23–38. doi:10.1007/s10584-014-1137-9.

Coppola, E., Nogherotto, R., Ciarlò, J. M., Giorgi, F., Meijgaard, E. Van, Iles, C., et al. (submitteda). Assessment of the European climate projections as simulated by the large EURO-CORDEX regional climate model ensemble. (submitted.

Coppola, E., Raffaele, F., Giorgi, F., Giuliani, G., Xuejie, G., Ciarlo, J., et al. (submittedb). Climate hazard indices projections based on CORDEX-CORE, CMIP5 and CMIP6 ensemble. *Clim. Dyn.* Submitted.

Coppola, E., Sobolowski, S., Pichelli, E., Raffaele, F., Ahrens, B., Anders, I., et al. (2018). A first-of-its-kind multi-model convection permitting ensemble for investigating convective phenomena over Europe and the Mediterranean. *Clim. Dyn.* doi:10.1007/s00382-018-4521-8.

Corner, A., Whitmarsh, L., and Xenias, D. (2012). Uncertainty, scepticism and attitudes towards climate change: biased assimilation and attitude polarisation. *Clim. Change* 114, 463–478. doi:10.1007/s10584-012-0424-6.

Coumou, D., and Rahmstorf, S. (2012). A decade of weather extremes. *Nat. Clim. Chang.* 2, 491–496. doi:10.1038/nclimate1452.

Cruz, F. T., Narisma, G. T., Dado, J. B., Singhruck, P., Tangang, F., Linarka, U. A., et al. (2017). Sensitivity of temperature to physical parameterization schemes of RegCM4 over the CORDEX-Southeast Asia region. *Int. J. Climatol.* 37, 5139–5153. doi:10.1002/joc.5151.

Cruz, F. T., and Sasaki, H. (2017). Simulation of Present Climate over Southeast Asia Using the Non-Hydrostatic Regional Climate Model. *SOLA* 13, 13–18. doi:10.2151/sola.2017-003.

CSIRO and Bureau of Meteorology (2015). Climate Change in Australia Information for Australia's Natural Resource Management Regions: Technical Report. Australia.

Cueto, O. R. G., Soto, N. S., Núñez, M. Q., Benítez, S. O., and Limón, N. V. (2013). Extreme temperature scenarios in Mexicali, Mexico under climate change conditions. *Atmósfera* 26, 509–520. doi:https://doi.org/10.1016/S0187-6236(13)71092-0.

Cueto, R. O. G., Martínez, A. T., and Ostos, E. J. (2010). Heat waves and heat days in an arid city in the northwest of México: current trends and in climate change scenarios. *Int. J. Biometeorol.* 54, 335—345. doi:10.1007/s00484-009-0283-7.

da Rocha, R. P., Reboita, M. S., Dutra, L. M. M., Llopart, M. P., and Coppola, E. (2014). Interannual variability associated with ENSO: present and future climate projections of RegCM4 for South America-CORDEX domain. *Clim. Change* 125, 95–109. doi:10.1007/s10584-014-1119-y.

Dahlke, S., and Maturilli, M. (2017). Contribution of Atmospheric Advection to the Amplified Winter Warming in the Arctic North Atlantic Region. *Adv. Meteorol.* 2017. doi:10.1155/2017/4928620.

Dai, A. (2011). Drought under global warming: A review. *Wiley Interdiscip. Rev. Clim. Chang.* doi:10.1002/wcc.81.

Darmaraki, S., Somot, S., Sevault, F., Nabat, P., Cabos Narvaez, W. D., Cavicchia, L., et al. (2019). Future evolution of Marine Heatwaves in the Mediterranean Sea. *Clim. Dyn.* doi:10.1007/s00382-019-04661-z.

Daron, J. (2015). Challenges in using a Robust Decision Making approach to guide climate change adaptation in South Africa. *Clim. Change* 132, 459–473. doi:10.1007/s10584-014-1242-9.

Daron, J. D., Lorenz, S., Wolski, P., Blamey, R. C., and Jack, C. (2015). Interpreting climate data visualisations to inform adaptation decisions. *Clim. Risk Manag.* 10, 17–26. doi:10.1016/J.CRM.2015.06.007.

Daron, J., Macadam, I., Kanamaru, H., Cinco, T., Katzfey, J., Scannell, C., et al. (2018). Providing future climate projections using multiple models and methods: insights from the Philippines. *Clim. Change* 148, 187–203. doi:10.1007/s10584-018-2183-5.

Dash, S. K., Kulkarni, M. A., Mohanty, U. C., and Prasad, K. (2009). Changes in the characteristics of rain events in India. *J. Geophys. Res. Atmos.* 114. doi:10.1029/2008JD010572.

Datta, R. T., Tedesco, M., Agosta, C., Fettweis, X., Kuipers Munneke, P., and Van Den Broeke, M. R. (2018). Melting over the northeast antarctic peninsula (1999-2009): Evaluation of a high-resolution regional climate model. *Cryosphere* 12, 2901–2922. doi:10.5194/tc-12-2901-2018.

Davy, R., Chen, L., and Hanna, E. (2018). Arctic amplification metrics. *Int. J. Climatol.* 38, 4384–4394. doi:10.1002/joc.5675.

de Abreu, R. C., Cunningham, C., Rudorff, C. M., Rudorff, N., Abatan, A. A., Tett, S. F. B., et al. (2019). Contribution of Anthropogenic Climate Change to April–May 2017 Heavy Precipitation over the Uruguay River Basin. *Bull. Am. Meteorol. Soc.* 100, S37–S41. doi:10.1175/BAMS-D-18-0102.1.

de Barros Soares, D., Lee, H., Loikith, P. C., Barkhordarian, A., and Mechoso, C. R. (2017a). Can significant trends be detected in surface air temperature and precipitation over South America in recent decades? *Int. J. Climatol.* 37, 1483–1493. doi:10.1002/joc.4792.

de Barros Soares, D., Lee, H., Loikith, P. C., Barkhordarian, A., and Mechoso, C. R. (2017b). Can significant trends be detected in surface air temperature and precipitation over South America in recent decades? *Int. J. Climatol.* 37, 1483–1493. doi:10.1002/joc.4792.

de Bruijn, K. M., Lips, N., Gersonius, B., and Middelkoop, H. (2016). The storyline approach: a new way to analyse and improve flood event management. *Nat. Hazards* 81, 99–121. doi:10.1007/s11069-015-2074-2.

de Carvalho, L. M. V., and Cavalcanti, I. F. A. (2016). "The South American Monsoon System (SAMS)," in *The Monsoons and Climate Change: Observations and Modeling*, eds. L. M. V. de Carvalho and C. Jones (Cham: Springer International Publishing), 121–148. doi:10.1007/978-3-319-21650-8_6.

de Jesus, E., da Rocha, R., Reboita, M., Llopart, M., Mosso Dutra, L., and Remedio, A. (2016). Contribution of cold fronts to seasonal rainfall in simulations over the southern La Plata Basin. *Clim. Res.* 68, 243–255. doi:10.3354/cr01358.

De Rydt, J., Gudmundsson, G. H., Rott, H., and Bamber, J. L. (2015). Modeling the instantaneous response of glaciers after the collapse of the Larsen B Ice Shelf. *Geophys. Res. Lett.* 42, 5355–5363. doi:10.1002/2015GL064355.

DeGaetano, A. T., and Castellano, C. M. (2017). Future projections of extreme precipitation intensity-duration-frequency curves for climate adaptation planning in New York State. *Clim. Serv.* 5, 23–35. doi:https://doi.org/10.1016/j.cliser.2017.03.003.

Degirmendžić, J., Kożuchowski, K., and Żmudzka, E. (2004). Changes of air temperature and precipitation in Poland in the period 1951–2000 and their relationship to atmospheric circulation. *Int. J. Climatol.* 24, 291–310. doi:10.1002/joc.1010.

Dekker, M. M., Haarsma, R. J., Vries, H. de, Baatsen, M., and Delden, A. J. va. (2018). Characteristics and development of European cyclones with tropical origin in reanalysis data. *Clim. Dyn.* 50, 445–455. doi:10.1007/s00382-017-3619-8.

Dell'Aquila, A., Mariotti, A., Bastin, S., Calmanti, S., Cavicchia, L., Deque, M., et al. (2018). Evaluation of simulated decadal variations over the Euro-Mediterranean region from ENSEMBLES to Med-CORDEX. *Clim. Dyn.* 51, 857–876. doi:10.1007/s00382-016-3143-2.

Delworth, T. L., and Zeng, F. (2014). Regional rainfall decline in Australia attributed to anthropogenic greenhouse gases and ozone levels. *Nat. Geosci* 7, 583–587. doi:10.1038/ngeo2201http://www.nature.com/ngeo/journal/v7/n8/abs/ngeo2201.html#supplementary-information.

Deng, H., and Chen, Y. (2017). Influences of recent climate change and human activities on water storage variations in Central Asia. *J. Hydrol.* 544, 46–57. doi:10.1016/j.jhydrol.2016.11.006.

Deng, H., Chen, Y., Wang, H., and Zhang, S. (2015). Climate change with elevation and its potential impact on water resources in the Tianshan Mountains, Central Asia. *Glob. Planet. Change* 135, 28–37. doi:https://doi.org/10.1016/j.gloplacha.2015.09.015.

Déqué, M., and Somot, S. (2008). Analysis of heavy precipitation for France using high resolution ALADIN RCM simulations. *Idöjaras Quaterly J. Hungarian Meteorol. Serv.* 112, PP. 179-190. Available at: https://hal-meteofrance.archives-ouvertes.fr/meteo-00370705/ [Accessed March 22, 2019].

Dessai, S., Bhave, A., Birch, C., Conway, D., Garcia-Carreras, L., Gosling, J. P., et al. (2018). Building narratives to characterise uncertainty in regional climate change through expert elicitation. *Environ. Res. Lett.* 13, 074005. doi:10.1088/1748-9326/aabcdd.

Dey, R., Lewis, S. C., Arblaster, J. M., and Abram, N. J. (2019). A review of past and projected changes in Australia's rainfall. *Wiley Interdiscip. Rev. Clim. Chang.* 0, e00577. doi:doi:10.1002/wcc.577.

Di Virgilio, G., Evans, J. P., Luca, A. Di, Grose, M. R., Round, V., and Thatcher, M. (submitted). Realised added value in dynamical downscaling of Australian climate change. (submitted.

Díaz, L. B., and Vera, C. S. (2017). Austral summer precipitation interannual variability and trends over Southeastern South America in CMIP5 models. *Int. J. Climatol.* 37, 681–695. doi:10.1002/joc.5031.

Diedhiou, A., Bichet, A., Wartenburger, R., Seneviratne, S. I., Rowell, D. P., Sylla, M. B., et al. (2018). Changes in climate extremes over West and Central Africa at 1.5 and 2 degree C global warming. *Environ. Res. Lett.* 13, 65020. doi:10.1088/1748-9326/aac3e5.

Dietrich, C., Wang, S., Schimanke, S., Gröger, M., Klein, B., Hordoir, B., et al. (submitted). Surface Heat Budget over the North Sea in Climate Change Simulations. (submitted.

Diffenbaugh, N. S., and Giorgi, F. (2012). Climate change hotspots in the CMIP5 global climate model ensemble. *Clim. Change*. doi:10.1007/s10584-012-0570-x.

Diffenbaugh, N. S., Scherer, M., and Ashfaq, M. (2013). Response of snow-dependent hydrologic extremes to continued global warming. *Nat. Clim. Chang.* 3, 379–384. doi:10.1038/nclimate1732.

Dike, V. N., Shimizu, M. H., Diallo, M., Lin, Z., Nwofor, O. K., and Chineke, T. C. (2015). Modelling present and future African climate using CMIP5 scenarios in HadGEM2-ES. *Int. J. Climatol.* doi:10.1002/joc.4084.

Dimri, A. P., Kumar, D., Choudhary, A., and Maharana, P. (2018a). Future changes over the Himalayas : Maximum and minimum temperature. *Glob. Planet. Change* 162, 212–234. doi:10.1016/j.gloplacha.2018.01.015.

Dimri, A. P., Kumar, D., Choudhary, A., and Maharana, P. (2018b). Future changes over the Himalayas: Mean temperature. *Glob. Planet. Change* 162, 235–251. doi:10.1016/J.GLOPLACHA.2018.01.014.

Diro, G. T., Giorgi, F., Fuentes-Franco, R., Walsh, K. J. E., Giuliani, G., and Coppola, E. (2014). Tropical cyclones in a regional climate change projection with RegCM4 over the CORDEX Central America domain. *Clim. Change* 125, 79–94. doi:10.1007/s10584-014-1155-7.

Diro, G. T., Tompkins, A. M., and Bi, X. (2012). Dynamical downscaling of ECMWF Ensemble seasonal forecasts over East Africa with RegCM3. *J. Geophys. Res. Atmos.* 117. doi:10.1029/2011JD016997.

Dobler, A., Haugen, J. E., and Benestad, R. E. (2016). Regional climate change projections for the Barents region. *Earth Syst. Dyn. Discuss.* 2016, 1–22. doi:10.5194/esd-2016-27.

Donat-Magnin, M., Jourdain, N., Gallée, H., Amory, C., Kittel, C., Fettweis, X., et al. (2019). Interannual Variability of Summer Surface Mass Balance and Surface Melting in the Amundsen Sector, West Antarctica. *Cryosph. Discuss.*, 1–35. doi:10.5194/tc-2019-109.

Donat, M. G., Alexander, L. V., Yang, H., Durre, I., Vose, R., Dunn, R. J. H., et al. (2013). Updated analyses of temperature and precipitation extreme indices since the beginning of the twentieth century: The HadEX2 dataset. *J. Geophys. Res. Atmos.* 118, 2098–2118. doi:10.1002/jgrd.50150.

Donat, M. G., Peterson, T. C., Brunet, M., King, A. D., Almazroui, M., Kolli, R. K., et al. (2014). Changes in extreme temperature and precipitation in the Arab region: Long-term trends and variability related to ENSO and NAO. *Int. J. Climatol.* doi:10.1002/joc.3707.

Dong, B., Sutton, R. T., and Shaffrey, L. (2017). Understanding the rapid summer warming and changes in temperature extremes since the mid-1990s over Western Europe. *Clim. Dyn.* 48, 1537–1554. doi:10.1007/s00382-016-3158-8.

Dosio, A., and Fischer, E. M. (2017). Will Half a Degree Make a Difference? Robust Projections of Indices of Mean and Extreme Climate in Europe Under 1.5°C, 2°C, and 3°C Global Warming. *Geophys. Res. Lett.* 45, 935–944. doi:10.1002/2017GL076222.

Dosio, A., and Panitz, H. J. (2016). Climate change projections for CORDEX-Africa with COSMO-CLM regional climate model and differences with the driving global climate models. *Clim. Dyn.* 46. doi:10.1007/s00382-015-2664-4.

Drobinski, P., Bastin, S., Arsouze, T., Beranger, K., Flaounas, E., and Stefanon, M. (2018). North-western Mediterranean sea-breeze circulation in a regional climate system model. *Clim. Dyn.* 51, 1077–1093. doi:10.1007/s00382-017-3595-z.

Drugé, T., Nabat, P., Mallet, M., and Somot, S. (2019). Model simulation of ammonium and nitrate aerosols distribution in the Euro-Mediterranean region and their radiative and climatic effects over 1979–2016. *Atmos. Chem. Phys.* 19, 3707–3731. doi:10.5194/acp-19-3707-2019.

Druyan, L. M., and Fulakeza, M. (2013). Downscaling reanalysis over continental Africa with a regional model: NCEP versus ERA Interim forcing. *Clim. Res.* doi:10.3354/cr01152.

Duan, A., and Xiao, Z. (2015). Does the climate warming hiatus exist over the Tibetan Plateau? *Sci. Rep.* 5, 13711. doi:10.1038/srep13711.

Duan, W., He, B., Takara, K., Luo, P., Hu, M., Alias, N. E., et al. (2015). Changes of precipitation amounts and extremes over Japan between 1901 and 2012 and their connection to climate indices. *Clim. Dyn.* 45, 2273–2292. doi:10.1007/s00382-015-2778-8.

Dunning, C. M., Black, E., and Allan, R. P. (2018). Later wet seasons with more intense rainfall over Africa under future climate change. *J. Clim.* doi:10.1175/JCLI-D-18-0102.1.

Dyrrdal, A. V., Stordal, F., and Lussana, C. (2018). Evaluation of summer precipitation from EURO-CORDEX fine-scale RCM simulations over Norway. *Int. J. Climatol.* 38, 1661–1677. doi:10.1002/joc.5287.

Easterling, D. R., Kunkel, K. E., Arnold, J. R., Knutson, T., LeGrande, A. N., Leung, L. R., et al. (2017). Precipitation change in the United States. doi:10.7930/J0H993CC.

Eicken, H. (1998). Deriving Modes and Rates of Ice Growth in the Weddell Sea from Microstructural, Salinity and Stable-Isotope Data. *Antarct. Sea Ice Phys. Process. Interact. Var.*, 89–122. doi:doi:10.1029/AR074p0089.

Eisen, O., Frezzotti, M., Genthon, C., Isaksson, E., Magand, O., van den Broeke, M. R., et al. (2008). Ground-based measurements of spatial and temporal variability of snow accumulation in East Antarctica. *Rev. Geophys.* 46. doi:10.1029/2006RG000218.

Elsner, J.B., Jagger, T. H. (2010). "On the Increasing Intensity of the Strongest Atlantic Hurricanes," in *Hurricanes and Climate Change* (Springer), 175–190. doi:10.1007/978-90-481-9510-7_1.

Elvidge, A. D., and Renfrew, I. A. (2016). The causes of foehn warming in the lee of mountains. *Bull. Am. Meteorol. Soc.* 97, 455–466. doi:10.1175/BAMS-D-14-00194.1.

Elvidge, A. D., Renfrew, I. A., King, J. C., Orr, A., Lachlan-Cope, T. A., Weeks, M., et al. (2015). Foehn jets over the Larsen C Ice Shelf, Antarctica. *Q. J. R. Meteorol. Soc.* 141, 698–713. doi:10.1002/qj.2382.

Endo, H., Kitoh, A., Mizuta, R., and Ishii, M. (2017). Future Changes in Precipitation Extremes in East Asia and Their Uncertainty Based on Large Ensemble Simulations with a High-Resolution AGCM. *SOLA* 13, 7–12. doi:10.2151/sola.2017-002.

Endris, H. S., Lennard, C., Hewitson, B., Dosio, A., Nikulin, G., and Panitz, H. J. (2016). Teleconnection responses in multi-GCM driven CORDEX RCMs over Eastern Africa. *Clim. Dyn.* doi:10.1007/s00382-015-2734-7.

Endris, H. S., Omondi, P., Jain, S., Lennard, C., Hewitson, B., Chang'a, L., et al. (2013). Assessment of the performance of CORDEX regional climate models in simulating East African rainfall. *J. Clim.* doi:10.1175/JCLI-D-12-00708.1.

Enfield, D. B., Mestas-Nuñez, A. M., and Trimble, P. J. (2001). The Atlantic Multidecadal Oscillation and its relation to rainfall and river flows in the continental U.S. *Geophys. Res. Lett.* 28, 2077–2080.

doi:10.1029/2000GL012745.
Engelbrecht, F., Adegoke, J., Bopape, M. J., Naidoo, M., Garland, R., Thatcher, M., et al. (2015). Projections of rapidly rising surface temperatures over Africa under low mitigation. *Environ. Res. Lett.* doi:10.1088/1748-9326/10/8/085004.
Espinoza, J. C., Ronchail, J., Frappart, F., Lavado, W., Santini, W., and Guyot, J. L. (2013). The Major Floods in the Amazonas River and Tributaries (Western Amazon Basin) during the 1970–2012 Period: A Focus on the 2012 Flood*. *J. Hydrometeorol.* 14, 1000–1008. doi:10.1175/JHM-D-12-0100.1.
Estilow, T. W., Young, A. H., and Robinson, D. A. (2015). A long-term Northern Hemisphere snow cover extent data record for climate studies and monitoring. *Earth Syst. Sci. Data* 7, 137–142. doi:10.5194/essd-7-137-2015.
Fan, F., Bradley, R. S., and Rawlins, M. A. (2014). Climate change in the northeastern US: regional climate model validation and climate change projections. *Clim. Dyn.* 43, 145–161. doi:10.1007/s00382-014-2198-1.
Fantini, A., Raffaele, F., Torma, C., Bacer, S., Coppola, E., Giorgi, F., et al. (2018). Assessment of multiple daily precipitation statistics in ERA-Interim driven Med-CORDEX and EURO-CORDEX experiments against high resolution observations. *Clim. Dyn.* 51, 877–900. doi:10.1007/s00382-016-3453-4.
Farinotti, D., Brinkerhoff, D. J., Clarke, G. K. C., Fürst, J. J., Frey, H., Gantayat, P., et al. (2017). How accurate are estimates of glacier ice thickness? Results from ITMIX, the Ice Thickness Models Intercomparison eXperiment. *Cryosphere* 11, 949–970. doi:10.5194/tc-11-949-2017.
Farinotti, D., Huss, M., Fürst, J. J., Landmann, J., Machguth, H., Maussion, F., et al. (2019). A consensus estimate for the ice thickness distribution of all glaciers on Earth. *Nat. Geosci.* 12. doi:10.1038/s41561-019-0300-3.
Favier, V., Agosta, C., Parouty, S., Durand, G., Delaygue, G., Gallée, H., et al. (2013). An updated and quality controlled surface mass balance dataset for Antarctica. *Cryosphere* 7, 583–597. doi:10.5194/tc-7-583-2013.
Fei, L., and Yong-Qi, G. (2015). The Project Siberian High in CMIP5 Models. *Atmos. Ocean. Sci. Lett.* 8, 179–184. doi:10.1080/16742834.2015.11447257.
Feng, R., Yu, R., Zheng, H., and Gan, M. (2018). Spatial and temporal variations in extreme temperature in Central Asia. *Int. J. Climatol.* 38, e388–e400. doi:10.1002/joc.5379.
Ferguson, C. R., Pan, M., and Oki, T. (2018). The Effect of Global Warming on Future Water Availability: CMIP5 Synthesis. *Water Resour. Res.* 54, 7791–7819. doi:10.1029/2018WR022792.
Fernandes, K., Giannini, A., Verchot, L., Baethgen, W., and Pinedo-Vasquez, M. (2015). Decadal covariability of Atlantic SSTs and western Amazon dry-season hydroclimate in observations and CMIP5 simulations. *Geophys. Res. Lett.* 42, 6793–6801. doi:10.1002/2015GL063911.
Fernández-Méndez, M., Olsen, L. M., Kauko, H. M., Meyer, A., Rösel, A., Merkouriadi, I., et al. (2018). Algal hot spots in a changing Arctic Ocean: Sea-ice ridges and the snow-ice interface. *Front. Mar. Sci.* 5. doi:10.3389/fmars.2018.00075.
Fernández, J., Frías, M. D., Cabos, W. D., Cofiño, A. S., Domínguez, M., Fita, L., et al. (2018). Consistency of climate change projections from multiple global and regional model intercomparison projects. *Clim. Dyn.* doi:10.1007/s00382-018-4181-8.
Fernandez, J. P. R., Franchito, S. H., Rao, V. B., and Llopart, M. (2017). Changes in Koppen-Trewartha climate classification over South America from RegCM4 projections. *Atmos. Sci. Lett.* 18, 427–434. doi:10.1002/asl.785.
Fischer, E. M., Beyerle, U., and Knutti, R. (2013). Robust spatially aggregated projections of climate extremes. *Nat. Clim. Chang.* 3, 1033. Available at: http://dx.doi.org/10.1038/nclimate2051.
Fischer, E. M., and Knutti, R. (2015). Anthropogenic contribution to global occurrence of heavy-precipitation and high-temperature extremes. *Nat. Clim. Chang.* 5, 560–564. doi:10.1038/nclimate2617.
Flaounas, E., Kelemen, F. D., Wernli, H., Gaertner, M. A., Reale, M., Sanchez-Gomez, E., et al. (2018). Assessment of an ensemble of ocean–atmosphere coupled and uncoupled regional climate models to reproduce the climatology of Mediterranean cyclones. *Clim. Dyn.* 51, 1023–1040. doi:10.1007/s00382-016-3398-7.
Flato, G., Marotzke, J., Abiodun, B., Braconnot, P., Chou, S. C., Collins, W., et al. (2013a). Chapter 9: Evaluation of Climate Models. *Clim. Chang. 2013 Phys. Sci. Basis. Contrib. Work. Gr. I to Fifth Assess. Rep. Intergov. Panel Clim. Chang.*, 741–866. doi:10.1017/CBO9781107415324.
Flato, G., Marotzke, J., Abiodun, B., Braconnot, P., Chou, S. C., Collins, W., et al. (2013b). IPCC 2013 AR5 - Chapter 9: Evaluation of Climate Models. *Clim. Chang. 2013 Phys. Sci. Basis. Contrib. Work. Gr. I to Fifth Assess. Rep. Intergov. Panel Clim. Chang.*, 741–866. doi:10.1017/CBO9781107415324.
Foresta, L., Gourmelen, N., Weissgerber, F., Nienow, P., Williams, J. J., Shepherd, A., et al. (2018). Heterogeneous and rapid ice loss over the Patagonian Ice Fields revealed by CryoSat-2 swath radar altimetry. *Remote Sens. Environ.* 211, 441–455. doi:10.1016/j.rse.2018.03.041.
Forster, P. M., Maycock, A. C., McKenna, C. M., and Smith, C. J. (2019). Latest climate models confirm need for urgent mitigation. *Nat. Clim. Chang.* doi:10.1038/s41558-019-0660-0.
Franzke, C. L. E., Lee, S., and Feldstein, S. B. (2017). Evaluating Arctic warming mechanisms in CMIP5 models. *Clim. Dyn.* 48, 3247–3260. doi:10.1007/s00382-016-3262-9.
Frey, H., Machguth, H., Huss, M., Huggel, C., Bajracharya, S., Bolch, T., et al. (2014). Estimating the volume of glaciers in the Himalayan-Karakoram region using different methods. *Cryosphere* 8, 2313–2333. doi:10.5194/tc-8-2313-2014.

Frezzotti, M., Scarchilli, C., Becagli, S., Proposito, M., and Urbini, S. (2013). A synthesis of the Antarctic surface mass balance during the last 800 yr. *Cryosphere* 7, 303–319. doi:10.5194/tc-7-303-2013.

Frieler, K., Clark, P. U., He, F., Buizert, C., Reese, R., Ligtenberg, S. R. M., et al. (2015). Consistent evidence of increasing Antarctic accumulation with warming. *Nat. Clim. Chang.* 5, 348. Available at: https://doi.org/10.1038/nclimate2574.

Frigg, R., Smith, L. A., and Stainforth, D. A. (2013). The myopia of imperfect climate models: The case of UKCP09. *Philos. Sci.* 80, 886–897. doi:10.1086/673892.

Frolov, A. V., Blinov, V. G., Golitsyn, G. S., Dymnikov, V. P., Izrael, Y. A., Kattsov, V. M., et al. (2014). *Second Roshydromet Assessment Report on Climate Change and its Consequences in the Russian Federation*. Available at: http://cc.voeikovmgo.ru/images/dokumenty/2016/od2/resume_ob_eng.pdf [Accessed April 3, 2019].

Fu, R., Yin, L., Li, W., Arias, P. A., Dickinson, R. E., Huang, L., et al. (2013). Increased dry-season length over southern Amazonia in recent decades and its implication for future climate projection. *Proc. Natl. Acad. Sci.* 110, 18110–18115. doi:10.1073/pnas.1302584110.

Fuentes-Franco, R., Coppola, E., Giorgi, F., Graef, F., and Pavia, E. G. (2014). Assessment of RegCM4 simulated inter-annual variability and daily-scale statistics of temperature and precipitation over Mexico. *Clim. Dyn.* 42, 629–647. doi:10.1007/s00382-013-1686-z.

Fuentes-Franco, R., Coppola, E., Giorgi, F., Pavia, E. G., Diro, G. T., and Graef, F. (2015). Inter-annual variability of precipitation over Southern Mexico and Central America and its relationship to sea surface temperature from a set of future projections from CMIP5 GCMs and RegCM4 CORDEX simulations. *Clim. Dyn.* 45, 425–440. doi:10.1007/s00382-014-2258-6.

Fuentes-Franco, R., Giorgi, F., Coppola, E., and Zimmermann, K. (2017). Sensitivity of tropical cyclones to resolution, convection scheme and ocean flux parameterization over Eastern Tropical Pacific and Tropical North Atlantic Oceans in the RegCM4 model. *Clim. Dyn.* 49, 547–561. doi:10.1007/s00382-016-3357-3.

Fumière, Q., Déqué, M., Nuissier, O., Somot, S., Alias, A., Caillaud, C., et al. (2019). Extreme rainfall in Mediterranean France during the fall: added value of the CNRM-AROME Convection-Permitting Regional Climate Model. *Clim. Dyn.* doi:10.1007/s00382-019-04898-8.

Fürst, J. J., Gillet-Chaulet, F., Benham, T. J., Dowdeswell, J. A., Grabiec, M., Navarro, F., et al. (2017). Application of a two-step approach for mapping ice thickness to various glacier types on Svalbard. *Cryosph.* 11, 2003–2032. doi:10.5194/tc-11-2003-2017.

Fyfe, J. C., Derksen, C., Mudryk, L., Flato, G. M., Santer, B. D., Swart, N. C., et al. (2017). Large near-term projected snowpack loss over the western United States. *Nat. Commun.* 8, 14996. doi:10.1038/ncomms14996.

Gaertner, M. Á., González-Alemán, J. J., Romera, R., Domínguez, M., Gil, V., Sánchez, E., et al. (2018). Simulation of medicanes over the Mediterranean Sea in a regional climate model ensemble: impact of ocean–atmosphere coupling and increased resolution. *Clim. Dyn.* 51, 1041–1057. doi:10.1007/s00382-016-3456-1.

Gaetani, M., Flamant, C., Bastin, S., Janicot, S., Lavaysse, C., Hourdin, F., et al. (2017). West African monsoon dynamics and precipitation: the competition between global SST warming and CO2 increase in CMIP5 idealized simulations. *Clim. Dyn.* doi:10.1007/s00382-016-3146-z.

Ganguli, P., and Coulibaly, P. (2019). Assessment of future changes in intensity-duration-frequency curves for Southern Ontario using North American (NA)-CORDEX models with nonstationary methods. *J. Hydrol. Reg. Stud.* 22, 100587. doi:https://doi.org/10.1016/j.ejrh.2018.12.007.

García-Díez, M., Fernández, J., and Vautard, R. (2015). An RCM multi-physics ensemble over Europe: multi-variable evaluation to avoid error compensation. *Clim. Dyn.* 45, 3141–3156. doi:10.1007/s00382-015-2529-x.

Gärtner-Roer, I., Naegeli, K., Huss, M., Knecht, T., Machguth, H., and Zemp, M. (2014). A database of worldwide glacier thickness observations. *Glob. Planet. Change* 122, 330–344. doi:10.1016/j.gloplacha.2014.09.003.

Gbobaniyi, E., Sarr, A., Sylla, M. B., Diallo, I., Lennard, C., Dosio, A., et al. (2014). Climatology, annual cycle and interannual variability of precipitation and temperature in CORDEX simulations over West Africa. *Int. J. Climatol.* 34. doi:10.1002/joc.3834.

Georgia's Third National Communication to the UNFCCC (2015).

Gevorgyan, A. (2014). Surface and tropospheric temperature trends in Armenia. *Int. J. Climatol.* 34, 3559–3573. doi:10.1002/joc.3928.

Gevorgyan, A., Melkonyan, H., Aleksanyan, T., Iritsyan, A., and Khalatyan, Y. (2016a). An assessment of observed and projected temperature changes in Armenia. *Arab. J. Geosci.* 9, 27. doi:10.1007/s12517-015-2167-y.

Gevorgyan, A., Melkonyan, H., Aleksanyan, T., Iritsyan, A., and Khalatyan, Y. (2016b). An assessment of observed and projected temperature changes in Armenia. *Arab. J. Geosci.* 9, 1–9. doi:10.1007/s12517-015-2167-y.

Ghebrezgabher, M. G., Yang, T., and Yang, X. (2016). Long-term trend of climate change and drought assessment in the Horn of Africa. *Adv. Meteorol.* 2016. doi:10.1155/2016/8057641.

Ghimire, S., Choudhary, A., and Dimri, A. P. (2018). Assessment of the performance of CORDEX-South Asia experiments for monsoonal precipitation over the Himalayan region during present climate: part I. *Clim. Dyn.* 50, 2311–2334. doi:10.1007/s00382-015-2747-2.

Gibba, P., Sylla, M. B., Okogbue, E. C., Gaye, A. T., Nikiema, M., and Kebe, I. (2019). State-of-the-art climate modeling of extreme precipitation over Africa: analysis of CORDEX added-value over CMIP5. *Theor. Appl.*

Climatol. doi:10.1007/s00704-018-2650-y.
Giese, E., Mossig, I., Rybski, D., and Bunde, A. (2007). Long-Term Analysis of Air Temperature Trends in Central Asia (Analyse langjähriger Zeitreihen der Lufttemperatur in Zentralasien). *Erdkunde* 61, 186–202. Available at: http://www.jstor.org/stable/25647984.
Giorgi, F., Coppola, E., Raffaele, F., Diro, G. T., Fuentes-Franco, R., Giuliani, G., et al. (2014). Changes in extremes and hydroclimatic regimes in the CREMA ensemble projections. *Clim. Change* 125, 39–51. doi:10.1007/s10584-014-1117-0.
Giorgi, F., Jones, C., and Asrar, G. (2009). Addressing climate information needs at the regional level: the CORDEX framework. *... Organ. Bull.* 58, 175–183.
Giorgi, F., Raffaele, F., and Coppola, E. (2019). The response of precipitation characteristics to global warming from climate projections. *Earth Syst. Dyn.* 10, 73–89. doi:10.5194/esd-10-73-2019.
Giorgi, F., Torma, C., Coppola, E., Ban, N., Schär, C., and Somot, S. (2016). Enhanced summer convective rainfall at Alpine high elevations in response to climate warming. *Nat. Geosci.* 9, 584–589. doi:10.1038/ngeo2761.
Giot, O., Termonia, P., Degrauwe, D., De Troch, R., Caluwaerts, S., Smet, G., et al. (2016). Validation of the ALARO-0 model within the EURO-CORDEX framework. *Geosci. Model Dev.* 9, 1143–1152. doi:10.5194/gmd-9-1143-2016.
GlaThiDa Consortium (2019). Glacier Thickness Database 3.0.1. doi:10.5904/wgms-glathida-2019-03.
Glisan, J. M., and Gutowski, W. J. (2014). WRF winter extreme daily precipitation over the North American CORDEX Arctic. *J. Geophys. Res.* 119, 10.738-10.748. doi:10.1002/2014JD021676.
Gloor, M., Barichivich, J., Ziv, G., Brienen, R., Schöngart, J., Peylin, P., et al. (2015). Recent Amazon climate as background for possible ongoing and future changes of Amazon humid forests. *Global Biogeochem. Cycles* 29, 1384–1399. doi:10.1002/2014GB005080.
GMENR (2015). Georgia's Third National Communication to the UNFCCC. Georgia Ministry of Environment and Natural Resources Available at: https://unfccc.int/resource/docs/natc/geonc3.pdf [Accessed April 2, 2019].
Goldenberg, S. B., Landsea, C. W., Mestas-Nuñez, A. M., and Gray, W. M. (2001). The recent increase in Atlantic hurricane activity: Causes and implications. *Science (80-.).* 293, 474–479. doi:10.1126/science.1060040.
Gonzalez-Hidalgo, J. C., Peña-Angulo, D., Brunetti, M., and Cortesi, N. (2016). Recent trend in temperature evolution in Spanish mainland (1951-2010): from warming to hiatus. *Int. J. Climatol.* 36, 2405–2416. doi:10.1002/joc.4519.
Gorodetskaya, I. V., Kneifel, S., Maahn, M., Van Tricht, K., Thiery, W., Schween, J. H., et al. (2015). Cloud and precipitation properties from ground-based remote-sensing instruments in East Antarctica. *Cryosph.* 9, 285–304. doi:10.5194/tc-9-285-2015.
Gorodetskaya, I. V., Tsukernik, M., Claes, K., Ralph, M. F., Neff, W. D., and Van Lipzig, N. P. M. (2014). The role of atmospheric rivers in anomalous snow accumulation in East Antarctica. *Geophys. Res. Lett.* 41, 6199–6206. doi:10.1002/2014GL060881.
Gorodetskaya, I. V., Van Lipzig, N. P. M., Van Den Broeke, M. R., Mangold, A., Boot, W., and Reijmer, C. H. (2013). Meteorological regimes and accumulation patterns at Utsteinen, Dronning Maud Land, East Antarctica: Analysis of two contrasting years. *J. Geophys. Res. Atmos.* 118, 1700–1715. doi:10.1002/jgrd.50177.
Gorte, T., Lenaerts, J. T. M., and Medley, B. (submitted). Scoring Antarctic surface mass balance in climate models to refine future projections. *Cryosph. Discuss.* (submitted. doi:https://doi.org/10.5194/tc-2019-240.
Gossart, A., Helsen, S., Lenaerts, J. T. M., Broucke, S. Vanden, van Lipzig, N. P. M., and Souverijns, N. (2019). An Evaluation of Surface Climatology in State-of-the-Art Reanalyses over the Antarctic Ice Sheet. *J. Clim.* 32, 6899–6915. doi:10.1175/JCLI-D-19-0030.1.
Goswami, B. N., Venugopal, V., Sengupta, D., Madhusoodanan, M. S., and Xavier, P. K. (2006). Increasing trend of extreme rain events over India in a warming environment. *Science* 314, 1442–5. doi:10.1126/science.1132027.
Graham, R. M., Cohen, L., Petty, A. A., Boisvert, L. N., Rinke, A., Hudson, S. R., et al. (2017). Increasing frequency and duration of Arctic winter warming events. *Geophys. Res. Lett.* 44, 6974–6983. doi:10.1002/2017GL073395.
Granskog, M. A., Rösel, A., Dodd, P. A., Divine, D., Gerland, S., Martma, T., et al. (2017). Snow contribution to first-year and second-year Arctic sea ice mass balance north of Svalbard. *J. Geophys. Res. Ocean.* 122, 2539–2549. doi:10.1002/2016JC012398.
Graversen, R. G., and Burtu, M. (2016). Arctic amplification enhanced by latent energy transport of atmospheric planetary waves. *Q. J. R. Meteorol. Soc.* 142, 2046–2054. doi:10.1002/qj.2802.
Grazioli, J., Genthon, C., Boudevillain, B., Duran-Alarcon, C., Del Guasta, M., Madeleine, J. B., et al. (2017). Measurements of precipitation in Dumont d'Urville, Adélie Land, East Antarctica. *Cryosphere* 11, 1797–1811. doi:10.5194/tc-11-1797-2017.
Gregory, J. M., and Huybrechts, P. (2006). Ice-sheet contributions to future sea-level change. *Philos. Trans. R. Soc. A Math. Phys. Eng. Sci.* 364, 1709–1732. doi:10.1098/rsta.2006.1796.
Grise, K. M., Son, S.-W., and Gyakum, J. R. (2013). Intraseasonal and Interannual Variability in North American Storm Tracks and Its Relationship to Equatorial Pacific Variability. *Mon. Weather Rev.* 141, 3610–3625. doi:10.1175/MWR-D-12-00322.1.
Gröger, M., Dieterich, C., Meier, M. H. E., and Schimanke, S. (2015). Thermal air–sea coupling in hindcast simulations for the North Sea and Baltic Sea on the NW European shelf. *Tellus A Dyn. Meteorol. Oceanogr.* 67, 26911.

doi:10.3402/tellusa.v67.26911.
Groisman, P. Y., Bulygina, O. N., Yin, X., Vose, R. S., Gulev, S. K., Hanssen-Bauer, I., et al. (2016). Recent changes in the frequency of freezing precipitation in North America and Northern Eurasia. *Environ. Res. Lett.* 11. doi:10.1088/1748-9326/11/4/045007.
Grose, M. R., Foster, S., Risbey, J. S., Osbrough, S., and Wilson, L. (2019a). Using indices of atmospheric circulation to refine southern Australian winter rainfall climate projections. *Clim. Dyn.* doi:10.1007/s00382-019-04880-4.
Grose, M. R., Narsey, S., Delage, F. P., Dowdy, A. J., Bador, M., Boschat, G., et al. (submitted). Insights from CMIP6 for Australia's future climate. *Earth's Futur.* (submitted.
Grose, M. R., Risbey, J. S., Moise, A. F., Osbrough, S., Heady, C., Wilson, L., et al. (2017). Constraints on Southern Australian Rainfall Change Based on Atmospheric Circulation in CMIP5 Simulations. *J. Clim.* 30, 225–242. doi:10.1175/jcli-d-16-0142.1.
Grose, M. R., Syktus, J., Thatcher, M., Evans, J. P., Ji, F., Rafter, T., et al. (2019b). The role of topography on projected rainfall change in mid-latitude mountain regions. *Clim. Dyn.* doi:10.1007/s00382-019-04736-x.
Grosvenor, D. P., King, J. C., Choularton, T. W., and Lachlan-Cope, T. (2014). Downslope föhn winds over the antarctic peninsula and their effect on the larsen ice shelves. *Atmos. Chem. Phys.* 14, 9481–9509. doi:10.5194/acp-14-9481-2014.
Gruza, G. V., Rankova, E. Y., Rocheva, E. V., and Smirnov, V. D. (2015). CURRENT GLOBAL WARMING: GEOGRAPHICAL AND SEASONAL FEATURES. *Фундаментальная и прикладная климатология* 2, 41–62. Available at: www.meteo.ru [Accessed November 13, 2019].
Gudmundsson, L., and Seneviratne, S. I. (2015). European drought trends. in *Extreme Hydrological Events - IAHS-IACS-IAG Joint Symposium JH1, 26th General Assembly of the International Union of Geodesy and Geophysics, Prague, Czech Republic, 22 June–2 July 2015* (Copernicus GmbH), 75–79. doi:https://doi.org/10.5194/piahs-369-75-2015.
Gulizia, C., and Camilloni, I. (2015). Comparative analysis of the ability of a set of CMIP3 and CMIP5 global climate models to represent precipitation in South America. *Int. J. Climatol.* 35, 583–595. doi:10.1002/joc.4005.
Gulizia, C., Camilloni, I., and Doyle, M. (2013). Identification of the principal patterns of summer moisture transport in South America and their representation by WCRP/CMIP3 global climate models. *Theor. Appl. Climatol.* 112, 227–241. doi:10.1007/s00704-012-0729-4.
Guo, D.-L., Sun, J.-Q., and Yu, E.-T. (2018a). Evaluation of CORDEX regional climate models in simulating temperature and precipitation over the Tibetan Plateau. *Atmos. Ocean. Sci. Lett.* 11, 219–227. doi:10.1080/16742834.2018.1451725.
Guo, D., Li, D., and Hua, W. (2017a). Quantifying air temperature evolution in the permafrost region from 1901 to 2014. *Int. J. Climatol.* 38, 66–76. doi:10.1002/joc.5161.
Guo, H., Bao, A., Liu, T., Jiapaer, G., Ndayisaba, F., Jiang, L., et al. (2018b). Spatial and temporal characteristics of droughts in Central Asia during 1966–2015. *Sci. Total Environ.* 624, 1523–1538. doi:https://doi.org/10.1016/j.scitotenv.2017.12.120.
Guo, H., Bao, A., Liu, T., Ndayisaba, F., He, D., Kurban, A., et al. (2017b). Meteorological drought analysis in the Lower Mekong Basin using satellite-based long-term CHIRPS product. *Sustain.* 9. doi:10.3390/su9060901.
Guo, H., Bao, A., Ndayisaba, F., Liu, T., Kurban, A., and De Maeyer, P. (2017c). Systematical Evaluation of Satellite Precipitation Estimates Over Central Asia Using an Improved Error-Component Procedure. *J. Geophys. Res. Atmos.* 122, 10,906-910,927. doi:10.1002/2017JD026877.
Guo, L., and Li, L. (2015). Variation of the proportion of precipitation occurring as snow in the Tian Shan Mountains, China. *Int. J. Climatol.* 35, 1379–1393. doi:10.1002/joc.4063.
Gutierrez, C., Somot, S., Nabat, P., Mallet, M., Corre, L., Van Meijgaard, E., et al. (submitted). Future evolution of surface solar radiation and photovoltaic potential in Europe: investigating the role of aerosols. *Environ. Res. Lett.* (submitted.
Gutiérrez, C., Somot, S., Nabat, P., Mallet, M., Gaertner, M. Á., and Perpiñán, O. (2018). Impact of aerosols on the spatiotemporal variability of photovoltaic energy production in the Euro-Mediterranean area. *Sol. Energy* 174, 1142–1152. doi:10.1016/J.SOLENER.2018.09.085.
Gutowski, J. W., Giorgi, F., Timbal, B., Frigon, A., Jacob, D., Kang, H. S., et al. (2016). WCRP COordinated Regional Downscaling EXperiment (CORDEX): A diagnostic MIP for CMIP6. *Geosci. Model Dev.* doi:10.5194/gmd-9-4087-2016.
Haag, I., Jones, P. D., and Samimi, C. (2019). Central Asia's changing climate: How temperature and precipitation have changed across time, space, and altitude. *Climate* 7. doi:10.3390/cli7100123.
Haapala, J., Lensu, M., Dumont, M., Renner, A. H. H., Granskog, M. A., and Gerland, S. (2013). Small-scale horizontal variability of snow, sea-ice thickness and freeboard in the first-year ice region north of Svalbard. *Ann. Glaciol.* 54, 261–266. doi:10.3189/2013AoG62A157.
Haarsma, R. J., Hazeleger, W., Severijns, C., de Vries, H., Sterl, A., Bintanja, R., et al. (2013). More hurricanes to hit western Europe due to global warming. *Geophys. Res. Lett.* 40, 1783–1788. doi:10.1002/grl.50360.
Haarsma, R. J., Roberts, M. J., Vidale, P. L., Catherine, A., Bellucci, A., Bao, Q., et al. (2016a). High Resolution Model Intercomparison Project (HighResMIP v1.0) for CMIP6. *Geosci. Model Dev.* 9, 4185–4208. doi:10.5194/gmd-9-

4185-2016.
Haarsma, R. J., Roberts, M., Vidale, P. L., Senior, C. A., Bellucci, A., Bao, Q., et al. (2016b). High Resolution Model Intercomparison Project (HighResMIP). *Geosci. Model Dev. Discuss.*, 1–35. doi:10.5194/gmd-2016-66.
HAM, S., LEE, J.-W., and YOSHIMURA, K. (2016). Assessing Future Climate Changes in the East Asian Summer and Winter Monsoon Using Regional Spectral Model. *J. Meteorol. Soc. Japan. Ser. II* 94A, 69–87. doi:10.2151/jmsj.2015-051.
Hamilton, C. D., Kovacs, K. M., Ims, R. A., and Lydersen, C. (2018). Haul-out behaviour of Arctic ringed seals (Pusa hispida): inter-annual patterns and impacts of current environmental change. *Polar Biol.* 41, 1063–1082. doi:10.1007/s00300-018-2260-2.
Hamman, J., Nijssen, B., Brunke, M., Cassano, J., Craig, A., DuVivier, A., et al. (2016). Land surface climate in the regional Arctic system model. *J. Clim.* 29, 6543–6562. doi:10.1175/JCLI-D-15-0415.1.
Han, S., and Yang, Z. (2013). Cooling effect of agricultural irrigation over Xinjiang, Northwest China from 1959 to 2006. *Environ. Res. Lett.* 8. doi:10.1088/1748-9326/8/2/024039.
Hannart, A., Vera, C., Cerne, B., and Otto, F. E. L. (2015a). Causal Influence of Anthropogenic Forcings on the Argentinian Heat Wave of December 2013. *Bull. Am. Meteorol. Soc.* 96, S41–S45. doi:10.1175/BAMS-D-15-00137.1.
Hannart, A., Vera, C., Cerne, B., and Otto, F. E. L. (2015b). Causal Influence of Anthropogenic Forcings on the Argentinian Heat Wave of December 2013. *Bull. Am. Meteorol. Soc.* 96, S41–S45. doi:10.1175/BAMS-D-15-00137.1.
Hansen, B. B., Isaksen, K., Benestad, R. E., Kohler, J., Pedersen, Å., Loe, L. E., et al. (2014). Warmer and wetter winters: Characteristics and implications of an extreme weather event in the High Arctic. *Environ. Res. Lett.* 9. doi:10.1088/1748-9326/9/11/114021.
Hao, M., Huang, J., Luo, Y., Chen, X., Lin, Y., Zhao, Z., et al. (2018). Narrowing the surface temperature range in CMIP5 simulations over the Arctic. *Theor. Appl. Climatol.* 132, 1073–1088. doi:10.1007/s00704-017-2161-2.
Hao, M., Luo, Y., Lin, Y., Zhao, Z., Wang, L., and Huang, J. (2019). Contribution of atmospheric moisture transport to winter Arctic warming. *Int. J. Climatol.* 39, 2697–2710. doi:10.1002/joc.5982.
Harold, J., Lorenzoni, I., Shipley, T. F., and Coventry, K. R. (2016). Cognitive and psychological science insights to improve climate change data visualization. *Nat. Clim. Chang.* 6, 1080–1089. doi:10.1038/nclimate3162.
Harris, A. J. L., Corner, A., Xu, J., and Du, X. (2013). Lost in translation? Interpretations of the probability phrases used by the Intergovernmental Panel on Climate Change in China and the UK. *Clim. Change* 121, 415–425. doi:10.1007/s10584-013-0975-1.
Harris, D. M. (2017). Telling the story of climate change: Geologic imagination, praxis, and policy. *Energy Res. Soc. Sci.* 31, 179–183. doi:10.1016/J.ERSS.2017.05.027.
Harris, I., Jones, P. D., Osborn, T. J., and Lister, D. H. (2014). Updated high-resolution grids of monthly climatic observations - the CRU TS3.10 Dataset. *Int. J. Climatol.* 34, 623–642. doi:10.1002/joc.3711.
Harter, D. E. V, Irl, S. D. H., Seo, B., Steinbauer, M. J., Gillespie, R., Triantis, K. A., et al. (2015). Impacts of global climate change on the floras of oceanic islands – Projections, implications and current knowledge. *Perspect. Plant Ecol. Evol. Syst.* 17, 160–183. doi:https://doi.org/10.1016/j.ppees.2015.01.003.
Hartmann, D. L., Tank, A. M. G. K., and Rusticucci, M. (2013). IPCC Fifth Assessment Report, Climate Change 2013: The Physical Science Basis. *IPCC* AR5, 31–39.
Harzallah, A., Jordà, G., Dubois, C., Sannino, G., Carillo, A., Li, L., et al. (2018). Long term evolution of heat budget in the Mediterranean Sea from Med-CORDEX forced and coupled simulations. *Clim. Dyn.* 51, 1145–1165. doi:10.1007/s00382-016-3363-5.
Hasson, S., Böhner, J., and Lucarini, V. (2015). Prevailing climatic trends and runo ff response from Hindukush – Karakoram – Himalaya , upper Indus basin. 579–653. doi:10.5194/esdd-6-579-2015.
Hasson, S., Lucarini, V., Khan, M. R., Petitta, M., Bolch, T., and Gioli, G. (2014). Early 21st century snow cover state over the western river basins of the Indus River system. 4077–4100. doi:10.5194/hess-18-4077-2014.
Hasson, S., Lucarini, V., and Pascale, S. (2013). Hydrological cycle over South and Southeast Asian river basins as simulated by PCMDI/CMIP3 experiments. *Earth Syst. Dyn.* 4, 199–217. doi:10.5194/esd-4-199-2013.
Hasson, S. ul, Böhner, J., and Chishtie, F. (2019a). Low fidelity of CORDEX and their driving experiments indicates future climatic uncertainty over Himalayan watersheds of Indus basin. *Clim. Dyn.* 52, 777–798. doi:10.1007/s00382-018-4160-0.
Hasson, S. ul, Böhner, J., and Chishtie, F. (2019b). Low fidelity of CORDEX and their driving experiments indicates future climatic uncertainty over Himalayan watersheds of Indus basin. *Clim. Dyn.* 52, 777–798. doi:10.1007/s00382-018-4160-0.
Hasson, S. ul, Böhner, J., and Chishtie, F. (2019c). Low fidelity of CORDEX and their driving experiments indicates future climatic uncertainty over Himalayan watersheds of Indus basin. *Clim. Dyn.* 52, 777–798. doi:10.1007/s00382-018-4160-0.
Hawkins, E., and Sutton, R. (2016). Connecting Climate Model Projections of Global Temperature Change with the Real World. *Bull. Am. Meteorol. Soc.* 97, 963–980. doi:10.1175/BAMS-D-14-00154.1.
Hazeleger, W., Van Den Hurk, B. J. J. M., Min, E., Van Oldenborgh, G. J., Petersen, A. C., Stainforth, D. A., et al.

(2015). Tales of future weather. *Nat. Clim. Chang.* 5. doi:10.1038/nclimate2450.
Henderson, G. R., and Leathers, D. J. (2009). European snow cover extent variability and associations with atmospheric forcings. *Int. J. Climatol.* 30, n/a-n/a. doi:10.1002/joc.1990.
Hernández-Díaz, L., Laprise, R., Sushama, L., Martynov, A., Winger, K., and Dugas, B. (2013). Climate simulation over CORDEX Africa domain using the fifth-generation Canadian Regional Climate Model (CRCM5). *Clim. Dyn.* doi:10.1007/s00382-012-1387-z.
Herrera, D. A., Ault, T. R., Fasullo, J. T., Coats, S. J., Carrillo, C. M., Cook, B. I., et al. (2018). Exacerbation of the 2013–2016 Pan-Caribbean Drought by Anthropogenic Warming. *Geophys. Res. Lett.* 45, 10,610-619,626. doi:10.1029/2018GL079408.
Herrera, D., and Ault, T. (2017). Insights from a New High-Resolution Drought Atlas for the Caribbean Spanning 1950–2016. *J. Clim.* 30, 7801–7825. doi:10.1175/JCLI-D-16-0838.1.
Herrera, S., Fernández, J., and Gutiérrez, J. M. (2016). Update of the Spain02 gridded observational dataset for EURO-CORDEX evaluation: assessing the effect of the interpolation methodology. *Int. J. Climatol.* 36, 900–908. doi:10.1002/joc.4391.
Hewitt, H. T., Copsey, D., Culverwell, I. D., Harris, C. M., Hill, R. S. R., Keen, A. B., et al. (2011). Design and implementation of the infrastructure of HadGEM3: the next-generation Met Office climate modelling system. *Geosci. Model Dev.* 4, 223–253. doi:10.5194/gmd-4-223-2011.
Hidalgo, H. G., Alfaro, E. J., and Quesada-Montano, B. (2017). Observed (1970--1999) climate variability in Central America using a high-resolution meteorological dataset with implication to climate change studies. *Clim. Change* 141, 13–28. doi:10.1007/s10584-016-1786-y.
Hijioka, Y., E. Lin, J.J. Pereira, R.T. Corlett, X. Cui, G.E. Insarov, R.D. Lasco, E. Lindgren, and A. Surjan, 2014 (2014). "No Title," in *Asia. In: Climate Change 2014: Impacts, Adaptation, and Vulnerability. Part B: Regional Aspects. Contribution of Working Group II to the Fifth Assessment Report of the Intergovernmental Panel on Climate Change*, eds. K. L. E. Barros, V.R., C.B. Field, D.J. Dokken, M.D. Mastrandrea, K.J. Mach, T.E. Bilir, M. Chatterjee and and L. L. W. Y.O. Estrada, R.C. Genova, B. Girma, E.S. Kissel, A.N. Levy, S. MacCracken, P.R. Mastrandrea (Cambridge University Press, Cambridge, United Kingdom and New York, NY, USA), 1327–1370.
Hines, K. M., Bromwich, D. H., Wang, S. H., Silber, I., Verlinde, J., and Lubin, D. (2019). Microphysics of summer clouds in central West Antarctica simulated by the Polar Weather Research and Forecasting Model (WRF) and the Antarctic Mesoscale Prediction System (AMPS). *Atmos. Chem. Phys.* 19, 12431–12454. doi:10.5194/acp-19-12431-2019.
Ho, E. H., and Budescu, D. V. (2019). Climate uncertainty communication. *Nat. Clim. Chang.* 9, 802–803. doi:10.1038/s41558-019-0606-6.
Hobgood, J. (2005). "Tropical Cyclones," in *Encyclopedia of World Climatology*, ed. J. E. Oliver (Dordrecht: Springer Netherlands), 750–755. doi:10.1007/1-4020-3266-8_213.
Hoell, A., Hoerling, M., Eischeid, J., Quan, X. W., and Liebmann, B. (2017). Reconciling theories for human and natural attribution of recent East Africa drying. *J. Clim.* doi:10.1175/JCLI-D-16-0558.1.
Hoerling, M., Hurrell, J., Eischeid, J., and Phillips, A. (2006). Detection and attribution of twentieth-century northern and southern African rainfall change. *J. Clim.* doi:10.1175/JCLI3842.1.
Holland, G., and Bruyère, C. L. (2014). Recent intense hurricane response to global climate change. *Clim. Dyn.* 42, 617–627. doi:10.1007/s00382-013-1713-0.
Howe, L. C., MacInnis, B., Krosnick, J. A., Markowitz, E. M., and Socolow, R. (2019). Acknowledging uncertainty impacts public acceptance of climate scientists' predictions. *Nat. Clim. Chang.* 9, 863–867. doi:10.1038/s41558-019-0587-5.
Hu, Z., Zhang, C., Hu, Q., and Tian, H. (2014). Temperature Changes in Central Asia from 1979 to 2011 Based on Multiple Datasets*. *J. Clim.* 27, 1143–1167. doi:10.1175/JCLI-D-13-00064.1.
Hu, Z., Zhou, Q., Chen, X., Qian, C., Wang, S., and Li, J. (2017). Variations and changes of annual precipitation in Central Asia over the last century. *Int. J. Climatol.* 37, 157–170. doi:10.1002/joc.4988.
Huang, A., Zhou, Y., Zhang, Y., Huang, D., Zhao, Y., and Wu, H. (2014a). Changes of the annual precipitation over central Asia in the twenty-first century projected by multimodels of CMIP5. *J. Clim.* 27, 6627–6646. doi:10.1175/JCLI-D-14-00070.1.
Huang, A., Zhou, Y., Zhang, Y., Huang, D., Zhao, Y., and Wu, H. (2014b). Changes of the Annual Precipitation over Central Asia in the Twenty-First Century Projected by Multimodels of CMIP5. *J. Clim.* 27, 6627–6646. doi:10.1175/JCLI-D-14-00070.1.
Huang, B., Polanski, S., and Cubasch, U. (2015). Assessment of precipitation climatology in an ensemble of CORDEX-East Asia regional climate simulations. *Clim. Res.* 64, 141–158. Available at: https://www.int-res.com/abstracts/cr/v64/n2/p141-158/.
Huang, B., Thorne, P. W., Banzon, V. F., Boyer, T., Chepurin, G., Lawrimore, J. H., et al. (2017a). Extended Reconstructed Sea Surface Temperature, Version 5 (ERSSTv5): Upgrades, Validations, and Intercomparisons. *J. Clim.* 30, 8179–8205. doi:10.1175/JCLI-D-16-0836.1.
Huang, J., Yu, H., Dai, A., Wei, Y., and Kang, L. (2017b). Drylands face potential threat under 2 °C global warming

target. *Nat. Clim. Chang.* 7, 417. Available at: https://doi.org/10.1038/nclimate3275.
Huffman, G. J., Adler, R. F., Bolvin, D. T., and Gu, G. (2009). Improving the global precipitation record: GPCP Version 2.1. *Geophys. Res. Lett.* 36. doi:10.1029/2009GL040000.
Hurd, C. L., Lenton, A., Tilbrook, B., and Boyd, P. W. (2018). Current understanding and challenges for oceans in a higher-CO2 world. *Nat. Clim. Chang.* 8, 686–694. doi:10.1038/s41558-018-0211-0.
Hurrel, J. W., Kushnir, Y., Visbeck, M., and Ottersen, G. (2003). An overview of the North Atlantic Oscillation. *Geophys. Monogr. Ser.*
Huss, M., and Farinotti, D. (2012). Distributed ice thickness and volume of all glaciers around the globe. *J. Geophys. Res. Earth Surf.* 117, 1–10. doi:10.1029/2012JF002523.
Huybrechts, P., Goelzer, H., Janssens, I., Driesschaert, E., Fichefet, T., Goosse, H., et al. (2011). Response of the Greenland and Antarctic Ice Sheets to Multi-Millennial Greenhouse Warming in the Earth System Model of Intermediate Complexity LOVECLIM. *Surv. Geophys.* 32, 397–416. doi:10.1007/s10712-011-9131-5.
Iacozza, J., and Ferguson, S. H. (2014). Spatio-temporal variability of snow over sea ice in western Hudson Bay, with reference to ringed seal pup survival. *Polar Biol.* 37, 817–832. doi:10.1007/s00300-014-1484-z.
IDOE (2017). Iran's third National Communacation to UNFCCC. Department of Environment of the Government of the Islamic Republic of Iran.
Iliasov, S., Zabenko, O., Gaidamak, N., Kirilenko, A., Myrsaliev, N., Shevchenko, V., et al. (2013). *Climate profile of the Kyrgyz Republic*. Bishkek.
Imada, Y., Watanabe, M., Kawase, H., Shiogama, H., and Arai, M. (2019). The July 2018 high temperature event in Japan could not have happened without human-induced global warming. *SOLA* 15A, 8–12. doi:10.2151/sola.15A-002.
Imbach, P., Chou, S. C., Lyra, A., Rodrigues, D., Rodriguez, D., Latinovic, D., et al. (2018). Future climate change scenarios in Central America at high spatial resolution. *PLoS One* 13, e0193570. doi:10.1371/journal.pone.0193570.
Indasi, V. (2019). Genealogy of Gridded Precipitation Datasets over Southern Africa. *prep*.
IPCC (2010). *Meeting Report of the Intergovernmental Panel on Climate Change Expert Meeting on Assessing and Combining Multi Model Climate Projections*. , eds. T. F. Stocker, D. Qin, G.-K. Plattner, M. Tignor, and P. M. Midgley IPCC Working Group I Technical Support Unit, University of Bern, Bern, Switzerland Available at: https://naturalsciences.ch/service/publications/75800-assessing-and-combining-multi-model-climate-projections [Accessed April 2, 2019].
IPCC (2012). Managing the Risks of Extreme Events and Disasters to Advance Climate Change Adaptation. A Special Report of Working Groups I and II of the Intergovernmental Panel on Climate Change. , eds. C. B. Field, V. Barros, T. F. Stocker, and Q. Dahe Cambridge, UK and New York, NY, USA: Cambridge University Press.
IPCC (2013a). IPCC Fifth Assessment Report (AR5). *IPCC*, s. 10-12.
IPCC (2013b). Working Group I Contribution to the IPCC Fifth Assessment Report, Climate Change 2013: The Physical Science Basis. *IPCC* AR5, 2014.
IPCC (2018a). Global Warming of 1.5°C. An IPCC Special Report on the impacts of global warming of 1.5°C above pre-industrial levels and related global greenhouse gas emission pathways, in the context of strengthening the global response to the threat of climate change,. , eds. V. Masson-Delmotte, P. Zhai, H.-O. Pörtner, D. Roberts, J. Skea, P. R. Shukla, et al. In Press.
IPCC (2018b). Special Report, Global Warming of 1.5° C (SR15).
IPCC (2018c). *Special report on 1.5 degree Global Warming*. Available at: http://report.ipcc.ch/sr15/pdf/sr15_spm_final.pdf.
IPCC (2018d). "Summary for Policymakers," in *Global Warming of 1.5°C. An IPCC Special Report on the impacts of global warming of 1.5°C above pre-industrial levels and related global greenhouse gas emission pathways, in the context of strengthening the global response to the threat of climate change,* eds. V. Masson-Delmotte, P. Zhai, H.-O. Pörtner, D. Roberts, J. Skea, P. R. Shukla, et al. (In Press), 32.
IPCC (2019a). Special Report on Climate Change and Land. *Ipcc*.
IPCC (2019b). Special report on the Ocean and Cryosphere in a Changing Climate. *Press*. doi:https://www.ipcc.ch/report/srocc/.
Ippolitov, I. I., Loginov, S. V., Kharyutkina, E. V., and Moraru, E. I. (2014). Climate variability over the Asian territory of Russia during 1975–2012. *Geogr. Nat. Resour.* 35, 310–318. doi:10.1134/S1875372814040027.
Iqbal, W., Syed, F. S., Sajjad, H., Nikulin, G., Kjellström, E., and Hannachi, A. (2017). Mean climate and representation of jet streams in the CORDEX South Asia simulations by the regional climate model RCA4. *Theor. Appl. Climatol.* 129, 1–19. doi:10.1007/s00704-016-1755-4.
Isaksen, K., Nordli, Ø., Førland, E. J., Łupikasza, E., Eastwood, S., and Niedźwiedź, T. (2016). Recent warming on Spitsbergen—Influence of atmospheric circulation and sea ice cover. *J. Geophys. Res. Atmos.* 121, 11,911-913,931. doi:10.1002/2016JD025606.
Islam, M. N., Almazroui, M., Dambul, R., Jones, P. D., and Alamoudi, A. O. (2015). Long-term changes in seasonal temperature extremes over Saudi Arabia during 1981-2010. *Int. J. Climatol.* 35, 1579–1592. doi:10.1002/joc.4078.

Iturbide, M., Bedia, J., Herrera, S., Baño-Medina, J., Fernández, J., Frías, M. D., et al. (2019). The R-based climate4R open framework for reproducible climate data access and post-processing. *Environ. Model. Softw.* 111, 42–54. doi:10.1016/j.envsoft.2018.09.009.

Iturbide, M., Gutiérrez, J. M., Alves, L., Bedia, J., Cerezo-Mota, R., Di Luca, A., et al. (submitted). An update of IPCC climate reference regions for subcontinental analysis of climate model data: definition and aggregated datasets. *Earth Syst. Sci. Data Discuss.* (submitted.

Ivanov, M., Warrach-Sagi, K., and Wulfmeyer, V. (2017). Field significance of performance measures in the context of regional climate model evaluation. Part 1: temperature. *Theor. Appl. Climatol.*, 1–19. doi:10.1007/s00704-017-2100-2.

Jacob, D. (2001). A note to the simulation of the annual and inter-annual variability of the water budget over the Baltic Sea drainage basin. *Meteorol Atmos Phys* 77, 61–73. doi:https://doi.org/10.1007/s007030170017.

Jacob, D., Kotova, L., Teichmann, C., Sobolowski, S. P., Vautard, R., Donnelly, C., et al. (2018). Climate Impacts in Europe Under +1.5°C Global Warming. *Earth's Futur.* doi:10.1002/2017EF000710.

James, R., Washington, R., Abiodun, B., Kay, G., Mutemi, J., Pokam, W., et al. (2018). Evaluating climate models with an African lens. *Bull. Am. Meteorol. Soc.* doi:10.1175/BAMS-D-16-0090.1.

Jeong, D. Il, and Sushama, L. (2018). Rain-on-snow events over North America based on two Canadian regional climate models. *Clim. Dyn.* 50, 303–316. doi:10.1007/s00382-017-3609-x.

Jin, C.-S., Cha, D. H., Lee, D. K., Suh, M. S., Hong, S. Y., Kang, H. S., et al. (2016). Evaluation of climatological tropical cyclone activity over the western North Pacific in the CORDEX-East Asia multi-RCM simulations. *Clim. Dyn.* 47, 765–778. doi:10.1007/s00382-015-2869-6.

Jin, Q., and Wang, C. (2017). A revival of Indian summer monsoon rainfall since 2002. *Nat. Clim. Chang.* 7, 587. Available at: https://doi.org/10.1038/nclimate3348.

Jin, Q., Wei, J., Yang, Z.-L., and Lin, P. (2017). Irrigation-Induced Environmental Changes around the Aral Sea: An Integrated View from Multiple Satellite Observations. *Remote Sens.* 9. doi:10.3390/rs9090900.

Joetzjer, E., Douville, H., Delire, C., and Ciais, P. (2013). Present-day and future Amazonian precipitation in global climate models: CMIP5 versus CMIP3. *Clim. Dyn.* 41, 2921–2936. doi:10.1007/s00382-012-1644-1.

Jones, C., and Carvalho, L. M. V. (2013). Climate Change in the South American Monsoon System: Present Climate and CMIP5 Projections. *J. Clim.* 26, 6660–6678. doi:10.1175/JCLI-D-12-00412.1.

Jones, D. A., Collins, D., Mcgree, S., Trewin, B. C., Skilling, E. J., Diamond, H. J., et al. (2013). An updated analysis of homogeneous temperature data at Pacific Island stations. in.

Jones, J. M., Gille, S. T., Goosse, H., Abram, N. J., Canziani, P. O., Charman, D. J., et al. (2016a). Assessing recent trends in high-latitude Southern Hemisphere surface climate. *Nat. Clim. Chang.* 6, 917–926. doi:10.1038/nclimate3103.

Jones, M. D., and Song, G. (2014). Making Sense of Climate Change: How Story Frames Shape Cognition. *Polit. Psychol.* 35, 447–476. doi:10.1111/pops.12057.

Jones, P. D., Harpham, C., Harris, I., Goodess, C. M., Burton, A., Centella-Artola, A., et al. (2016b). Long-term trends in precipitation and temperature across the Caribbean. *Int. J. Climatol.* 36, 3314–3333. doi:10.1002/joc.4557.

Jones, P. D., Lister, D. H., Osborn, T. J., Harpham, C., Salmon, M., and Morice, C. P. (2012). Hemispheric and large-scale land-surface air temperature variations: An extensive revision and an update to 2010. *J. Geophys. Res. Atmos.* 117, n/a-n/a. doi:10.1029/2011JD017139.

Juneng, L., Tangang, F., Chung, J. X., Ngai, S. T., Tay, T. W., Narisma, G., et al. (2016). Sensitivity of Southeast Asia rainfall simulations to cumulus and air-sea flux parameterizations in RegCM4. *Clim. Res.* 69, 59–77. doi:10.3354/cr01386.

Jury, M. R. (2013). Climate trends in southern Africa. *S. Afr. J. Sci.* doi:10.1590/sajs.2013/980.

Jury, M. W., Herrera, S., Gutiérrez, J. M., and Barriopedro, D. (2018). Blocking representation in the ERA-Interim driven EURO-CORDEX RCMs. *Clim. Dyn.* doi:10.1007/s00382-018-4335-8.

Kalognomou, E. A., Lennard, C., Shongwe, M., Pinto, I., Favre, A., Kent, M., et al. (2013). A diagnostic evaluation of precipitation in CORDEX models over Southern Africa. *J. Clim.* doi:10.1175/JCLI-D-12-00703.1.

Kamil, S., Almazroui, M., Kang, I. S., Hanif, M., Kucharski, F., Abid, M. A., et al. (2019). Long-term ENSO relationship to precipitation and storm frequency over western Himalaya–Karakoram–Hindukush region during the winter season. *Clim. Dyn.* doi:10.1007/s00382-019-04859-1.

Kang, I. S., Rashid, I. U., Kucharski, F., Almazroui, M., and Alkhalaf, A. K. (2015). Multidecadal changes in the relationship between ENSO and wet-season precipitation in the Arabian Peninsula. *J. Clim.* doi:10.1175/JCLI-D-14-00388.1.

Kang, S., Im, E.-S., and Eltahir, E. A. B. (2019). Future climate change enhances rainfall seasonality in a regional model of western Maritime Continent. *Clim. Dyn.* 52, 747–764. doi:10.1007/s00382-018-4164-9.

Kaplan, A., Cane, M. A., Kushnir, Y., Clement, A. C., Blumenthal, M. B., and Rajagopalan, B. (1998). Analyses of global sea surface temperature 1856-1991. *J. Geophys. Res. Ocean.* 103, 18567–18589. doi:10.1029/97JC01736.

Kapnick, S. B., Delworth, T. L., Ashfaq, M., Malyshev, S., and Milly, P. C. D. (2014). Snowfall less sensitive to warming in Karakoram than in Himalayas due to a unique seasonal cycle. *Nat. Geosci.* 7, 834–840. doi:10.1038/ngeo2269.

Karki, R., Hasson, S. ul, Gerlitz, L., Talchabhadel, R., Schickhoff, U., Scholten, T., et al. (2019). Rising mean and extreme near surface air temperature across Nepal. *Int. J. Climatol.*, joc.6344. doi:10.1002/joc.6344.

Karmacharya, J., New, M., Jones, R., and Levine, R. (2016). Added value of a high-resolution regional climate model in simulation of intraseasonal variability of the South Asian summer monsoon. doi:10.1002/joc.4767.

Karmalkar, A. V., Taylor, M. A., Campbell, J., Stephenson, T., New, M., Centella, A., et al. (2013). A review of observed and projected changes in climate for the islands in the Caribbean. *Atmósfera* 26, 283–309. doi:10.1016/S0187-6236(13)71076-2.

Karmalkar, A. V., Bradley, R. S., and Diaz, H. F. (2011). Climate change in Central America and Mexico: regional climate model validation and climate change projections. *Clim. Dyn.* 37, 605–629. doi:10.1007/s00382-011-1099-9.

Karmalkar, A. V (2018). Interpreting Results from the NARCCAP and NA-CORDEX Ensembles in the Context of Uncertainty in Regional Climate Change Projections. *Bull. Am. Meteorol. Soc.* 99, 2093–2106. doi:10.1175/BAMS-D-17-0127.1.

Katragkou, E., García-Díez, M., Vautard, R., Sobolowski, S., Zanis, P., Alexandri, G., et al. (2015). Regional climate hindcast simulations within EURO-CORDEX: evaluation of a WRF multi-physics ensemble. *Geosci. Model Dev.* 8, 603–618. doi:10.5194/gmd-8-603-2015.

Kattsov, V. M., Shkolnik, I. M., and Efimov, S. V. (2017a). Climate change projections in Russian regions: The detailing in physical and probability spaces. *Russ. Meteorol. Hydrol.* 42, 452–460. doi:10.3103/S1068373917070044.

Kattsov, V. M., Shkolnik, I. M., and Efimov, S. V (2017b). Climate change projections in Russian regions: The detailing in physical and probability spaces. *Russ. Meteorol. Hydrol.* 42, 452–460. doi:10.3103/S1068373917070044.

Kattsov, V. M., Walsh, J. E., Chapman, W. L., Govorkova, V. A., Pavlova, T. V., and Zhang, X. (2007). Simulation and Projection of Arctic Freshwater Budget Components by the IPCC AR4 Global Climate Models. *J. Hydrometeorol.* 8, 571–589. doi:10.1175/jhm575.1.

Katzfey, J., Nguyen, K., McGregor, J., Hoffmann, P., Ramasamy, S., Nguyen, H. Van, et al. (2016). High-resolution simulations for Vietnam - methodology and evaluation of current climate. *Asia-Pacific J. Atmos. Sci.* 52, 91–106. doi:10.1007/s13143-016-0011-2.

Kaufman, D. S., Schneider, D. P., McKay, N. P., Ammann, C. M., Bradley, R. S., Briffa, K. R., et al. (2009). Recent warming reverses long-term arctic cooling. *Science (80-.).* doi:10.1126/science.1173983.

Kause, A., Townsend, T., and Gaissmaier, W. (2019). Framing Climate Uncertainty: Frame Choices Reveal and Influence Climate Change Beliefs. *Weather. Clim. Soc.* 11, 199–215. doi:10.1175/WCAS-D-18-0002.1.

Kaye, N. R., Hartley, A., and Hemming, D. (2012). Mapping the climate: guidance on appropriate techniques to map climate variables and their uncertainty. *Geosci. Model Dev.* 5, 245–256. doi:10.5194/gmd-5-245-2012.

Kendon, E. J., Ban, N., Roberts, N. M., Fowler, H. J., Roberts, M. J., Chan, S. C., et al. (2016). Do Convection-Permitting Regional Climate Models Improve Projections of Future Precipitation Change? *Bull. Am. Meteorol. Soc.* 98, 79–93. doi:10.1175/BAMS-D-15-0004.1.

Kendon, E. J., Roberts, N. M., Fowler, H. J., Roberts, M. J., Chan, S. C., and Senior, C. A. (2014). Heavier summer downpours with climate change revealed by weather forecast resolution model. *Nat. Clim. Chang.* 4, 570–576. doi:10.1038/nclimate2258.

Kennedy, J. J., Rayner, N. A., Smith, R. O., Parker, D. E., and Saunby, M. (2011a). Reassessing biases and other uncertainties in sea surface temperature observations measured in situ since 1850: 1. Measurement and sampling uncertainties. *J. Geophys. Res. Atmos.* 116. doi:10.1029/2010JD015218.

Kennedy, J. J., Rayner, N. A., Smith, R. O., Parker, D. E., and Saunby, M. (2011b). Reassessing biases and other uncertainties in sea surface temperature observations measured in situ since 1850: 2. Biases and homogenization. *J. Geophys. Res. Atmos.* 116. doi:10.1029/2010JD015220.

Kharyutkina, E. V., Loginov, S. V., and Ippolitov, I. I. (2016). Influence of radiation and circulation factors on climate change in Western Siberia at the end of the 20th century and beginning of the 21st century. *Izv. - Atmos. Ocean Phys.* 52, 579–586. doi:10.1134/S0001433816060098.

Khlebnikova, E. I., Kattsov, V. M., Pikaleva, A. A., and Shkolnik, I. M. (2018). Assessment of Climate Change Impacts on the Economic Development of the Russian Arctic in the 21st Century. *Russ. Meteorol. Hydrol.* 43, 347–356. doi:10.3103/S1068373918060018.

Khlebnikova, E. I., Rudakova, Y. L., Sall', I. A., Efimov, S. V, and Shkolnik, I. M. (2019a). Changes in Indicators of Temperature Extremes in the 21st Century: Ensemble Projections for the Territory of Russia. *Russ. Meteorol. Hydrol.* 44, 159–168. doi:10.3103/S1068373919030014.

Khlebnikova, E. I., Rudakova, Y. L., and Shkolnik, I. M. (2019b). Changes in Precipitation Regime over the Territory of Russia: Data of Regional Climate Modeling and Observations. *Russ. Meteorol. Hydrol.* 44, 431–439. doi:10.3103/S106837391907001X.

Khlebnikova, E. I., Rudakova, Y. L., and Shkolnik, I. M. (2019c). Changes in Precipitation Regime over the Territory of Russia: Data of Regional Climate Modeling and Observations. *Russ. Meteorol. Hydrol.* 44, 431–439. doi:10.3103/S106837391907001X.

Kieu-Thi, X., Vu-Thanh, H., Nguyen-Minh, T., Le, D., Nguyen-Manh, L., Takayabi, I., et al. (2016). Rainfall and Tropical Cyclone Activity over Vietnam Simulated and Projected by the Non-Hydrostatic Regional Climate Model - NHRCM. *J. Meteorol. Soc. Japan. Ser. II* 94A, 135–150. doi:10.2151/jmsj.2015-057.

Kim, H.-S., Chung, Y.-S., Tans, P. P., and Yoon, M.-B. (2016a). Climatological variability of air temperature and precipitation observed in South Korea for the last 50 years. *Air Qual. Atmos. Heal.* 9, 645–651. doi:10.1007/s11869-015-0366-z.

Kim, I. W., Oh, J., Woo, S., and Kripalani, R. H. (2018). Evaluation of precipitation extremes over the Asian domain: observation and modelling studies. *Clim. Dyn.* 52, 1–26. doi:10.1007/s00382-018-4193-4.

Kim, J. Y., and Kim, K. Y. (2019). Relative role of horizontal and vertical processes in the physical mechanism of wintertime Arctic amplification. *Clim. Dyn.* 52, 6097–6107. doi:10.1007/s00382-018-4499-2.

Kim, Y., Jun, M., Min, S.-K., Suh, M.-S., and Kang, H.-S. (2016b). Spatial analysis of future East Asian seasonal temperature using two regional climate model simulations. *Asia-Pacific J. Atmos. Sci.* 52, 237–249. doi:10.1007/s13143-016-0022-z.

King, J. C., Kirchgaessner, A., Bevan, S., Elvidge, A. D., Kuipers Munneke, P., Luckman, A., et al. (2017). The Impact of Föhn Winds on Surface Energy Balance During the 2010–2011 Melt Season Over Larsen C Ice Shelf, Antarctica. *J. Geophys. Res. Atmos.* 122, 12,062-12,076. doi:10.1002/2017JD026809.

Kirono, D. G., Butler, J. R., McGregor, J. L., Ripaldi, A., Katzfey, J., and Nguyen, K. (2015). Historical and future seasonal rainfall variability in Nusa Tenggara Barat Province, Indonesia: Implications for the agriculture and water sectors. *Clim. Risk Manag.* 12, 45–58. doi:10.1016/j.crm.2015.12.002.

Kisembe, J., Favre, A., Dosio, A., Lennard, C., Sabiiti, G., and Nimusiima, A. (2018). Evaluation of rainfall simulations over Uganda in CORDEX regional climate models. *Theor. Appl. Climatol.* doi:10.1007/s00704-018-2643-x.

KITOH, A. (2017). The Asian Monsoon and its Future Change in Climate Models: A Review. *J. Meteorol. Soc. Japan. Ser. II* 95, 7–33. doi:10.2151/jmsj.2017-002.

Kivinen, S., Rasmus, S., Jylhä, K., and Laapas, M. (2017). Long-Term Climate Trends and Extreme Events in Northern Fennoscandia (1914–2013). *Climate* 5, 16. doi:10.3390/cli5010016.

Kjellström, E., Nikulin, G., Strandberg, G., Christensen, O. B., Jacob, D., Keuler, K., et al. (2018). European climate change at global mean temperature increases of 1.5 and 2 °C above pre-industrial conditions as simulated by the EURO-CORDEX regional climate models. *Earth Syst. Dyn.* 9, 459–478. doi:10.5194/esd-9-459-2018.

Klutse, N. A. B., Ajayi, V. O., Gbobaniyi, E. O., Egbebiyi, T. S., Kouadio, K., Nkrumah, F., et al. (2018). Potential impact of 1.5 °C and 2 °C global warming on consecutive dry and wet days over West Africa. *Environ. Res. Lett.* doi:10.1088/1748-9326/aab37b.

Klutse, N. A. B., Sylla, M. B., Diallo, I., Sarr, A., Dosio, A., Diedhiou, A., et al. (2016). Daily characteristics of West African summer monsoon precipitation in CORDEX simulations. *Theor. Appl. Climatol.* 123. doi:10.1007/s00704-014-1352-3.

Knippertz, P., Christoph, M., and Speth, P. (2003). Long-term precipitation variability in Morocco and the link to the large-scale circulation in recent and future climates. *Meteorol. Atmos. Phys.* doi:10.1007/s00703-002-0561-y.

Knowles, N. (2015). Trends in snow cover and related quantities at weather stations in the conterminous United States. *J. Clim.* 28, 7518–7528. doi:10.1175/JCLI-D-15-0051.1.

Knutson, T. R., and Zeng, F. (2018). Model Assessment of Observed Precipitation Trends over Land Regions: Detectable Human Influences and Possible Low Bias in Model Trends. *J. Clim.* 31, 4617–4637. doi:10.1175/JCLI-D-17-0672.1.

Kobashi, T., Kawamura, K., Severinghaus, J. P., Barnola, J. M., Nakaegawa, T., Vinther, B. M., et al. (2011). High variability of Greenland surface temperature over the past 4000 years estimated from trapped air in an ice core. *Geophys. Res. Lett.* 38. doi:10.1029/2011GL049444.

Kobashi, T., Severinghaus, J. P., Barnola, J. M., Kawamura, K., Carter, T., and Nakaegawa, T. (2010). Persistent multi-decadal Greenland temperature fluctuation through the last millennium. *Clim. Change*. doi:10.1007/s10584-009-9689-9.

Koenigk, T., Berg, P., and Döscher, R. (2015). Arctic climate change in an ensemble of regional CORDEX simulations. *Polar Res.* 34, 1–19. doi:10.3402/polar.v34.24603.

Kohnemann, S. H. E., Heinemann, G., Bromwich, D. H., and Gutjahr, O. (2017). Extreme Warming in the Kara Sea and Barents Sea during the Winter Period 2000–16. *J. Clim.* 30, 8913–8927. doi:10.1175/JCLI-D-16-0693.1.

Kokorev, V. A., and Sherstiukov, A. B. (2015). METEOROLOGICAL DATA FOR STUDYING THE CURRRENT AND PROJECTED FOR THE FUTURE CLIMATE CHANGE IN RUSSIA. *Arctica.Natural Sci.* 3, 5–23. Available at: http://meteo.ru.

Komarov, V. S., Lomakina, N. Y., Lavrinenko, A. V., and Ily'in, S. N. (2010). Changes of the atmospheric boundary layer climates of Siberia in the period of global warming. Part 1. Anomalies and trends of the air temperature. *OpticsAtmOcean* 23, 942–950.

Komurcu Bayraktar, M., Emanuel, K. A., Huber, M., and Acosta, R. P. (2018). High-Resolution Climate Projections for the Northeastern United States Using Dynamical Downscaling at Convection-Permitting Scales.

Kossin, J. P. (2018). A global slowdown of tropical-cyclone translation speed. *Nature* 558, 104–107. doi:10.1038/s41586-018-0158-3.

Kossin, J. P., Emanuel, K. A., and Vecchi, G. A. (2014). The poleward migration of the location of tropical cyclone maximum intensity. *Nature* 509, 349–352. doi:10.1038/nature13278.

Kossin, J. P., Olander, T. L., and Knapp, K. R. (2013). Trend analysis with a new global record of tropical cyclone intensity. *J. Clim.* 26, 9960–9976. doi:10.1175/JCLI-D-13-00262.1.

Koster, R. D., Dirmeyer, P. A., Hahmann, A. N., Ijpelaar, R., Tyahla, L., Cox, P., et al. (2002). Comparing the Degree of Land–Atmosphere Interaction in Four Atmospheric General Circulation Models. *J. Hydrometeorol.* 3, 363–375. doi:10.1175/1525-7541(2002)003<0363:CTDOLA>2.0.CO;2.

Koster, R. D., Suarez, M. J., and Heiser, M. (2000). Variance and Predictability of Precipitation at Seasonal-to-Interannual Timescales. *J. Hydrometeorol.* 1, 26–46. doi:10.1175/1525-7541(2000)001<0026:VAPOPA>2.0.CO;2.

Kotcher, J. E., Myers, T. A., Vraga, E. K., Stenhouse, N., and Maibach, E. W. (2017). Does Engagement in Advocacy Hurt the Credibility of Scientists? Results from a Randomized National Survey Experiment. *Environ. Commun.* 11, 415–429. doi:10.1080/17524032.2016.1275736.

Kotlarski, S., Keuler, K., Christensen, O. B., Colette, A., Déqué, M., Gobiet, A., et al. (2014). Regional climate modeling on European scales: a joint standard evaluation of the EURO-CORDEX RCM ensemble. *Geosci. Model Dev.* 7, 1297–1333. doi:10.5194/gmd-7-1297-2014.

Kotlarski, S., Szabó, P., Herrera, S., Räty, O., Keuler, K., Soares, P. M., et al. (2017). Observational uncertainty and regional climate model evaluation: A pan-European perspective. *Int. J. Climatol.*, 1–20. doi:10.1002/joc.5249.

Kovacs, K. M., Aguilar, A., Aurioles, D., Burkanov, V., Campagna, C., Gales, N., et al. (2012). Global threats to pinnipeds. *Mar. Mammal Sci.* 28, 414–436. doi:10.1111/j.1748-7692.2011.00479.x.

Kozhakhmetov, P. Z., and Nikiforova, L. N. (2016). *Weather disasters in Kazakhstan in the context of global climate change*. Astana Available at: https://new.kazhydromet.kz/upload/pagefiles/nits/УКИ НИЦ/Climate Change_09-2017_RUS_Light.pdf [Accessed April 3, 2019].

Krakovska, S. V. (2018). Optimal ensemble of regional climate models for the ssessment of temperature regime change in Ukraine. *Nat. Manag.* 12, 114–126.

Krakovska, S. V., Palamarchuk, L. V., Gnatiuk, N. . V., Shpytal, T. M., and Shedemenko, I. P. (2017). CHANGES IN PRECIPITATION DISTRIBUTION IN UKRAINE FOR THE 21ST CENTURY BASED ON DATA OF REGIONAL CLIMATE MODEL ENSEMBLE. *Geoinformatika* 64, 62–74. Available at: https://www.researchgate.net/publication/322103650.

Krakovska, S. V., Palamarchuk, L. V., and Shpytal, T. M. (2019). Climatic projections of heating season in Ukraine up to the middle of the 21st century. *Geofiz. Zhurnal* 41, 144–164. doi:doi.org/10.24028/gzh.0203-3100.v41i6.2019.190072.

Krasting, J. P., Broccoli, A. J., Dixon, K. W., and Lanzante, J. R. (2013). Future changes in northern hemisphere snowfall. *J. Clim.* 26, 7813–7828. doi:10.1175/JCLI-D-12-00832.1.

Krieger, G., Moreira, A., Fiedler, H., Hajnsek, I., Werner, M., Younis, M., et al. (2007). TanDEM-X: A Satellite Formation for High-Resolution SAR Interferometry. *IEEE Trans. Geosci. Remote Sens.* 45, 3317–3341. doi:10.1109/TGRS.2007.900693.

Krishnan, R., Sabin, T. P., Ayantika, D. C., Kitoh, A., Sugi, M., Murakami, H., et al. (2013). Will the South Asian monsoon overturning circulation stabilize any further? *Clim. Dyn.* doi:10.1007/s00382-012-1317-0.

Krishnan, R., Sabin, T. P., Vellore, R., Mujumdar, M., Sanjay, J., Goswami, B. N., et al. (2016). Deciphering the desiccation trend of the South Asian monsoon hydroclimate in a warming world. *Clim. Dyn.* 47, 1007–1027. doi:10.1007/s00382-015-2886-5.

Krishnan, R., Shrestha, A. B., Ren, G., Rajbhandari, R., Saeed, S., Sanjay, J., et al. (2019a). "Unravelling Climate Change in the Hindu Kush Himalaya: Rapid Warming in the Mountains and Increasing Extremes," in *The Hindu Kush Himalaya Assessment* (Springer International Publishing), 57–97. doi:10.1007/978-3-319-92288-1_3.

Krishnan, R., Shrestha, A. B., Ren, G., Rajbhandari, R., Saeed, S., Sanjay, J., et al. (2019b). "Unravelling Climate Change in the Hindu Kush Himalaya: Rapid Warming in the Mountains and Increasing Extremes," in *The Hindu Kush Himalaya Assessment* (Cham: Springer International Publishing), 57–97. doi:10.1007/978-3-319-92288-1_3.

Kröner, N., Kotlarski, S., Fischer, E., Lüthi, D., Zubler, E., and Schär, C. (2017). Separating climate change signals into thermodynamic, lapse-rate and circulation effects: theory and application to the European summer climate. *Clim. Dyn.* 48, 3425–3440. doi:10.1007/s00382-016-3276-3.

Kruger, A. C., and Sekele, S. S. (2013). Trends in extreme temperature indices in South Africa: 1962-2009. *Int. J. Climatol.* doi:10.1002/joc.3455.

Kruger, A. C., and Shongwe, S. (2004). Temperature trends in South Africa: 1960-2003. *Int. J. Climatol.* doi:10.1002/joc.1096.

Kug, J.-S., Jeong, J.-H., Jang, Y.-S., Kim, B.-M., Folland, C. K., Min, S.-K., et al. (2015). Two distinct influences of Arctic warming on cold winters over North America and East Asia. *Nat. Geosci.* 8, 759–762. doi:10.1038/ngeo2517.

Kuipers Munneke, P., Luckman, A. J., Bevan, S. L., Smeets, C. J. P. P., Gilbert, E., van den Broeke, M. R., et al. (2018). Intense Winter Surface Melt on an Antarctic Ice Shelf. *Geophys. Res. Lett.* 45, 7615–7623.

doi:10.1029/2018GL077899.
Kulkarni, A., Deshpande, N., Kothawale, D., Sabade, S., Ramarao, M., Sabin, T., et al. (2017). "Observed climate variability and change over India," in *Climate Change over INDIA: An Interim Report*, eds. R. Krishnan and J. Sanjay (Centre for Climate Change Research, IITM), 3–9.
Kumi, N., and Abiodun, B. J. (2018). Potential impacts of 1.5 °c and 2 °c global warming on rainfall onset, cessation and length of rainy season in West Africa. *Environ. Res. Lett.* doi:10.1088/1748-9326/aab89e.
Kunkel, K. E., Palecki, M. A., Hubbard, K. G., Robinson, D. A., Redmond, K. T., and Easterling, D. R. (2007). Trend identification in twentieth-century U.S. snowfall: The challenges. *J. Atmos. Ocean. Technol.* 24, 64–73. doi:10.1175/JTECH2017.1.
Kunkel, K. E., Robinson, D. A., Champion, S., Yin, X., Estilow, T., and Frankson, R. M. (2016). Trends and Extremes in Northern Hemisphere Snow Characteristics. *Curr. Clim. Chang. Reports* 2, 65–73. doi:10.1007/s40641-016-0036-8.
Kurtz, N. T., and Farrell, S. L. (2011). Large-scale surveys of snow depth on Arctic sea ice from Operation IceBridge. *Geophys. Res. Lett.* 38, n/a-n/a. doi:10.1029/2011GL049216.
Kusunoki, S. (2017). Future changes in global precipitation projected by the atmospheric model MRI-AGCM3.2H with a 60-km size. *Atmosphere (Basel).* 8, 6–14. doi:10.3390/atmos8050093.
Kusunoki, S. (2018a). Future changes in precipitation over East Asia projected by the global atmospheric model MRI-AGCM3.2. *Clim. Dyn.* 51, 4601–4617. doi:10.1007/s00382-016-3499-3.
Kusunoki, S. (2018b). Is the global atmospheric model MRI-AGCM3.2 better than the CMIP5 atmospheric models in simulating precipitation over East Asia? *Clim. Dyn.* 51, 4489–4510. doi:10.1007/s00382-016-3335-9.
Kusunoki, S., Mizuta, R., and Hosaka, M. (2015). Future changes in precipitation intensity over the Arctic projected by a global atmospheric model with a 60-km grid size. *Polar Sci.* 9, 277–292. doi:https://doi.org/10.1016/j.polar.2015.08.001.
Kwan, M. S., Tangang, F. T., and Juneng, L. (2014). Present-day regional climate simulation over Malaysia and western Maritime Continent region using PRECIS forced with ERA40 reanalysis. *Theor. Appl. Climatol.* 115, 1–14. doi:10.1007/s00704-013-0873-5.
Lakoff, G. (2010). Why it Matters How We Frame the Environment. *Environ. Commun.* 4, 70–81. doi:10.1080/17524030903529749.
Lange, B. A., Haas, C., Charette, J., Katlein, C., Campbell, K., Duerksen, S., et al. (2019). Contrasting ice algae and snow-dependent irradiance relationships between landfast first-year and multi-year sea ice. *Geophys. Res. Lett.* doi:10.1029/2019gl082873.
Lange, S. (2019). EartH2Observe, WFDEI and ERA-Interim data Merged and Bias-corrected for ISIMIP (EWEMBI). V. 1.1. GFZ Data Services. doi:http://doi.org/10.5880/pik.2019.004.
Larue, F., Royer, A., De Sève, D., Langlois, A., Roy, A., and Brucker, L. (2017). Validation of GlobSnow-2 snow water equivalent over Eastern Canada. *Remote Sens. Environ.* 194, 264–277. doi:10.1016/j.rse.2017.03.027.
Latif, M. (2017). Analysis of rainfall trends over Indo-Pakistan summer monsoon and related dynamics based on CMIP5 climate. doi:10.1002/joc.5391.
Latif, M., Syed, F. S., and Hannachi, A. (2017). Rainfall trends in the South Asian summer monsoon and its related large-scale dynamics with focus over Pakistan. *Clim. Dyn.* 48, 3565–3581. doi:10.1007/s00382-016-3284-3.
Laxon, S. W., Giles, K. A., Ridout, A. L., Wingham, D. J., Willatt, R., Cullen, R., et al. (2013). CryoSat-2 estimates of Arctic sea ice thickness and volume. *Geophys. Res. Lett.* 40, 732–737. doi:10.1002/grl.50193.
Leach, N., Li, S., Sparrow, S., van Oldenborgh, G. J., Lott, F. C., Weisheimer, A., et al. (2019). "Anthropogenic influence on the 2018 summer warm spell in Europe: the impact of different spatio-temporal scales," in *Explaining extreme events from a climate perspective* (Bulletin of the American Meteorological Society). Available at: https://www.ametsoc.org/ams/index.cfm/publications/bulletin-of-the-american-meteorological-society-bams/explaining-extreme-events-from-a-climate-perspective/.
Leduc, M., Mailhot, A., Frigon, A., Martel, J.-L., Ludwig, R., Brietzke, G. B., et al. (2019). The ClimEx Project: A 50-Member Ensemble of Climate Change Projections at 12-km Resolution over Europe and Northeastern North America with the Canadian Regional Climate Model (CRCM5). *J. Appl. Meteorol. Climatol.* 58, 663–693. doi:10.1175/JAMC-D-18-0021.1.
Lee, J.-Y., Kwon, M., Yun, K.-S., Min, S.-K., Park, I.-H., Ham, Y.-G., et al. (2017). The long-term variability of Changma in the East Asian summer monsoon system: A review and revisit. *Asia-Pacific J. Atmos. Sci.* 53, 257–272. doi:10.1007/s13143-017-0032-5.
Legasa, M. N., Manzanas, R., Fernández, J., Herrera, S., Iturbide, M., Moufouma-Okia, W., et al. (submitted). Assessing potential conflicts and grand ensemble 2 generation in multi-domain CORDEX regional 3 projections. *Geophys. Res. Lett.* (submitted.
Lelieveld, J., Proestos, Y., Hadjinicolaou, P., Tanarhte, M., Tyrlis, E., and Zittis, G. (2016). Strongly increasing heat extremes in the Middle East and North Africa (MENA) in the 21st century. *Clim. Change*. doi:10.1007/s10584-016-1665-6.
Lemos, M. C., Kirchhoff, C. J., and Ramprasad, V. (2012). Narrowing the climate information usability gap. *Nat. Clim. Chang.* 2, 789–794. doi:10.1038/nclimate1614.

Lenaerts, J. T. M., Fyke, J., and Medley, B. (2018). The Signature of Ozone Depletion in Recent Antarctic Precipitation Change: A Study With the Community Earth System Model. *Geophys. Res. Lett.* 45, 12,931-12,939. doi:10.1029/2018GL078608.

Lenaerts, J. T. M., Medley, B., van den Broeke, M. R., and Wouters, B. (2019). Observing and Modeling Ice Sheet Surface Mass Balance. *Rev. Geophys.* 57, 376–420. doi:10.1029/2018RG000622.

Lenaerts, J. T. M., van Meijgaard, E., van den Broeke, M. R., Ligtenberg, S. R. M., Horwath, M., and Isaksson, E. (2013). Recent snowfall anomalies in Dronning Maud Land, East Antarctica, in a historical and future climate perspective. *Geophys. Res. Lett.* 40, 2684–2688. doi:10.1002/grl.50559.

Lenaerts, J. T. M., Vizcaino, M., Fyke, J., van Kampenhout, L., and van den Broeke, M. R. (2016). Present-day and future Antarctic ice sheet climate and surface mass balance in the Community Earth System Model. *Clim. Dyn.* 47, 1367–1381. doi:10.1007/s00382-015-2907-4.

Lenderink, G., Belušić, D., Fowler, H. J., Kjellström, E., Lind, P., van Meijgaard, E., et al. (2019). Systematic increases in the thermodynamic response of hourly precipitation extremes in an idealized warming experiment with a convection-permitting climate model. *Environ. Res. Lett.* 14, 074012. doi:10.1088/1748-9326/ab214a.

Lenderink, G., Van Den Hurk, B. J. J. M., Klein Tank, A. M. G., Van Oldenborgh, G. J., Van Meijgaard, E., De Vries, H., et al. (2014). Preparing local climate change scenarios for the Netherlands using resampling of climate model output. *Environ. Res. Lett.* 9. doi:10.1088/1748-9326/9/11/115008.

Lennard, C., Nikulin, G., Dosio, A., and Moufouma-Okia, W. (2018). On the need for regional climate information over Africa under varying levels of global warming. *Environ. Res. Lett.* doi:10.1088/1748-9326/aab2b4.

Lewandowsky, S., Oreskes, N., Risbey, J. S., Newell, B. R., and Smithson, M. (2015). Seepage: The effect of climate denial on the scientific community. *Glob. Environ. Chang.* 33, 1–13. doi:10.1016/j.gloenvcha.2015.02.013.

Li, B., Chen, Y., Shi, X., Chen, Z., and Li, W. (2013). Temperature and precipitation changes in different environments in the arid region of northwest China. *Theor. Appl. Climatol.* 112, 589–596. doi:10.1007/s00704-012-0753-4.

Li, D., Yin, B., Feng, J., Dosio, A., Geyer, B., Qi, J. F., et al. (2018a). Present climate evaluation and added value analysis of dynamically downscaled simulations of CORDEX-East Asia. *J. Appl. Meteorol. Climatol.* 57, 2317–2341. doi:10.1175/JAMC-D-18-0008.1.

Li, D., Zhou, T., Zou, L., Zhang, W., and Zhang, L. (2018b). Extreme High-Temperature Events Over East Asia in 1.5°C and 2°C Warmer Futures: Analysis of NCAR CESM Low-Warming Experiments. *Geophys. Res. Lett.* 45, 1541–1550. doi:10.1002/2017GL076753.

Li, H., Xu, C. Y., Beldring, S., Tallaksen, L. M., and Jain, S. K. (2016). Water resources under climate change in himalayan basins. *Water Resour. Manag.* 30, 843–859. doi:10.1007/s11269-015-1194-5.

Li, J., Liu, Z., Yao, Z., and Wang, R. (2019). Comprehensive assessment of Coupled Model Intercomparison Project Phase 5 global climate models using observed temperature and precipitation over mainland Southeast Asia. *Int. J. Climatol.* 39, 4139–4153. doi:10.1002/joc.6064.

Li, J., Yu, R., Yuan, W., Chen, H., Sun, W., and Zhang, Y. (2015a). Precipitation over East Asia simulated by NCAR CAM5 at different horizontal resolutions. *J. Adv. Model. Earth Syst.* 7, 774–790. doi:10.1002/2014MS000414.

Li, Q., Yang, S., Xu, W., Wang, X. L., Jones, P., Parker, D., et al. (2015b). China experiencing the recent warming hiatus. *Geophys. Res. Lett.* 42, 889–898. doi:10.1002/2014GL062773.

Li, Q., Zhang, L., Xu, W., Zhou, T., Wang, J., Zhai, P., et al. (2017). Comparisons of Time Series of Annual Mean Surface Air Temperature for China since the 1900s: Observations, Model Simulations, and Extended Reanalysis. *Bull. Am. Meteorol. Soc.* 98, 699–711. doi:10.1175/BAMS-D-16-0092.1.

Liebmann, B., Bladé, I., Funk, C., Allured, D., Quan, X. W., Hoerling, M., et al. (2017). Climatology and interannual variability of boreal spring wet season precipitation in the eastern horn of Africa and implications for its recent decline. *J. Clim.* doi:10.1175/JCLI-D-16-0452.1.

Limsakul, A., and Singhruck, P. (2016). Long-term trends and variability of total and extreme precipitation in Thailand. *Atmos. Res.* 169, 301–317. doi:10.1016/J.ATMOSRES.2015.10.015.

Lin, L., Gettelman, A., Xu, Y., Wu, C., Wang, Z., Rosenbloom, N., et al. (2019). CAM6 simulation of mean and extreme precipitation over Asia: sensitivity to upgraded physical parameterizations and higher horizontal resolution. *Geosci. Model Dev.* 12, 3773–3793. doi:10.5194/gmd-12-3773-2019.

Lind, P., Lindstedt, D., Kjellström, E., Jones, C., Lind, P., Lindstedt, D., et al. (2016). Spatial and Temporal Characteristics of Summer Precipitation over Central Europe in a Suite of High-Resolution Climate Models. *J. Clim.* 29, 3501–3518. doi:10.1175/JCLI-D-15-0463.1.

Lindsay, R., Wensnahan, M., Schweiger, A., and Zhang, J. (2014). Evaluation of seven different atmospheric reanalysis products in the arctic. *J. Clim.* 27, 2588–2606. doi:10.1175/JCLI-D-13-00014.1.

Lindvall, J., and Svensson, G. (2015). The diurnal temperature range in the CMIP5 models. *Clim. Dyn.* 44, 405–421. doi:10.1007/s00382-014-2144-2.

Lioubimtseva, E., and Cole, R. (2006). Uncertainties of Climate Change in Arid Environments of Central Asia. *Rev. Fish. Sci.* 14, 29–49. doi:10.1080/10641260500340603.

Liu, C., Ikeda, K., Rasmussen, R., Barlage, M., Newman, A. J., Prein, A. F., et al. (2017a). Continental-scale convection-permitting modeling of the current and future climate of North America. *Clim. Dyn.* 49, 71–95. doi:10.1007/s00382-016-3327-9.

Liu, H. W., Zhou, T. J., Zhu, Y. X., and Lin, Y. H. (2012). The strengthening East Asia summer monsoon since the early 1990s. *Chinese Sci. Bull.* 57, 1553–1558. doi:10.1007/s11434-012-4991-8.

Liu, M., Vecchi, G. A., Smith, J. A., and Murakami, H. (2017b). The Present-Day Simulation and Twenty-First-Century Projection of the Climatology of Extratropical Transition in the North Atlantic. *J. Clim.* 30, 2739–2756. doi:10.1175/JCLI-D-16-0352.1.

Liu, W., Lim, W. H., Sun, F., Mitchell, D., Wang, H., Chen, D., et al. (2018). Global Freshwater Availability Below Normal Conditions and Population Impact Under 1.5 and 2 °C Stabilization Scenarios. *Geophys. Res. Lett.* 45, 9803–9813. doi:10.1029/2018GL078789.

Liu, X., Cheng, Z., Yan, L., and Yin, Z. Y. (2009). Elevation dependency of recent and future minimum surface air temperature trends in the Tibetan Plateau and its surroundings. *Glob. Planet. Change* 68, 164–174. doi:10.1016/j.gloplacha.2009.03.017.

Llopart, M., Coppola, E., Giorgi, F., da Rocha, R. P., and Cuadra, S. V. (2014a). Climate change impact on precipitation for the Amazon and La Plata basins. *Clim. Change* 125, 111–125. doi:10.1007/s10584-014-1140-1.

Llopart, M., Coppola, E., Giorgi, F., da Rocha, R. P., and Cuadra, S. V. (2014b). Climate change impact on precipitation for the Amazon and La Plata basins. *Clim. Change* 125, 111–125. doi:10.1007/s10584-014-1140-1.

Llopart, M., Simões Reboita, M., and Porfírio da Rocha, R. (2019). Assessment of multi-model climate projections of water resources over South America CORDEX domain. *Clim. Dyn.* doi:10.1007/s00382-019-04990-z.

Loginov, V. F., Lysenko, S. A., Danilovich, S., Kamyshenka, H. A., Kalyada, V. V., Melnik, V. I., et al. (2018). CLIMATE RESEARCH IN THE INSTITUTE FOR NATURE MANAGEMENT OF THE NATIONAL ACADEMY OF SCIENCES OF BELARUS. *Nat. Manag.* 1, 67–86.

Loginov, S. V, Ippolitov, I. I., and Kharyutkina, E. V (2014). The relationship of surface air temperature, heat balance at the surface, and radiative balance at the top of atmosphere over the Asian territory of Russia using reanalysis and remote-sensing data. *Int. J. Remote Sens.* 35, 5878–5898. doi:10.1080/01431161.2014.945007.

Loh, J. Le, Tangang, F., Juneng, L., Hein, D., and Lee, D.-I. (2016). Projected rainfall and temperature changes over Malaysia at the end of the 21st century based on PRECIS modelling system. *Asia-Pacific J. Atmos. Sci.* 52, 191–208. doi:10.1007/s13143-016-0019-7.

López-Franca, N., Zaninelli, P., Carril, A., Menéndez, C., and Sánchez, E. (2016). Changes in temperature extremes for 21st century scenarios over South America derived from a multi-model ensemble of regional climate models. *Clim. Res.* 68, 151–167. doi:10.3354/cr01393.

Lorenz, S., Dessai, S., Forster, P. M., and Paavola, J. (2015). Tailoring the visual communication of climate projections for local adaptation practitioners in Germany and the UK. *Philos. Trans. R. Soc. A Math. Phys. Eng. Sci.* 373, 20140457. doi:10.1098/rsta.2014.0457.

Loupian, E., Burtsev, M. A., Bartalev, S. A., and Kashnitskii, A. (2015). IKI center for collective use of satellite data archiving , processing and analysis systems aimed at solving the problems of environmental study and monitoring. *Curr. Probl. Remote Sens. Earth From Sp.* 12, 263–284.

Lowe, J., Bernie, D., Bett, P., Bricheno, L., Brown, S., Calvert, D., et al. (2018). UKCP18 science overview report. Available at: https://www.metoffice.gov.uk/pub/data/weather/uk/ukcp18/science-reports/UKCP18-Overview-report.pdf.

Lucas-Picher, P., Somot, S., Déqué, M., Decharme, B., and Alias, A. (2013). Evaluation of the regional climate model ALADIN to simulate the climate over North America in the CORDEX framework. *Clim. Dyn.* 41, 1117–1137. doi:10.1007/s00382-012-1613-8.

Lucas-Picher, P., Wulff-Nielsen, M., Christensen, J. H., Aoalgeirsdóttir, G., Mottram, R., and Simonsen, S. B. (2012). Very high resolution regional climate model simulations over Greenland: Identifying added value. *J. Geophys. Res. Atmos.* 117. doi:10.1029/2011JD016267.

Luckman, A., Elvidge, A., Jansen, D., Kulessa, B., Kuipers Munneke, P., King, J., et al. (2014). Surface melt and ponding on Larsen C Ice Shelf and the impact of föhn winds. *Antarct. Sci.* 26, 625–635. doi:10.1017/S0954102014000339.

Luo, M., Liu, T., Frankl, A., Duan, Y., Meng, F., Bao, A., et al. (2018). Defining spatiotemporal characteristics of climate change trends from downscaled GCMs ensembles: how climate change reacts in Xinjiang, China. *Int. J. Climatol.* 38, 2538–2553. doi:10.1002/joc.5425.

Luo, M., Liu, T., Meng, F., Duan, Y., Bao, A., Frankl, A., et al. (2019). Spatiotemporal characteristics of future changes in precipitation and temperature in Central Asia. *Int. J. Climatol.* 39, 1571–1588. doi:10.1002/joc.5901.

Lupo, A., and Kininmonth, W. (2013). Global Climate Models and Their Limitations. *Clim. Chang. Reconsidered II Phys. Sci.*, 7–148. doi:10.1038/ncomms2656.

Lussana, C., Saloranta, T., Skaugen, T., Magnusson, J., Tveito, O. E., and Andersen, J. (2018). seNorge2 daily precipitation, an observational gridded dataset over Norway from 1957 to the present day. *Earth Syst. Sci. Data; Katlenburg-Lindau* 10, 235–249. doi:http://dx.doi.org/10.5194/essd-10-235-2018.

Lyon, B. (2014). Seasonal drought in the Greater Horn of Africa and its recent increase during the March-May long rains. *J. Clim.* doi:10.1175/JCLI-D-13-00459.1.

Lyon, B., and Dewitt, D. G. (2012). A recent and abrupt decline in the East African long rains. *Geophys. Res. Lett.* doi:10.1029/2011GL050337.

LYRA, A. de A., CHOU, S. C., and SAMPAIO, G. de O. (2016). Sensitivity of the Amazon biome to high resolution climate change projections. *Acta Amaz.* 46, 175–188. doi:10.1590/1809-4392201502225.

MacKellar, N., New, M., and Jack, C. (2014). Observed and modelled trends in rainfall and temperature for South Africa: 1960-2010. *S. Afr. J. Sci.* doi:10.1590/sajs.2014/20130353.

Maenza, R. A., Agosta, E. A., and Bettolli, M. L. (2017). Climate change and precipitation variability over the western 'Pampas' in Argentina. *Int. J. Climatol.* 37, 445–463. doi:10.1002/joc.5014.

Magaña, V., Amador, J. A., and Medina, S. (1999). The Midsummer Drought over Mexico and Central America. *J. Clim.* 12, 1577–1588. doi:10.1175/1520-0442(1999)012<1577:TMDOMA>2.0.CO;2.

Maldonado, T., Rutgersson, A., Alfaro, E., Amador, J., and Claremar, B. (2016). Interannual variability of the midsummer drought in Central America and the connection with sea surface temperatures. *Adv. Geosci.* 42, 35–50. doi:10.5194/adgeo-42-35-2016.

Maloney, E. D., Camargo, S. J., Chang, E., Colle, B., Fu, R., Geil, K. L., et al. (2014a). North American climate in CMIP5 experiments: Part III: Assessment of twenty-first-century projections. *J. Clim.* 27, 2230–2270. doi:10.1175/JCLI-D-13-00273.1.

Maloney, E. D., Camargo, S. J., Chang, E., Colle, B., Fu, R., Geil, K. L., et al. (2014b). North American Climate in CMIP5 Experiments: Part III: Assessment of Twenty-First-Century Projections. *J. Clim.* 27, 2230–2270. doi:10.1175/JCLI-D-13-00273.1.

Manabe, S., and Stouffer, R. J. (1980). Sensitivity of a global climate model to an increase of CO_2 concentration in the atmosphere. *J. Geophys. Res.* 85, 5529. doi:10.1029/JC085iC10p05529.

Mannig, B., Müller, M., Starke, E., Merkenschlager, C., Mao, W., Zhi, X., et al. (2013). Dynamical downscaling of climate change in Central Asia. *Glob. Planet. Change* 110, 26–39. doi:10.1016/j.gloplacha.2013.05.008.

Manomaiphiboon, K., Octaviani, M., Torsri, K., and Towprayoon, S. (2013). Projected changes in means and extremes of temperature and precipitation over Thailand under three future emissions scenarios. *Clim. Res.* 58, 97–115. doi:10.3354/cr01188.

Manzanas, R., Amekudzi, L. K., Preko, K., Herrera, S., and Gutiérrez, J. M. (2014). Precipitation variability and trends in Ghana: An intercomparison of observational and reanalysis products. *Clim. Change*. doi:10.1007/s10584-014-1100-9.

Manzanas, R., Brands, S., San-Martín, D., Lucero, A., Limbo, C., and Gutiérrez, J. M. (2015). Statistical downscaling in the tropics can be sensitive to reanalysis choice: A case study for precipitation in the Philippines. *J. Clim.* 28, 4171–4184. doi:10.1175/JCLI-D-14-00331.1.

Maraun, D., Widmann, M., and Gutiérrez, J. M. (2018). Statistical downscaling skill under present climate conditions: A synthesis of the VALUE perfect predictor experiment. *Int. J. Climatol.* doi:10.1002/joc.5877.

Maraun, D., Widmann, M., Gutiérrez, J. M., Kotlarski, S., Chandler, R. E., Hertig, E., et al. (2015). VALUE: A framework to validate downscaling approaches for climate change studies. *Earth's Futur.* 3, 1–14. doi:10.1002/2014EF000259.

Marengo, J. A., and Espinoza, J. C. (2016). Extreme seasonal droughts and floods in Amazonia: causes, trends and impacts. *Int. J. Climatol.* 36, 1033–1050. doi:10.1002/joc.4420.

Marengo, J. A., Liebmann, B., Grimm, A. M., Misra, V., Silva Dias, P. L., Cavalcanti, I. F. A., et al. (2012). Recent developments on the South American monsoon system. *Int. J. Climatol.* 32, 1–21. doi:10.1002/joc.2254.

Marengo, J. A., Souza, C. M., Thonicke, K., Burton, C., Halladay, K., Betts, R. A., et al. (2018). Changes in Climate and Land Use Over the Amazon Region: Current and Future Variability and Trends. *Front. Earth Sci.* 6. doi:10.3389/feart.2018.00228.

Marengo, J. A., Torres, R. R., and Alves, L. M. (2017). Drought in Northeast Brazil—past, present, and future. *Theor. Appl. Climatol.* 129, 1189–1200. doi:10.1007/s00704-016-1840-8.

Marengo, J., Alves, L., and Torres, R. (2016). Regional climate change scenarios in the Brazilian Pantanal watershed. *Clim. Res.* 68, 201–213. doi:10.3354/cr01324.

Mariotti, A., Pan, Y., Zeng, N., and Alessandri, A. (2015). Long-term climate change in the Mediterranean region in the midst of decadal variability. *Clim. Dyn.* 44, 1437–1456. doi:10.1007/s00382-015-2487-3.

Martinez-Austria, P. F., and Bandala, E. R. (2017). Temperature and Heat-Related Mortality Trends in the Sonoran and Mojave Desert Region. *Atmosphere (Basel).* 8. doi:10.3390/atmos8030053.

Martínez-Austria, P. F., Bandala, E. R., and Patiño-Gómez, C. (2016). Temperature and heat wave trends in northwest Mexico. *Phys. Chem. Earth, Parts A/B/C* 91, 20–26. doi:10.1016/j.pce.2015.07.005.

Martínez-Castro, D., Porfirio da Rocha, R., Bezanilla-Morlot, A., Alvarez-Escudero, L., Reyes-Fernández, J. P., Silva-Vidal, Y., et al. (2006). Sensitivity studies of the RegCM3 simulation of summer precipitation, temperature and local wind field in the Caribbean Region. *Theor. Appl. Climatol.* doi:10.1007/s00704-005-0201-9.

Martínez-Castro, D., Vichot-Llano, A., Bezanilla-Morlot, A., Centella-Artola, A., Campbell, J., Giorgi, F., et al. (2018). The performance of RegCM4 over the Central America and Caribbean region using different cumulus parameterizations. *Clim. Dyn.* 50, 4103–4126. doi:10.1007/s00382-017-3863-y.

Martínez-Castro, D., Vichot-Llano, A., Bezanilla-Morlot, A., Centella-Artola, A., Campbell, J., and Viloria-Holguin, C. (2016). Performance of RegCM-4.3 over the Caribbean region using differentconfigurations of the Tiedtke convective parameterization scheme. *Rev. Climatol.* 16, 77–98. Available at:

http://www.climatol.eu/reclim/reclim16f.pdf.
Martinez Sanchez, J. N., and Cavazos, T. (2014). Eastern Tropical Pacific hurricane variability and landfalls on Mexican coasts. *Clim. Res.* 58, 221–234. doi:10.3354/cr01192.
Martynov, A., Laprise, R., Sushama, L., Winger, K., Šeparović, L., and Dugas, B. (2013). Reanalysis-driven climate simulation over CORDEX North America domain using the Canadian Regional Climate Model, version 5: model performance evaluation. *Clim. Dyn.* 41, 2973–3005. doi:10.1007/s00382-013-1778-9.
Matthes, H., Rinke, A., and Dethloff, K. (2015). Recent changes in Arctic temperature extremes: Warm and cold spells during winter and summer. *Environ. Res. Lett.* 10, 114020. doi:10.1088/1748-9326/10/11/114020.
Maturilli, M., Herber, A., and König-Langlo, G. (2015). Surface radiation climatology for Ny-Ålesund, Svalbard (78.9° N), basic observations for trend detection. *Theor. Appl. Climatol.* 120, 331–339. doi:10.1007/s00704-014-1173-4.
Maure, G., Pinto, I., Ndebele-Murisa, M., Muthige, M., Lennard, C., Nikulin, G., et al. (2018). The southern African climate under 1.5 °c and 2 °c of global warming as simulated by CORDEX regional climate models. *Environ. Res. Lett.* doi:10.1088/1748-9326/aab190.
Maussion, F., Butenko, A., Champollion, N., Dusch, M., Eis, J., Fourteau, K., et al. (2019). The Open Global Glacier Model (OGGM) v1.1. *Geosci. Model Dev.* 12, 909–931. doi:10.5194/gmd-12-909-2019.
Mayer, S., Fox Maule, C., Sobolowski, S., Bøssing Christensen, O., Danielsen Sørup, H. J., Antonia Sunyer, M., et al. (2015). Identifying added value in high-resolution climate simulations over Scandinavia. *Tellus A Dyn. Meteorol. Oceanogr.* 67, 24941. doi:10.3402/tellusa.v67.24941.
Mayowa, O. O., Pour, S. H., Shahid, S., Mohsenipour, M., Harun, S. Bin, Heryansyah, A., et al. (2015). Trends in rainfall and rainfall-related extremes in the east coast of peninsular Malaysia. *J. Earth Syst. Sci.* 124, 1609–1622. doi:10.1007/s12040-015-0639-9.
Mba, W. P., Longandjo, G.-N. T., Moufouma-Okia, W., Bell, J.-P., James, R., Vondou, D. A., et al. (2018). Consequences of 1.5 °C and 2 °C global warming levels for temperature and precipitation changes over Central Africa. *Environ. Res. Lett.* 13, 055011. doi:10.1088/1748-9326/aab048.
Mccrary, R. R., Mcginnis, S., and Mearns, L. O. (2017). Evaluation of snow water equivalent in NARCCAP simulations, including measures of observational uncertainty. *J. Hydrometeorol.* 18, 2425–2452. doi:10.1175/JHM-D-16-0264.1.
McCrary, R. R., and Mearns, L. O. (2019). Quantifying and Diagnosing Sources of Uncertainty in Midcentury Changes in North American Snowpack from NARCCAP. *J. Hydrometeorol.* 20, 2229–2252. doi:10.1175/JHM-D-18-0248.1.
McDermid, S. S., and Winter, J. (2017). Anthropogenic forcings on the climate of the Aral Sea: A regional modeling perspective. *Anthropocene* 20, 48–60. doi:https://doi.org/10.1016/j.ancene.2017.03.003.
McGrath, D., Colgan, W., Bayou, N., Muto, A., and Steffen, K. (2013). Recent warming at Summit, Greenland: Global context and implications. *Geophys. Res. Lett.* 40, 2091–2096. doi:10.1002/grl.50456.
McGree, S., Whan, K., Jones, D., Alexander, L. V, Imielska, A., Diamond, H., et al. (2014). An updated assessment of trends and variability in total and extreme rainfall in the western Pacific. *Int. J. Climatol.* 34, 2775–2791. doi:10.1002/joc.3874.
McLean, N. M., Stephenson, T. S., Taylor, M. A., and Campbell, J. D. (2015). Characterization of Future Caribbean Rainfall and Temperature Extremes across Rainfall Zones. *Adv. Meteorol.* 2015, 1–18. doi:10.1155/2015/425987.
McMahon, R., Stauffacher, M., and Knutti, R. (2015). The unseen uncertainties in climate change: reviewing comprehension of an IPCC scenario graph. *Clim. Change* 133, 141–154. doi:10.1007/s10584-015-1473-4.
McSweeney, C. F., and Jones, R. G. (2016). How representative is the spread of climate projections from the 5 CMIP5 GCMs used in ISI-MIP? *Clim. Serv.* doi:10.1016/j.cliser.2016.02.001.
Mearns, L. (NCAR), McGinnis, S. (NCAR), and Korytina, D. (NCAR) (2017). The NA-CORDEX dataset, version 1.0. NCAR Climate Data Gateway. doi:doi.org/10.5065/D6SJ1JCH.
Mearns, L., Gutowski, W., Jones, R., Leung, L., McGinnis, S., Nunes, A., et al. (2009). A Regional Climate Change Assessment Program for North America. *EOS Trans.* 90, 311. doi:10.1029/2009EO360002.
Medley, B., Joughin, I., Das, S. B., Steig, E. J., Conway, H., Gogineni, S., et al. (2013). Airborne-radar and ice-core observations of annual snow accumulation over Thwaites Glacier, West Antarctica confirm the spatiotemporal variability of global and regional atmospheric models. *Geophys. Res. Lett.* 40, 3649–3654. doi:10.1002/grl.50706.
Medley, B., McConnell, J. R., Neumann, T. A., Reijmer, C. H., Chellman, N., Sigl, M., et al. (2018). Temperature and Snowfall in Western Queen Maud Land Increasing Faster Than Climate Model Projections. *Geophys. Res. Lett.* 45, 1472–1480. doi:10.1002/2017GL075992.
Medley, B., and Thomas, E. R. (2019). Increased snowfall over the Antarctic Ice Sheet mitigated twentieth-century sea-level rise. *Nat. Clim. Chang.* 9, 34–39. doi:10.1038/s41558-018-0356-x.
Meehl, G. A., Stocker, T. F., Collins, W. D., Friedlingstein, P., Gaye, A. T., Gregory, J. M., et al. (2007). "2007: Global Climate Projections," in *Climate Change 2007: Contribution of Working Group I to the Fourth Assessment Report of the Intergovernmental Panel on Climate Change*, 747–846. Available at: http://www.ipcc.ch/pdf/assessment-report/ar4/wg1/ar4-wg1-chapter10.pdf.
Mei, R., Ashfaq, M., Rastogi, D., Leung, L. R., and Dominguez, F. (2015). Dominating controls for wetter South Asian summer monsoon in the twenty-first century. *J. Clim.* 28, 3400–3419. doi:10.1175/JCLI-D-14-00355.1.

Meleshko, V. P., Mirvis, V. M., Govorkova, V. A., Baidin, A. V., Pavlova, T. V., and Lvova, T. Y. (2019). The Arctic Climate Warming and Extremely Cold Winters in North Eurasia during 1979–2017. *Russ. Meteorol. Hydrol.* 44, 223–230. doi:10.3103/S1068373919040010.

Melissa McLean, N., Stephenson, T., Taylor, M., and Campbell, J. (2015). Characterization of Future Caribbean Rainfall and Temperature Extremes across Rainfall Zones. *Adv. Meteorol.* 2015, 1–18. doi:10.1155/2015/425987.

Mendes, D., Marengo, J. A., Rodrigues, S., and Oliveira, M. (2014). Downscaling Statistical Model Techniques for Climate Change Analysis Applied to the Amazon Region. *Adv. Artif. Neural Syst.* 2014, 1–10. doi:10.1155/2014/595462.

Méndez, M., and Magaña, V. (2010). Regional Aspects of Prolonged Meteorological Droughts over Mexico and Central America. *J. Clim.* 23, 1175–1188. doi:10.1175/2009JCLI3080.1.

Menéndez, C., Zaninelli, P., Carril, A., and Sánchez, E. (2016a). Hydrological cycle, temperature, and land surface-atmosphere interaction in the La Plata Basin during summer: response to climate change. *Clim. Res.* 68, 231–241. doi:10.3354/cr01373.

Menéndez, C., Zaninelli, P., Carril, A., and Sánchez, E. (2016b). Hydrological cycle, temperature, and land surface-atmosphere interaction in the La Plata Basin during summer: response to climate change. *Clim. Res.* 68, 231–241. doi:10.3354/cr01373.

Meque, A., and Abiodun, B. J. (2015). Simulating the link between ENSO and summer drought in Southern Africa using regional climate models. *Clim. Dyn.* doi:10.1007/s00382-014-2143-3.

Merkouriadi, I., Liston, G. E., Graham, R. M., and Granskog, M. A. (2019). Quantifying the potential for snow-ice formation in the Arctic Ocean. *Geophys. Res. Lett.*, 2019GL085020. doi:10.1029/2019GL085020.

Meyer, J., Want, S.-Y., Gillies, R., and Joon, J.-H. (submitted). Evaluating CORDEX-NA performance and future change to western U.S. precipitation and modes of variability. *J. Hydrol.* (submitted.

Miao, C., Duan, Q., Sun, Q., Huang, Y., Kong, D., Yang, T., et al. (2014). Assessment of CMIP5 climate models and projected temperature changes over Northern Eurasia. *Environ. Res. Lett. Environ. Res. Lett* 9, 12. doi:10.1088/1748-9326/9/5/055007.

Michelangeli, P.-A., Vautard, R., and Legras, B. (1995). Weather Regimes: Recurrence and Quasi Stationarity. *J. Atmos. Sci.* 52, 1237–1256. doi:10.1175/1520-0469(1995)052<1237:WRRAQS>2.0.CO;2.

Min, S. K., and Hense, A. (2007). A Bayesian assessment of climate change using multimodel ensembles. Part II: Regional and seasonal mean surface temperatures. *J. Clim.* doi:10.1175/JCLI4178.1.

Ministry for the Environment (2018). Climate Change Projections for New Zealand: Atmosphere Projections Based on Simulations from the IPCC Fifth Assessment, 2nd Edition. Wellington, New Zealand.

Mioduszewski, J. R., Rennermalm, A. K., Robinson, D. A., and Mote, T. L. (2014a). Attribution of snowmelt onset in Northern Canada. *J. Geophys. Res. Atmos.* 119, 9638–9653. doi:10.1002/2013JD021024.

Mioduszewski, J. R., Rennermalm, A. K., Robinson, D. A., and Mote, T. L. (2014b). Journal of Geophysical Research : Atmospheres Attribution of snowmelt onset in Northern Canada. 9638–9653. doi:10.1002/2013JD021024.Received.

Mishra, V. (2015a). Climatic uncertainty in HImalaya. *J. Geophys. Res. Atmos.*, 1–17. doi:10.1002/2014JD022650.Received.

Mishra, V. (2015b). Climatic uncertainty in Himalayan water towers. *J. Geophys. Res. Atmos.* 120, 2689–2705. doi:10.1002/2014JD022650.

Mishra, V. (2015c). Climatic uncertainty in Himalayan water towers. *J. Geophys. Res.* 120, 2689–2705. doi:10.1002/2014JD022650.

Mohan, A., and Topp, K. (2018). India's energy future: Contested narratives of change. *Energy Res. Soc. Sci.* 44, 75–82. doi:10.1016/J.ERSS.2018.04.040.

Mokhov, I. I. (2015). Contemporary climate changes in the Arctic. *Her. Russ. Acad. Sci.* 85, 265–271. doi:10.1134/S1019331615030168.

Mokhov, I. I., Timazhev, A. V., and Lupo, A. R. (2014). Changes in atmospheric blocking characteristics within Euro-Atlantic region and Northern Hemisphere as a whole in the 21st century from model simulations using RCP anthropogenic scenarios. *Glob. Planet. Change* 122, 265–270. doi:10.1016/J.GLOPLACHA.2014.09.004.

Monaghan, A. J., Bromwich, D. H., Fogt, R. L., Wang, S.-H., Mayewski, P. A., Dixon, D. A., et al. (2006). Insignificant Change in Antarctic Snowfall Since the International Geophysical Year. *Science (80-.).* 313, 827–831. doi:10.1126/science.1128243.

Moon, S., and Ha, K.-J. (2017). Temperature and precipitation in the context of the annual cycle over Asia: Model evaluation and future change. *Asia-Pacific J. Atmos. Sci.* 53, 229–242. doi:10.1007/s13143-017-0024-5.

Mora, C., Frazier, A. G., Longman, R. J., Dacks, R. S., Walton, M. M., Tong, E. J., et al. (2013). The projected timing of climate departure from recent variability. *Nature*. doi:10.1038/nature12540.

Moreau, L., Groth, P., Cheney, J., Lebo, T., and Miles, S. (2015). The rationale of PROV. *J. Web Semant.* doi:10.1016/j.websem.2015.04.001.

Mote, P. W., Li, S., Lettenmaier, D. P., Xiao, M., and Engel, R. (2018). Dramatic declines in snowpack in the western US. *npj Clim. Atmos. Sci.* 1. doi:10.1038/s41612-018-0012-1.

Mote, P. W., Rupp, D. E., Li, S., Sharp, D. J., Otto, F., Uhe, P. F., et al. (2016). Perspectives on the causes of

exceptionally low 2015 snowpack in the western United States. *Geophys. Res. Lett.* 43, 10,910-980,988. doi:10.1002/2016GL069965.

Mottram, R., Hansen, N., Kittel, C., Van Wessem, M., Agosta, C., Amory, C., et al. (submitted). What is the Surface Mass Balance of Antarctica? An Intercomparison of Regional Climate Model Estimates. (submitted. Available at: http://www.cordex.org/.

Mottram, R., Nielsen, K. P., Gleeson, E., and Yang, X. (2017). Modelling Glaciers in the HARMONIE-AROME NWP model. *Adv. Sci. Res.* 14, 323–334. doi:10.5194/asr-14-323-2017.

Mouhamed, L., Traore, S. B., Alhassane, A., and Sarr, B. (2013). Evolution of some observed climate extremes in the West African Sahel. *Weather Clim. Extrem.* doi:10.1016/j.wace.2013.07.005.

Mourão, C., Chou, S. C., and Marengo, J. (2016). Downscaling Climate Projections over La Plata Basin. *Atmos. Clim. Sci.* 06, 1–12. doi:10.4236/acs.2016.61001.

Mudryk, L. R., Derksen, C., Howell, S., Laliberté, F., Thackeray, C., Sospedra-Alfonso, R., et al. (2018). Canadian snow and sea ice: Historical trends and projections. *Cryosphere* 12, 1157–1176. doi:10.5194/tc-12-1157-2018.

Mudryk, L. R., Derksen, C., Kushner, P. J., and Brown, R. (2015). Characterization of Northern Hemisphere snow water equivalent datasets, 1981-2010. *J. Clim.* 28, 8037–8051. doi:10.1175/JCLI-D-15-0229.1.

Murphy, C., Wilby, R. L., Matthews, T. K. R., Thorne, P., Broderick, C., Fealy, R., et al. (2019). Multi-century trends to wetter winters and drier summers in the England and Wales precipitation series explained by observational and sampling bias in early records. *Int. J. Climatol.*, joc.6208. doi:10.1002/joc.6208.

Nabat, P., Solmon, F., Mallet, M., Kok, J. F., and Somot, S. (2012). Dust emission size distribution impact on aerosol budget and radiative forcing over the Mediterranean region: a regional climate model approach. *Atmos. Chem. Phys.* 12, 10545–10567. doi:10.5194/acp-12-10545-2012.

Nabat, P., Somot, S., Cassou, C., Mallet, M., Michou, M., Bouniol, D., et al. (submitted). Modulation of radiative aerosols effects by atmospheric circulation over the Euro-Mediterranean region. (submitted.

Nabat, P., Somot, S., Mallet, M., Chiapello, I., Morcrette, J. J., Solmon, F., et al. (2013). A 4-D climatology (1979–2009) of the monthly tropospheric aerosol optical depth distribution over the Mediterranean region from a comparative evaluation and blending of remote sensing and model products. *Atmos. Meas. Tech.* 6, 1287–1314. doi:10.5194/amt-6-1287-2013.

Nabat, P., Somot, S., Mallet, M., Michou, M., Sevault, F., Driouech, F., et al. (2015a). Dust aerosol radiative effects during summer 2012 simulated with a coupled regional aerosol-atmosphere-ocean model over the Mediterranean. *Atmos. Chem. Phys.* 15. doi:10.5194/acp-15-3303-2015.

Nabat, P., Somot, S., Mallet, M., Sanchez-Lorenzo, A., and Wild, M. (2014). Contribution of anthropogenic sulfate aerosols to the changing Euro-Mediterranean climate since 1980. *Geophys. Res. Lett.* 41, 5605–5611. doi:10.1002/2014GL060798.

Nabat, P., Somot, S., Mallet, M., Sevault, F., Chiacchio, M., and Wild, M. (2015b). Direct and semi-direct aerosol radiative effect on the Mediterranean climate variability using a coupled regional climate system model. *Clim. Dyn.* 44, 1127–1155. doi:10.1007/s00382-014-2205-6.

National Academies of Sciences and Medicine (2017). *Communicating Science Effectively*. Washington, D.C.: National Academies Press doi:10.17226/23674.

Navarro-Estupiñan, J., Robles-Morua, A., Vivoni, E. R., Zepeda, J. E., Montoya, J. A., and Verduzco, V. S. (2018). Observed trends and future projections of extreme heat events in Sonora, Mexico. *Int. J. Climatol.* 38, 5168–5181. doi:10.1002/joc.5719.

Nengker, T.; Choudhary, A.; Dimri, A. P. (2018). Assessment of the performance of CORDEX-SA experiments in simulating seasonal mean temperature over the Himalayan region for the present climate: Part I. *Clim. Dyn.* 50, 2411–2441. doi:10.1007/s00382-017-3597-x.

Nesbitt, S. W., Gochis, D. J., and Lang, T. J. (2008). The Diurnal Cycle of Clouds and Precipitation along the Sierra Madre Occidental Observed during NAME-2004: Implications for Warm Season Precipitation Estimation in Complex Terrain. *J. Hydrometeorol.* 9, 728–743. doi:10.1175/2008JHM939.1.

Neukom, R., Luterbacher, J., Villalba, R., Küttel, M., Frank, D., Jones, P. D., et al. (2010). Multi-centennial summer and winter precipitation variability in southern South America. *Geophys. Res. Lett.* 37. doi:10.1029/2010GL043680.

New, M., Hewitson, B., Stephenson, D. B., Tsiga, A., Kruger, A., Manhique, A., et al. (2006). Evidence of trends in daily climate extremes over southern and west Africa. *J. Geophys. Res. Atmos.* doi:10.1029/2005JD006289.

New Zealand Ministry for the Environment & Statistics (2017). New Zealand's Environmental Reporting Series: Our atmosphere and climate 2017.

Ngo-Duc, T., Kieu, C., Thatcher, M., Nguyen-Le, D., and Phan-Van, T. (2014). Climate projections for Vietnam based on regional climate models. *Clim. Res.* 60, 199–213. doi:10.3354/cr01234.

Ngo-Duc, T., Tangang, F. T., Santisirisomboon, J., Cruz, F., Trinh-Tuan, L., Nguyen-Xuan, T., et al. (2017). Performance evaluation of RegCM4 in simulating extreme rainfall and temperature indices over the CORDEX-Southeast Asia region. *Int. J. Climatol.* 37, 1634–1647. doi:10.1002/joc.4803.

Nguyen-Xuan, T., Ngo-Duc, T., Kamimera, H., Trinh-Tuan, L., Matsumoto, J., Inoue, T., et al. (2016). The Vietnam Gridded Precipitation (VnGP) Dataset: Construction and Validation. *SOLA* 12, 291–296. doi:10.2151/sola.2016-

057.
Nguyen, K. C. and K. J. W. (2001). Interannual, Decadal, and Transient Greenhouse Simulation of Tropical Cyclone–like Vortices in a Regional Climate Model of the South Pacific. *J. Clim.* 14, 3043–3054.
Niang, I., Ruppel, O. C., Abdrabo, M. A., Essel, A., Lennard, C., Padgham, J., et al. (2014). Chapter 22 - Africa. *Clim. Chang. 2014 Impacts, Adapt. Vulnerability - Contrib. Work. Gr. II to Fifth Assess. Rep. Intergov. Panel Clim. Chang.* doi:10.1017/CBO9781107415386.002.
Nicolas, J. P., and Bromwich, D. H. (2011). Precipitation Changes in High Southern Latitudes from Global Reanalyses: A Cautionary Tale. *Surv. Geophys.* 32, 475–494. doi:10.1007/s10712-011-9114-6.
Nicolas, J. P., and Bromwich, D. H. (2014). New Reconstruction of Antarctic Near-Surface Temperatures: Multidecadal Trends and Reliability of Global Reanalyses. *J. Clim.* 27, 8070–8093. doi:10.1175/JCLI-D-13-00733.1.
Nicolas, J. P., Vogelmann, A. M., Scott, R. C., Wilson, A. B., Cadeddu, M. P., Bromwich, D. H., et al. (2017). January 2016 extensive summer melt in West Antarctica favoured by strong El Niño. *Nat. Commun.* 8. doi:10.1038/ncomms15799.
Nicolaus, M., Katlein, C., Maslanik, J., and Hendricks, S. (2012). Changes in Arctic sea ice result in increasing light transmittance and absorption. *Geophys. Res. Lett.* 39, 2012GL053738. doi:10.1029/2012GL053738.
Nikulin, G., Lennard, C., Dosio, A., Kjellström, E., Chen, Y., Hansler, A., et al. (2018a). The effects of 1.5 and 2 degrees of global warming on Africa in the CORDEX ensemble. *Environ. Res. Lett.* doi:10.1088/1748-9326/aab1b1.
Nikulin, G., Lennard, C., Dosio, A., Kjellström, E., Chen, Y., Hansler, A., et al. (2018b). The effects of 1.5 and 2 degrees of global warming on Africa in the CORDEX ensemble. *Environ. Res. Lett.* doi:10.1088/1748-9326/aab1b1.
Ning, L., and Bradley, R. S. (2015). Snow occurrence changes over the central and eastern United States under future warming scenarios. *Sci. Rep.* 5, 1–8. doi:10.1038/srep17073.
Niranjan Kumar, K., Entekhabi, D., and Molini, A. (2015). Hydrological extremes in hyperarid regions: A diagnostic characterization of intense precipitation over the Central Arabian Peninsula. *J. Geophys. Res.* doi:10.1002/2014JD022341.
Nisbet, M. C., and Markowitz, E. (2016). *Strategic science communication on environmental issues*. American Association for the Advancement of Science Available at: https://mcmprodaaas.s3.amazonaws.com/s3fs-public/content_files/NisbetMarkowitz_StrategicSciCommOnEnvironmentalIssues_WhitePaper.pdf.
Nkrumah, F., Vischel, T., Panthou, G., Klutse, N. A. B., Adukpo, D. C., and Diedhiou, A. (2019). Recent Trends in the Daily Rainfall Regime in Southern West Africa. *Atmosphere (Basel).* 10, 741. doi:10.3390/atmos10120741.
Nobre, C. A., Sampaio, G., Borma, L. S., Castilla-Rubio, J. C., Silva, J. S., and Cardoso, M. (2016). Land-use and climate change risks in the Amazon and the need of a novel sustainable development paradigm. *Proc. Natl. Acad. Sci.* 113, 10759 LP – 10768. Available at: http://www.pnas.org/content/113/39/10759.abstract.
Noël, B., Van De Berg, W. J., Van Meijgaard, E., Kuipers Munneke, P., Van De Wal, R. S. W., and Van Den Broeke, M. R. (2015). Evaluation of the updated regional climate model RACMO2.3: Summer snowfall impact on the Greenland Ice Sheet. *Cryosphere* 9, 1831–1844. doi:10.5194/tc-9-1831-2015.
Nordli, Ø., Przybylak, R., Ogilvie, A. E. J., and Isaksen, K. (2014). Long-term temperature trends and variability on spitsbergen: The extended svalbard airport temperature series, 1898-2012. *Polar Res.* 33. doi:10.3402/polar.v33.21349.
Notaro, M., Bennington, V., and Vavrus, S. (2015). Dynamically Downscaled Projections of Lake-Effect Snow in the Great Lakes Basin* ,+. *J. Clim.* 28, 1661–1684. doi:10.1175/JCLI-D-14-00467.1.
Ongoma, V., Chena, H., and Gaoa, C. (2018). Projected changes in mean rainfall and temperature over east Africa based on CMIP5 models. *Int. J. Climatol.* doi:10.1002/joc.5252.
Onstott, R. G. (1992). SAR and Scatterometer Signatures of Sea Ice. *Microw. Remote Sens. Sea Ice*, 73–104. doi:doi:10.1029/GM068p0073.
Onyutha, C., Tabari, H., Rutkowska, A., Nyeko-Ogiramoi, P., and Willems, P. (2016). Comparison of different statistical downscaling methods for climate change rainfall projections over the Lake Victoria basin considering CMIP3 and CMIP5. *J. Hydro-Environment Res.* doi:10.1016/j.jher.2016.03.001.
Osakada, Y., and Nakakita, E. (2018). Future Change of Occurrence Frequency of Baiu Heavy Rainfall and Its Linked Atmospheric Patterns by Multiscale Analysis. *SOLA* 14, 79–85. doi:10.2151/sola.2018-014.
Osborn, T. J., Wallace, C. J., Harris, I. C., and Melvin, T. M. (2016). Pattern scaling using ClimGen: monthly-resolution future climate scenarios including changes in the variability of precipitation. *Clim. Change* 134, 353–369. doi:10.1007/s10584-015-1509-9.
Osima, S., Indasi, V. S., Zaroug, M., Endris, H. S., Gudoshava, M., Misiani, H. O., et al. (2018). Projected climate over the Greater Horn of Africa under 1.5 °c and 2 °c global warming. *Environ. Res. Lett.* doi:10.1088/1748-9326/aaba1b.
Otto, F. E. L., Haustein, K., Uhe, P., Coelho, C. A. S., Aravequia, J. A., Almeida, W., et al. (2015). Factors Other Than Climate Change, Main Drivers of 2014/15 Water Shortage in Southeast Brazil. *Bull. Am. Meteorol. Soc.* 96, S35–S40. doi:10.1175/BAMS-D-15-00120.1.
Outten, S. D., and Esau, I. (2012). A link between Arctic sea ice and recent cooling trends over Eurasia. *Clim. Change*

110, 1069–1075. doi:10.1007/s10584-011-0334-z.
Overland, J., Dunlea, E., Box, J. E., Corell, R., Forsius, M., Kattsov, V., et al. (2019). The urgency of Arctic change. *Polar Sci.* doi:10.1016/j.polar.2018.11.008.
Overland, J. E., Dethloff, K., Francis, J. A., Hall, R. J., Hanna, E., Kim, S.-J., et al. (2016). Nonlinear response of mid-latitude weather to the changing Arctic. *Nat. Clim. Chang.* 6, 992–999. doi:10.1038/nclimate3121.
Overland, J. E., Wang, M., Walsh, J. E., and Stroeve, J. C. (2014). Future Arctic climate changes: Adaptation and mitigation time scales. *Earth's Futur.* 2, 68–74. doi:10.1002/2013ef000162.
Ozturk, T., Turp, M. T., Türkeş, M., and Kurnaz, M. L. (2017). Projected changes in temperature and precipitation climatology of Central Asia CORDEX Region 8 by using RegCM4.3.5. *Atmos. Res.* 183, 296–307. doi:10.1016/j.atmosres.2016.09.008.
Ozturk, T., Turp, M. T., Türkeş, M., and Kurnaz, M. L. (2018). Future projections of temperature and precipitation climatology for CORDEX-MENA domain using RegCM4.4. *Atmos. Res.* 206, 87–107. doi:10.1016/j.atmosres.2018.02.009.
Pachauri, R. K. (2014). *Climate Change 2014 Synthesis Report*.
Pachauri, R. K., and Reisinger, A. (2007). IPCC fourth assessment report. *IPCC Fourth Assess. Rep.* 1, 976. Available at: http://www.construible.es/construible%5Cbiblioteca%5Cpresentacion_informe_ipcc.pdf%5Cnpapers2://publication/uuid/DD3ABB67-E411-4C0F-A29C-DA693B95B789.
Pal, S., Chang, H.-I., Castro, C. L., and Dominguez, F. (2019). Credibility of Convection-Permitting Modeling to Improve Seasonal Precipitation Forecasting in the Southwestern United States. *Front. Earth Sci.* 7, 11. doi:10.3389/feart.2019.00011.
Palazzi, E., Hardenberg, J. Von, and Terzago, S. (2015). Precipitation in the Karakoram-Himalaya : a CMIP5 view. *Clim. Dyn.*, 21–45. doi:10.1007/s00382-014-2341-z.
Palazzi, E., Von Hardenberg, J., and Provenzale, A. (2013). Precipitation in the hindu-kush karakoram himalaya: Observations and future scenarios. *J. Geophys. Res. Atmos.* 118, 85–100. doi:10.1029/2012JD018697.
Palerme, C., Genthon, C., Claud, C., Kay, J. E., Wood, N. B., and L'Ecuyer, T. (2017). Evaluation of current and projected Antarctic precipitation in CMIP5 models. *Clim. Dyn.* 48, 225–239. doi:10.1007/s00382-016-3071-1.
Palerme, C., Kay, J. E., Genthon, C., L'Ecuyer, T., Wood, N. B., and Claud, C. (2014). How much snow falls on the Antarctic ice sheet? *Cryosph.* 8, 1577–1587. doi:10.5194/tc-8-1577-2014.
Palomino-Lemus, R., Córdoba-Machado, S., Gámiz-Fortis, S. R., Castro-Díez, Y., and Esteban-Parra, M. J. (2015). Summer precipitation projections over northwestern South America from CMIP5 models. *Glob. Planet. Change* 131, 11–23. doi:10.1016/j.gloplacha.2015.05.004.
Palomino-Lemus, R., Córdoba-Machado, S., Gámiz-Fortis, S. R., Castro-Díez, Y., and Esteban-Parra, M. J. (2017). Climate change projections of boreal summer precipitation over tropical America by using statistical downscaling from CMIP5 models. *Environ. Res. Lett.* 12, 124011. doi:10.1088/1748-9326/aa9bf7.
Palomino-Lemus, R., Córdoba-Machado, S., Gámiz-Fortis, S. R., Castro-Díez, Y., and Esteban-Parra, M. J. (2018). High-resolution boreal winter precipitation projections over tropical America from CMIP5 models. *Clim. Dyn.* 51, 1773–1792. doi:10.1007/s00382-017-3982-5.
Panday, P. K., Thibeault, J., and Frey, K. E. (2015). Changing temperature and precipitation extremes in the Hindu Kush-Himalayan region: An analysis of CMIP3 and CMIP5 simulations and projections. *Int. J. Climatol.* 35, 3058–3077. doi:10.1002/joc.4192.
Panitz, H. J., Dosio, A., Büchner, M., Lüthi, D., and Keuler, K. (2014). COSMO-CLM (CCLM) climate simulations over CORDEX-Africa domain: Analysis of the ERA-Interim driven simulations at 0.44° and 0.22° resolution. *Clim. Dyn.* doi:10.1007/s00382-013-1834-5.
Panthou, G., Lebel, T., Vischel, T., Quantin, G., Sane, Y., Ba, A., et al. (2018a). Rainfall intensification in tropical semi-arid regions: The Sahelian case. *Environ. Res. Lett.* doi:10.1088/1748-9326/aac334.
Panthou, G., Mailhot, A., Laurence, E., and Talbot, G. (2014). Relationship between surface temperature and extreme rainfalls: A multi-time-scale and event-based analysis. *J. Hydrometeorol.* doi:10.1175/JHM-D-14-0020.1.
Panthou, G., Vrac, M., Drobinski, P., Bastin, S., and Li, L. (2018b). Impact of model resolution and Mediterranean sea coupling on hydrometeorological extremes in RCMs in the frame of HyMeX and MED-CORDEX. *Clim. Dyn.* 51, 915–932. doi:10.1007/s00382-016-3374-2.
Park, C., Min, S.-K., Lee, D., Cha, D.-H., Suh, M.-S., Kang, H.-S., et al. (2016). Evaluation of multiple regional climate models for summer climate extremes over East Asia. *Clim. Dyn.* 46, 2469–2486. doi:10.1007/s00382-015-2713-z.
Partasenok, I. S., Geyer, B., and Melnik, V. I. (2015). Studies of possible scenarios of changes in the climate of Belarus based on ensemble concep. *roceedings Hydrometcentre Russ.* 358, 99–111.
Pavlidis, V., Katragkou, E., Prein, A., Georgoulias, A., Kartsios, S., Zanis, P., et al. (submitted). Investigating the impact of aerosol climatologies in regional climate model simulations over Europe. (submitted.
Pazos, M., and Mendoza, B. (2013). Landfalling tropical cyclones along the Eastern Pacific coast between the sixteenth and twentieth centuries. *J. Clim.* 26, 4219–4230. doi:10.1175/JCLI-D-11-00411.1.
Peel, M. C., Finlayson, B. L., and McMahon, T. A. (2007). Updated world map of the Köppen-Geiger climate classification. *Hydrol. Earth Syst. Sci.* 11, 1633–1644. doi:10.5194/hess-11-1633-2007.

Peng, X., Zhang, T., Frauenfeld, O. W., Wang, K., Sun, W., and Luo, J. (2019). Evaluation and quantification of surface air temperature over Eurasia based on CMIP5 models. *Clim. Res.* 77, 167–180. doi:10.3354/cr01549.

Perevedentsev, Y. P., Vasil'ev, A. A., Shantalinskii, K. M., and Gur'yanov, V. V. (2017). Long-term variations in surface air pressure and surface air temperature in the Northern Hemisphere mid-latitudes. *Russ. Meteorol. Hydrol.* 42, 461–470. doi:10.3103/S1068373917070056.

Perovich, D. K., and Polashenski, C. (2012). Albedo evolution of seasonal Arctic sea ice. *Geophys. Res. Lett.* 39, n/a-n/a. doi:10.1029/2012GL051432.

Perovich, D., Polashenski, C., Arntsen, A., and Stwertka, C. (2017). Anatomy of a late spring snowfall on sea ice. *Geophys. Res. Lett.* 44, 2802–2809. doi:10.1002/2016GL071470.

Peterson, T. C., Taylor, M. A., Demeritte, R., Duncombe, D. L., Burton, S., Thompson, F., et al. (2002). Recent changes in climate extremes in the Caribbean region. *J. Geophys. Res. Atmos.* 107, ACL 16-1-ACL 16-9. doi:10.1029/2002JD002251.

Pfeffer, W. T., Arendt, A. A., Bliss, A., Bolch, T., Cogley, J. G., Gardner, A. S., et al. (2014). The randolph glacier inventory: A globally complete inventory of glaciers. *J. Glaciol.* 60, 537–552. doi:10.3189/2014JoG13J176.

Pham, T. Van, Brauch, J., Früh, B., and Ahrens, B. (2017). Simulation of snowbands in the Baltic Sea area with the coupled atmosphere-ocean-ice model COSMO-CLM/NEMO. *Meteorol. Zeitschrift* 26, 71–82. doi:10.1127/metz/2016/0775.

Pichelli, E., Coppola, E., Sobolowski, S., Ban, N., Giorgi, F., Stocchi, P., et al. (submitted). The first multi-model ensemble of regional climate simulations at kilometer-scale resolution part 2: future precipitation projections. *Clim. Dyn.* (submitted.

Pinto, I., Jack, C., and Hewitson, B. (2018). Process-based model evaluation and projections over southern Africa from Coordinated Regional Climate Downscaling Experiment and Coupled Model Intercomparison Project Phase 5 models. *Int. J. Climatol.* doi:10.1002/joc.5666.

Pinto, I., Lennard, C., Tadross, M., Hewitson, B., Dosio, A., Nikulin, G., et al. (2016). Evaluation and projections of extreme precipitation over southern Africa from two CORDEX models. *Clim. Change*. doi:10.1007/s10584-015-1573-1.

Pithan, F., and Mauritsen, T. (2014). Arctic amplification dominated by temperature feedbacks in contemporary climate models. *Nat. Geosci.* 7, 181–184. doi:10.1038/ngeo2071.

Planos Gutiérrez, E. O., Rivero Vega, R., and Guevara Velazco, V. (2012). *Impacto del Cambio Climático y Medidas de Adaptación en Cuba*. , eds. E. O. Planos Gutiérrez, R. Rivero Vega, and V. Guevara Velazco La Habana, Cuba: Agencia de Medio Ambiente, Ministerio de Ciencia Tecnología y Medio Ambiente Available at: http://www.redciencia.cu/geobiblio/paper/2012_Planos_Impacto y Adaptacion, Libro.pdf.

Poan, E. D., Gachon, P., Laprise, R., Aider, R., and Dueymes, G. (2018). Investigating added value of regional climate modeling in North American winter storm track simulations. *Clim. Dyn.* 50, 1799–1818. doi:10.1007/s00382-017-3723-9.

Porter, C., Morin, P., Howat, I., Noh, M.-J., Bates, B., Peterman, K., et al. (2018). ArcticDEM. doi:https://doi.org/10.7910/DVN/OHHUKH.

Prakash, S. (2019). Performance assessment of CHIRPS, MSWEP, SM2RAIN-CCI, and TMPA precipitation products across India. *J. Hydrol.* doi:10.1016/j.jhydrol.2019.01.036.

Prakash, S., Mitra, A. K., Momin, I. M., Pai, D. S., Rajagopal, E. N., and Basu, S. (2014). Comparison of TMPA-3B42 Versions 6 and 7 Precipitation Products with Gauge-Based Data over India for the Southwest Monsoon Period. *J. Hydrometeorol.* 16, 346–362. doi:10.1175/jhm-d-14-0024.1.

Prein, A. F., Bukovsky, M. S., Mearns, L. O., Bruyère, C. L., and Done, J. M. (2019). Simulating North American Weather Types With Regional Climate Models. *Front. Environ. Sci.* 7, 36. doi:10.3389/fenvs.2019.00036.

Prein, A. F., and Gobiet, A. (2017). Impacts of uncertainties in European gridded precipitation observations on regional climate analysis. *Int. J. Climatol.* 37, 305–327. doi:10.1002/joc.4706.

Prein, A. F., Gobiet, A., Truhetz, H., Keuler, K., Goergen, K., Teichmann, C., et al. (2016). Precipitation in the EURO-CORDEX 0.11° and 0.44° simulations: high resolution, high benefits? *Clim. Dyn.* 46, 383–412. doi:10.1007/s00382-015-2589-y.

Prein, A. F., Langhans, W., Fosser, G., Ferrone, A., Ban, N., Goergen, K., et al. (2015). A review on regional convection-permitting climate modeling: Demonstrations, prospects, and challenges. *Rev. Geophys.* 53, 323–361. doi:10.1002/2014RG000475.

Prein, A. F., Liu, C., Ikeda, K., Trier, S. B., Rasmussen, R. M., Holland, G. J., et al. (2017a). Increased rainfall volume from future convective storms in the US. *Nat. Clim. Chang.* 7, 880–884. doi:10.1038/s41558-017-0007-7.

Prein, A., Rasmussen, R., and Stephens, G. (2017b). Challenges and Advances in Convection Permitting Climate Modeling. *Bull. Am. Meteorol. Soc.* May, 1027–1029. doi:doi.org/10.1175/BAMS-D-16-0263.1.

Previdi, M., and Polvani, L. M. (2016). Anthropogenic impact on Antarctic surface mass balance, currently masked by natural variability, to emerge by mid-century. *Environ. Res. Lett.* 11. doi:10.1088/1748-9326/11/9/094001.

Pulak Guhathakurta and Jayashree V Revadekar (2017). "Observed Variability and Long-Term Trends of Rainfall Over India," in *Observed Climate Variability and Change over the Indian Region* (Singapore: Springer, Singapore).

Rabinovich, A., and Morton, T. A. (2012). Unquestioned Answers or Unanswered Questions: Beliefs About Science

Guide Responses to Uncertainty in Climate Change Risk Communication. *Risk Anal.* 32, 992–1002. doi:10.1111/j.1539-6924.2012.01771.x.

Raga, G., Bracamontes-Cevallos, B., Farfán, L., and Romero-Centeno, R. (2012). Landfalling tropical cyclones on the Pacific coast of Mexico: 1850-2010 (edited by T. Cavazos). *Atmósfera* 26. Available at: https://www.revistascca.unam.mx/atm/index.php/atm/article/view/28630.

Raghavan, S. V., Hur, J., and Liong, S. Y. (2018a). Evaluations of NASA NEX-GDDP data over Southeast Asia: present and future climates. *Clim. Change* 148, 503–518. doi:10.1007/s10584-018-2213-3.

Raghavan, S. V., Vu, M. T., and Liong, S. Y. (2016). Regional climate simulations over Vietnam using the WRF model. *Theor. Appl. Climatol.* 126, 161–182. doi:10.1007/s00704-015-1557-0.

Raghavan, S. V, Liu, J., Nguyen, N. S., Vu, M. T., and Liong, S.-Y. (2018b). Assessment of CMIP5 historical simulations of rainfall over Southeast Asia. *Theor. Appl. Climatol.* 132, 989–1002. doi:10.1007/s00704-017-2111-z.

Rahmawati, N., and Lubczynski, M. W. (2018). Validation of satellite daily rainfall estimates in complex terrain of Bali Island, Indonesia. *Theor. Appl. Climatol.* 134, 513–532. doi:10.1007/s00704-017-2290-7.

Rajbhandari, R., Shrestha, A. B., Kulkarni, A., Patwardhan, S. K., and Bajracharya, S. R. (2015). Projected changes in climate over the Indus river basin using a high resolution regional climate model (PRECIS). 339–357. doi:10.1007/s00382-014-2183-8.

Rajbhandari, R., Shrestha, A. B., and Wahid, S. (2016). Projection of Future Climate over the Koshi River Basin Based on CMIP5 GCMs. 190–204.

Rajczak, J., and Schär, C. (2017). Projections of Future Precipitation Extremes Over Europe: A Multimodel Assessment of Climate Simulations. *J. Geophys. Res. Atmos.* 122, 10,773-10,800. doi:10.1002/2017JD027176.

Ramarao, M. V. S., Sanjay, J., Krishnan, R., Mujumdar, M., Bazaz, A., and Revi, A. (2018). On observed aridity changes over the semiarid regions of India in a warming climate. *Theor. Appl. Climatol.*, 1–10. doi:10.1007/s00704-018-2513-6.

Ramsankaran, R., Pandit, A., and Azam, M. F. (2018). Spatially distributed ice-thickness modelling for Chhota Shigri Glacier in western Himalayas, India. *Int. J. Remote Sens.* 39, 3320–3343. doi:10.1080/01431161.2018.1441563.

Rao, V. B., Franchito, S. H., Santo, C. M. E., and Gan, M. A. (2016). An update on the rainfall characteristics of Brazil: seasonal variations and trends in 1979-2011. *Int. J. Climatol.* 36, 291–302. doi:10.1002/joc.4345.

Rapaić, M., Brown, R., Markovic, M., and Chaumont, D. (2015). An Evaluation of Temperature and Precipitation Surface-Based and Reanalysis Datasets for the Canadian Arctic, 1950-2010. *Atmos. - Ocean* 53, 283–303. doi:10.1080/07055900.2015.1045825.

Rasmussen, R., Ikeda, K., Liu, C., Gochis, D., Clark, M., Dai, A., et al. (2014). Climate Change Impacts on the Water Balance of the Colorado Headwaters: High-Resolution Regional Climate Model Simulations. *J. Hydrometeorol.* 15, 1091–1116. doi:10.1175/JHM-D-13-0118.1.

Ratna, S., Ratnam, J., Behera, S., Tangang, F., and Yamagata, T. (2017). Validation of the WRF regional climate model over the subregions of Southeast Asia: climatology and interannual variability. *Clim. Res.* 71, 263–280. doi:10.3354/cr01445.

Raup, B., Racoviteanu, A., Khalsa, S. J. S., Helm, C., Armstrong, R., and Arnaud, Y. (2007). The GLIMS geospatial glacier database: A new tool for studying glacier change. *Glob. Planet. Change* 56, 101–110. doi:10.1016/j.gloplacha.2006.07.018.

Rauthe, M., Steiner, H., Riediger, U., Mazurkiewicz, A., and Gratzki, A. (2013). A Central European precipitation climatology – Part I: Generation and validation of a high-resolution gridded daily data set (HYRAS). *Meteorol. Zeitschrift* 22, 235–256. doi:10.1127/0941-2948/2013/0436.

Reboita, M., Dutra, L., and Dias, C. (2016). Diurnal cycle of precipitation simulated by RegCM4 over South America: present and future scenarios. *Clim. Res.* 70, 39–55. doi:10.3354/cr01416.

Reboita, M. S., da Rocha, R. P., de Souza, M. R., and Llopart, M. (2018). Extratropical cyclones over the southwestern South Atlantic Ocean: HadGEM2-ES and RegCM4 projections. *Int. J. Climatol.* 38, 2866–2879. doi:10.1002/joc.5468.

Reboita, M. S., da Rocha, R. P., Dias, C. G., and Ynoue, R. Y. (2014). Climate Projections for South America: RegCM3 Driven by HadCM3 and ECHAM5. *Adv. Meteorol.* 2014, 1–17. doi:10.1155/2014/376738.

Reboita, M. S., Reale, M., da Rocha, R. P., Giorgi, F., Giuliani, G., Coppola, E., et al. (submitted). Future Changes in the Wintertime Cyclonic Activity over the CORDEX-CORE Southern Hemisphere domains in a Multi-Model Approach. *Clim. Dyn.* (submitted.

Rehman, N., Adnan, M., and Ali, S. (2018). Assessment of CMIP5 climate models over south Asia and climate change projections over Pakistan under representative concentration pathways. *Int. J. Glob. Warm.* 16, 381–415. doi:10.1504/IJGW.2018.095994.

Ren, Y. Y., Ren, G. Y., Sun, X. B., Shrestha, A. B., You, Q. L., Zhan, Y. J., et al. (2017a). Observed changes in surface air temperature and precipitation in the Hindu Kush Himalayan region over the last 100-plus years. *Adv. Clim. Chang. Res.* 8, 148–156. doi:10.1016/j.accre.2017.08.001.

Ren, Y., Zhou, B., Song, L., and Xiao, Y. (2017b). Interannual variability of western North Pacific subtropical high, East Asian jet and East Asian summer precipitation: CMIP5 simulation and projection. *Quat. Int.* 440, 64–70.

doi:https://doi.org/10.1016/j.quaint.2016.08.033.
Rendfrey, T., Bukovsky, M., and McGinnis, S. (2018). NA-CORDEX Visualization Collection. *UCAR/NCAR*. doi://doi.org/10.5065/90ZF-H771.
Requena, A. I., Burn, D. H., and Coulibaly, P. (2019). Estimates of gridded relative changes in 24-h extreme rainfall intensities based on pooled frequency analysis. *J. Hydrol.* 577, 123940. doi:https://doi.org/10.1016/j.jhydrol.2019.123940.
Retchless, D. P., and Brewer, C. A. (2016). Guidance for representing uncertainty on global temperature change maps. *Int. J. Climatol.* 36, 1143–1159. doi:10.1002/joc.4408.
Reyer, C. P. O., Otto, I. M., Adams, S., Albrecht, T., Baarsch, F., Cartsburg, M., et al. (2017). Climate change impacts in Central Asia and their implications for development. *Reg. Environ. Chang.* 17, 1639–1650. doi:10.1007/s10113-015-0893-z.
Rhoades, A. M., Jones, A. D., and Ullrich, P. A. (2018). Assessing Mountains as Natural Reservoirs With a Multimetric Framework. *Earth's Futur.* 6, 1221–1241. doi:10.1002/2017EF000789.
Ricker, R., Hendricks, S., Kaleschke, L., Tian-Kunze, X., King, J., and Haas, C. (2017). A weekly Arctic sea-ice thickness data record from merged CryoSat-2 and SMOS satellite data. *Cryosph.* 11, 1607–1623. doi:10.5194/tc-11-1607-2017.
Rignot, E., Mouginot, J., Scheuchl, B., van den Broeke, M., van Wessem, M. J., and Morlighem, M. (2019). Four decades of Antarctic Ice Sheet mass balance from 1979–2017. *Proc. Natl. Acad. Sci.* 116, 1095–1103. doi:10.1073/pnas.1812883116.
Ringard, J., Chiriaco, M., Bastin, S., and Habets, F. (2019). Recent trends in climate variability at the local scale using 40 years of observations: the case of the Paris region of France. *Atmos. Chem. Phys.* 19, 13129–13155. doi:10.5194/acp-19-13129-2019.
Ringard, J., Dieppois, B., Rome, S., Diedhiou, A., Pellarin, T., Konaré, A., et al. (2016). The intensification of thermal extremes in west Africa. *Glob. Planet. Change*. doi:10.1016/j.gloplacha.2015.12.009.
Roehrig, R., Bouniol, D., Guichard, F., Hourdin, F. déric, and Redelsperger, J. L. (2013). The present and future of the west african monsoon: A process-oriented assessment of CMIP5 simulations along the AMMA transect. *J. Clim.* doi:10.1175/JCLI-D-12-00505.1.
Rohde, R., Muller, R., Jacobsen, R., Perlmutter, S., Rosenfeld, A., Wurtele, J., et al. (2013). Berkeley Earth Temperature Averaging Process. *Geoinformatics Geostatistics An Overv.* 1, 1–13. doi:10.4172/gigs.1000103.
Rohini, P., Rajeevan, M., and Srivastava, A. K. (2016). On the Variability and Increasing Trends of Heat Waves over India. *Sci. Rep.* 6, 26153. Available at: https://doi.org/10.1038/srep26153.
Rösel, A., Itkin, P., King, J., Divine, D., Wang, C., Granskog, M. A., et al. (2018). Thin Sea Ice, Thick Snow, and Widespread Negative Freeboard Observed During N-ICE2015 North of Svalbard. *J. Geophys. Res. Ocean.* 123, 1156–1176. doi:10.1002/2017JC012865.
ROSHYDROMET (2019). A REPORT ON CLIMATE FEATURES ON THE TERRITORY OF THE RUSSIAN FEDERATION IN 2018. Moscow.
Rowell, D. P. (2013). Simulating SST teleconnections to Africa: What is the state of the art? *J. Clim.* doi:10.1175/JCLI-D-12-00761.1.
Rowell, D. P., Booth, B. B. B., Nicholson, S. E., and Good, P. (2015). Reconciling past and future rainfall trends over East Africa. *J. Clim.* doi:10.1175/JCLI-D-15-0140.1.
Rowell, D. P., Senior, C. A., Vellinga, M., and Graham, R. J. (2016). Can climate projection uncertainty be constrained over Africa using metrics of contemporary performance? *Clim. Change*. doi:10.1007/s10584-015-1554-4.
Roxy, M. K., Ghosh, S., Pathak, A., Athulya, R., Mujumdar, M., Murtugudde, R., et al. (2017). A threefold rise in widespread extreme rain events over central India. *Nat. Commun.* 8. doi:10.1038/s41467-017-00744-9.
Roxy, M. K., Ritika, K., Terray, P., Murtugudde, R., Ashok, K., and Goswami, B. N. (2015). Drying of Indian subcontinent by rapid Indian Ocean warming and a weakening land-sea thermal gradient. *Nat. Commun.* 6, 7423. Available at: https://doi.org/10.1038/ncomms8423.
Royal Meteorological Society (2019). Warming Stripes show the changing climate across the globe. Available at: https://www.rmets.org/news/warming-stripes-show-changing-climate-across-globe [Accessed December 19, 2019].
Rupp, D. E., Mote, P. W., Bindoff, N. L., Stott, P. a., and Robinson, D. a. (2013). Detection and Attribution of Observed Changes in Northern Hemisphere Spring Snow Cover. *J. Clim.* 26, 6904–6914. doi:10.1175/JCLI-D-12-00563.1.
Ruscica, R. C., Menéndez, C. G., and Sörensson, A. A. (2016a). Land surface-atmosphere interaction in future South American climate using a multi-model ensemble. *Atmos. Sci. Lett.* 17, 141–147. doi:10.1002/asl.635.
Ruscica, R. C., Menéndez, C. G., and Sörensson, A. A. (2016b). Land surface-atmosphere interaction in future South American climate using a multi-model ensemble. *Atmos. Sci. Lett.* 17, 141–147. doi:10.1002/asl.635.
Russo, E., Kirchner, I., Pfahl, S., Schaap, M., and Cubasch, U. (2019). Sensitivity studies with the Regional Climate Model COSMO-CLM 5.0 over the CORDEX Central Asia Domain. *Geosci. Model Dev. Discuss.* 2019, 1–33. doi:10.5194/gmd-2019-22.
Russo, S., Marchese, A. F., Sillmann, J., and Immé, G. (2016). When will unusual heat waves become normal in a

warming Africa? *Environ. Res. Lett.* doi:10.1088/1748-9326/11/5/054016.
Rusticucci, M., Kyselý, J., Almeira, G., and Lhotka, O. (2016). Long-term variability of heat waves in Argentina and recurrence probability of the severe 2008 heat wave in Buenos Aires. *Theor. Appl. Climatol.* 124, 679–689. doi:10.1007/s00704-015-1445-7.
Rutgersson, A., Jaagus, J., Schenk, F., Stendel, M., Bärring, L., Briede, A., et al. (2015). "Recent Change—Atmosphere," in (Springer, Cham), 69–97. doi:10.1007/978-3-319-16006-1_4.
Ruti, P. M., Somot, S., Giorgi, F., Dubois, C., Flaounas, E., Obermann, A., et al. (2016). Med-CORDEX initiative for Mediterranean climate studies. *Bull. Am. Meteorol. Soc.* 97. doi:10.1175/BAMS-D-14-00176.1.
Sa'adi, Z., Shahid, S., Ismail, T., Chung, E.-S., and Wang, X.-J. (2017). Trends analysis of rainfall and rainfall extremes in Sarawak, Malaysia using modified Mann–Kendall test. *Meteorol. Atmos. Phys.*, 1–15. doi:10.1007/s00703-017-0564-3.
Sabin, R. K. T. P., and Mujumdar, R. V. M. (2016). Deciphering the desiccation trend of the South Asian monsoon hydroclimate in a warming world. *Clim. Dyn.* 47, 1007–1027. doi:10.1007/s00382-015-2886-5.
Sabin, T. P. ., Krishnan, R., Ghattas, J., Denvil, S., Dufresne, J. L., Hourdin, F., et al. (2013). High resolution simulation of the South Asian monsoon using a variable resolution global climate model. *Clim. Dyn.* 41, 173–194. doi:10.1007/s00382-012-1658-8.
Saeed, F., and Athar, H. (2018). Assessment of simulated and projected climate change in Pakistan using IPCC AR4-based AOGCMs. 967–980.
Saha, A., Ghosh, S., Sahana, A. S., and Rao, E. P. (2014). Failure of CMIP5 climate models in simulating post-1950 decreasing trend of Indian monsoon. *Geophys. Res. Lett.* 41, 7323–7330. doi:10.1002/2014GL061573.
Salio, P., Hobouchian, M. P., García Skabar, Y., and Vila, D. (2015). Evaluation of high-resolution satellite precipitation estimates over southern South America using a dense rain gauge network. *Atmos. Res.* doi:10.1016/j.atmosres.2014.11.017.
Salman, S. A., Shahid, S., Ismail, T., Chung, E.-S., and Al-Abadi, A. M. (2017). Long-term trends in daily temperature extremes in Iraq. *Atmos. Res.* 198, 97–107. doi:10.1016/J.ATMOSRES.2017.08.011.
Salman, S. A., Shahid, S., Ismail, T., Rahman, N. bin A., Wang, X., and Chung, E.-S. (2018). Unidirectional trends in daily rainfall extremes of Iraq. *Theor. Appl. Climatol.* 134, 1165–1177. doi:10.1007/s00704-017-2336-x.
Samuelsson, P., Jones, C. G., Will´En, U., Ullerstig, A., Gollvik, S., Hansson, U., et al. (2011). The Rossby Centre Regional Climate model RCA3: model description and performance. *Tellus A Dyn. Meteorol. Oceanogr.* 63, 4–23. doi:10.1111/j.1600-0870.2010.00478.x.
Sanchez-Gomez, E., and Somot, S. (2018). Impact of the internal variability on the cyclone tracks simulated by a regional climate model over the Med-CORDEX domain. *Clim. Dyn.* 51. doi:10.1007/s00382-016-3394-y.
Sanchez-Lorenzo, A., Wild, M., Brunetti, M., Guijarro, J. A., Hakuba, M. Z., Calbó, J., et al. (2015). Reassessment and update of long-term trends in downward surface shortwave radiation over Europe (1939–2012). *J. Geophys. Res. Atmos.* 120, 9555–9569. doi:10.1002/2015JD023321.
Sánchez, E., Solman, S., Remedio, A. R. C., Berbery, H., Samuelsson, P., Da Rocha, R. P., et al. (2015a). Regional climate modelling in CLARIS-LPB: a concerted approach towards twentyfirst century projections of regional temperature and precipitation over South America. *Clim. Dyn.* 45, 2193–2212. doi:10.1007/s00382-014-2466-0.
Sánchez, E., Solman, S., Remedio, A. R. C., Berbery, H., Samuelsson, P., Da Rocha, R. P., et al. (2015b). Regional climate modelling in CLARIS-LPB: a concerted approach towards twentyfirst century projections of regional temperature and precipitation over South America. *Clim. Dyn.* 45, 2193–2212. doi:10.1007/s00382-014-2466-0.
Sanjay, J., Krishnan, R., Shrestha, A. B., Rajbhandari, R., and Ren, G.-Y. (2017a). Downscaled climate change projections for the Hindu Kush Himalayan region using CORDEX South Asia regional climate models. *Adv. Clim. Chang. Res.* 8, 185–198. doi:10.1016/J.ACCRE.2017.08.003.
Sanjay, J., Krishnan, R., Shrestha, A. B., Rajbhandari, R., and Ren, G. Y. (2017b). Downscaled climate change projections for the Hindu Kush Himalayan region using CORDEX South Asia regional climate models. *Adv. Clim. Chang. Res.* 8, 185–198. doi:10.1016/j.accre.2017.08.003.
Sanjay, J., Krishnan, R., Shrestha, A. B., Rajbhandari, R., and Ren, G. Y. (2017c). Downscaled climate change projections for the Hindu Kush Himalayan region using CORDEX South Asia regional climate models. *Adv. Clim. Chang. Res.* 8, 185–198. doi:10.1016/j.accre.2017.08.003.
Sanjay, J., Ramarao, M. V. S., Mujumdar, M., and Krishnan, R. (2017d). "Regional Climate Change Scenarios," in *Springer Geology* (Springer), 285–304. doi:10.1007/978-981-10-2531-0_16.
Sanogo, S., Fink, A. H., Omotosho, J. A., Ba, A., Redl, R., and Ermert, V. (2015). Spatio-temporal characteristics of the recent rainfall recovery in West Africa. *Int. J. Climatol.* 35, 4589–4605. doi:10.1002/joc.4309.
Saros, J. E., Anderson, N. J., Juggins, S., McGowan, S., Yde, J. C., Telling, J., et al. (2019). Arctic climate shifts drive rapid ecosystem responses across the West Greenland landscape. *Environ. Res. Lett.* 14, 074027. doi:10.1088/1748-9326/ab2928.
Sarr, A. B., Camara, M., and Diba, I. (2015). Spatial Distribution of Cordex Regional Climate Models Biases over West Africa. *Int. J. Geosci.* doi:10.4236/ijg.2015.69081.
Sarthi, P. P., Ghosh, S., and Kumar, P. (2015). Possible future projection of Indian Summer Monsoon Rainfall (ISMR) with the evaluation of model performance in Coupled Model Inter-comparison Project Phase 5 (CMIP5). *Glob.*

Planet. Change 129, 92–106. doi:10.1016/j.gloplacha.2015.03.005.
Satgé, F., Ruelland, D., Bonnet, M.-P., Molina, J., and Pillco, R. (2019). Consistency of satellite-based precipitation products in space and over time compared with gauge observations and snow- hydrological modelling in the Lake Titicaca region. *Hydrol. Earth Syst. Sci.* 23, 595–619. doi:10.5194/hess-23-595-2019.
Saurral, R. I., Camilloni, I. A., and Barros, V. R. (2017). Low-frequency variability and trends in centennial precipitation stations in southern South America. *Int. J. Climatol.* 37, 1774–1793. doi:10.1002/joc.4810.
Scambos, T. A., Berthier, E., Haran, T., Shuman, C. A., Cook, A. J., Ligtenberg, S. R. M., et al. (2014). Detailed ice loss pattern in the northern Antarctic Peninsula: Widespread decline driven by ice front retreats. *Cryosphere* 8, 2135–2145. doi:10.5194/tc-8-2135-2014.
Schaller, N., Kay, A. L., Lamb, R., Massey, N. R., van Oldenborgh, G. J., Otto, F. E. L., et al. (2016). Human influence on climate in the 2014 southern England winter floods and their impacts. *Nat. Clim. Chang.* 6, 627–634. doi:10.1038/nclimate2927.
Schardong, A., and Simonovic, S. (2019). Application of Regional Climate Models for Updating Intensity-Duration-Frequency Curves Under Climate Change. *Int. J. Environ. Clim. Chang.* 9, 311–330. doi:10.9734/IJECC/2019/v9i530117.
Schiermeier, Q. (2018). Droughts, heatwaves and floods: How to tell when climate change is to blame. *Nature* 560, 20–22. doi:10.1038/d41586-018-05849-9.
Schilling, J., Freier, K. P., Hertig, E., and Scheffran, J. (2012). Climate change, vulnerability and adaptation in North Africa with focus on Morocco. *Agric. Ecosyst. Environ.* doi:10.1016/j.agee.2012.04.021.
Schneider, U., Becker, A., Finger, P., Meyer-Christoffer, A., Rudolf, B., and Ziese, M. (2011). GPCC Full Data Reanalysis Version 6.0 at 1.0°: Monthly Land-Surface Precipitation from Rain-Gauges built on GTS-based and Historic Data. doi:10.5676/DWD_GPCC/FD_M_V6_100.
Schneider, U., Becker, A., Finger, P., Meyer-Christoffer, A., Ziese, M., and Rudolf, B. (2014). GPCC's new land surface precipitation climatology based on quality-controlled in situ data and its role in quantifying the global water cycle. *Theor. Appl. Climatol.* 115, 15–40. doi:10.1007/s00704-013-0860-x.
Schwingshackl, C., Davin, E. L., Hirschi, M., Sørland, S. L., Wartenburger, R., and Seneviratne, S. I. (2019). Regional climate model projections underestimate future warming due to missing plant physiological CO 2 response. *Environ. Res. Lett.* 14, 114019. doi:10.1088/1748-9326/ab4949.
Scian, B., and Pierini, J. (2013). Variability and trends of extreme dry and wet seasonal precipitation in Argentina. A retrospective analysis. *Atmósfera* 26, 3–26. doi:10.1016/S0187-6236(13)71059-2.
Scott, R. C., Nicolas, J. P., Bromwich, D. H., Norris, J. R., Lubin, D., Scott, R. C., et al. (2019). Meteorological Drivers and Large-Scale Climate Forcing of West Antarctic Surface Melt. *J. Clim.* 32, 665–684. doi:10.1175/JCLI-D-18-0233.1.
Screen, J. A., and Simmonds, I. (2010). Increasing fall-winter energy loss from the Arctic Ocean and its role in Arctic temperature amplification. *Geophys. Res. Lett.* doi:10.1029/2010GL044136.
Sein, D. V., Mikolajewicz, U., Gröger, M., Fast, I., Cabos, W., Pinto, J. G., et al. (2015). Regionally coupled atmosphere-ocean- sea ice-marine biogeochemistry model ROM: 1. Description and validation. *J. Adv. Model. Earth Syst.* doi:https://doi.org/10.1002/2014MS000357.
Sellami, H., Benabdallah, S., La Jeunesse, I., and Vanclooster, M. (2016). Quantifying hydrological responses of small Mediterranean catchments under climate change projections. *Sci. Total Environ.* doi:10.1016/j.scitotenv.2015.07.006.
Sellar, A. A., Jones, C. G., Mulcahy, J., Tang, Y., Yool, A., Wiltshire, A., et al. UKESM1: Description and evaluation of the UK Earth System Model. *J. Adv. Model. Earth Syst.* 0. doi:10.1029/2019MS001739.
Semenov, V. A. (2016). Link between anomalously cold winters in Russia and sea-ice decline in the Barents Sea. *Izv. Atmos. Ocean. Phys.* 52, 225–233. doi:10.1134/S0001433816030105.
Semenov, V. A., Mokhov, I. I., and Latif, M. (2012). Influence of the ocean surface temperature and sea ice concentration on regional climate changes in Eurasia in recent decades. *Izv. Atmos. Ocean. Phys.* 48, 355–372. doi:10.1134/S0001433812040135.
Šeparović, L., Alexandru, A., Laprise, R., Martynov, A., Sushama, L., Winger, K., et al. (2013). Present climate and climate change over North America as simulated by the fifth-generation Canadian regional climate model. *Clim. Dyn.* 41, 3167–3201. doi:10.1007/s00382-013-1737-5.
Serreze, M. C., and Barry, R. G. (2011). Processes and impacts of Arctic amplification: A research synthesis. *Glob. Planet. Change* 77, 85–96. doi:10.1016/j.gloplacha.2011.03.004.
Serreze, M. C., Walsh, J. E., Chapin III, F. S., Osterkamp, T., Dyurgerov, M., Romanovsky, V., et al. (2000). Observational Evidence of Recent Change in the Northern High-Latitude Environment. *Clim. Chang.* 46, 159–207. doi:10.1023/A:100550403.
Sevault, F., Somot, S., Alias, A., Dubois, C., Lebeaupin-Brossier, C., Nabat, P., et al. (2014). A fully coupled Mediterranean regional climate system model: design and evaluation of the ocean component for the 1980–2012 period. *Tellus A Dyn. Meteorol. Oceanogr.* 66, 23967. doi:10.3402/tellusa.v66.23967.
Sharma, A., Huang, H.-P., Zavialov, P., and Khan, V. (2018). Impact of Desiccation of Aral Sea on the Regional Climate of Central Asia Using WRF Model. *Pure Appl. Geophys.* 175, 465–478. doi:10.1007/s00024-017-1675-y.

Shean, D. E., Alexandrov, O., Moratto, Z. M., Smith, B. E., Joughin, I. R., Porter, C., et al. (2016). An automated, open-source pipeline for mass production of digital elevation models (DEMs) from very-high-resolution commercial stereo satellite imagery. *ISPRS J. Photogramm. Remote Sens.* 116, 101–117. doi:https://doi.org/10.1016/j.isprsjprs.2016.03.012.

Shepherd, A., Ivins, E., Rignot, E., Smith, B., van den Broeke, M., Velicogna, I., et al. (2018a). Mass balance of the Antarctic Ice Sheet from 1992 to 2017. *Nature* 558, 219–222. doi:10.1038/s41586-018-0179-y.

Shepherd, A., Ivins, E., Rignot, E., Smith, B., van den Broeke, M., Velicogna, I., et al. (2019). Mass balance of the Greenland Ice Sheet from 1992 to 2018. *Nature*. doi:10.1038/s41586-019-1855-2.

Shepherd, T. G., Boyd, E., Calel, R. A., Chapman, S. C., Dessai, S., Dima-West, I. M., et al. (2018b). Storylines: an alternative approach to representing uncertainty in physical aspects of climate change. *Clim. Change* 151, 555–571. doi:10.1007/s10584-018-2317-9.

Sherstyukov, B. G. (2016). The climatic conditions of the Arctic and new approaches to the forecast of the climate change. *Арктика и Север*, 39–67. doi:10.17238/issn2221-2698.2016.24.39.

Shkolnik, I. M., and Efimov, S. V. (2013). Cyclonic activity in high latitudes as simulated by a regional atmospheric climate model: Added value and uncertainties. *Environ. Res. Lett.* 8. doi:10.1088/1748-9326/8/4/045007.

Shkolnik, I., Pavlova, T., Efimov, S., and Zhuravlev, S. (2018). Future changes in peak river flows across northern Eurasia as inferred from an ensemble of regional climate projections under the IPCC RCP8.5 scenario. *Clim. Dyn.* 50, 215–230. doi:10.1007/s00382-017-3600-6.

Shongwe, M. E., Lennard, C., Liebmann, B., Kalognomou, E.-A., Ntsangwane, L., Pinto, I., et al. (2015). An evaluation of CORDEX regional climate models in simulating precipitation over Southern Africa. *Atmos. Sci. Lett.* doi:10.1002/asl2.538.

Shrestha, A., Agrawal, N., Alfthan, B., Bajracharya, S., Maréchal, J., and van Oort, B. (2015). *the Himalayan Climate and Water Atlas*.

Shvidenko, A., Buksha, I., Krakovska, S., and Lakyda, P. (2017). Vulnerability of Ukrainian forests to climate change. *Sustain.* 9. doi:10.3390/su9071152.

Siew, J. H., Tangang, F. T., and Juneng, L. (2013). Evaluation of CMIP5 coupled atmosphere-ocean general circulation models and projection of the Southeast Asian winter monsoon in the 21st century. *Int. J. Climatol.* 34, n/a-n/a. doi:10.1002/joc.3880.

Sillmann, J., Kharin, V. V., Zhang, X., Zwiers, F. W., and Bronaugh, D. (2013a). Climate extremes indices in the CMIP5 multimodel ensemble: Part 1. Model evaluation in the present climate. *J. Geophys. Res. Atmos.* 118, 1716–1733. doi:10.1002/jgrd.50203.

Sillmann, J., Kharin, V. V., Zhang, X., Zwiers, F. W., and Bronaugh, D. (2013b). Climate extremes indices in the CMIP5 multimodel ensemble: Part 1. Model evaluation in the present climate. *J. Geophys. Res. Atmos.* 118, 1716–1733. doi:10.1002/jgrd.50203.

Sillmann, J., Kharin, V. V., Zwiers, F. W., Zhang, X., and Bronaugh, D. (2013c). Climate extremes indices in the CMIP5 multimodel ensemble: Part 2. Future climate projections. *J. Geophys. Res. Atmos.* 118, 2473–2493. doi:10.1002/jgrd.50188.

Silva, W. L., Dereczynski, C., Chou, S. C., and Cavalcanti, I. (2014). Future Changes in Temperature and Precipitation Extremes in the State of Rio de Janeiro (Brazil). *Am. J. Clim. Chang.* 03, 353–365. doi:10.4236/ajcc.2014.34031.

Silvestri, G., and Vera, C. (2009). Nonstationary Impacts of the Southern Annular Mode on Southern Hemisphere Climate. *J. Clim.* 22, 6142–6148. doi:10.1175/2009JCLI3036.1.

Singh Swati A4 - Ghosh, Subimal A4 - Sahana, A. S. A4 - Vittal, H. A4 - Karmakar, Subhankar, S. A.-S. (2017). Do dynamic regional models add value to the global model projections of Indian monsoon? *Clim. Dyn.* v. 48, 1375-1397–2017 v.48 nos.3–4. doi:10.1007/s00382-016-3147-y.

Singh, D., Tsiang, M., Rajaratnam, B., and Diffenbaugh, N. S. (2014). Observed changes in extreme wet and dry spells during the South Asian summer monsoon season. *Nat. Clim. Chang.* 4, 456. Available at: https://doi.org/10.1038/nclimate2208.

Singh, M. S., Kuang, Z., Maloney, E. D., Hannah, W. M., and Wolding, B. O. (2017). Increasing potential for intense tropical and subtropical thunderstorms under global warming. *Proc. Natl. Acad. Sci. U. S. A.* 114, 11657–11662. doi:10.1073/pnas.1707603114.

Skansi, M. de los M., Brunet, M., Sigró, J., Aguilar, E., Arevalo Groening, J. A., Bentancur, O. J., et al. (2013). Warming and wetting signals emerging from analysis of changes in climate extreme indices over South America. *Glob. Planet. Change* 100, 295–307. doi:10.1016/j.gloplacha.2012.11.004.

Slingo, J., and Palmer, T. (2011). Uncertainty in weather and climate prediction. *Philos. Trans. R. Soc. A Math. Phys. Eng. Sci.* 369, 4751–4767. doi:10.1098/rsta.2011.0161.

Soares dos Santos, T., Mendes, D., and Rodrigues Torres, R. (2016). Artificial neural networks and multiple linear regression model using principal components to estimate rainfall over South America. *Nonlinear Process. Geophys.* 23, 13–20. doi:10.5194/npg-23-13-2016.

Soares, P. M. M., and Cardoso, R. M. (2018). A simple method to assess the added value using high-resolution climate distributions: application to the EURO-CORDEX daily precipitation. *Int. J. Climatol.* 38, 1484–1498. doi:10.1002/joc.5261.

Solman, S. (2016a). Systematic temperature and precipitation biases in the CLARIS-LPB ensemble simulations over South America and possible implications for climate projections. *Clim. Res.* 68, 117–136. doi:10.3354/cr01362.
Solman, S. (2016b). Systematic temperature and precipitation biases in the CLARIS-LPB ensemble simulations over South America and possible implications for climate projections. *Clim. Res.* 68, 117–136. doi:10.3354/cr01362.
Solman, S. A. (2013). Regional Climate Modeling over South America: A Review. *Adv. Meteorol.* 2013, 1–13. doi:10.1155/2013/504357.
Solman, S. A., Nuñez, M. N., and Cabré, M. F. (2008). Regional climate change experiments over southern South America. I: present climate. *Clim. Dyn.* 30, 533–552. doi:10.1007/s00382-007-0304-3.
Solman, S. A., Sanchez, E., Samuelsson, P., da Rocha, R. P., Li, L., Marengo, J., et al. (2013). Evaluation of an ensemble of regional climate model simulations over South America driven by the ERA-Interim reanalysis: model performance and uncertainties. *Clim. Dyn.* 41, 1139–1157. doi:10.1007/s00382-013-1667-2.
Song, S., and Bai, J. (2016). Increasing Winter Precipitation over Arid Central Asia under Global Warming. *Atmosphere (Basel).* 7. doi:10.3390/atmos7100139.
Soraisam, B., Karumuri, A., and D.S., P. (2018). Uncertainties in observations and climate projections for the North East India. *Glob. Planet. Change* 160, 96–108. doi:10.1016/j.gloplacha.2017.11.010.
Sørland, S. L., Schär, C., Lüthi, D., and Kjellström, E. (2018a). Bias patterns and climate change signals in GCM-RCM model chains. *Environ. Res. Lett.* 13, 074017. doi:10.1088/1748-9326/aacc77.
Sørland, S. L., Schär, C., Lüthi, D., and Kjellström, E. (2018b). Bias patterns and climate change signals in GCM-RCM model chains. *Environ. Res. Lett.* 13, 074017. doi:10.1088/1748-9326/aacc77.
Souverijns, N., Gossart, A., Demuzere, M., Lenaerts, J. T. M., Medley, B., Gorodetskaya, I. V, et al. (2019). A New Regional Climate Model for POLAR-CORDEX: Evaluation of a 30-Year Hindcast with COSMO-CLM2 Over Antarctica. *J. Geophys. Res. Atmos.* 124, 1405–1427. doi:10.1029/2018JD028862.
Souvignet, M., Gaese, H., Ribbe, L., Kretschmer, N., and Oyarzún, R. (2010). Statistical downscaling of precipitation and temperature in north-central Chile: an assessment of possible climate change impacts in an arid Andean watershed. *Hydrol. Sci. J.* 55, 41–57. doi:10.1080/02626660903526045.
Sperber, K. R., Annamalai, H., Kang, I. S., Kitoh, A., Moise, A., Turner, A., et al. (2013). The Asian summer monsoon: An intercomparison of CMIP5 vs. CMIP3 simulations of the late 20th century. *Clim. Dyn.* 41, 2711–2744. doi:10.1007/s00382-012-1607-6.
Spielhagen, R. F., Werner, K., Sørensen, S. A., Zamelczyk, K., Kandiano, E., Budeus, G., et al. (2011). Enhanced modern heat transfer to the arctic by warm atlantic water. *Science (80-.).* doi:10.1126/science.1197397.
Spinoni, J., Barbosa, P., Bucchignani, E., Cassano, J., Cavazos, T., Christensen, J. H., et al. (2019). Future global meteorological drought hotspots: a study based on CORDEX data. *J. Clim.*, JCLI-D-19-0084.1. doi:10.1175/JCLI-D-19-0084.1.
Spinoni, J., Szalai, S., Szentimrey, T., Lakatos, M., Bihari, Z., Nagy, A., et al. (2015). Climate of the Carpathian Region in the period 1961-2010: Climatologies and trends of 10 variables. *Int. J. Climatol.* 35, 1322–1341. doi:10.1002/joc.4059.
Srivastava, A. K., and Delsole, T. (2014). Robust forced response in South Asian summer monsoon in a future climate. *J. Clim.* 27, 7849–7860. doi:10.1175/JCLI-D-13-00599.1.
Srivastava, A. K., Kothawale, D. R., and Rajeevan, M. N. (2017a). "Observed Climate Variability and Change over the Indian Region," in doi:10.1007/978-981-10-2531-0.
Srivastava, A. K., Kothawale, D. R., and Rajeevan, M. N. (2017b). "Variability and Long-Term Changes in Surface Air Temperatures Over the Indian Subcontinent," in *Observed Climate Variability and Change over the Indian Region* (Springer India). doi:10.1007/978-981-10-2531-0_2.
Srivastava, A. K., Revadekar, J. V., and Rajeevan, M. (2019). "Regional Climates: Asia: South Asia," in *STATE OF THE CLIMATE IN 2018*, eds. J. Blunden and D. Arndt (Bulletin of the American Meteorological Society), S236–S240. Available at: https://journals.ametsoc.org/doi/pdf/10.1175/2019BAMSStateoftheClimate.1.
Stennett-Brown, R., Jones, J. J., Stephenson, T., and Taylor, M. (2017). Future Caribbean temperature and rainfall extremes from statistical downscaling: statistical downscaling of Caribbean temperature and rainfall. *Int. J. Climatol.* 37. doi:10.1002/joc.5126.
Stenni, B., Curran, M. A. J., Abram, N. J., Orsi, A., Goursaud, S., Masson-Delmotte, V., et al. (2017). Antarctic climate variability on regional and continental scales over the last 2000 years. *Clim. Past* 13, 1609–1634. doi:10.5194/cp-13-1609-2017.
Stephenson, T. S., Vincent, L. A., Allen, T., Van Meerbeeck, C. J., McLean, N., Peterson, T. C., et al. (2014). Changes in extreme temperature and precipitation in the Caribbean region, 1961–2010. *Int. J. Climatol.* 34, 2957–2971. doi:10.1002/joc.3889.
Steptoe, H., Jones, S. E. O., and Fox, H. (2018). Correlations Between Extreme Atmospheric Hazards and Global Teleconnections: Implications for Multihazard Resilience. *Rev. Geophys.* 56, 50–78. doi:10.1002/2017RG000567.
Stott, P. (2016). How climate change affects extreme weather events. *Science (80-.).* 352, 1517–1518. doi:10.1126/science.aaf7271.
Stott, P. A., Christidis, N., and Betts, R. A. (2011). Changing return periods of weather-related impacts: The attribution

challenge. *Clim. Change*. doi:10.1007/s10584-011-0265-8.
Stott, P. A., Gillett, N. P., Hegerl, G. C., Karoly, D. J., Stone, D. A., Zhang, X., et al. (2010). Detection and attribution of climate change: A regional perspective. *Wiley Interdiscip. Rev. Clim. Chang.* doi:10.1002/wcc.34.
Stroeve, J., Holland, M. M., Meier, W., Scambos, T., and Serreze, M. (2007). Arctic sea ice decline: Faster than forecast. *Geophys. Res. Lett.* doi:10.1029/2007GL029703.
Stuecker, M. F., Bitz, C. M., Armour, K. C., Proistosescu, C., Kang, S. M., Xie, S. P., et al. (2018). Polar amplification dominated by local forcing and feedbacks. *Nat. Clim. Chang.* 8, 1076–1081. doi:10.1038/s41558-018-0339-y.
Sun, H., Wang, A., Zhai, J., Huang, J., Wang, Y., Wen, S., et al. (2018a). Impacts of global warming of 1.5 °C and 2.0 °C on precipitation patterns in China by regional climate model (COSMO-CLM). *Atmos. Res.* 203, 83–94. doi:10.1016/j.atmosres.2017.10.024.
Sun, Q., Miao, C., Duan, Q., Ashouri, H., Sorooshian, S., and Hsu, K. L. (2018b). A Review of Global Precipitation Data Sets: Data Sources, Estimation, and Intercomparisons. *Rev. Geophys.* doi:10.1002/2017RG000574.
Sun, Y., Zhang, X., Zwiers, F. W., Song, L., Wan, H., Hu, T., et al. (2014). Rapid increase in the risk of extreme summer heat in Eastern China. *Nat. Clim. Chang.* 4, 1082.
Supari, S., Tangang, F., Juneng, L., Cruz, F., Chung, J., Ngai, S. T., et al. (submitted). Multi-model Projections of Precipitation Extremes in Southeast Asia based on CORDEX-Southeast Asia simulations. (submitted.
Supari, Tangang, F., Juneng, L., and Aldrian, E. (2017). Observed changes in extreme temperature and precipitation over Indonesia. *Int. J. Climatol.* 37, 1979–1997. doi:10.1002/joc.4829.
Surazakov, A., and Aizen, V. (2010). Positional accuracy evaluation of declassified hexagon KH-9 mapping camera imagery. *Photogramm. Eng. Remote Sensing* 76, 603–608. doi:10.14358/PERS.76.5.603.
Suriano, Z. J., and Leathers, D. J. (2016). Twenty-first century snowfall projections within the eastern Great Lakes region: Detecting the presence of a lake-induced snowfall signal in GCMs. *Int. J. Climatol.* 36, 2200–2209. doi:10.1002/joc.4488.
Susskind, J., Schmidt, G. A., Lee, J. N., and Iredell, L. (2019). Recent global warming as confirmed by AIRS. *Environ. Res. Lett.* 14. doi:10.1088/1748-9326/aafd4e.
Suzuki-Parker, A., Kusaka, H., Takayabu, I., Dairaku, K., Ishizaki, N. N., and Ham, S. (2018). Contributions of GCM/RCM Uncertainty in Ensemble Dynamical Downscaling for Precipitation in East Asian Summer Monsoon Season. *SOLA* 14, 97–104. doi:10.2151/sola.2018-017.
Syed, F. S., Giorgi, F., Pal, J. S., and Keay, K. (2010). Regional climate model simulation of winter climate over central-southwest Asia, with emphasis on NAO and ENSO effects. *Int. J. Climatol.* 30, 220–235. doi:10.1002/joc.1887.
Syed, F. S., Iqbal, W., Syed, A. A. B., and Rasul, G. (2014). Uncertainties in the regional climate models simulations of South-Asian summer monsoon and climate change. *Clim. Dyn.* 42, 2079–2097. doi:10.1007/s00382-013-1963-x.
Syed, F. S., Latif, M., Al-Maashi, A., and Ghulam, A. (2019). Regional climate model RCA4 simulations of temperature and precipitation over the Arabian Peninsula: sensitivity to CORDEX domain and lateral boundary conditions. *Clim. Dyn.* doi:10.1007/s00382-019-04974-z.
Sylla, M. B., Faye, A., Klutse, N. A. B., and Dimobe, K. (2018). Projected increased risk of water deficit over major West African river basins under future climates. *Clim. Change* 151, 247–258. doi:10.1007/s10584-018-2308-x.
Sylla, M. B., Giorgi, F., Coppola, E., and Mariotti, L. (2013). Uncertainties in daily rainfall over Africa: Assessment of gridded observation products and evaluation of a regional climate model simulation. *Int. J. Climatol.* 33, 1805–1817. doi:10.1002/joc.3551.
Sylla, M. B., Nikiema, P. M., Gibba, P., Kebe, I., and Klutse, N. A. B. (2016). *Climate change over West Africa: Recent trends and future projections*. doi:10.1007/978-3-319-31499-0_3.
Tabary, P., Dupuy, P., Gueguen, C., Moulin, L., Laurantin, O., Merlier, C., et al. (2011). A 10-year (1997-2006) reanalysis of Quantitative Precipitation Estimation over France: methodology and first results. IAHS Publ Available at: http://web13.extendcp.co.uk/iahs.info/uploads/dms/15900.351 Abstracts 53.pdf [Accessed March 22, 2019].
Takhsha, M., Nikiéma, O., Lucas-Picher, P., Laprise, R., Hernández-Díaz, L., and Winger, K. (2018). Dynamical downscaling with the fifth-generation Canadian regional climate model (CRCM5) over the CORDEX Arctic domain: effect of large-scale spectral nudging and of empirical correction of sea-surface temperature. *Clim. Dyn.* 51, 161–186. doi:10.1007/s00382-017-3912-6.
Tan, J., Jakob, C., Rossow, W. B., and Tselioudis, G. (2015). Increases in tropical rainfall driven by changes in frequency of organized deep convection. *Nature* 519, 451–454. doi:10.1038/nature14339.
Tang, J., Li, Q., Wang, S., Lee, D.-K., Hui, P., Niu, X., et al. (2016). Building Asian climate change scenario by multi-regional climate models ensemble. Part I: surface air temperature. *Int. J. Climatol.* 36, 4241–4252. doi:10.1002/joc.4628.
Tangang, F., Chung, J. X., Juneng, L., Supari, Salimun, E., Ngai, S. T., et al. (submitted). Projected future changes in rainfall in Southeast Asia based on multi-model simulations of CORDEX Southeast Asia. *Clim. Dyn.* (submitted.
Tangang, F., Santisirisomboon, J., Juneng, L., Salimun, E., Chung, J., Supari, S., et al. (2019). Projected future changes in mean precipitation over Thailand based on multi-model regional climate simulations of CORDEX Southeast Asia. *Int. J. Climatol.* 39, 5413–5436. doi:10.1002/joc.6163.

Tangang, F., Supari, S., Chung, J. X., Cruz, F., Salimun, E., Ngai, S. T., et al. (2018). Future changes in annual precipitation extremes over Southeast Asia under global warming of 2°C. *APN Sci. Bull.* 8, 3–8. doi:10.30852/sb.2018.436.

Tatebe, H., Ogura, T., Nitta, T., Komuro, Y., Ogochi, K., Takemura, T., et al. (2019). Description and basic evaluation of simulated mean state, internal variability, and climate sensitivity in MIROC6. *Geosci. Model Dev.* 12, 2727–2765. doi:10.5194/gmd-12-2727-2019.

Taylor, A. L., Dessai, S., and de Bruin, W. B. (2015). Communicating uncertainty in seasonal and interannual climate forecasts in Europe. *Philos. Trans. R. Soc. A Math. Phys. Eng. Sci.* 373, 20140454. doi:10.1098/rsta.2014.0454.

Taylor, C. M., Belusic, D., Guichard, F., Parker, D. J., Vischel, T., Bock, O., et al. (2017). Frequency of extreme Sahelian storms tripled since 1982 in satellite observations. *Nature*. doi:10.1038/nature22069.

Taylor, M. A., and Alfaro, E. J. (2005). "Central America and the Caribbean, Climate of," in *Encyclopedia of World Climatology*, ed. J. E. Oliver (Dordrecht: Springer Netherlands), 183–189. doi:10.1007/1-4020-3266-8_37.

Taylor, M. A., Centella, A., Charlery, J., Bezanilla, A., Campbell, J., Borrajero, I., et al. (2013). The Precis Caribbean Story: Lessons and Legacies. *Bull. Am. Meteorol. Soc.* 94, 1065–1073. doi:10.1175/BAMS-D-11-00235.1.

Taylor, M. A., Clarke, L. A., Centella, A., Bezanilla, A., Stephenson, T. S., Jones, J. J., et al. (2018). Future Caribbean Climates in a World of Rising Temperatures: The 1.5 vs 2.0 Dilemma. *J. Clim.* 31, 2907–2926. doi:10.1175/JCLI-D-17-0074.1.

Taylor, M. A., Stephenson, T. S., Chen, A. A., and Stephenson, K. A. (2012). Climate Change and the Caribbean: Review and Response. *Caribb. Stud.* 40, 169–200. doi:10.1353/crb.2012.0020.

Teichmann, C., Bülow, K., Otto, J., Pfeifer, S., Rechid, D., Sieck, K., et al. (2018). Avoiding Extremes: Benefits of Staying below +1.5 °C Compared to +2.0 °C and +3.0 °C Global Warming. *Atmosphere (Basel).* 9, 115. doi:10.3390/atmos9040115.

Teichmann, C., Jacob, D., Remedio, A. R., Remke, T., Buntemeyer, L., Hoffmann, P., et al. (submitted). Assessing mean climate change signals in the global CORDEX-CORE ensemble. *Clim. Dyn.* Submitted.

Terzago, S., von Hardenberg, J., Palazzi, E., and Provenzale, A. (2017). Snow water equivalent in the Alps as seen by gridded data sets, CMIP5 and CORDEX climate models. *Cryosph.* 11, 1625–1645. doi:10.5194/tc-11-1625-2017.

Teufel, B., Sushama, L., Huziy, O., Diro, G. T., Jeong, D. I., Winger, K., et al. (2019). Investigation of the mechanisms leading to the 2017 Montreal flood. *Clim. Dyn.* 52, 4193–4206. doi:10.1007/s00382-018-4375-0.

Thirumalai, K., DiNezio, P. N., Okumura, Y., and Deser, C. (2017). Extreme temperatures in Southeast Asia caused by El Niño and worsened by global warming. *Nat. Commun.* 8, 15531. doi:10.1038/ncomms15531.

Thomas, E. R., Hosking, J. S., Tuckwell, R. R., Warren, R. A., and Ludlow, E. C. (2015). Twentieth century increase in snowfall in coastal West Antarctica. *Geophys. Res. Lett.* 42, 9387–9393. doi:10.1002/2015GL065750.

Thomas, E. R., Melchior Van Wessem, J., Roberts, J., Isaksson, E., Schlosser, E., Fudge, T. J., et al. (2017). Regional Antarctic snow accumulation over the past 1000 years. *Clim. Past* 13, 1491–1513. doi:10.5194/cp-13-1491-2017.

Thompson, E., Frigg, R., and Helgeson, C. (2016). Expert Judgment for Climate Change Adaptation. *Philos. Sci.* 83, 1110–1121. doi:10.1086/687942.

Thorne, P. W., Parker, D. E., Tett, S. F. B., Jones, P. D., McCarthy, M., Coleman, H., et al. (2005). Revisiting radiosonde upper air temperatures from 1958 to 2002. *J. Geophys. Res.* 110, D18105. doi:10.1029/2004JD005753.

Tian, T., Boberg, F., Bøssing Christensen, O., Hesselbjerg Christensen, J., She, J., and Vihma, T. (2013). Resolved complex coastlines and land–sea contrasts in a high-resolution regional climate model: a comparative study using prescribed and modelled SSTs. *Tellus A Dyn. Meteorol. Oceanogr.* 65, 19951. doi:10.3402/tellusa.v65i0.19951.

Tierney, J. E., Ummenhofer, C. C., and DeMenocal, P. B. (2015). Past and future rainfall in the Horn of Africa. *Sci. Adv.* doi:10.1126/sciadv.1500682.

Tímea, K., and Anda, A. (2017). Analysis of precipitation time series at Keszthely, Hungary (1871–2014). *Időjárás* 121, 63–78.

Timm, O. E., Giambelluca, T. W., and Diaz, H. F. (2015). Statistical downscaling of rainfall changes in Hawai'i based on the CMIP5 global model projections. *J. Geophys. Res. Atmos.* 120, 92–112. doi:10.1002/2014JD022059.

Tingley, M. P., and Huybers, P. (2013). Recent temperature extremes at high northern latitudes unprecedented in the past 600 years. *Nature*. doi:10.1038/nature11969.

Top, S. et al. (submitted). Evaluation of regional climate models ALARO-0 and REMO at 0.22° resolution over the CORDEX Central Asia domain. *GMD* (submitted.

Torma, C. (9998). Evaluation of EURO-CORDEX and Med-CORDEX regional climate model ensembles over the Carpathian Region using the high resolution gridded observational database: CARPATCLIM. *Idojárás* (in press).

Torma, C., and Giorgi, F. (submitted). On the evidence of orographical modulation of regional fine scale precipitation change signals: The Carpathians. (submitted.

Torma, C., Giorgi, F., and Coppola, E. (2015). Added value of regional climate modeling over areas characterized by complex terrain-Precipitation over the Alps. *J. Geophys. Res. Atmos.* 120, 3957–3972. doi:10.1002/2014JD022781.

Torres, R. R., and Marengo, J. A. (2013a). Uncertainty assessments of climate change projections over South America. *Theor. Appl. Climatol.* 112, 253–272. doi:10.1007/s00704-012-0718-7.

Torres, R. R., and Marengo, J. A. (2013b). Uncertainty assessments of climate change projections over South America. *Theor. Appl. Climatol.* 112, 253–272. doi:10.1007/s00704-012-0718-7.
Torzhkov, I. O., Kushnir, E. A., Konstantinov, A. V, Koroleva, T. S., Efimov, S. V, and Shkolnik, I. M. (2019). Assessment of Future Climate Change Impacts on Forestry in Russia. *Russ. Meteorol. Hydrol.* 44, 180–186. doi:10.3103/S1068373919030038.
Tramblay, Y., and Somot, S. (2018). Future evolution of extreme precipitation in the Mediterranean. *Clim. Change* 151, 289–302. doi:10.1007/s10584-018-2300-5.
Trenberth, K. E. (2012). Framing the way to relate climate extremes to climate change. *Clim. Change* 115, 283–290. doi:10.1007/s10584-012-0441-5.
Trewin, B. (2018). The Australian Climate Observations Reference Network –Surface Air Temperature (ACORN-SAT) version 2.
Trinh-Tuan, L., Matsumoto, J., Tangang, F. T., Juneng, L., Cruz, F., Narisma, G., et al. (2018). Application of Quantile Mapping Bias Correction for Mid-future Precipitation Projections over Vietnam. *Sci. Online Lett. Atmos.* 15, 1–6. doi:10.2151/sola.
Tripathi, O. P., and Dominguez, F. (2013). Effects of spatial resolution in the simulation of daily and subdaily precipitation in the southwestern US. *J. Geophys. Res. Atmos.* 118, 7591–7605. doi:10.1002/jgrd.50590.
Troin, M., Vrac, M., Khodri, M., Caya, D., Vallet-Coulomb, C., Piovano, E., et al. (2016). A complete hydro-climate model chain to investigate the influence of sea surface temperature on recent hydroclimatic variability in subtropical South America (Laguna Mar Chiquita, Argentina). *Clim. Dyn.* 46, 1783–1798. doi:10.1007/s00382-015-2676-0.
Trusel, L. D., Frey, K. E., Das, S. B., Karnauskas, K. B., Kuipers Munneke, P., van Meijgaard, E., et al. (2015). Divergent trajectories of Antarctic surface melt under two twenty-first-century climate scenarios. *Nat. Geosci.* 8, 927–932. doi:10.1038/ngeo2563.
Turner, J., Barrand, N. E., Bracegirdle, T. J., Convey, P., Hodgson, D. A., Jarvis, M., et al. (2014). Antarctic climate change and the environment: an update. *Polar Rec. (Gr. Brit).* 50, 237–259. doi:10.1017/S0032247413000296.
Turner, J., Lu, H., White, I., King, J. C., Phillips, T., Hosking, J. S., et al. (2016). Absence of 21st century warming on Antarctic Peninsula consistent with natural variability. *Nature* 535, 411. Available at: https://doi.org/10.1038/nature18645.
Turner, J., Phillips, T., Thamban, M., Rahaman, W., Marshall, G. J., Wille, J. D., et al. (2019). The Dominant Role of Extreme Precipitation Events in Antarctic Snowfall Variability. *Geophys. Res. Lett.* 46, 3502–3511. doi:10.1029/2018GL081517.
Turton, J. V., Kirchgaessner, A., Ross, A. N., and King, J. C. (2017). Does high-resolution modelling improve the spatial analysis of föhn flow over the Larsen C Ice Shelf? *Weather* 72, 192–196. doi:10.1002/wea.3028.
Ummenhofer, C. C., Sen Gupta, A., and England, M. H. (2009). Causes of Late Twentieth-Century Trends in New Zealand Precipitation. *J. Clim.* 22, 3–19. doi:10.1175/2008JCLI2323.1.
USGCRP (2017). Climate Science Special Report: Fourth National Climate Assessment, Vol 1. Washingrton, D.C.
Vaittinada Ayar, P., Vrac, M., Bastin, S., Carreau, J., Déqué, M., and Gallardo, C. (2016). Intercomparison of statistical and dynamical downscaling models under the EURO- and MED-CORDEX initiative framework: present climate evaluations. *Clim. Dyn.* 46, 1301–1329. doi:10.1007/s00382-015-2647-5.
Valdés-Pineda, R., Valdés, J. B., Diaz, H. F., and Pizarro-Tapia, R. (2016). Analysis of spatio-temporal changes in annual and seasonal precipitation variability in South America-Chile and related ocean–atmosphere circulation patterns. *Int. J. Climatol.* doi:10.1002/joc.4532.
van den Besselaar, E. J. M., van der Schrier, G., Cornes, R. C., Iqbal, A. S., Klein Tank, A. M. G., Besselaar, E. J. M. van den, et al. (2017). SA-OBS: A Daily Gridded Surface Temperature and Precipitation Dataset for Southeast Asia. *J. Clim.* 30, 5151–5165. doi:10.1175/JCLI-D-16-0575.1.
van den Hurk, B., Hewitt, C., Jacob, D., Bessembinder, J., Doblas-Reyes, F., and Döscher, R. (2018). The match between climate services demands and Earth System Models supplies. *Clim. Serv.* 12, 59–63. doi:10.1016/J.CLISER.2018.11.002.
van der Bilt, W., Bakke, J., Smedsrud, L. H., Sund, M., Schuler, T., Westermann, S., et al. (2019). Climate in Svalbard 2100.
Van Khiem, M., Redmond, G., McSweeney, C., and Thuc, T. (2014). Evaluation of dynamically downscaled ensemble climate simulations for Vietnam. *Int. J. Climatol.* 34, 2450–2463. doi:10.1002/joc.3851.
Van Pham, T., Brauch, J., Dieterich, C., Frueh, B., and Ahrens, B. (2014). New coupled atmosphere-ocean-ice system COSMO-CLM/NEMO: assessing air temperature sensitivity over the North and Baltic Seas. *Oceanologia* 56, 167–189. doi:10.5697/OC.56-2.167.
van Vuuren, D. P., Edmonds, J., Kainuma, M., Riahi, K., Thomson, A., Hibbard, K., et al. (2011). The representative concentration pathways: An overview. *Clim. Change* 109, 5–31. doi:10.1007/s10584-011-0148-z.
van Wessem, J. M., van de Berg, W. J., Noël, B. P. Y., van Meijgaard, E., Amory, C., Birnbaum, G., et al. (2018). Modelling the climate and surface mass balance of polar ice sheets using RACMO2 – Part 2: Antarctica (1979–2016). *Cryosph.* 12, 1479–1498. doi:10.5194/tc-12-1479-2018.
Vautard, R., Gobiet, A., Jacob, D., Belda, M., Colette, A., Déqué, M., et al. (2013). The simulation of European heat

waves from an ensemble of regional climate models within the EURO-CORDEX project. *Clim. Dyn.* 41, 2555–2575. doi:10.1007/s00382-013-1714-z.

Vautard, R., Kadygrov, N., Iles, C., Boberg, F., and Buonomo, E. (submitted). Evaluation of the large EURO-CORDEX regional climate model ensemble. (submitted.

Vera, C. S., and Díaz, L. (2015). Anthropogenic influence on summer precipitation trends over South America in CMIP5 models. *Int. J. Climatol.* 35, 3172–3177. doi:10.1002/joc.4153.

Vermishev, M., and Moir, S. eds. (2015). *Armenia's Third National Communication on Climate Change*. Yerevan: "Lusabats" Publishing House Available at: http://www.nature-ic.am/wp-content/uploads/2013/10/1.Armenias-TNC_2015_ENG.pdf [Accessed April 2, 2019].

Vicente-Serrano, S. M., López-Moreno, J. I., Correa, K., Avalos, G., Bazo, J., Azorin-Molina, C., et al. (2018). Recent changes in monthly surface air temperature over Peru, 1964-2014. *Int. J. Climatol.* 38, 283–306. doi:10.1002/joc.5176.

Vicente-Serrano, S. M., Rodríguez-Camino, E., Domínguez-Castro, F., El Kenawy, A., and Azorín-Molina, C. (2017). An updated review on recent trends in observational surface atmospheric variables and their extremes over Spain. *Cuad. Investig. Geogr.* 43, 209–232. doi:10.18172/cig.3134.

Vichot-Llano, A., Bezanilla-Morlot, A., Martínez-Castro, D., and Centella-Artola, A. (2019). Present situation of the application of downscaling methods to the climate change pr ojections in Central America and the Caribbean. *Rev. Cuba. Meteorol.* 25. Available at: http://rcm.insmet.cu/index.php/rcm/article/view/467.

Vichot-Llano, A., and Martínez-Castro, D. (2017). Estado actual de las representación de los principales factores del clima del Caribe por modelos climáticos regionales. Estudios de sensibilidad y validación. *Rev. Cuba. Meteorol.* 23, 232–261. Available at: http://rcm.insmet.cu/index.php/rcm/article/view/243/238.

Vichot-Llano, A., Martínez-Castro, D., Centella-Artola, A., and Bezanilla-Morlot, A. (2014). Sensibilidad al cambio de dominio y resolución de tres configuraciones del modelo climático regional RegCM 4.3 para la región de América Central y el Caribe. *Rev. Climatol.* 14, 45–62. Available at: http://webs.ono.com/reclim11/reclim14e.pdf.

Vidal, J.-P., Martin, E., Franchistéguy, L., Baillon, M., and Soubeyroux, J.-M. (2010). A 50-year high-resolution atmospheric reanalysis over France with the Safran system. *Int. J. Climatol.* 30, 1627–1644. doi:10.1002/joc.2003.

Vignon, É., Traullé, O., and Berne, A. (2019). On the fine vertical structure of the low troposphere over the coastal margins of East Antarctica. *Atmos. Chem. Phys.* 19, 4659–4683. doi:10.5194/acp-19-4659-2019.

Villafuerte, M. Q., and Matsumoto, J. (2015). Significant influences of global mean temperature and ENSO on extreme rainfall in Southeast Asia. *J. Clim.* 28, 1905–1919. doi:10.1175/JCLI-D-14-00531.1.

Villafuerte, M. Q., Matsumoto, J., Akasaka, I., Takahashi, H. G., Kubota, H., and Cinco, T. A. (2014). Long-term trends and variability of rainfall extremes in the Philippines. *Atmos. Res.* 137, 1–13. doi:10.1016/j.atmosres.2013.09.021.

Vincent, L. A., Zhang, X., Brown, R. D., Feng, Y., Mekis, E., Milewska, E. J., et al. (2015). Observed Trends in Canada's Climate and Influence of Low-Frequency Variability Modes. *J. Clim.* 28, 4545–4560. doi:10.1175/JCLI-D-14-00697.1.

Vinther, B. M., Jones, P. D., Briffa, K. R., Clausen, H. B., Andersen, K. K., Dahl-Jensen, D., et al. (2010). Climatic signals in multiple highly resolved stable isotope records from Greenland. *Quat. Sci. Rev.* doi:10.1016/j.quascirev.2009.11.002.

Viste, E., Korecha, D., and Sorteberg, A. (2013). Recent drought and precipitation tendencies in Ethiopia. *Theor. Appl. Climatol.* doi:10.1007/s00704-012-0746-3.

Vizy, E. K., and Cook, K. H. (2012). Mid-twenty-first-century changes in extreme events over northern and tropical Africa. *J. Clim.* doi:10.1175/JCLI-D-11-00693.1.

Vogel, M. M., Zscheischler, J., and Seneviratne, S. I. (2018). Varying soil moisture–atmosphere feedbacks explain divergent temperature extremes and precipitation projections in central Europe. *Earth Syst. Dyn.* 9, 1107–1125. doi:10.5194/esd-9-1107-2018.

Voldoire, A., Saint-Martin, D., Sénési, S., Decharme, B., Alias, A., Chevallier, M., et al. (2019). Evaluation of CMIP6 DECK Experiments With CNRM-CM6-1. *J. Adv. Model. Earth Syst.* 11, 2177–2213. doi:10.1029/2019MS001683.

Vose, R. S., Easterling, D. R., Kunkel, K. E., LeGrande, A. N., and Wehner, M. F. (2017). "Temperature changes in the United States," in *Climate Science Special Report: Fourth National Climate Assessment, Volume I*, eds. D. J. Wuebbles, D. W. Fahey, K. A. Hibbard, D. J. Dokken, B. C. Stewart, and T. K. Maycock (Washington, DC, USA: U.S. Global Change Research Program), 185–206. doi:10.7930/J0N29V45.

Vuille, M., Franquist, E., Garreaud, R., Lavado Casimiro, W. S., and Cáceres, B. (2015). Impact of the global warming hiatus on Andean temperature. *J. Geophys. Res. Atmos.* 120, 3745–3757. doi:10.1002/2015JD023126.

Wainwright, C. M., Marsham, J. H., Keane, R. J., Rowell, D. P., Finney, D. L., Black, E., et al. (2019). 'Eastern African Paradox' rainfall decline due to shorter not less intense Long Rains. *npj Clim. Atmos. Sci.* doi:10.1038/s41612-019-0091-7.

Walsh, K. ~J. ~E., Nguyen, K.-C., and McGregor, J. ~L. (2004). Fine-resolution regional climate model simulations of

the impact of climate change on tropical cyclones near Australia. *Clim. Dyn.* 22, 47–56. doi:10.1007/s00382-003-0362-0.

Walsh, K. J. E., Fiorino, M., Landsea, C. W., and McInnes, K. L. (2007). Objectively Determined Resolution-Dependent Threshold Criteria for the Detection of Tropical Cyclones in Climate Models and Reanalyses. *J. Clim.* 20, 2307–2314. doi:10.1175/JCLI4074.1.

Walsh, K. J. E., McBride, J. L., Klotzbach, P. J., Balachandran, S., Camargo, S. J., Holland, G., et al. (2016). Tropical cyclones and climate change. *WIREs Clim. Chang.* 7, 65–89. doi:10.1002/wcc.371.

Walters, D., Boutle, I., Brooks, M., Melvin, T., Stratton, R., Vosper, S., et al. (2017). The Met Office Unified Model Global Atmosphere 6.0/6.1 and JULES Global Land 6.0/6.1 configurations. *Geosci. Model Dev.* 10, 1487–1520. doi:10.5194/gmd-10-1487-2017.

Wang, B., Wu, Z., Li, J., Liu, J., Chang, C.-P., Ding, Y., et al. (2008). How to Measure the Strength of the East Asian Summer Monsoon. *J. Clim.* 21, 4449–4463. doi:10.1175/2008JCLI2183.1.

Wang, C., Zhang, L., Lee, S. K., Wu, L., and Mechoso, C. R. (2014). A global perspective on CMIP5 climate model biases. *Nat. Clim. Chang.* doi:10.1038/nclimate2118.

Wang, G., Power, S. B., and McGree, S. (2016). Unambiguous warming in the western tropical Pacific primarily caused by anthropogenic forcing. *Int. J. Climatol.* 36, 933–944. doi:10.1002/joc.4395.

Wang, J., and Kotamarthi, V. R. (2015). High-resolution dynamically downscaled projections of precipitation in the mid and late 21st century over North America. *Earth's Futur.* 3, 268–288. doi:10.1002/2015EF000304.

Wang, L., and Chen, W. (2014). The East Asian winter monsoon: re-amplification in the mid-2000s. *Chinese Sci. Bull.* 59, 430–436. doi:10.1007/s11434-013-0029-0.

Wang, S., Dieterich, C., Döscher, R., Höglund, A., Hordoir, R., Meier, H. E. M., et al. (2015). Development and evaluation of a new regional coupled atmosphere–ocean model in the North Sea and Baltic Sea. *Tellus A Dyn. Meteorol. Oceanogr.* 67, 24284. doi:10.3402/tellusa.v67.24284.

Wang, T., Miao, J.-P., Sun, J.-Q., and Fu, Y.-H. (2018). Intensified East Asian summer monsoon and associated precipitation mode shift under the 1.5 °C global warming target. *Adv. Clim. Chang. Res.* 9, 102–111. doi:https://doi.org/10.1016/j.accre.2017.12.002.

Wang, X. L., Xu, H., Qian, B., Feng, Y., and Mekis, E. (2017). Adjusted Daily Rainfall and Snowfall Data for Canada. *Atmos. - Ocean* 55, 155–168. doi:10.1080/07055900.2017.1342163.

Wang, Y. (2009). How Do Outer Spiral Rainbands Affect Tropical Cyclone Structure and Intensity? *J. Atmos. Sci.* 66, 1250–1273. doi:10.1175/2008JAS2737.1.

Watterson, I. G., Bathols, J., and Heady, C. (2014). What influences the skill of climate models over the continents? *Bull. Am. Meteorol. Soc.* doi:10.1175/BAMS-D-12-00136.1.

Webster, M. A., Rigor, I. G., Nghiem, S. V., Kurtz, N. T., Farrell, S. L., Perovich, D. K., et al. (2014). Interdecadal changes in snow depth on Arctic sea ice. *J. Geophys. Res. Ocean.* 119, 5395–5406. doi:10.1002/2014jc009985.

Webster, M., Gerland, S., Holland, M., Hunke, E., Kwok, R., Lecomte, O., et al. (2018). Snow in the changing sea-ice systems. *Nat. Clim. Chang.* 8, 946–953. doi:10.1038/s41558-018-0286-7.

Wegmann, M., Orsolini, Y., and Zolina, O. (2018). Warm Arctic−cold Siberia: comparing the recent and the early 20th-century Arctic warmings. *Environ. Res. Lett.* 13, 025009. doi:10.1088/1748-9326/aaa0b7.

Wen, G., Huang, G., Hu, K., Qu, X., Tao, W., and Gong, H. (2014). Changes in the characteristics of precipitation over northern Eurasia. *Theor. Appl. Climatol.* 119, 653–665. doi:10.1007/s00704-014-1137-8.

Wester, P., Mishra, A., Mukherji, A., and Shrestha, A. B. eds. (2019). *The Hindu Kush Himalaya Assessment*. Cham: Springer International Publishing doi:10.1007/978-3-319-92288-1.

WGMS (2017). Global Glacier Change Bulletin No. 2 (2014-2015). , eds. M. Zemp, S. U. Nussbaumer, I. Gärtner-Roer, J. Huber, H. Machguth, F. Paul, et al. WGMS.

Whan, K., Alexander, L. V, Imielska, A., McGree, S., Jones, D., Ene, E., et al. (2014). Trends and variability of temperature extremes in the tropical Western Pacific. *Int. J. Climatol.* 34, 2585–2603. doi:10.1002/joc.3861.

Whan, K., and Zwiers, F. (2016). Evaluation of extreme rainfall and temperature over North America in CanRCM4 and CRCM5. *Clim. Dyn.* 46, 3821–3843. doi:10.1007/s00382-015-2807-7.

Whan, K., and Zwiers, F. (2017). The impact of ENSO and the NAO on extreme winter precipitation in North America in observations and regional climate models. *Clim. Dyn.* 48, 1401–1411. doi:10.1007/s00382-016-3148-x.

Whetton, P. H., Grose, M. R., and Hennessy, K. J. (2016). A short history of the future: Australian climate projections 1987–2015. *Clim. Serv.* 2–3, 1–14. doi:10.1016/j.cliser.2016.06.001.

Whetton, P., Hennessy, K., Clarke, J., McInnes, K., and Kent, D. (2012). Use of Representative Climate Futures in impact and adaptation assessment. *Clim. Change* 115, 433–442. doi:10.1007/s10584-012-0471-z.

Whittleston, D., Nicholson, S. E., Schlosser, A., and Entekhabi, D. (2017). Climate models lack jet-rainfall coupling over West Africa. *J. Clim.* doi:10.1175/JCLI-D-16-0579.1.

Whyte, F. S., Taylor, M. A., Stephenson, T. S., and Campbell, J. D. (2008). Features of the Caribbean low level jet. *Int. J. Climatol.* 28, 119–128. doi:10.1002/joc.1510.

Wilkinson, M. D., Dumontier, M., Aalbersberg, Ij. J., Appleton, G., Axton, M., Baak, A., et al. (2016). The FAIR Guiding Principles for scientific data management and stewardship. *Sci. Data* 3, 160018. doi:10.1038/sdata.2016.18.

Wille, J. D., Favier, V., Dufour, A., Gorodetskaya, I. V., Turner, J., Agosta, C., et al. (2019). West Antarctic surface melt triggered by atmospheric rivers. *Nat. Geosci.* 12, 911–916. doi:10.1038/s41561-019-0460-1.

William Landsea, C. (2015). Comments on "Monitoring and Understanding Trends in Extreme Storms: State of Knowledge." *Bull. Am. Meteorol. Soc.* 96, 1175–1176. doi:10.1175/BAMS-D-13-00211.1.

Williams, A. P., and Funk, C. (2011). A westward extension of the warm pool leads to a westward extension of the Walker circulation, drying eastern Africa. *Clim. Dyn.* doi:10.1007/s00382-010-0984-y.

WMO (2017). *WMO Guidelines on the Calculation of Climate Normals (WMO-No. 1203)*. WMO. , ed. World Meteorological Organization (WMO) Geneva: World Meteorological Organization (WMO) Available at: https://library.wmo.int/doc_num.php?explnum_id=4166.

WMO (2018). *Guidance on Good Practices for Climate Services User Engagement: Expert Team on User Interface for Climate Services*. World Meteorological Organization, WMO-No. 1214 Available at: https://library.wmo.int/index.php?lvl=notice_display&id=20254#.XKX5raBKhaQ.

Woo, S., Prakash, G., Jai, S., Oh, H., and Min, K. (2019). Projection of seasonal summer precipitation over Indian sub - continent with a high - resolution AGCM based on the RCP scenarios. *Meteorol. Atmos. Phys.* 131, 897–916. doi:10.1007/s00703-018-0612-7.

Wright, D. M., Posselt, D. J., and Steiner, A. L. (2013). Sensitivity of lake-effect snowfall to lake ice cover and temperature in the great lakes region. *Mon. Weather Rev.* 141, 670–689. doi:10.1175/MWR-D-12-00038.1.

Wu, C.-H., Freychet, N., Chen, C.-A., and Hsu, H.-H. (2017). East Asian presummer precipitation in the CMIP5 at high versus low horizontal resolution. *Int. J. Climatol.* 37, 4158–4170. doi:10.1002/joc.5055.

Wu, T., Lu, Y., Fang, Y., Xin, X., Li, L., Li, W., et al. (2019). The Beijing Climate Center Climate System Model (BCC-CSM): the main progress from CMIP5 to CMIP6. *Geosci. Model Dev.* 12, 1573–1600. doi:10.5194/gmd-12-1573-2019.

Wu, Y., and Polvani, L. M. (2017). Recent Trends in Extreme Precipitation and Temperature over Southeastern South America: The Dominant Role of Stratospheric Ozone Depletion in the CESM Large Ensemble. *J. Clim.* 30, 6433–6441. doi:10.1175/JCLI-D-17-0124.1.

Xie, P., and Arkin, P. A. (1996). Analyses of Global Monthly Precipitation Using Gauge Observations, Satellite Estimates, and Numerical Model Predictions. *J. Clim.* 9, 840–858. doi:10.1175/1520-0442(1996)009<0840:AOGMPU>2.0.CO;2.

Xie, P., Arkin, P. A., and Janowiak, J. E. (2007). "CMAP: The CPC merged analysis of precipitation," in *Advances in Global Change Research* (Dordrecht: Springer Netherlands), 319–328. doi:10.1007/978-1-4020-5835-6_25.

Xie, Y., Liu, Y., and Huang, J. (2016). Overestimated Arctic warming and underestimated Eurasia mid-latitude warming in CMIP5 simulations. *Int. J. Climatol.* 36, 4475–4487. doi:10.1002/joc.4644.

Xu, C., Li, J., Zhao, J., Gao, S., and Chen, Y. (2015). Climate variations in northern Xinjiang of China over the past 50 years under global warming. *Quat. Int.* 358, 83–92. doi:https://doi.org/10.1016/j.quaint.2014.10.025.

Xu, K., Wu, C., and Hu, B. X. (2019a). Projected changes of temperature extremes over nine major basins in China based on the CMIP5 multimodel ensembles. *Stoch. Environ. Res. Risk Assess.* 33, 321–339. doi:10.1007/s00477-018-1569-2.

Xu, M., Kang, S., Wu, H., and Yuan, X. (2018). Detection of spatio-temporal variability of air temperature and precipitation based on long-term meteorological station observations over Tianshan Mountains, Central Asia. *Atmos. Res.* 203, 141–163. doi:https://doi.org/10.1016/j.atmosres.2017.12.007.

Xu, Y., Jones, A., and Rhoades, A. (2019b). A quantitative method to decompose SWE differences between regional climate models and reanalysis datasets. *Sci. Rep.* 9, 1–11. doi:10.1038/s41598-019-52880-5.

Yan, L., and Liu, X. (2014). Has climatic warming over the Tibetan Plateau paused or continued in recent years. *J. Earth Ocean Atmos. Sci* 1, 13–28.

Yang, J., Fang, G., Chen, Y., and De-Maeyer, P. (2017). Climate change in the Tianshan and northern Kunlun Mountains based on GCM simulation ensemble with Bayesian model averaging. *J. Arid Land* 9, 622–634. doi:10.1007/s40333-017-0100-9.

Yang, W., Seager, R., Cane, M. A., and Lyon, B. (2015). The rainfall annual cycle bias over East Africa in CMIP5 coupled climate models. *J. Clim.* doi:10.1175/JCLI-D-15-0323.1.

Yao, J., Yang, Q., Mao, W., Zhao, Y., and Xu, X. (2016). Precipitation trend–Elevation relationship in arid regions of the China. *Glob. Planet. Change* 143, 1–9. doi:https://doi.org/10.1016/j.gloplacha.2016.05.007.

Yao, J., Zhou, T., Guo, Z., Chen, X., Zou, L., and Sun, Y. (2017). Improved Performance of High-Resolution Atmospheric Models in Simulating the East Asian Summer Monsoon Rain Belt. *J. Clim.* 30, 8825–8840. doi:10.1175/JCLI-D-16-0372.1.

Ye, H. (2018). Changes in duration of dry and wet spells associated with air temperatures in Russia. *Environ. Res. Lett.* 13, 034036. doi:10.1088/1748-9326/aaae0d.

Ye, H., Fetzer, E. J., Behrangi, A., Wong, S., Lambrigtsen, B. H., Wang, C. Y., et al. (2016). Increasing daily precipitation intensity associated with warmer air temperatures over northern Eurasia. *J. Clim.* 29, 623–636. doi:10.1175/JCLI-D-14-00771.1.

Ye, H., Fetzer, E. J., Wong, S., and Lambrigtsen, B. H. (2017a). Rapid decadal convective precipitation increase over Eurasia during the last three decades of the 20th century. *Sci. Adv.* 3, e1600944. doi:10.1126/sciadv.1600944.

Ye, H., Fetzer, E. J., Wong, S., Lambrigtsen, B. H., Wang, T., Chen, L., et al. (2017b). Erratum to: More frequent showers and thunderstorm days under a warming climate: evidence observed over Northern Eurasia from 1966 to 2000 (Climate Dynamics, (2017), 49, 5-6, (1933-1944), 10.1007/s00382-016-3412-0). *Clim. Dyn.* 49, 3619. doi:10.1007/s00382-016-3511-y.

Ye, H., Fetzer, E. J., Wong, S., Lambrigtsen, B. H., Wang, T., Chen, L., et al. (2017c). More frequent showers and thunderstorm days under a warming climate: evidence observed over Northern Eurasia from 1966 to 2000. *Clim. Dyn.* 49, 1933–1944. doi:10.1007/s00382-016-3412-0.

Yeh, S. W., Cai, W., Min, S. K., McPhaden, M. J., Dommenget, D., Dewitte, B., et al. (2018). ENSO Atmospheric Teleconnections and Their Response to Greenhouse Gas Forcing. *Rev. Geophys.* 56, 185–206. doi:10.1002/2017RG000568.

Yin, L., Fu, R., Shevliakova, E., and Dickinson, R. E. (2013). How well can CMIP5 simulate precipitation and its controlling processes over tropical South America? *Clim. Dyn.* 41, 3127–3143. doi:10.1007/s00382-012-1582-y.

Yiou, P., Cattiaux, J., Faranda, D., Kadygrov, N., Jézéquel, A., Naveau, P., et al. (2019). "Analyses of the Northern European summer heatwave of 2018," in *Explaining extreme events from a climate perspective* (Bulletin of the American Meteorological Society). Available at: https://www.ametsoc.org/ams/index.cfm/publications/bulletin-of-the-american-meteorological-society-bams/explaining-extreme-events-from-a-climate-perspective/.

Yoon, J.-H. (2016). Multi-model analysis of the Atlantic influence on Southern Amazon rainfall. *Atmos. Sci. Lett.* 17, 122–127. doi:10.1002/asl.600.

Yoon, J.-H., Ruby Leung, L., and Correia, J. (2012). Comparison of dynamically and statistically downscaled seasonal climate forecasts for the cold season over the United States. *J. Geophys. Res. Atmos.* 117. doi:10.1029/2012JD017650.

Yoon, J. H., Wang, S. Y. S., Gillies, R. R., Kravitz, B., Hipps, L., and Rasch, P. J. (2015). Increasing water cycle extremes in California and in relation to ENSO cycle under global warming. *Nat. Commun.* 6, 1–6. doi:10.1038/ncomms9657.

Yu, R., Li, J., Zhang, Y., and Chen, H. (2015). Improvement of rainfall simulation on the steep edge of the Tibetan Plateau by using a finite-difference transport scheme in CAM5. *Clim. Dyn.* 45, 2937–2948. doi:10.1007/s00382-015-2515-3.

Yu, Y., Pi, Y., Yu, X., Ta, Z., Sun, L., Disse, M., et al. (2019). Climate change, water resources and sustainable development in the arid and semi-arid lands of Central Asia in the past 30 years. *J. Arid Land* 11, 1–14. doi:10.1007/s40333-018-0073-3.

Yuan, X., Wang, W., Cui, J., Meng, F., Kurban, A., and De Maeyer, P. (2017). Vegetation changes and land surface feedbacks drive shifts in local temperatures over Central Asia. *Sci. Rep.* 7, 1–8. doi:10.1038/s41598-017-03432-2.

Zaninelli, P. G., Menéndez, C. G., Falco, M., López-Franca, N., and Carril, A. F. (2019a). Future hydroclimatological changes in South America based on an ensemble of regional climate models. *Clim. Dyn.* 52, 819–830. doi:10.1007/s00382-018-4225-0.

Zaninelli, P. G., Menéndez, C. G., Falco, M., López-Franca, N., and Carril, A. F. (2019b). Future hydroclimatological changes in South America based on an ensemble of regional climate models. *Clim. Dyn.* 52, 819–830. doi:10.1007/s00382-018-4225-0.

Zappa, G., Shepherd, T. G., Zappa, G., and Shepherd, T. G. (2017). Storylines of Atmospheric Circulation Change for European Regional Climate Impact Assessment. *J. Clim.* 30, 6561–6577. doi:10.1175/JCLI-D-16-0807.1.

Zazulie, N., Rusticucci, M., and Raga, G. B. (2017). Regional climate of the subtropical central Andes using high-resolution CMIP5 models—part I: past performance (1980–2005). *Clim. Dyn.* 49, 3937–3957. doi:10.1007/s00382-017-3560-x.

Zemp, M., Frey, H., Gärtner-Roer, I., Nussbaumer, S. U., Hoelzle, M., Paul, F., et al. (2015). Historically unprecedented global glacier decline in the early 21st century. *J. Glaciol.* 61, 745–762. doi:10.3189/2015JoG15J017.

Zemp, M., Huss, M., Thibert, E., Eckert, N., McNabb, R., Huber, J., et al. (2019). Global glacier mass changes and their contributions to sea-level rise from 1961 to 2016. *Nature* 568, 382–386. doi:10.1038/s41586-019-1071-0.

Zentek, R. and Heinemann, G. (2019). Verification of the regional atmospheric model CCLM v5.0 with conventional data and Lidar measurements in Antarctica. *Geosci. Model Dev. Discuss.* doi:10.5194/gmd-2019-141.

Zhang, D., Yang, C., Ju, Q., Yang, T., Gu, H., and Yu, Z. (2018a). High-resolution ensemble projections and uncertainty assessment of regional climate change over China in CORDEX East Asia. *Hydrol. Earth Syst. Sci.* 22, 3087–3103. doi:10.5194/hess-22-3087-2018.

Zhang, H., Ouyang, Z., Zheng, H., and Wang, X. (2009). Recent climate trends on the northern slopes of the Tianshan Mountains, Xinjiang, China. *J. Mt. Sci.* 6, 255–265. doi:10.1007/s11629-009-0236-y.

Zhang, M., Chen, Y., Shen, Y., and Li, B. (2019a). Tracking climate change in Central Asia through temperature and precipitation extremes. *J. Geogr. Sci.* 29, 3–28. doi:10.1007/s11442-019-1581-6.

Zhang, M., Chen, Y., Shen, Y., and Li, Y. (2017). Changes of precipitation extremes in arid Central Asia. *Quat. Int.* 436, 16–27. doi:https://doi.org/10.1016/j.quaint.2016.12.024.

Zhang, M., Luo, G., Cao, X., Hamdi, R., Li, T., Cai, P., et al. (2019b). Numerical Simulation of the Irrigation Effects on Surface Fluxes and Local Climate in Typical Mountain-Oasis-Desert Systems in the Central Asia Arid Area. *J.*

Geophys. Res. Atmos. n/a. doi:10.1029/2019JD030507.
Zhang, M., Mariotti, A., Lin, Z., Ramasmamy, V., Lamarque, J., Xie, Z., et al. (2018b). Coordination to Understand and Reduce Global Model Biases by U.S. and Chinese Institutions. *Bull. Am. Meteorol. Soc.* 99, ES109–ES113. doi:10.1175/BAMS-D-17-0301.1.
Zhang, R. (2015). Changes in East Asian summer monsoon and summer rainfall over eastern China during recent decades. *Sci. Bull.* 60, 1222–1224. doi:10.1007/s11434-015-0824-x.
Zhao, S., Li, J., Yu, R., and Chen, H. (2015). Recent Reversal of the Upper-Tropospheric Temperature Trend and its Role in Intensifying the East Asian Summer Monsoon. *Sci. Rep.* 5. doi:10.1038/srep11847.
Zheng, W., Pritchard, M. E., Willis, M. J., Tepes, P., Gourmelen, N., Benham, T. J., et al. (2018). Accelerating glacier mass loss on Franz Josef Land, Russian Arctic. *Remote Sens. Environ.* 211, 357–375. doi:10.1016/j.rse.2018.04.004.
Zhou, C., and Wang, K. (2017a). Contrasting Daytime and Nighttime Precipitation Variability between Observations and Eight Reanalysis Products from 1979 to 2014 in China. *J. Clim.* 30, 6443–6464. doi:10.1175/JCLI-D-16-0702.1.
Zhou, C., and Wang, K. (2017b). Quantifying the Sensitivity of Precipitation to the Long-Term Warming Trend and Interannual–Decadal Variation of Surface Air Temperature over China. *J. Clim.* 30, 3687–3703. doi:10.1175/JCLI-D-16-0515.1.
Zhou, L., Dickinson, R. E., Dai, A., and Dirmeyer, P. (2010). Detection and attribution of anthropogenic forcing to diurnal temperature range changes from 1950 to 1999: Comparing multi-model simulations with observations. *Clim. Dyn.* doi:10.1007/s00382-009-0644-2.
Zhou, T., Chen, X., Wu, B., Guo, Z., Sun, Y., Zou, L., et al. (2017a). A Robustness Analysis of CMIP5 Models over the East Asia-Western North Pacific Domain. *Engineering* 3, 773–778. doi:https://doi.org/10.1016/J.ENG.2017.05.018.
Zhou, T., Song, F., Ha, K.-J., and Chen, X. (2017b). "Decadal Change of East Asian Summer Monsoon: Contributions of Internal Variability and External Forcing," in *The Global Monsoon System*, 327–336. doi:10.1142/9789813200913_0026.
Zhou, W., Tang, J., Wang, X., Wang, S., Niu, X., and Wang, Y. (2016). Evaluation of regional climate simulations over the CORDEX-EA-II domain using the COSMO-CLM model. *Asia-Pacific J. Atmos. Sci.* 52, 107–127. doi:10.1007/s13143-016-0013-0.
Zhou, X., Matthes, H., Rinke, A., Huang, B., Yang, K., and Dethlo, K. (2019). Simulating Arctic 2-m air temperature and its linear trends using the HIRHAM5 regional climate model. 217, 137–149. doi:10.1016/j.atmosres.2018.10.022.
Zittis, G., and Hadjinicolaou, P. (2017). The effect of radiation parameterization schemes on surface temperature in regional climate simulations over the MENA-CORDEX domain. *Int. J. Climatol.* 37, 3847–3862. doi:10.1002/joc.4959.
Zou, L., and Zhou, T. (2016). A regional ocean–atmosphere coupled model developed for CORDEX East Asia: assessment of Asian summer monsoon simulation. *Clim. Dyn.* 47, 3627–3640. doi:10.1007/s00382-016-3032-8.

Appendix Atlas.A

[START TABLE ATLAS.A.1 HERE]

Table Atlas.A.1: Overview of observational datasets for North, West and Central Asia

Observed datasets	Domain	P	T	Data type	Spatial resolution	Temporal resolution	Period	Reference
CLIMATER	Russia Kazakhstan Turkmenistan Georgia Armenia Tajikistan Uzbekistan	x	Mean Min Max	Stations	600 stations	Daily Monthly	1874–present (each station available individually)	Russian Research Institute of Hydrometeorological Information - World Data Center (RIHMI-WDC) aisori.meteo.ru/climater (Bulygina et al., 2014)
HadGHCND	Global	-	Min Max	Gridded	2.5° lat x 3.75° lon grid	Daily	1950–present	Met Office Hadley Centre observations datasets www.metoffice.gov.uk/hadobs/hadghcnd/ (Caesar et al., 2006)
HadAT2 gridded radiosonde temperature product: anomalies relative to the monthly 1966–1995 climatology	Global	-	Min Max	Gridded on pressure levels 850, 700, 500, 300, 200, 150, 100, 50, 30 hPa	10° lon x 5° lat grid	Monthly	1950–2012	Met Office Hadley Centre observations datasets www.metoffice.gov.uk/hadobs/hadat/hadat2.html (Thorne et al., 2005)
CRUTEM4	Global	-	Min Max	Gridded	5° grid	Daily	1850–present	Met Office Hadley Centre observations datasets www.metoffice.gov.uk/hadobs/crutem4/ (Jones et al., 2012)
CCU 'IKI-Monitoring' satellite data archive	Global	-	x	Satellite images	Satellite-dependent	Daily	1984–present	Center for collective use of satellite data (CCU 'IKI-Monitoring'), Space Research Institute of the Russian Academy of Sciences (IKI RAS) ckp.geosmis.ru/default.aspx?page=6 (Loupian et al., 2015)
CPC Merged Analysis of Precipitation (CMAP)	Global	x	-	Gridded	2.5° lat – 2.5° lon grid	Monthly	1979–2019	NOAA/OAR/ESRL PSD, Boulder, CO, USA www.esrl.noaa.gov/psd/data/gridded/data.cmap.html#detail (Xie et al., 2007)

Note: The symbols x and - in the precipitation (P) and temperature (T) columns indicate that data are respectively available and unavailable. 'Mean', 'Min' and 'Max' specify which type of temperature data is available.

[END TABLE ATLAS.A.1 HERE]

[START TABLE ATLAS.A.2 HERE]

Table Atlas A.2: Overview of national and other climate change assessments.

Country	Reference period	Time horizons	RCPs or emission scenarios	National / Other	Reference
Armenia	1961–1990	2011–2040 2041–2070 2071–2100.	RCP6.0 RCP8.5	National Other	(Gevorgyan, 2014; Vermishev and Moir, 2015; Gevorgyan et al., 2016b)
Azerbaijan	1961–1990		1, 2, 3, 4, 5°C 21 CMIP5 climate models	Other	National average climate information from ClimGen, climate information for Azerbaijan crudata.uea.ac.uk/~timo/climgen/national/web/Azerbaijan/projs_seas.htm (Osborn et al., 2016)
Bahrain	1986–2005	2080–2099	RCP2.6 RCP4.5 RCP6.0 RCP8.5	Other	Climate Change Knowledge Portal climateknowledgeportal.worldbank.org/country/bahrain/climate-data-projections (World Bank Climate Change Knowledge Portal)
Georgia	1986–2010	2021–2050 2071–2100	A2 A1B B1	National	(Georgia's Third National Communication to the UNFCCC, 2015)
Iran	1982–2009	2016–2030	B1 A2 A1B	National	(IDOE, 2017)
Iraq	1961–2005	2070–2099		Other	(Salman et al., 2017)
Kazakhstan	1986–2005	2016–2035 2046–2065 2081–2099	RCP4.5 RCP8.5 42 CMIP5 models	National	(Kozhakhmetov and Nikiforova, 2016)
Kyrgyzstan	1961–1990	2020 2050 2080 2100	16 CMIP3 models A2	National	(Iliasov et al., 2013)
Russia	1981–2000	2011–2030 2041–2060 2080–2099	RCP4.5 RCP8.5	National	Climate Center of Roshydromet cc.voeikovmgo.ru/ru/klimat/izmenenie-klimata-rossii-v-21-veke (Frolov et al., 2014)
Tajikistan	1961–1990	2011–2041 2041–2070 2071–2099	RCP2.6 RCP8.5	Other	(Aalto et al., 2017)
Turkmenistan	1990	2020 2040 2060 2080 2100	A1FI B1 a MAGICC / SCENGEN	National	(Allaberdiyev, 2010)
Uzbekistan	1850–2005	2011–2100	RCP2.6 RCP4.5 RCP8.5	Other	(Huang et al., 2014b)

[END TABLE ATLAS.A.2 HERE]

[START TABLE ATLAS.A.3 HERE]

Table Atlas.A.3: South America NWS region. If both increase and decrease are indicated, papers have shown different change signal or the signal is mixed over the region, i.e. there are positive and negative changes in the same region and it is difficult to assess the climate signal.

Season	Climate variables changes			
	Precipitation GCMs	Precipitation RCMs	Temperature GCMs	Temperature RCMs
DJF	Increase[a]	Increase[a]	Increase[a]	Increase[a]
MAM		Decrease[b]		
JJA	Decrease or increase[c]	Decrease[c]	Increase[c]	Increase[c]
SON				
Annual	Increase[d]	Decrease[d]	Increase[d]	Increase[d]

Notes:
(a) (Chou et al., 2014a; Coppola et al., 2014b; Giorgi et al., 2014; Reboita et al., 2014; LYRA et al., 2016; Llopart et al., 2019)
(b) (Ruscica et al., 2016b)
(c) (Chou et al., 2014a; Coppola et al., 2014b; Giorgi et al., 2014; Reboita et al., 2014; LYRA et al., 2016; Llopart et al., 2019)
(d) (Coppola et al., 2014b; LYRA et al., 2016)

[END TABLE ATLAS.A.3 HERE]

[START TABLE ATLAS.A.4 HERE]

Table Atlas.A.4: As Table Atlas.A.3, but for the South America AMZ region.

Season	Climate variables changes			
	Precipitation GCMs	Precipitation RCMs	Temperature GCMs	Temperature RCMs
DJF	Decrease[a]	Decrease[a]	Increase[a]	Increase[a]
MAM		Decrease[b]		Increase[b]
JJA	Decrease[c]	Decrease[c]	Increase[c]	Increase[c]
SON		Decrease[d]		Increase[d]
Annual	Decrease[e]	Decrease[e]	Increase[e]	Increase[e]

Notes:
(a) (Chou et al., 2014a; Coppola et al., 2014a; Llopart et al., 2014a, 2019; Reboita et al., 2014; LYRA et al., 2016)
(b) (Chou et al., 2014a; Ruscica et al., 2016b)
(c) (Chou et al., 2014a; Coppola et al., 2014a; Llopart et al., 2014a, 2019; Reboita et al., 2014; LYRA et al., 2016)
(d) (Chou et al., 2014a; Ruscica et al., 2016b)
(e) (Coppola et al., 2014a; LYRA et al., 2016)

[END Table Atlas.A.4 HERE]

[START Table Atlas.A.5 HERE]

Table Atlas.A.5: As Table Atlas.A.3, but for the South America SAM region.

Season	Climate variables changes			
	Precipitation GCMs	Precipitation RCMs	Temperature GCMs	Temperature RCMs
DJF	Increase[a]	Decrease or increase[a]	Increase[a]	Increase[a]
MAM		Decrease[b]		Increase[b]
JJA	Decrease[c]	Decrease or increase[c]	Increase[c]	Increase[c]
SON		Decrease[d]		Increase[d]
Annual	Decrease[e]	Decrease[e]	Increase[e]	Increase[e]

Notes:
(a) (Chou et al., 2014a; Coppola et al., 2014a; Llopart et al., 2014a, 2019; Reboita et al., 2014; LYRA et al., 2016; Marengo et al., 2016)
(b) (Chou et al., 2014a; Ruscica et al., 2016b)
(c) (Chou et al., 2014a; Coppola et al., 2014a; Llopart et al., 2014a, 2019; Reboita et al., 2014; LYRA et al., 2016; Marengo et al., 2016)
(d) (Chou et al., 2014a; Ruscica et al., 2016b)
(e) (Coppola et al., 2014a; LYRA et al., 2016)

[END TABLE ATLAS.A.5 HERE]

[START TABLE ATLAS.A.6 HERE]

Table Atlas.A.6: As Table Atlas.A.3, but for the South America NEB region.

Season	Climate variables changes			
	Precipitation GCMs	Precipitation RCMs	Temperature GCMs	Temperature RCMs
DJF	Increase[a]	Decrease or increase[a]	Increase[a]	Increase[a]
MAM		Decrease or increase[b]		Increase[b]
JJA	Decrease or increase[c]	Decrease or increase[c]	Increase[c]	Increase[c]
SON		Decrease[d]		Increase[d]
Annual	Increase[e]	Decrease[e]	Increase[e]	Increase[e]

Notes:
(a) (Chou et al., 2014a; Coppola et al., 2014a; Llopart et al., 2014a, 2019; Reboita et al., 2014; LYRA et al., 2016; Marengo et al., 2016)
(b) (Chou et al., 2014a; Ruscica et al., 2016b; Marengo et al., 2017)
(c) (Chou et al., 2014a; Coppola et al., 2014a; Llopart et al., 2014a, 2019; Reboita et al., 2014; LYRA et al., 2016; Marengo et al., 2017)
(d) (Chou et al., 2014a; Ruscica et al., 2016a; Marengo et al., 2017)
(e) (Coppola et al., 2014a; LYRA et al., 2016; Marengo et al., 2017; Zaninelli et al., 2019b)

[END TABLE ATLAS.A.6 HERE]

[START Table Atlas.A.7 HERE]

Table Atlas.A.7: As Table Atlas.A.3, but for the South America SWS region.

Season	Climate variables changes			
	Precipitation GCMs	Precipitation RCMs	Temperature GCMs	Temperature RCMs
DJF	Decrease or increase[a]	Decrease or increase[a]	Increase[a]	Increase[a]
MAM		Decrease[b]		Increase[b]
JJA	Decrease[c]	Decrease[c]	Increase[c]	Increase[c]
SON		Decrease[d]		Increase[d]
Annual	Decrease[e]	Decrease or increase[e]	Increase[e]	Increase[e]

Notes:
(a) (Chou et al., 2014a; Coppola et al., 2014a; Llopart et al., 2014a, 2019; Reboita et al., 2014; Cabré et al., 2016)
(b) (Cabré et al., 2016; Ruscica et al., 2016a)
(c) (Chou et al., 2014a; Coppola et al., 2014a; Llopart et al., 2014a, 2019; Reboita et al., 2014; Cabré et al., 2016)
(d) (Cabré et al., 2016; Ruscica et al., 2016a)
(e) (Coppola et al., 2014a; Barros et al., 2015; LYRA et al., 2016)

[END TABLE ATLAS.A.7 HERE]

[START TABLE ATLAS.A.8 HERE]

Table Atlas.A.8: As Table Atlas.A.3, but for the South America SES region.

Season	Climate variables changes			
	Precipitation GCMs	Precipitation RCMs	Temperature GCMs	Temperature RCMs
DJF	Decrease or increase[a]	Increase[a]	Increase[a]	Increase[a]
MAM		Increase[b]		Increase[b]
JJA	Decrease or increase[c]	Decrease or increase[c]	Increase[c]	Increase[c]
SON		Decrease or increase[d]		Increase[d]
Annual	Decrease or increase[e]	Decrease or increase[e]	Increase[e]	Increase[e]

Notes:
(a) (Chou et al., 2014a; Coppola et al., 2014a; Llopart et al., 2014a, 2019; Reboita et al., 2014; LYRA et al., 2016; Mourão et al., 2016; Maenza et al., 2017)
(b) (Chou et al., 2014a; Ruscica et al., 2016a)
(c) (Chou et al., 2014a; Coppola et al., 2014a; Llopart et al., 2014a, 2019; Reboita et al., 2014; LYRA et al., 2016; Mourão et al., 2016)
(d) (Chou et al., 2014a; Cabré et al., 2016; Ruscica et al., 2016a)
(e) (Coppola et al., 2014a; Barros et al., 2015; LYRA et al., 2016)

[END Table Atlas.A.8 HERE]

[START Table Atlas.A.9 HERE]

Table Atlas A.9: As Table Atlas.A.3, but for the South America SSA region.

Season	Climate variables changes			
	Precipitation GCMs	Precipitation RCMs	Temperature GCMs	Temperature RCMs
DJF	Decrease[a]	Decrease or increase[a]	Increase[a]	Increase[a]
MAM		Increase[b]		Increase[b]
JJA	Decrease or increase[c]	Decrease or increase[c]	Increase[c]	Increase[c]
SON		Decrease[d]		Increase[d]
Annual	Decrease or increase[e]	Decrease or increase[e]	Increase[e]	Increase[e]

Notes:
(a) (Chou et al., 2014a; Coppola et al., 2014a; Llopart et al., 2014a, 2019; Reboita et al., 2014)
(b) (Cabré et al., 2016)
(c) (Chou et al., 2014a; Coppola et al., 2014a; Llopart et al., 2014a, 2019; Reboita et al., 2014)
(d) (Cabré et al., 2016)
(e) (Coppola et al., 2014a; Barros et al., 2015; Zaninelli et al., 2019b)
(f) (Chou et al., 2014; Giorgi et al., 2014; López-Franca et al., 2016; Sillmann et al., 2013b)

[END TABLE ATLAS.A.9 HERE]

Figures

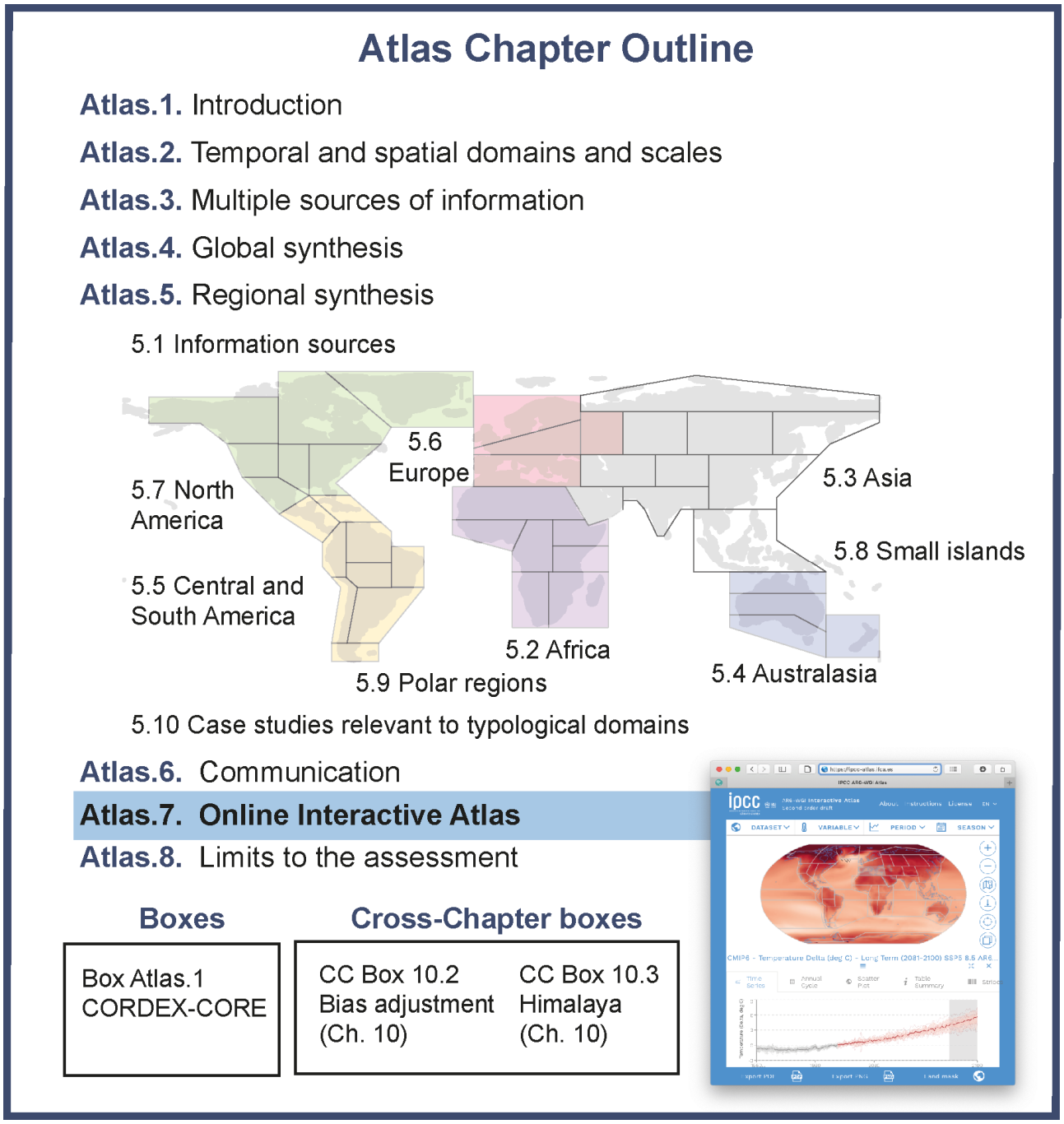

Figure Atlas.1: The main components of the Atlas Chapter with, bottom right, a screen-shot from the online Interactive Atlas.

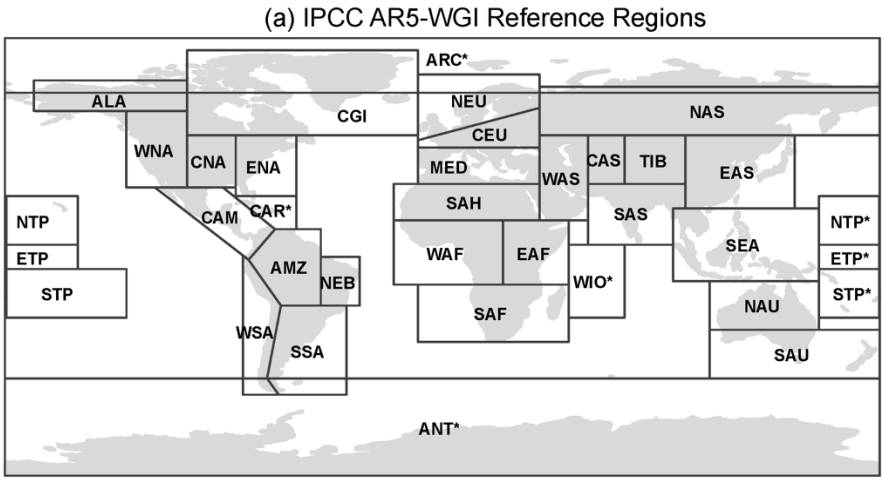

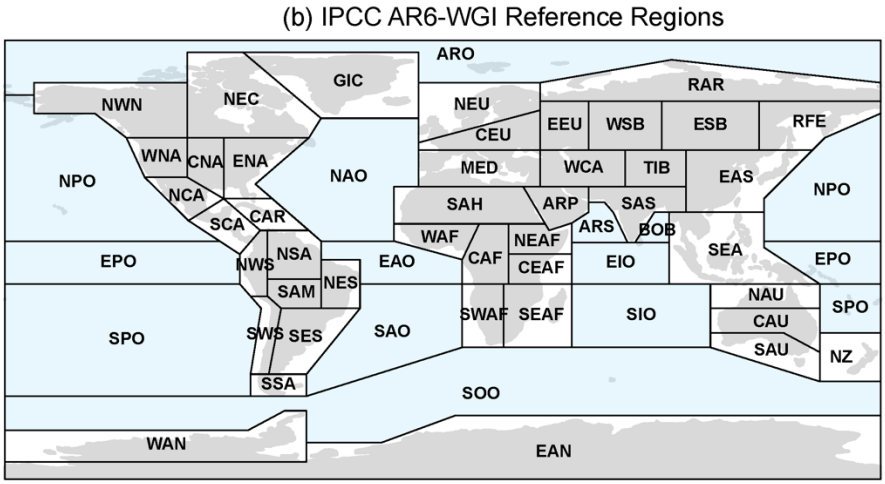

1	GIC	Greenland/Iceland
2	NEC	N.E.Canada
3	CNA	C.North-America
4	ENA	E.North-America
5	NWN	N.W.North-America
6	WNA	W.North-America
7	NCA	N.Central-America
8	SCA	S.Central-America
9	CAR	Caribbean
10	NWS	N.W.South-America
11	SAM	South-American-Monsoon
12	SSA	S.South-America
13	SWS	S.W.South-America
14	SES	S.E.South-America
15	NSA	N.South-America
16	NES	N.E.South-America
17	NEU	N.Europe
18	CEU	C.Europe
19	EEU	E.Europe
20	MED	Mediterranean

21	WAF	West-Africa
22	SAH	Sahara
23	NEAF	North-East-Africa
24	CEAF	Central-East-Africa
25	SWAF	South-West-Africa
26	SEAF	South-Eeast-Africa
27	CAF	Central-Africa
28	RAR	Russian-Arctic
29	RFE	Russian-Far-East
30	ESB	E.Siberia
31	WSB	W.Siberia
32	WCA	W.C.Asia
33	TIB	Tibetan-Plateau
34	EAS	E.Asia
35	ARP	Arabian-Peninsula
36	SAS	S.Asia
37	SEA	S.E.Asia

38	NAU	N.Australia
39	CAU	C.Australia
40	SAU	S.Australia
41	NZ	New-Zealand
42	EAN	E.Antarctica
43	WAN	W.Antarctica
44	ARO	Arctic-Ocean
45	NPO	N.Pacific-Ocean
46	EPO	Equatorial.Pacific-Ocean
47	SPO	S.Pacific-Ocean
48	NAO	N.Atlantic-Ocean
49	EAO	Equatorial.Atlantic-Ocean
50	SAO	S.Atlantic-Ocean
51	ARS	Arabian-Sea
52	BOB	Bengal-Gulf
53	EIO	Equatorial.Indic-Ocean
54	SIO	S.Indic-Ocean
55	SOO	Southern-Ocean

Figure Atlas.2: Reference AR5 (a) and AR6 (b) WGI regions (Iturbide et al., *submitted*). The latter includes both land and ocean regions and it is used as the standard for the regional analysis of atmospheric variables in the Atlas Chapter and Interactive Atlas. The definition of the regions and companion notebooks and scripts are available at the ATLAS GitHub (reference-regions section) (Atlas GitHub, 2020).

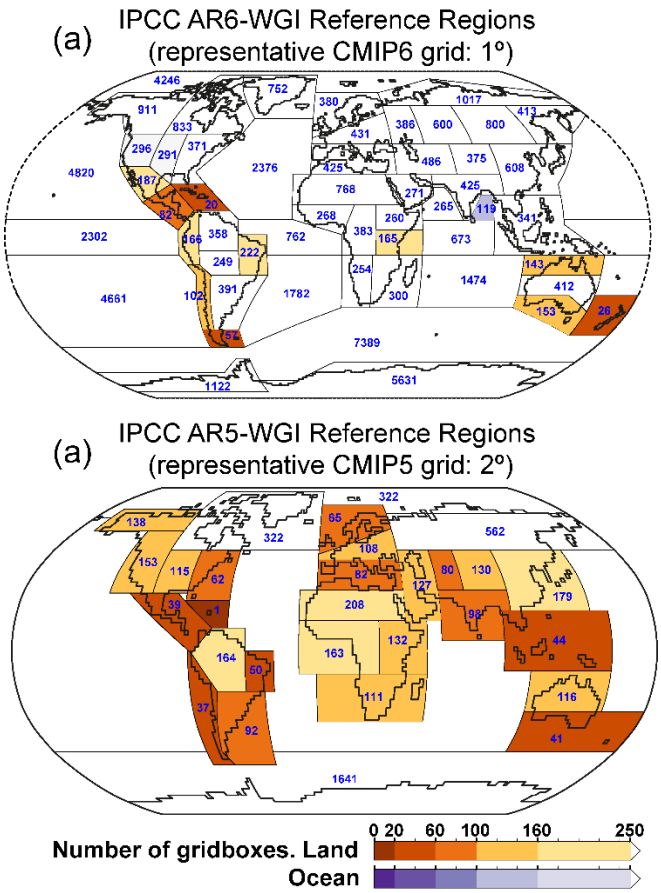

Figure Atlas.3: Number of land gridboxes (blue number) for the (a) AR6 and (b) AR5 reference regions for the representative grid-boxes of the CMIP6 (1° horizontal resolution) and CMIP5 (2° horizontal resolution) model outputs. Colour shading indicate regions with fewer than 250 grid-boxes (darkest shading if fewer than 20 grid-boxes). The polygons in the figures show the climate reference regions shown in Figure Atlas.2:; adapted from Iturbide et al. (*submitted*). This figure can be reproduced from the ATLAS GitHub (reference regions and grids sections) (Atlas GitHub, 2020).

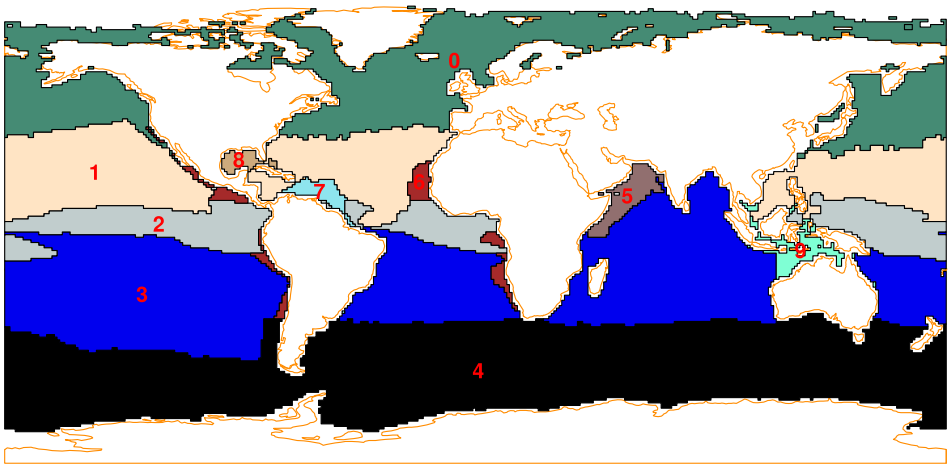

Figure Atlas.4: Ten oceanic regions defined by their biological activity used for the regional analysis of oceanic variables in the Interactive Atlas.

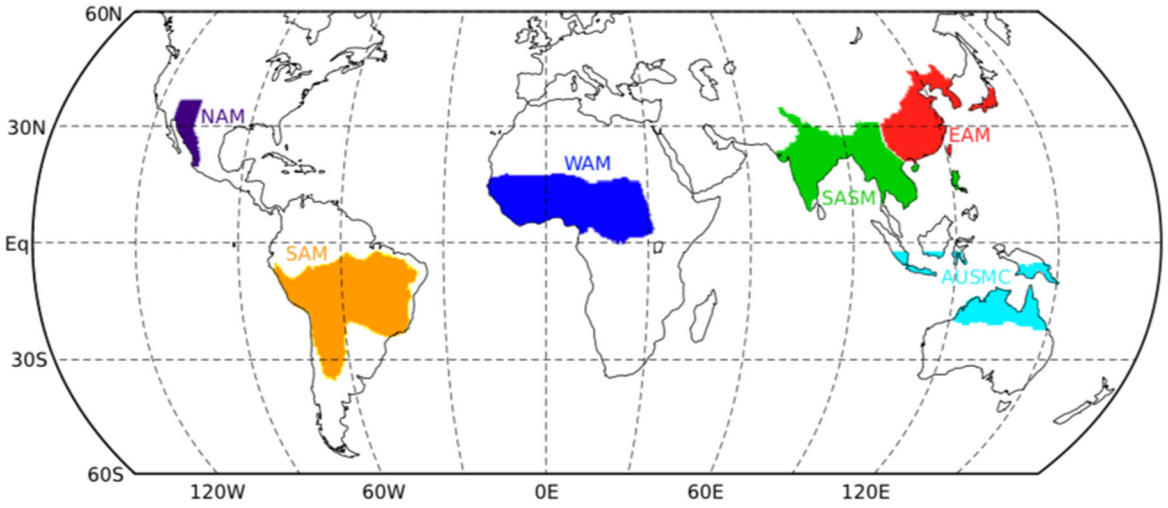

Figure Atlas.5: Land monsoon regions of North America (NAM), South America (SAM), Africa (WAM), Asia (SASM and EAM) and Australasia (AUSMC). These regions can be used alternatively to the reference regions for the regional analysis of atmospheric variables in the Interactive Atlas.

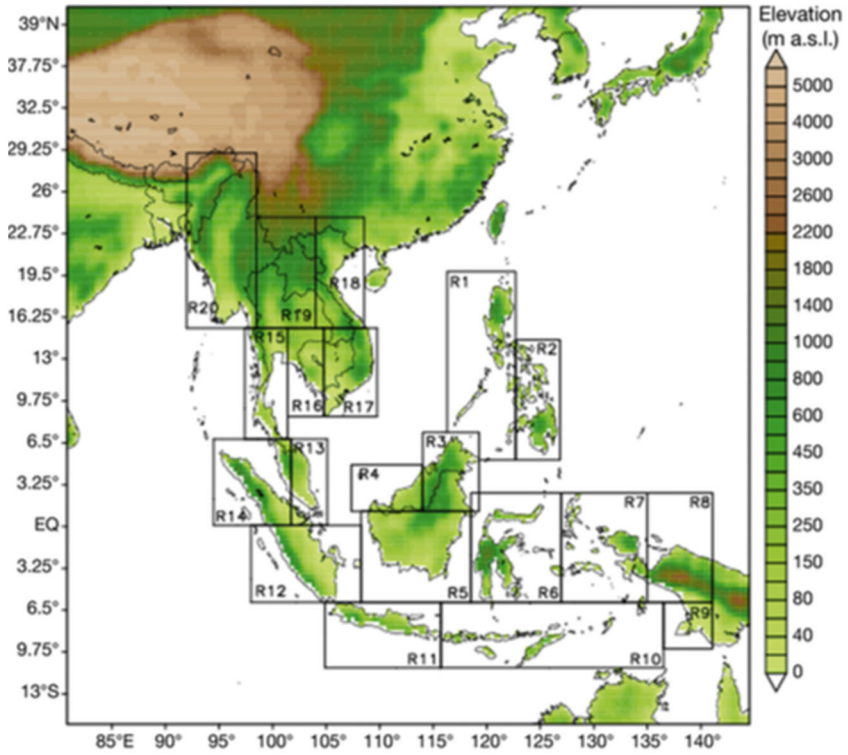

Figure Atlas.6: CORDEX-SEA subregions based on historical rainfall climatology and variability (Juneng et al., 2016).

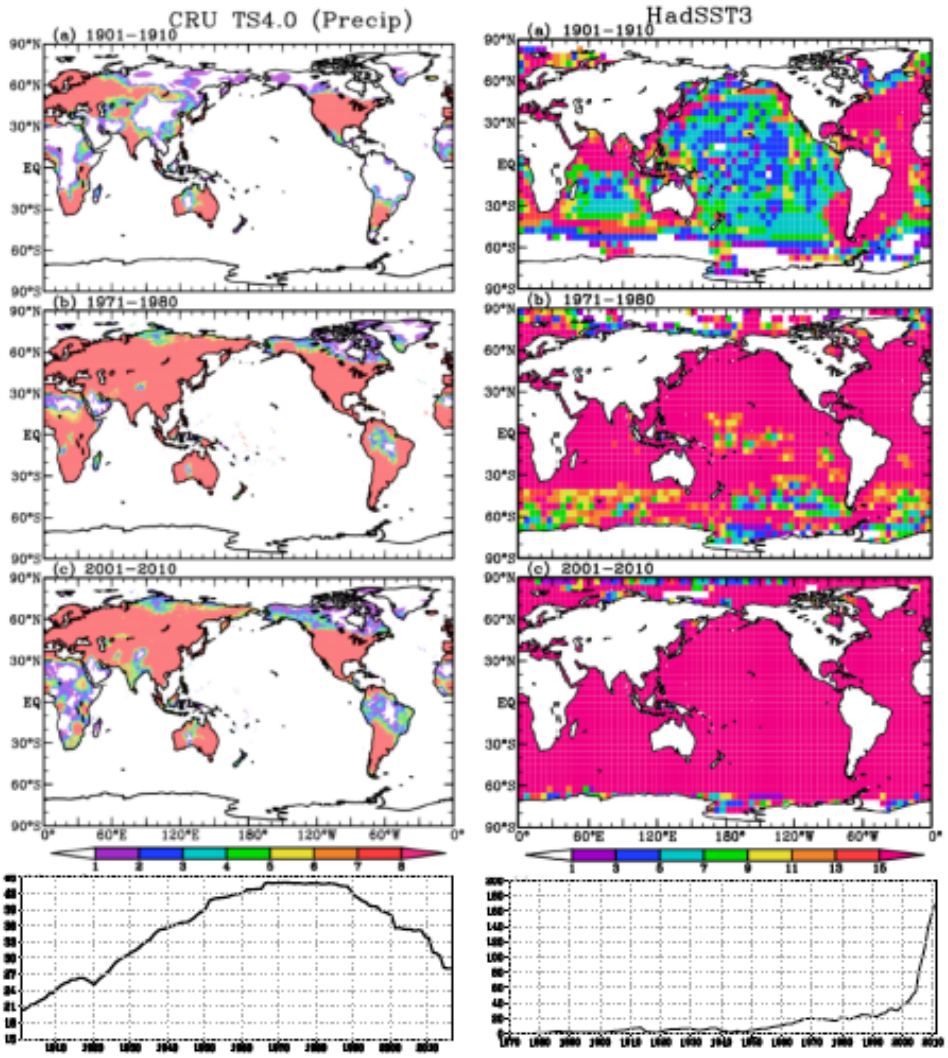

Figure Atlas.7: Left: Number of stations per 0.5 x 0.5 grid cell reported over the period of 1901–1910, 1971–1980, and 2001–2010 (top 1-3) and global total number of stations reported over the entire globe for precipitation for CRU TS4.0 dataset (bottom). Right: same as left except the HadSST3 dataset.

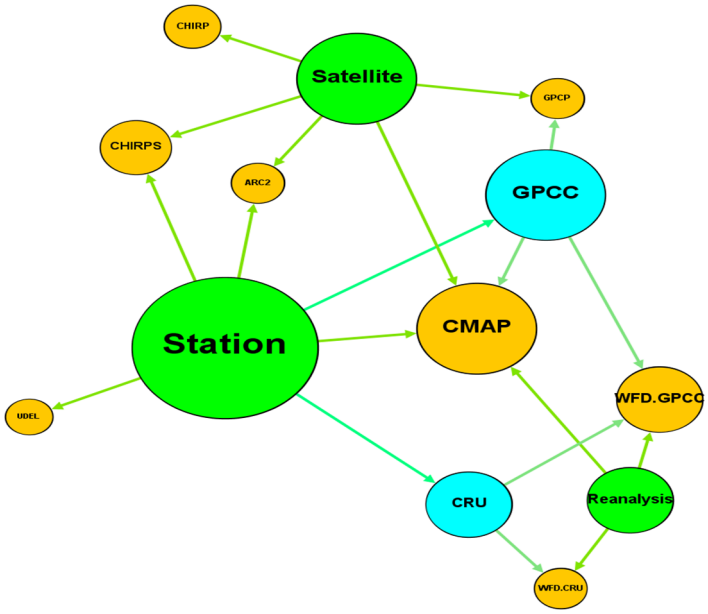

Figure Atlas.8: Relationship between gridded precipitation dataset and three classes of input data; station, satellite and reanalysis. Input datasets are shown in green, blue shows gridded datasets that are used as input to others shown in orange. (Indasi, 2019)

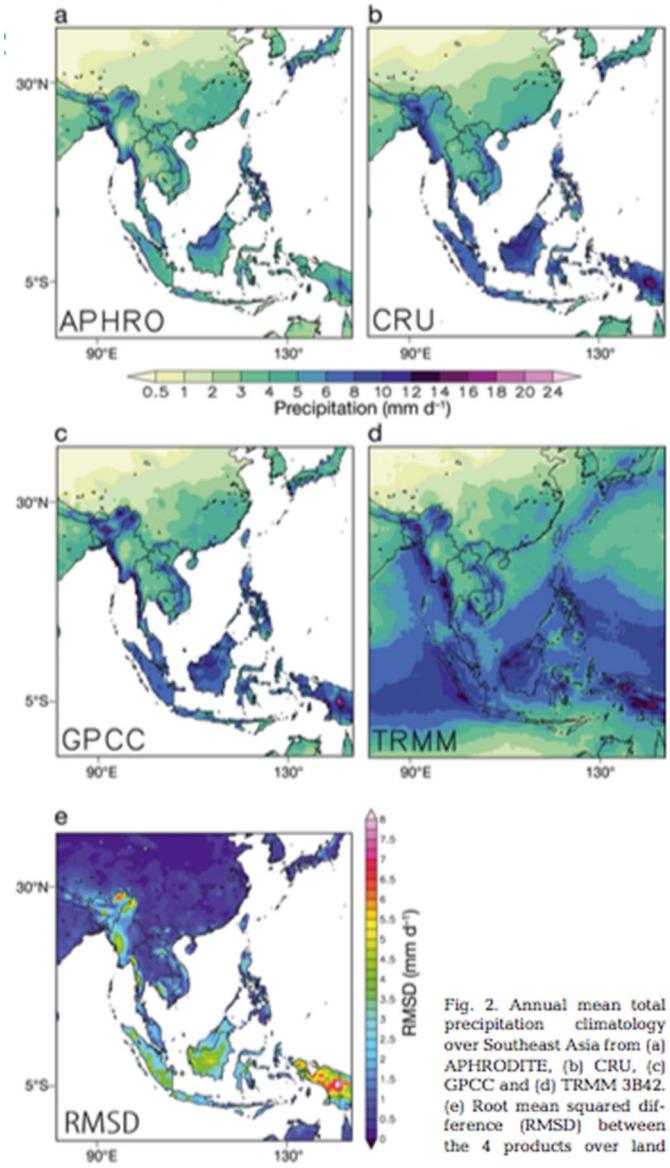

Fig. 2. Annual mean total precipitation climatology over Southeast Asia from (a) APHRODITE, (b) CRU, (c) GPCC and (d) TRMM 3B42. (e) Root mean squared difference (RMSD) between the 4 products over land

Figure Atlas.9: Differences in precipitation values in the different observation datasets in Southeast Asia (from Juneng et al., 2016).

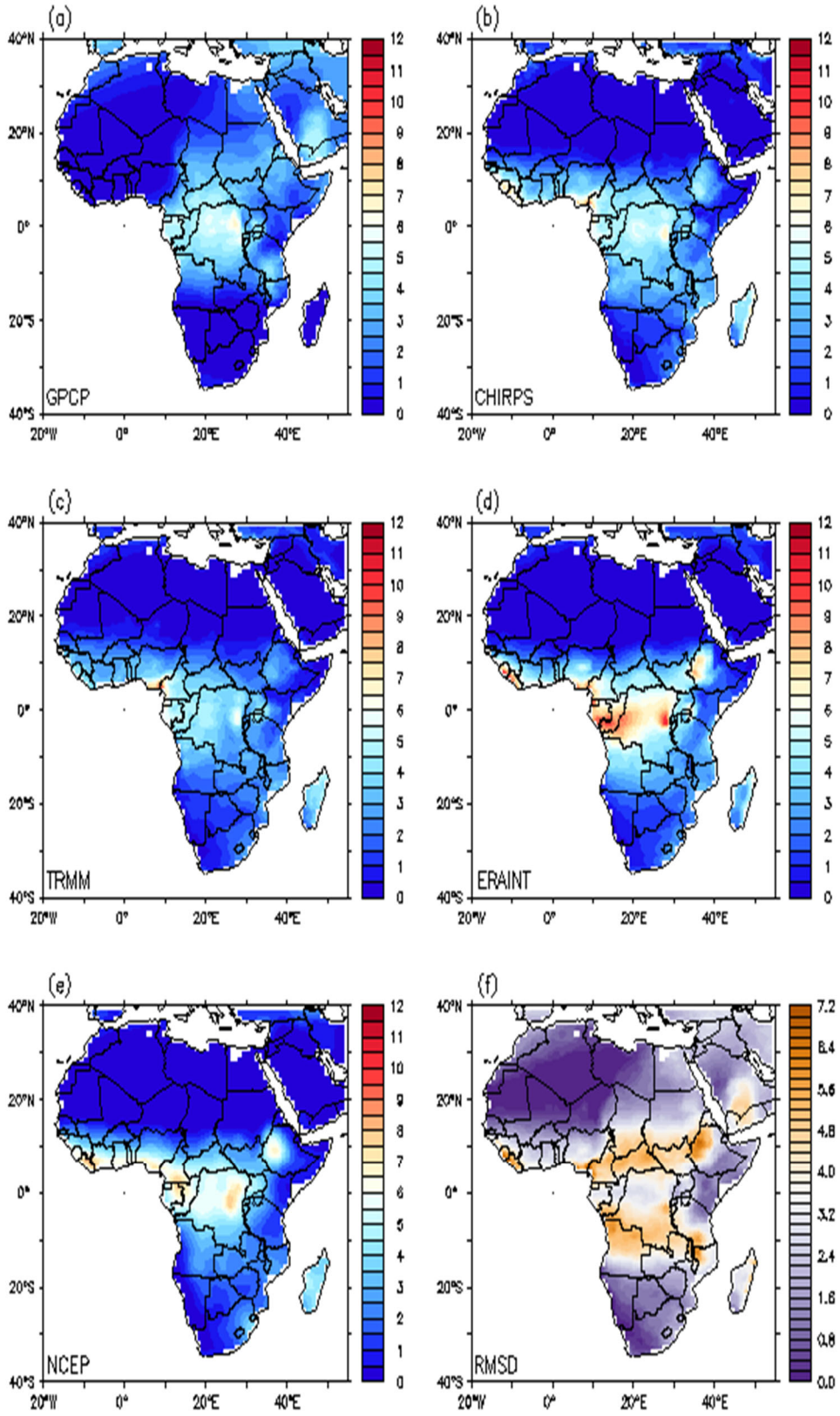

Figure Atlas.10: Similar to Figure Atlas.9: but for Africa.

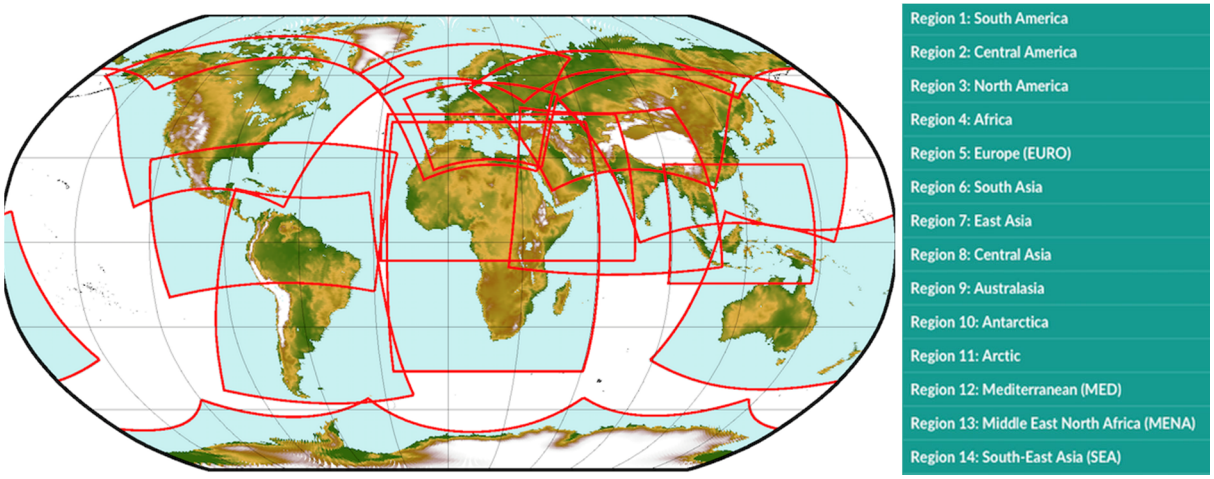

Figure Atlas.11: CORDEX domains and the topography corresponding to 0.44º resolution.

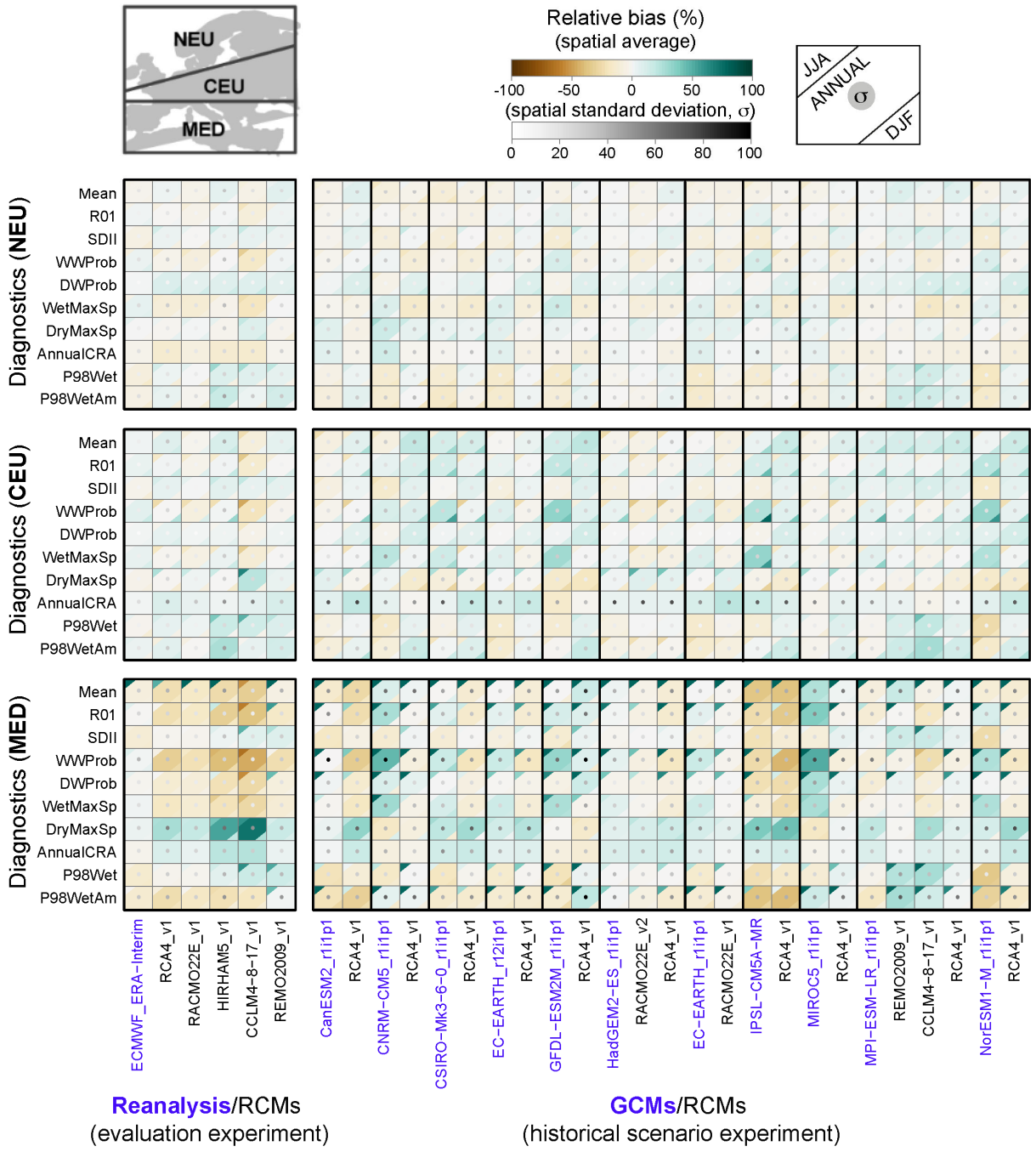

Figure Atlas.12: Evaluation (relative bias) of precipitation-based diagnostics shown separately for the three European subdomains NEU, CEU and MED for reanalysis- and historical GCM-driven RCM simulations showing annual and seasonal results (as shown in the legend). The colour matrices show the mean spatial biases of the different diagnostics (in rows) and columns are organized in blocks corresponding to each of the GCMs (blue labels, including ERA-Interim in first place slightly separated) together with their coupled RCMs (black labels). This allows to compare the bias of the RCM with that of the driving GCM. All diagnostic biases are relative with respect to the observational reference (EWEMBI).

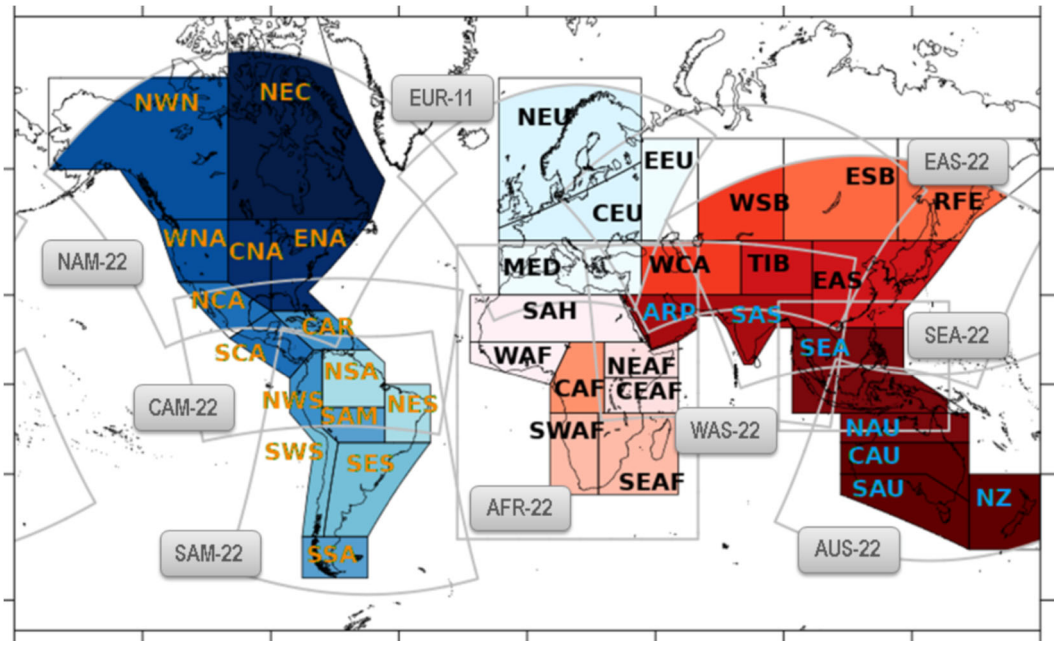

Box Atlas.1, Figure 1: Nine domains used for global coverage in CORDEX CORE; see Figure Atlas.11: for the full list of CORDEX domains (Teichmann et al., submitted).

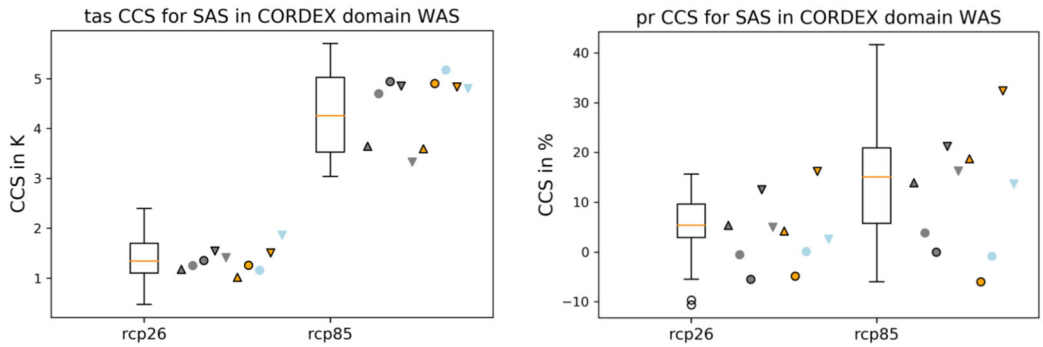

Box Atlas.1, Figure 2: Temperatures (left) and precipitation (right) climate change signals at the end of the century (2070-2099) for the entire CMIP5 ensemble (box-whisker plots) and the CORDEX-CORE driving GCMs of the respective CORDEX-CORE results in the SAS (South Asia) reference regions. The driving GCMs with low, medium and high equilibrium climate sensitivity are plotted as gray triangles pointing upwards, circle and triangle pointing downwards, respectively and the corresponding RCM results are drawn using the same symbols as before, but in orange for REMO and in blue for RegCM (Teichmann et al., submitted).

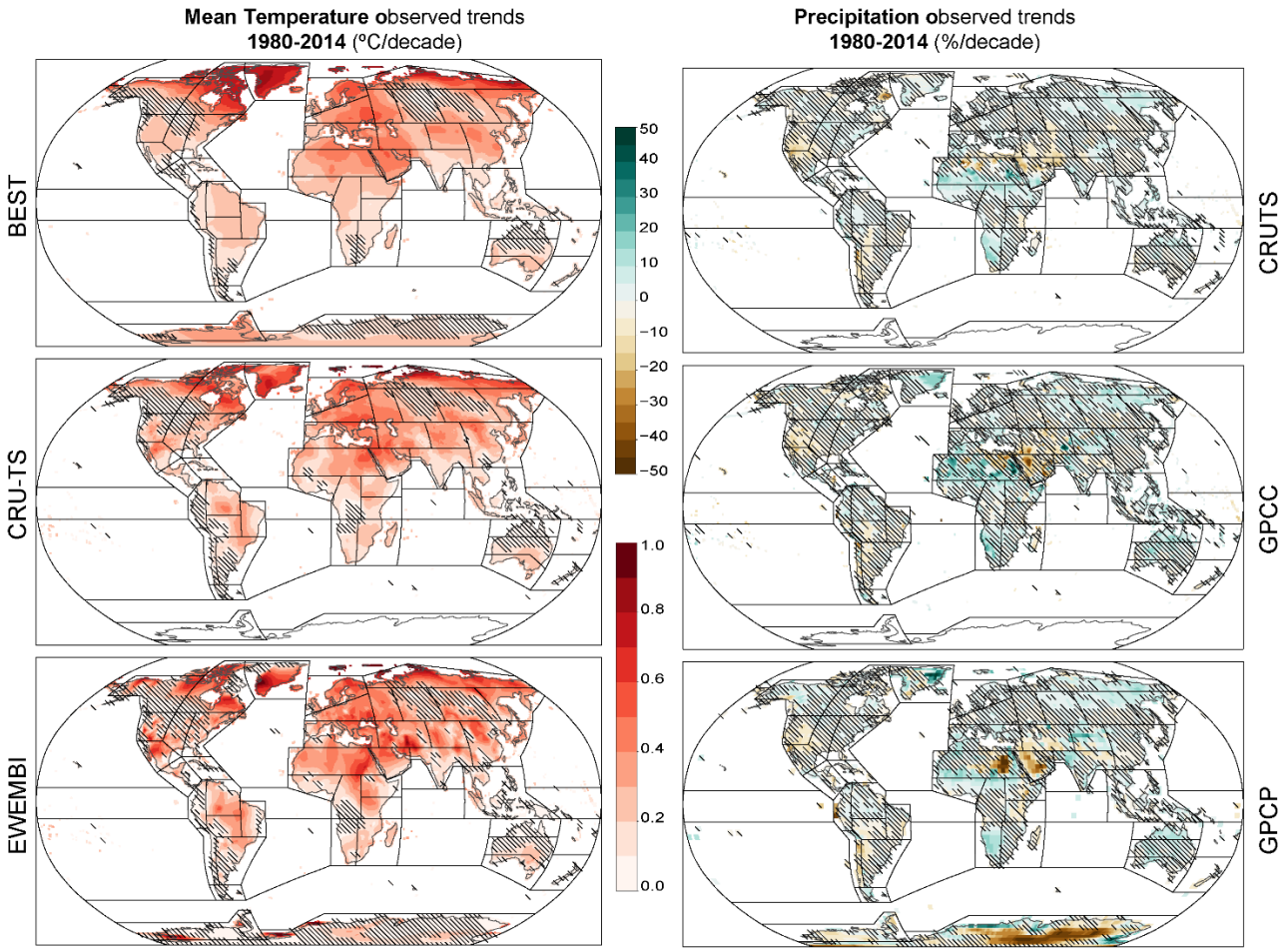

Figure Atlas.13: Observed trends of annual mean surface air temperature (left-hand column) and precipitation (right-hand column) – see Section Atlas.3 for details of the datasets. Observed linear trends are calculated for the common 1980–2014 period from three different datasets and are expressed as ºC per decade and relative change (with respect to the climatological value) per decade, respectively. Hatching indicates regions where trends are not significant (at a 0.1 significance level) and the black lines mark out the reference regions defined in Section Atlas.2.

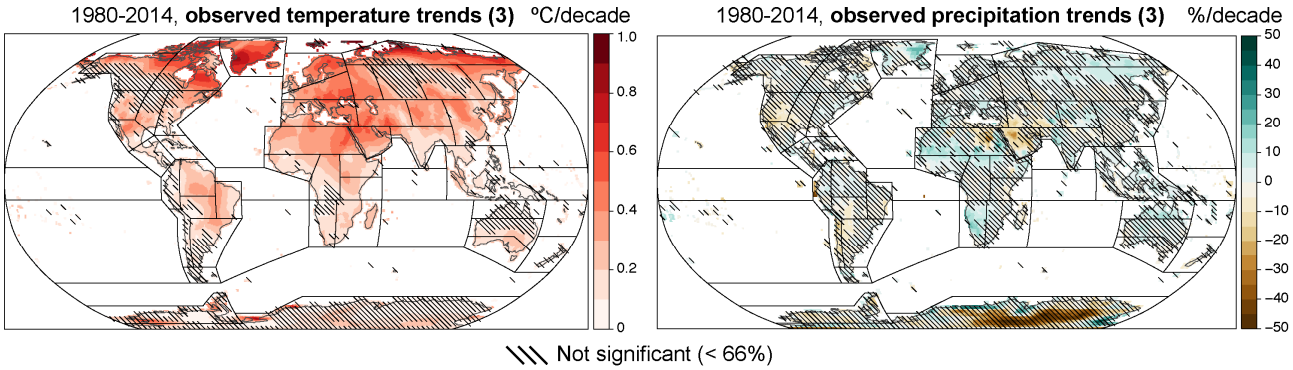

Figure Atlas.14: Consensus on the observed trends from the three observational datasets shown in Figure Atlas.13: (CRU TS, BERKELEY and EWEMBI for temperature; CRU TS, GPCC and GPCP for precipitation). Hatching indicates regions where no or only one dataset provides a significant trend. Linear trends are calculated for the common 1980–2014 period and expressed in °C per decade (temperature) and % relative change per decade (precipitation) with respect to the climatological mean over this period.

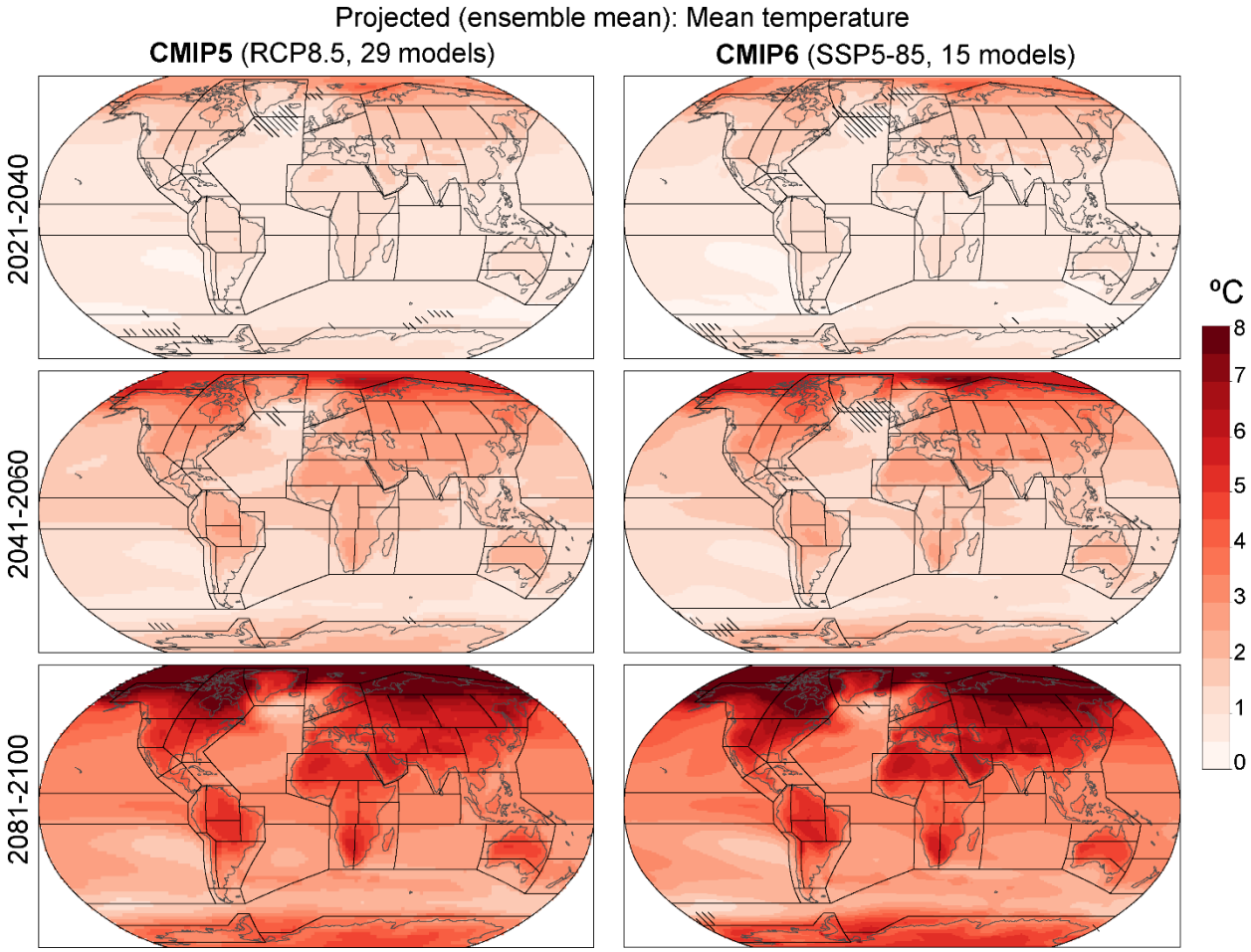

Figure Atlas.15: Future projected changes of annual mean surface air temperature in the CMIP5 (left-hand column) and CMIP6 (right-hand column) ensembles. Projected changes are calculated as the climatology differences for near-term (2021–2040), medium-term (2041–2060) and long-term (2081–2100) periods for the emissions scenario RCP8.5 (SSP5-8.5 for CMIP6) with respect to the historical (1986–2005) period; values are expressed as ºC. Hatching indicates lack of model agreement (less than 80% of agreement; as defined in Nikulin et al., 2018) and the black lines mark out the reference regions defined in Section Atlas.2. Similar analysis for other indices and scenarios (including warming levels) are available at the Interactive Atlas (http://ipcc-atlas.ifca.es).

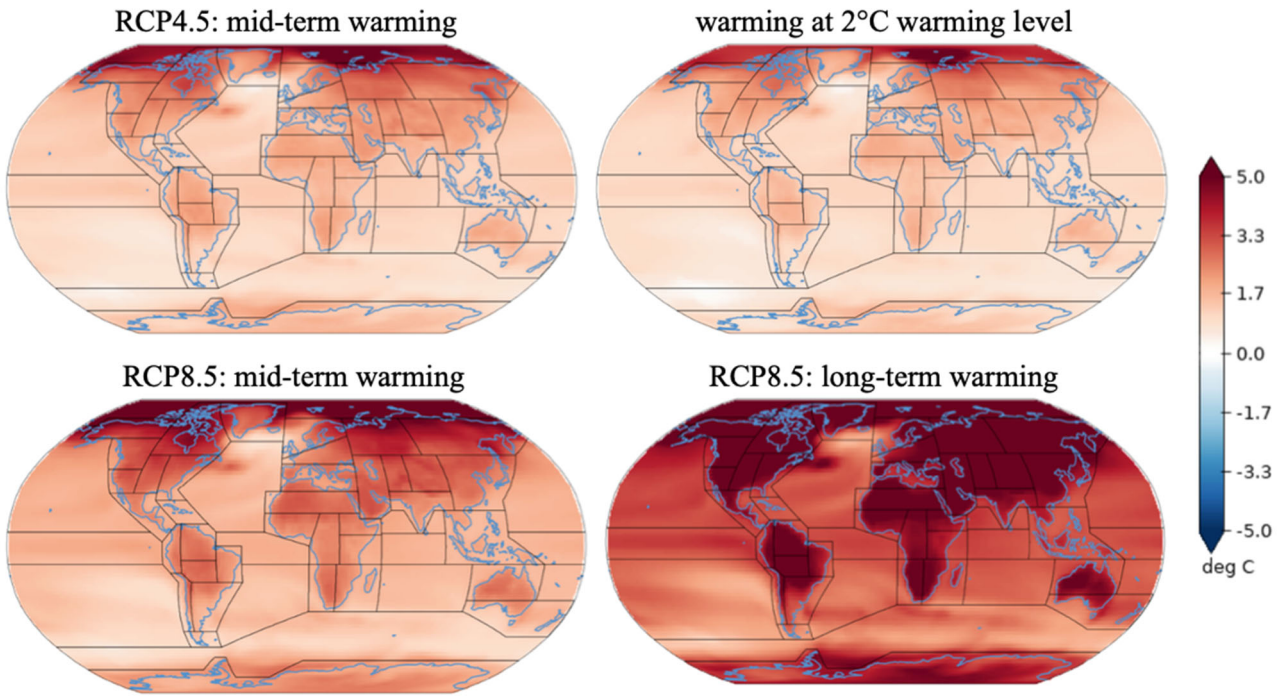

Figure Atlas.16: Global temperature changes projected for mid century (left-hand column) under RCP4.5 (top) and RCP8.5 (bottom) compared to, in the right column, a global mean warming level of 2°C (top) and at the end of the century under RCP8.5 emissions (bottom) from an ensemble of nine CMIP5 GCMs. Note that the future period warmings are calculated against a baseline period of 1986–2005 whereas the global mean warming level is defined with respect to a 'pre-industrial' baseline of 1861–1890. Thus, the other three RCP-based maps would show greater warmings with respect to this earlier baseline.

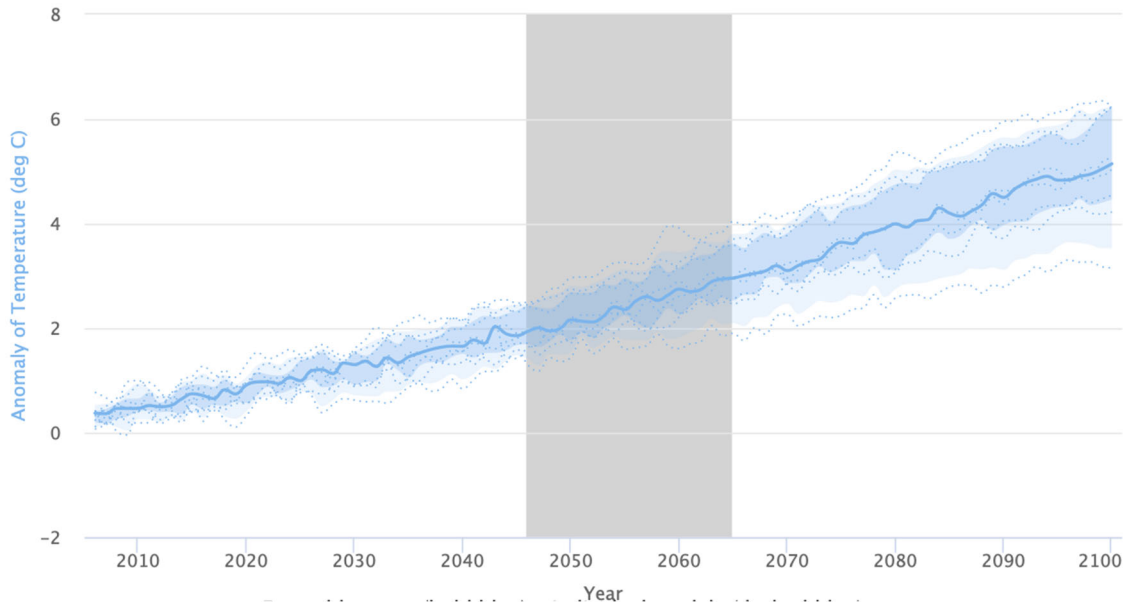

Figure Atlas.17: Global average surface air temperature increases projected by nine CMIP5 models under the RCP8.5 emissions scenario from 2005 to 2100 relative to a 1986–2005 baseline.

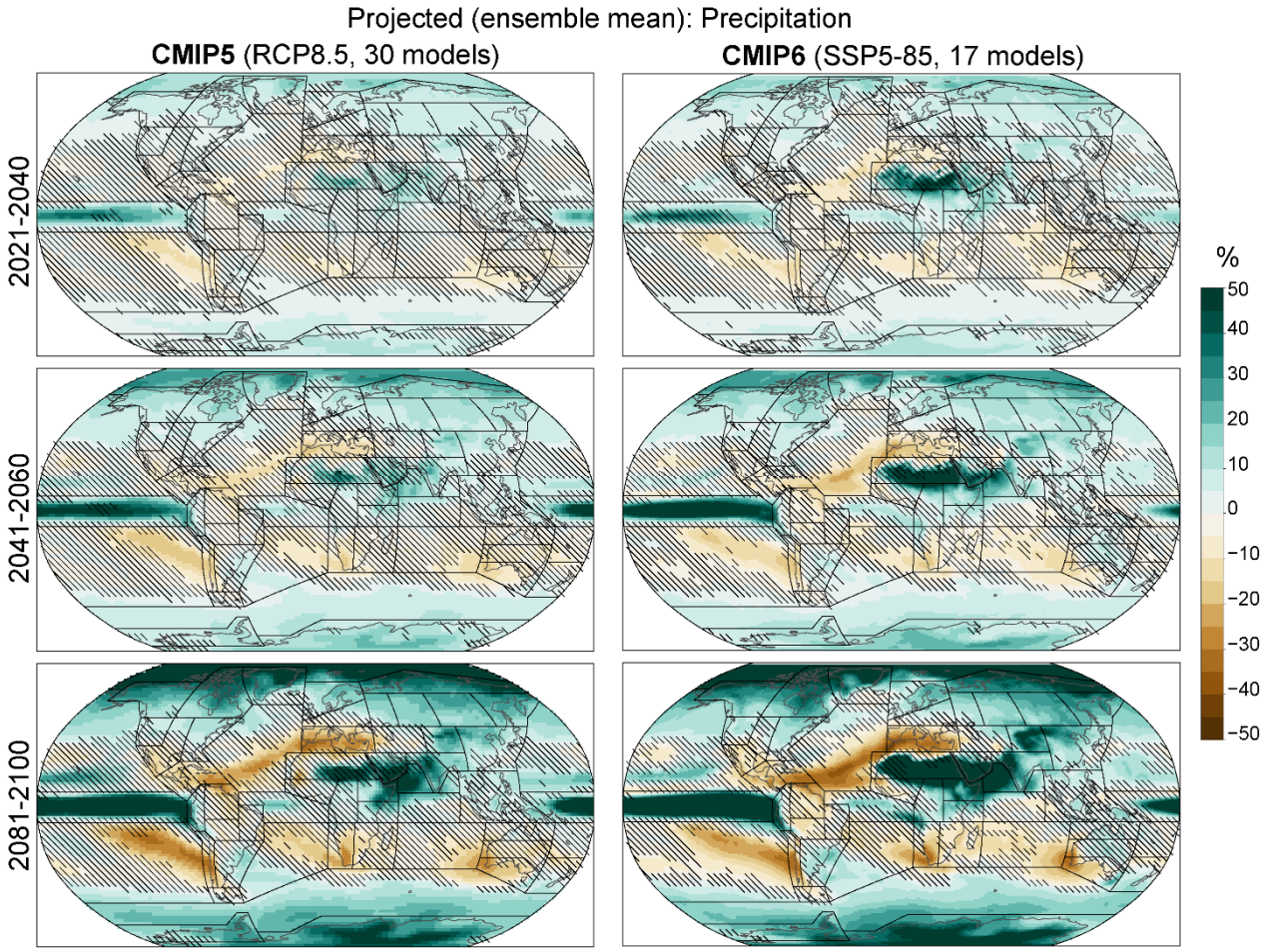

Figure Atlas.18: Future projected changes of annual mean precipitation in the CMIP5 (left-hand column) and CMIP6 (right-hand column) ensembles. Projected changes are calculated as the climatology differences for near-term (2021-2040), medium-term (2041-20160| and long-term (2081-2100) periods for the emissions scenario RCP8.5 (SSP5-8.5 for CMIP6) with respect to the historical period (1986-2005); values are expressed relative differences (%). Hatching indicates lack of model agreement (less than 80% of agreement; as defined in Nikulin et al., 2018) and the black lines mark out the reference regions defined in Section Atlas.2. Similar analysis for other indices and scenarios (including warming levels) are available at the Interactive Atlas (http://ipcc-atlas.ifca.es).

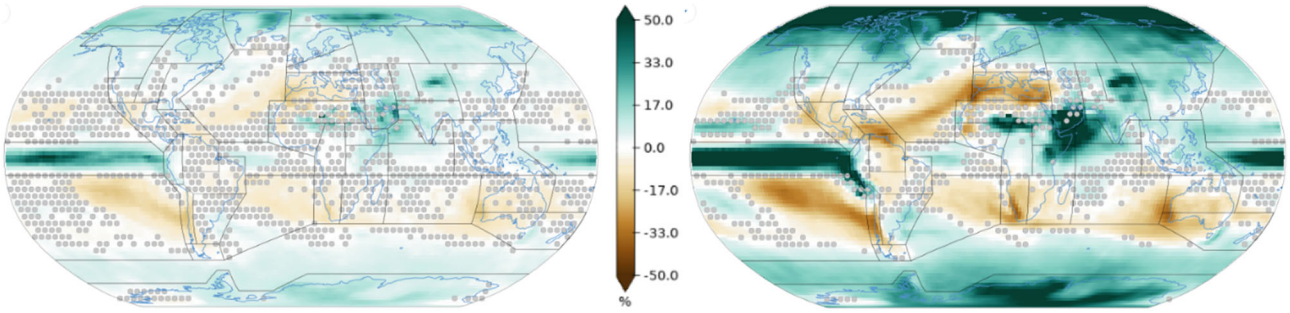

Figure Atlas.19: Global precipitation changes projected at 2°C global mean warming compared to pre-industrial levels (left) and for 2081–2100 under RCP8.5 emissions compared to the 1986–2005 period (right) from an ensemble of nine CMIP5 GCMs. Regions are stippled where less than six out of the nine models agree on the sign of the change (noting that this assessment does not take into account whether the individual models' projected changes are significant).

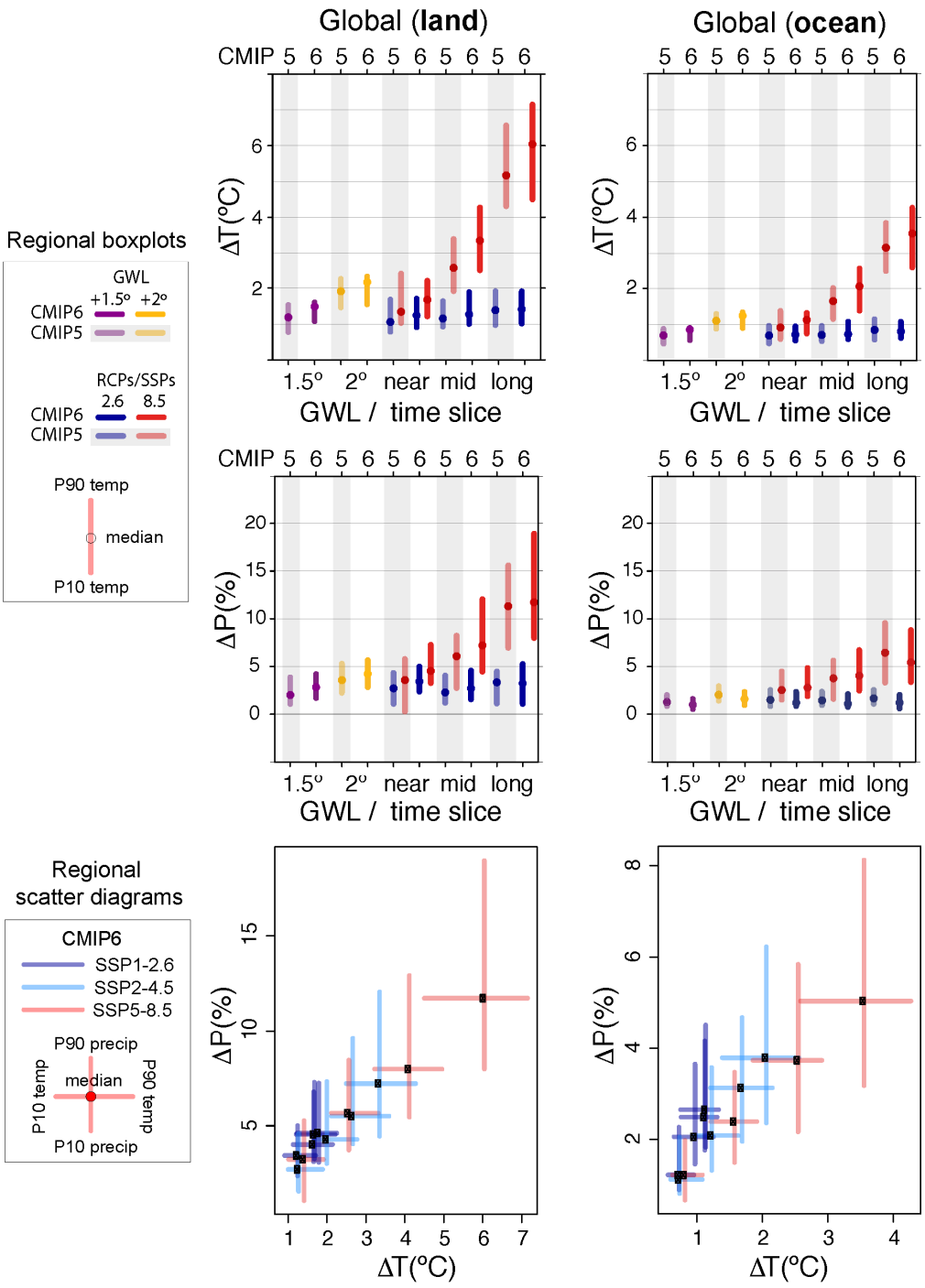

Figure Atlas.20: Changes in annual mean surface air temperature and precipitation averaged over global land (left) and the global oceans (right). The top two rows show the median (dots) and 10th–90th percentile range across each model ensemble for temperature and precipitation changes respectively, for two datasets (CMIP5 and CMIP6) and two scenarios (SSP1-2.6/RCP2.6 and SSP5-8.5/RCP8.5). The first four bars represent the additional warming projected relative to the historical baseline period of 1995-2014 to reach the two global warming levels (GWL; +1.5°C and +2°C) and the remaining six the projected changes over three time periods (near-term 2021–2040, mid-term 2041–2060 and long-term 2081–2100) compared to this same historical baseline period.
The bottom row shows scatter diagrams of temperature against precipitation changes, displaying the median (dots) and 10th–90th percentile ranges for four future periods (2021–2040, 2041–2060, 2061–2080, 2081–2100) compared to the historical baseline period, as obtained from CMIP6 projections for three scenarios (SSP1-2.6, SSP2-4.5 and SSP5-8.5). Changes are absolute for temperature and relative for precipitation. (The script used to generate this figure is available online (Atlas GitHub, 2020) and similar results can be generated in the Interactive Atlas for flexibly defined seasonal periods.)

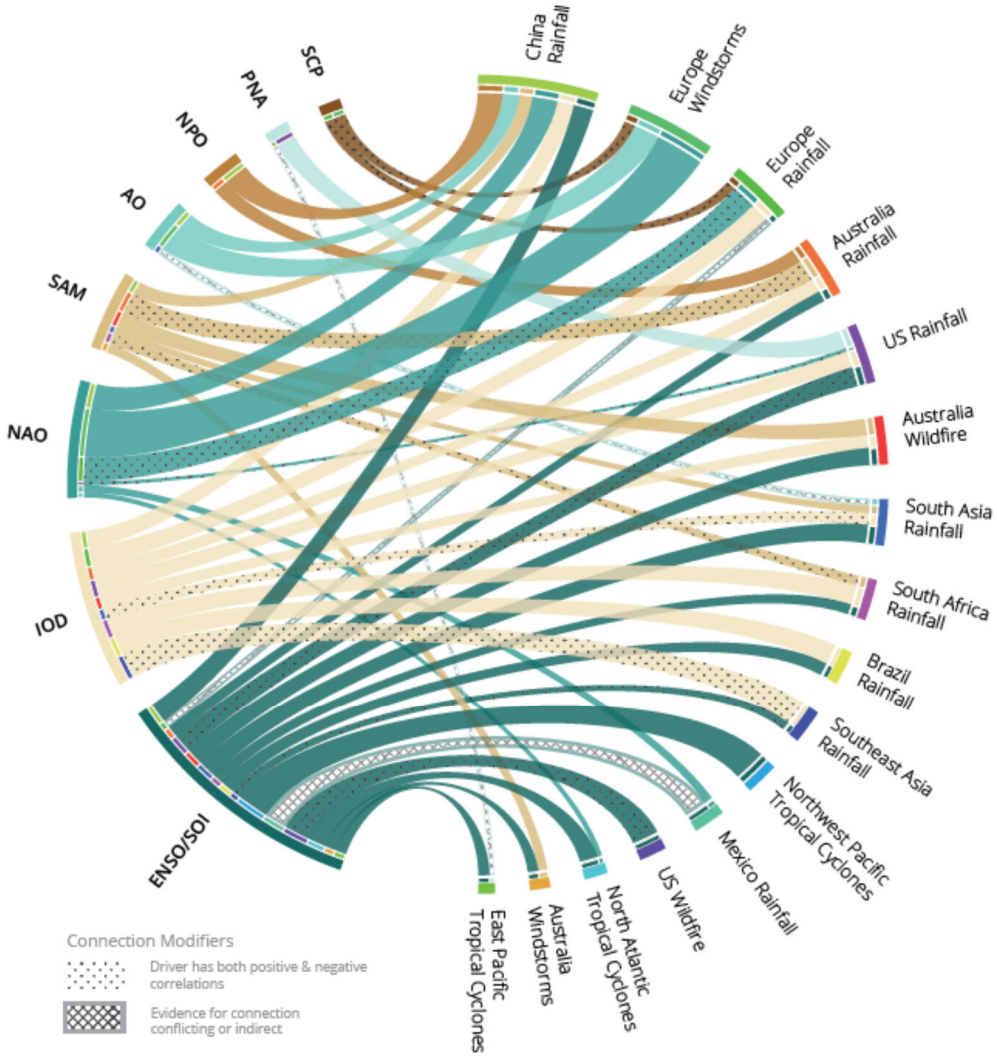

Figure Atlas.21: Influence of major modes of variability on regional extreme events relevant to assessing multi-hazard resilience (Steptoe et al., 2018). Ribbon colours define the driver from which they originate and their width is proportional to the correlation. Hatching represent where there is conflicting evidence for a correlation or where the driver is not directly related to the hazard and dots represent drivers that have both a positive and negative correlation with the hazard.

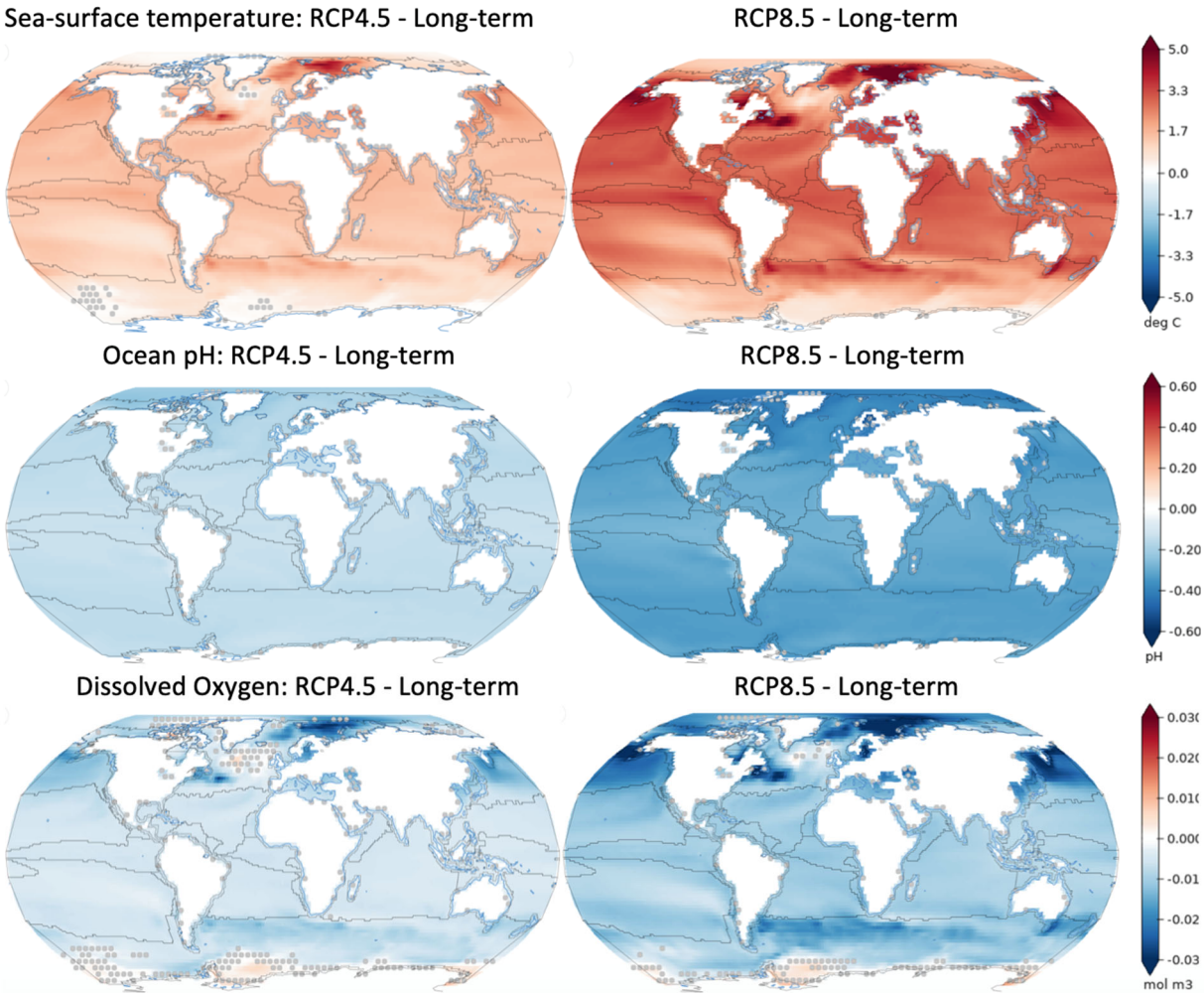

Figure Atlas.22: Projected changes in sea surface temperature (top), ocean pH (middle) and dissolved oxygen (bottom) for 2081–2100 under the RCP4.5 (left-hand column) and 8.5 (right-hand column) emissions compared to a 1986–2005 baseline period from an ensemble of nine CMIP5 GCMs. Regions are stippled where less than six out of the nine models do not agree on the sign of the change (noting that this assessment does not take into account whether the individual models' projected changes are significant)

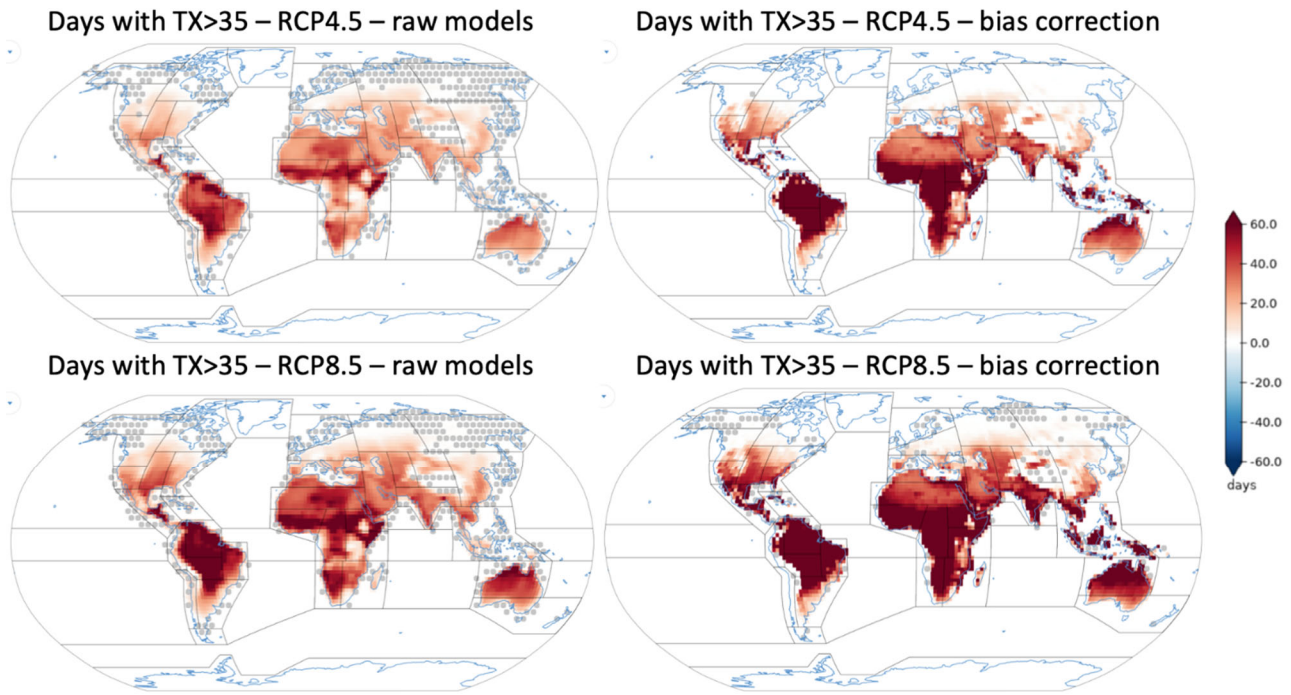

Figure Atlas.23: Projected changes in the number of days per year in which the maximum temperature exceeds 35°C from an ensemble of nine CMIP5 GCMs (the ensemble mean is considered in all cases). The top/bottom rows correspond to a future mid-term period 2046–2065 (compared to 1986–2005) under the RCP4.5/8.5 emissions scenarios respectively considering the raw model data (left-hand column) and bias adjusted (EQM method) data (right-hand column). Regions are stippled where less than six out of the nine models agree on the sign of the change (noting that this assessment does not take into account whether the individual models' projected changes are significant). *[The Interactive Atlas shows the results for two alternative bias correction methods; see Annex VII for more details.]*

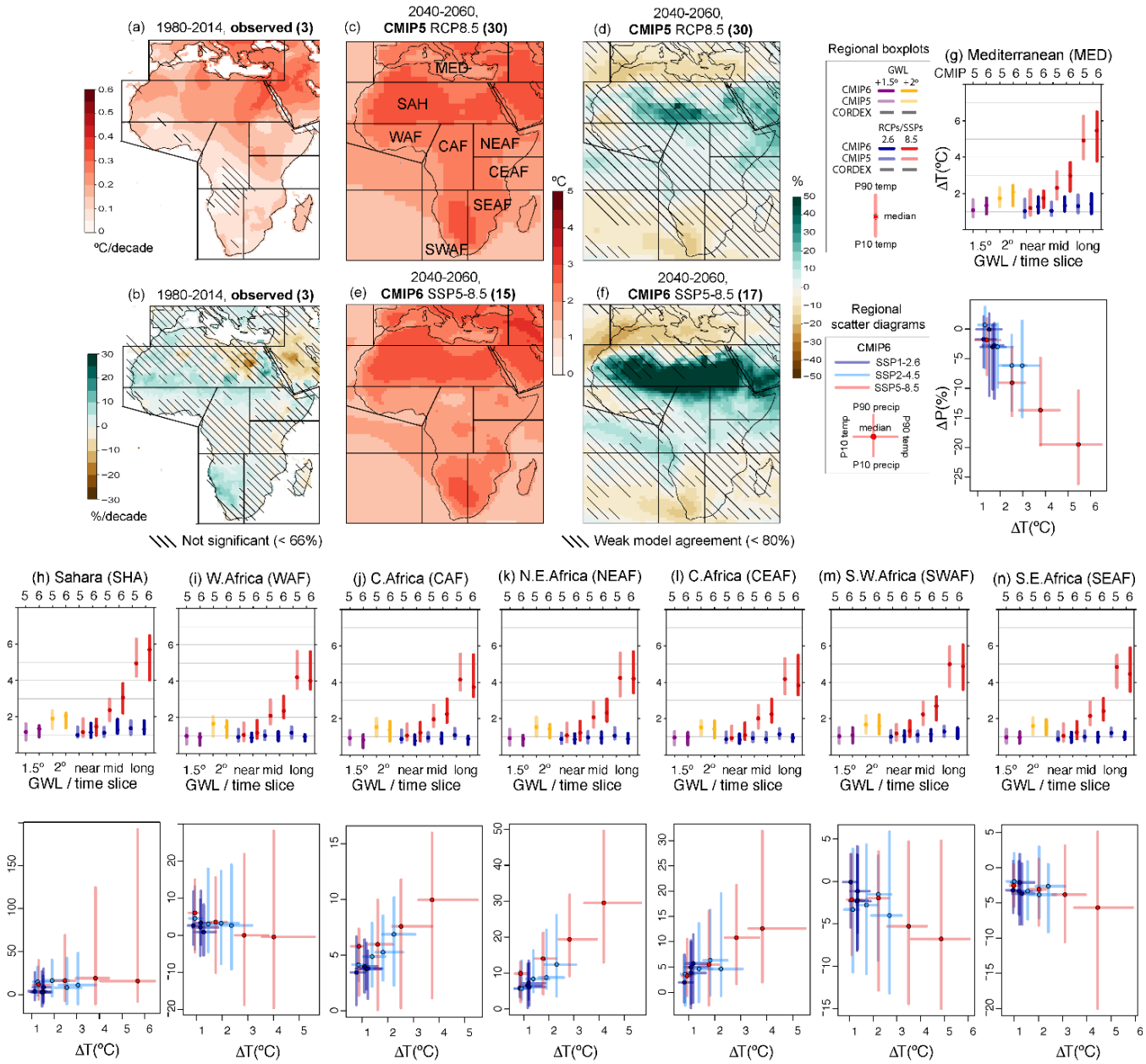

Figure Atlas.24: (a–b) Mean observed trends of annual mean surface air temperature and precipitation for three datasets (CRU TS, BERKELEY and EWEMBI for temperature; CRU TS, GPCC and GPCP for precipitation). Hatching indicates regions where no or only one dataset provides a significant trend. Linear trends are calculated for the common 1980–2014 period and expressed in °C per decade (temperature) and % relative change per decade (precipitation) with respect to the climatological mean over this period.

(c–f) Climate change projections of annual mean surface air temperature and precipitation from CMIP5 (30 models) and CMIP6 (17 models) calculated as the differences in the climatological average for RCP8.5 and SSP5-8.5 respectively, for the period 2041–2060 with respect to the historical 1995–2014 period and expressed as °C (temperature) and % relative change (precipitation). Hatching indicates weak model agreement on the sign of the change (less than 80% as defined in Nikulin et al., 2018).

(g–n) Regional mean changes in annual mean surface air temperature and precipitation for the eight African regions (MED, SHA, WAF, CAF, NEAF, CEAF, SWAF and SEAF). The top row shows the median (dots) and 10th–90th percentile range across each model ensemble for annual mean temperature changes, for two datasets (CMIP5 and CMIP6) and two scenarios (SSP1-2.6/RCP2.6 and SSP5-8.5/RCP8.5). The first four bars represent the additional warming projected relative to the historical baseline 1995–2014 period to reach the two global warming levels (GWL; +1.5°C and

+2°C) and the remaining six projected changes over three time periods (near-term 2021–2040, mid-term 2041–2060 and long-term 2081–2100) compared to this same historical baseline period. The bottom row shows scatter diagrams of temperature against precipitation changes, displaying the median (dots) and 10th–90th percentile ranges for four future periods (2021–2040, 2041–2060, 2061–2080, 2081–2100) compared to the historical baseline period, as obtained from CMIP6 projections for three scenarios (SSP1-2.6, SSP2-4.5 and SSP5-8.5). Changes are absolute for temperature and relative for precipitation.
(The script used to generate this figure is available online (Atlas GitHub, 2020) and similar results can be generated in the Interactive Atlas for flexibly defined seasonal periods.)

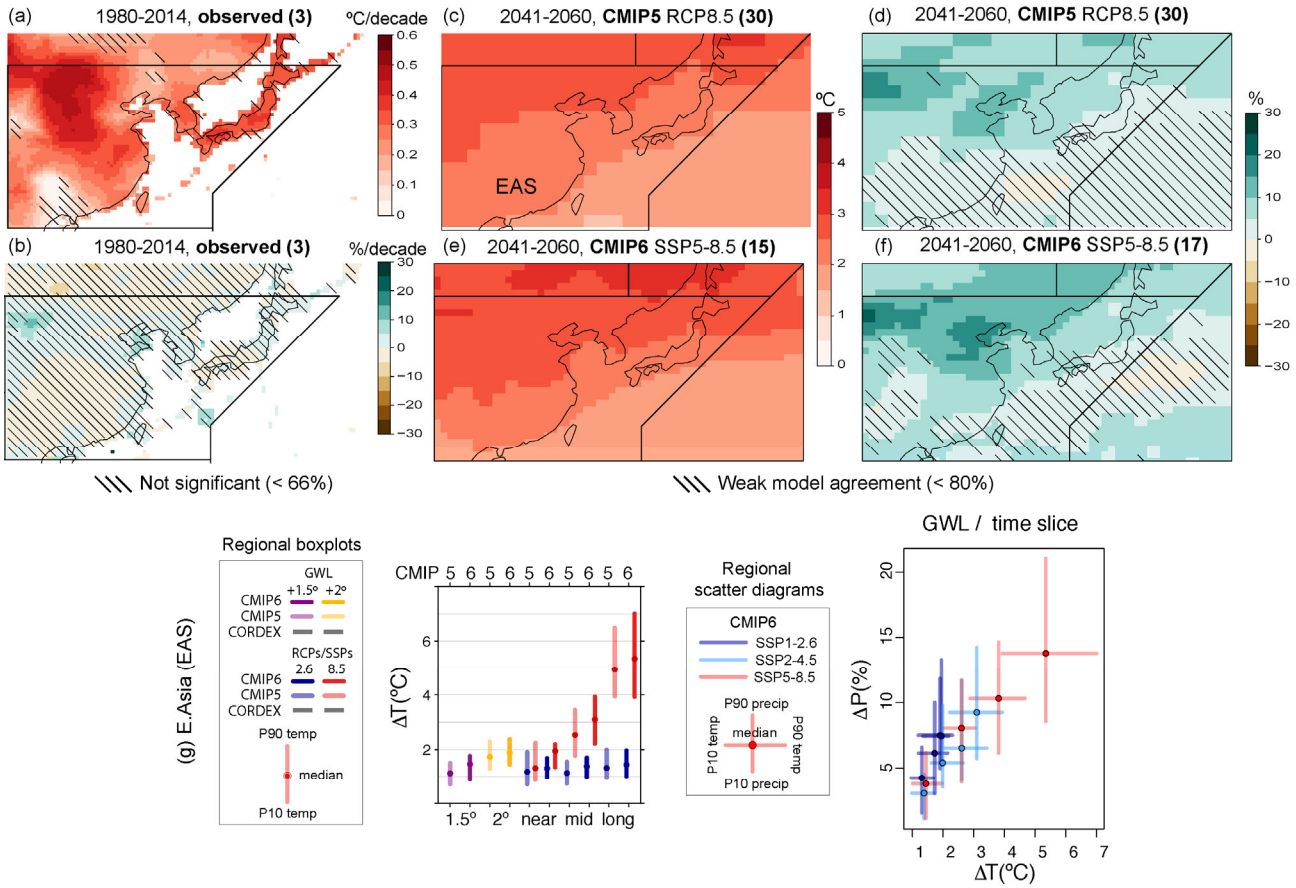

Figure Atlas.25: (a–b) Mean observed trends of annual mean surface air temperature and precipitation for three datasets (CRU TS, BERKELEY and EWEMBI for temperature; CRU TS, GPCC and GPCP for precipitation). Hatching indicates regions where no or only one dataset provides a significant trend. Linear trends are calculated for the common 1980–2014 period and expressed in °C per decade (temperature) and % relative change per decade (precipitation) with respect to the climatological mean over this period.
(c–f) Climate change projections of annual mean surface air temperature and precipitation from CMIP5 (30 models) and CMIP6 (17 models) calculated as the differences in the climatological average for RCP8.5 and SSP5-8.5 respectively, for the period 2041–2060 with respect to the historical 1995–2014 period and expressed as °C (temperature) and % relative change (precipitation). Hatching indicates weak model agreement on the sign of the change (less than 80% as defined in Nikulin et al., 2018).
(g) Regional mean changes in annual mean surface air temperature and precipitation for the East Asian region. The left plot shows the median (dots) and 10th–90th percentile range across each model ensemble for annual mean temperature changes, for two datasets (CMIP5 and CMIP6) and two scenarios (SSP1-2.6/RCP2.6 and SSP5-8.5/RCP8.5). The first four bars represent the additional warming projected relative to the historical baseline 1995–2014 period to reach the two global warming levels (GWL; +1.5°C and +2°C) and the remaining six projected changes over three time periods (near-term 2021–2040, mid-term 2041–2060 and long-term 2081–2100) compared to this same historical baseline period. The right plot shows a scatter diagram of temperature against precipitation changes, displaying the median (dots) and 10th–90th percentile ranges for four future periods (2021–2040, 2041–2060, 2061–2080, 2081–2100) compared to the historical baseline period, as obtained from CMIP6 projections for three scenarios (SSP1-2.6, SSP2-4.5 and SSP5-8.5). Changes are absolute for temperature and relative for precipitation.
(The script used to generate this figure is available online (Atlas GitHub, 2020) and similar results can be generated in the Interactive Atlas for flexibly defined seasonal periods.)

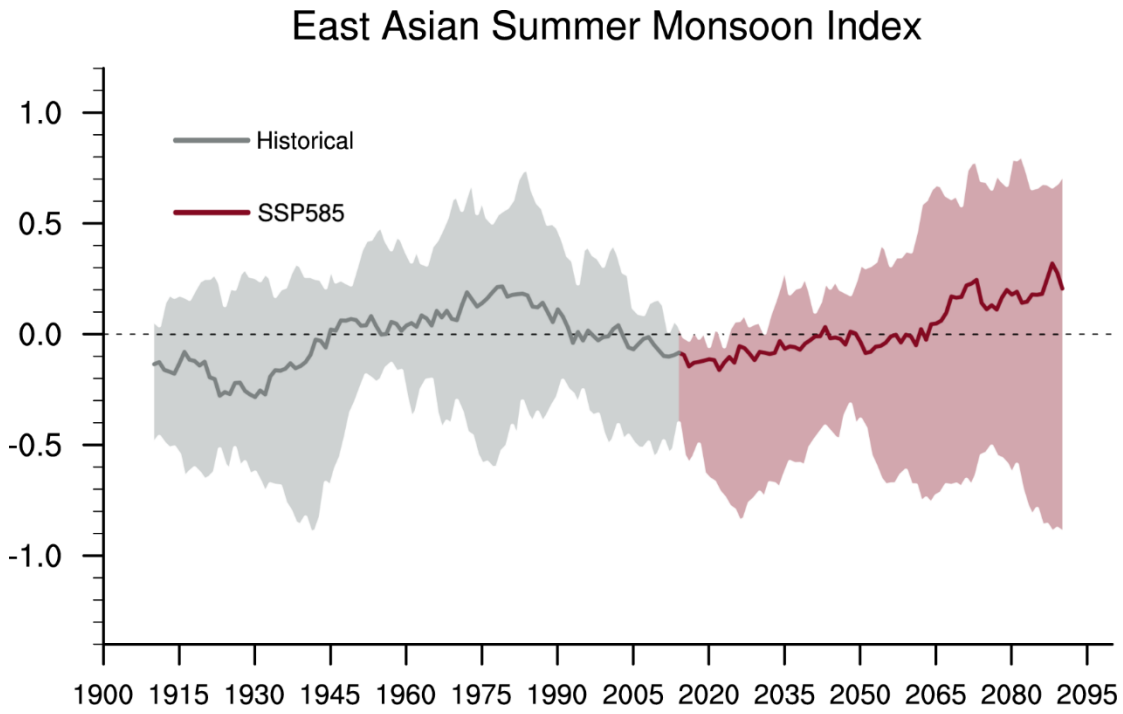

Figure Atlas.26: Time series of East Asian Summer Monsoon index (21-year running mean) over 1900-2100. Historical (gray), SSP5-85 (red) simulations by 12 CMIP6 model ensembles are shown in 10th and 90th (shading), and 50th (thick line) percentile. The index is defined as normalized June-July-August sea level pressure difference between 110°E and 160°E from 10°N to 50°N (Wang et al., 2008).

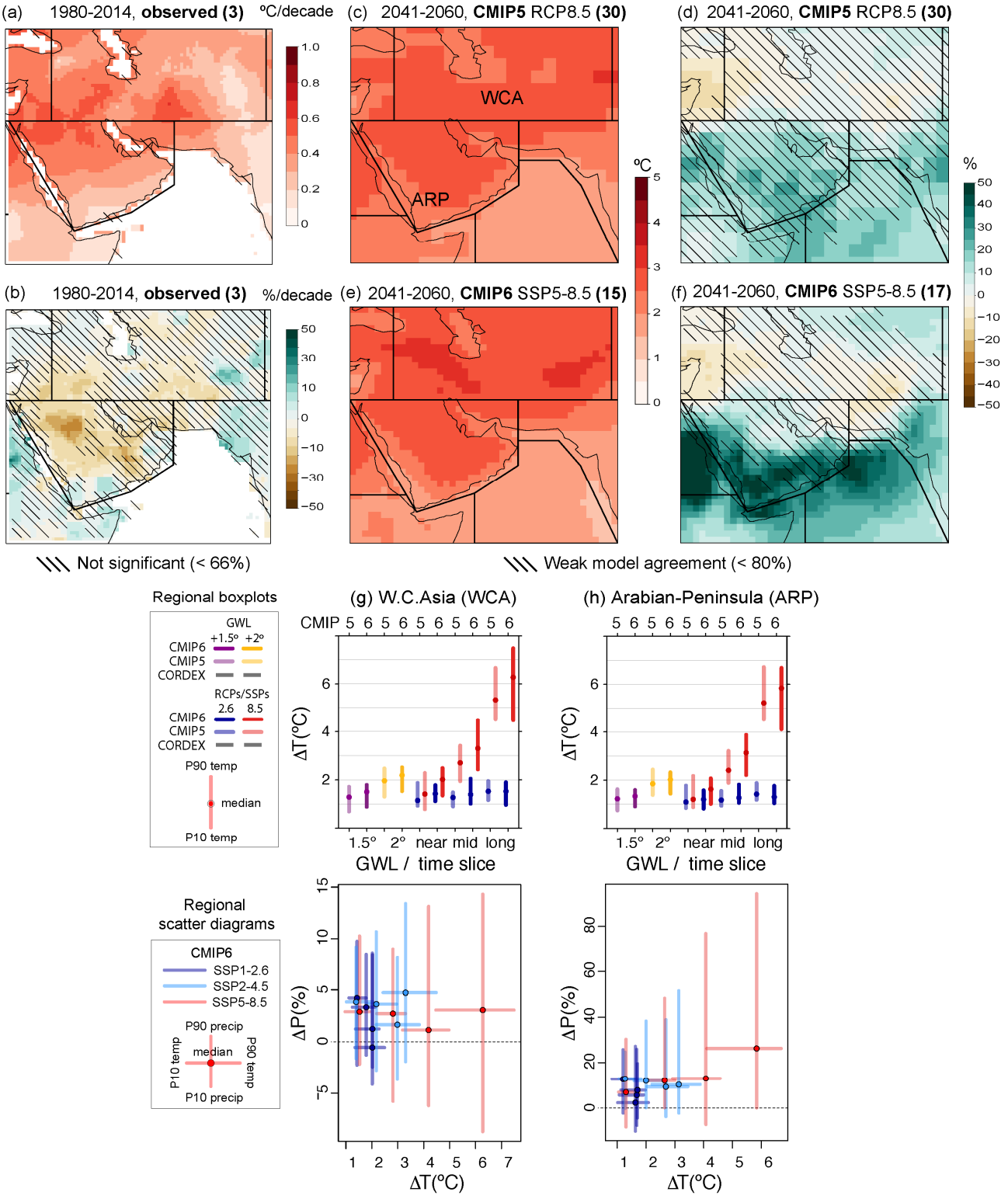

Figure Atlas.27: (a–b) Mean observed trends of annual mean surface air temperature and precipitation for three datasets (CRU TS, BERKELEY and EWEMBI for temperature; CRU TS, GPCC and GPCP for precipitation). Hatching indicates regions where no or only one dataset provides a significant trend. Linear trends are calculated for the common 1980–2014 period and expressed in °C per decade (temperature) and % relative change per decade (precipitation) with respect to the climatological mean over this period.
(c–f) Climate change projections of annual mean surface air temperature and precipitation from CMIP5 (30 models) and CMIP6 (17 models) calculated as the differences in the climatological average for RCP8.5 and SSP5-8.5 respectively, for the period 2041–2060 with respect to the historical

1995–2014 period and expressed as °C (temperature) and % relative change (precipitation). Hatching indicates weak model agreement on the sign of the change (less than 80% as defined in Nikulin et al., 2018).
(g–h) Regional mean changes in annual mean surface air temperature and precipitation for the two Middle East Asia regions (WCA and ARP). The top row shows the median (dots) and 10th–90th percentile range across each model ensemble for annual mean temperature changes, for two datasets (CMIP5 and CMIP6) and two scenarios (SSP1-2.6/RCP2.6 and SSP5-8.5/RCP8.5). The first four bars represent the additional warming projected relative to the historical baseline 1995–2014 period to reach the two global warming levels (GWL; +1.5°C and +2°C) and the remaining six projected changes over three time periods (near-term 2021–2040, mid-term 2041–2060 and long-term 2081–2100) compared to this same historical baseline period. The bottom row shows scatter diagrams of temperature against precipitation changes, displaying the median (dots) and 10th–90th percentile ranges for four future periods (2021–2040, 2041–2060, 2061–2080, 2081–2100) compared to the historical baseline period, as obtained from CMIP6 projections for three scenarios (SSP1-2.6, SSP2-4.5 and SSP5-8.5). Changes are absolute for temperature and relative for precipitation.
(The script used to generate this figure is available online (Atlas GitHub, 2020) and similar results can be generated in the Interactive Atlas for flexibly defined seasonal periods.)

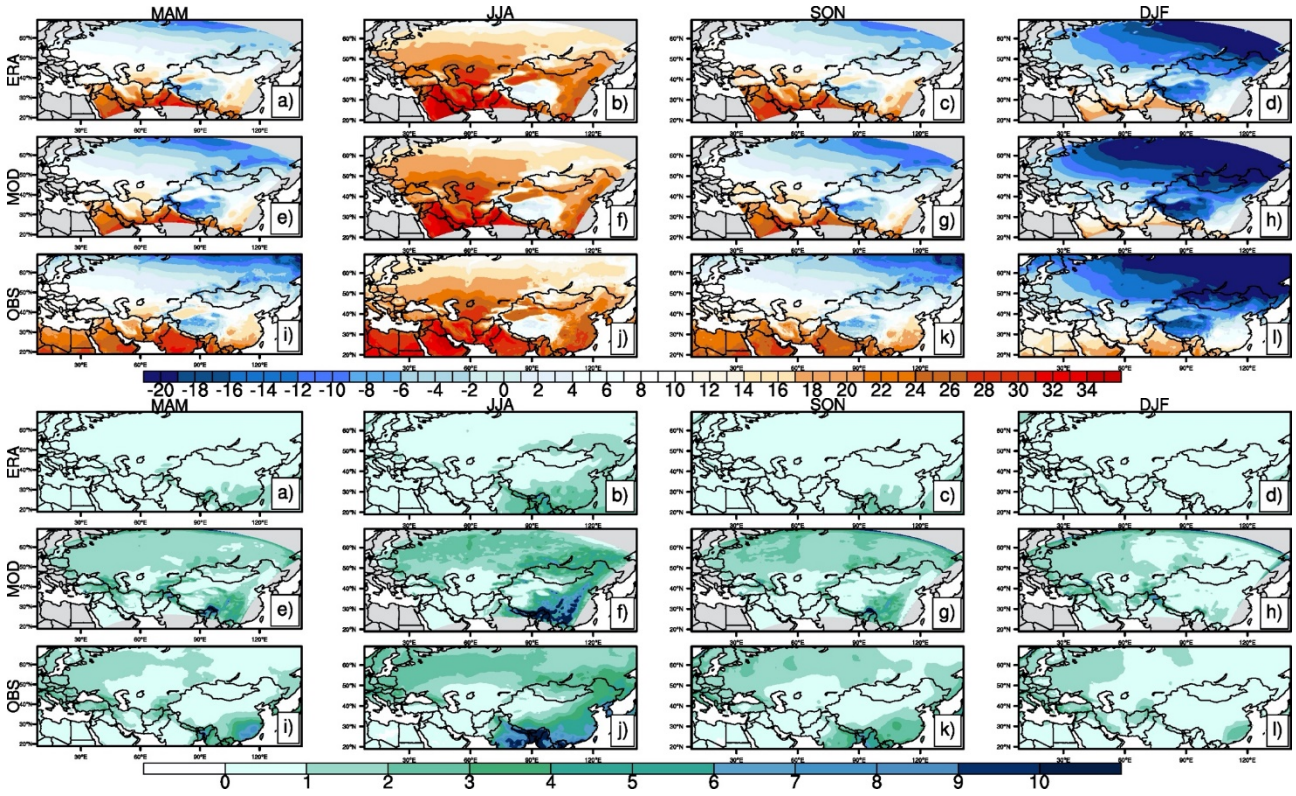

Figure Atlas.28: Seasonal air temperature (°C, blue to red) and precipitation (mm day^{-1}, pale green to blue) for the domain centred over Central Asia for the period 1981–2000, for ERA-Interim dataset (ERA; a–d), RegCM4.3.5 driven by the ERA-Interim (MOD; e–h) and CRU observational dataset (OBS; i–l), for spring (a, e, i), summer (b, f, j), autumn (c, g, k) and winter (d, h, l) seasons (Ozturk et al., 2017).

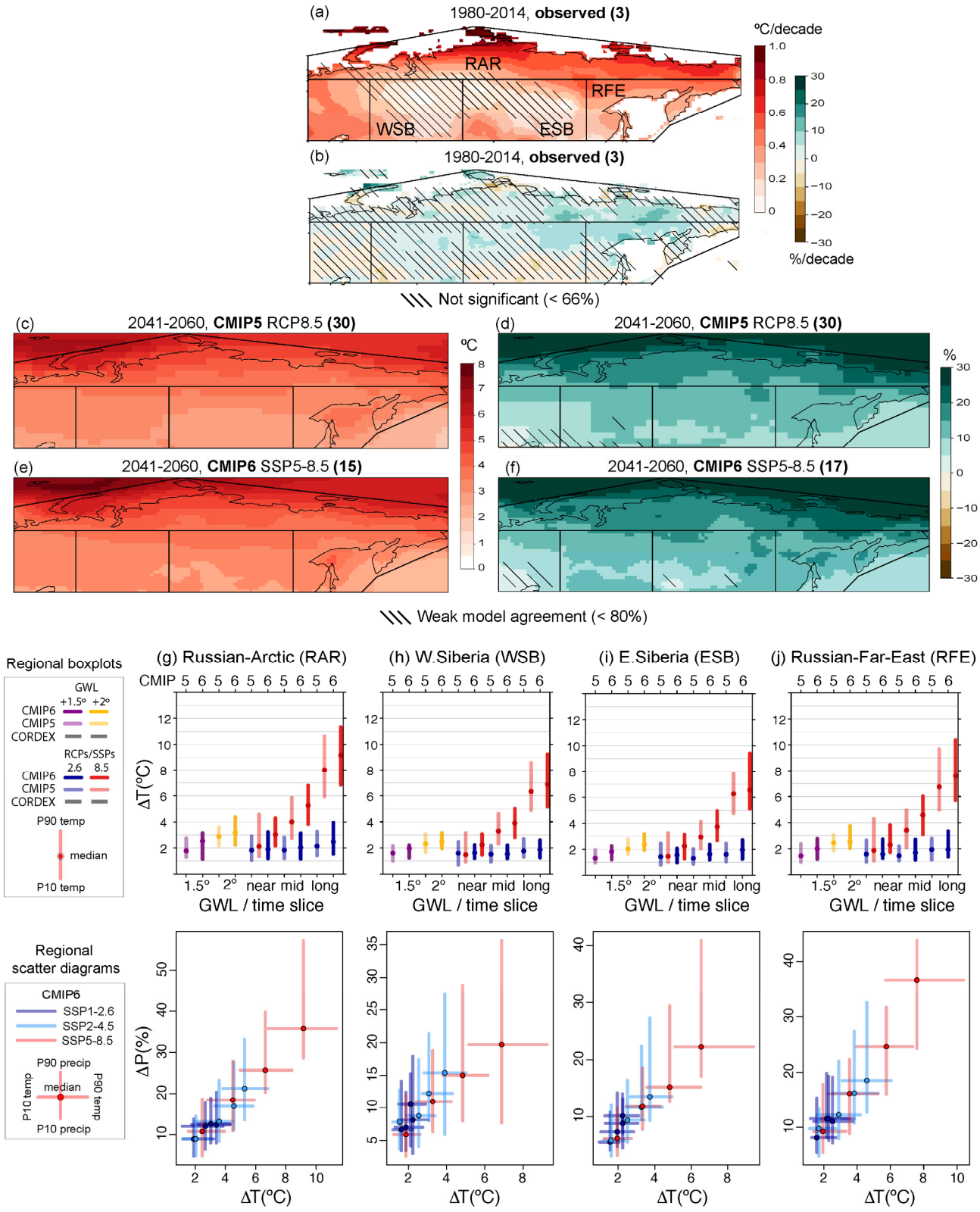

Figure Atlas.29: (a–b) Mean observed trends of annual mean surface air temperature and precipitation for three datasets (CRU TS, BERKELEY and EWEMBI for temperature; CRU TS, GPCC and GPCP for precipitation). Hatching indicates regions where no or only one dataset provides a significant trend. Linear trends are calculated for the common 1980–2014 period and expressed in °C per decade (temperature) and % relative change per decade (precipitation) with respect to the climatological mean over this period.
(c–f) Climate change projections of annual mean surface air temperature and precipitation from CMIP5 (30 models) and CMIP6 (17 models) calculated as the differences in the climatological

average for RCP8.5 and SSP5-8.5 respectively, for the period 2041–2060 with respect to the historical 1995–2014 period and expressed as °C (temperature) and % relative change (precipitation). Hatching indicates weak model agreement on the sign of the change (less than 80% as defined in Nikulin et al., 2018).
(g–j) Regional mean changes in annual mean surface air temperature and precipitation for the four North Asia regions (RAR, WSB, ESB and RFE). The top row shows the median (dots) and 10th–90th percentile range across each model ensemble for annual mean temperature changes, for two datasets (CMIP5 and CMIP6) and two scenarios (SSP1-2.6/RCP2.6 and SSP5-8.5/RCP8.5). The first four bars represent the additional warming projected relative to the historical baseline 1995–2014 period to reach the two global warming levels (GWL; +1.5°C and +2°C) and the remaining six projected changes over three time periods (near-term 2021–2040, mid-term 2041–2060 and long-term 2081–2100) compared to this same historical baseline period. The bottom row shows scatter diagrams of temperature against precipitation changes, displaying the median (dots) and 10th–90th percentile ranges for four future periods (2021–2040, 2041–2060, 2061–2080, 2081–2100) compared to the historical baseline period, as obtained from CMIP6 projections for three scenarios (SSP1-2.6, SSP2-4.5 and SSP5-8.5). Changes are absolute for temperature and relative for precipitation.
(The script used to generate this figure is available online (Atlas GitHub, 2020) and similar results can be generated in the Interactive Atlas for flexibly defined seasonal periods.)

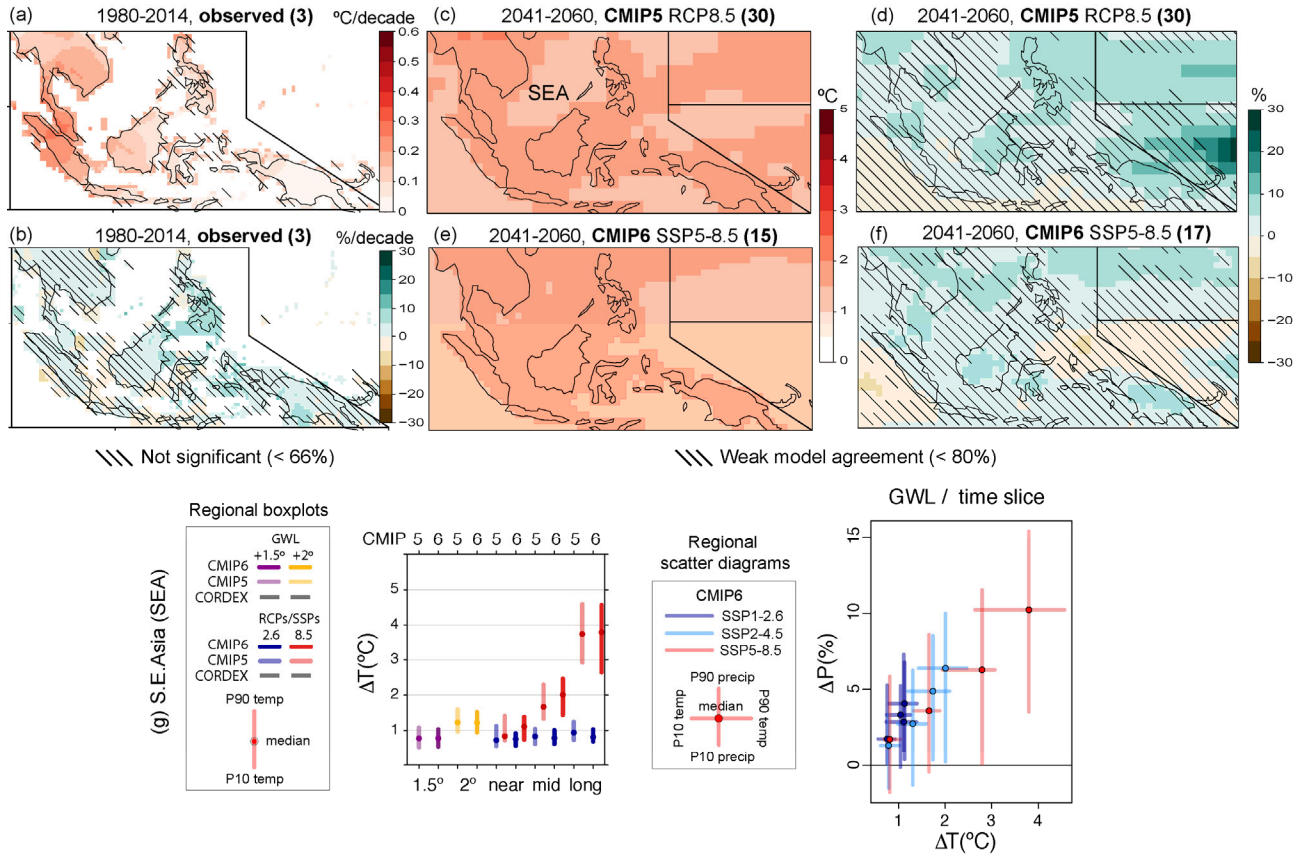

Figure Atlas.30: (a–b) Mean observed trends of annual mean surface air temperature and precipitation for three datasets (CRU TS, BERKELEY and EWEMBI for temperature; CRU TS, GPCC and GPCP for precipitation). Hatching indicates regions where no or only one dataset provides a significant trend. Linear trends are calculated for the common 1980–2014 period and expressed in °C per decade (temperature) and % relative change per decade (precipitation) with respect to the climatological mean over this period.
(c–f) Climate change projections of annual mean surface air temperature and precipitation from CMIP5 (30 models) and CMIP6 (17 models) calculated as the differences in the climatological average for RCP8.5 and SSP5-8.5 respectively, for the period 2041–2060 with respect to the historical 1995–2014 period and expressed as °C (temperature) and % relative change (precipitation). Hatching indicates weak model agreement on the sign of the change (less than 80% as defined in Nikulin et al., 2018).
(g) Regional mean changes in annual mean surface air temperature and precipitation for the Southeast Asia region. The left plot shows the median (dots) and 10th–90th percentile range across each model ensemble for annual mean temperature changes, for two datasets (CMIP5 and CMIP6) and two scenarios (SSP1-2.6/RCP2.6 and SSP5-8.5/RCP8.5). The first four bars represent the additional warming projected relative to the historical baseline 1995–2014 period to reach the two global warming levels (GWL; +1.5°C and +2°C) and the remaining six projected changes over three time periods (near-term 2021–2040, mid-term 2041–2060 and long-term 2081–2100) compared to this same historical baseline period. The right plot shows a scatter diagram of temperature against precipitation changes, displaying the median (dots) and 10th–90th percentile ranges for four future periods (2021–2040, 2041–2060, 2061–2080, 2081–2100) compared to the historical baseline period, as obtained from CMIP6 projections for three scenarios (SSP1-2.6, SSP2-4.5 and SSP5-8.5). Changes are absolute for temperature and relative for precipitation.
(The script used to generate this figure is available online (Atlas GitHub, 2020) and similar results can be generated in the Interactive Atlas for flexibly defined seasonal periods.)

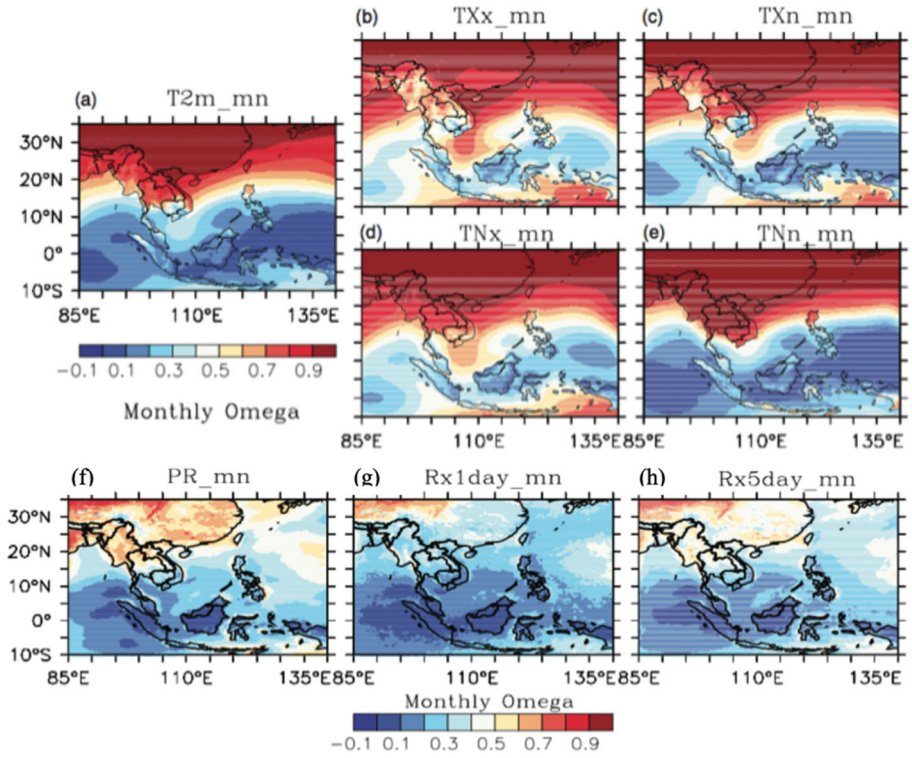

Figure Atlas.31: Similarity index omega between the different CORDEX-SEA historical simulations for different temperature-based (a-e) and precipitation extreme indices (f-h) (from Ngo-Duc et al., 2017).

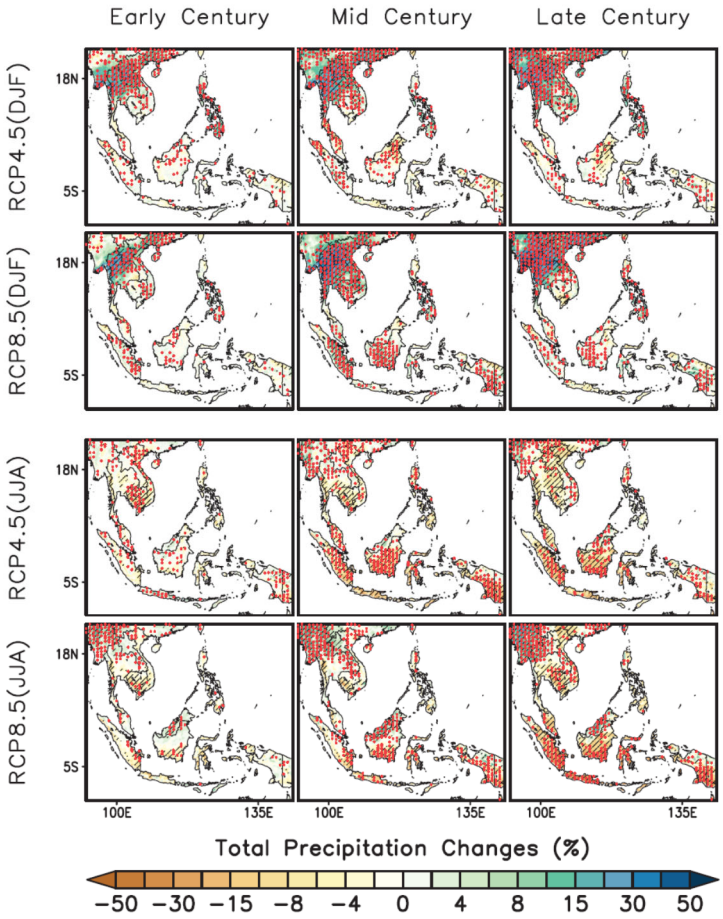

Figure Atlas.32: The projected changes in mean precipitation expressed as a percentage (%) relative to the mean in the historical period. Hatching indicates the changes are significant at 95% level above random noise while dots are showing robustness at 95% (Tangang et al., *submitted*).

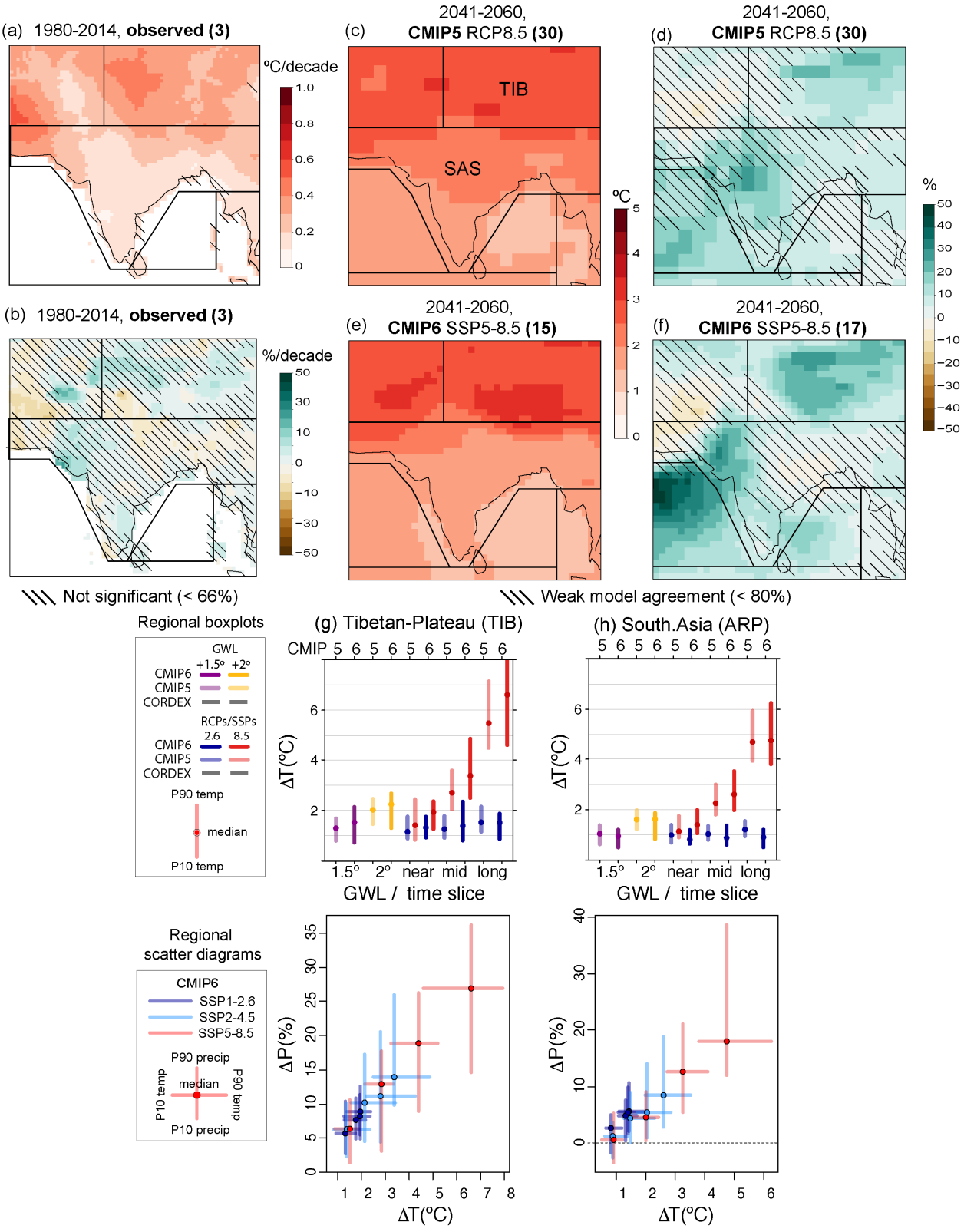

Figure Atlas.33: (a–b) Mean observed trends of annual mean surface air temperature and precipitation for three datasets (CRU TS, BERKELEY and EWEMBI for temperature; CRU TS, GPCC and GPCP for precipitation). Hatching indicates regions where no or only one dataset provides a significant trend. Linear trends are calculated for the common 1980–2014 period and expressed in °C per decade (temperature) and % relative change per decade (precipitation) with respect to the climatological mean over this period.
(c–f) Climate change projections of annual mean surface air temperature and precipitation from

CMIP5 (30 models) and CMIP6 (17 models) calculated as the differences in the climatological average for RCP8.5 and SSP5-8.5 respectively, for the period 2041–2060 with respect to the historical 1995–2014 period and expressed as °C (temperature) and % relative change (precipitation). Hatching indicates weak model agreement on the sign of the change (less than 80% as defined in Nikulin et al., 2018).

(g–h) Regional mean changes in annual mean surface air temperature and precipitation for the Tibetan Plateau and South Asia. The top row shows the median (dots) and 10th–90th percentile range across each model ensemble for annual mean temperature changes, for two datasets (CMIP5 and CMIP6) and two scenarios (SSP1-2.6/RCP2.6 and SSP5-8.5/RCP8.5). The first four bars represent the additional warming projected relative to the historical baseline 1995–2014 period to reach the two global warming levels (GWL; +1.5°C and +2°C) and the remaining six projected changes over three time periods (near-term 2021–2040, mid-term 2041–2060 and long-term 2081–2100) compared to this same historical baseline period. The bottom row shows scatter diagrams of temperature against precipitation changes, displaying the median (dots) and 10th–90th percentile ranges for four future periods (2021–2040, 2041–2060, 2061–2080, 2081–2100) compared to the historical baseline period, as obtained from CMIP6 projections for three scenarios (SSP1-2.6, SSP2-4.5 and SSP5-8.5). Changes are absolute for temperature and relative for precipitation.

(The script used to generate this figure is available online (Atlas GitHub, 2020) and similar results can be generated in the Interactive Atlas for flexibly defined seasonal periods.)

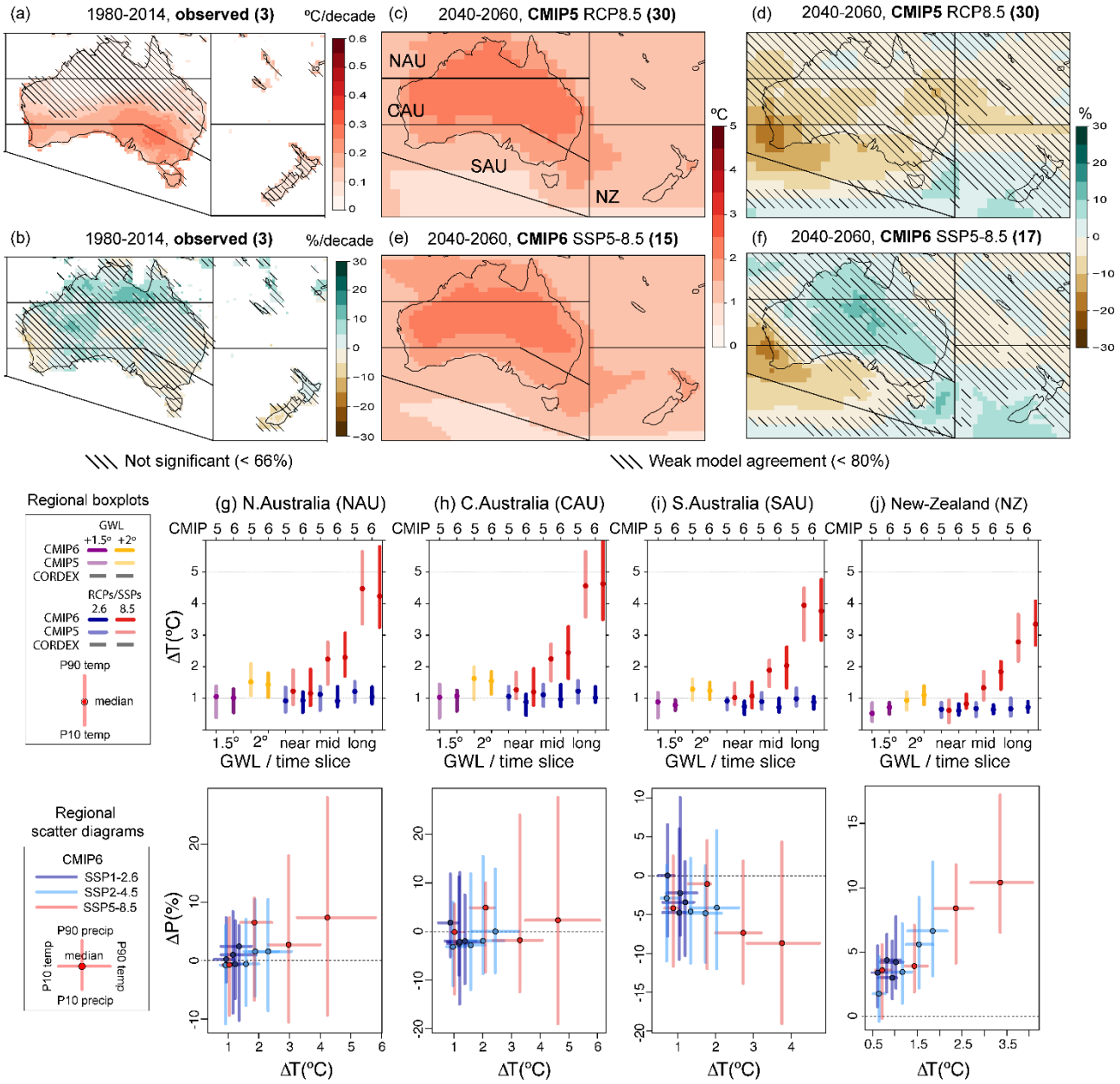

Figure Atlas.34: (a–b) Mean observed trends of annual mean surface air temperature and precipitation for three datasets (CRU TS, BERKELEY and EWEMBI for temperature; CRU TS, GPCC and GPCP for precipitation). Hatching indicates regions where no or only one dataset provides a significant trend. Linear trends are calculated for the common 1980–2014 period and expressed in °C per decade (temperature) and % relative change per decade (precipitation) with respect to the climatological mean over this period.

(c–f) Climate change projections of annual mean surface air temperature and precipitation from CMIP5 (30 models) and CMIP6 (17 models) calculated as the differences in the climatological average for RCP8.5 and SSP5-8.5 respectively, for the period 2041–2060 with respect to the historical 1995–2014 period and expressed as °C (temperature) and % relative change (precipitation). Hatching indicates weak model agreement on the sign of the change (less than 80% as defined in Nikulin et al., 2018).

(g-j) Regional mean changes in annual mean surface air temperature and precipitation for the four Australasian regions (NAU, CAU, SAU and NZ). The top row shows the median (dots) and 10th–90th percentile range across each model ensemble for annual mean temperature changes, for two datasets (CMIP5 and CMIP6) and two scenarios (SSP1-2.6/RCP2.6 and SSP5-8.5/RCP8.5). The first four bars represent the additional warming projected relative to the historical baseline 1995–2014 period to reach the two global warming levels (GWL; +1.5°C and +2°C) and the remaining six projected changes over three time periods (near-term 2021–2040, mid-term 2041–2060 and long-term 2081–

2100) compared to this same historical baseline period. The bottom row shows scatter diagrams of temperature against precipitation changes, displaying the median (dots) and 10th–90th percentile ranges for four future periods (2021–2040, 2041–2060, 2061–2080, 2081–2100) compared to the historical baseline period, as obtained from CMIP6 projections for three scenarios (SSP1-2.6, SSP2-4.5 and SSP5-8.5). Changes are absolute for temperature and relative for precipitation.
(The script used to generate this figure is available online (Atlas GitHub, 2020) and similar results can be generated in the Interactive Atlas for flexibly defined seasonal periods.)

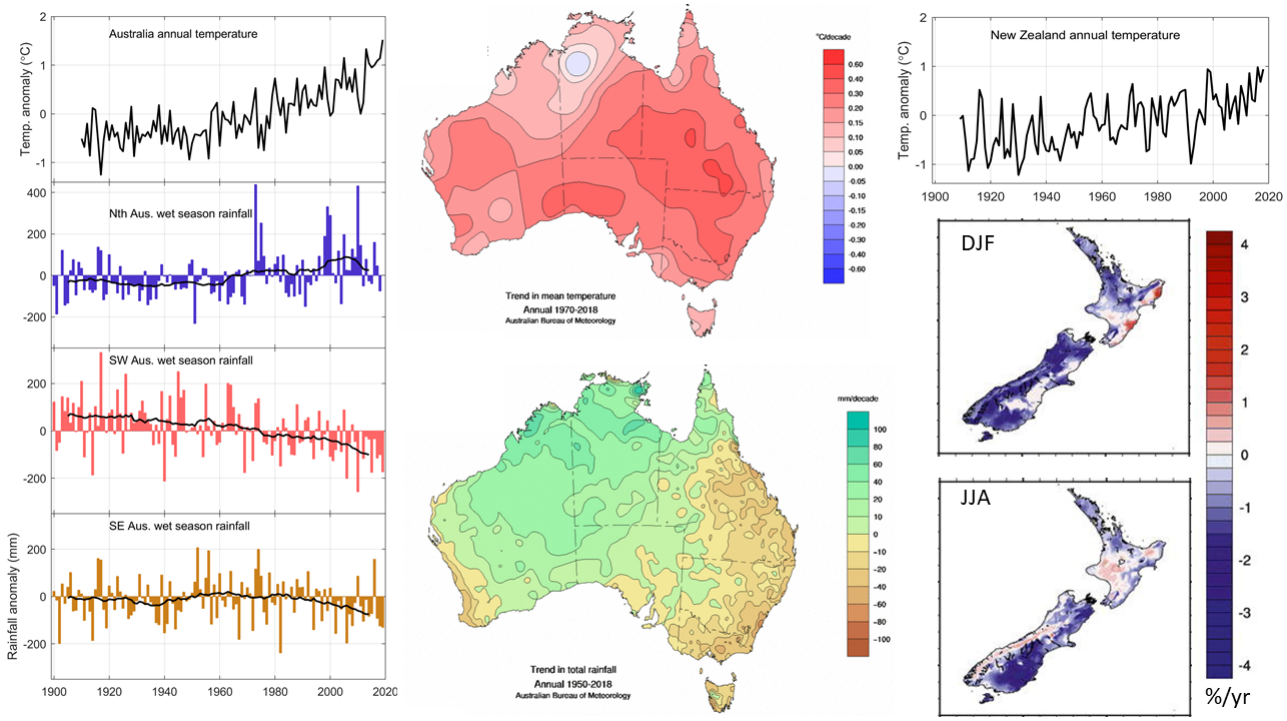

Figure Atlas.35: Observed trends in temperature and rainfall for Australia and New Zealand from high-quality regional datasets; Left: time series of anomalies from 1961-1990 average, Australian northern wet season is Oct-Apr and southern wet season is Apr-Oct (adapted from BoM and CSIRO 2018); Centre: maps show annual linear trends for 1970-2019 for temperature to illustrate warming minimum in northwest Australia in this period, 1950-2019 in mean annual rainfall; right: New Zealand mean annual temperature from NIWA, maps show trends in summer and winter rainfall in 1979 to 2006 in the NIWA climate database taken from (Ummenhofer et al., 2009).

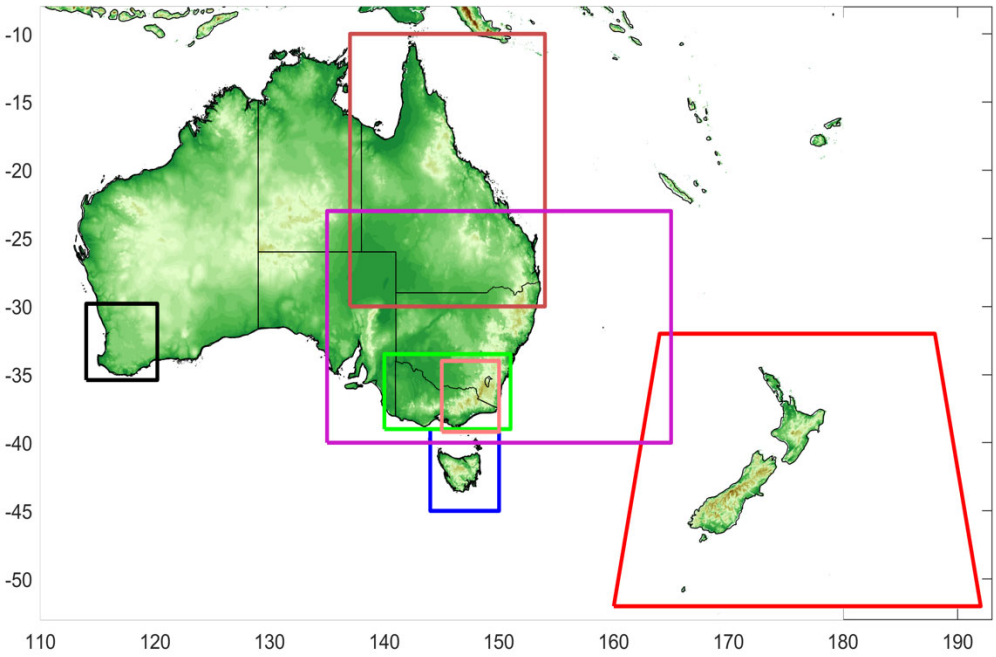

Figure Atlas.36: Domains of notable regional dynamical downscaling studies in Australasia offering the potential for regional added value in climate change projections. NIWA projections for New Zealand (red), NARCliM work for eastern Australia (purple) and southwest Western Australia regional projections (black) use limited area models and the entire model domain is shown, Victorian Climate Projections 2019 (green), Queensland (brown), Climate Futures for the Alps (light brown) and Climate Futures for Tasmania (blue) use stretched-grid global models and the high-resolution domain is shown. Surface height is indicated by the colour scale, showing studies are generally focused on areas of notable topographic features, where cases of 'added value' in temperature and rainfall projections were found.

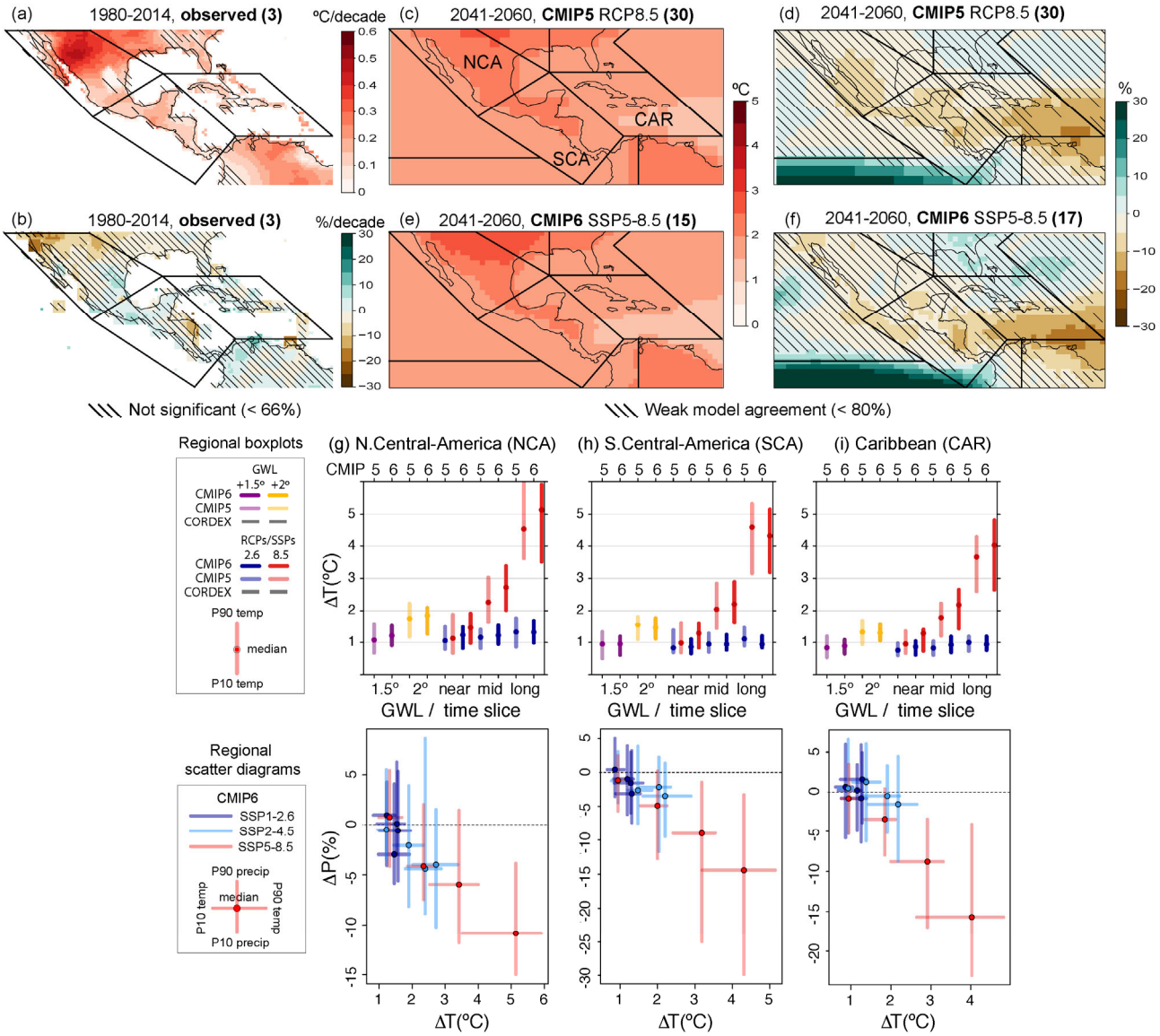

Figure Atlas.37: (a–b) Mean observed trends of annual mean surface air temperature and precipitation for three datasets (CRU TS, BERKELEY and EWEMBI for temperature; CRU TS, GPCC and GPCP for precipitation). Hatching indicates regions where no or only one dataset provides a significant trend. Linear trends are calculated for the common 1980–2014 period and expressed in °C per decade (temperature) and % relative change per decade (precipitation) with respect to the climatological mean over this period.

(c–f) Climate change projections of annual mean surface air temperature and precipitation from CMIP5 (30 models) and CMIP6 (17 models) calculated as the differences in the climatological average for RCP8.5 and SSP5-8.5 respectively, for the period 2041–2060 with respect to the historical 1995–2014 period and expressed as °C (temperature) and % relative change (precipitation). Hatching indicates weak model agreement on the sign of the change (less than 80% as defined in Nikulin et al., 2018).

(g–i) Regional mean changes in annual mean surface air temperature and precipitation for the three Central American regions (NCA, SCA and CAR). The top row shows the median (dots) and 10th–90th percentile range across each model ensemble for annual mean temperature changes, for two datasets (CMIP5 and CMIP6) and two scenarios (SSP1-2.6/RCP2.6 and SSP5-8.5/RCP8.5). The first four bars represent the additional warming projected relative to the historical baseline 1995–2014 period to reach the two global warming levels (GWL; +1.5°C and +2°C) and the remaining six projected changes over three time periods (near-term 2021–2040, mid-term 2041–2060 and long-term 2081–2100) compared to this same historical baseline period. The bottom row shows scatter diagrams of temperature against precipitation changes, displaying the median (dots) and 10th–90th percentile ranges for four future periods (2021–2040, 2041–2060, 2061–2080, 2081–2100) compared to the

historical baseline period, as obtained from CMIP6 projections for three scenarios (SSP1-2.6, SSP2-4.5 and SSP5-8.5). Changes are absolute for temperature and relative for precipitation.
(The script used to generate this figure is available online (Atlas GitHub, 2020) and similar results can be generated in the Interactive Atlas for flexibly defined seasonal periods.)

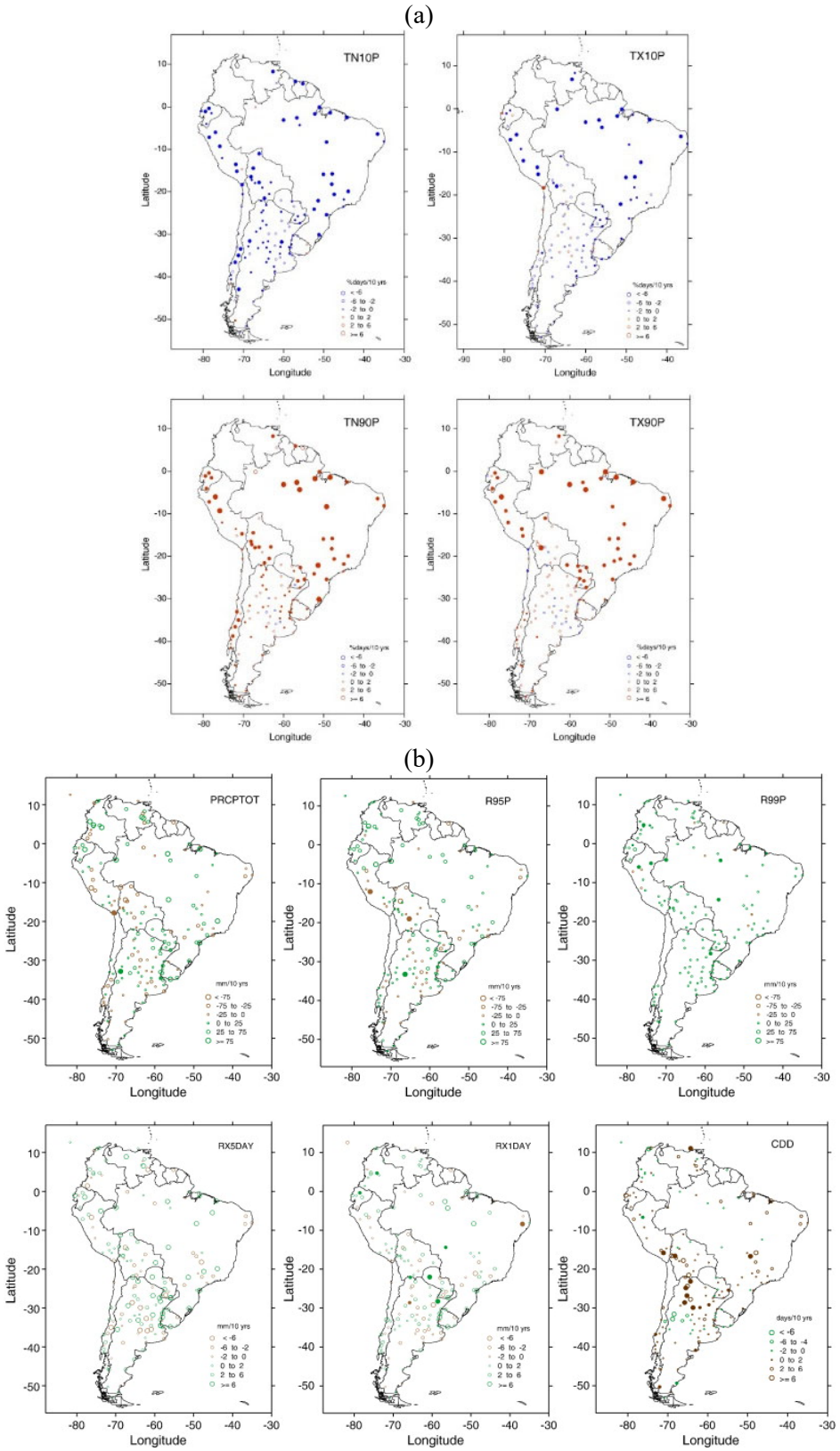

Figure Atlas.38: Local robust trends estimated annually for the 1969–2009 period for (a) cold nights (upper left), cold days (upper right), warm nights (bottom left) and warm days (bottom right) and (b) for annual total rainfall (upper left), very wet days (upper central), extremely wet days (upper right), annual maximum consecutive 5-day precipitation (bottom left), annual maximum 1-day precipitation (bottom central) and consecutive dry days (bottom right). (Skansi et al., 2013)

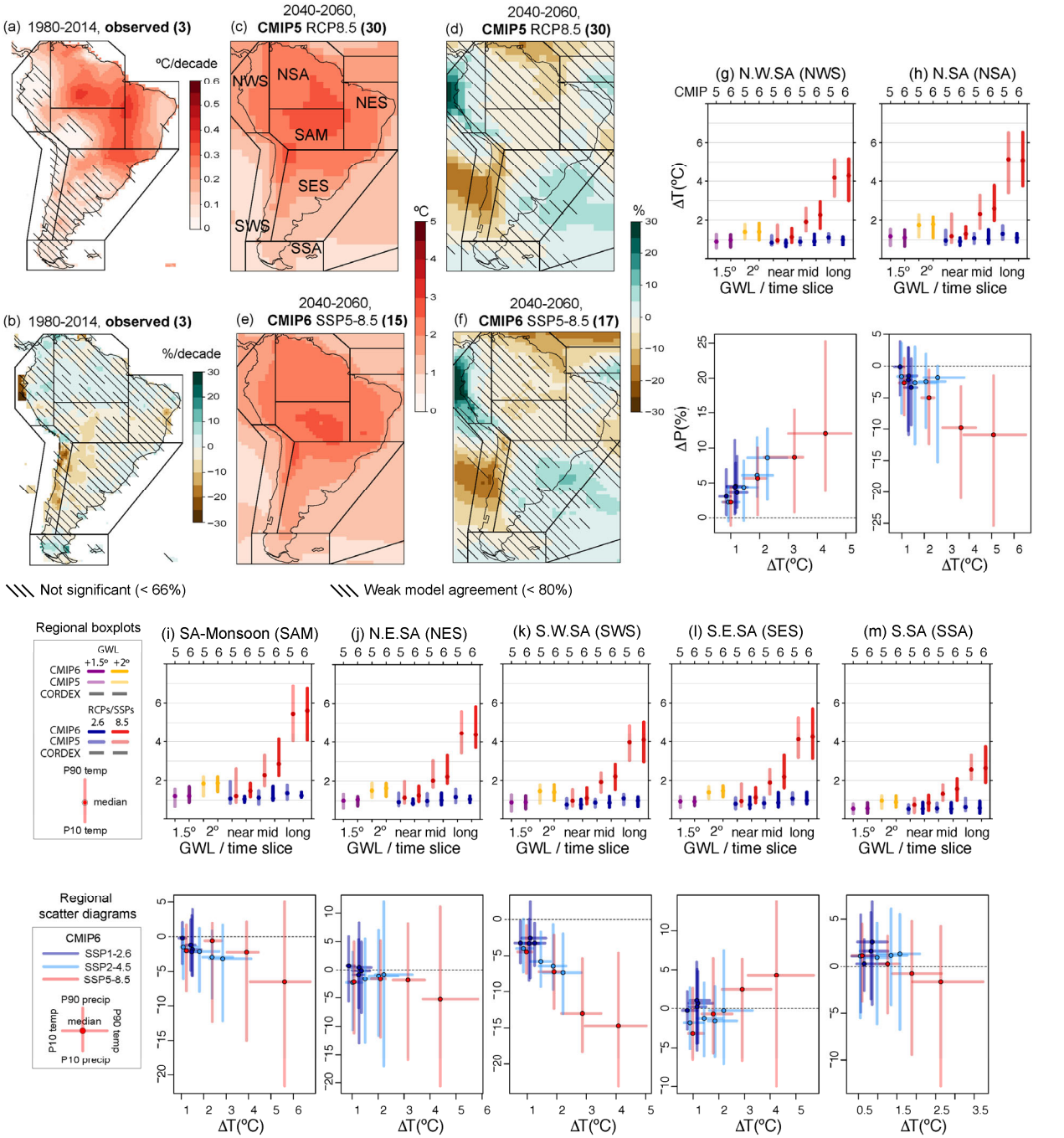

Figure Atlas.39: (a–b) Mean observed trends of annual mean surface air temperature and precipitation for three datasets (CRU TS, BERKELEY and EWEMBI for temperature; CRU TS, GPCC and GPCP for precipitation). Hatching indicates regions where no or only one dataset provides a significant trend. Linear trends are calculated for the common 1980–2014 period and expressed in °C per decade (temperature) and % relative change per decade (precipitation) with respect to the climatological mean over this period.
(c–f) Climate change projections of annual mean surface air temperature and precipitation from CMIP5 (30 models) and CMIP6 (17 models) calculated as the differences in the climatological average for RCP8.5 and SSP5-8.5 respectively, for the period 2041–2060 with respect to the historical 1995–2014 period and expressed as °C (temperature) and % relative change (precipitation). Hatching indicates weak model agreement on the sign of the change (less than 80% as defined in Nikulin et al., 2018).
(g–m) Regional mean changes in annual mean surface air temperature and precipitation for the seven South American regions (NWS, NSA, SAM, NES, SWS, SES and SSA). The top row shows the median (dots) and 10th–90th percentile range across each model ensemble for annual mean temperature changes, for two datasets (CMIP5 and CMIP6) and two scenarios (SSP1-2.6/RCP2.6 and

SSP5-8.5/RCP8.5). The first four bars represent the additional warming projected relative to the historical baseline 1995–2014 period to reach the two global warming levels (GWL; +1.5°C and +2°C) and the remaining six projected changes over three time periods (near-term 2021–2040, mid-term 2041–2060 and long-term 2081–2100) compared to this same historical baseline period. The bottom row shows scatter diagrams of temperature against precipitation changes, displaying the median (dots) and 10th–90th percentile ranges for four future periods (2021–2040, 2041–2060, 2061–2080, 2081–2100) compared to the historical baseline period, as obtained from CMIP6 projections for three scenarios (SSP1-2.6, SSP2-4.5 and SSP5-8.5). Changes are absolute for temperature and relative for precipitation.
(The script used to generate this figure is available online (Atlas GitHub, 2020) and similar results can be generated in the Interactive Atlas for flexibly defined seasonal periods.)

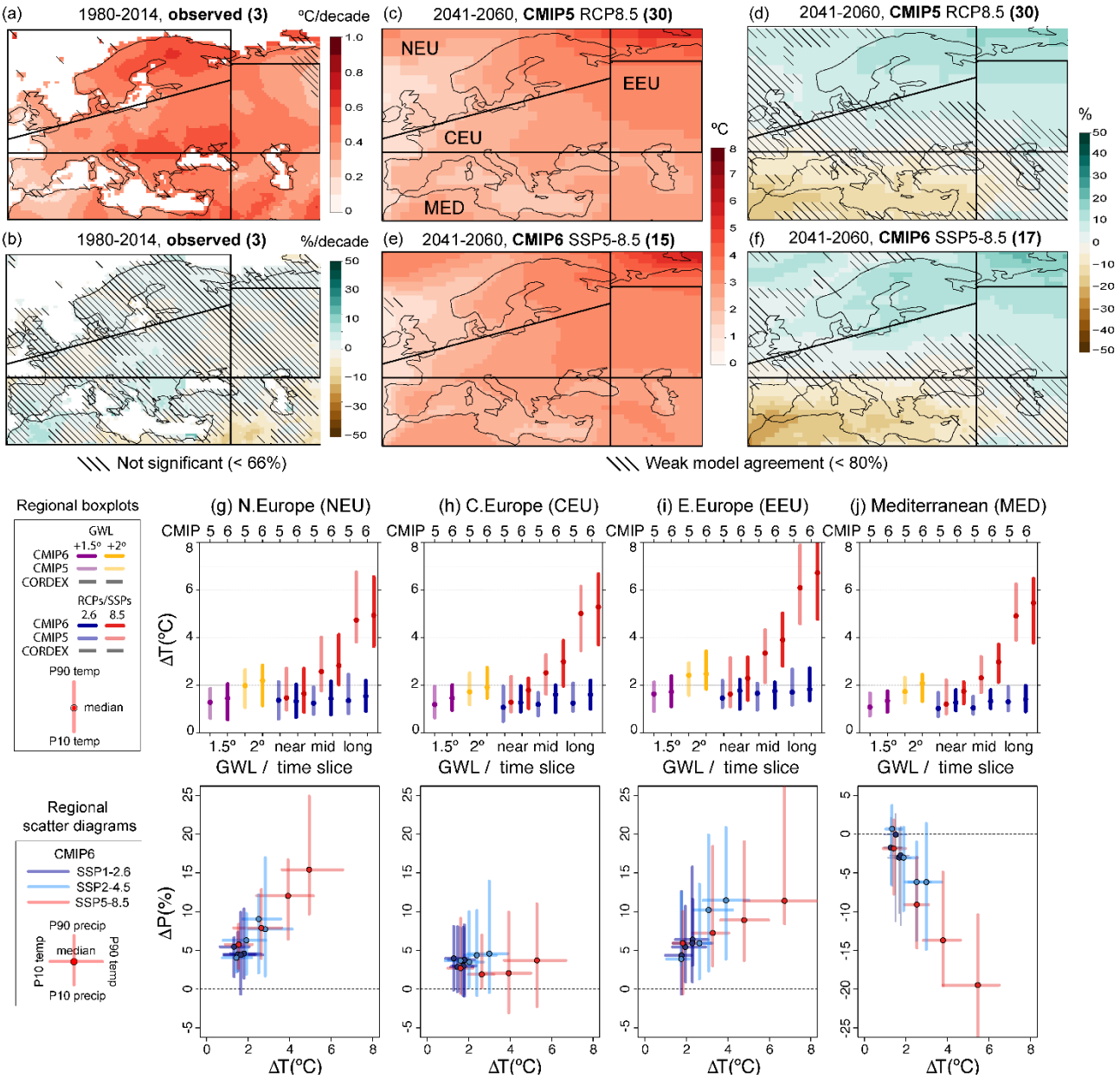

Figure Atlas.40: (a–b) Mean observed trends of annual mean surface air temperature and precipitation for three datasets (CRU TS, BERKELEY and EWEMBI for temperature; CRU TS, GPCC and GPCP for precipitation). Hatching indicates regions where no or only one dataset provides a significant trend. Linear trends are calculated for the common 1980–2014 period and expressed in °C per decade (temperature) and % relative change per decade (precipitation) with respect to the climatological mean over this period.

(c–f) Climate change projections of annual mean surface air temperature and precipitation from CMIP5 (30 models) and CMIP6 (17 models) calculated as the differences in the climatological average for RCP8.5 and SSP5-8.5 respectively, for the period 2041–2060 with respect to the historical 1995–2014 period and expressed as °C (temperature) and % relative change (precipitation). Hatching indicates weak model agreement on the sign of the change (less than 80% as defined in Nikulin et al., 2018).

(g–j) Regional mean changes in annual mean surface air temperature and precipitation for the four European regions (NEU, CEU, MED and EEU). The top row shows the median (dots) and 10th–90th percentile range across each model ensemble for annual mean temperature changes, for two datasets (CMIP5 and CMIP6) and two scenarios (SSP1-2.6/RCP2.6 and SSP5-8.5/RCP8.5). The first four bars represent the additional warming projected relative to the historical baseline 1995–2014 period to reach the two global warming levels (GWL; +1.5°C and +2°C) and the remaining six projected

changes over three time periods (near-term 2021–2040, mid-term 2041–2060 and long-term 2081–2100) compared to this same historical baseline period. The bottom row shows scatter diagrams of temperature against precipitation changes, displaying the median (dots) and 10th–90th percentile ranges for four future periods (2021–2040, 2041–2060, 2061–2080, 2081–2100) compared to the historical baseline period, as obtained from CMIP6 projections for three scenarios (SSP1-2.6, SSP2-4.5 and SSP5-8.5). Changes are absolute for temperature and relative for precipitation.
(The script used to generate this figure is available online (Atlas GitHub, 2020) and similar results can be generated in the Interactive Atlas for flexibly defined seasonal periods.)

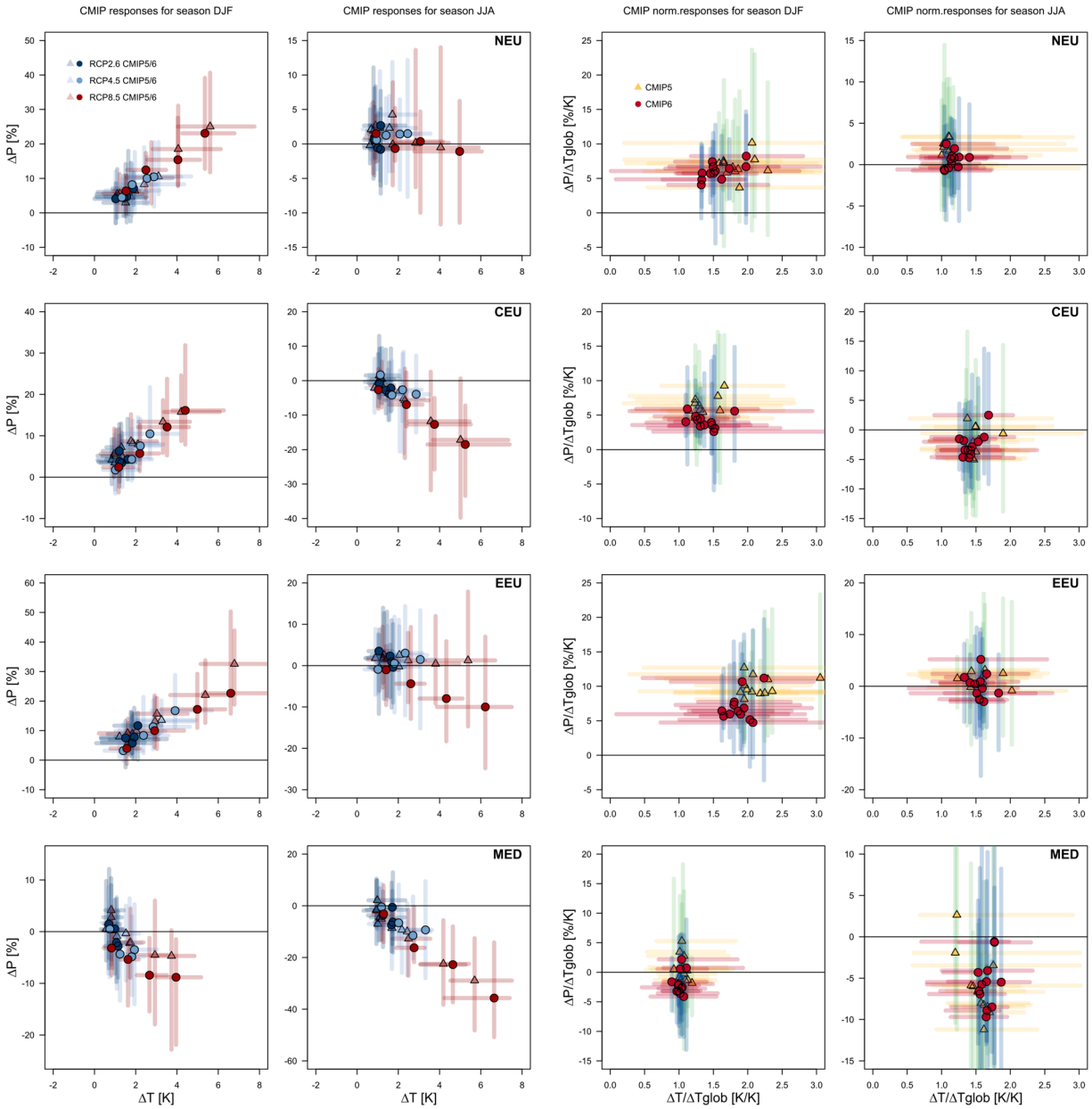

Figure Atlas.41: Regional mean changes in seasonal mean temperature and precipitation for DJF and JJA for the European regions NEU, CEU, EEU and MED for CMIP5 and a subset of CMIP6. Left 2 columns show absolute temperature and relative precipitation change for 3 emission scenarios and 4 20-year time slices between 2020 and 2100 relative to 1995-2014; right 2 columns show the change normalized by the global mean annual mean temperature change. Horizontal and vertical error bars represent the 10% and 90% percentile value from the mean values calculated across the ensemble of included models. See text for details. Results are generated with the Interactive Atlas (http://ipcc-atlas.ifca.es, system version 24 January 2020).

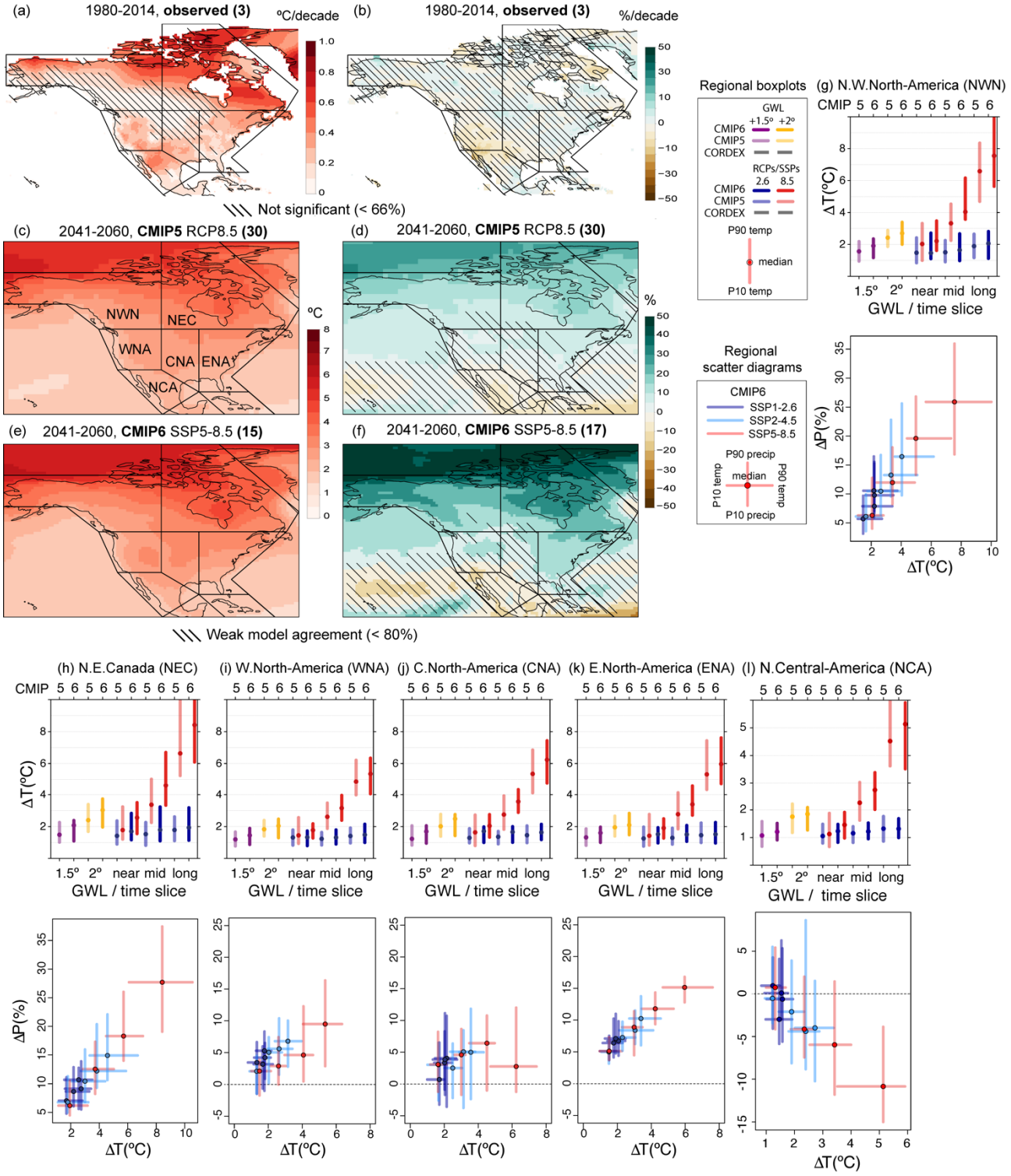

Figure Atlas.42: (a–b) Mean observed trends of annual mean surface air temperature and precipitation for three datasets (CRU TS, BERKELEY and EWEMBI for temperature; CRU TS, GPCC and GPCP for precipitation). Hatching indicates regions where no or only one dataset provides a significant trend. Linear trends are calculated for the common 1980–2014 period and expressed in °C per decade (temperature) and % relative change per decade (precipitation) with respect to the climatological mean over this period.
(c–f) Climate change projections of annual mean surface air temperature and precipitation from CMIP5 (30 models) and CMIP6 (17 models) calculated as the differences in the climatological average for RCP8.5 and SSP5-8.5 respectively, for the period 2041–2060 with respect to the historical

1995–2014 period and expressed as °C (temperature) and % relative change (precipitation). Hatching indicates weak model agreement on the sign of the change (less than 80% as defined in Nikulin et al., 2018).
(g–k) Regional mean changes in annual mean surface air temperature and precipitation for the five North American regions (NWN, NEC, WNA, CNA and ENA). The top row shows the median (dots) and 10th–90th percentile range across each model ensemble for annual mean temperature changes, for two datasets (CMIP5 and CMIP6) and two scenarios (SSP1-2.6/RCP2.6 and SSP5-8.5/RCP8.5). The first four bars represent the additional warming projected relative to the historical baseline 1995–2014 period to reach the two global warming levels (GWL; +1.5°C and +2°C) and the remaining six projected changes over three time periods (near-term 2021–2040, mid-term 2041–2060 and long-term 2081–2100) compared to this same historical baseline period. The bottom row shows scatter diagrams of temperature against precipitation changes, displaying the median (dots) and 10th–90th percentile ranges for four future periods (2021–2040, 2041–2060, 2061–2080, 2081–2100) compared to the historical baseline period, as obtained from CMIP6 projections for three scenarios (SSP1-2.6, SSP2-4.5 and SSP5-8.5). Changes are absolute for temperature and relative for precipitation.
(The script used to generate this figure is available online (Atlas GitHub, 2020) and similar results can be generated in the Interactive Atlas for flexibly defined seasonal periods.)

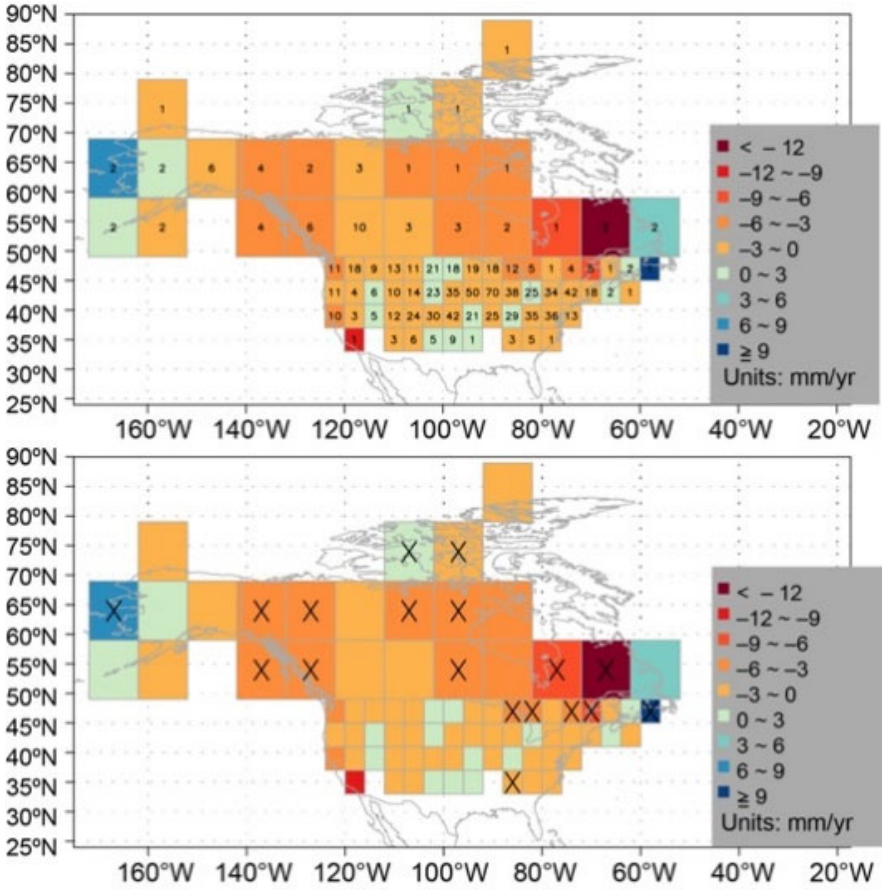

Figure Atlas.43: Grid box trends (mm yr^{-1}) in annual maximum snow depth for cold season periods of 1960/1961 to 2014/2015. (top) Numbers indicate number of stations available in that grid box. (bottom) Boxes with 'x' indicate statistically significant trends at the $p < 0.05$ level of significance (Vose et al., 2017).

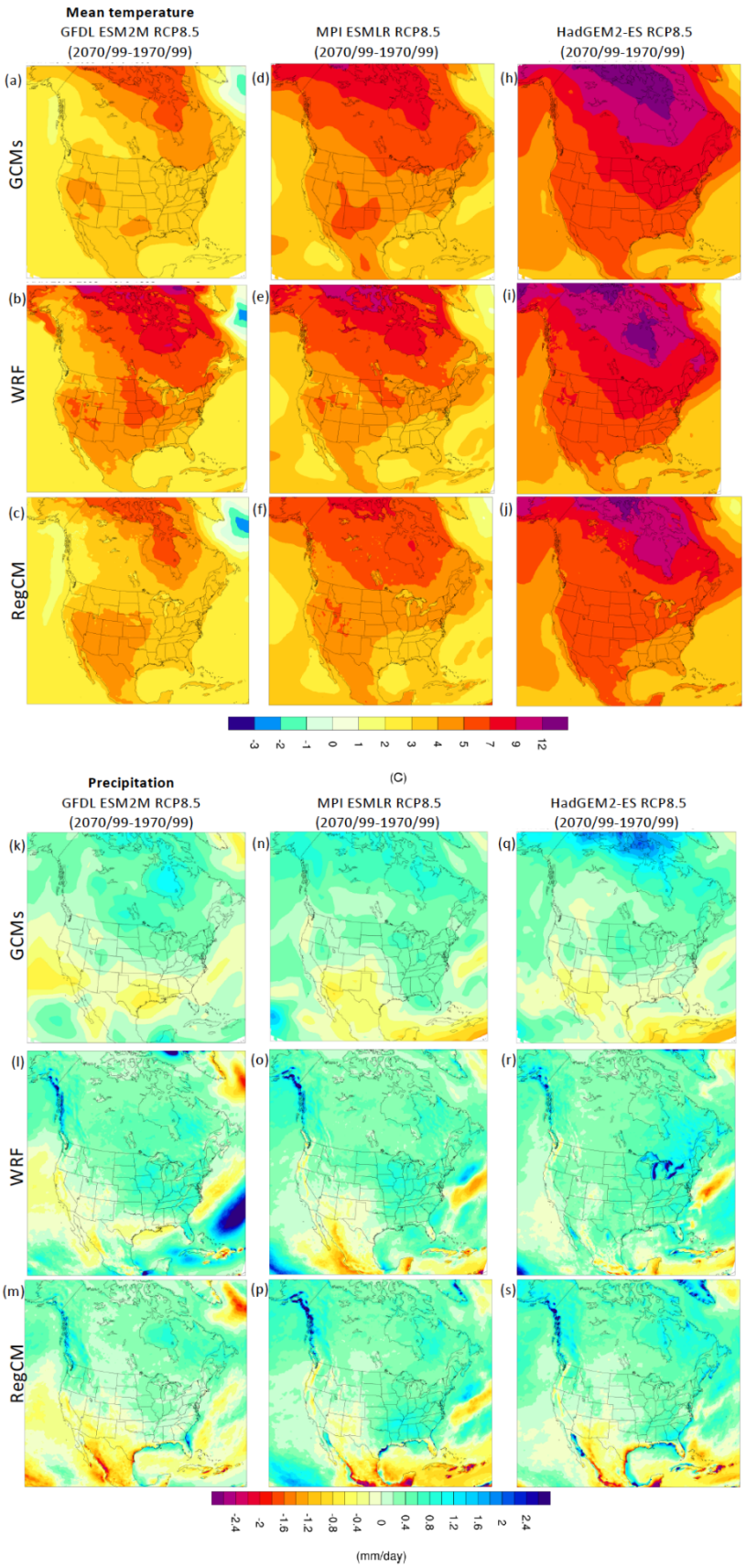

Figure Atlas.44: Changes in the annual mean surface air temperature (top) and precipitation (bottom) by three GCMs (GFDL ESM2M, MPI ESM-LR, HadGEM2-ES) and two RCMs (WRF and RegCM4) nested in the GCMs.

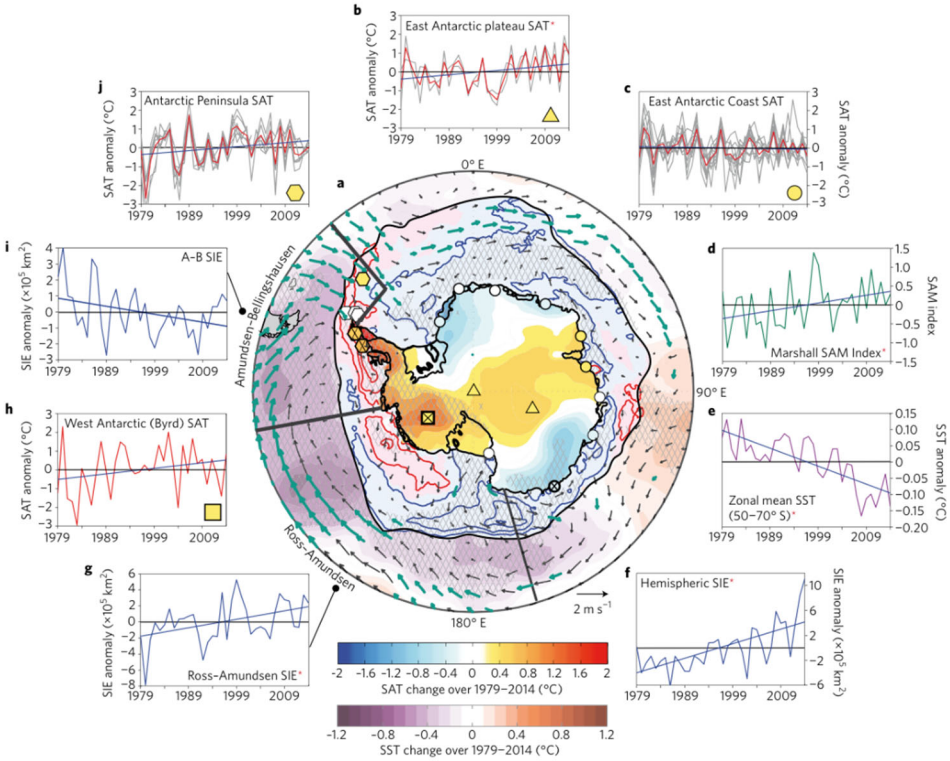

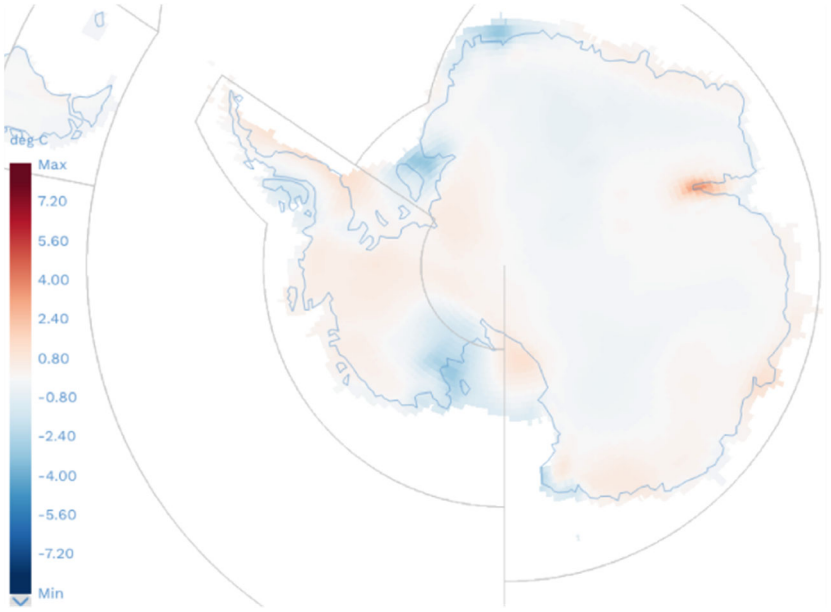

Figure Atlas.45: a) Surface air temperature (SAT) and sea surface temperature (SST) change over the 1979–2014 period based on observational records (Jones et al., 2016a). b) Air temperature change during the 1995–2014 period based on EWEMBI data (from Interactive Atlas available at http://ipcc-atlas.ifca.es). Thin black lines denote WAN and EAN, the two main reference regions as used in the Interactive Atlas for Antarctica.

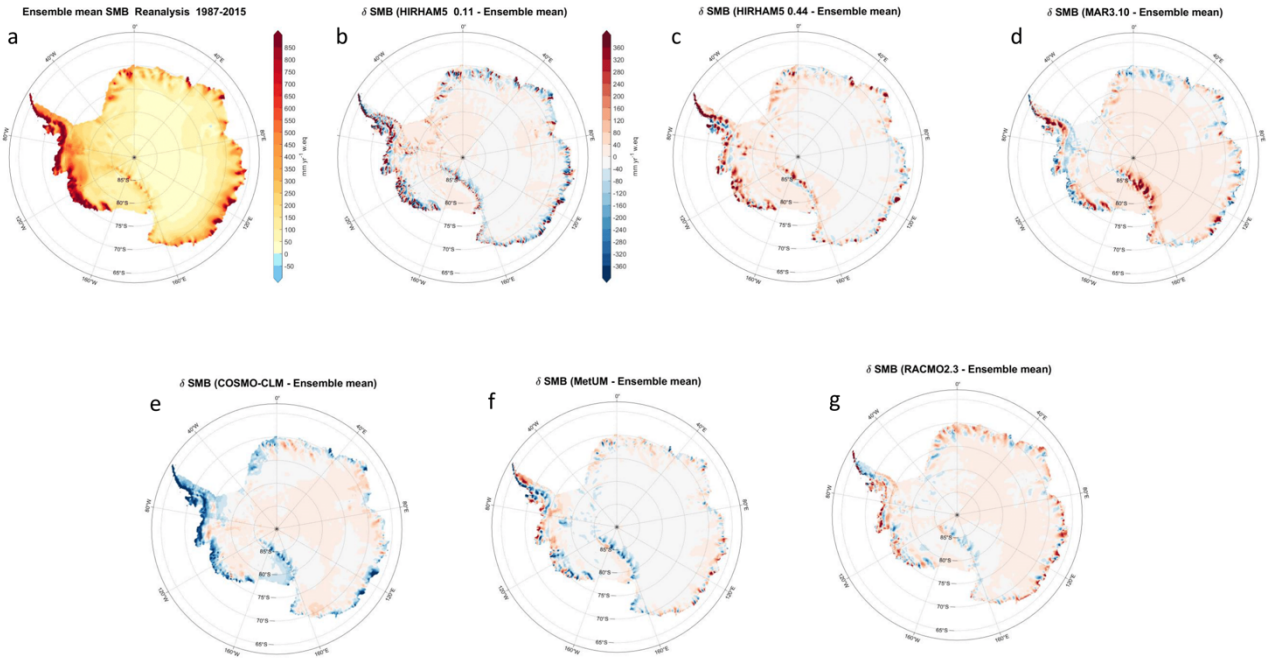

Figure Atlas.46: Maps of Antarctic mean surface mass balance from Polar CORDEX forced by ERA-Interim reanalysis (taken from Mottram et al. (*submitted*)). The models are MetUM, COSMO-CLM2, RACMO2.1p, HIRHAM, MAR v3.10 and RACMO2.3p2. The period is 1980 to 2010 with the exception of COSMO-CLM2 where the time series starts in 1987.

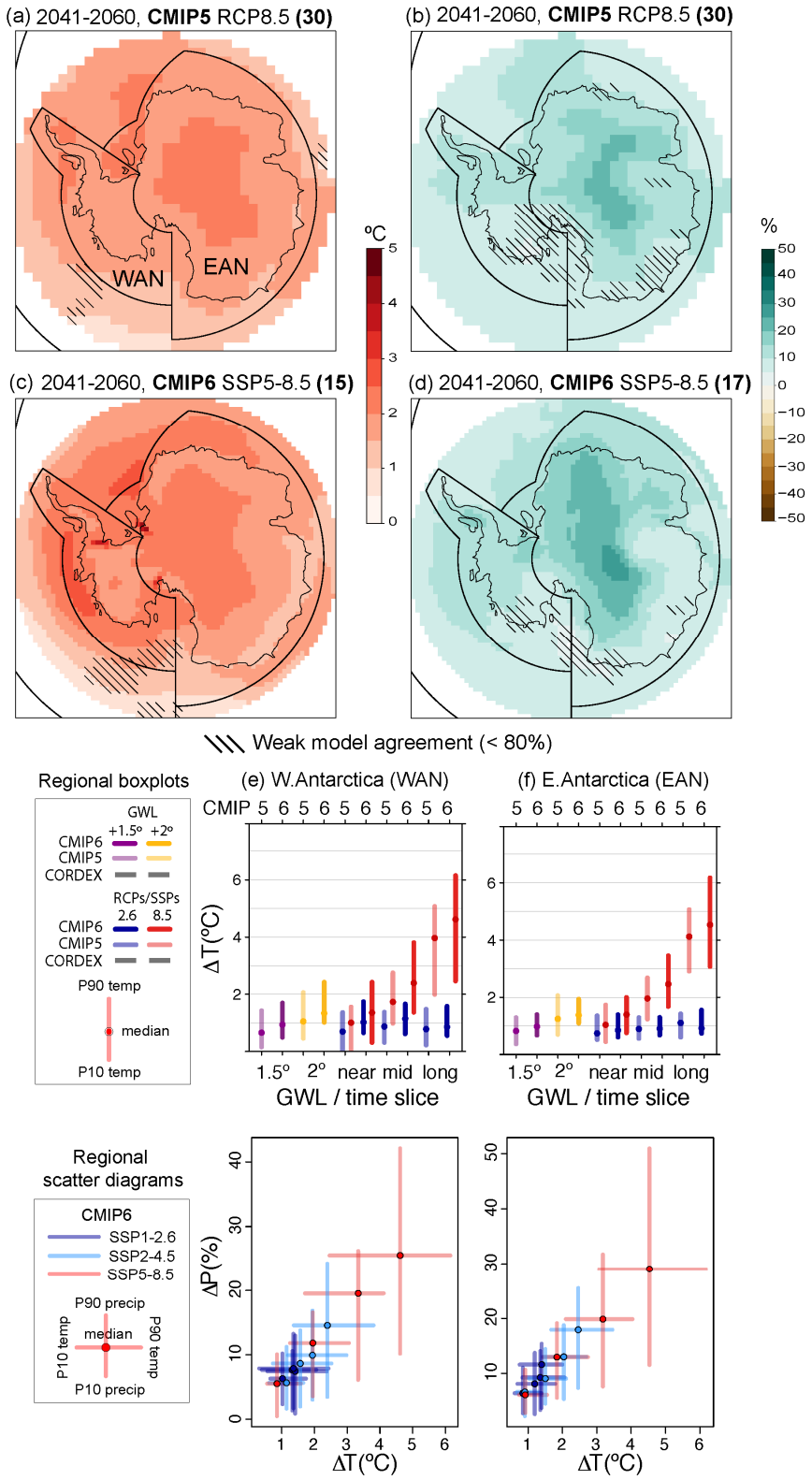

Figure Atlas.47: (a–d) Climate change projections of annual mean surface air temperature and precipitation from CMIP5 (30 models) and CMIP6 (17 models) calculated as the differences in the climatological average for RCP8.5 and SSP5-8.5 respectively, for the period 2041–2060 with respect to the historical 1995–2014 period and expressed as °C (temperature) and % relative change (precipitation). Hatching indicates weak model agreement on the sign of the change (less than 80% as defined in Nikulin et al., 2018).
(e–f) Regional mean changes in annual mean surface air temperature and precipitation for the two Antarctic regions (WAN and EAN). The top row shows the median (dots) and 10th–90th percentile

range across each model ensemble for annual mean temperature changes, for two datasets (CMIP5 and CMIP6) and two scenarios (SSP1-2.6/RCP2.6 and SSP5-8.5/RCP8.5). The first four bars represent the additional warming projected relative to the historical baseline 1995–2014 period to reach the two global warming levels (GWL; +1.5°C and +2°C) and the remaining six projected changes over three time periods (near-term 2021–2040, mid-term 2041–2060 and long-term 2081–2100) compared to this same historical baseline period. The bottom row shows scatter diagrams of temperature against precipitation changes, displaying the median (dots) and 10th–90th percentile ranges for four future periods (2021–2040, 2041–2060, 2061–2080, 2081–2100) compared to the historical baseline period, as obtained from CMIP6 projections for three scenarios (SSP1-2.6, SSP2-4.5 and SSP5-8.5). Changes are absolute for temperature and relative for precipitation.
(The script used to generate this figure is available online (Atlas GitHub, 2020) and similar results can be generated in the Interactive Atlas for flexibly defined seasonal periods.)

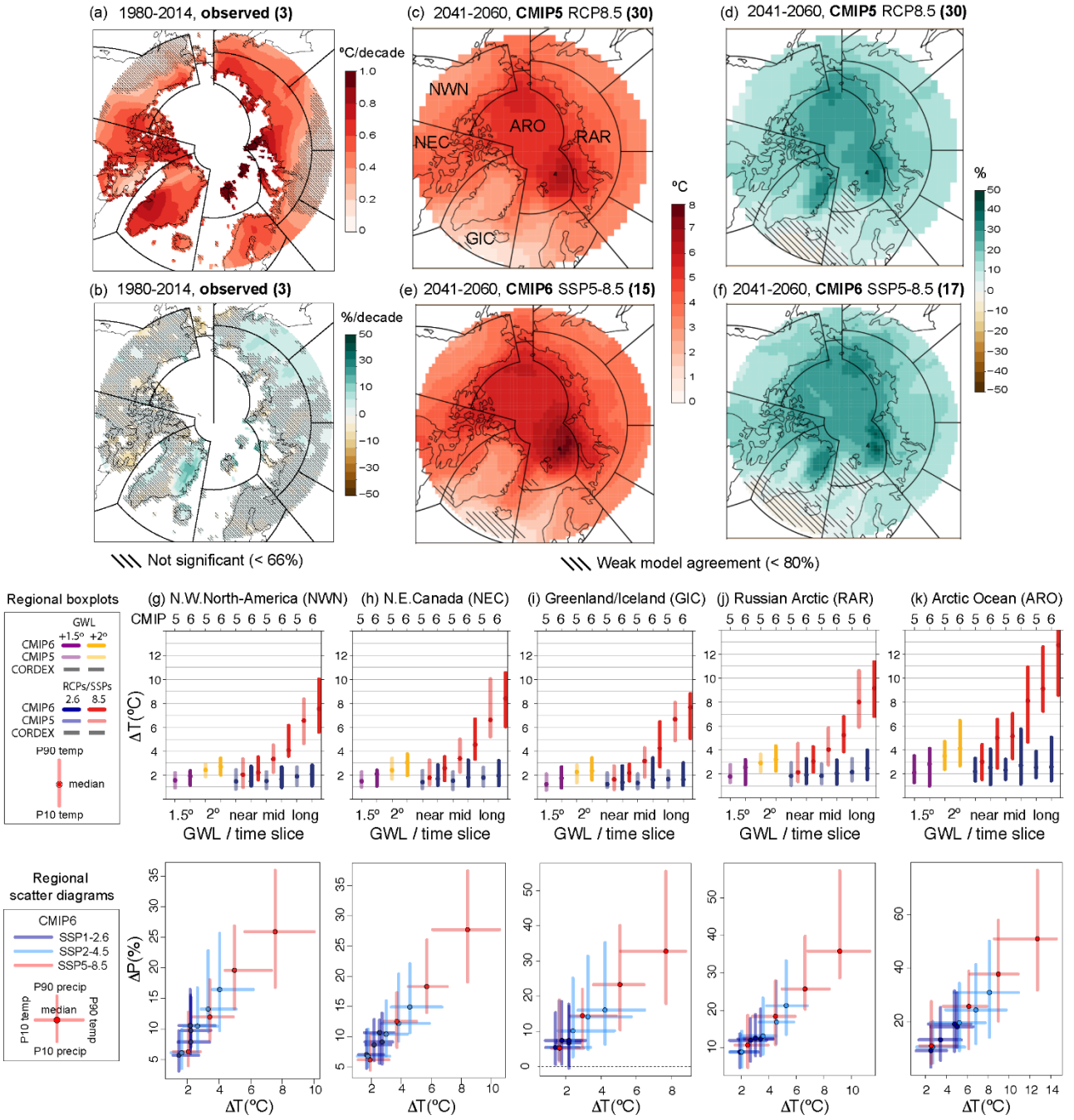

Figure Atlas.48: (a–b) Mean observed trends of annual mean surface air temperature and precipitation for three datasets (CRU TS, BERKELEY and EWEMBI for temperature; CRU TS, GPCC and GPCP for precipitation). Hatching indicates regions where no or only one dataset provides a significant trend. Linear trends are calculated for the common 1980–2014 period and expressed in °C per decade (temperature) and % relative change per decade (precipitation) with respect to the climatological mean over this period.
(c–f) Climate change projections of annual mean surface air temperature and precipitation from CMIP5 (30 models) and CMIP6 (17 models) calculated as the differences in the climatological average for RCP8.5 and SSP5-8.5 respectively, for the period 2041–2060 with respect to the historical 1995–2014 period and expressed as °C (temperature) and % relative change (precipitation). Hatching indicates weak model agreement on the sign of the change (less than 80% as defined in Nikulin et al., 2018).
(g–k) Regional mean changes in annual mean surface air temperature and precipitation for the five Arctic regions (ARO, RAR, GIC, NEC and NWN). The top row shows the median (dots) and 10th–90th percentile range across each model ensemble for annual mean temperature changes, for two datasets (CMIP5 and CMIP6) and two scenarios (SSP1-2.6/RCP2.6 and SSP5-8.5/RCP8.5). The first

four bars represent the additional warming projected relative to the historical baseline 1995–2014 period to reach the two global warming levels (GWL; +1.5°C and +2°C) and the remaining six projected changes over three time periods (near-term 2021–2040, mid-term 2041–2060 and long-term 2081–2100) compared to this same historical baseline period. The bottom row shows scatter diagrams of temperature against precipitation changes, displaying the median (dots) and 10th–90th percentile ranges for four future periods (2021–2040, 2041–2060, 2061–2080, 2081–2100) compared to the historical baseline period, as obtained from CMIP6 projections for three scenarios (SSP1-2.6, SSP2-4.5 and SSP5-8.5). Changes are absolute for temperature and relative for precipitation.
(The script used to generate this figure is available online (Atlas GitHub, 2020) and similar results can be generated in the Interactive Atlas for flexibly defined seasonal periods.)

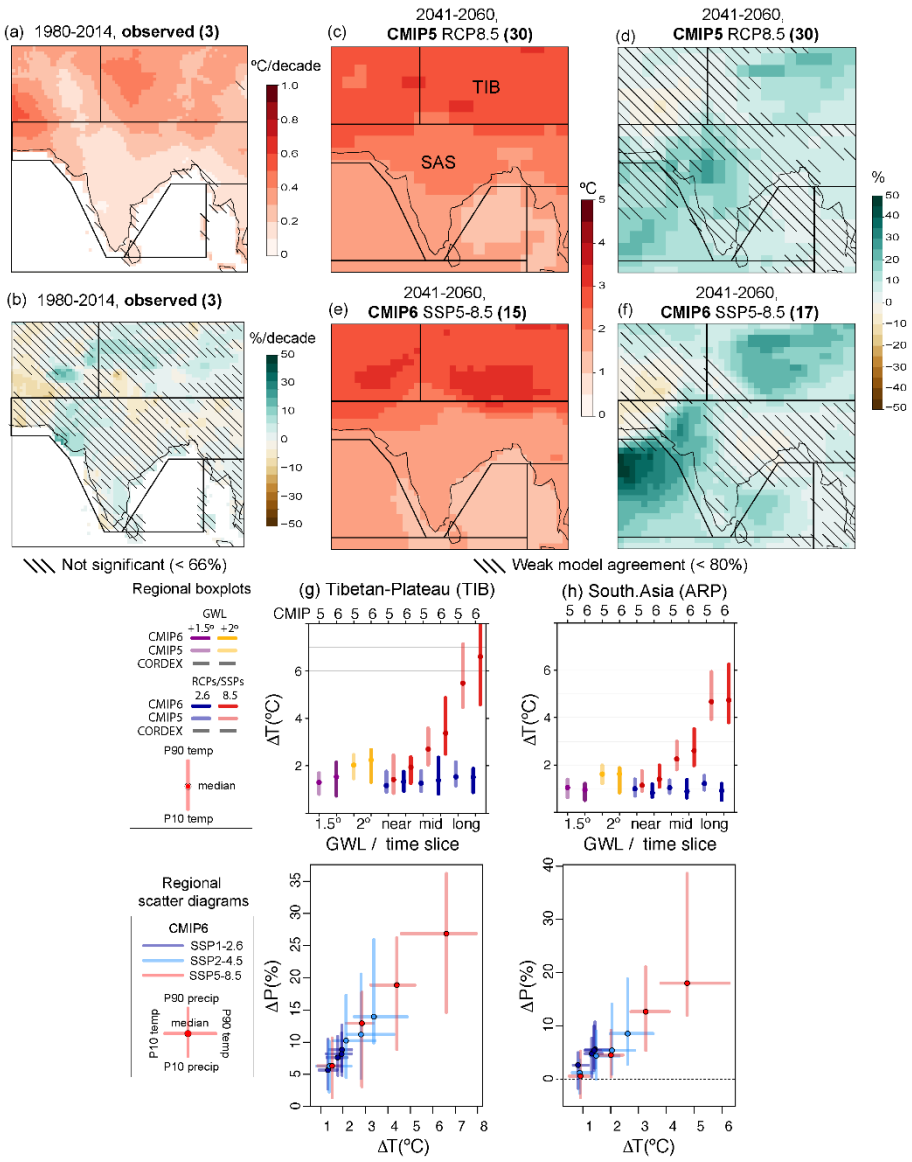

Figure Atlas.49: (a–b) Mean observed trends of annual mean surface air temperature and precipitation for three datasets (CRU TS, BERKELEY and EWEMBI for temperature; CRU TS, GPCC and GPCP for precipitation). Hatching indicates regions where no or only one dataset provides a significant trend. Linear trends are calculated for the common 1980–2014 period and expressed in °C per decade (temperature) and % relative change per decade (precipitation) with respect to the climatological mean over this period.

(c–f) Climate change projections of annual mean surface air temperature and precipitation from CMIP5 (30 models) and CMIP6 (17 models) calculated as the differences in the climatological average for RCP8.5 and SSP5-8.5 respectively, for the period 2041–2060 with respect to the historical 1995–2014 period and expressed as °C (temperature) and % relative change (precipitation). Hatching indicates weak model agreement on the sign of the change (less than 80% as defined in Nikulin et al., 2018).

(g–h) Regional mean changes in annual mean surface air temperature and precipitation for the Tibetan Plateau and South Asia. The top row shows the median (dots) and 10th–90th percentile range across each model ensemble for annual mean temperature changes, for two datasets (CMIP5 and CMIP6) and two scenarios (SSP1-2.6/RCP2.6 and SSP5-8.5/RCP8.5). The first four bars represent the additional warming projected relative to the historical baseline 1995–2014 period to reach the two global warming levels (GWL; +1.5°C and +2°C) and the remaining six projected changes over three time periods (near-term 2021–2040, mid-term 2041–2060 and long-term 2081–2100) compared to this same historical baseline period. The bottom row shows scatter diagrams of temperature against precipitation changes, displaying the median (dots) and 10th–90th percentile ranges for four future periods (2021–2040, 2041–2060, 2061–2080, 2081–2100) compared to the historical baseline period,

as obtained from CMIP6 projections for three scenarios (SSP1-2.6, SSP2-4.5 and SSP5-8.5). Changes are absolute for temperature and relative for precipitation.
(The script used to generate this figure is available online (Atlas GitHub, 2020) and similar results can be generated in the Interactive Atlas for flexibly defined seasonal periods.)

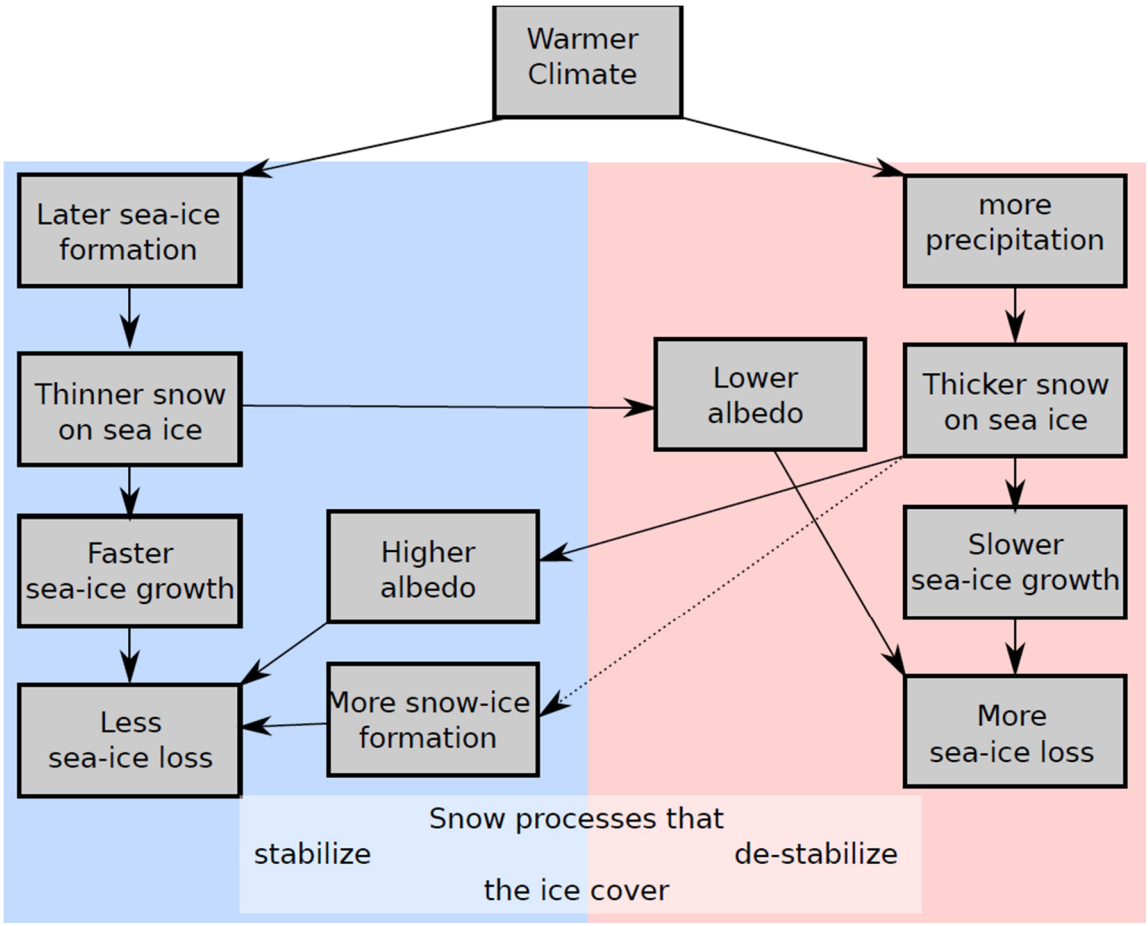

Figure Atlas.50: Conceptual flow diagram of relevant snow-on-sea-ice processes.

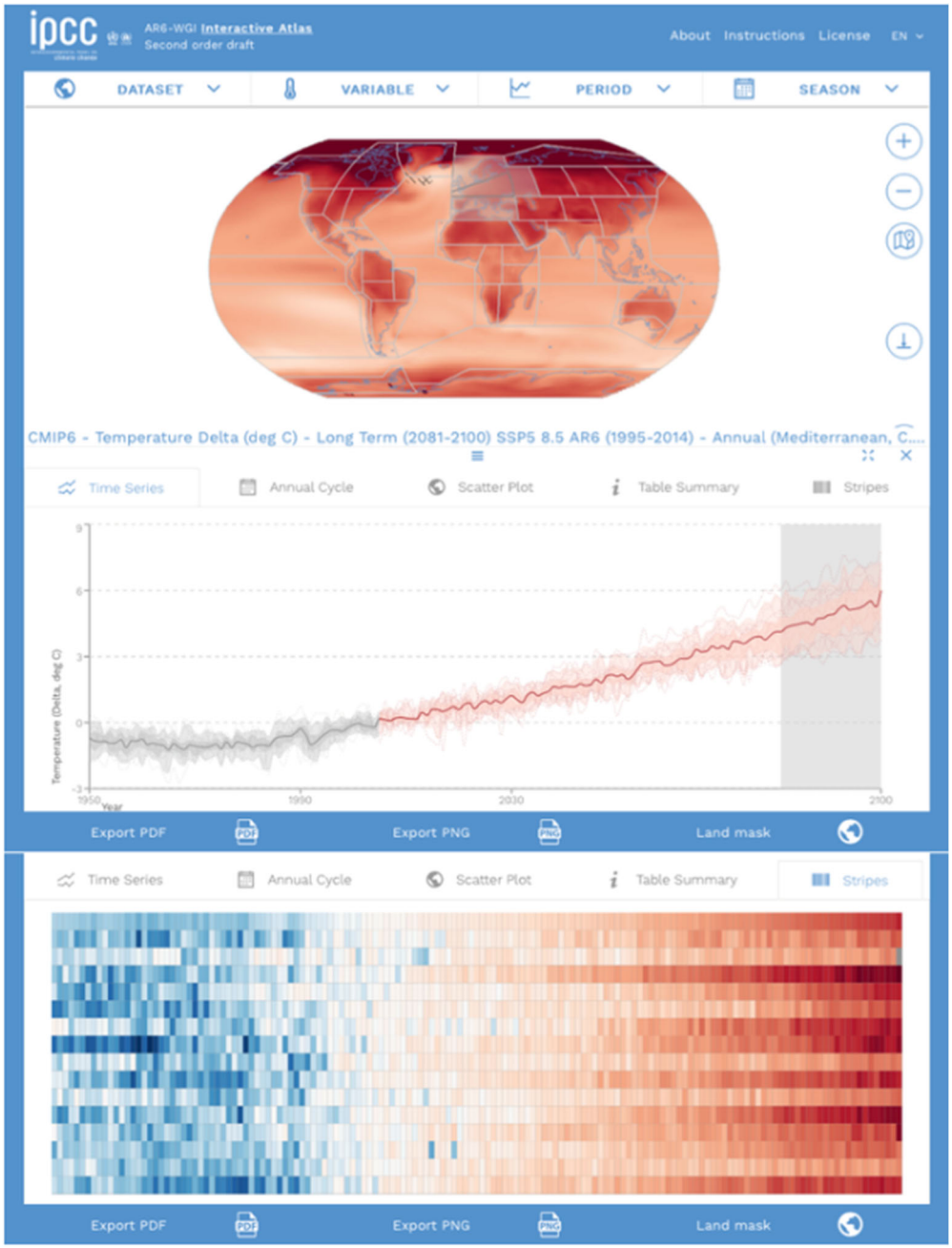

Figure Atlas.51: The Interactive Atlas incorporates different visualisations to present climate information such as standard spatial maps (top) and time series (middle), but also more modern visual representations like the (piled) stripes plots (bottom). These examples correspond to CMIP6 annual mean temperature for the SSP5-8.5 scenario. The spatial map shows the climate change signal for the long-term period (2081–2100) with respect to the 1995–2014 baseline period. Regional information – for the aggregated European regions selected in the map – for both the historical and future periods are displayed using time series (middle panel, historical 1950–2014 period in grey and 2015–2100 projections in red) and, alternatively, as a stripe plot formed by the piled stripes of the different models (this figure illustrates a strong warming pattern emerging from the interannual and model variability).

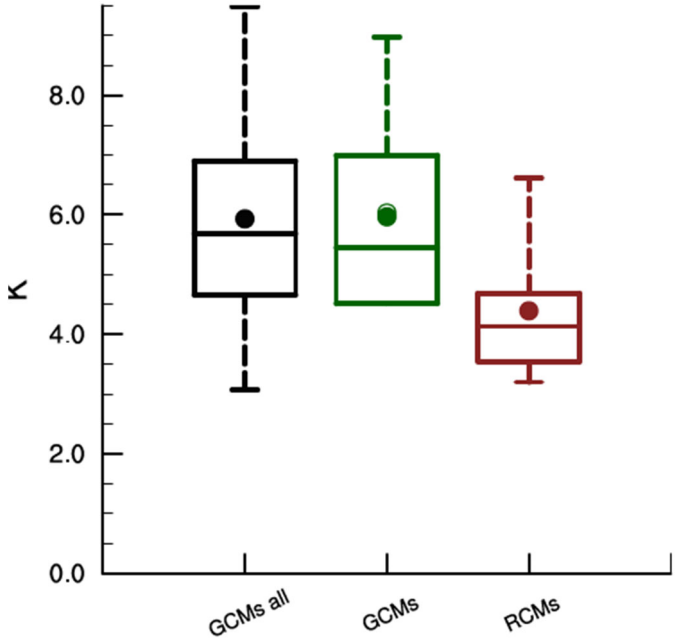

Figure Atlas.52: Mean European June-July-August surface temperature change between the 1970–1999 and 2070–2099 periods for RCP8.5 using an ensemble of CMIP5 GCMs (black), a subset of these used to drive an ensemble of RCMs (green) and the RCMs (red). (Source: Boé et al., *submitted*).

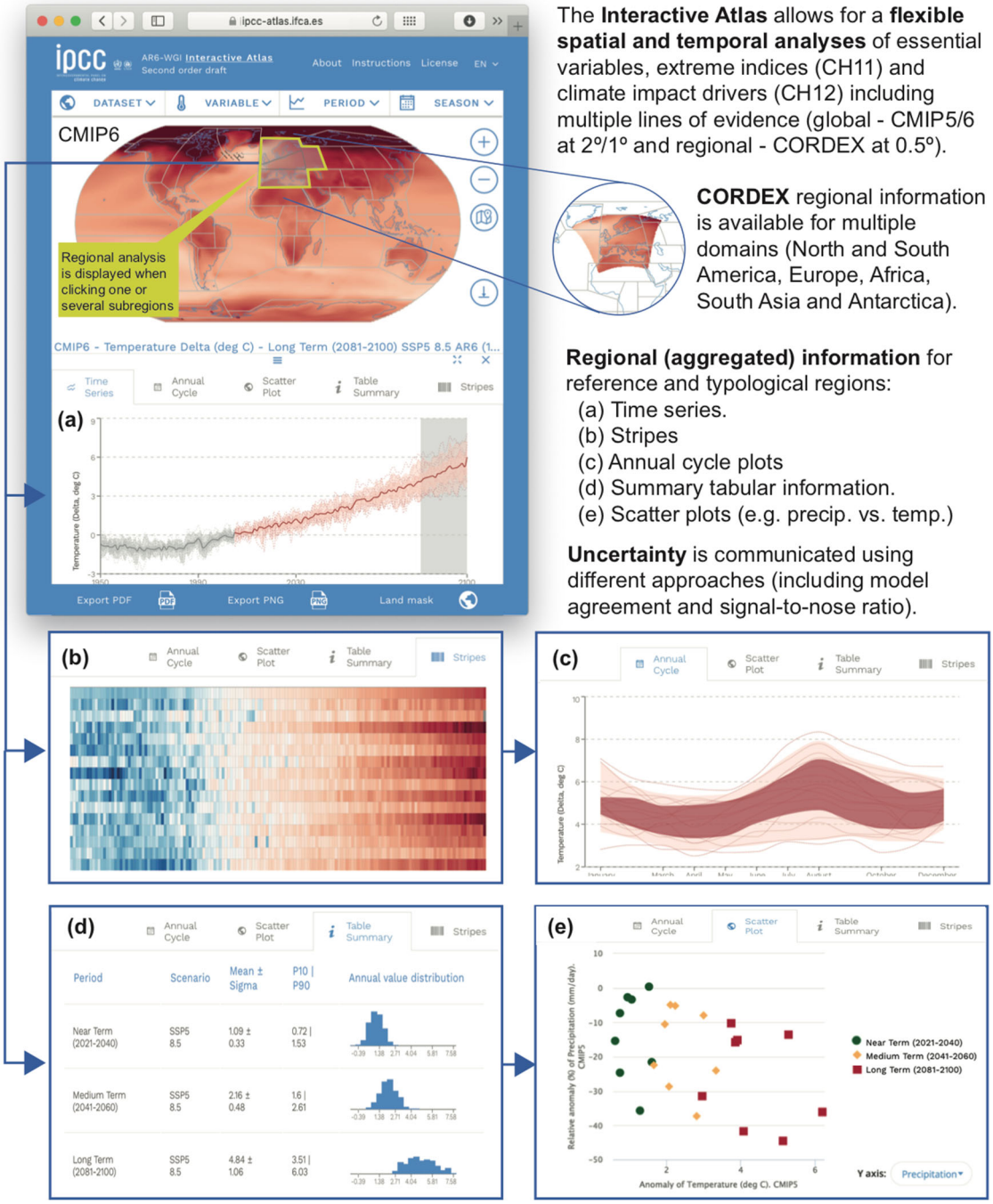

Figure Atlas.53: Screenshots from the Interactive Atlas showing the main interface and WGI Reference regions (top map) and various formats for displaying summary information over the reference regions (bottom five graphics panels). Other details of model ensembles, resolutions etc are displayed in the text of the figure.

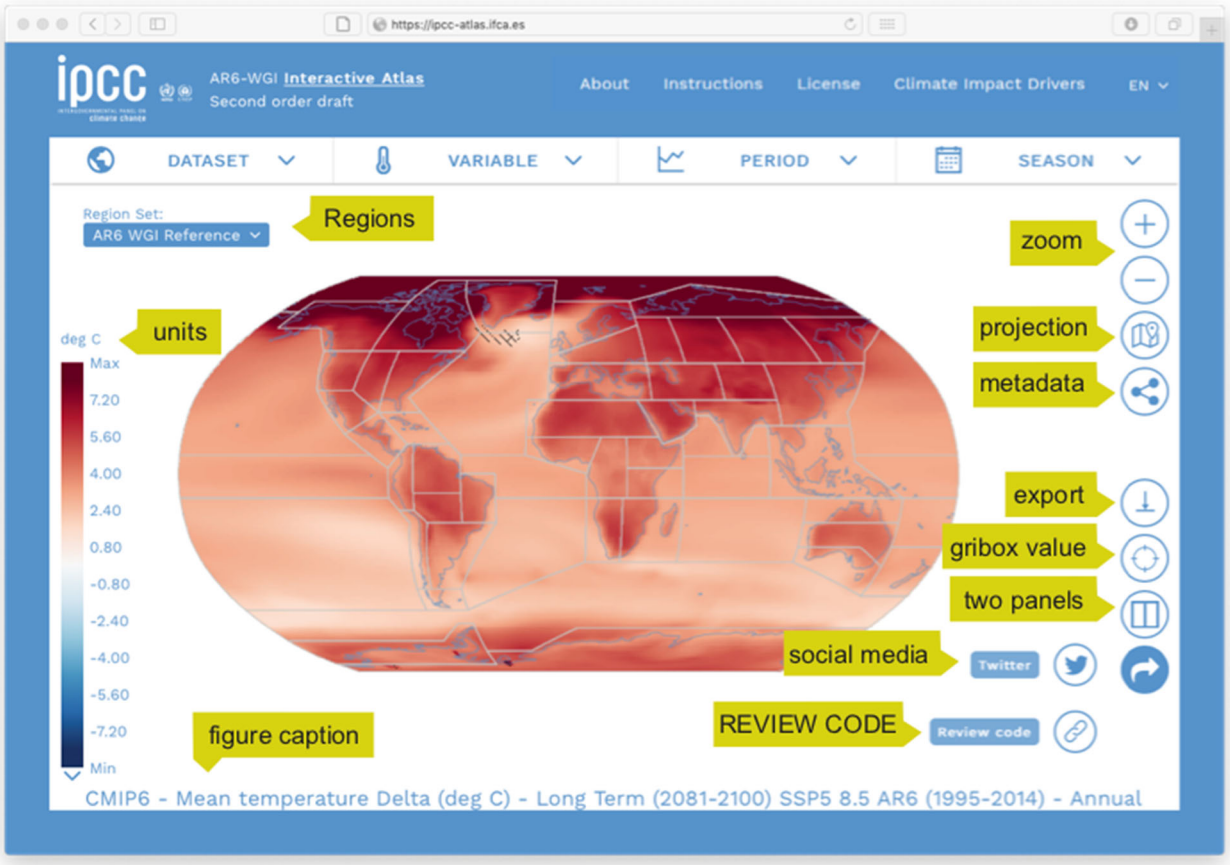

Figure Atlas.54: A screenshot illustrating the main window of the AR6 WGI Interactive Atlas, which displays a global map of the climate change signal for annual mean temperature from the CMIP6 dataset for the long-term future period (2081-2100) using the AR6 baseline (1995-2014). The main controls at the top of the window allow selecting the *dataset* (CMIP6, CMIP5 or different CORDEX domains, at 2º, 1º and 0.5º horizontal resolution, respectively), *variable* (atmospheric and oceanic variables and indices), *scenario* (currently SSP1-2.6, 2-4.5 and 5-8.5 –or RCP2.6, 4.5 and 8.5– for different time slices and 1.5º, 2º and 3º warming levels) and *season* (annual, standard seasons and user-defined ones). Regional information for a particular region can be obtained interactively by clicking on the map over one or several sub-regions; see Figure Atlas.55:). Note that the full URL (as copied from the browser) tracks all the information of the current choice (a short 'review code' can be obtained as shown in the figure).

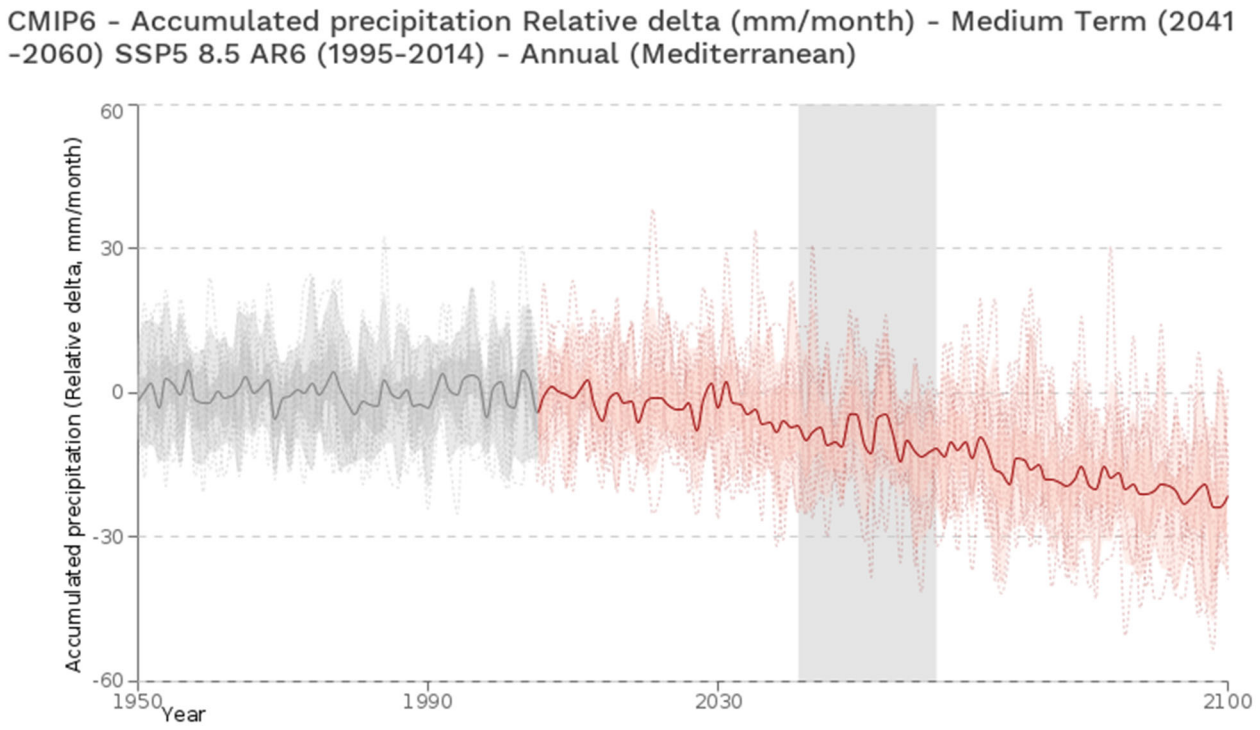

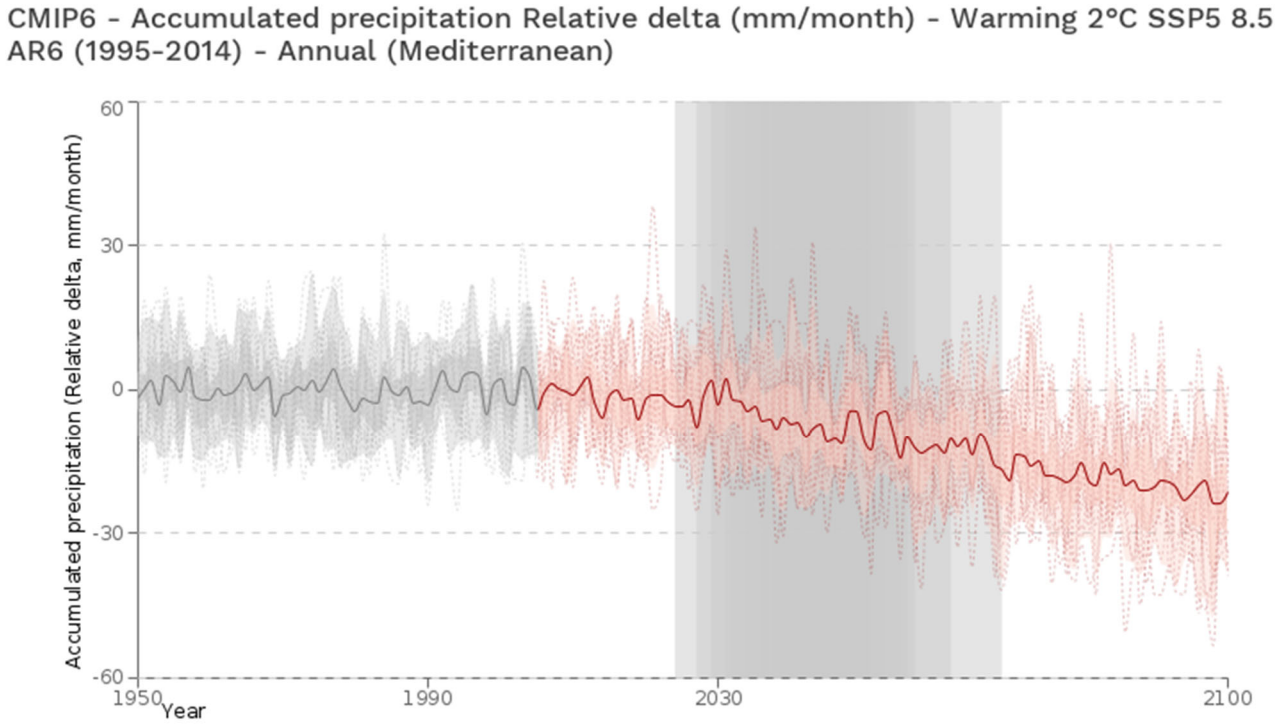

Figure Atlas.55: Regional information for a selected region (the Mediterranean) in the form of a time series for a mid-term time slice (top) and a 2ºC warming level (bottom). Note that the corresponding periods are indicated with grey shading (with intensity proportional to the number of models including each particular year for the case of the warming levels). Fine granularity is provided by hovering over a particular point, obtaining information of particular models. These figures have been exported directly from the Interactive Atlas (as bitmap or PDF files).

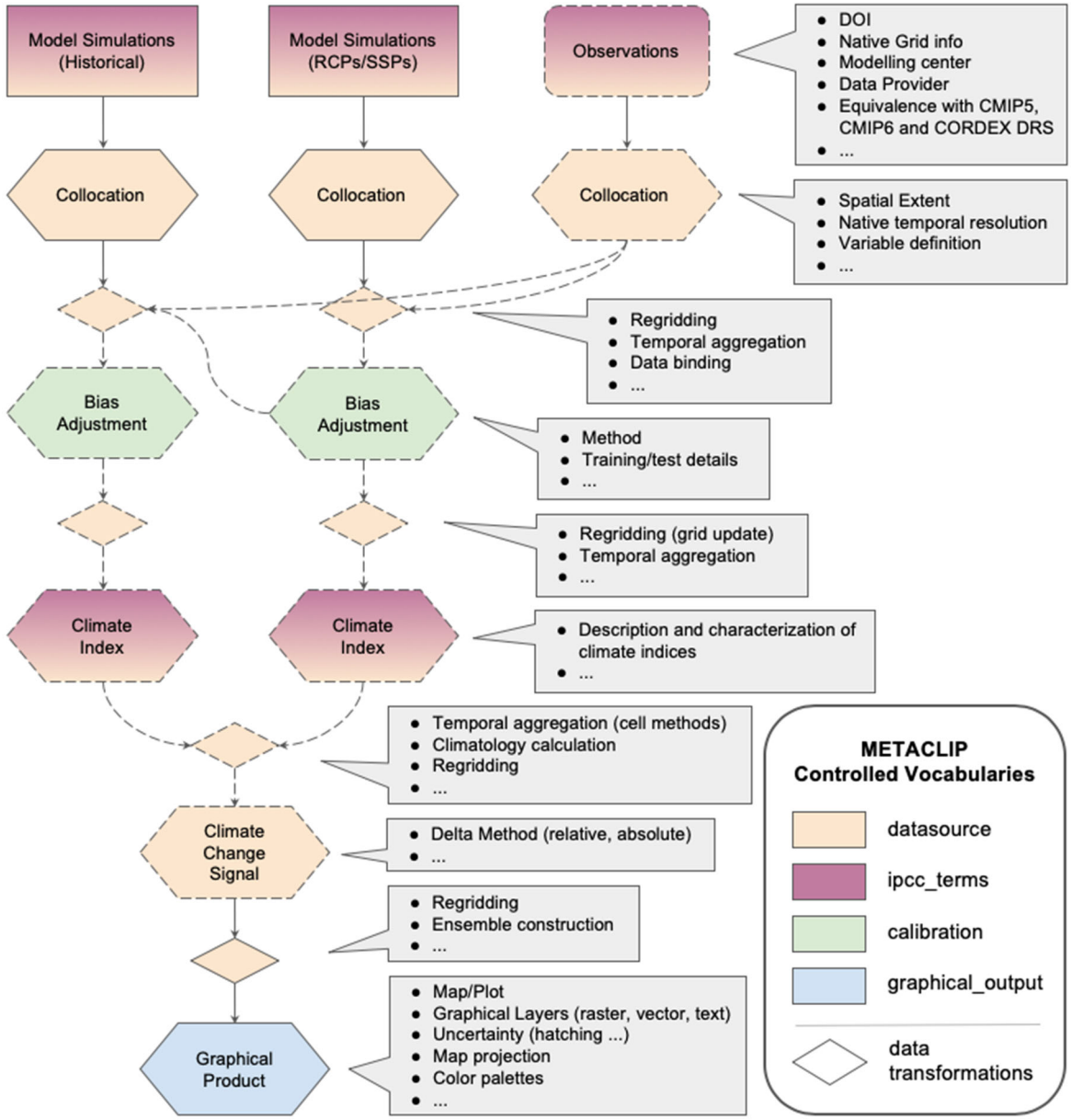

Figure Atlas.56: Schematic representation of the generation workflow, from database description, subsetting and data transformation to final graphical product generation (maps and plots). Product-dependent workflow steps are depicted with dashed borders. METACLIP specifically considers the different intermediate steps consisting of various data transformations, bias adjustment, climate index calculation and graphical product generation, providing a semantic description of each stage and the different elements involved. The different controlled vocabularies describing each stage are indicated by the colors. The gradient indicates that both ipcc_terms and datasource vocabularies are involved, usually meaning that specific individual instances have been defined in ipcc_terms extending generic classes of datasource. Both datasource and ipcc_terms vocabularies, dealing with the primary data sources, have specific annotation properties linking their own features with the CMIP5, CMIP6 and CORDEX Data Reference Syntax, taking as reference their respective controlled vocabularies. All products generated by the Interactive Atlas provide a METACLIP provenance description, including a persistent link to a reproducible source code under version control.

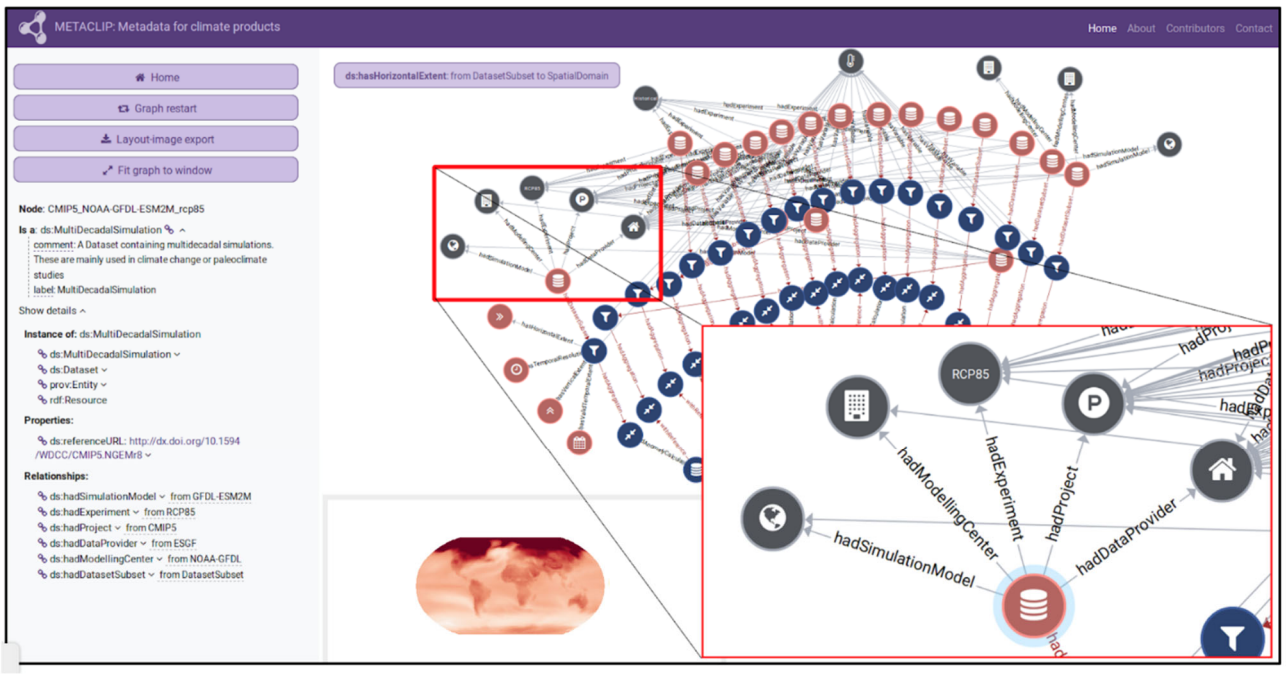

Figure Atlas.57: Screenshot of the METACLIP Interpreter for provenance visualization (metaclip.org), displaying the provenance of a temperature anomaly map downloaded from the Interactive Atlas as a PNG file with attached METACLIP metadata (METACLIP export option). The blow-up shows a specific dataset (CMIP5 RcP8.5) used to produce the map. It shows details about the dataset provenance such as its DOI identifying the source of data, the experiment (RCP 8.5), the modelling centre, GCM information, data provider and associated Project (CMIP5). The interface allows the user to expand the detail of information if needed by clicking in each of the nodes and reading the metadata in the left panel. It is also possible zooming in/out, scrolling and saving a user-defined position of the graph.

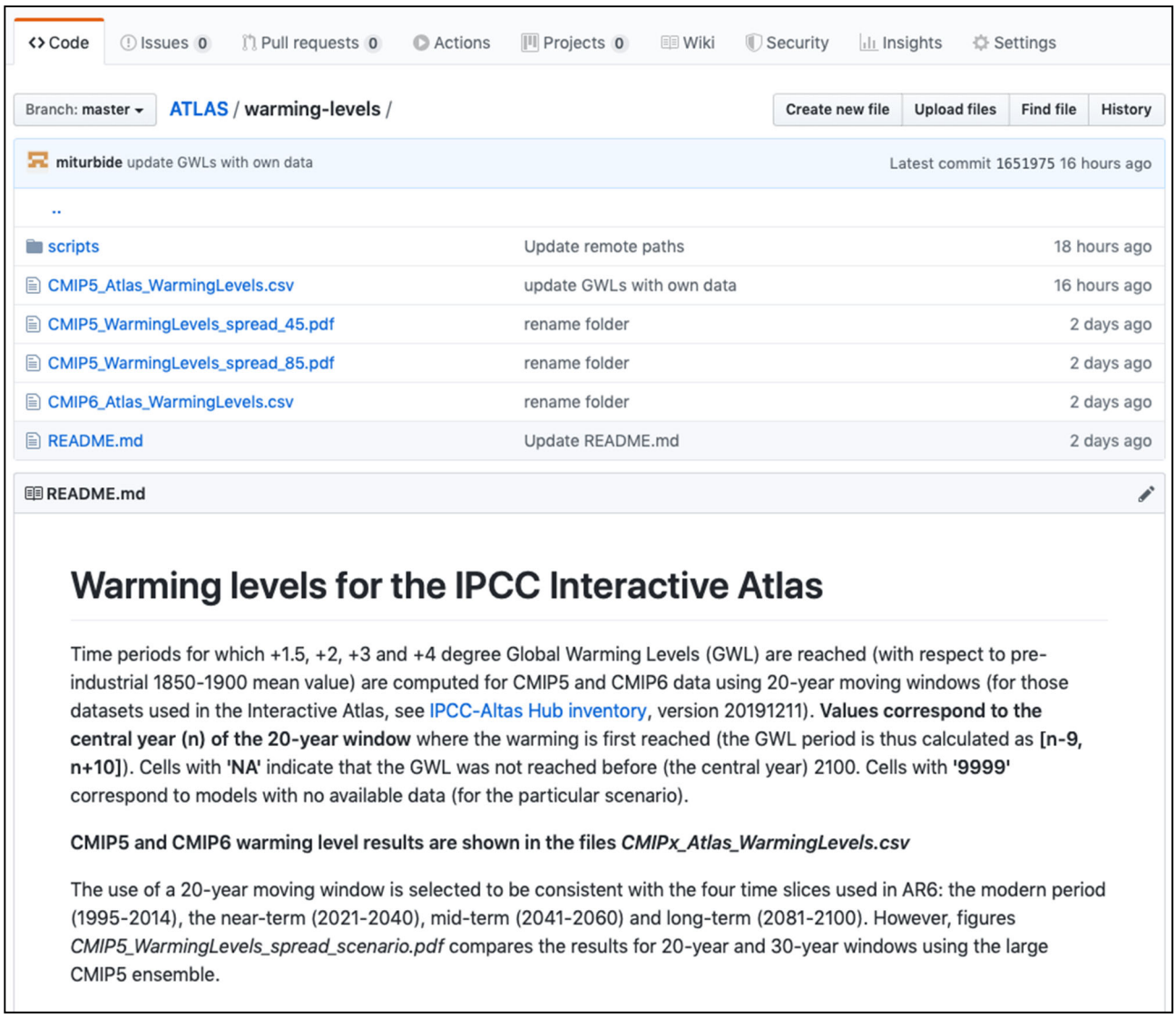

FAQ Atlas.4, Figure 1: Screenshot of the GitHub repository containing the scripts and results of the warming level calculations for CMIP5 and CMIP6 models, together with some sensitivity studies to the effect of the length of the moving window.